

JPL PUBLICATION 78-38

Viking Navigation

W. J. O'Neil, R. P. Rudd, D. L. Farless,
C. E. Hildebrand, R. T. Mitchell,
K. H. Rourke, et al.
Jet Propulsion Laboratory

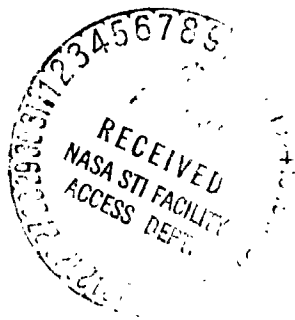
E. A. Euler
Martin Marietta Aerospace

(NASA-CR-162917) VIKING NAVIGATION (Jet
Propulsion Lab.) 322 p HC A14/MF A01
CSCL 22B

N80-21397
TRFO
N80-21403
Unclass
47593

G3/15

November 15, 1979



National Aeronautics and
Space Administration

Jet Propulsion Laboratory
California Institute of Technology
Pasadena, California

JPL PUBLICATION 78-38

Viking Navigation

W. J. O'Neil, R. P. Rudd, D. L. Farless,
C. E. Hildebrand, R. T. Mitchell,
K. H. Rourke, et al.
Jet Propulsion Laboratory

E. A. Euler
Martin Marietta Aerospace

November 15, 1979

National Aeronautics and
Space Administration

Jet Propulsion Laboratory
California Institute of Technology
Pasadena, California

The research described in this publication was carried out by the Jet Propulsion Laboratory, California Institute of Technology, under NASA Contract No NAS7-100

Abstract

NASA soft-landed two Viking spacecraft on Mars in the summer of 1976. These were the free world's first landings on another planet. This report provides a final, comprehensive description of the navigation of the Viking spacecraft throughout their flight from Earth launch to Mars landing. The flight path design, actual inflight control, and postflight reconstruction are discussed in detail. The report is comprised of an introductory chapter followed by five chapters which essentially correspond to the organization of the Viking navigation operations, namely, Trajectory Description, Interplanetary Orbit Determination, Satellite Orbit Determination, Maneuver Analysis, and Lander Flight Path Analysis. To the extent appropriate, each chapter describes the preflight analyses upon which the operational strategies and performance predictions were based. The inflight results are then discussed and compared with the preflight predictions and, finally, the results of any postflight analyses are presented.

Contents

Introduction	1
W. J. O'Neil and R. P. Rudd	
I. Flight Path Design	5
II. Viking 1 Inflight Synopsis	16
III. Viking 2 Inflight Synopsis	20
References	27
Appendix. Definitions of Terminology	28
Figures	
1a. FPAG personnel	3
1b. FPAG functional organization	4
2. Viking flight team functional organization	9
3. SPFPAD operations schedule	11
4. Lander descent	13
5. Accessible area constraints	13
6. Accessible area fixed to orbit	14
7. Inertial landing point	14
8. Orbit plane design	14
9. Viking 1 orbit insertion design	15
10. Viking 1 B-plane delivery requirements	15
11. Timing offset	15
12. Orbital operations plan	16
13. Viking 1 heliocentric trajectory	17
14. Viking 1 launch accuracy	17
15. Viking 1 Earth departure control	17
16. Viking 1 interplanetary delivery	18
17. Viking 1 Mars approach control	19
18. Viking 1 Mars orbit insertion	20
19. Viking 1 actual site acquisitions	20
20. Descent sequence	21
21. Landing accuracy	21
22. Viking 2 heliocentric trajectory	21
23. Viking 2 launch accuracy	22
24. Viking 2 midcourse aimpoints	22

25.	Viking 2 unbiased near-Earth midcourse maneuver	23
26.	Viking 2 Earth departure control	24
27.	Viking 2 midcourse targeted and achieved aimpoints	25
28.	VO 1 and VO 2 ground tracks	26
29.	Viking 2 landing region	26

Trajectory Description 30

D. L. Farless, L. H. Dicken, and R. E. Diehl

I. Launch Phase 30

II. Interplanetary Phase 31

A.	Heliocentric Orbit Description	31
B.	Near-Earth Midcourse Maneuver Effects	33
C.	Solar Pressure Effects	33
D.	Interplanetary Trajectory Data	33

III. Encounter Phase 33

IV. Mars Orbit Phase 37

Tables

1.	Viking 1 launch trajectory mark event list	30
2.	Viking 2 launch trajectory mark event list	31
3.	Orbital data	31
4.	Heliocentric orbit elements	32
5.	Areocentric orbit elements	37
6.	VO-1 Mars orbit elements	38
7.	VO-2 Mars orbit elements	44
8.	Mars orbit trim maneuver execution times	47

Figures

1.	Targeted and achieved injection aimpoints for Viking launches	31
2.	Viking 1 heliocentric trajectory	32
3.	Viking 2 heliocentric trajectory	32
4.	Targeted and achieved midcourse maneuver aimpoints for Viking	33
5.	Viking 1 geocentric range	34
6.	Viking 1 geocentric range rate	34
7.	Viking 1 geocentric declination	34
8.	Viking 1 geocentric right ascension	34
9.	Viking 1 heliocentric range	35
10.	Viking 1 areocentric range	35

11. Viking 2 geocentric range	35
12. Viking 2 geocentric range rate	35
13. Viking 2 geocentric declination	36
14. Viking 2 geocentric right ascension	36
15. Viking 2 heliocentric range	36
16. Viking 2 areocentric range	36

Interplanetary Orbit Determination 48

K. H. Rourke, N. Jerath, C. H. Acton, W. G. Breckenridge, J. K. Campbell,
C. S. Christensen, A. J. Donegan, H. M. Koble, N. A. Mottinger, G. C.
Rinker, and F. B. Winn

I. Introduction	48
II. Mission Description	49
III. Orbit Determination System Fundamentals	49
A. Trajectory Models	50
B. Observation Models	50
C. Radio Data Models	50
D. Optical Data Models	51
E. Filter Models	51
F. Orbit Determination Process	52
G. Critical Orbit Determination Inputs	53
H. Orbit Determination Errors	54
IV. Orbit Determination Software System	54
V. Orbit Determination Strategy	55
A. Radio and Optical Orbit Determination	55
B. Approach Observation Schedules	58
C. Orbit Estimation Strategies	58
VI. Orbit Determination Results	60
A. Launch/Earth Departure Phase	60
B. Cruise Phase	60
VII. Long-Arc Radio Data Processing	62
A. Inflight Processing	62
B. Postflight Processing	64
VIII. Solar Pressure Model Improvement	68

IX. Optical Measurements Processing	73
A. Optical Measurement System	73
B. Optical Observables	73
C. Sequence Data and Pointing Optimization	74
D. Data Flow and Management	74
E. Telemetry Data Processing	74
F. Picture Data Processing	74
G. Optical Observables Generation	75
H. Processing Results	75
X. Approach Orbit Determination Evaluation	75
XI. Inflight Orbit Determination Solution Compilation	79
XII. DSN Station Location Evaluation	80
A. Theoretical Background	81
B. Data Coverage and Calibrations	82
C. Preliminary Solutions	83
D. Final Solutions	83
XIII. Satellite Ephemeris Evaluation	101
A. Wilkins' Angles	101
B. Analysis of Approach Optical Data for Ephemeris Determination	102
C. Satellite Ephemeris from VO-1 and VO-2	104
XIV. Conclusions	106
References	108
Tables	
1. Mission events	49
2. Optical observables	51
3. Orbit determination system error model	54
4. OD software inputs	55
5. OD software outputs	56
6. OD software glossary	56
7. Typical operations sequence	56
8. Mission requirements and radio capability	57
9. Data treatment	60
10. Launch departure solutions	61
11. B-plane summary of Viking 1 postflight long-arc data processing	64

12.	Comparison of solutions for Viking 1 solar pressure parameters	68
13.	Comparison of inflight solutions for Viking 1 and Viking 2 solar pressure parameters	73
14.	Pointing knowledge accuracy	75
15.	Detrended target residuals	76
16.	Orbit estimate deliveries	78
17.	Viking 1 cruise solution summary	84
18.	Viking 1 approach phase solutions (ODP)	85
19.	Viking 1 approach phase solutions (ONP)	88
20.	Viking 2 cruise solution summary	90
21.	Viking 2 approach phase solutions (ODP)	91
22.	Viking 2 approach phase solutions (ONP)	93
23.	Location set 44	95
24.	Summary of Viking 1 and 2 radiometric data sets	95
25.	Summary of charged particle calibration sets	95
26.	Viking 1 uncalibrated corrections to LS44	99
27.	Viking 1 calibrated corrections to LS44	99
28.	Viking 2 uncalibrated corrections to LS44	100
29.	Viking 2 calibrated corrections to LS44	100
30.	Final Viking corrections to LS44	100
31.	Combined Viking 1 and 2 station location solutions	100
32.	Viking nominal Deimos ephemeris	102
33.	Parameter set selection for satellite ephemeris	103
34.	Data strategy selection for satellite ephemeris	103
35.	Effect of degrading a priori uncertainty on satellite ephemeris	103
36.	Optical measurement biases	104
37.	Deimos ephemeris parameter updates	104
38.	Deimos ephemeris update evaluation	104
39.	Deimos ephemeris using Viking approach optical data	105

Figures

1.	Mission events	49
2.	Orbit determination process	52
3.	Orbit determination software interfaces	55
4a.	Mission requirements and radio capability: departure	57
4b.	Mission requirements and radio capability: approach	57
5.	Optical observations	59

6.	Optical observable	59
7.	Optical accuracy	59
8.	Optical observation schedules	59
9.	Viking 1 launch phase solutions	61
10.	Viking 2 launch phase solutions	61
11.	Viking 1 cruise solutions	62
12.	Viking 2 cruise solutions	63
13.	Viking 1 long-arc solutions	63
14.	Viking 2 long-arc solutions	63
15.	Viking 1 long-arc inflight calibrated doppler residuals	65
16.	Viking 1 long-arc postflight calibrated doppler residuals	66
17.	Viking 2 long-arc inflight calibrated doppler residuals	67
18.	Viking 1 long-arc postflight uncalibrated doppler residuals	69
19.	Viking 1 long-arc postflight calibrated doppler residuals, doppler-only fit	70
20.	Viking 1 long-arc postflight uncalibrated range residuals	71
21.	Viking 1 long-arc postflight calibrated range residuals	72
22.	Viking 1 Mars residuals	76
23.	Viking 2 Mars residuals	76
24.	Viking 1 Deimos residuals	76
25.	Viking 2 Deimos residuals	76
26a.	Viking 1 approach solution histories, pre AMC 1: ODP	79
26b.	Viking 1 approach solution histories, pre AMC 1: ONP	79
27a.	Viking 1 approach solution histories, pre AMC 2: ODP	80
27b.	Viking 1 approach solution histories, pre AMC 2: ONP	80
28a.	Viking 1 approach solution histories, pre MOI: ODP	81
28b.	Viking 1 approach solution histories, pre MOI: ONP	81
29a.	Viking 2 approach solution histories, pre AMC: ODP	82
29b.	Viking 2 approach solution histories, pre AMC: ONP	82
30a.	Viking 2 approach solution histories, pre MOI: ODP	83
30b.	Viking 2 approach solution histories, pre MOI: ONP	83
31.	A cylindrical coordinate system for a DSN station	95
32.	Viking 1 uncalibrated doppler residuals	96
33.	Viking 2 uncalibrated doppler residuals	97
34.	Viking 1 calibrated doppler residuals	98
35.	Viking 2 calibrated doppler residuals	99
36.	Final Viking spin axis and longitude corrections to LS44	101

37. Wilkins' angles	101
38. VO-1 postfit Deimos residuals	102
39. VO-1 postfit Deimos residuals; loose a priori	104
40. VO-1 pre-update Deimos residuals	105
41. VO-1 post-update Deimos residuals	105
42. VO-1 post-update Deimos residuals, biases solved for	105
Satellite Orbit Determination	109
C. E. Hildebrand, E. J. Christensen, D. H. Boggs, G. H. Born, B. G. Williams, and Z. Shippony	
I. Introduction	109
II. Overview of Viking Satellite OD Activities	111
A. Support Activities	111
B. Methods	112
III. Initial Orbit Convergence	113
A. The Convergence Problem for Short Data Arcs	113
B. Preflight Simulation Analysis	114
C. Viking 1 and 2 Initial Orbit Convergence	117
IV. Short Arc Orbit Determination	121
A. Preflight Analysis	121
B. Inflight Results	121
C. Late Update Strategies	124
D. Constrained State Estimates During Extended Mission	126
E. PVRA: Efficient Spacecraft State Estimation in Orbit Phase	127
F. Media Effects on OD Accuracy	128
V. Modeling Gravitational Accelerations	132
A. Preflight Analysis	132
B. A Linear Piecewise Batch Estimator	134
C. VO-1 Experience	134
D. VO-2 Experience	136
E. Gravity Estimation in Extended Mission	137
F. Conclusions	141
VI. Viking Lander Position Determination	142
A. Information Content of VL Radio Tracking Data	142
B. Preflight Analysis	143
C. Inflight Results	143

VII. The Mass of Phobos from Viking Flybys	145
A. Introduction	145
B. Encounter Geometry	145
C. Preflight and Real-Time Estimates	145
D. Postflight Estimates	150
E. Concluding Remarks	150

VIII. Conclusions and Recommendations	151
--	-----

References	151
-----------------------------	-----

Tables

1. Areocentric orbital elements of Viking 1	110
2. Areocentric orbital elements of Viking 2	110
3. Post-MOI initial state uncertainties	114
4. Post-MOI convergence worst-direction error	115
5. VO-1 first orbit convergence history	119
6. VO-2 first orbit convergence history	120
7. Trim maneuver description	125
8. Normalized spherical harmonic coefficients for Mars $\times 10^5$	137
9. Areocentric orbital elements of Viking 1 and Viking 2	139
10. VL position and Mars spin axis direction estimates at five days after touchdown	143
11. Phobos encounter parameters	150

Figures

1. Viking orbit phase navigation related events	111
2. Range-rate time history for different values of orbital period	114
3. Worst-direction diagram in phase space	115
4. Viking 1 eccentricity convergence profile	116
5. Viking 2 $\Omega_{p_{01}}$ convergence profile	116
6. Viking 1 semi-major axis convergence profile	117
7. Viking 1 worst-direction convergence profile	117
8. Viking 2 worst-direction convergence profile	118
9. Viking 1 first orbit period estimate evolution	118
10. Viking 1 first orbit $\Omega_{p_{01}}$ estimate evolution	120
11. Viking 2 first orbit period estimate evolution	120

12.	Viking 2 first orbit Ω_{pos} estimate evolution	121
13.	Viking 1 orbit knowledge accuracy	122
14.	Viking 2 orbit knowledge accuracy	122
15.	Viking 1 and 2 two-way range residuals using DF84	123
16.	Preflight and actual Viking 1 periapse position prediction accuracy	124
17.	Late update orbit period errors	125
18.	Late update plane-of-sky node errors	126
19.	Effect of a priori constraints on orbital period uncertainty	127
20.	Effect of a priori constraints on time periapsis passage	128
21.	Phase change for VO-1 DSS 63 10/15/77 pass	129
22.	VO-2 first orbit worst-case media-induced period error	130
23.	VO-2 first orbit worst-case media-induced Ω_{pos} error	131
24.	Errors in predicted times of periapsis (t_p) incurred using a 6X6 gravity field estimated using three revolutions ($P_{116} - P_{119}$) of partially calibrated S/X data	131
25.	Errors in predicted Ω_{pos} incurred using a 6X6 gravity field estimated using three revolutions ($P_{116} - P_{119}$) of partially calibrated S/X data	131
26.	Schematic representation of the change in period (ΔP) through periapsis	132
27.	Definition of the graphic node β	133
28.	RSS position error before and after gravity sensing over two revolutions of Viking 1. The figure represents a typical case from a preflight covariance analysis where errors in gravity, station locations, ephemeris and mass of Mars were considered	133
29.	Change in period as a function of graphic node at periapsis based on a 6X6 VO-1 combined field determined over $P_2 - P_{46}$	135
30.	Difference in the change in period (VO-1 6X6 combined field - nominal) as a function of graphic node at periapsis	135
31.	Uncertainty in the change in period as a function of graphic node at periapsis based on the nominal field and a VO-1 6X6 field determined over $P_3 - P_5$	135
32.	Uncertainty in the change in period as a function of graphic node at periapsis based on the nominal field and a 6X6 VO-1 combined field determined over $P_2 - P_{46}$	136
33.	Change in period as a function of periapsis passage based on nominal and VO-1 determined gravity fields and observations for the first 20 days	136
34.	Errors in predicted times of periapsis t_p and predicted changes in period ΔP incurred using the nominal gravity field on VO-2 (prediction started as P_7)	137
35.	Errors in predicted times of periapsis t_p and predicted changes in period ΔP incurred using the 6X6 VO-1 and VO-2 combined field on VO-2 (prediction started at P_7)	137

36. Uncertainty in the change in period as a function of graphic node at periapsis based on the nominal field and the 6X6 VO-1 and VO-2 combined field	138
37. Comparison of ΔP (β) between various gravity fields and the nominal gravity field evaluated for the first VO-1 synchronous phase	138
38. Timing uncertainty mapped for $H_p = 300$ km, VO-1, using COMBIX/AVE covariance	140
39. Error in timing predictions based on observed errors in delta period (Revs. 264-273)	141
40. Comparison of ΔP errors	141
41. Viking lander tracking geometry	142
42. Viking lander doppler signatures	143
43. Standard deviations of Viking lander position and Mars spin axis direction from radio tracking (pre-flight)	144
44. VL radio tracking coverage for five days following touchdown	145
45. Standard deviations of Viking lander position and Mars spin axis direction from radio tracking (in-flight)	146
46. Phobos encounters	147
47. VO-1 and Phobos encounter geometry	147
48. Orbit period change vs B-plane encounter location	148
49. Range-rate change vs B-plane encounter location	149

Maneuver Analysis 153
R. T. Mitchell, D. L. Farless, J. K. Miller, G. R. Hintz, M. I. Adams, N. P. Dwivedi, and D. L. Gray

I. Interplanetary Maneuvers	153
A. Choice of Maneuver Dates	153
B. Launch	154
C. Emergency Early Maneuver Strategy	154
D. Summary of Maneuvers Performed	156
E. Maneuver Mechanization	160
II. Orbit Insertion	161
A. Viking 1	162
B. Viking 2	167
III. Orbit Trim Maneuvers	169
A. Prelanding Maneuver Strategies	170
B. Maneuver Mechanization	182
C. Maneuver Constraints	183
D. Trim Maneuver Software	184

E. Viking 1 Trim Maneuvers	184
F. Viking 2 Trim Maneuvers	198

References	211
-----------------------------	------------

Tables

1. Prelaunch plan for midcourse maneuver locations	154
2. Targeted and achieved encounter conditions	156
3. Maneuver data	157
4. Viking 1 MOI command update site acquisition tradeoffs	166
5. Viking 1 MOI command update ΔV budget	166
6. Final MOI parameters and related data for Vikings 1 and 2	167
7. Trajectory data – Viking 1 insertion	167
8. Viking 2 post-MOI orbital parameters	169
9. Viking 2 orbit insertion parameters	169
10. Inflight a priori execution errors (99%)	183
11. Design quantities: velocity increment and ignition time	185
12. Design quantities: turns	185
13. Trajectory data	186
14. Viking 1 landing site targeting adjustments	191
15. Candidate Viking 2 landing sites	199
16. Viking 2 landing site adjustments	203
17. MOT-3 and MOT-4 trajectory summary for Viking 2	205

Figures

1. Viking 1 injection dispersions	155
2. Viking 2 injection dispersions	155
3. Viking 1 EEM energy envelopes	155
4. Viking 1 midcourse aimpoints	157
5. Viking 1 midcourse aimpoints, detail	157
6. Viking 2 midcourse aimpoints	158
7. Viking 1 first midcourse Earth/Sun cone and clock angles during turns	158
8. Viking 1 midcourse 1 dispersions	159
9. Viking 2 unbiased first maneuver	160
10. Viking 2 biased first maneuver	161
11. Viking 2 first maneuver velocity in critical plane coordinates	162
12. Examples of B-plane turns quantization	162
13. Viking 1 orbit geometry	163

14. Viking 2 MOI geometry	163
15. Viking 1 insertion timing strategy	163
16. Viking 1 approach midcourse B-plane delivery	163
17. ΔV trades for h_p correction at MOI/trim, $\Delta\theta = 0$ deg	164
18. ΔV trades for h_p correction at MOI/trim, $\Delta\theta = 2$ deg	164
19. ΔV trades for h_p correction at MOI/trim, $\Delta\theta = -2$ deg	164
20. Viking 1 post-MOI period dispersion	165
21. Roll-yaw turn variations for Viking 1 MOI	165
22. Ignition time sensitivity to h_p error	165
23. Effect on post-MOI orbit dispersions of updating MOI parameters based on post AMC-2 orbit knowledge	166
24. Viking 1 Earth/Sun traces for MOI	167
25. Viking 2 nominal post-insertion orbit timing	168
26. Viking 2 approach control and knowledge	168
27. Viking 2 approach trajectory history	168
28. Viking 2 period change vs ignition time error	169
29. ΔV cost for correcting periapsis altitude errors at MOI vs in orbit for Viking 2	169
30. Viking 2 Earth/Sun traces for MOI	170
31. Viking 2 MOI burn tracking data residuals	170
32. Satellite orbit control for lander separation	171
33. Timing definitions	171
34. Separation orbit time phasing	172
35. VL/VO timing relationships	172
36. Reconnaissance parameters	172
37. Definition of tilt angle ϕ_{tilt}	173
38. Flight plane velocity space	174
39. Period gradients for Viking 1	175
40. Periapsis altitude gradients for Viking 1	175
41. Right ascension of ascending node and inclination gradients for Viking 1	175
42. Argument of periapsis gradients for Viking 1	175
43. Time to periapsis gradients for Viking 1	176
44. LATPER gradients for Viking 1	176
45. Sun elevation angle gradients for Viking 1	176
46. Period gradients for Viking 2	176
47. Periapsis altitude gradients for Viking 2	177

48.	Right ascension of node and inclination gradients for Viking 2	177
49.	Argument of periapsis gradients for Viking 2	177
50.	Time to periapsis gradients for Viking 2	177
51.	LATPER gradients for Viking 2	178
52.	Sun elevation angle gradients for Viking 2	178
53.	Partial of period and periapsis altitude with respect to velocity for a sunline maneuver on Viking 1	178
54.	Partial of LATPER with respect to velocity for a sunline maneuver on Viking 1	178
55.	Partial of period and periapsis altitude with respect to velocity for a sunline maneuver on Viking 2	179
56.	Partial of LATPER with respect to velocity for a sunline maneuver on Viking 2	179
57.	Viking 1 timing strategy	179
58.	Latitude correction trim	180
59.	Viking 2 timing strategy and reconnaissance opportunities for EMA < 9 deg	181
60.	Definition of ellipse orientation angle ψ	181
61.	Definition of vertical impact point	181
62.	Site acquisition geometry for Viking 2	182
63.	Viking maneuver pointing constraints	183
64.	MOT site acquisition strategies	185
65.	Site acquisition for July 4, 1976, landing	187
66.	Viking orbit geometry	188
67.	Landing site rendezvous	188
68.	A-1 site acquisition probability	189
69.	MOT-3 velocity cost analysis for Viking 1, $\Delta p = -1$ min	189
70.	VL accessible area and landing dispersion ellipse with MOT-3	190
71.	A1NW acquisition with MOT-4, $LATPER_{TD} = 23^\circ N$	190
72.	A1NW acquisition without MOT-4	190
73.	P20 tilt and VL accessible area	191
74.	MOT PER update for Viking 1	192
75.	Site acquisition for Viking 1	192
76.	MOT-6 period control vs true anomaly	193
77.	MOT-6 ΔV -cost vs true anomaly	193
78.	Site acquisition strategy following MOT-5	193
79.	VL parameters R30 – R35	194
80.	Station-keeping strategy for Viking 1	194
81.	SKT-2 ΔV geometry for Viking 1	195

82.	SKT-2 accuracy analysis	195
83.	VL-2/VO-1 relay geometry	195
84.	Viking 1 walk analysis	195
85.	VO-1 walk timeline	196
86.	MOT-7 geometry for Viking 1	196
87.	MOT-7 turns doppler for Viking 1	197
88.	MOT-8/9 geometry for Viking 1	198
89.	Viking 1 timeline	198
90.	VL-2/VO-1 offset	198
91.	Viking 2 site certification/acquisition	199
92.	Viking 2 orbit timing at MOT-1	200
93.	Orbit plane for Viking 2	201
94.	MOT-1 ΔV geometry for Viking 2	202
95.	Viking 2 orbit timing at MOT-2	202
96.	Maneuver update analysis for Viking 2 MOT-2	203
97.	MOT-2 geometry for Viking 2	203
98.	Viking 2 site acquisition	204
99.	MOT-3 ΔV cost analysis for a sunline maneuver on Viking 2	204
100.	MOT-3 h_p and LATPER changes for a sunline maneuver on Viking 2	204
101.	MOT-4 ΔV cost analysis for a sunline maneuver on Viking 2	204
102.	MOT-4 h_p and LATPER changes for a sunline maneuver on Viking 2	205
103.	MOT-3/MOT-4 geometries for Viking 2	206
104.	Preliminary MOT-3/MOT-4 VL accessible area for Viking 2	207
105.	Post-MOT-4 VL accessible area for Viking 2	208
106.	Sun direction in velocity space	209
107.	Viking 2 plane geometry (MOT-1)	210
108.	VL-2/VO-2 relay sensitivity to timing offset	210
109.	Viking 2 plane change cost	211
110.	Viking 2 plane change geometry	211

Lander Flight Path Analysis 212
E.A. Euler, G. L. Adams, and F. W. Hopper

I. Introduction	212
A. LFPAT Software	212
B. Operational Activities	213

II. Preflight VL Capability Estimate	216
A. Maximum Accessible Area	217
B. Targeting Region and Preferred Targeting Region	220
C. Landing Accuracy	221
D. Additional Design Considerations	222
III. Preliminary VL Trajectory Design History and Validation	224
A. Preliminary VL-1 Trajectory Design History and Validation	224
B. Preliminary VL-2 Trajectory Design History and Validation	227
IV. Final VL Trajectory Design and Descent Parameters	228
A. Nominal VL Descent Trajectory Design	228
B. Descent Flight Load Parameters	229
C. Descent Trajectory Dispersions	234
D. Descent Relay Performance	234
V. Reconstructed VL Flight Path Summary	234
VI. Entry Trajectory Reconstruction	241
A. Description of Process	241
B. Data	252
C. Entry Trajectory Reconstruction Results	252
D. Vehicle Subsystem Performance	270
VII. Environmental Estimates	274
A. Reconstructed Atmosphere/Winds	274
B. Terrain Profiles	279
VIII. Postland Relay Link	286
A. Procedures, Requirements, and ICL Definition	286
B. Actual VL Relay Link Performance History	286
References	299
Tables	
1. Preseparation timeline	214
2. Preflight system and mission constraints	216
3. Summary of descent trajectory designs for candidate VL-1 LS's	226
4. VL descent trajectory design summary	229
5. Trajectory-related descent guidance parameters	230
6. Predicted VL entry and touchdown dispersions	235
7. VL-1 descent constraints checklist	236

8.	VL-2 descent constraints checklist	236
9.	Descent reconstruction summary	239
10.	Actual vs predict VL SOE	240
11.	VL entry flight path angle and touchdown errors resulting from each deorbit control error	241
12.	A priori entry state and covariance	253
13.	Instrument bias and scale factors	254
14.	Model parameters and uncertainties	254
15.	ODP landed position fixes, 1σ uncertainties	254
16.	Viking trajectory/atmosphere reconstruction summary: Viking 1 reconstruction	255
17.	Viking trajectory/atmosphere reconstruction summary: Viking 2 reconstruction	256
18.	Viking trajectory/atmosphere reconstruction summary: VL-1, 1σ uncertainties in estimates	257
19.	Viking trajectory/atmosphere reconstruction summary: VL-2, 1σ uncertainties in estimates	257
20.	Initial measurement residuals	267
21.	Measurement residuals, VL-1 and VL-2, smoothed trajectories	269

Figures

1.	Descent validation process	214
2.	VL-1 altitude vs time during entry phase	215
3.	VL-2 altitude vs time during entry phase	215
4.	99% design wind magnitude profile	217
5.	Sensitivity of q_{max} to entry errors	217
6.	Sensitivity of stagnation point heating rate to entry errors	218
7.	Sensitivity of total stagnation heat load to entry errors	218
8.	Parachute phase dynamic pressure and Mach No. vs altitude	218
9.	Descent trajectory geometry	219
10.	Maximum accessible area	220
11.	Dispersions (3σ) over targeting region	220
12.	Targeting regions	221
13.	SMA of the 0.99 landing dispersion ellipse over the targeting region	221
14.	Components of touchdown dispersion ellipse SMA and SMB over targeting region	221
15.	VL terrain height capability	223
16.	Terminal descent contours	224

17.	VL-1 landing site and targeting region history	225
18.	Final VL-1 targeting region and landing site	225
19.	Targeting region and landing site	227
20.	Nominal VL descent trajectory	228
21.	VO-1/VL-1 relative geometry at deorbit	232
22.	VO-2/VL-2 relative geometry at deorbit	233
23.	Predicted VL-1 descent relay link performance	237
24.	Predicted VL-2 descent relay link performance	238
25.	VL-1 landing site error	240
26.	VL-2 landing site error	240
27.	Reconstructed and observed VL-1 descent relay performance	242
28.	Reconstructed and observed VL-2 descent relay performance	247
29.	VL-1 nominal terrain height profile	254
30.	VL-2 nominal terrain height profile	254
31.	VL-1 altitude above reference areoid vs time	258
32.	VL-1 altitude above reference areoid vs range	258
33.	VL-1 range from entry vs time	258
34.	VL-1 altitude above reference areoid vs range	258
35.	VL-1 relative velocity vs time	259
36.	VL-1 relative flight path angle vs time	259
37.	VL-1 relative azimuth vs time	259
38.	VL-1 aerocentric latitude vs time	259
39.	VL-1 longitude vs time	260
40.	VL-1 ground trace near touchdown	260
41.	VL-1 terminal descent performance	260
42.	VL-1 planet relative sigma vs time	260
43.	VL-1 planet relative sigma vs time (detail)	261
44.	VL-1 planet relative beta vs time	261
45.	VL-1 planet relative alpha vs time	261
46.	VL-1 Euler PSI vs time	262
47.	VL-1 Euler theta vs time	263
48.	VL-2 altitude above reference areoid vs time	263
49.	VL-2 range from entry vs time	263
50.	VL-2 altitude above reference areoid vs range	263
51.	VL-2 altitude above reference areoid vs range	264
52.	VL-2 relative velocity vs time	264
53.	VL-2 relative flight path angle vs time	264

54.	VL-2 relative azimuth vs time	264
55.	VL-2 latitude vs time	265
56.	VL-2 longitude vs time	265
57.	VL-2 latitude vs longitude	265
58.	VL-2 terminal descent performance	265
59.	VL-2 planet relative sigma vs time	266
60.	VL-2 planet relative beta vs time	266
61.	VL-2 planet relative alpha vs time	266
62.	VL-2 Euler PSI vs time	266
63.	VL-2 Euler theta vs time	267
64.	VL-2 Euler PSI vs time (detail)	268
65.	VL-2 Euler theta vs time	269
66.	VL-1 dynamic pressure vs time	271
67.	VL-1 Mach No. vs time	271
68.	VL-2 dynamic pressure vs time	271
69.	VL-2 Mach No. vs time	271
70.	Planet relative angle of attack vs Mach No.	272
71.	Atmosphere estimation loops	273
72.	VL-1 and VL-2 wind estimation uncertainties	273
73.	VL-1 ambient pressure (< .1 mb) vs altitude	275
74.	VL-1 ambient pressure (> .1 mb) vs altitude	276
75.	VL-1 density (< 10 ⁻⁷ gm/cc) vs altitude	277
76.	VL-1 density (> 10 ⁻⁷ gm/cc) vs altitude	278
77.	VL-1 altitude above reference aeroid vs temperature	279
78.	VL-2 ambient pressure (< .1 mb) vs altitude	280
79.	VL-2 ambient pressure (> .1 mb) vs altitude	281
80.	VL-2 density (< 10 ⁻⁷ gm/cc) vs altitude	282
81.	VL-2 density (> 10 ⁻⁷ gm/cc) vs altitude	283
82.	VL-2 altitude above reference areoid vs temperature	284
83.	Atmosphere estimation uncertainties (10)	284
84.	VL-1 altitude above reference areoid vs wind magnitude	284
85.	VL-1 altitude above reference areoid vs wind azimuth	285
86.	VL-2 altitude above reference surface vs wind magnitude	285
87.	VL-2 altitude above reference surface vs wind azimuth	285
88.	VL-1 terrain height profile	285
89.	VL-2 terrain height profile	285

90.	VL-1 transmission start times	287
91.	VL-2 transmission start times	287
92.	VL-1/VO-1 relay link performance (sol 9/ICL)	288
93.	VL-1/VO-1 1-W mode relay link performance (sol 2)	289
94.	VL-1/VL-1 relay link performance (sol 26)	290
95.	VL-1/VO-1 10-W relay link performance (sol 42)	291
96.	VL-1 antenna pattern traces	292
97.	VO-1 antenna pattern traces	293
98.	VL-2/VO-2 relay link performance (sol 5/ICL)	294
99.	VL-2 antenna pattern traces for VO-2 and VO-1 relay links	295
100.	VO antenna pattern traces for VL-2/VO-2 and VL-2/VO-1 relay links	296
101.	VL-2/VO-2 relay link performance (sol 20)	297
102.	VL-2/VO-1 relay link performance (sol 45)	298

Introduction

W. J. O'Neil and R. P. Rudd

The free world's first landing on another planet was accomplished by the Viking 1 Lander when it flawlessly soft-landed on the Martian plain Chryse Planitia at 04:53 PDT, July 20, 1976. Less than two months later, the Viking 2 Lander performed an equally magnificent landing on the Martian plain Utopia Planitia at 15:37 PDT, September 3. It is particularly significant that the very first attempt at such an extraordinary feat was completely successful. Viking 1 landed within 30 km of its target more than 300 million km from Earth. Viking 2 landed within 10 km of its target. Both landers have transmitted a tremendous amount of high-quality scientific data to Earth via relay links with their parent vehicles, Viking Orbiter 1 and Orbiter 2. Both Viking spacecraft consisted of a Lander attached to an Orbiter. The Orbiter was designed to carry the Lander into Mars orbit, observe candidate landing sites with television and infrared (IR) instruments, deliver the Lander to the required position and velocity to begin its descent, and to subsequently relay data from the Lander to Earth during descent and throughout the Lander's 90-day surface mission. By "station-keeping" the Orbiter in a near Mars-synchronous orbit (24.6-h period), the Orbiter flew over the lander once each Martian day maintaining a 30-60 minute communication link during which it received and recorded Lander data at 16 kbps. Between the daily links the data was played back to Earth at 8 kbps. In addition to relaying the Lander data, both Orbiters also

transmitted tens of thousands of television pictures and IR observations of Mars obtained by the Orbiters' own science instruments. Comprehensive discussions of the science data obtained by the Landers and the Orbiters are presented in Ref. 1.

This publication presents a final, comprehensive report on the design, control, and reconstruction of the flight paths of all four Viking vehicles. The initial work on the flight path including the specification of requirements on the flight hardware was done by the Viking Navigation Working Group (NWG) from 1970 to 1973. In 1973 the Viking Flight Path Analysis Group (FPAG) absorbed the functions and most of the membership of the NWG. The FPAG continued the flight path design, developed the navigation strategies, procedures, and operational software and, ultimately, performed the inflight navigation. Viking navigation included the precise determination of the spacecraft trajectories (classically referred to as orbit determination), prediction of the trajectories, design of the propulsive maneuvers required to effect the necessary trajectory changes, and calculation of the Lander descent guidance parameters.

The FPAG was a multi-agency team led by the Jet Propulsion Laboratory (JPL) with members from JPL, Langley

Research Center, Martin Marietta Aerospace Co., General Electric Co., and Analytical Mechanics Associates, Inc. Figures 1a and 1b present the FPAG as it existed during the primary missions. Figure 1a lists the membership of each team and gives the affiliation of each member in recognition of the contribution of his organization. One of the most significant factors contributing to the totally cohesive inflight operation of the FPAG was that excellent working relationships were developed over the many years the FPAG worked as a team in preparing for flight. During the flight all members were co-located and functioned as a unit without regard to company affiliation.

Figure 1b identifies the functions of each FPAG team. The Interplanetary Orbit Determination Team (IPODT) was responsible for trajectory determination and prediction to the point of engine ignition for Mars Orbit Insertion (MOI). The Satellite Orbit Determination Team (SATODT) was responsible for these functions after MOI. The SATODT was also responsible for determining the landed location of each Lander based on radio tracking of the Lander. Radiometric tracking data (two-way doppler and range) provided by the JPL Deep Space Network (DSN) was the principal data type used in the orbit determination process. The Tracking Data Conditioning Team (TDCT) was responsible for editing and calibrating the data for use in the JPL Orbit Determination Program (ODP). The ODP was the primary orbit determination tool. All the FPAG software operated in the Univac 1108 computers at JPL. During the Mars approach phases, optical tracking data were also extensively used in the OD process. The optical data were obtained by imaging either Mars or its natural satellite Deimos against the star background with the Orbiter television system.

The Orbiter Maneuver and Trajectory Team (OMATT) was responsible for developing the maneuver strategies and designing each individual propulsive maneuver required to deliver the Viking Spacecraft to the proper position and velocity for initiating the Lander descent. The orbit defined by this position and velocity was known as the "separation orbit" -- the key navigation interface between the Orbiter and the Lander. Specification of the separation orbit was a joint responsibility of the Lander Flight Path Analysis Team (LFPAT) and the OMATT. The strategy for achieving the separation orbit was complicated by the necessity to observe a variety of candidate landing sites under stringent observation conditions prior to the Project commitment to land. The OMATT was also responsible for the postlanding strategies and individual maneuvers required to station-keep the Orbiter with respect to the Lander to maintain adequate relay geometry and, alternatively, to desynchronize the Orbiter, causing it to "walk" around the planet in order to obtain global science observations. Unlike its predecessor, Mariner 9, the Viking

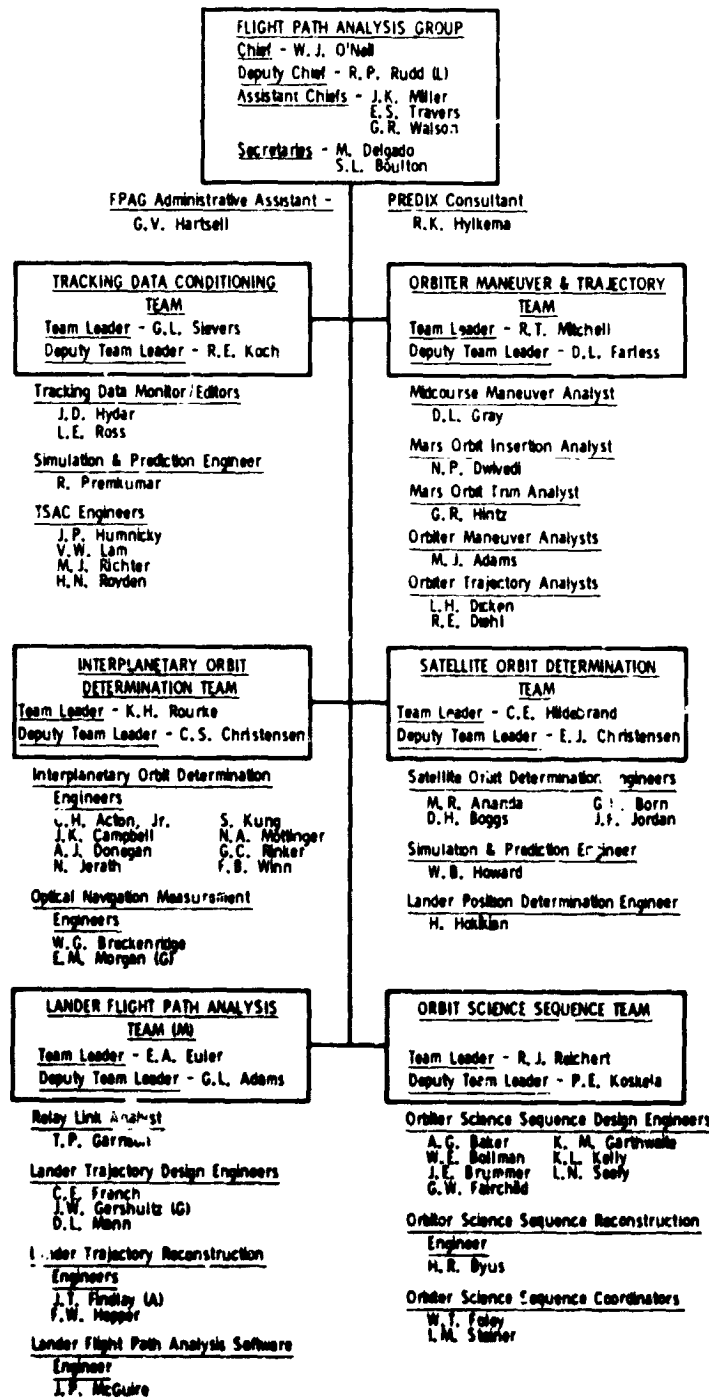
Project routinely utilized attitude maneuvers of the spacecraft to overcome the physical limitations of the Orbiter scan platform in order to point the science instruments in any direction and/or align an instrument raster in a preferred way around its boresight. The design of these "non-propulsive" maneuvers was a joint responsibility of the OMATT and the Orbiter Science Sequence Team (OSST). Finally, the OMATT also generated all Viking Spacecraft/Orbiter trajectory data required by the Project.

The principal maneuver tools of the OMATT were the Midcourse Maneuver Operations Program (MMOP), the Mars Orbit Insertion Operations Program (MOIOP), and the Mars Orbit Trim Operations Program (MOTOP). Each program had a design and analysis capability including Monte Carlo simulations with appropriate approximations for predicting trajectory control accuracy and propellant expenditure statistics. Each program also had a single maneuver, high-precision targeting capability. The JPL *n*-body, double-precision trajectory program, DPTRAJ, was the principal trajectory tool and was the Project standard for flight path computations except for the atmospheric phase of the Lander descent.

The Lander Flight Path Analysis Team (LFPAT) was responsible for the design and control of the Lander flight path from separation to touchdown. This involved the precision targeting of the Lander's deorbit maneuver, generation of the attitude to be commanded at key points along the trajectory, and specification of timed backup commands for critical events to be sensed onboard. All the Lander descent commands were stored in the Lander's Guidance, Control and Sequencing Computer (GCSC) days before separation, S, with a routine update performed at S-39 hours and, as required, updates at S-9.5 and S-3.5 hours. Following separation the descent was completely autonomous -- no command could be received by the Lander until it was on the Mars surface. Basically, the Lander attitude commands were 3×3 transformation matrices relating the desired attitude to the Lander's attitude at the instant of separation. Attitude changes were specified for the deorbit maneuver burn(s), beginning of descent coast, mid-coast, pre-entry, and entry. Attitude control was maintained with an RCS hot gas system until 0.05 g was sensed. After 0.05 g, aerodynamic stability maintained pitch and yaw control; an RCS was required for roll control all the way to touchdown. It was crucially important to maintain the proper angle of attack with the RCS to the 0.05 g point. This was accomplished by initiating a programmed pitch maneuver in concert with the pre-entry attitude command.

The LFPAT targeted the deorbit maneuver and generated the attitude command parameters using the Lander Targeting Operations Program (LTOP). The Lander Trajectory Simula-

ORIGIN...
OF POOR QUALITY



Affiliations: Lander Flight Path Analysis Team personnel at Martin Marietta (M)
 except as noted. All other personnel JPL or JPL contractors
 except as noted.

L - Langley Research Center

G - General Electric Co.

A - Analytical Mechanics Associates, Inc.

Fig. 1a. FPAG personnel

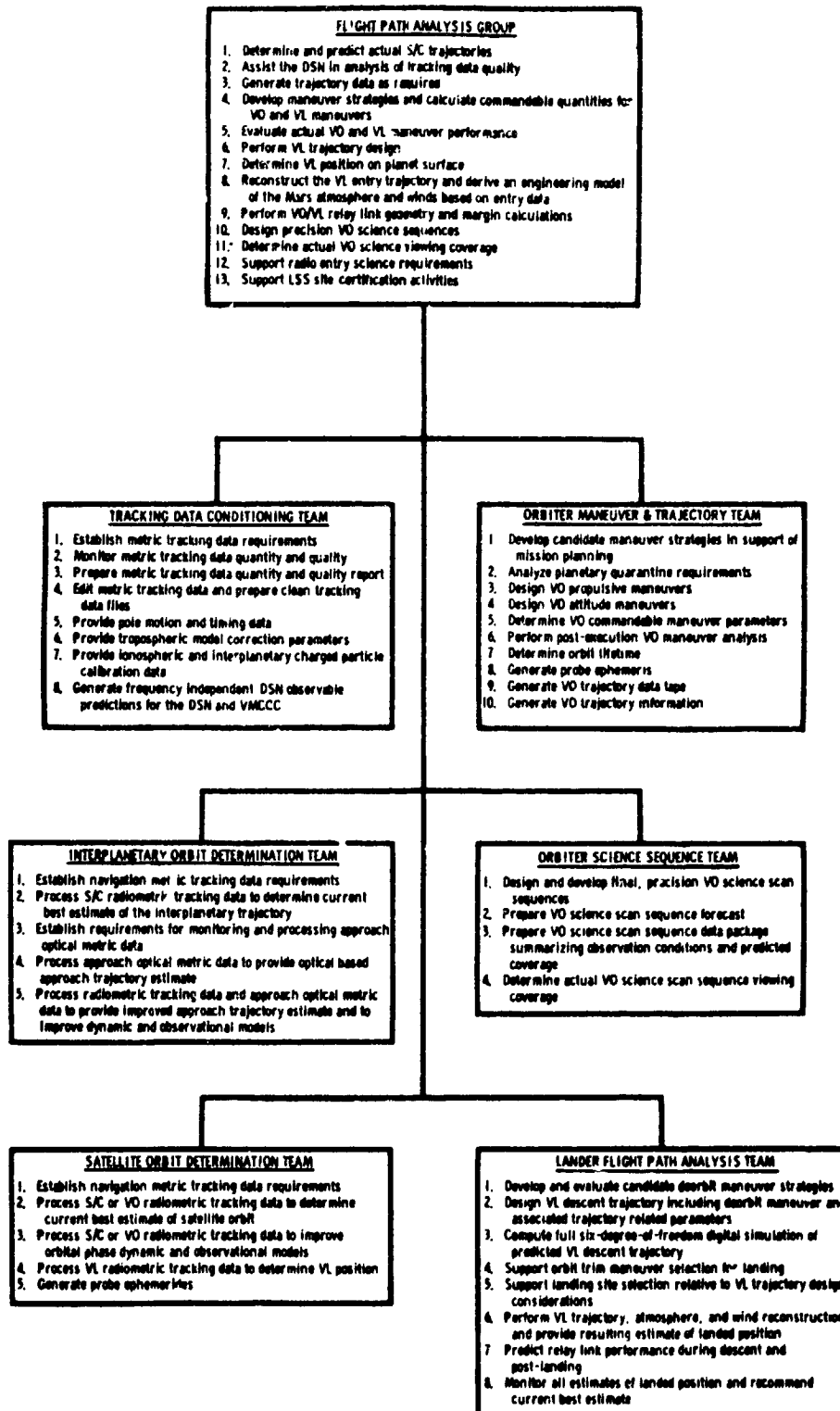


Fig. 1b. FPAG functional organization

tion (LATS) program was the Project standard for computation of the Lander's descent through the Mars atmosphere. LATS was a six-degree-of-freedom, high-fidelity simulation including the Lander's attitude control system response characteristics. The LFPAT used LATS to verify the descent guidance parameters generated by LTOP. These parameters were independently checked to the 0.05 g point by OMATT using DPTRAJ and auxiliary software. External to FPAG, the Lander Support Office (LSO) at Martin Marietta Aerospace in Denver performed a complete simulation of the descent based on the GCSC command load using the Viking Control and Simulation Facility (VCSF). The VCSF contained a hybrid analog-digital facility utilizing bit-by-bit simulation.

The LFPAT was also responsible for reconstructing the Lander trajectory from separation to touchdown using telemetered onboard measurements from the IRU and pressure and temperature probes in conjunction with best estimates of the separation state vector and the landed location based on radio tracking data. The PREPR (Preprocessor for Lander Trajectory and Atmosphere Reconstruction) Program was used to smooth the telemetered data and compensate the IRU data for cg offset affects. It was also used to fill data gaps with simulated data from LATS (subsequent processing required continuous data). The Lander Trajectory and Atmosphere Reconstruction Program (LTARP) was then used to estimate the trajectory based on the "sensed" data file prepared by PREPR and the estimates of the separation state and landed location provided by the Satellite Orbit Determination Team.

Finally, the LFPAT was responsible for predicting the performance of the Lander-to-Orbiter relay links. The Postland Relay Link Program (RLINK) was the primary tool for this. RLINK solved the geometrical problem of determining the path of the Lander-to-Orbiter line-of-sight through the antenna gain patterns of both vehicles based on the input trajectory of the Orbiter and the input attitudes of both vehicles. The resulting predictions of link margin (in dB) vs time were used to establish when to turn the Lander transmitter and Orbiter receiver on and off.

The foregoing has merely identified the primary functions of the FPAG teams. In subsequent chapters of this report, each team reports in full detail its inflight and postflight activities, including all pertinent numerical results. (The only exception is the Orbiter Science Sequence Team; its activities are reported in Ref. 2.) Each chapter is essentially self-contained and the sequential order of the chapters is arbitrary. Consequently, the reader may direct his immediate attention to the chapter(s) of his primary interest.

Figure 2, which was extracted from Ref. 3, presents a functional description of the total Viking Flight Team (VFT)

organization. The figure is included here to show the relationships between the FPAG and the other elements of the VFT. The total membership of the VFT exceeded 800 people during the primary mission.

The FPAG was instrumental in developing an operational scheduling format that resulted in working schedules providing considerable detail (event times resolution to 10 min) yet remarkable clarity for tens of days of the mission at a glance. An example schedule in its actual working form is shown in Fig. 3. These schedules were unique in providing for immediate reconciliation of trajectory events (e.g., time of perapsis), command windows, and personnel schedules (particularly metabolic considerations).

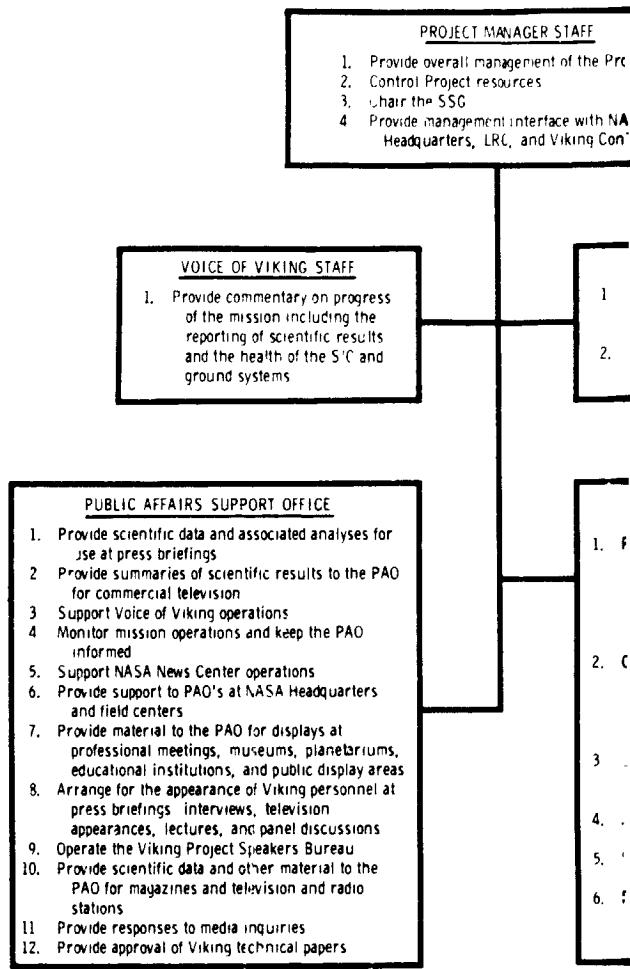
The remainder of this introduction is devoted to an overview of the Viking flight path design followed by synopsis of the inflight navigation activities on both Viking missions from launch to landing.

Please note that a complete list of acronym definitions is given in an appendix to this *Introduction*. Most readers will find it necessary to refer to this list for terminology used throughout the remainder of this report.

I. Flight Path Design

As stated earlier, each Viking spacecraft consisted of a Lander attached to an Orbiter. The Orbiter was designed to carry the Lander into Mars orbit and perform a series of orbit trim maneuvers to deliver the Lander into the separation orbit. The requirements for site observations pre-landing and daily post-landing Lander to Orbiter relay radio transmissions dictated the design of a Mars synchronous separation orbit with a periapsis altitude of 1500 km. The Mars synchronous orbital period is 24.6 h. The period control accuracy requirement was ± 4 min to ensure adequate relay communications geometry for at least five (Mars) days after landing without any reliance on Lander transmitter or Orbiter receiver timing adjustment commands from earth. The tolerance on periapsis altitude was -50 km, +150 km. The lower limit was based on relay considerations; the upper limit on constraining landing dispersions.

The Lander was designed to perform a deorbit maneuver shortly after separation from the Orbiter while in the separation orbit to effect its descent and atmospheric entry. The relationship between the separation orbit and the descent trajectory is illustrated in Fig. 4. During descent the Lander's electrical power was supplied by batteries which were charged by the Orbiter prior to separation. Battery capacity constrained the maximum allowable descent coast time (from



FOLDOUT FRAME

1

FOLDOUT FRAME

2

PRECEDING PAGE BLANK NOT FILMED

6 AND 7

PROJECT MANAGER STAFF
 Provide overall management of the Project
 Control Project resources
 Chair the SSG
 Provide management interface with NASA
 Headquarters, LRC, and Viking Contractors

PROJECT MANAGER OFFICE
 1. Provide overall management of the Project
 2. Control Project resources
 3. Provide independent assessment of major mission decisions
 4. Provide task leadership for technical problem solving as required
 5. Chair the SSG
 6. Provide PAC support including commentary on mission progress

SENIOR STAFF
 1. Provide recommendations needed in making major mission decisions
 2. Support the control of VFT resources

MISSION DIRECTORATE OFFICE
 1. Provide overall direction of the mission
 2. Review and approve Mission Profiles, SOE's and commands
 3. Assure the resolution of operational problems involving two or more directorates
 4. Provide administrative support
 5. Provide overall direction, coordination and integration of any VFT test and training activities
 6. Operate and maintain the VPSS in support of any VFT test and training
 7. Provide GDS performance analysis
 8. Provide a focal point for diagnosis, analysis and following of all problems experienced by the VFT in using the GDS
 9. Provide software maintenance and control
 10. Manage the operational failure reporting system

ENGINEERING OFFICE
 1. Provide the Project Manager and Mission Director an independent assessment of major decisions, contingency planning, S/C data S/C emergencies and corrective actions
 2. Organize and integrate additional resources of personnel and test systems to supplement VFT resources when required by S/C emergencies or anomalies
 3. Serve as technical troubleshooter upon request of Project Manager or the Mission Director
 4. Assess and recommend resolution of system interface problems
 5. Serve on Project and VFT directorate review panels as required
 6. Review development and test operations plans from a systems engineering viewpoint

SCIENCE ANALYSIS & MISSION PLANNING DIRECTORATE
 1. Provide data and recommendations needed in making major mission decisions
 2. Recommend mission science decisions
 3. Recommend revisions to Mission Profile and/or S/C SOE requirements to optimize science data return
 4. Generate Mission Profiles
 5. Perform first order S/C and ground system constraint checks
 6. Predict, analyze, evaluate, and report VL science instrument and Surface Sampler status and performance
 7. Establish science data return and processing requirements and priorities
 8. Provide data processing for analysis of science data
 9. Provide landing site certification data analysis and recommendations
 10. Maintain and operate the science analysis software
 11. Operate the STL and SPM
 12. Operate the IPF
 13. Operate the GRE
 14. Provide real-time evaluation support to MCD during critical mission operations
 15. Prepare science reports and Project reports

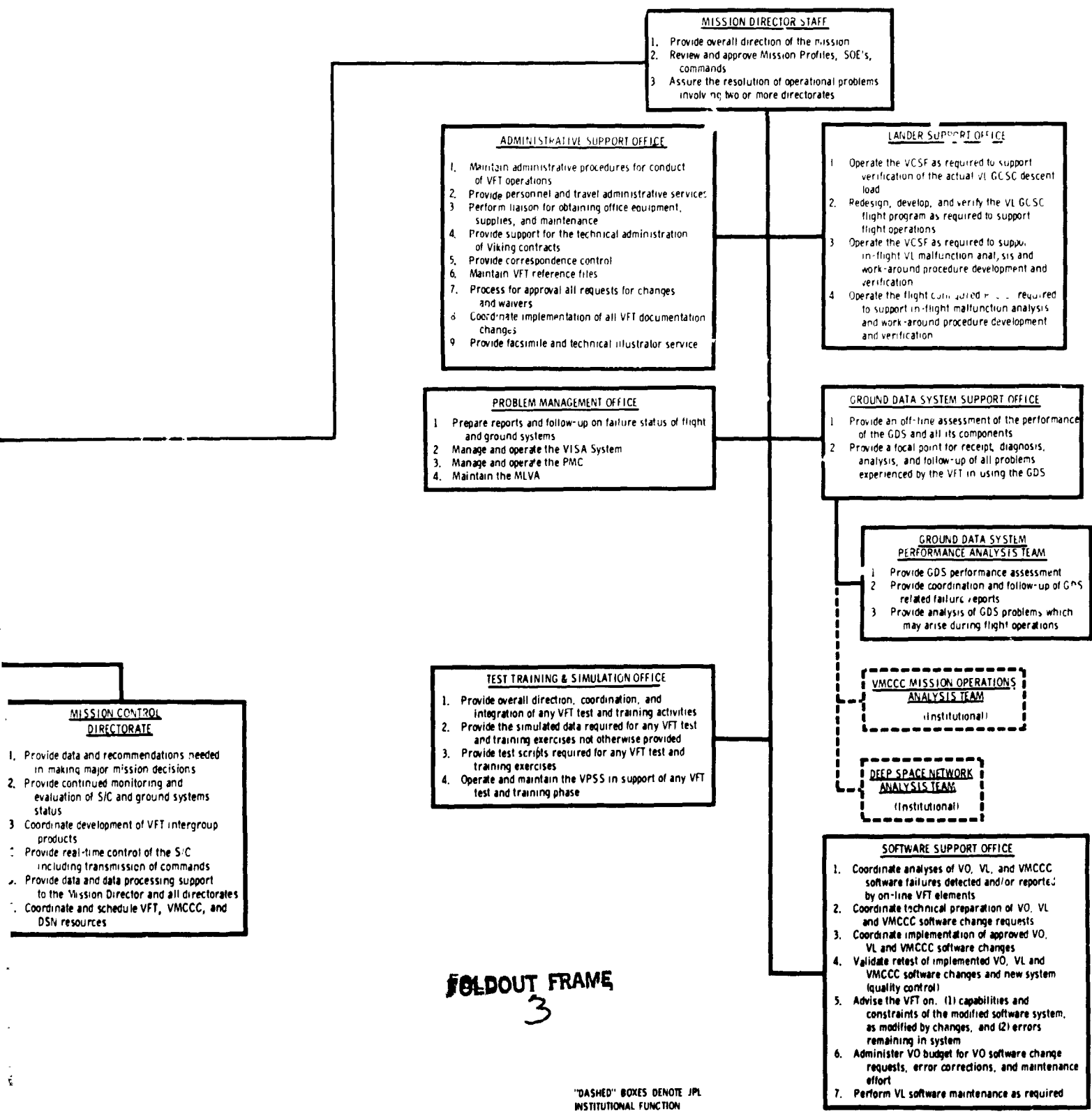
SPACECRAFT PERFORMANCE & FLIGHT PATH ANALYSIS DIRECTORATE
 1. Provide data and recommendations needed in making major mission decisions
 2. Generate S/C SOE's
 3. Predict, analyze, and evaluate S/C performance including VO science instrument performance
 4. Generate commands
 5. Provide and update TM calibration tables
 6. Determine and predict actual S/C, VO, and VL trajectories and maneuvers, and VO viewing coverage
 7. Provide Mars atmosphere and wind models based on entry data
 8. Establish metric tracking and S/C performance data processing requirements and priorities
 9. Provide real-time evaluation support to MCD during critical mission operations
 10. Support LSS site certification activities
 11. Define VL test requirements for LSO support

MISSION DIRECTORATE
 1. Provide data and recommendations needed in making major mission decisions
 2. Provide continued evaluation of S/C status
 3. Coordinate development products
 4. Provide real-time coordination including transmission to the Mission Director
 5. Provide data and data to the Mission Director
 6. Coordinate and schedule DSN resources

FOLDOUT FRAME

2

ORIGINAL PAGE IS OF PGOR QUALITY



FOLDOUT FRAME
3

"DASHED" BOXES DENOTE JPL INSTITUTIONAL FUNCTION

ORIGINAL PAGE IS OF POOR QUALITY

- SCIENCE ANALYSIS & MISSION PLANNING DIRECTORATE**
1. Provide data and recommendations needed in making major mission decisions.
 2. Recommend mission science decisions.
 3. Recommend revisions to Mission Profile and/or V/SOE requirements to optimize science data return.
 4. Generate Mission Profiles.
 5. Perform first order S/C and ground system constraint checks.
 6. Predict, analyze, evaluate and report V/L science instrument and Surface Sampler status and performance.
 7. Establish science data return and processing requirements and priorities.
 8. Provide data processing for analysis of science data.
 9. Provide landing site certification data analysis and recommendations.
 10. Maintain and operate the science analysis software.
 11. Operate the STL and SPM.
 12. Operate the GRE.
 13. Provide real time evaluation support to M/D during critical mission operations.
 14. Prepare science reports and Project reports.

- IMAGE PROCESSING STAFF**
1. Support evaluation of VO and VL camera performance and update calibration data files.
 2. Update and maintain on-line library of VO and VL camera images.
 3. Assist OIT and LIT members in use of interactive consoles.
 4. Provide on set up, monitoring and documentation of imaging batch processing requests.
 5. Provide on set up, monitoring and documentation of VO and VL imaging RDR processing requests.
 6. Maintain IPF software utilized in support of OIT and LIT activities.

- LANDING SITE STAFF**
1. Analyze and interpret V/S images of landing sites.
 2. Perform photogrammetric analysis of V/S images of landing sites.
 3. Mosaic V/S images of landing sites.
 4. Analyze and interpret MARDI landing site data.
 5. Analyze and interpret IRIM landing site data.
 6. Correlate all VO landing site data.
 7. Correlate VO landing site data with Earth based observation data.
 8. Analyze and interpret VL-1 data for use in certifying Mission 2 landing site, including mapping the atmosphere to the Mission 2 site.
 9. Prepare reports on the candidate landing sites and recommend sites to SA & MPC Director.
 10. Identify secondary sites, if necessary.
 11. Identify and certify alternate sites, if necessary.
 12. Recommend alternate sites, if necessary.

- ORBITER SCIENCE GROUP**
1. Recommend revisions to Mission Profile and/or VO SOE requirements to enhance science data return based on:
 - a) Knowledge acquired from Viking data.
 - b) Better than planned systems performance.
 2. Recommend revisions to Mission Profile and/or SOE requirements necessitated by lower than planned systems performance or failures.
 3. Review and concur with all Mission Profile and/or VO SOE changes that affect VO science.
 4. Establish VO science data return and processing requirements and priorities.
 5. Maintain and operate the VO science analysis software.
 6. Support LSS site certification activities.
 7. Prepare VO science reports and Project reports.

- LANDER SCIENCE GROUP**
1. Recommend revisions to Mission Profile and/or VL SOE requirements to enhance VL science data return based on:
 - a) Knowledge acquired from Viking data.
 - b) Better than planned systems performance.
 2. Recommend revisions to Mission Profile and/or VL SOE requirements necessitated by lower than planned systems performance or failures.
 3. Review and concur with all Mission Profile and/or VL SOE changes that affect VL science.
 4. Report VL science instrument status and performance.
 5. Establish VL science data return and processing requirements and priorities.
 6. Maintain and operate the VL science analysis software.
 7. Operate the STL and SPM.
 8. Operate the GRE.
 9. Support LSS site certification activities.
 10. Prepare VL science reports and Project reports.

1. Generate
2. Perform
3. constrain
4. Support

- ORBITER SCIENCE TEAMS**
1. Reduce and analyze VO science data necessary to support the conduct of mission operations.
 2. Recommend revisions to Mission Profile and/or VO SOE requirements to enhance VO science data return based on:
 - a) Knowledge acquired from Viking data.
 - b) Better than planned systems performance.
 3. Recommend revisions to Mission Profile and/or VO SOE requirements to enhance VO science data return necessitated by lower than planned systems performance or failures.
 4. Review and concur with all Mission Profile and/or VO SOE changes that affect VO science.
 5. Define required VO science instrument settings for the nominal mission and revise as necessary as required for VO science.
 6. Perform special tests, calibrations and studies as required for VO science.
 7. Establish VO science data return and processing requirements and priorities.
 8. Maintain and operate the VO science analysis software.
 9. Support the MCD in VO science data record preparation, data processing and computer data analysis.
 10. Provide interpreted VO science data for use as public information.
 11. Support LSS site certification activities.
 12. Prepare VO science reports and Project reports.

- LANDER SCIENCE TEAMS**
1. Reduce and analyze VL science and science instrument performance data necessary to support the conduct of mission operations.
 2. Recommend revisions to Mission Profile and/or VL SOE requirements to enhance science data return based on:
 - a) Knowledge acquired from Viking data.
 - b) Better than planned systems performance.
 3. Recommend revisions to Mission Profile and/or VL SOE requirements to enhance science data return necessitated by lower than planned systems performance or failures.
 4. Develop the Biology Investigation SOE.
 5. Review and concur with all Mission Profile and/or VL SOE changes that affect VL science.
 6. Define required VL science instrument settings for the nominal mission and revise as necessary.
 7. Maintain VL science instrument performance files.
 8. Define VL science instrument TM channel alarm limits.
 9. Monitor and analyze downlink data to determine VL science instrument actual performance.
 10. Report VL science instrument performance analysis results and operational status.
 11. Determine impacts of VL performance and planned VL science SOE's on VL science instrument performance.
 12. Analyze and diagnose VL science instrument anomalies and recommend alternate procedures.
 13. Prepare VL science instrument performance reports.
 14. Perform special VL science tests, calibrations, and studies as required.
 15. Establish VL science data return and processing requirements and priorities.
 16. Maintain and operate the VL science analysis software.
 17. Prepare surface model for each landing site.
 18. Operate the SPM.
 19. Operate the GRE.
 20. Support the MCD in VL data record preparation, data processing, and computer data analysis.
 21. Provide interpreted VL science data for use as public information.
 22. Support LSS site certification activities.
 23. Prepare VL science reports and Project reports.

- SURFACE SAMPLER TEAM**
1. Monitor and evaluate Surface Sampler status and performance.
 2. Determine the impacts of VL performance on the Surface Sampler.
 3. Report Surface Sampler status to Lander Science Teams.
 4. Support the development of VL SOE's involving use of the Surface Sampler.
 5. Operate and maintain the STL as required to develop and verify VL SOE's.
 6. Verify the safety of commands which include Surface Sampler operations.
 7. Support preparation of models of the Martian surface for each landing site.
 8. Provide to the Lander Science Teams the data needed to resolve conflicts on Surface Sampler usage.
 9. Prepare Surface Sampler performance reports.

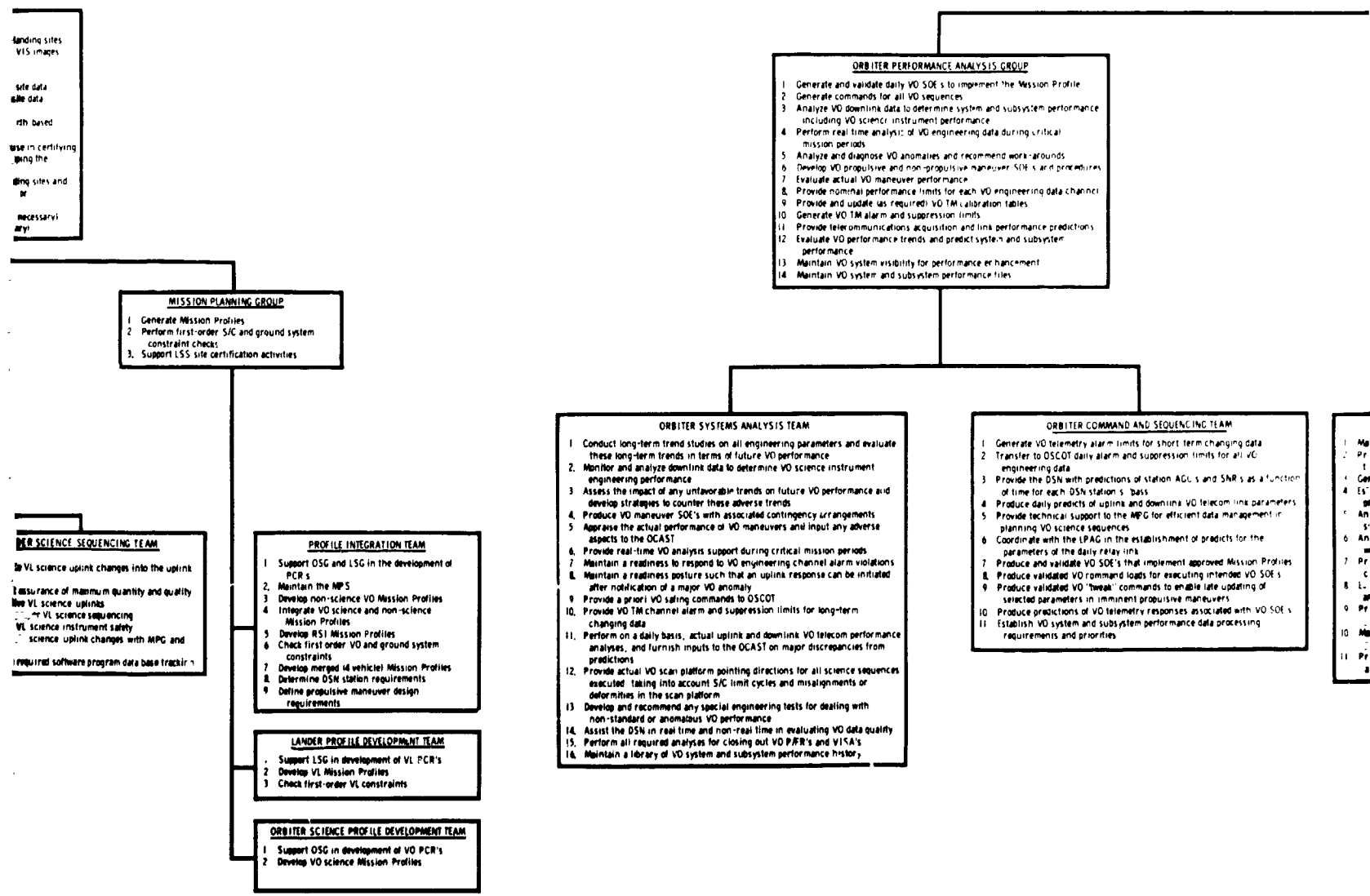
- LANDER SCIENCE DATA MANAGEMENT TEAM**
1. Prepare input run requests for VL science analysis programs.
 2. Perform product inspection for outputs of VL science analysis program runs.
 3. Distribute VL science analysis program run products to science teams.
 4. Coordinate activities of Lander Science Team Data Processing personnel with respect to instrument performance evaluation.
 5. Assist in budgeting and control of Lander Science Team computer usage.

- LANDER SCIENCE SEQUENCING TEAM**
1. Integrate VL science uplink changes into the uplink MOS.
 2. Support assurance of maximum quantity and quality of adaptive VL science uplinks.
 3. Assure proper VL science sequencing.
 4. Assure VL science instrument safety.
 5. Coordinate science uplink changes with MPG and LCAST.
 6. Provide required software program data base track.

ORBITER SCIENCE
LANDER SCIENCE
SURFACE SAMPLER

BOLDOUT FRAME

1



FOLDOUT FRAME
2

ORBITER PERFORMANCE ANALYSIS GROUP

- SPACECRAFT PERFORMANCE & FLIGHT PATH ANALYSIS DIRECTORATE**
1. Provide data and recommendations needed in making major mission decisions
 2. Generate S/C SOE's
 3. Predict, analyze and evaluate S/C performance including VO science instrument performance
 4. Generate commands
 5. Provide and update TM calibration tables and alarm limits
 6. Determine and predict actual S/C VO and VL trajectories and maneuvers and VO viewing coverage
 7. Provide Mars atmosphere and wind models based on entry data
 8. Establish metric tracking and S/C performance data processing requirements and priorities
 9. Provide real time evaluation support to MCD during critical mission operations
 10. Support LSS site certification activities
 11. Define VL test requirements for LSO support

- LANDER PERFORMANCE ANALYSIS GROUP**
1. Generate and validate daily VL SOE's required to implement Mission Profile
 2. Generate VL commands
 3. Maintain VL system and subsystem performance files
 4. Provide and update (as required) the VL TM calibration tables
 5. Generate VL TM channel alarm limits
 6. Establish VL system and subsystem performance data processing requirements and priorities
 7. Analyze downlink data to determine VL system and subsystem actual performance
 8. Analyze and diagnose VL anomalies, recommend work-arounds
 9. Predict VL TM responses and provide alarm limit changes associated with SOE changes
 10. Evaluate VL performance trends and predict system and subsystem performance
 11. Provide VL telecommunications acquisition and link performance predictions
 12. Maintain VL system visibility for performance enhancement
 13. Support LSS site certification activities
 14. Define VL test requirements for LSO support

- FLIGHT PATH ANALYSIS GROUP**
1. Determine and predict actual S/C trajectories
 2. Assist the DSN in analysis of tracking data quality
 3. Generate trajectory data as required
 4. Develop maneuver strategies and calculate commandable quantities for VO and VL maneuvers
 5. Evaluate actual VO and VL maneuver performance
 6. Perform VL trajectory design
 7. Determine VL position on planet surface
 8. Reconstruct the VL entry trajectory and derive an engineering model of the Mars atmosphere and winds based on entry data
 9. Perform VO/VL relay link geometry and margin calculations
 10. Design precision VO science sequences
 11. Determine actual VO science viewing coverage
 12. Support radio entry science requirements
 13. Support LSS site certification activities

- LANDER SYSTEMS ANALYSIS TEAM**
1. Maintain VL system and subsystem performance files
 2. Provide and update (as required) VL TM calibration tables
 3. Generate VL TM channel alarm limits
 4. Establish VL system and subsystem performance data processing requirements and priorities
 5. Analyze downlink data to determine VL system and subsystem actual performance
 6. Analyze and diagnose VL anomalies, recommend work-arounds
 7. Predict VL TM responses and provide alarm limit changes associated with SOE changes
 8. Evaluate VL performance trends and predict system and subsystem performance
 9. Provide VL telecommunications acquisition and link performance predictions
 10. Maintain VL system and subsystem visibility for performance enhancement
 11. Provide supplemental VL entry phase support at JPL as required

- LANDER COMMAND AND SEQUENCING TEAM**
1. Generate and validate daily VL SOE's required to implement the Mission Profile
 2. Generate VL commands

- TRACKING DATA CONDITIONING TEAM**
1. Establish metric tracking data requirements
 2. Monitor metric tracking data quantity and quality
 3. Prepare metric tracking data quantity and quality report
 4. Edit metric tracking data and prepare clean tracking data files
 5. Provide pole motion and timing data
 6. Provide tropospheric model correction parameters
 7. Provide ionospheric and interplanetary charged particle calibration data
 8. Generate frequency independent DSN observable predictions for the DSN and VMCC

- ORBITER MANEUVER & TRAJECTORY TEAM**
1. Develop candidate maneuver strategies in support of mission planning
 2. Analyze planetary quarantine requirements
 3. Design VO propulsive maneuvers
 4. Design VO attitude maneuvers
 5. Determine VO commandable maneuver parameters
 6. Perform post-execution VO maneuver analysis
 7. Determine orbit lifetime
 8. Generate probe ephemeris
 9. Generate VO trajectory data tape
 10. Generate VO trajectory information

- INTERPLANETARY ORBIT DETERMINATION TEAM**
1. Establish navigation metric tracking data requirements
 2. Process S/C radiometric tracking data to determine current best estimate of the interplanetary trajectory
 3. Establish requirements for monitoring and processing approach optical metric data
 4. Process approach optical metric data to provide optical based approach trajectory estimate
 5. Process radiometric tracking data and approach optical metric data to provide improved approach trajectory estimate and to improve dynamic and observational models

- ORBITER SCIENCE SEQUENCE TEAM**
1. Design and develop final, precision VO science scan sequences
 2. Prepare VO science scan sequence forecast
 3. Prepare VO science scan sequence data package summarizing observation conditions and predicted coverage
 4. Determine actual VO science scan sequence viewing coverage

- SATELLITE ORBIT DETERMINATION TEAM**
1. Establish navigation metric tracking data requirements
 2. Process S/C or VO radiometric tracking data to determine current best estimate of satellite orbit
 3. Process S/C or VO radiometric tracking data to improve orbital phase dynamic and observational models
 4. Process VL radiometric tracking data to determine VL position
 5. Generate probe ephemerides

- LANDER FLIGHT ATM ANALYSIS TEAM**
1. Develop and evaluate candidate descent maneuver strategies
 2. Design VL descent trajectory including descent maneuver and associated trajectory related parameters
 3. Compute full six-degree-of-freedom digital simulation of predicted VL descent trajectory
 4. Support orbit trim maneuver selection for landing
 5. Support landing site selection relative to VL trajectory design considerations
 6. Perform VL trajectory, atmosphere and wind reconstruction and provide resulting estimate of landed position
 7. Predict relay link performance during descent and post-landing
 8. Monitor all estimates of landed position and recommend current best estimate

ING TEAM

changing data for all VO

and SNR's as a function

telecom link parameters

data management in

predicts for the

Provided Mission Profiles

intended VO SOE's

late updating of

maneuvers

associated with VO SOE's

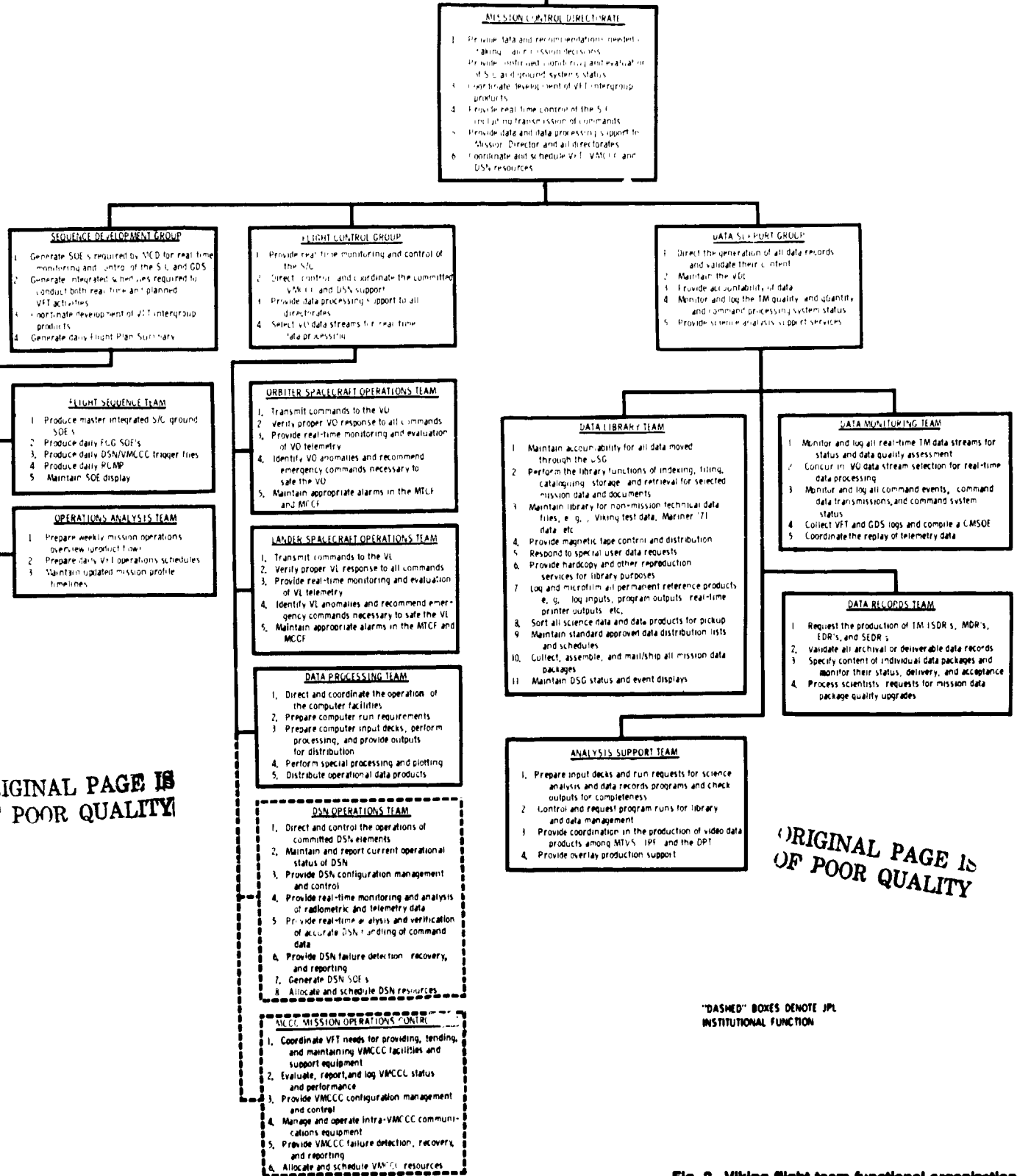
data processing

ORIGINAL PAGE IS
OF POOR QUALITY

SOLDOUT FRAME

ORIGINAL PAGE IS
OF POOR QUALITY

ORIGINAL PAGE IS
OF POOR QUALITY



"DASHED" BOXES DENOTE JPL INSTITUTIONAL FUNCTION
















Fig. 2. Viking flight team functional organization

SCOUT FRAME
4

PDT	UTC
2400	0700
2200	0500
2000	0300
1800	0100
1600	2300
1400	2100
1200	1900
1000	1700
0800	1500
0600	1300
0400	1100
0200	0900
0000	0700

DAY NO. (PDT)
DAY of
MONTH (PDT)
SEPARATION_A

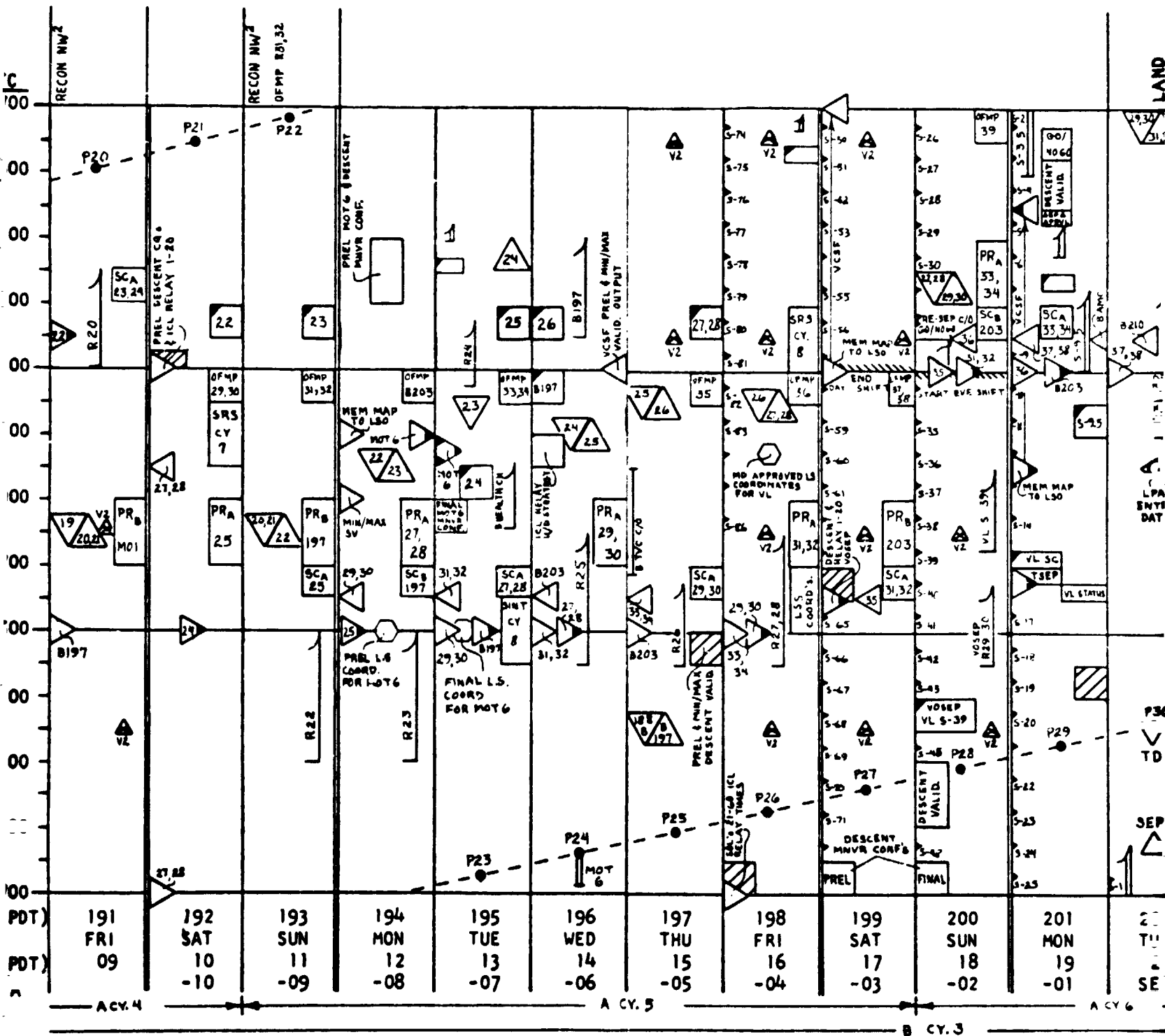
LEGEND

-  - END VO SEQUENCE REV x
 -  - START VO SEQUENCE REV x
 -  - FPAG OUTPUT REV x: SSP
 -  - OPAG INPUT: VODEV
 -  - CMD WINDOW REV x
 -  - LATE UPDATE
CMD WINDOW REV x
 -  - (3 DARK CORNERS) -
LATE UPDATE
 -  - V1 CONTROL PICTURE TRIAD
 -  - V1 KNOWLEDGE PICTURE
 -  - CMD CONF REV x
 -  - SPFPAD MTG
 -  - PREL PROD REVIEW
 -  - SEQ (CMD - MTG
LSS INPUT REV x
 -  - PP-PHOTO PARAM
COVERAGE OPTIONS
REV x. FPAG-LSS
 -  - ORCOL REV x
- DARK TIP = FINAL
OPEN TIP = PREL.

ORIGINAL FILED
OF BOOK 1000000000

EDDOUT FRAME

1



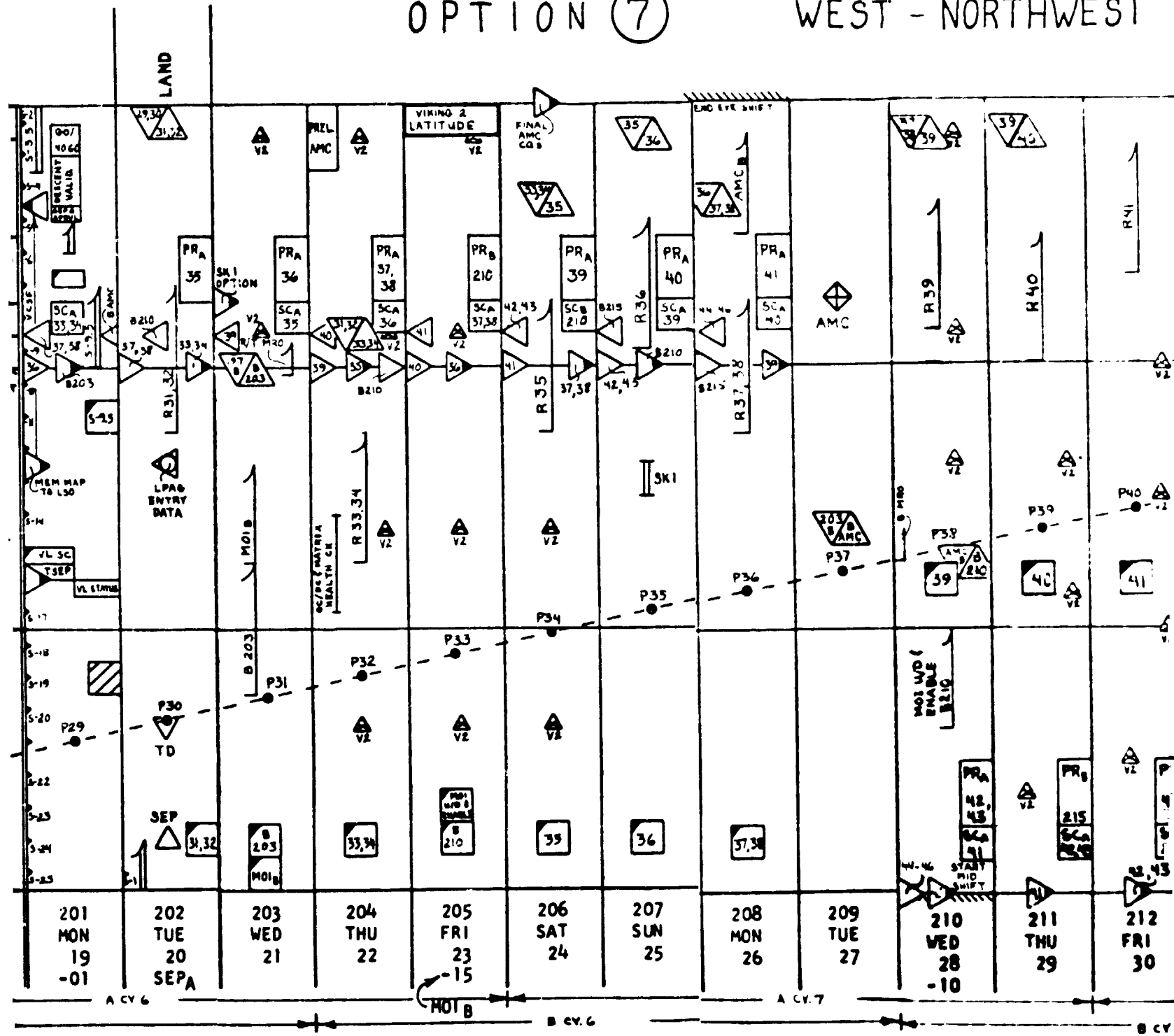
FOLDOUT FRAME



ORIGINAL PAGE IS OF POOR QUALITY

OPTION 7

WEST - NORTHWEST



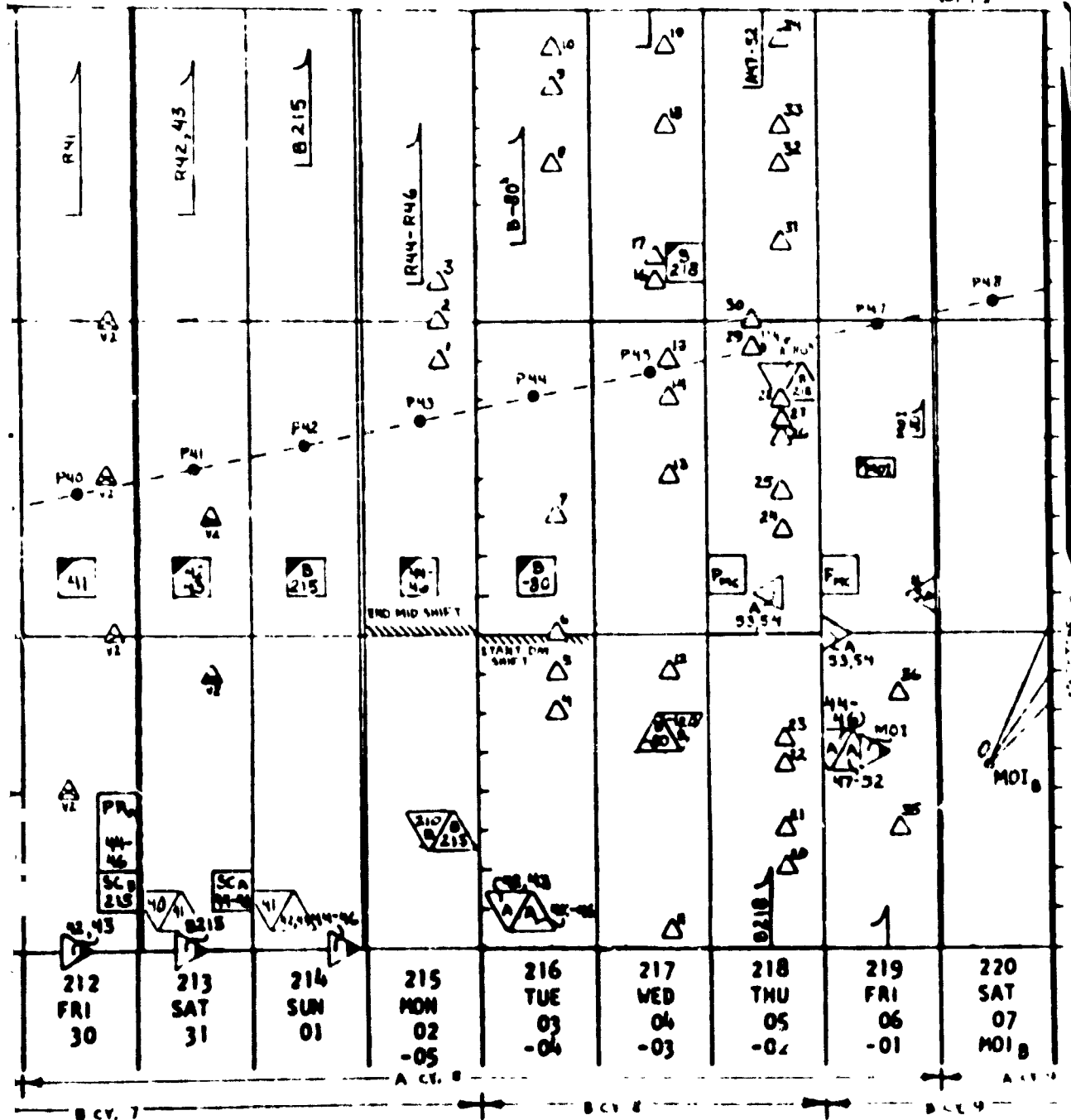
ORIGINAL PAGE 13
OF POOR QUALITY

SOLDOUT FRAME
3

ORIG
OF P

EST (WNW)

DSN VIEW PERIODS
REV 1.8



REVISION 0 - 1947.8

FOLDOUT FRAME

Fig. 3. SPPAD operations schedule

ORIGINAL PAGE IS OF POOR QUALITY

PRECEDING PAGE BLANK NOT FILMED

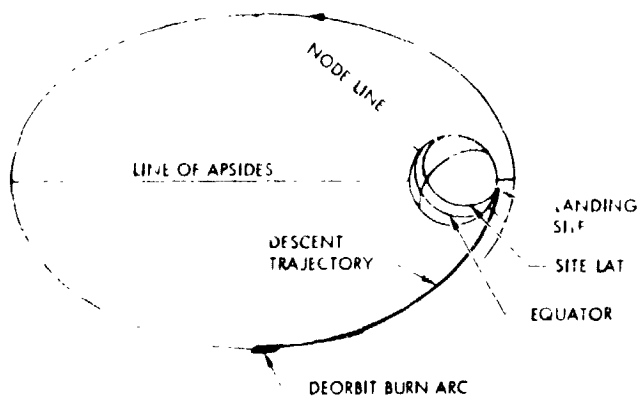


Fig. 4. Lander descent

separation to entry) to 5 h. To provide adequate margin with respect to aerodynamic structural and thermal loads and skipout in the presence of trajectory dispersions and any one of the five "equally likely" Martian design atmospheres, the targetable entry corridor was constrained to be the flight path angle range from -16.2 to -17.4 deg at 800,000 ft altitude at a speed less than 4.625 k/s. The Lander Capsule RCS mounted on the aeroshell, which was used for attitude control during descent, was also used to impart the deorbit velocity increment. Approximately 85% of the RCS fuel was allocated for deorbit yielding a maximum velocity increment capability of 156 m/s. Finally, to assure adequate relay communication from the Lander to the Orbiter throughout descent and for 11 minutes after landing, the Lander was to be 20 deg ahead (i.e., downrange) of the Orbiter at the moment of entry.

The constraints on the foregoing parameters - coast time, entry flight path angle, deorbit velocity increment, and lead angle - determined the accessible landing area with respect to the separation orbit as illustrated in Fig. 5. PER is the downrange surface angle from the separation orbit periapsis; XR is the arc distance away from the separation orbit plane. One degree of Mars surface angle is equivalent to about 60 km. Observe that the maximum achievable crossrange was constrained by the 5-h coast limit and the maximum available deorbit velocity of 156 m/s. The downrange limit was determined by the shallow entry and the 156-m/s limits; uprange by the steep entry and the 5-h coast limits. Actually the crossrange capability was somewhat arbitrarily reduced to ± 3 deg to avoid the rapid growth in landing dispersions which would result beyond ± 3 deg. Also, as the coast time increases, the required deorbit velocity increment decreases. In order to minimize entry mass the maximum deorbit velocity increment of 156 m/s was to be expended. Therefore, for long coasts it would have been necessary to use a "two-burn" deorbit maneuver totalling 156 m/s but designed so that the second burn would partly cancel the effect of the first yielding the

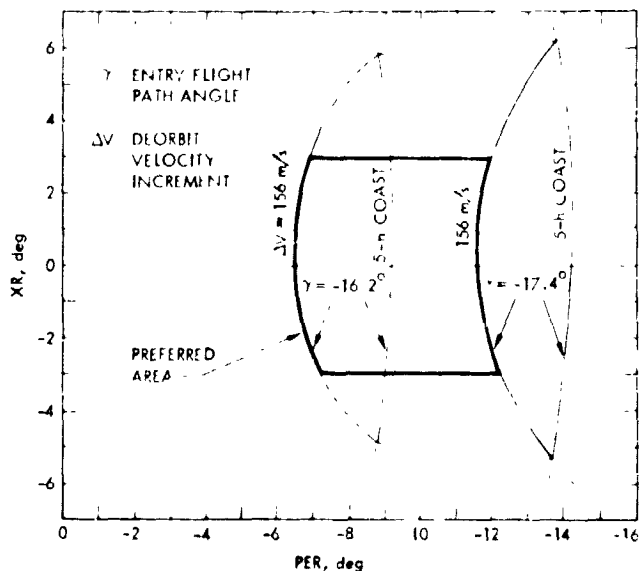


Fig. 5. Accessible area constraints

required net increment of less than 156 m/s. Since it was undesirable to use long coast times and two-burn deorbit maneuvers, the extreme uprange capability was to be avoided as indicated in Fig. 5. The above margin considerations dictated a "preferred" targeting region wherein the Lander could be targeted to land up to three degrees away from the orbit plane and 2.5 deg downrange or uprange of the midpoint. The targeting controls were the direction, magnitude, and location (in the separation orbit) of the deorbit maneuver. Since the accessible landing area was "fixed" to the separation orbit as illustrated in Fig. 6, the separation orbit had to be controlled to "capture" the landing site within the accessible area so that the Lander could reach the site within the capabilities and constraints described above.

The elevation of the Sun at the landing site at the time of landing was a crucial parameter in the orbit design. The best observations of the landing area would be obtained when the Orbiter/Lander spacecraft was flying over the accessible area. Following landing, the relay links would also occur in this overflight region, and real-time television from the Lander was to be obtained during the links. Consequently, TV imaging of the landing area both from orbit and on the surface necessitated a sun elevation angle (SEA) at landing that would yield good shadowing. As shown in Fig. 7, the landing SEA and the landing site latitude uniquely determined the landing point in inertial space.

The ballistic approach to any planet is along a hyperbola whose focus is at the planet's center and whose inbound asymptote approximates the straight line motion relative to

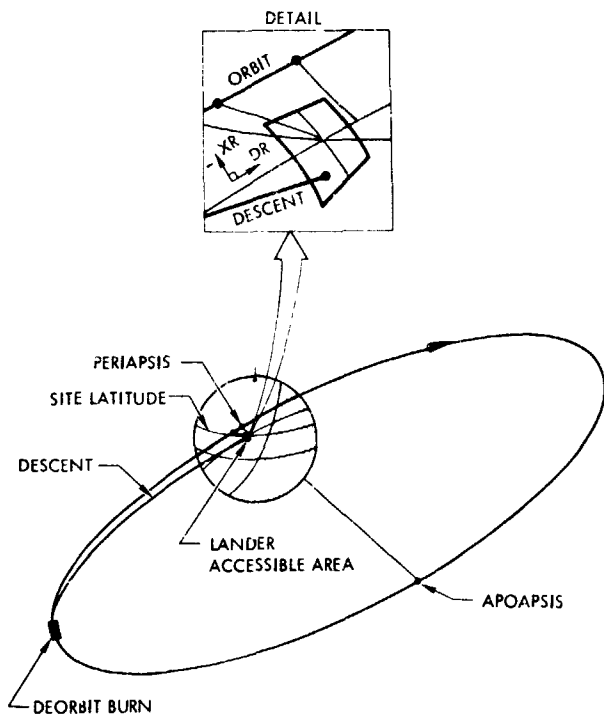


Fig. 6. Accessible area fixed to orbit

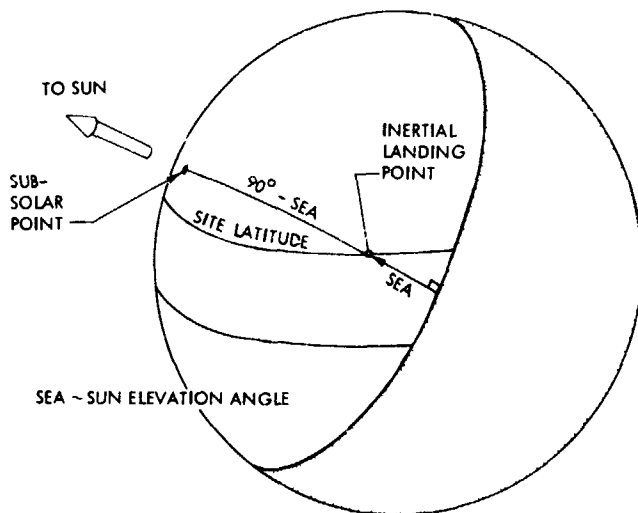


Fig. 7. Inertial landing point

the planet as the spacecraft enters the planet's sphere of influence. The "S-vector" which is parallel to the asymptote and passes through the planet center is fundamental in the orbit design. It corresponds to what would be a vertical impact trajectory as shown in Fig. 8. The Earth-to-Mars interplanetary trajectory, which is uniquely determined by the launch and arrival dates, establishes the S-vector. The plane of any

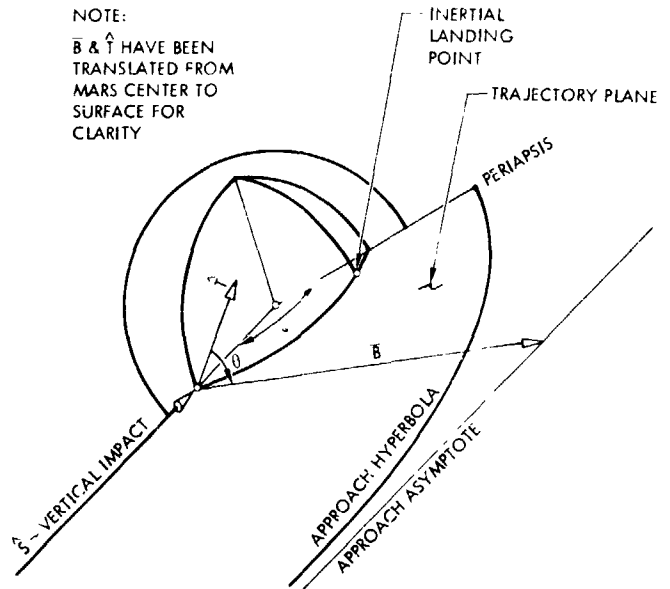


Fig. 8. Orbit plane design

possible approach trajectory contains the S-vector; therefore, the plane can be changed only by rotation about the S-vector. A coplanar orbit insertion maneuver is the most efficient transfer from the hyperbolic "flyby" trajectory to Mars orbit. Accordingly, the orientation (θ around \hat{S}) of the approach trajectory plane was controlled with midcourse maneuvers to contain the inertial landing point in the plane as illustrated in Fig. 8. Thus, the vertical impact point, the inertial landing point, and the planet center uniquely specify the orbit plane. The orientation ψ of the orbit within its plane was controlled to center the accessible area over the landing point (Figs. 8 and 9). The approach trajectory was targeted to minimize the orbit insertion velocity increment required to transfer to the orbit prescribed above. As illustrated in Fig. 9 this was essentially a tangential transfer. The insertion velocity increment for Viking 1 would nominally be about 1250 m/s - 85% of the total Orbiter capability. Viking 2 would require about 1100 m/s for insertion into a 28.7-h orbit initially.

An aiming plane passing through the planet center and perpendicular to the S-vector known as the "B-plane" is used to avoid nonlinearities in targeting. The approach trajectory is controlled by controlling the point at which its asymptote pierces the B-plane. This is the point at which the spacecraft would fly through the B-plane if the planet has no mass (i.e., if there were no gravitational bending). The vector in the B-plane from the planet center to the asymptote is known as the "B-vector"; it corresponds to the semi-minor axis of the hyperbola. Knowledge and control of both the B-vector and the time of arrival are the essence of interplanetary navigation.

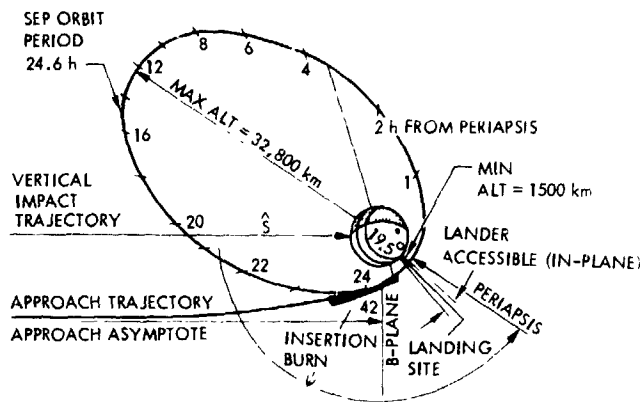


Fig. 9. Viking 1 orbit insertion design

The Viking 1 B-plane is presented in Fig. 10. In this view the planet appears as it would to an observer on the spacecraft during the approach. The T-axis in the B-plane lies in the ecliptic and is used as the reference direction for measuring θ . (R completes the right-handed R-S-T frame.) The edge of the trajectory plane coincides with the B-vector; thus, the aim angle θ completely orients the trajectory plane. The Viking 1 B-vector was to be controlled to within 5 deg and 700 km of the target, resulting in the approach control accuracy requirement zone shown. This control requirement would ensure that even in the presence of 0.99 orbit insertion errors, the orbit could be adjusted with small orbit trim maneuvers within the site acquisition propellant budget to achieve the required separation orbit, i.e., to correct periapsis altitude to within the allowed tolerance and to capture the landing site within the Lander accessible area. The orbit insertion errors would be due to errors in the knowledge of the approach trajectory (i.e., "orbit determination" errors) at the time the insertion

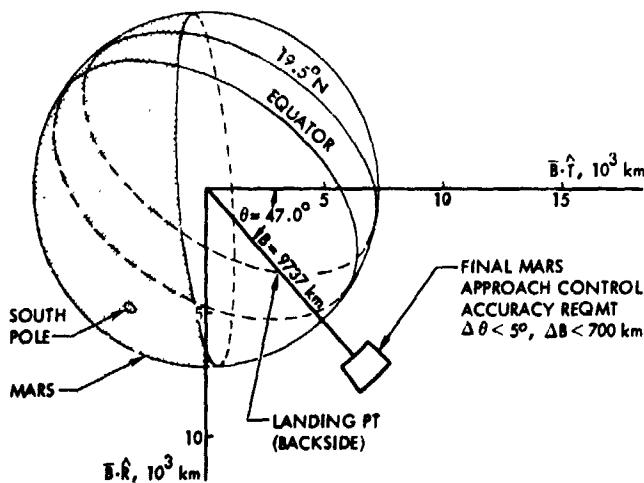


Fig. 10. Viking 1 B-plane delivery requirements

commands were calculated on the ground and the execution errors of the spacecraft in performing the maneuver. In concert with the control requirement, the B-vector knowledge requirement was set at 3 deg and 500 km. The Viking 2 requirements were 7 deg and 500 km and 5 deg and 350 km for control and knowledge, respectively. The requirements differed because the geometry of the two missions differed significantly.

In the foregoing discussion the landing point was treated as a point in inertial space specified by site latitude and sun elevation. The timing of the spacecraft in orbit had to be precisely controlled so that the intended landing site on the Mars surface would, in fact, be under the Lander at the moment of touchdown. The parameter "timing offset" was introduced to achieve this control. Consider the meridian fixed to the center of the Lander accessible area as illustrated in Fig. 11. Timing offset was defined to be the time required for the spacecraft to reach this "inertial" meridian after the landing site has crossed it.

The Viking 1 in-orbit maneuver strategy for acquiring the landing site is depicted in Fig. 12. To obtain adequate site certification observations of the intended landing area the timing offset had to be less than one hour. To capture the site within the Lander accessible area the offset of the Orbiter at the landing periapsis was to be 8 ± 8 min. Recall that the Lander leads the Orbiter during descent; therefore, the nominal Orbiter timing offset had to be positive at landing. To expedite site certification and land 15 revolutions after insertion, the strategy was to:

- (1) Control the arrival time at Mars such that the timing offset immediately after insertion (i.e., periapsis-0) would not exceed 15 min.

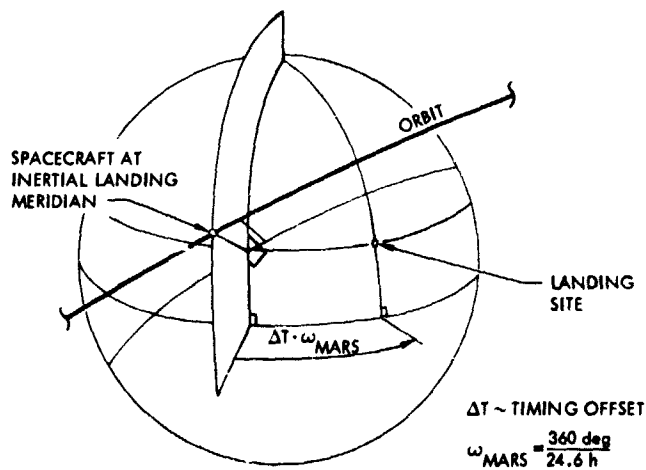


Fig. 11. Timing offset

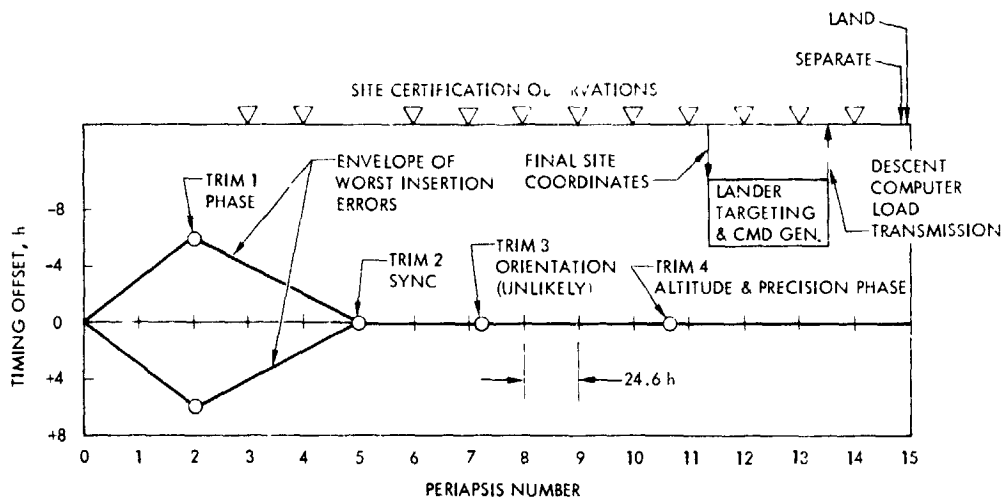


Fig. 12. Orbital operations plan

- (2) Insert into a very nearly Mars synchronous orbit such that the 8-min offset would result at periapsis-15.

To aid the understanding of Fig. 12, consider a 1-hour subsynchronous postinsertion orbit (i.e., 23.6-h period). The spacecraft will complete its first revolution in 1 hour less than a Mars day; thus the landing site will be 1 hour west (timing offset = -1.0 h) of the meridian when the spacecraft is at the meridian. The converse holds for the supersynchronous case, and the problem is completely linear. The knowledge requirement for generation of the orbit insertion commands discussed earlier and the spacecraft execution accuracy ensured that the 0.99 error in the postinsertion period would not exceed 3 h. A "phasing" maneuver was scheduled at Periapsis-2 to change the orbit period such that the timing offset would be zero at Periapsis-5. A "synchronizing" maneuver would be performed at Periapsis-5 to drive the offset to +8 min at Periapsis-15. Owing to their smaller size and the vast improvement in orbit determination "knowledge" once in orbit, these trim maneuvers would be at least a hundred times more accurate in period control than the insertion maneuver (i.e., 1 min vs 3 h). An orientation correction maneuver was scheduled near Periapsis-7 to move the accessible area in the approach and insertion maneuvers. A fourth maneuver was scheduled to correct the periapsis altitude and perform any appropriate vernier timing adjustment in the revolution preceding Periapsis-11. Final orbit determination and Lander targeting and commanding would then be performed between Periapsis-11 and Periapsis-14 as indicated in Fig. 12. This maneuver strategy guaranteed acquiring the landing site within the 150 m/s velocity budget allocated for navigation dispersions; 25 m/s was suballocated for midcourse maneuvers, 125 m/s for insertion maneuver adjustments and the site

acquisition orbit trims. The foregoing presented the "pre-launch" site acquisition strategy for Viking 1. The Viking 2 strategy, which was significantly different, is described in the *Maneuver Analysis* chapter.

The salient features of the flight path design and control strategy as it existed at launch have been presented. The actual inflight performance will now be discussed.

II. Viking 1 Inflight Synopsis

Viking 1 was launched by a Titan IIIE/Centaur launch vehicle on August 20, 1975, on the 10-month journey to Mars depicted in Fig. 13. The launch aimpoint was intentionally biased about 0.3 million km from Mars as shown in Fig. 14. The arrival time was biased about one day late. These biases satisfied the following constraints: (1) the probability of impacting Mars with unsterilized hardware was to be less than 10^{-6} ; (2) the first maneuver was to exceed 2 m/s to ensure propulsion stability; and (3) the maneuver attitude was to allow communication over the spacecraft low-gain antenna.

The crosses (+) in Fig. 14 show the variety of orbit determination solutions obtained during the first few hours after launch. By 12 h after launch sufficient tracking data (doppler and range) were available to determine the solution very well. All subsequent solutions were nicely clustered within the area indicated; thus, the Centaur injection error was about 2σ . The first midcourse maneuver scheduled for launch plus seven days was targeted directly to the center of the approach control zone discussed earlier (and to the final desired arrival time). This zone lies within the dot on Fig. 14. An enlarged view of the zone is shown in Fig. 15, where the 3σ

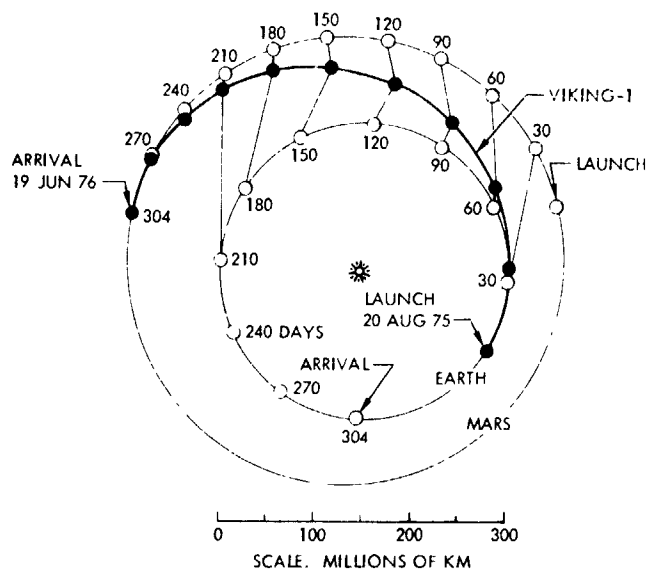


Fig. 13. Viking 1 heliocentric trajectory

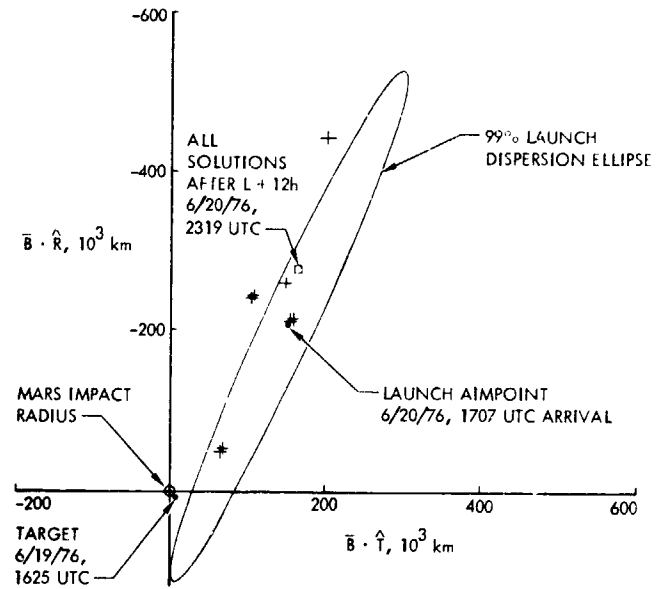


Fig. 14. Viking 1 launch accuracy

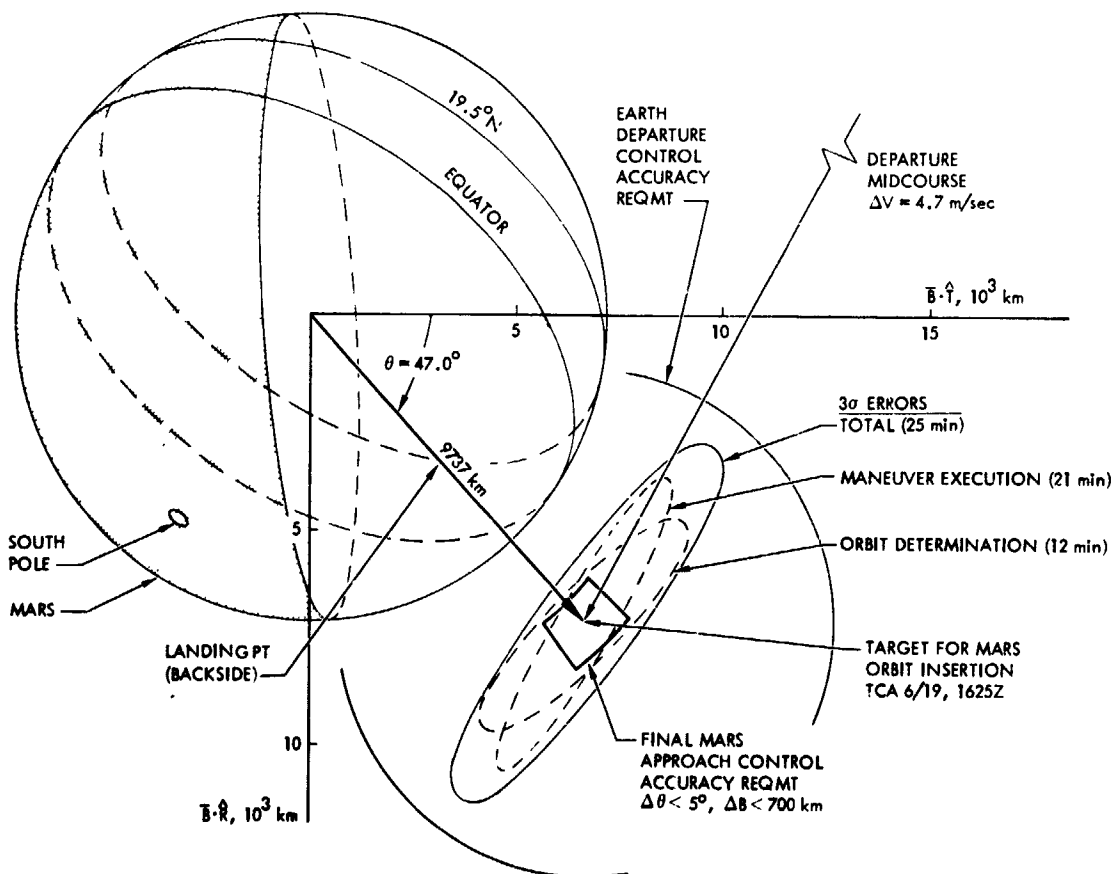


Fig. 15. Viking 1 Earth departure control

orbit determination and execution errors for the 4.7 m/s midcourse are displayed. The major orbit determination error source was the uncertainty in the solar pressure force that would act on the spacecraft throughout its journey to Mars. This uncertainty could be reduced only after several months of tracking, at which point the solar pressure coefficients could be accurately estimated in the orbit determination process. Note that the orbit determination and maneuver execution errors were comparable and their combined total was small enough to avoid planetary quarantine biasing and was well within the earth departure control requirement. The departure control requirement was set at 6000 km to ensure that the approach midcourse maneuvers would be sufficiently small that their errors would be inconsequential compared to the approach orbit determination errors. After about a week of post-midcourse tracking, it was clear that the actual execution error was indeed small and no further maneuvers would be required until Mars approach.

During the nine-month interplanetary "cruise," the navigation emphasis was on refining the trajectory and observational models. These refinements were very important to providing the capability to do "radio-only" redetermination of the trajectory between the two scheduled approach midcourse maneuvers. This effort resulted in significant adjustments of the solar pressure coefficients and the Australian tracking station locations. The effort also produced a "best" long-(tracking) arc estimate of the trajectory utilizing all available tracking data. This long-arc estimate provided the baseline for encounter operations.

The encounter operations schedule provided for approach maneuvers at both 30 and 10 days before arrival. A series of observations of Mars and stars by the Orbiter television cameras was scheduled prior to each maneuver opportunity. These observations were used to aid in the orbit determination process but were not to be relied upon to meet navigation requirements. The first optical series confirmed the long-arc radio solution, and it was then clear that a single approach midcourse at 10 days before arrival would easily correct the existing delivery error. The final delivery error would be essentially the orbit determination error at the time the midcourse was calculated. Therefore, the 10-day midcourse was preferred since the second optical series could be analyzed prior to its design.

The short-arc (~3 weeks) radio and optical orbit determination solutions did not agree as well as expected with the long-arc radio-only solution. There was more confidence in the short-arc radio plus optical. Furthermore, it was fully demonstrated that if this solution was used in targeting the approach midcourse while the long-arc radio was actually the right solution, the consequences would be minimal. In this event,

the periapsis altitude would be about 150 km lower, but this error would be easily correctable with the inorbit maneuver strategy described earlier. Accordingly, the short-arc radio plus optical solution was adopted without reservation. Fig. 16 presents this final premaneuver solution and its uncertainty. Observe that the 3σ uncertainty would be well within the approach control zone following the maneuver since the execution error would be negligible. Note also that the interplanetary delivery error (i.e., the error prior to the approach midcourse) was about 1800 km, corresponding to about 1.5σ with respect to the delivery accuracy predicted for the departure control. Most of this error was due to solar pressure prediction error as expected.

When the propulsion system was repressurized two days before the midcourse, the pressure regulator in the propellant feed system leaked such that the pressure buildup by the time of orbit insertion would be much too high for safe engine operation. It was possible to avoid this buildup by again sealing off the pressurant supply with a pyro valve as it had been sealed throughout interplanetary cruise. However, if this were done, the mission would be lost if the last pyro "open" valve did not open when commanded just before insertion. Consequently, it was decided to leave the system open and reduce the pressure with large approach midcourse maneuvers. Accordingly, two maneuvers of 50 and 60 m/s were executed at 9 and 4 days before arrival, respectively. The approach midcourse that had been designed to correct the navigation error was only 3.7 m/s.

In order to minimize propellant cost, these two maneuvers were designed as retro maneuvers to reduce the approach speed and thereby reduce the insertion velocity requirement.

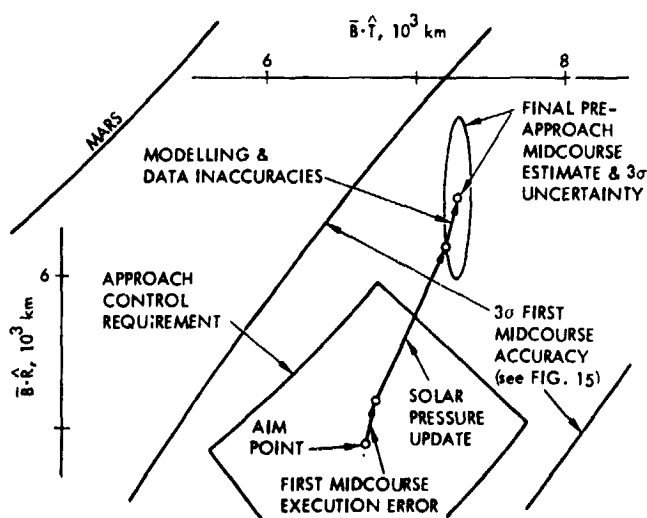


Fig. 16. Viking 1 Interplanetary delivery

The insertion requirement would be reduced about 1 m/s for every 2 m/s of retro during approach. However, these retro maneuvers would also delay the Mars arrival by about 6.5 h so that at least the first part of the site acquisition/certification strategy discussed earlier (Fig. 12) was now invalid because the initial timing offset would be +6.5 h. To get back to the original timeline as quickly as possible without any further propellant penalties, it was decided to insert into a 42.5-h orbit so that the spacecraft would nominally overfly the landing site at the end of the first revolution – the 6.5-h arrival delay plus the 42.5-h period would be equivalent to two revolutions in the synchronous orbit. The first orbit trim would be performed during this overflight to synchronize the orbit (i.e., reduce the period to 24.6 h). The periapsis at the end of the first revolution was called Periapsis-2 to maintain the original relationship between periapsis numbering and mission events (e.g., trim-1 was still scheduled at “Periapsis-2”).

An important factor in the decision to do the large maneuvers instead of closing the propulsion system was the excellent actual performance of the optical orbit determination process. Radio data alone could not adequately redetermine the approach trajectory in the few days between these maneuvers, but the optical data could. If the optical process had not been working so well, it is unlikely that these large maneuvers would have been attempted. Figure 17 illustrates the maneuver performance. The predicted delivery error ellipse for each was dominated by the spacecraft execution error owing to both the large size of the maneuvers and to the excellent orbit determination performance. The aimpoint was moved progressively away from the planet due to the increased bending of the trajectory that would occur at the lower approach speeds and also due to the larger initial orbit. Note that both maneuvers were executed very well. The final delivery error was less than 30 km in the B-plane and less than 10 s in arrival time. A third series of Mars/stars observations between the maneuvers was indeed instrumental in achieving this accuracy.

A series of observations of the Mars' satellite Deimos against the star background was used as planned to precisely determine the final approach trajectory for calculation of the orbit insertion maneuver commands. The last observation was made 37 h before arrival and incorporated in the orbit determination as quickly as possible. The updated estimate was then used to calculate updated insertion commands, which were transmitted to the spacecraft at 16 h before arrival. The updated estimate was in error by less than 10 km based on postflight analysis.

The insertion maneuver was extremely accurate. The lander accessible area was positioned within 0.1 deg of the ideal

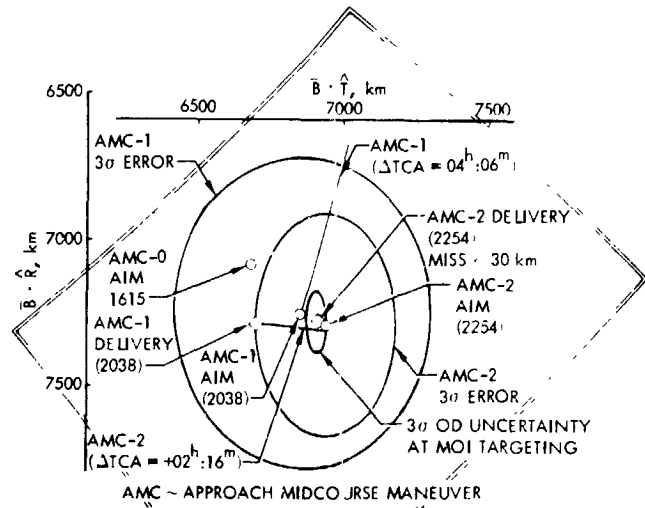


Fig. 17. Viking 1 Mars approach control

inertial location. The orbit period error was only 8 min; therefore, it was possible to attempt achieving the separation orbit directly with the single trim at Periapsis-2. The altitude was already well within tolerance at 1513 km. The initial orbit is contrasted with the separation orbit in Fig. 18.

The principal difficulty in directly achieving the separation orbit with the first trim was accurately predicting the timing offset at Periapsis-15. Because of uncertainties in the Mars gravitational harmonics the actual orbital period in each future revolution was rather unpredictable. However, the Mariner 9 derived gravity field proved to be very accurate, and after several revolutions of tracking, it was clear that the first trim had, in fact, perfectly acquired the primary landing site as illustrated in Fig. 19. It is seen that the primary site A1 at 34.0°W 19.5°N had been captured virtually in the center of the accessible area for a July 4 landing. Only 10 m/s of the 150 m/s navigation velocity budget was expended (to correct navigation errors) in acquiring the A1 site!

Several days before the last prelanding scheduled trim opportunity near Periapsis-11, the A1 site was abandoned because features observed in the site area implied hazardous terrain. A new site A1R about 100 km southeast of A1 was then considered. A trim was designed for the opportunity near Periapsis-11 to cause the A1R to “drift” to the center of the entry corridor for the July 4 landing. Lander descent trajectories were targeted to A1R for separation orbits with and without the trim. Before a decision was reached whether or not to trim before descending to A1R, it was decided that A1R was too hazardous and that a safer area probably existed to the northwest. Accordingly, a maneuver strategy was developed to start a westward migration with a period trim at

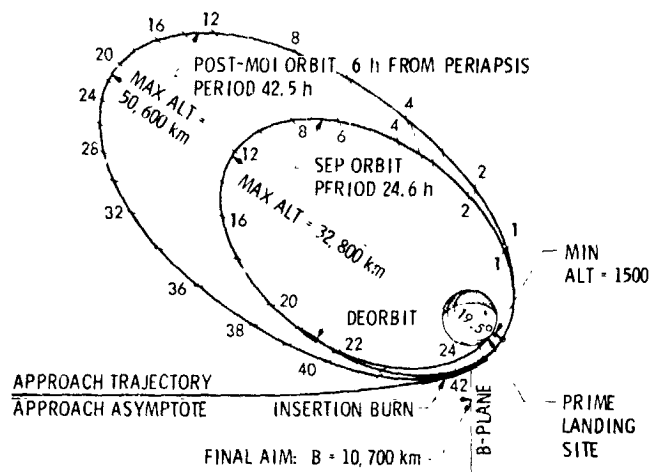


Fig. 18. Viking 1 Mars orbit insertion

Periaresis-16 followed by an orbit orientation trim near Periaresis-19 to move the accessible area as far north as prudent based on observations yet to be made. When it became clear prior to Periaresis-16 that the accessible area should be moved one degree north, the strategy was modified to combine the orientation adjustment and the start of the migration into the trim near Periaresis-19. The actual landing site was selected during the migration; its coordinates 47.5°W 22.4°N warranted resynchronizing the orbit at Periaresis-24. Thus the site was captured in the accessible area for a July 20 landing as shown in Fig. 19.

The orbit determination performance was exceptionally good throughout the entire site acquisition phase. For example, the time of Periaresis-19 was predicted within one second eight revolutions earlier. All three of the prelanding trims were executed so accurately that their errors were truly inconsequential.

The final Lander targeting resulted in a nominal entry flight path angle of -16.9° (only 0.1° from ideal), a 3.1-h coast time, and utilized a 156-m/s single-burn deorbit maneuver. The navigation parameters transmitted to the Lander computer 39 h before separation included attitude command matrices for deorbit, descent coast, preentry, and entry. The parachute deployment altitude, terminal descent ignition altitude, and the altitude-vs-velocity descent guidance profiles were set at the standard values. Following separation the Lander executed a flawless, autonomous descent as illustrated in Fig. 20. Fig. 21 presents the Viking 1 landing accuracy. Observe that the Viking 1 landed within 30 km of its target, which corresponds to a 1σ landing error. The Viking 2 landing accuracy of 10 km is also shown.

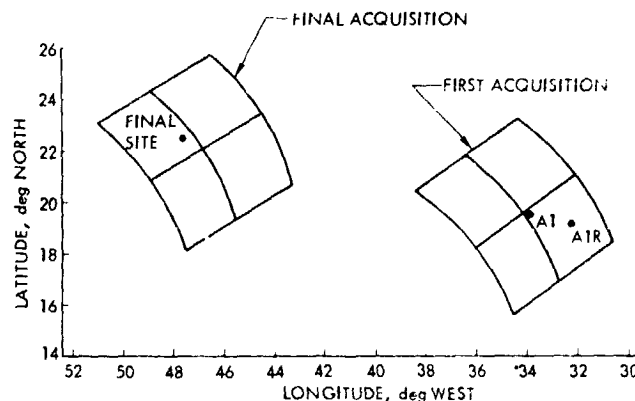


Fig. 19. Viking 1 actual site acquisitions

III. Viking 2 Inflight Synopsis

Viking 2 was launched by a Titan IIIE/Centaur launch vehicle on September 9, 1975, and targeted for a Mars arrival date of August 8, 1976. The 11-month journey to Mars is illustrated in Fig. 22. As with Viking 1, the launch aimpoint was biased to satisfy planetary quarantine requirements, to assure the first midcourse maneuver would exceed 2 mps, and to guarantee two-way communications during the first midcourse maneuver burn. Figure 23 shows this intentional biasing, the 99% launch vehicle dispersion ellipse and the early orbit determination history.

The crosses (+) in Fig. 23 indicate the orbit determination solutions obtained during the first few hours after launch. By 10 hours after launch, the orbit solutions had stabilized and further premidcourse solutions were clustered within the area indicated. The Viking 2 Centaur injection performance was approximately 2σ .

The first midcourse maneuver for Viking 2 was scheduled for 10 days after launch. A velocity change of approximately 8 mps was necessary to achieve the required final Mars encounter conditions. However, for reasons to be described, this first midcourse maneuver was targeted to a different set of Mars encounter conditions. This resulted in the necessity to execute a near Mars midcourse maneuver to achieve the required final Mars encounter conditions. Figure 24 illustrates these two sets of encounter conditions. The "target for MOI" point is the required final Mars encounter condition to establish the proper Mars orbit for landing site reconnaissance and landing. The "M/C1 target" is the aimpoint for the first midcourse maneuver.

Initial maneuver analysis indicated that the first midcourse maneuver could be targeted directly to the required final Mars encounter conditions while still satisfying the required plane-

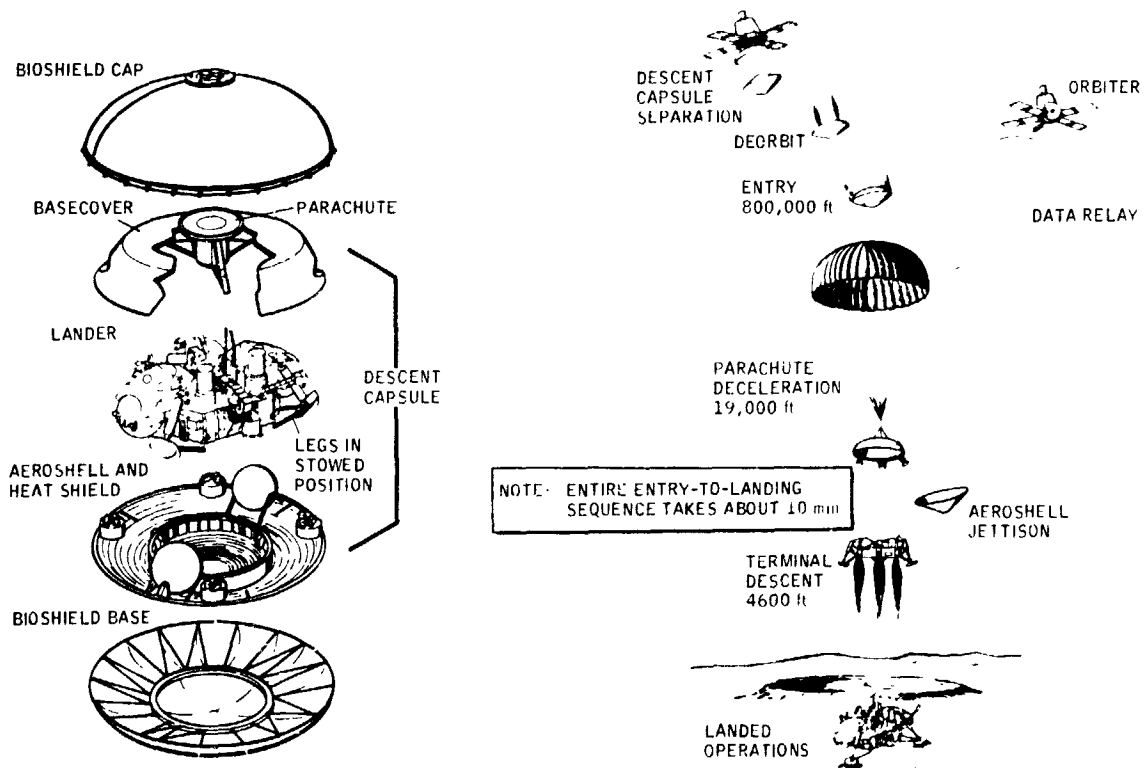


Fig. 20. Descent sequence

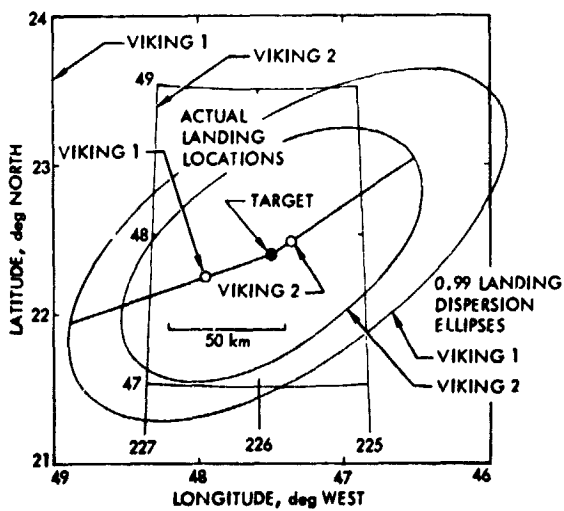


Fig. 21. Landing accuracy

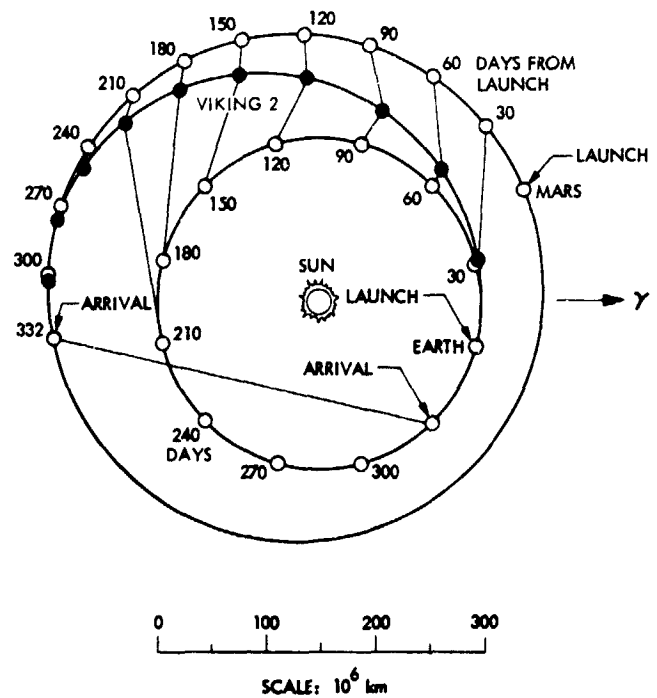


Fig. 22. Viking 2 heliocentric trajectory

ORIGINAL PAGE IS
OF POOR QUALITY

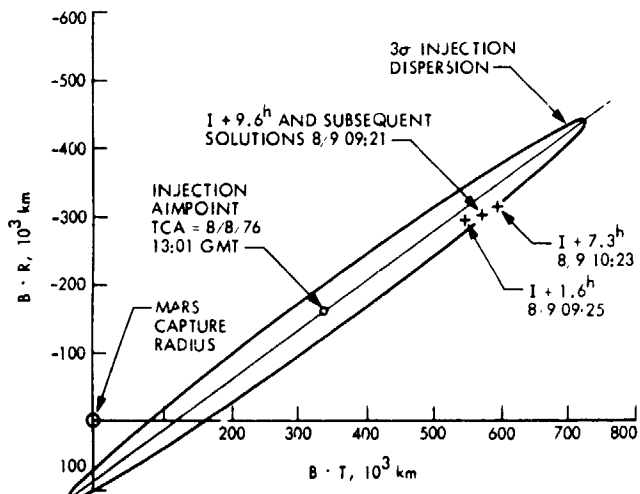


Fig. 23. Viking 2 launch accuracy

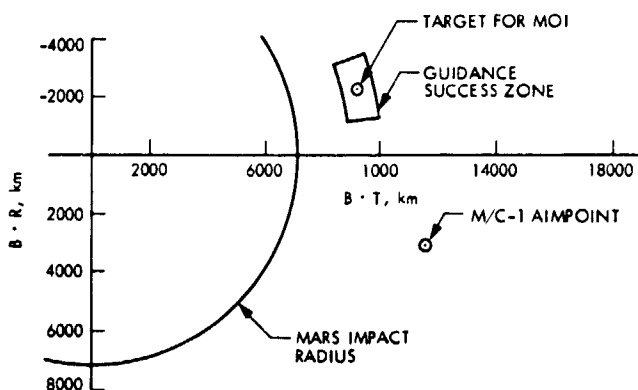


Fig. 24. Viking 2 midcourse aimpoints

tary quarantine probability of impact constraints. However, because of the size and orientation of the midcourse maneuver dispersion ellipse, this could result in the spacecraft being on a Mars impact trajectory following the execution of the maneuver. Should this be the case (approximately 20% probability, Fig. 25), a decision would have to be made to either (1) execute a second near-Earth midcourse maneuver to correct the execution errors of the first maneuver or (2) leave the spacecraft on the impact trajectory until Mars arrival, correcting the error with a near-Mars midcourse maneuver. Since it was almost a certainty that at least one Mars approach midcourse maneuver would be required in any event, and the ΔV penalty for biasing the near-Earth midcourse maneuver to avoid impact was relatively small (less than 5 mps), it was decided to bias the targeted Mars aimpoint. This biased aimpoint is indicated in Fig. 26 along with the midcourse

maneuver dispersion ellipse and its orbit determination and execution error components. The biased aimpoint was selected to (1) assure that the probability of being on an impact trajectory following the first midcourse maneuver execution was less than 1%, (2) maximize the ability to achieve a Mars orbit if the spacecraft could perform only the insertion maneuver but no more midcourse maneuvers, (3) assure that the Mars approach midcourse maneuver spacecraft attitude would provide communication in the burn attitude, and (4) minimize the additional ΔV expenditure resulting from the bias. The resulting ΔV for this near-Earth midcourse maneuver was 8.1 mps.

As with Viking 1, the major orbit determination error at the time of the maneuver was the uncertainty in the solar pressure force. After about a week of postmidcourse tracking it was clear that the actual maneuver execution error was indeed small and no further maneuvers would be required until Mars approach.

The navigation activities during the interplanetary cruise phase for Viking 2 were similar to those for Viking 1. Short-arc solutions were generated on a weekly basis including the previous three weeks' doppler and ranging data. These weekly trajectory estimates were used to prepare tracking predicts for the DSN stations providing mission support. Every three to four weeks a long-arc solution was generated including all of the doppler and range data after the near-Earth midcourse maneuver. Comparisons of these short- and long-arc solutions and the consistency of the solutions as the data arc increases provided the means for validating the orbit determination process and verifying the orbit determination models (e.g., station locations, solar pressure). These analyses combined with the Viking 1 cruise orbit determinations resulted in the adjustments to the solar pressure coefficients and the Australian tracking station locations.

The encounter operations began 40 days before Mars arrival. Extensive radio and optical tracking data processing was completed during this 40-day time period in support of a near-Mars midcourse maneuver 10 days before encounter and the Mars Orbit Insertion (MOI) maneuver. During the encounter operations phase, the optical navigation tracking schedule for Viking 2 differed from the Viking 1 schedule. For Viking 2, three sets of star-Mars-star triads were scheduled prior to the encounter-minus-10-day midcourse maneuver rather than the two sets for Viking 1. This allowed an early optical-only orbit determination for comparison with the radio and radio-plus-optical solutions, and was important for Viking 2 because of the concern over degraded radio tracking data as a result of increased solar plasma activity. This increased plasma activity was due to the smaller Sun-Earth spacecraft angle for Viking 2 (Viking 2 encounter occurred

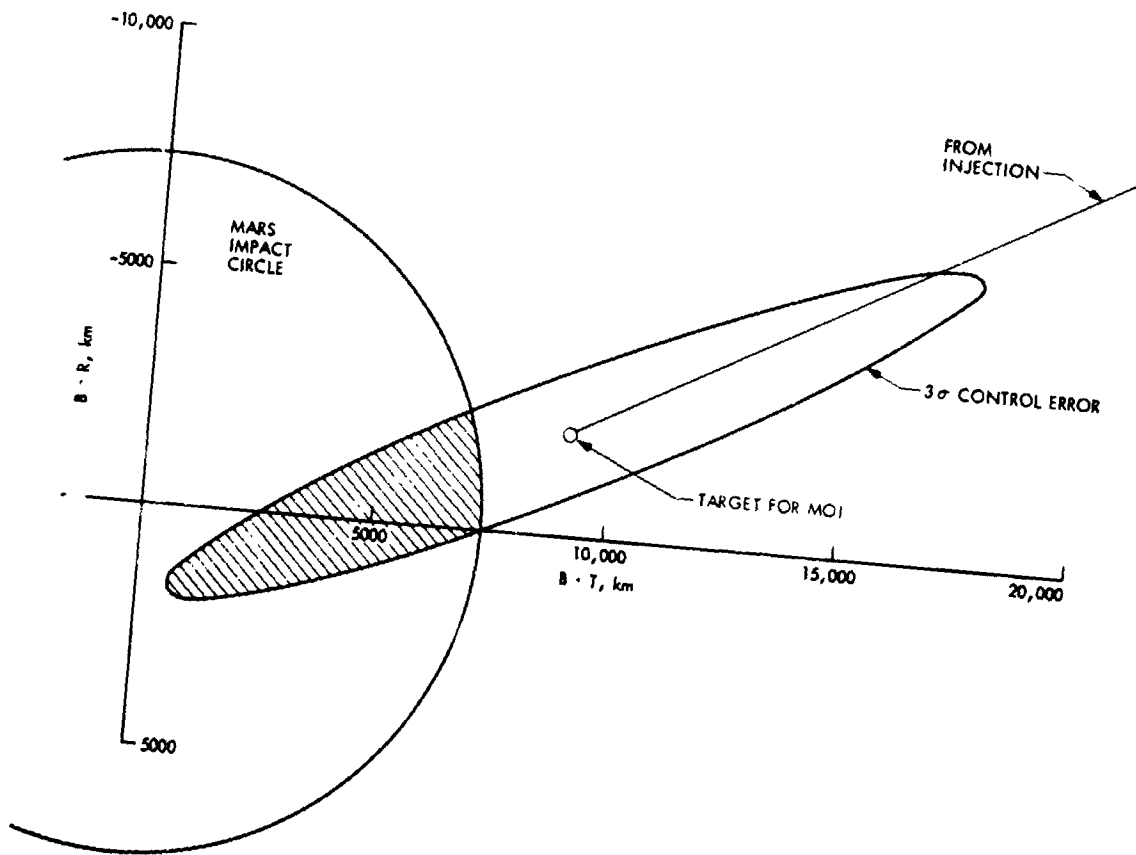


Fig. 25. Viking 2 unblended near-Earth midcourse maneuver

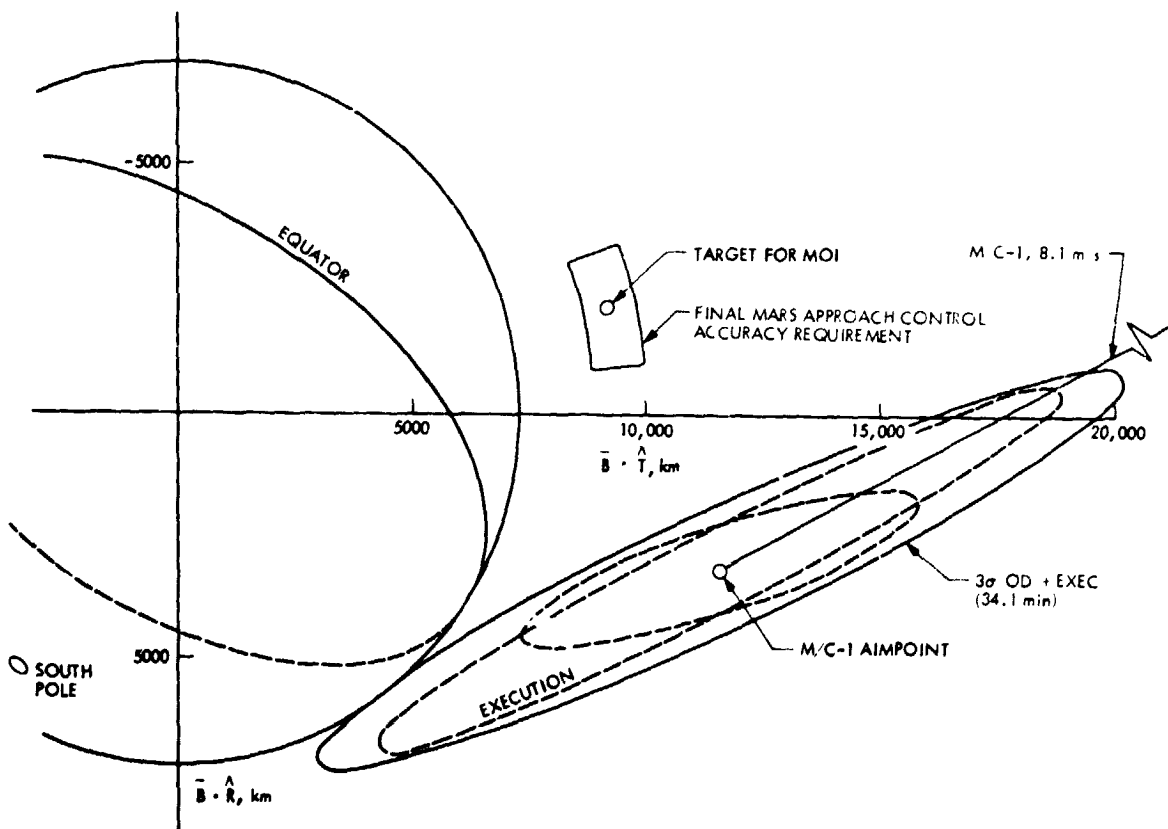


Fig. 26. Viking 2 Earth departure control

closer to solar conjunction than the Viking 1 encounter). In addition to the different optical navigation tracking schedule for Viking 2, revised long-arc radio tracking data processing procedures were implemented based on postencounter analysis of the Viking 1 radio data. These revised procedures resulted in much improved long-arc radio orbit determination solutions over the Viking 1 experience. These solutions exhibited close agreement with the short-arc radio only and radio-plus-optical solutions. The Viking 2 Mars approach midcourse maneuver was executed at encounter minus 10 days. The ΔV for this maneuver was 9.2 mps. Because of the pressure regulator problem on Viking 1, it was decided to delay repressurizing the orbiter propulsion system until as late as possible before MOI. As a result of this decision, the encounter-minus-10-day maneuver was performed in the "blowdown" mode. The propulsion system pressurization from the near-Earth maneuver was sufficient to allow the 9.2 mps near-Mars maneuver to be executed without additional pressurization. Figure 27 illustrates the near-Earth midcourse aimpoint and the achieved B-plane conditions, the difference being primarily a result of the solar pressure modeling error. Also shown is the Mars approach midcourse (AMC) maneuver targeted aimpoint, the achieved B-plane conditions and the final Mars approach control accuracy requirement zone.

Following the successful completion of the near-Mars midcourse maneuver, additional optical navigation observations consisting first of star-Mars-star triads and then Deimos-star single frames were acquired. These observations combined with continuous radiometric tracking data coverage were used to first confirm the midcourse maneuver execution accuracy and then to determine the maneuver parameters for the MOI maneuver. The preliminary MOI maneuver parameters were determined based on radio and optical tracking data to six

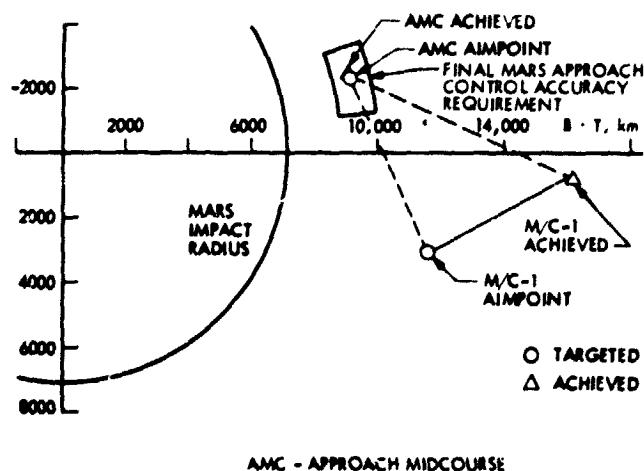


Fig. 27. Viking 2 midcourse targeted and achieved aimpoints.

days before encounter. As a result of the excellent Viking 2 approach orbit determination performance, the planned maneuver update at 16 hours before encounter was not required. Post-encounter trajectory reconstruction verified the B-plane error of less than 40 km for the encounter-minus-6-day orbit determination.

Because of the pressure regulator leak experience on Viking 1, the pyro-valve for repressurizing the fuel and oxidizer tanks for Viking 2 was not fired until about 13 hours before MOI. This was accomplished without incident, and although a small leak was indicated after the repressurization it was not a factor in the orbit insertion operations.

The MOI maneuver was accomplished on August 7, 1976, placing the spacecraft in a Mars orbit inclined 55.2 deg to the equator, with a periapsis altitude of 1519 km and a period of 27.623 hours. These parameters compare with the targeted values of 55.0 deg, 1500 km and 27.414 h. The dispersion from the targeted values were all within the expected tolerances.

The target orbit period of 27.414 h for the post-MOI orbit was selected to allow a landing site survey to be conducted over 360 deg in longitude between the latitudes of 40 and 50 deg north prior to landing site selection. With the super-synchronous orbit the spacecraft progressively "walked" around the planet in 40-deg steps. At each periapsis passage, low-altitude observations of a region of the planet displaced 40 deg from the previous periapsis passage could be obtained. This provided the opportunity to evaluate two of three specified potential landing areas for VL-2. These three potential landing areas were in the longitude regions of B1 (345 to 15°W), B2 (90 to 140°W) and B3 (200 to 270°W). While VO-2 surveyed the B2 and B3 sites, the B1 site was surveyed with VO-1 from its synchronous orbit over the VL-1 landing site. Figure 28 illustrates the inertial ground tracks of the two Viking orbiters.

Because of the +12-min orbit period error, the orbit was "walking" around the planet at a rate approximately 2.9 deg per revolution faster than desired. That is, at each periapsis passage the spacecraft was progressively 2.9 deg further west from the nominal plan. In order to eliminate the effect of this orbit period error and regain the nominal timeline and landing site survey profile, a trim maneuver strategy employing maneuvers on revs 2 and 6 was executed. The first of these maneuvers reduced the orbit period by approximately 19 min; the second maneuver resulted in an orbit with the nominal orbit period. Thus, between revs 2 and 6 the orbit was "walking" at a rate approximately 1.5 deg per revolution less than desired. When the maneuver on rev 6 was completed, the effect of the initial orbit period error had been nullified. This

VO 1 & VO 2
GROUNDTRACKS
SEPTEMBER 3, 1976
(VIEWED FROM 30°
ABOVE THE SUN).

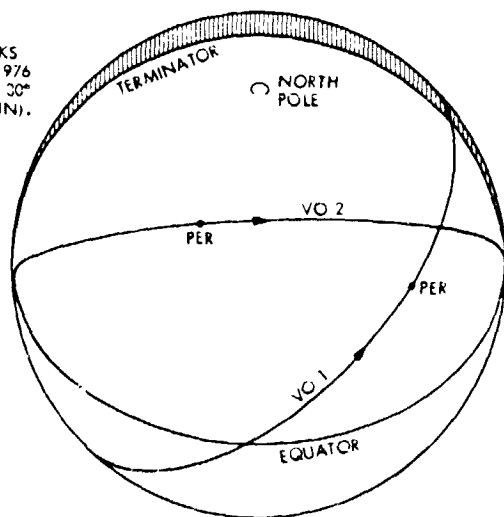


Fig. 28. VO 1 and VO 2 ground tracks

strategy provided reconnaissance of the B2 region on revs 4 through 8 and the B3 region on revs 9 through 11. In addition to correcting the orbit period, the periapsis altitude was also corrected to the desired 1500 km.

The orbit geometry and nature of the trajectory corrections to be made resulted in an opportunity to execute these maneuvers in a unique manner with some definite advantages. It was found that each of these maneuvers could be executed while maintaining a Sun-Canopus acquired spacecraft attitude. This had the advantage of eliminating the usually necessary spacecraft turns to achieve the burn attitude. By eliminating these turns, the inherent spacecraft risk in leaving the celestial references was avoided as well as the possible need for the spacecraft going into a battery share mode if the yaw turn positioned the solar panels too far from the sunline. The major navigation advantage, however, was the reduction in the pointing contribution to the maneuver execution errors and the resulting increased orbit control accuracy. The maneuvers on revs 2 and 6 were successfully executed in this Sun-Canopus acquired attitude, a technique that was used a number of times throughout the remainder of the mission operations.

The orbit period established with the trim maneuver on rev 6 resulted, as designed, in the spacecraft being in the middle of the B1 landing region when it passed through the PER point (the center of the accessible area; see Fig. 5) on rev 19. If the selected landing site had been in the B1 region, a trim maneuver on rev 19 would have been performed to acquire the final landing orbit with the sync maneuver occurring on rev 21. However, reconnaissance data indicated that both the B1 and B2 regions were too hazardous.

Accordingly, an area was selected in the B3 region specified as $48.0^{\circ}\text{N} \pm 1.5^{\circ}$ areographic latitude and $226.0^{\circ}\text{W} \pm 2.0^{\circ}$ longitude.

In order to establish the separation orbit to reach this landing region, trim maneuvers near periapsis on revs 16 and 18 were planned, with landing to occur near periapsis on rev 25. Since the landing site was currently specified as a region and not a point, the maneuver strategy was to "center" the separation orbit such that (1) VL entry flight path angle changes could be used for down-track adjustments and (2) VL cross ranging could be used for out-of-plane adjustments. Fig. 29 illustrates this alignment of the lander accessible area and the specified landing region.

In order to center the lander accessible area within the specified landing region, an increase in latitude of the PER point was required. This was combined with the orbit period changes necessary to establish the proper spacecraft landing site time-space relationship. MOT 3, executed on rev 16, decreased the orbit period by 3 h 21 min and increased the latitude of PER by 1.5 deg. MOT 4 executed on rev 18 increased the orbit period to be Mars synchronous and further increased PER latitude by 0.3 deg. These two trim maneuvers were also executed while maintaining Sun/Canopus acquisition, providing the benefit of reduced maneuver execution errors.

Satellite orbit determination activities during this time period consisted of generating both short-arc (single rev) and long-arc (multi-rev) solutions. The Viking 2 supersync orbit

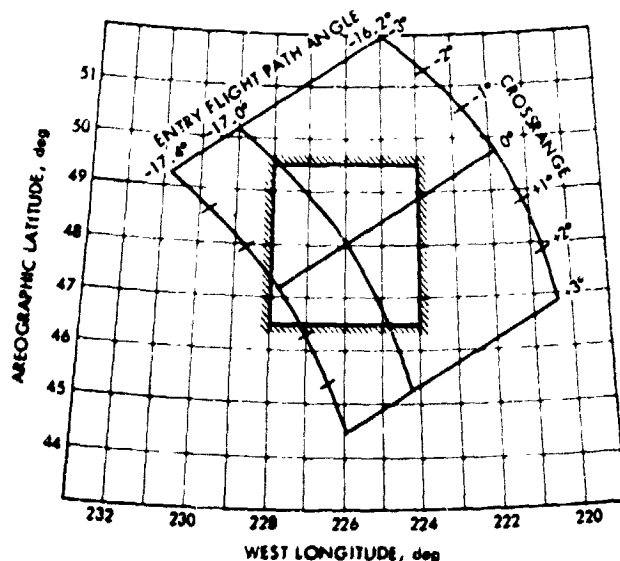


Fig. 29. Viking 2 landing region

period, while providing data for updating the Mars gravity field, made prediction less accurate than Viking 1 because of the varying terrain at each periapsis passage. This increased the importance of late updates to key site certification observations and trim maneuvers. After the MOT 4 sync maneuver was executed the prediction capability improved to the same level as that achieved with Viking 1.

At separation minus 84 hours, the final landing site location was selected - 225.9°W and 47.9°N. Lander deorbit and descent parameters were then determined and transmitted to the spacecraft at separation minus 39 hours. Landing occurred near periapsis on rev 25, September 3, 1976. Lander targeting to achieve this landing site consisted of an entry angle of -17.0 deg and a cross range of 0.1 deg. The coast time was 3.1 hours and the Lander lead angle at the time of entry was 20 deg.

At Lander separation, an anomaly in the Orbiter attitude control system caused a loss of the Orbiter's roll reference.

This resulted in the loss of the real-time Lander telemetry during descent because of the off-Earth pointing of the orbiter high-gain antenna. Fortunately, in accordance with the nominal plan, the Lander-to-Orbiter relay data were recorded on the Orbiter tape recorder and played back after landing when the Orbiter roll attitude was reestablished. During the time period when real-time telemetry was not available, Lander events were monitored by observing the changes in the relay link reception. These changes were monitored on the ground via the Orbiter engineering low-rate channel transmitted over the Orbiter low-gain antenna.

Reconstruction of the Lander trajectory following the Orbiter replay of the Lander relay data confirmed near nominal performance with a landing accuracy of 10 km. This was illustrated in Fig. 21 along with the 99% landing dispersion ellipse.

References

1. Soffen, G. A., et al., "Scientific Results of the Viking Project," *Journal of Geophysical Research*, Vol. 82, No. 28 Sept. 30, 1977, American Geophysical Union, Washington, D. C., Library of Congress No. 77-23719.
2. Koskela, P. E., *Viking Orbiter Picture Catalog*, Jet Propulsion Laboratory, Pasadena, Calif. (in press).
3. Robins, C. H., Jr., "Viking Flight Team Organization and Staffing," M75-150-5, Jet Propulsion Laboratory, Pasadena, Calif., June 23, 1976 (an internal document).

Appendix

Definitions of Terminology

A/S	aeroshell	IPL	Image Processing Laboratory
ACS	Attitude Control System	IPODT	Interplanetary Orbit Determination Team
AGC	automatic gain control	IR	infrared
AMC	approach mid-course	IRTM	infrared thermal mapper
APF	argument of periapsis	IRU	inertial reference unit
ATBS	accelerometer thermal bias shift	ISDR	Intermediate System Data Record
BER	bit error rate	JPL	Jet Propulsion Laboratory
CA	in-plane pointing angle	kbps	kilobits per second
CBE	current best estimate	L/D	lift-to-drag ratio
CD	drag coefficient	LAN	longitude of ascending node
CL	lift coefficient	LATPER	latitude of PER
CLA	out-of-plane pointing angle	LATS	lander trajectory simulation
CMD	command	LCAST	Lander Command and Sequencing Team
CMSOE	command sequence of events	LFPAT	Lander Flight Path Analysis Team
DECSET	downlink decommutation and decalibration set	LGA	low gain antenna
DN	data number	LPAG	Lander Performance Analysis Group
DPODP	Double Precision Orbit Determination Program	LRC	Langlely Research Center
DPT	Data Processing Team	LS	landing site
DPTRAJ	Double Precision Trajectory Program	LSG	Lander Science Group
DR	downrange	LSO	Lander Support Office
DRVID	differenced range versus integrated doppler	LSS	Landing Site Staff
DSG	Data Support Group	LTARP	Lander Trajectory and Atmosphere Reconstruction Program
DSN	Deep Space Network	LTOP	Lander Targeting Operations Program
DSS	Deep Space Station	LTR	lander trajectory reconstruction
E	encounter	M	Mach number
E	entry	M/C	midcourse
EDR	Experiment Data Record	MAWD	Mars atmospheric water detector
EEM	emergency early maneuver	MCCC	Mission Control and Computing Center
EMA	emission angle	MCCF	Mission Control and Computing Facility
EME	Earth mean equator	MCD	Mission Control Directorate
ERT	Earth received time	MCR	midcourse correction required
ESLE	equivalent station location error	MDR	Master Data Record
EXEC	execution	MEQ	Mars mean equator
FCG	Flight Control Group	MLVA	master list of Viking anomalies
FOV	field of view	MMOP	Midcourse Maneuver Operations Program
FPAG	Flight Path Analysis Group	MOI	Mars orbit insertion
GCSC	Guidance Control and Sequencing Computer	MOIOP	Mars Orbit Insertion Operations Program
GDS	Ground Data System	MOT	Mars orbit trim
GMT	Greenwich Mean Time	MOTOP	Mars Orbit Trim Operations Program
GRE	ground-reconstruction equipment	MPG	Mission Planning Group
HGA	high gain antenna	MPS	mission profile strategy
I	inclination	MSL	mean surface level
I	injection	MTCF	Mission Test Computing Facility
IC	initial conditions	MTVS	Mission and Test Video System
ICL	initial computer load	OD	orbit determination
INA	incidence angle	ODP	Orbit Determination Program
INC	inclination	OIT	Orbiter Imaging Team
IPF	Image Processing Facility		

OMATT	Orbiter Maneuver and Trajectory Team	SEP	Sun-Earth-Probe
OMSET	optical measurement set	SKT	station keeping time
ONP	Optical Navigation Program	SMA, SMMA	semi-major axis
OPAG	Orbiter Performance Analysis Group	SMB, SMIA	semi-minor axis
OSCOT	Orbiter Spacecraft Operations Team	SNR	signal-to-noise ratio
OSG	Orbiter Science Group	SOE	sequence of events
OSST	Orbiter Science Sequence Team	SOL	Mars day
OWLT	one way light time	SPFPAD	Spacecraft Performance and Flight Path Analysis Directorate
P/B	playback	SPM	shadow prediction model
PAO	Public Affairs Office	SSG	Science Steering Group
PCR	Profile Change Request	STL	science test lander
PDT	Pacific daylight time	TCA	time of closest approach
PER	true anomaly of landing site with respect to VO separation orbit	TD	touchdown
PFR	Problem Failure Report	TDCT	Tracking Data Conditioning Team
PMC	Problem Management Center	TDLR	terminal descent and landing radar
PP	post processor	TIGN	time of ignition
PQ	planetary quarantine	TM	telemetry
PREDIX	DSN Prediction System	TSAC	tracking system analytic calibration
PREPR	preprocessor for lander trajectory reconstruction	TSEP	time of separation
PSA	partial step algorithm	UAMS	upper atmosphere mass spectrometer
PTC	Proof Test Capsule	UTC	Universal Time Coordinated
PVRA	path-vary-regress-accum	VCSF	Viking Control and Simulation Facility
q	dynamic pressure	VDL	Viking Data Library
Q	heat load	VFT	Viking Flight Team
\dot{Q}	heating rate	VIS	Visual Imaging Subsystem
QSS	quasi-statistical sum	VISA	Viking Incident, Surprise, or Anomaly Report
RA	right ascension	VL	Viking Lander
RCA	radius of closest approach	VLBI	very long baseline interferometry
RCM ^P	reconstituted mission profile	VLC	Viking Lander Capsule
RCS	Reaction Control System	VMCCC	Viking Mission Control and Computing Center
RDR	Reduced Data Record	VMCOE	Viking modified classical orbital elements
RLINK	Post Landing Relay Link Program	VO	Viking Orbiter
RPA	retarding potential analyzer	VPSS	Viking Project Simulation System
RSI	radio science investigation	XR	crossrange
RTI	real-time imaging	α	angle of attack
S.SEP	separation	β	angle of sideslip
SAMPD	Science and Mission Planning Directorate	γ	flight path angle
SATODT	Satellite Orbit Determination Team	γ_E	flight path angle at entry
SEA	Sun elevation angle	ΔV	velocity increment
SEAPER	Sun elevation angle at PER	ψ	apsidal rotation
SEDR	Supplementary Experiment Data Record	θ	aiming angle in B-plane

Trajectory Description

D. L. Farless, L. H. Dicken, and R. E. Diehl

I. Launch Phase

The two Viking '75 spacecraft were launched by Titan IIIE booster vehicles with Centaur D-1T high-energy upper stages. The two launch vehicles were the third and fourth Titan/Centaur combinations to be launched and were designated as vehicles TC-3 and TC-4. The launch trajectories utilized a parking orbit coast phase between two Centaur thrusting phases. Both launches were conducted from Launch Complex LC-41 at the Air Force Eastern Test Range.

Viking 1 was successfully launched on August 20, 1975, after a nine-day delay. The delay was caused, first, by failure of a thrust-vector-control valve in one of the Titan solid rocket boosters and later by a discharged battery on the Viking Orbiter (VO) which necessitated replacement of the entire spacecraft with the second spacecraft. Liftoff came at 21 h 22 min 0.6 s GMT, only 0.6 s after the nominal open-window launch time for this day. Launch azimuth was 96.57 deg, and the required Centaur parking orbit coast time was 15 min 20 s. Table 1 shows the nominal and actual Mark Event times for the Viking 1 launch.

Viking 2 was launched 20 days later on September 9, 1975, after several days of delay because of trouble with the orbiter's S-band radio subsystem. Liftoff came at 18 h 39 min 0 s, once again right on the open-window launch time at an azimuth of 96.51 deg. Nominal and actual Mark Event times for this

launch are presented in Table 2. Nominal Centaur parking orbit coast time for this launch was 18 min 13 s.

Both launches were essentially nominal, well within expected dispersions. Table 3 presents post-separation geocentric orbit elements for both spacecraft. These data are

Table 1. Viking 1 launch trajectory mark event list

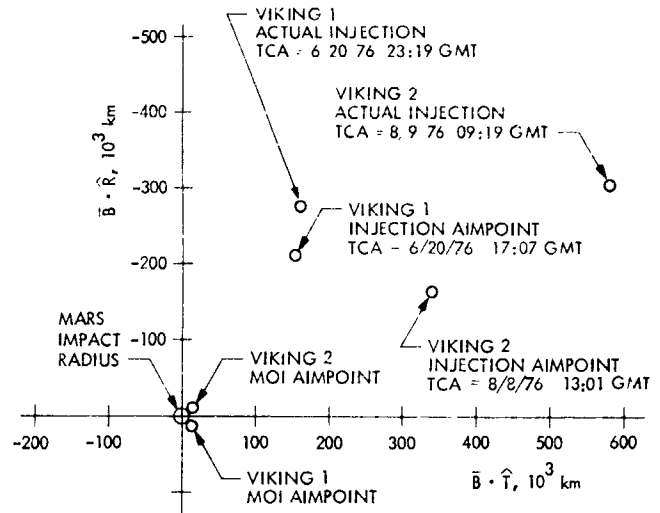
Mark	Event	Nominal time	Actual time
0	Launch	21:22:00	21:22:00.6
1	Heat shield jettison	21:23:40	21:23:40.2
2	Stage I ignition	21:23:51	21:23:51.0
3	Stage I/O separation (jettison SRM)	21:24:02	21:24:01.9
4	Stage I shutdown	21:26:16	21:26:19.7
5	Stage I jettison	21:26:17	21:26:20.4
6	Stage II ignition	21:26:17	21:26:20.3
7	Jettison Centaur standard shroud	21:26:28	21:26:32.3
8	Stage II shutdown	21:29:40	21:29:40.9
9	Stage II jettison	21:29:46	21:29:54.6
10	Centaur first main engine start (MES1)	21:29:56	21:30:05.9
11	Centaur first main engine cutoff (MEC01)/park orbit insertion	21:32:03	21:32:11.6
12	Centaur second main engine start (MES2)	21:47:23	21:47:33.0
13	Centaur second main engine cutoff (MEC02)	21:52:44	21:52:48.0

Launch date: 8/20/75
 Launch time: 21:22:00
 Arrival date: 6/19/76

Table 2. Viking 2 launch trajectory mark event list

Mark	Event	Nominal time	Actual time
0	Launch	18:39:00	18:38:59.96
1	Heat shield jettison	18:40:40	18:40:40.0
2	Stage I ignition	18:40:51	18:40:52.0
3	Stage I/O separation (jettison SRM)	18:41:02	18:41:07.9
4	Stage I shutdown	18:43:16	18:43:21.0
5	Stage I jettison	18:43:17	18:43:21.6
6	Stage II ignition	18:43:17	18:43:21.8
7	Jettison Centaur standard shroud	18:43:28	18:43:33.3
8	Stage II shutdown	18:46:40	18:46:50.0
9	Stage II jettison	18:46:46	18:46:53.2
10	Centaur first main engine start (MES1)	18:46:56	18:47:05.1
11	Centaur first main engine cutoff (MEC01)/park orbit insertion	18:49:09	18:49:13.2
12	Centaur second main engine start (MES2)	19:07:22	19:07:27.0
13	Centaur second main engine cutoff (MEC02)	19:12:25	19:12:27.8

Launch date: 9/9/75
 Launch time: 18:39:00
 Arrival date: 8/7/76



NOTE: TCA IS TIME OF CLOSEST APPROACH ON THE HYPERBOLA

Fig. 1. Targeted and achieved injection aimpoints for Viking launches

Table 3. Orbital data
 (Earth mean equator and equinox of 1950.0 coordinate reference)

Parameter	Post-separation geocentric orbit elements		Injection orbit elements from launch polynomials	
	Viking 1	Viking 2	Viking 1	Viking 2
Epoch, GMT	8/20/75, 21:52:43.4	9/9/75, 19:12:24.0	8/20/75, 21:52:44	9/9/75, 19:12:25
Periapsis radius, km	6,561.0	6,557.1	6,562.7	6,558.8
Semi-major axis, km	-18,842.2	-26,502.4	-18,849.7	-26,466.1
Eccentricity	1.3482	1.2474	1.3482	1.2478
Inclination, deg	29.29	29.31	29.34	29.39
Longitude of ascending node, deg	104.48	83.56	104.40	83.52
Argument of periapsis, deg	-159.71	-148.66	-159.66	-148.64
Time past periapsis, s	136.9	130.9	138.6	134.6
Trajectory energy, km ² /s ²	21.155	15.040	21.146	15.061
Declination of outgoing asymptote, deg	-10.48	-2.63	-10.47	-2.63

based on the best orbit estimates obtained prior to the near-Earth midcourse maneuver on each spacecraft. For comparison, the injection orbit elements, based on the nominal launch polynomials, are included in Table 3. Figure 1 is a display of the injection targets and actual achieved injections in the B-plane. Also shown are the final targets required for the nominal Mars Orbit Insertion (MOI). The injection aimpoints were biased away from these MOI aimpoints to insure that planetary quarantine (PQ) requirements were met in consideration of expected launch vehicle dispersions, to guarantee a minimum required ΔV for the first maneuver, and to insure that the spacecraft attitude for the first maneuver would allow real-time communications during the burn.

II. Interplanetary Phase

A. Heliocentric Orbit Description

The two Viking spacecraft were inserted into Type II Class II interplanetary trajectories from Earth to Mars. That is, they traversed more than 180 deg of true anomaly from launch to encounter and arrival occurred after apoapsis of the transfer orbit. Plots of the two trajectories are shown in Figs. 2 and 3, along with positions of the Earth and Mars. The pre-near-Earth midcourse maneuver heliocentric orbit elements for the two Viking interplanetary trajectories are presented in Table 4. The epochs of these conditions are the times of the first midcourse maneuvers. The total central angle traveled

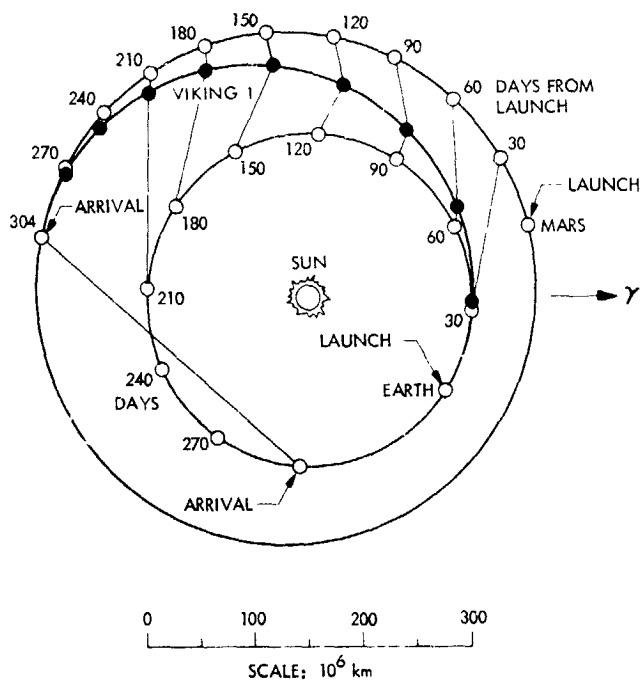


Fig. 2. Viking 1 heliocentric trajectory

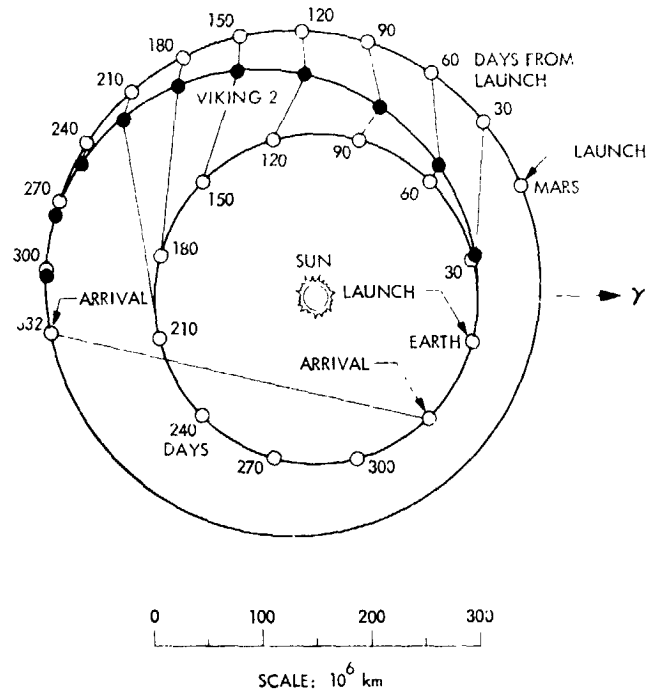


Fig. 3. Viking 2 heliocentric trajectory

Table 4. Heliocentric orbit elements
(Earth mean orbit plane and equinox of 1950.0 coordinate reference)

Parameter	Pre-midcourse		Post-midcourse	
	Viking 1	Viking 2	Viking 1	Viking 2
Epoch, GMT	8/27/75, 18:30:00	9/19/75, 16:30:00	8/27/75, 19:59:12	9/19/75, 6:59:12
Periapsis radius, km	149.778×10^6	150.584×10^6	149.779×10^6	150.58×10^6
Semimajor axis, km	199.644×10^6	200.168×10^6	199.728×10^6	200.29×10^6
Eccentricity	0.24978	0.24771	0.25008	0.24813
Inclination, deg	4.48	2.92	4.48	2.92
Longitude of ascending node, deg	146.72	165.82	146.72	165.83
Argument of periapsis, deg	198.70	185.02	198.68	184.97
Time past periapsis, days	-10.0899	5.5947	-10.0076	5.6439

from launch to encounter for Viking 1 was 201 deg in 304 days and for Viking 2 was 203 deg in 332 days.

Launch occurred on the descending node of the transfer orbit in each case, so the majority of the trajectory was flown below the ecliptic plane but encounter with Mars was above the ecliptic plane. It is interesting to note that, although Viking 1 was launched first and encountered Mars first, Viking 2 actually passed Viking 1 and reached the orbit of Mars first. Mars having not yet arrived at this point in its orbit, Viking 2 continued on to apoapsis of its heliocentric orbit before encountering Mars on the way back toward the Sun. Meanwhile, Viking 1 was overtaken near apoapsis of its heliocentric ellipse by the faster moving Mars.

B. Near-Earth Midcourse Maneuver Effects

Both Viking launches required that the aimpoint at Mars be biased away from the planet. For this reason, at least one midcourse (M/C) maneuver, executed shortly after launch, was mandatory. For both spacecraft, one near-Earth M/C, 7 to 10 days after launch, was sufficient to meet all mission requirements. In the case of Viking 2, the M/C maneuver was also biased away from the desired final target as discussed in *Maneuver Analysis*. Figure 4 is a sketch of the B-plane at Mars showing the achieved post-M/C encounter points along with the targeted aimpoints for the M/C designs. Table 4 lists the post-M/C heliocentric orbit elements for Viking 1 and Viking 2. These are the best estimates of the two-body interplanetary orbits for the two Viking spacecraft.

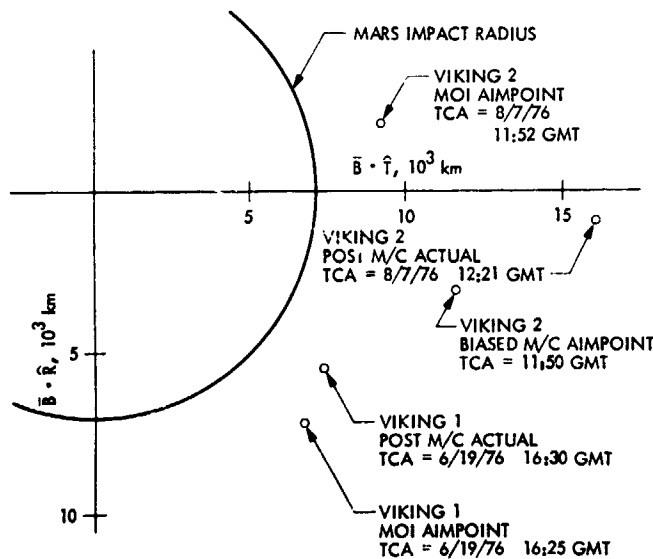


Fig. 4. Targeted and achieved midcourse maneuver aimpoints for Viking

C. Solar Pressure Effects

The effect of solar radiation pressure acting on the Viking spacecraft throughout the interplanetary phase of the trajectories is to cause a change in the encounter point relative to Mars of about 20,000 kilometers. This effect was allowed for in targeting the launches and the near-Earth M/C maneuvers by calculating the solar pressure effects using the best estimate of the solar radiation constant and the dimensions of the spacecraft. However, several months into the mission, solution for actual solar pressure effects indicated modification to the spacecraft solar pressure model to allow for solar radiation impingement in areas of the spacecraft not previously included in the model. These changes caused the encounter points for both spacecraft to move by about 1000 km relative to Mars.

D. Interplanetary Trajectory Data

Time history plots of several parameters relative to the interplanetary trajectories are presented in Figs. 5 through 10 for Viking 1 and in Figs. 11 through 16 for Viking 2. In each case, the first two figures plot geocentric range and range rate, the next two figures plot geocentric declination and right ascension (relative to Earth equator and equinox of 1950.0), and the last two figures plot heliocentric and areocentric range. All data are plotted against calendar date.

III. Encounter Phase

Only one encounter phase M/C maneuver was planned for Viking 1, to take place 10 days before encounter. However, a leaking pressure regulator valve was encountered when the pyrotechnic squib valve, which sealed off the high pressure gas supply during cruise, was opened shortly before the maneuver. To reduce the pressure accumulating in the propellant tanks, two M/C maneuvers were executed, one on June 10, 1976, at 11:00 GMT, about 10 days before encounter and another on June 15 at 14:00 GMT, about 4 days before encounter. Since these maneuvers had to be large — about 50 meters/second — to achieve the required reduction in propellant tank pressure, they were used to reduce the Mars-relative velocity of the spacecraft. This delayed the arrival time by a total of over 6 hours and also decreased the required MOI maneuver ΔV .

Table 5 presents areocentric encounter orbit elements for Viking 1 before the approach midcourse maneuvers and after each of the two maneuvers. The changes in the encounter orbit geometry were dictated by changing MOI requirements as detailed in the *Maneuver Analysis* chapter of this document.

Viking 2 required only one encounter phase M/C maneuver — the leaky valve problem was precluded by waiting until shortly before MOI to open the squib valve and doing the

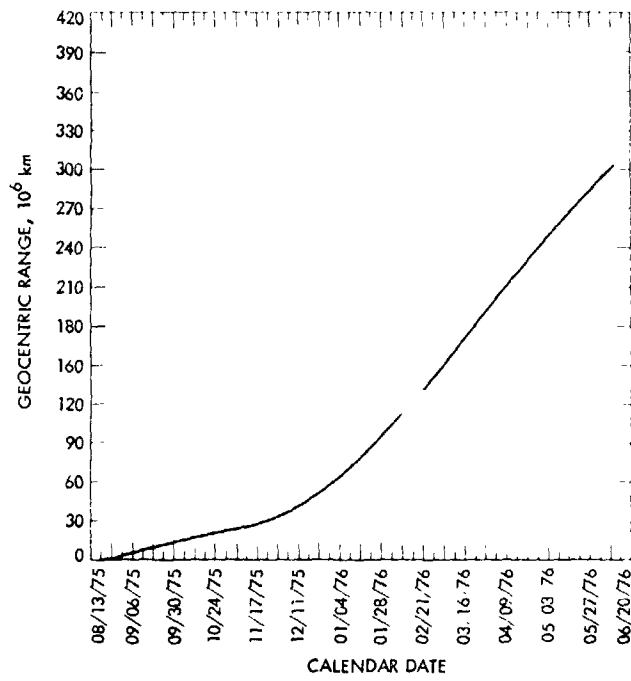


Fig. 5. Viking 1 geocentric range

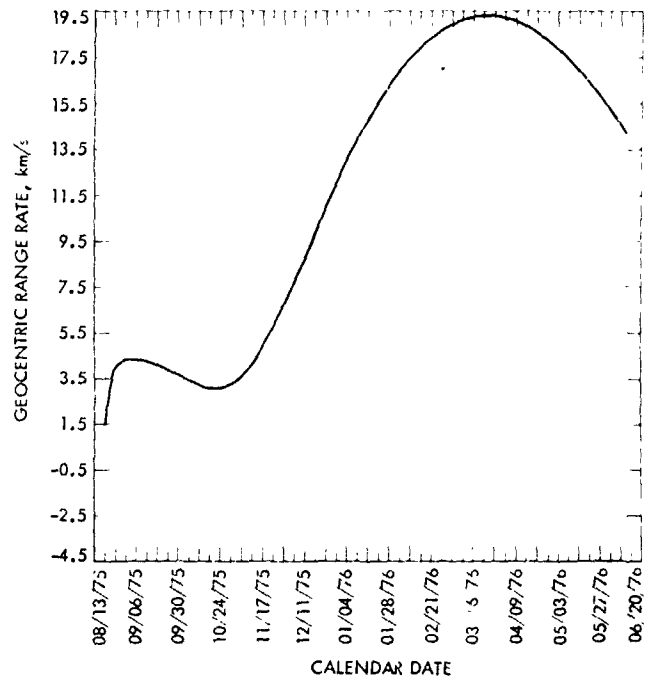


Fig. 6. Viking 1 geocentric range rate

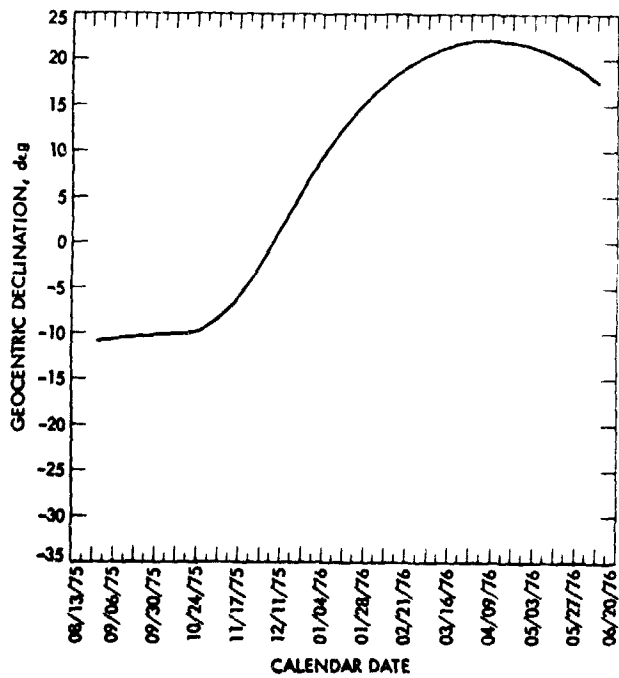


Fig. 7. Viking 1 geocentric declination

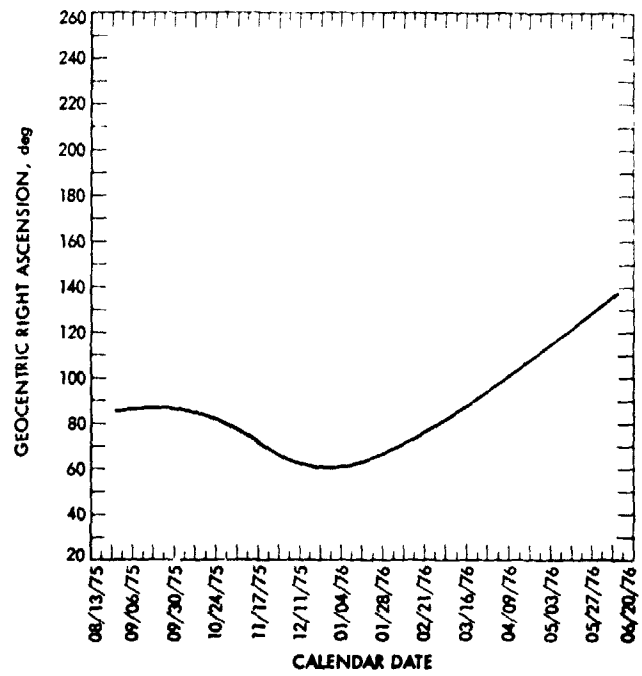


Fig. 8. Viking 1 geocentric right ascension

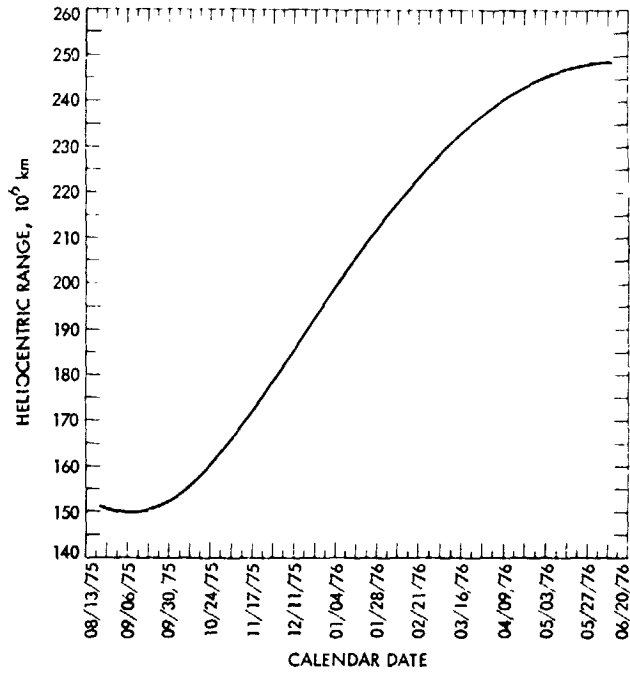


Fig. 9. Viking 1 heliocentric range

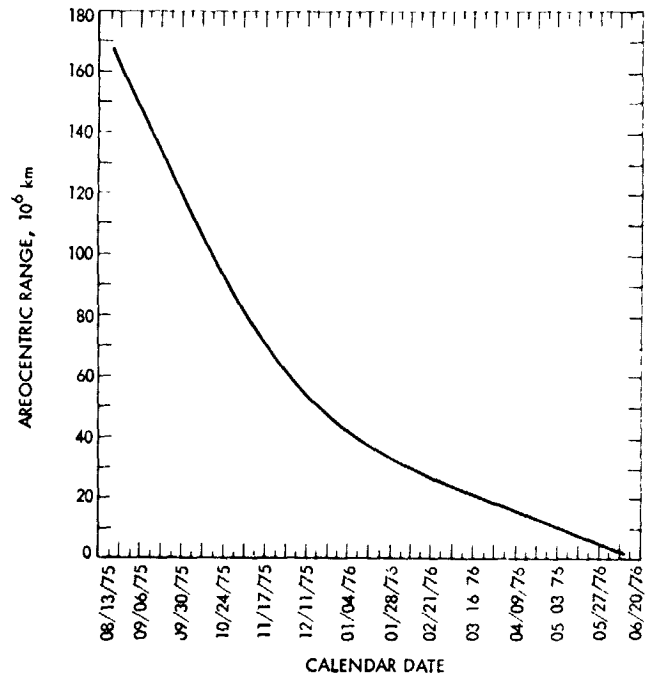


Fig. 10. Viking 1 areocentric range

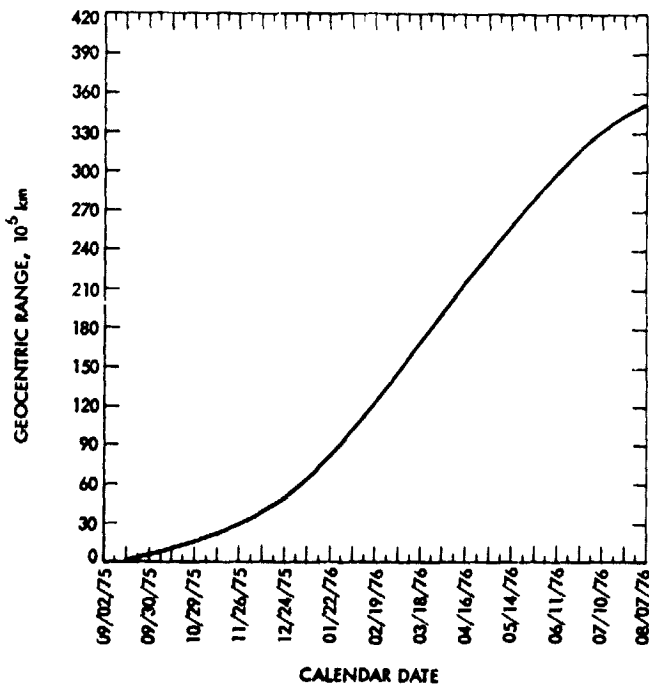


Fig. 11. Viking 2 geocentric range

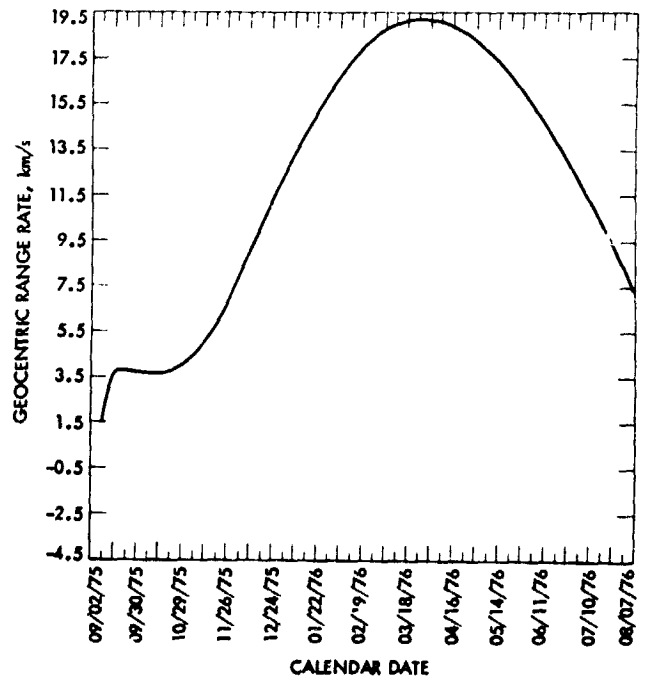


Fig. 12. Viking 2 geocentric range rate

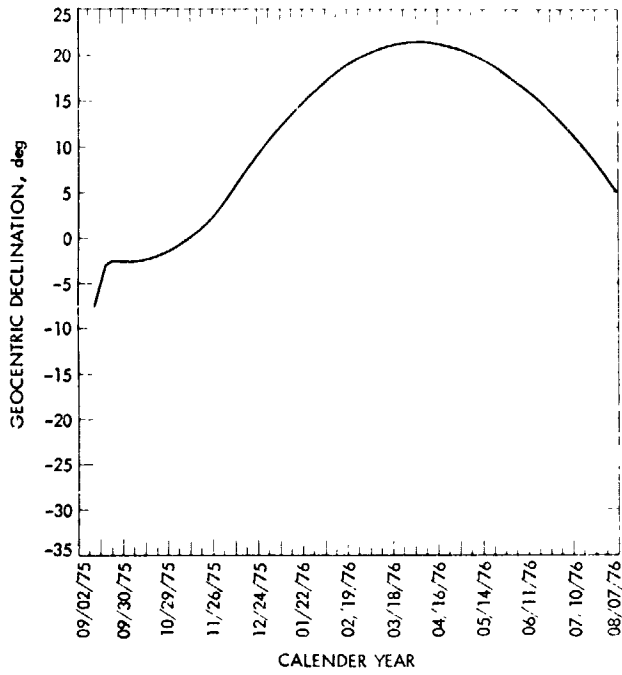


Fig. 13. Viking 2 geocentric declination

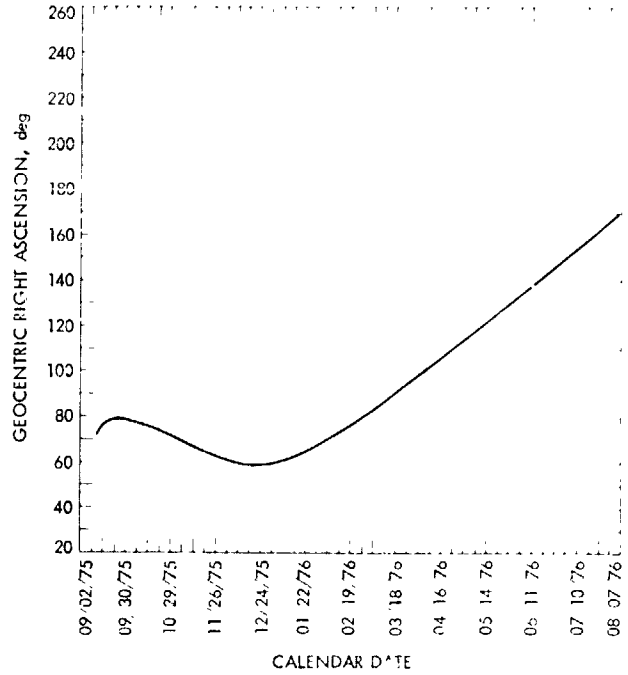


Fig. 14. Viking 2 geocentric right ascension

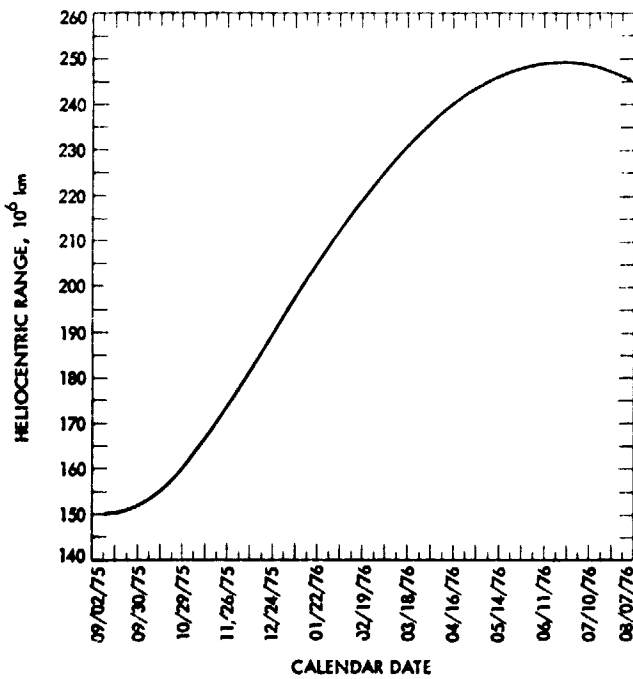


Fig. 15. Viking 2 heliocentric range

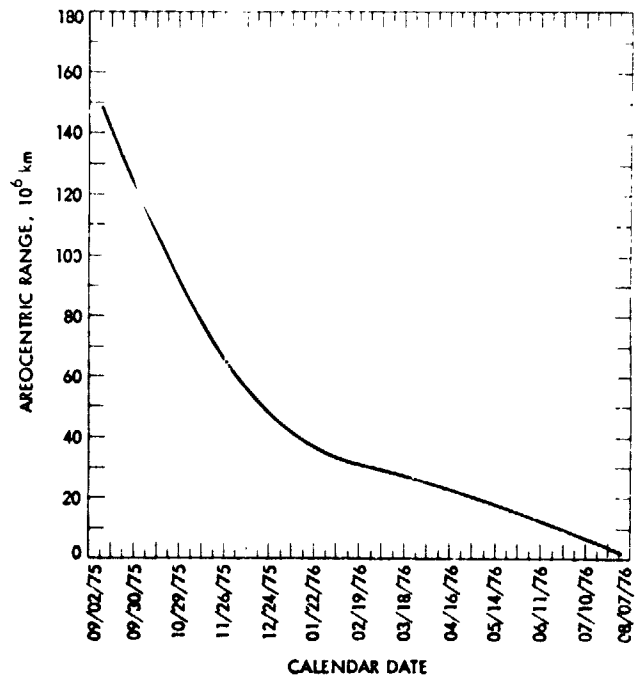


Fig. 16. Viking 2 areocentric range

**Table 5. Areocentric orbit elements
(Mars mean equator and equinox of date coordinate reference)**

Parameter	Viking 1			Viking 2	
	Pre-approach M/C	Post-approach M/C 1	Post-approach M/C 2	Pre-approach M/C	Post-approach M/C
Radius of closest approach, km	5170.9	5510.5	5561.6	11172.7	5050.7
Semimajor axis, km	-5774.6	-6005.8	6279.7	6184.9	6167.1
Eccentricity	1.8955	1.9175	1.8856	2.8064	1.8190
Inclination, deg	36.44	38.44	38.01	42.81	55.18
Longitude of ascending node, deg	116.76	132.18	129.87	53.89	36.52
Argument of periapsis, deg	25.71	12.98	15.38	57.82	81.98
Time of periapsis passage, GMT	6/19/76	6/19/76	6/19/76	8/07/76	8/07/76
	16:31:23	20:37:50	22:54:09	12:21:13	11:45:05
Hyperbolic excess velocity, km/s	2.723	2.670	2.612	2.631	2.635

M/C in the blowdown mode. The M/C maneuver was executed about 10 days before encounter on July 28, 1976, at 01 00 GMT. Table 5 lists the areocentric orbit elements at encounter before and after the M/C.

IV. Mars Orbit Phase

On June 19, 1976, at 22:59 GMT, Viking 1 was inserted into a highly elliptical orbit about Mars after a 38-min MOI motor burn. The orbit elements after MOI for each orbit revolution up to the end of the nominal mission are presented in Table 6. The definition of rev number is as follows: A rev is measured from apoapsis to apoapsis with apoapsis being the start of each rev; i.e., apoapsis number 1 precedes periapsis number 1. Orbit insertion is assumed to occur on rev 0 so that the first apoapsis is the start of rev 1. An immediate exception to this rule was made with Viking 1. Because of the large approach M/C maneuvers executed with this spacecraft, Viking 1 was inserted into a 42.5-h-period orbit instead of the planned 24.6-h orbit. The period was reduced to 24.6 h by a Mars orbit trim (MOT) maneuver near periapsis at the end of the first full rev. This periapsis would normally have been numbered "1" but it occurred on the GMT day and time at

which the second periapsis would have occurred if the nominal mission profile had been followed. In order to preserve the day/rev number sequence which had previously been established, the first rev of Viking 1 was labeled rev 2 and there was no rev 1. This is the reason Table 6 begins with rev number 2.

Viking 2 was inserted into Mars orbit seven weeks later on August 7, 1976, at 12 09 GMT after a 39-min MOI motor burn. Table 7 lists the rev-by-rev orbit elements for this spacecraft through the end of the nominal mission.

Periodic discontinuities may be observed in the normal progression of the orbit elements in these tables. These will usually be the result of MOT maneuvers, as between revs 2 and 3 in Table 6. A list of MOT maneuver execution times is included here as Table 8 to aid in identifying these points. This list is complete regardless of the absence of some MOT numbers. A number of trim maneuvers were planned and designed but never executed. Some other, generally small, discontinuities in the orbit elements are attributable to updates in orbit determination solutions, lack of tracking data, or poor orbit determination due to noisy data during solar conjunction.

Table 6. VO-1 Mars orbit elements

Rev. No.	Apoapsis/Periapsis GMT date and time, 1976		Period, h	RCA, km	INC (MEQ), deg	LAN (MFO), deg	APF (MEQ), deg
2	6/20	20:16:56	42.35210	4907.19	37.688	129.7960	39.7596
	6/21	17:28:15					
3	6/22	05:47:19	24.66124	4907.10	37.8787	129.6765	39.9378
	6/22	18:07:55					
4	6/23	06:27:40	24.65884	4907.03	37.8849	129.5454	40.1125
	6/23	18:47:26					
5	6/24	07:07:06	24.65640	4906.96	37.8911	129.4145	40.2872
	6/24	19:26:48					
6	6/25	07:46:24	24.65393	4906.89	37.8975	129.2837	40.4619
	6/25	20:06:01					
7	6/26	08:25:32	24.65143	4906.81	37.9039	129.1531	40.6365
	6/26	20:45:05					
8	6/27	09:04:32	24.64889	4906.73	37.9104	129.0226	40.8111
	6/27	21:24:00					
9	6/28	09:43:22	24.64633	4906.65	37.9169	128.8922	40.9856
	6/28	22:02:45					
10	6/29	10:22:03	24.64374	4906.56	37.9235	128.7620	41.1601
	6/29	22:41:22					
11	6/30	11:00:35	24.64113	4906.46	37.9301	128.6319	41.3346
	6/30	23:19:49					
12	7/01	11:38:57	24.63850	4906.37	37.9368	128.5019	41.5091
	7/01	23:58:06					
13	7/02	12:17:10	24.63586	4906.26	37.9435	128.3720	41.6835
	7/03	00:36:14					
14	7/03	12:55:13	24.63320	4906.15	37.9502	128.2423	41.8579
	7/04	01:14:13					
15	7/04	13:33:07	24.63052	4906.04	37.9570	128.1126	42.0322
	7/05	01:52:01					
16	7/05	14:10:51	24.62784	4905.92	37.9638	127.9830	42.2065
	7/06	02:29:40					
17	7/06	14:48:25	24.62514	4905.80	37.9706	127.8534	42.3808
	7/07	03:06:30					
18	7/07	15:25:10	24.62280	4905.74	37.9757	127.7264	42.5505
	7/08	03:43:51					
19	7/08	16:02:28	24.62012	4905.62	37.9876	127.5949	42.7449
	7/09	04:20:38					
20	7/09	16:43:52	24.77574	4906.92	37.6949	124.7660	44.8918
	7/10	05:06:44					
21	7/10	17:30:17	24.77270	4906.70	37.7165	124.6130	45.1146
	7/11	05:53:28					
22	7/11	18:16:33	24.76986	4906.54	37.7235	124.4851	45.2906
	7/12	06:39:39					
23	7/12	19:02:38	24.76700	4906.38	37.7306	124.3578	45.4665
	7/13	07:25:39					
24	7/13	19:48:34	24.76415	4906.22	37.7277	124.2390	45.6123
	7/14	08:11:31					
25	7/14	20:31:03	24.65140	4902.50	37.7007	124.1978	45.8188
	7/15	08:50:35					
26	7/15	21:10:02	24.64859	4902.33	37.7078	124.0713	45.9953
	7/16	09:29:29					
27	7/16	21:48:51	24.64579	4902.17	37.7148	123.9451	46.1717
	7/17	10:08:13					
28	7/17	22:27:30	24.64300	4901.99	37.7218	123.8189	46.3481
	7/18	10:46:47					
29	7/18	23:05:59	24.64022	4901.81	37.7288	123.6928	46.5244
	7/19	11:25:11					

Table 6 (contd)

Rev. No.	Apoapsis/Periapsis GMT date and time, 1976		Period, h	RCA, km	INC (MI Q), deg	LAN (MFO), deg	API (MEQ), deg
30	7/19	23:44:18	24.63744	4901.63	37.7358	123.5669	46.7008
	7/20	12:03:26					
31	7/21	00:22:31	24.63667	4902.19	37.7424	123.4365	46.8761
	7/21	12:41:37					
32	7/22	01:00:37	24.63391	4902.00	37.7493	123.3108	47.0524
	7/22	13:19:38					
33	7/23	01:38:34	24.63115	4901.81	37.7562	123.1852	47.2286
	7/23	13:57:30					
34	7/24	02:16:20	24.62840	4901.60	37.7631	123.0596	47.4048
	7/24	14:35:11					
35	7/25	02:53:57	24.62565	4901.40	37.7700	122.9341	47.5811
	7/25	15:12:43					
36	7/26	03:31:23	24.62291	4901.19	37.7768	122.8087	47.7572
	7/26	15:50:05					
37	7/27	04:08:40	24.62016	4900.97	37.7836	122.6833	47.9334
	7/27	16:27:17					
38	7/28	04:45:47	24.61742	4900.76	37.7905	122.5579	48.1096
	7/28	17:04:19					
39	7/29	05:22:44	24.61468	4900.53	37.7972	122.4325	48.2858
	7/29	17:41:11					
40	7/30	05:59:32	24.61194	4900.30	37.8040	122.3072	48.4620
	7/30	18:17:53					
41	7/31	06:36:09	24.60919	4900.07	37.8108	122.1818	48.6381
	7/31	18:54:26					
42	8/01	07:12:36	24.60644	4899.83	37.8176	122.0564	48.8143
	8/01	19:30:48					
43	8/02	07:50:13	24.60569	4900.09	37.8143	121.9410	48.9604
	8/02	20:07:01					
44	8/03	08:28:06	24.63793	4898.84	37.9011	121.7756	49.3066
	8/03	20:43:03					
45	8/04	09:06:26	24.63777	4898.80	37.9009	121.7778	49.3035
	8/04	21:25:34					
46	8/05	09:44:36	24.63507	4898.50	37.9074	121.6530	49.4790
	8/05	22:03:40					
47	8/06	10:22:37	24.63237	4898.21	37.9139	121.5282	49.6545
	8/06	22:41:36					
48	8/07	11:00:28	24.62968	4897.90	37.9203	121.4035	49.8301
	8/07	23:19:22					
49	8/08	11:38:10	24.62700	4897.60	37.9267	121.2788	50.0056
	8/08	23:56:58					
50	8/09	12:15:42	24.62432	4897.29	37.9330	121.1542	50.1812
	8/10	00:34:26					
51	8/10	12:53:04	24.62165	4896.97	37.9394	121.0296	50.3568
	8/11	01:11:43					
52	8/11	13:30:17	24.61898	4896.65	37.9457	120.9050	50.5324
	8/12	01:48:51					
53	8/12	14:07:20	24.61632	4896.33	37.9520	120.7804	50.7080
	8/13	02:25:49					
54	8/13	14:44:13	24.61366	4896.01	37.9582	120.6559	50.8836
	8/14	03:02:38					
55	8/14	15:20:57	24.61100	4895.68	37.9645	120.5313	51.0593
	8/15	03:39:17					
56	8/15	15:57:31	24.60853	4895.34	37.9707	120.4066	51.2349
	8/16	04:15:46					
57	8/16	16:33:56	24.60567	4895.01	37.9769	120.2820	51.4105
	8/17	04:52:06					

Table 6 (contd)

Rev. No.	Apoapsis/Periapsis GMT date and time, 1976		Period, h	RC A, km	INC (MI O), deg	LAN (MI O), deg	API (MI O), deg
58	8/17	17 10 11	24.60299	4894.66	37.9831	120.1573	51.5862
	8/18	05 28 17					
59	8/18	17 46 17	24.60032	4894.32	37.9893	120.0325	51.7618
	8/19	06 04 17					
60	8/19	18 27 13	24.59763	4893.97	37.9955	119.9077	51.9375
	8/20	06 40 08					
61	8/20	18 57 59	24.59494	4893.62	38.0017	119.7828	52.1132
	8/21	07 15 50					
62	8/21	19 33 35	24.59224	4893.27	38.0079	119.6578	52.2888
	8/22	07 51 22					
63	8/22	20 09 02	24.58954	4892.92	38.0141	119.5328	52.4645
	8/23	08 26 43					
64	8/23	20 44 19	24.58682	4892.56	38.0203	119.4076	52.6401
	8/24	09 01 56					
65	8/24	21 19 27	24.58409	4892.20	38.0265	119.2823	52.8157
	8/25	09 36 58					
66	8/25	21 54 24	24.58135	4891.84	38.0327	119.1570	52.9914
	8/26	10 11 50					
67	8/26	22 29 11	24.57861	4891.47	38.0388	119.0314	53.1670
	8/27	10 46 33					
68	8/27	23 03 49	24.57586	4891.10	38.0450	118.9058	53.3426
	8/28	11 21 06					
69	8/28	23 38 17	24.57310	4890.73	38.0512	118.7800	53.5182
	8/29	11 55 29					
70	8/30	00 12 35	24.57033	4890.36	38.0574	118.6540	53.6938
	8/30	12 29 41					
71	8/31	00 46 43	24.56756	4889.99	38.0636	118.5278	53.8693
	8/31	13 03 44					
72	9/01	01 20 40	24.56479	4889.62	38.0697	118.4015	54.0449
	9/01	13 37 37					
73	9/02	01 54 28	24.56201	4889.24	38.0759	118.2750	54.2204
	9/02	14 11 20					
74	9/03	02 28 06	24.55924	4888.87	38.0820	118.1482	54.3959
	9/03	14 44 53					
75	9/04	03 01 34	24.55648	4888.49	38.0881	118.0213	54.5714
	9/04	15 18 16					
76	9/05	03 34 52	24.55373	4888.11	38.0942	117.8942	54.7469
	9/05	15 51 29					
77	9/06	04 08 00	24.55099	4887.73	38.1002	117.7668	54.9224
	9/06	16 24 32					
78	9/07	04 40 59	24.54827	4887.35	38.1062	117.6391	55.0978
	9/07	16 57 26					
79	9/08	05 13 01	24.54397	4886.80	38.1260	117.5068	55.2883
	9/08	17 29 20					
80	9/09	05 45 34	24.54113	4886.43	38.1320	117.3787	55.4637
	9/09	18 01 48					
81	9/10	06 17 56	24.53831	4886.05	38.1379	117.2504	55.6391
	9/10	18 34 05					
82	9/11	06 50 09	24.53550	4885.47	38.1538	117.1219	55.8244
	9/11	19 06 14					
83	9/12	06 02 33	21.87715	4885.17	38.1295	116.9917	56.0344
	9/12	16 59 03					
84	9/13	03 55 10	21.87698	4884.82	38.1321	116.8512	56.2054
	9/13	14 51 29					
85	9/14	01 47 49	21.87793	4884.37	38.1297	116.7192	56.3801
	9/14	12 44 10					

Table 6 (contd)

Rev. No.	Apoapsis/Perapsis GMT date and time, 1976		Period, h	RCA, km	INC (MEQ). deg	LAN (MEQ). deg	API (MEQ). deg
86	9/14	23:40:33	21.87928	4884.18	38.1279	116.5934	56.5552
	9/15	10:36:55					
87	9/15	21:33:17	21.87912	4884.22	38.1309	116.4682	56.7330
	9/16	08:29:40					
88	9/16	19:25:56	21.87615	4883.81	38.1374	116.3309	56.9122
	9/17	06:22:14					
89	9/17	17:18:31	21.87634	4883.22	38.1359	116.1862	57.0898
	9/18	04:14:49					
90	9/18	15:11:13	21.88004	4882.92	38.1282	116.0534	57.2693
	9/19	02:07:37					
91	9/19	13:04:00	21.87961	4882.64	38.1297	115.9277	57.4505
	9/20	00:00:24					
92	9/20	10:56:42	21.87727	4882.42	38.1043	115.7753	57.6303
	9/20	21:53:02					
93	9/21	08:59:57	22.22920	4835.90	38.3090	115.7176	57.9874
	9/21	20:06:51					
94	9/22	07:13:42	22.22968	4885.43	38.3025	115.5870	58.1616
	9/22	18:20:36					
95	9/23	05:27:32	22.23107	4885.14	38.3000	115.4602	58.3349
	9/23	16:34:28					
96	9/24	03:41:26	22.23192	4885.16	38.1004	115.2467	58.5102
	9/24	14:48:23					
97	9/25	03:08:11	24.64537	4909.35	38.1579	115.0810	59.7747
	9/25	15:27:33					
98	9/26	03:46:50	24.64313	4909.09	38.1634	114.9552	59.9485
	9/26	16:06:08					
99	9/27	04:25:21	24.64092	4908.82	38.1690	114.8295	60.1224
	9/27	16:44:35					
100	9/28	05:03:44	24.63874	4908.56	38.1744	114.7038	60.2964
	9/28	17:22:54					
101	9/29	05:42:00	24.63658	4908.30	38.1799	114.5782	60.4703
	9/29	18:01:06					
102	9/30	07:20:08	24.63444	4908.05	38.1852	114.4526	60.6443
	9/30	18:34:10					
103	10/01	06:58:09	24.63243	4907.74	38.2104	114.3375	60.8217
	10/01	19:17:07					
104	10/02	07:36:02	24.63033	4907.49	38.2157	114.2120	60.9956
	10/02	19:54:57					
105	10/03	08:13:47	24.62824	4907.24	38.2209	114.0865	61.1696
	10/03	20:32:38					
106	10/04	08:51:25	24.62616	4906.99	38.2261	113.9610	61.3437
	10/04	21:10:12					
107	10/05	09:28:55	24.62409	4906.74	38.2313	113.8355	61.5178
	10/05	21:47:39					
108	10/06	10:06:18	24.62202	4906.49	38.2364	113.7100	61.6919
	10/06	22:24:58					
109	10/07	10:43:34	24.61996	4906.24	38.2415	113.5844	61.8661
	10/07	23:02:10					
110	10/08	11:20:42	24.61789	4905.99	38.2466	113.4588	62.0404
	10/08	23:39:14					
111	10/09	11:57:43	24.61582	4905.74	38.2517	113.3331	62.2147
	10/10	00:16:11					
112	10/10	12:34:44	24.61419	4905.52	38.2304	113.1893	62.4120
	10/11	00:53:10					
113	10/11	13:11:31	24.61213	4905.31	38.2354	113.0635	62.5865
	10/12	01:29:53					

Table 6 (contd)

Rev. No.	Apoapsis/Perapsis GMT date and time, 1976		Period, h	RCA, km	INC (MIQ), deg	LAN (MIQ), deg	API (MEQ), deg
114	10/12	13:48:11	24.61005	4905.09	38.2405	112.9376	62.7609
	10/13	02:06:29					
115	10/13	14:24:43	24.60795	4904.87	38.2455	112.8117	62.9355
	10/14	02:42:58					
116	10/14	15:01:08	24.60584	4904.65	38.2505	112.6856	63.1101
	10/15	03:19:19					
117	10/15	15:37:25	24.60370	4904.43	38.2556	112.5594	63.2847
	10/16	03:55:32					
118	10/16	16:13:35	24.60153	4904.20	38.2606	112.4332	63.4594
	10/17	04:31:38					
119	10/17	16:49:36	24.59934	4903.98	38.2657	112.3067	63.6342
	10/18	05:07:35					
120	10/18	17:25:30	24.59711	4903.75	38.2708	112.1802	63.8090
	10/19	05:43:25					
121	10/19	18:01:16	24.59485	4903.52	38.2759	112.0535	63.9839
	10/20	06:19:06					
122	10/20	18:36:53	24.59254	4903.29	38.2810	111.9267	64.1589
	10/21	06:54:40					
123	10/21	19:12:22	24.59020	4903.05	38.2861	111.7996	64.3339
	10/22	07:30:04					
124	10/22	19:47:42	24.58780	4902.81	38.2913	111.6724	64.5089
	10/23	08:05:21					
125	10/23	20:22:54	24.58536	4902.57	38.2965	111.5450	64.6840
	10/24	08:40:28					
126	10/24	20:57:57	24.58286	4902.32	38.3018	111.4174	64.8592
	10/25	09:15:26					
127	10/25	21:32:51	24.58030	4902.07	38.3071	111.2896	65.0345
	10/26	09:50:15					
128	10/26	22:07:35	24.57768	4901.82	38.3125	111.1615	65.2097
	10/27	10:24:55					
129	10/27	22:42:10	24.57499	4901.56	38.3179	111.0332	65.3851
	10/28	10:59:25					
130	10/28	23:16:35	24.57224	4901.29	38.3233	110.9046	65.5605
	10/29	11:33:45					
131	10/29	23:50:50	24.56942	4901.02	38.3288	110.7758	65.7359
	10/30	12:07:55					
132	10/31	00:24:55	24.56652	4900.74	38.3344	110.6466	65.9114
	10/31	12:41:55					
133	11/01	00:58:49	24.56355	4900.45	38.3400	110.5171	66.0870
	11/01	13:15:44					
134	11/02	01:32:32	24.56050	4900.16	38.3457	110.3873	66.2625
	11/02	13:49:22					
135	11/03	02:06:05	24.55736	4899.86	38.3515	110.2572	66.4382
	11/03	14:22:48					
136	11/04	02:39:26	24.55414	4899.55	38.3573	110.1266	66.6138
	11/04	14:56:03					
137	11/05	03:12:35	24.55084	4899.23	38.3631	109.9957	66.7895
	11/05	15:29:06					
138	11/06	03:45:32	24.54746	4898.90	38.3690	109.8644	66.9652
	11/06	16:01:57					
139	11/07	04:18:17	24.54399	4898.57	38.3750	109.7326	67.1409
	11/07	16:34:36					
140	11/08	04:50:49	24.54043	4898.22	38.3810	109.6004	67.3166
	11/08	17:07:02					
141	11/09	05:23:08	24.53680	4897.86	38.3871	109.4677	67.4924
	11/09	17:39:14					

Table 6 (contd)

Rev. No.	Apoapsis/Perapsis GMT date and time, 1976		Period, h	RCA, km	INC (MEQ), deg	LAN (MEQ), deg	APF (MEQ), deg
142	11/10	05:55:14	24.53309	4897.49	38.3932	109.3345	67.6681
	11/10	18:11:14					
143	11/11	06:27:06	24.52930	4897.11	38.3993	109.2008	67.8438
	11/11	18:42:59					
144	11/12	06:58:45	24.52544	4896.72	38.4054	109.0666	68.0195
	11/12	19:14:31					
145	11/13	07:30:10	24.52153	4896.31	38.4115	108.9318	68.1952
	11/13	19:45:49					
146	11/14	08:01:21	24.51756	4895.89	38.4176	108.7964	68.3708
	11/14	20:16:52					
147	11/15	08:32:17	24.51356	4895.47	38.4237	108.6605	68.5464
	11/15	20:47:41					

Table 7. VO-2 Mars orbit elements

Rev. No.	Apoapsis/Periapsis GMT date and time, 1976		Period, h	RCA, km	INC (MI Q), deg	LAN (MI Q), deg	API (MI Q), deg
1	8/08	01:27:53	27.623	4912.2	55.17	36.37	69.32
	8/08	15:16:35					
2	8/09	05:05:11	27.620	4912.4	55.18	36.28	69.36
	8/09	18:53:53					
3	8/10	08:33:16	27.313	4893.0	55.20	36.07	66.77
	8/10	22:12:40					
4	8/11	11:52:10	27.317	4892.9	55.21	36.00	69.81
	8/12	01:31:41					
5	8/12	15:11:26	27.325	4893.0	55.20	35.90	69.86
	8/13	04:51:12					
6	8/13	18:30:49	27.321	4892.8	55.21	35.80	69.90
	8/14	08:10:28					
7	8/14	21:52:53	27.413	4895.0	55.21	35.72	70.02
	8/15	11:35:17					
8	8/16	01:17:44	27.415	4895.3	55.20	35.63	70.08
	8/16	15:00:12					
9	8/17	04:42:45	27.419	4895.3	55.19	35.53	70.15
	8/17	18:25:20					
10	8/18	08:07:56	27.420	4895.3	55.19	35.43	70.20
	8/18	21:50:33					
11	8/19	11:33:04	27.417	4895.6	55.19	35.33	70.25
	8/20	01:15:36					
12	8/20	14:57:57	27.412	4895.7	55.20	35.24	70.31
	8/21	04:40:20					
13	8/21	18:22:51	27.417	4895.7	55.19	35.15	70.37
	8/22	08:05:23					
14	8/22	21:48:07	27.424	4895.8	55.18	35.04	70.42
	8/23	11:30:52					
15	8/24	01:13:25	27.418	4895.8	55.19	34.94	70.46
	8/24	14:55:59					
16	8/25	04:38:23	27.413	4896.0	55.19	34.85	70.52
	8/25	18:21:31					
17	8/26	06:22:43	24.040	4818.3	55.65	34.78	72.66
	8/26	18:23:57					
18	8/27	06:25:12	24.042	4818.6	55.65	34.70	72.71
	8/27	18:26:29					
19	8/28	06:45:15	24.622	4883.0	55.39	34.40	73.65
	8/28	19:03:56					
20	8/29	07:22:35	24.622	4882.9	55.38	34.38	73.66
	8/29	19:41:16					
21	8/30	07:59:56	24.622	4883.3	55.38	34.29	73.73
	8/30	20:18:37					
22	8/31	08:37:17	24.622	4883.6	55.38	34.20	73.79
	8/31	20:55:58					
23	9/01	09:14:38	24.622	4884.0	55.38	34.11	73.86
	9/01	21:33:20					
24	9/02	09:52:00	24.623	4884.4	55.38	34.02	73.92
	9/02	22:10:42					
25	9/03	10:29:23	24.623	4884.8	55.38	33.93	73.99
	9/03	22:48:05					
26	9/04	11:06:51	24.626	4885.5	55.39	33.85	74.03
	9/04	23:25:39					
27	9/05	11:44:26	24.626	4886.0	55.39	33.77	74.09
	9/06	00:03:15					
28	9/06	12:22:02	24.626	4886.4	55.39	33.68	74.15
	9/07	00:40:51					

Table 7 (contd)

Rev. No.	Apoapsis/Periapsis GMT date and time, 1976		Period, h	RCA, km	INC (MI-Q), deg	LAN (MI-Q), deg	API (MI-Q), deg
29	9/07	12:59:39	24.626	4886.8	55.39	33.59	74.21
	9/08	01:18:28					
30	9/08	13:37:16	24.627	4887.2	55.39	33.50	74.28
	9/09	01:56:06					
31	9/09	14:14:55	24.627	4887.7	55.39	33.41	74.33
	9/10	02:33:46					
32	9/10	14:52:35	24.628	4888.2	55.39	33.32	74.40
	9/11	03:11:26					
33	9/11	15:30:21	24.628	4888.6	55.39	33.23	74.46
	9/12	03:49:09					
34	9/12	16:08:00	24.628	4889.0	55.39	33.14	74.53
	9/13	04:26:52					
35	9/13	16:45:44	24.629	4889.5	55.39	33.05	74.59
	9/14	05:04:37					
36	9/14	17:23:30	24.629	4890.0	55.39	32.95	74.66
	9/15	05:42:25					
37	9/15	18:01:18	24.630	4890.5	55.39	32.86	74.73
	9/16	06:20:14					
38	9/16	18:39:08	24.630	4890.9	55.39	32.77	74.79
	9/17	06:58:05					
39	9/17	19:17:01	24.631	4891.4	55.39	32.68	74.85
	9/18	07:35:58					
40	9/18	19:54:55	24.632	4891.8	55.39	32.59	74.92
	9/19	08:13:53					
41	9/19	20:32:52	24.632	4892.4	55.39	32.51	74.97
	9/20	08:51:52					
42	9/20	21:10:52	24.633	4892.9	55.39	32.42	75.03
	9/21	09:29:53					
43	9/21	21:48:54	24.634	4893.3	55.39	32.33	75.10
	9/22	10:07:57					
44	9/22	22:26:59	24.635	4893.8	55.39	32.24	75.16
	9/23	10:46:03					
45	9/23	23:05:07	24.636	4894.3	55.39	32.15	75.22
	9/24	11:24:13					
46	9/24	23:43:20	24.637	4894.9	55.38	32.04	75.31
	9/25	12:02:27					
47	9/26	00:21:35	24.638	4895.4	55.38	31.95	75.38
	9/26	12:40:44					
48	9/27	00:59:54	24.639	4895.9	55.38	31.86	75.44
	9/27	13:19:05					
49	9/28	01:38:17	24.640	4896.4	55.38	31.76	75.50
	9/28	13:57:30					
50	9/29	02:16:44	24.641	4897.0	55.38	31.71	75.53
	9/29	14:38:27					
51	9/30	02:57:44	24.643	4925.5	55.34	31.27	75.89
	9/30	15:17:01					
52	10/01	04:56:43	26.794	4902.3	74.90	54.60	68.34
	10/01	18:20:16					
53	10/02	07:44:16	26.794	4902.3	74.90	54.60	68.34
	10/02	21:08:07					
54	10/03	10:32:07	26.800	4902.1	74.89	54.56	68.28
	10/03	23:56:08					
55	10/04	13:20:13	26.802	4902.0	74.89	54.51	68.22
	10/05	02:44:19					
56	10/05	16:08:19	26.800	4902.2	74.89	54.44	68.18
	10/06	05:32:21					

Table 7 (contd)

Rev. No	Apoapsis/Periapsis GMT date and time, 1976		Period, h	RCA, km	INC (MFQ), deg	LAN (MEQ), deg	APF (MEQ), deg
57	10/06	18:56:08	26.793	4902.6	74.89	54.40	68.13
	10/07	08:19:56					
58	10/07	21:43:35	26.788	4902.6	74.89	54.36	68.09
	10/08	11:07:15					
59	10/09	00:31:06	26.795	4902.5	74.88	54.31	68.06
	10/09	13:54:59					
60	10/10	03:19:10	26.806	4902.6	74.87	54.27	67.99
	10/10	16:43:23					
61	10/11	06:07:31	26.805	4902.6	74.88	54.25	67.86
	10/11	19:31:42					
62	10/12	08:55:33	26.795	4902.4	74.89	54.21	67.80
	10/12	22:19:27					
63	10/13	11:43:06	26.789	4902.7	74.90	54.16	67.76
	10/14	01:06:48					
64	10/14	14:30:32	26.791	4903.0	74.90	54.12	67.73
	10/15	03:54:19					
65	10/15	17:18:15	26.798	4902.9	74.89	54.07	67.68
	10/16	06:42:13					
66	10/16	20:06:23	26.802	4902.7	74.88	54.03	67.60
	10/17	09:30:29					
67	10/17	22:54:31	26.801	4903.0	74.88	53.98	67.54
	10/18	12:18:35					
68	10/19	01:42:25	26.795	4903.4	74.89	53.94	67.48
	10/19	15:06:18					
69	10/20	04:29:56	26.788	4903.6	74.89	53.90	67.44
	10/20	17:53:37					
70	10/21	07:17:21	26.791	4903.5	74.89	53.85	67.41
	10/21	20:41:11					
71	10/22	10:05:16	26.803	4903.6	74.87	53.79	67.37
	10/22	23:29:24					
72	10/23	12:53:36	26.807	4903.8	74.87	53.75	67.29
	10/24	02:17:51					
73	10/24	15:41:48	26.799	4903.7	74.87	53.71	67.21
	10/25	05:05:48					
74	10/25	18:29:20	26.790	4903.8	74.88	53.67	67.17
	10/26	07:53:14					
75	10/26	21:16:55	26.790	4904.2	74.88	53.62	67.13
	10/27	10:40:39					
76	10/28	00:04:32	26.796	4904.3	74.87	53.58	67.09
	10/28	13:28:28					
77	10/29	02:52:29	26.801	4904.1	74.87	53.53	67.03
	10/29	16:16:33					
78	10/30	05:40:37	26.802	4904.3	74.86	53.48	66.97
	10/30	19:04:43					
79	10/31	08:28:39	26.797	4904.7	74.87	53.41	66.96
	10/31	21:52:36					
80	11/01	11:16:17	26.790	4905.1	74.87	53.36	66.91
	11/02	00:40:00					
81	11/02	14:03:40	26.789	4905.1	74.87	53.32	66.88
	11/03	03:27:22					
82	11/03	16:51:21	26.800	4905.2	74.86	53.27	66.83
	11/04	06:15:22					
83	11/04	19:39:35	26.808	4905.4	74.85	53.23	66.76
	11/05	09:03:51					
84	11/05	22:27:54	26.802	4905.4	74.86	53.18	66.69
	11/06	11:51:59					

Table 7 (contd)

Rev. No.	Apoapsis/Periapsis GMT date and time, 1976		Period, h	RCA, km	INC (MEQ), deg	LAN (MEQ), deg	API (MLQ), deg
85	11/07	01:15:44	26.792	4905.5	74.87	53.15	66.63
	11/07	14:39:32					
86	11/08	04:03:14	26.789	4905.7	74.86	53.14	66.49
	11/08	17:26:56					
87	11/09	06:50:45	26.794	4906.0	74.86	53.10	66.45
	11/09	20:14:36					
88	11/10	09:38:36	26.800	4906.2	74.85	53.11	66.43
	11/10	23:02:38					
89	11/11	12:26:42	26.803	4906.2	74.85	52.99	66.36
	11/12	01:50:49					
90	11/12	15:14:47	26.799	4906.6	74.85	52.94	66.30
	11/13	04:38:48					
91	11/13	18:02:32	26.792	4907.1	74.86	52.90	66.25
	11/14	07:26:19					
92	11/14	20:49:57	26.788	4907.2	74.86	52.86	66.22
	11/15	10:13:37					
93	11/15	23:37:29	26.796	4907.3	74.85	52.82	66.18
	11/16	13:01:23					

Table 8. Mars orbit trim (MOT) maneuver execution times

Spacecraft	Maneuver	Ignition	
		Date	Time (GMT), 1976
V-1	MOT 1	6/21	17:26
V-1	MOT 5	7/09	00:40
V-1	MOT 6	7/14	07:12
V-1	SKT 2 ^a	8/03	03:00
V-2	MOT 1	8/09	17:16
V-2	MOT 2	8/14	08:31
V-2	MOT 3	8/25	17:48
V-2	MOT 4	8/27	20:26
V-1	MOT 7	9/11	19:04
V-1	MOT 8	9/20	22:15
V-1	MOT 9	9/24	15:10
V-2	MOT 5A	9/29	04:33
V-2	MOT 5	9/30	21:08

^aThis trim was for lander relay station keeping purposes and was labeled SKT for that reason.

Interplanetary Orbit Determination

K. H. Rourke, N. Jerath, C. H. Acton, W. G. Breckenridge, J. K. Campbell, C. S. Christensen,
A. J. Donegan, H. M. Koble, N. A. Mottinger, G. C. Riniker, and F. B. Winn

I. Introduction

This chapter presents a general description of the Viking interplanetary orbit determination activity extending from launch to Mars encounter. The emphasis is on the technical fundamentals of the problem, basic strategies and data types used, quantitative results, and specific conclusions derived from the inflight experience. Special attention is given to the use of the spacecraft-based optical measurements and their first application as a principal navigational data type for an interplanetary mission. The optical-based orbit determination in fact was the primary contributor to the exceptional interplanetary navigation accuracy experienced by both Viking missions. The Viking application of optical orbit determination relied in large part on the technology developed and demonstrated by the Mariner 9 Optical Navigation Demonstration (Refs. 1-3).

The contents of this chapter can be summarized as follows: Section II presents a brief description of Viking navigation-related interplanetary events. Section III discusses the principles of the various orbit determination system elements. The description includes the identification and quantification of

the major system errors. Section IV surveys the software system established for the orbit determination data processing. Section V discusses the orbit determination strategies employed for Viking, including strategy rationale developed using a simplified model of the spacecraft-based optical observables. Section VI describes the salient results of the launch, departure, and cruise orbit determination operations. Section VII describes the long-arc radio data processing results. Section VIII describes the inflight solar pressure model improvement resulting from inflight analysis. Section IX describes the operational processes required to reduce raw spacecraft-based observations into data usable for orbit determination. Section X describes the collection of inflight approach orbit determination results and evaluates their accuracy with respect to precision post-flight reconstruction results. The complete set of interplanetary OD solutions are compiled and tabulated in Section XI. Section XII discusses the DSN station locations at some length and Section XIII contains an analysis of satellite ephemeris related issues. Section XIV concludes the article with some general statements drawn from the Viking inflight experience, with emphasis on conclusions that may assist orbit determination efforts on future interplanetary missions.

II. Mission Description

Table 1 and Fig. 1 depict the prime interplanetary orbit determination related events that occurred during the Viking missions. The critical events for navigation and orbit determination are the execution of the spacecraft midcourse correction (M/C) and Mars orbit insertion (MOI) maneuvers. The departure corrections were required to remove expected launch vehicle errors. The approach midcourse corrections were needed to remove errors in the departure corrections, in the trajectory prediction, and in general to ensure the required accuracy of the delivery of the Viking spacecraft to Mars. During the Viking 1 approach, two corrections were made before insertion instead of the normally expected single correction. The second correction, executed just 4 days before Mars encounter, was not necessary for navigational purposes, but was required to relieve propellant overpressurization caused by a valve malfunction onboard the Viking 1 spacecraft. Following the approach M/C, the interplanetary orbit determination activity was completed with the delivery of estimates supporting the computation of the Mars orbit insertion maneuver commands.

For each maneuver, the accuracy of the specific orbit estimate used to derive the maneuver commands directly affected the accuracy of the maneuver itself. For approach and orbit insertion maneuvers, the orbit determination accuracy largely determined the accuracy of the post-maneuver trajectory.

At the times indicated in Table 1, best orbit estimates were required in support of maneuver calculations. At these points,

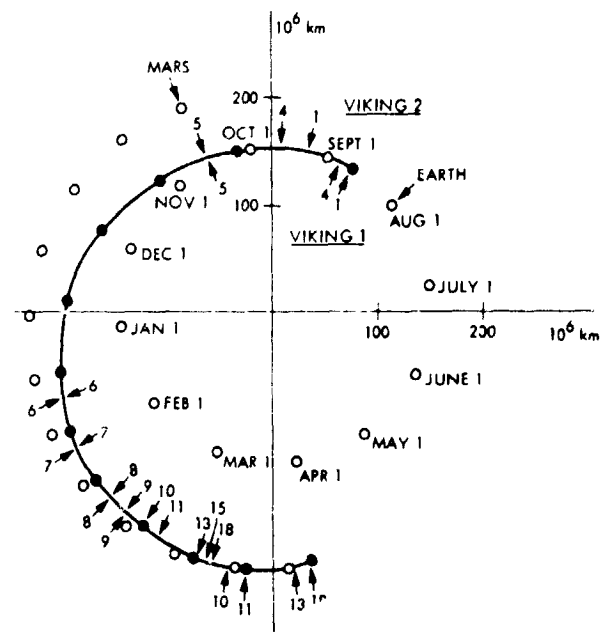


Fig. 1. Mission events

the available navigation observations (radio tracking data from the Deep Space Network and onboard optical observations from the spacecraft) were incorporated into best estimates. The best estimates were passed by the Interplanetary Orbit Determination Team to other elements of the Viking Flight Path Analysis Group for the maneuver analysis and the ultimate generation of spacecraft executable commands.

Table 1 also lists events aiding the direct navigation support, including navigation model refinement and the spacecraft instrument checkout and scan calibration activity. The instrument checkout and scan calibration activity were crucial to the preparation for obtaining the spacecraft-based optical measurements.

Table 1. Mission events

Event	Viking 1	Viking 2
1. Launch	8/20/75	9/9/75
2. Initial estimate	L + 3 h	L + 3 h
3. Final departure M/C estimate	8/25/75	9/17/75
4. Departure M/C	8/27/75	9/19/75
5. Orbiter instrument checkout	10/13/75	10/9/75
6. Scan platform calibration 1	2/9/76	2/13/76
7. Solar pressure model update	3/10/76	3/10/76
8. Scan platform calibration 2	4/11/76	4/14/76
9. Navigation model finalization	4/25/76	4/25/76
10. Start planetary operations	5/10/76	5/29/76
11. Start optical navigation	5/17/76	7/6/76
12. Final approach M/C-1 estimate	6/6/76	7/25/76
13. Approach M/C-1	6/10/76	7/28/76
14. Final approach M/C-2 estimate	6/14/76	
15. Approach M/C-2	6/15/76	
16. Preliminary MOI estimate	6/17/76	7/31/76
17. Final MOI estimate	6/18/76	8/6/76
18. MOI	6/19/76	8/7/76

III. Orbit Determination System Fundamentals

The orbit determination system used for Viking has as inputs ground-based radio metric and spacecraft-based optical observations. These input data are then "fit" in a least-squares sense to obtain a "solution" of the spacecraft state (position and velocity) at a reference epoch. This "solved for" state is numerically integrated to obtain an estimated spacecraft trajectory.

The orbit determination process requires three sets of models: *trajectory models* determine the spacecraft trajectory in an inertial coordinate system; *observation models* relate the

observations to the spacecraft trajectory; *filter models* determine how the observations are fit to obtain the solution.

A. Trajectory Models

The equations of motion of a spacecraft in the solar system are given by

$$\mathbf{r}(t) = f[\mathbf{r}(t), t]$$

where \mathbf{r} is the position vector and t is time. The terms in the acceleration function f include gravitational forces of the sun, the planets, and their satellites. The parameters in this model are the masses of the respective celestial bodies and their positions relative to the spacecraft at any given time. Their positions are obtained by planetary ephemeris interpolation.

There are also nongravitational accelerations. Solar pressure is the major such acceleration and depends on the spacecraft mass, size, and orientation, as well as on reflectivities of various spacecraft components and the orientation and distance of the spacecraft with respect to the Sun. There can also be uncontrolled outgassing, e.g., attitude control leaks. In the case of Viking, venting of air and water vapor from the lander parachute and bioshield insulation was also a significant effect. The third type of spacecraft acceleration is caused by the engine firing when a maneuver is performed.

B. Observation Models

For each observable obtained, a computed observable is calculated, based on the current nominal spacecraft trajectory. The two are differenced to form a "residual." The vector of residuals forms the right-hand side of the data equation that the filter uses. The length of this vector is minimized in a least-squares sense when a solution is formed. Following is a brief summary of how the observables are computed.

C. Radio Data Models

There were two types of radio metric data used in orbit determination for Viking. Doppler is a measure of the difference in frequency of the carrier signal received from the spacecraft compared to that transmitted. The observable is an average of this difference over some sample time T . It can be expressed in terms of range rate or differenced range between the spacecraft and station as:

$$f(t) = \frac{f_0}{T} \int_{t-T/2}^{t+T/2} \frac{\dot{\rho}(\tau)}{c} d\tau$$

$$= \frac{f_0}{T} \left[\frac{\rho(t+T/2) - \rho(t-T/2)}{c} \right]$$

where ρ is the range, f_0 is the transmitted frequency, and c is the speed of light.

Range is given by the round-trip transmit time of a signal from the station to the spacecraft and return. Thus:

$$\rho(t_{receive}) = t_{receive} - t_{transmit}$$

$$= \frac{|\mathbf{r}(t_r) - \mathbf{r}(t_{S/C})|}{c}$$

$$+ \frac{|\mathbf{r}(t_{S/C}) - \mathbf{r}(t_t)|}{c}$$

+ relativity corrections,

where $\mathbf{r}(t_t) + \mathbf{r}(t_r)$ are position vectors of the station at transmit and receive times, and $\mathbf{r}(t_{S/C})$ is the position of the spacecraft at the time the signal is received there and retransmitted toward Earth. To obtain these vectors requires an ephemeris interpolation to find the position of Earth, knowledge of the station location, and knowledge of UT and polar motion (Earth rotation rate changes and Earth wobble). See Ref. 4 for a detailed discussion of radio observational models.

Radio metric data is affected in two ways by the media through which the radio waves pass. First, the Earth's troposphere slows the velocity of a signal passing through it, which is especially important at low elevations where the signal path through the atmosphere is comparatively long. All radio metric data are corrected for tropospheric effects with a seasonal model that is a function of the spacecraft elevation angle.

Second, there are charged particles both in the Earth's ionosphere and in clouds of space plasma streaming outward from the Sun. A modulation on a carrier signal (for example, the modulation used for the range measurement) is slowed by an amount proportional to the total number of electrons encountered along the propagation path. An approximation for this "group velocity" is

$$V_g = c \left(1 - 1/2 K \frac{N}{f^2} \right)$$

where c is the speed of light, N is the electron density, f is the carrier frequency, and K is a constant. The small velocity decrease, due to plasma, increases the transmit time as seen in the range observable by an amount

$$\Delta t = 1/2 \frac{K}{f^2} \left(\int_{station(t_p)}^{S/C} N dl + \int_{S/C}^{station(t_p)} N dl \right)$$

The phase velocity, which determines the doppler observable, is similarly influenced by plasma. The phase velocity is increased, however; i.e.,

$$V_p = c \left(1 + 1/2 K \frac{N}{f^2} \right)$$

The total phase change is the integral of V_p along the propagation path

$$\phi = \int_1 V_p dt = c \left(1 + 1/2 \frac{K}{f^2} \int_1 N dt \right)$$

The net change in electron content along a propagation path can be determined by differencing integrated doppler from relative range. This procedure takes advantage of the opposite, but equal, influences the plasma has on group and phase velocities. This difference is called DRVID (for Differenced Range Versus Integrated Doppler) and was used to correct the doppler data in some of the solutions discussed in Section X.

The range observables must be calibrated for the transit time of the range signal within the ground station and within the spacecraft. This calibration is measured and computed for each pass of data.

D. Optical Data Models

The optical observables used in Viking orbit determination are a "line" number and "pixel" number of the optical center of an image of either Mars or Deimos. The line and pixel numbers give the location on the TV raster formed by one of the vidicon cameras onboard the spacecraft. These observables along with the camera pointing direction give an angular measurement between either Mars or Deimos and a fixed inertial direction.

A camera optical model relates the electromagnetic image to the theoretical physical image. A camera alignment model, attitude control telemetry, and star images are used to determine camera pointing direction. The Mars limb model defines the line and pixel of the planet center given an image of a disc or partial disc. The Mars and satellite ephemerides are needed, along with the spacecraft ephemeris, to give the inertial direction needed for the computed observable.

Table 2 describes the process used to transform an inertial vector from the spacecraft to an object into line and pixel numbers. The optical measurements system and the end-to-end processing of the measurements are described in detail in Section IX.

E. Filter Models

The filter used in the Viking Orbit Determination Program (ODP) is a minimum variance filter. It is formulated as a "Square Root Information Filter" (Ref. 5). It can be operated in two modes: a batch or weighted least-squares mode where all data are used together for a solution, and a sequential mode where the time span of data is divided into smaller batches. In the sequential mode, there are stochastic parameters whose values change from batch to batch, but are statistically correlated. Details on the application of estimation techniques to orbit determination are given in Refs. 6 and 7.

In obtaining a solution, a list of parameters to be estimated and a list of parameters to be "considered" are chosen. The estimate list includes the spacecraft state (position and velocity at some epoch) and possibly parameters from the trajectory and/or data models (e.g., solar pressure parameters, station locations, and Mars mass or ephemeris). "Consider" parameters are not solved for in the solution, but are parameters whose uncertainty increases the uncertainty (covariance) of the solution.

Table 2. Optical observables

\bar{r}	$= \bar{r}_0 + [K] \cdot \left\{ \bar{d} + [F] \bar{v}_c \right\}$
\bar{v}_c	$= [C] \cdot [P] \cdot [A] \cdot [R] \cdot \bar{v}_1$
\bar{r}	= image location (line and pixel)
\bar{r}_0	= location of Visual Imaging System (VIS) line of sight (line and pixel)
K	= VIS scan raster transformation, linear part (line and pixel/millimeter)
\bar{d}	= nonlinear distortion error as a function of image position, F \bar{v}_c (mm)
F	= optics model, transforms from \bar{v}_c to image position (mm)
\bar{v}_c	= unit vector to object in camera coordinates
C	= transformation for camera alignment wrt scan platform
P	= transformation, scan platform wrt spacecraft body coordinates, includes gimbal angles
A	= transformation for attitude control motion of spacecraft body wrt spacecraft nominal orientation
R	= transformation from inertial/reference coordinates to spacecraft nominal orientation
\bar{v}_1	= unit vector to object in inertial/reference coordinates

The a priori statistics of both the estimated and consider parameters must be chosen. The observation set to be included in the solution along with the observation weights must be selected. If the sequential filter mode is used, the batch sizes, the correlation time, the set of stochastic parameters, and the a priori statistics also must be chosen.

F. Orbit Determination Process

Figure 2 illustrates the orbit determination process by describing the data flow between the three sets of models discussed. It is divided into four horizontal sections. Section I

consists of inputs; Section II, data preparation; Section III, the mainline processing; and Section IV is a list of decisions made by the orbit determination analyst.

This process was implemented for Viking by the orbit determination software system described in Section IV. The major elements of this system, which actually consist of subsystems of separate UNIVAC 1108 computer programs, are the Orbit Determination Program (ODP), the Optical Navigation Program (ONP), and the Optical Measurements Set (OMSET).

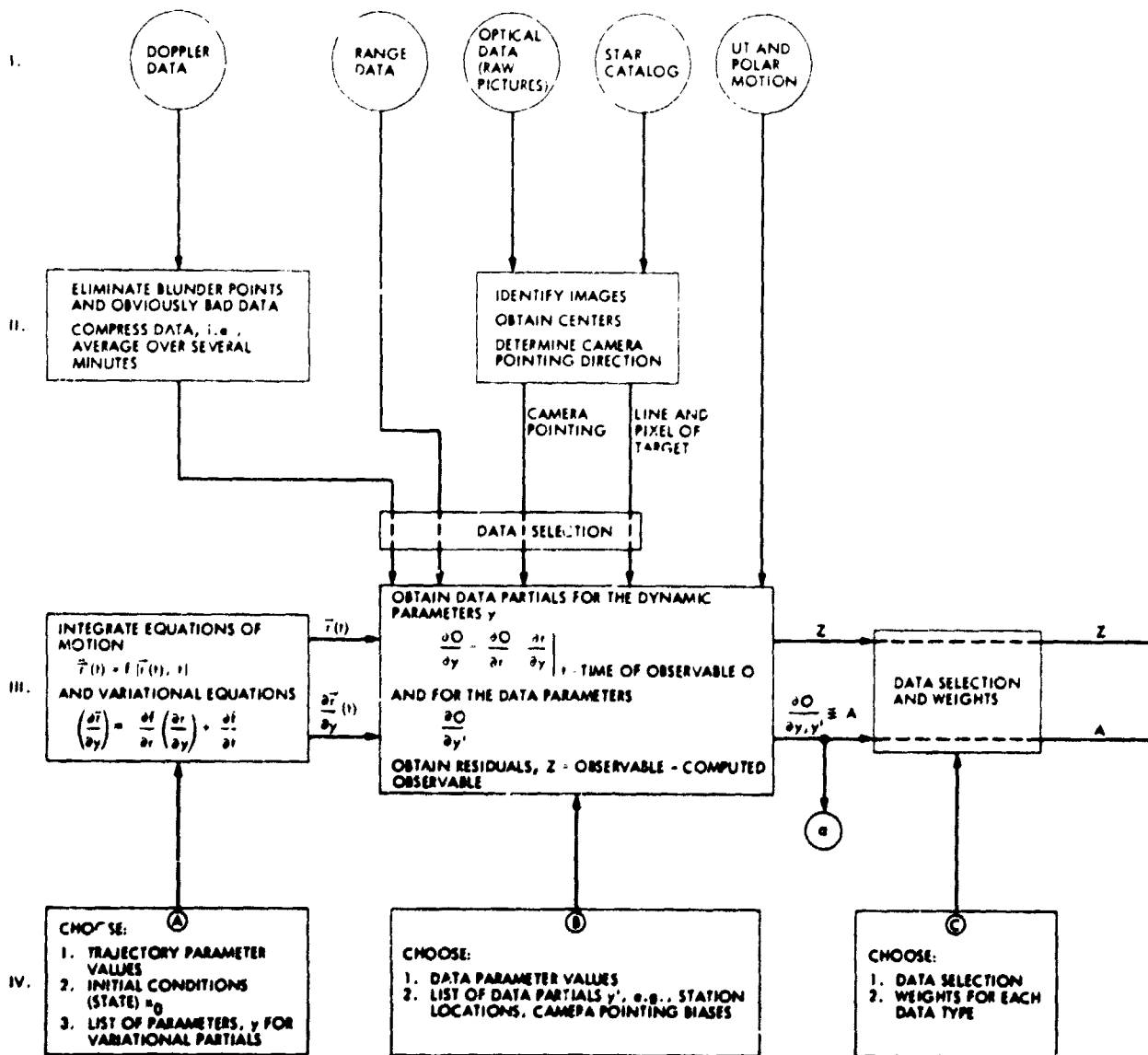


Fig. 2. Orbit determination process

G. Critical Orbit Determination Inputs

The orbit determination process requires, in addition to the observation data described previously, input values for numerous fundamental constants and parameters required by the trajectory and observation models. The most critical of these inputs, those most strongly affecting the orbit determination output, are summarized below, along with their corresponding external sources.

- (1) Planetary ephemeris supplied by the JPL planetary ephemeris development program.
- (2) Tracking station locations, supplied by the NASA Office of Tracking and Data Acquisition.

(3) Spacecraft a priori solar pressure coefficients supplied by Viking spacecraft engineering personnel.

(4) Deimos satellite ephemeris supplied by research supported by the Mariner 9 Optical Navigation Demonstration (Ref. 8).

(5) Timing, polar motion, and transmission media calibration supplied by the tracking system analytic calibration element of the JPL Operations Support Office.

Accuracy values for these data and the associated effects on orbit determination are described in the following subsection.

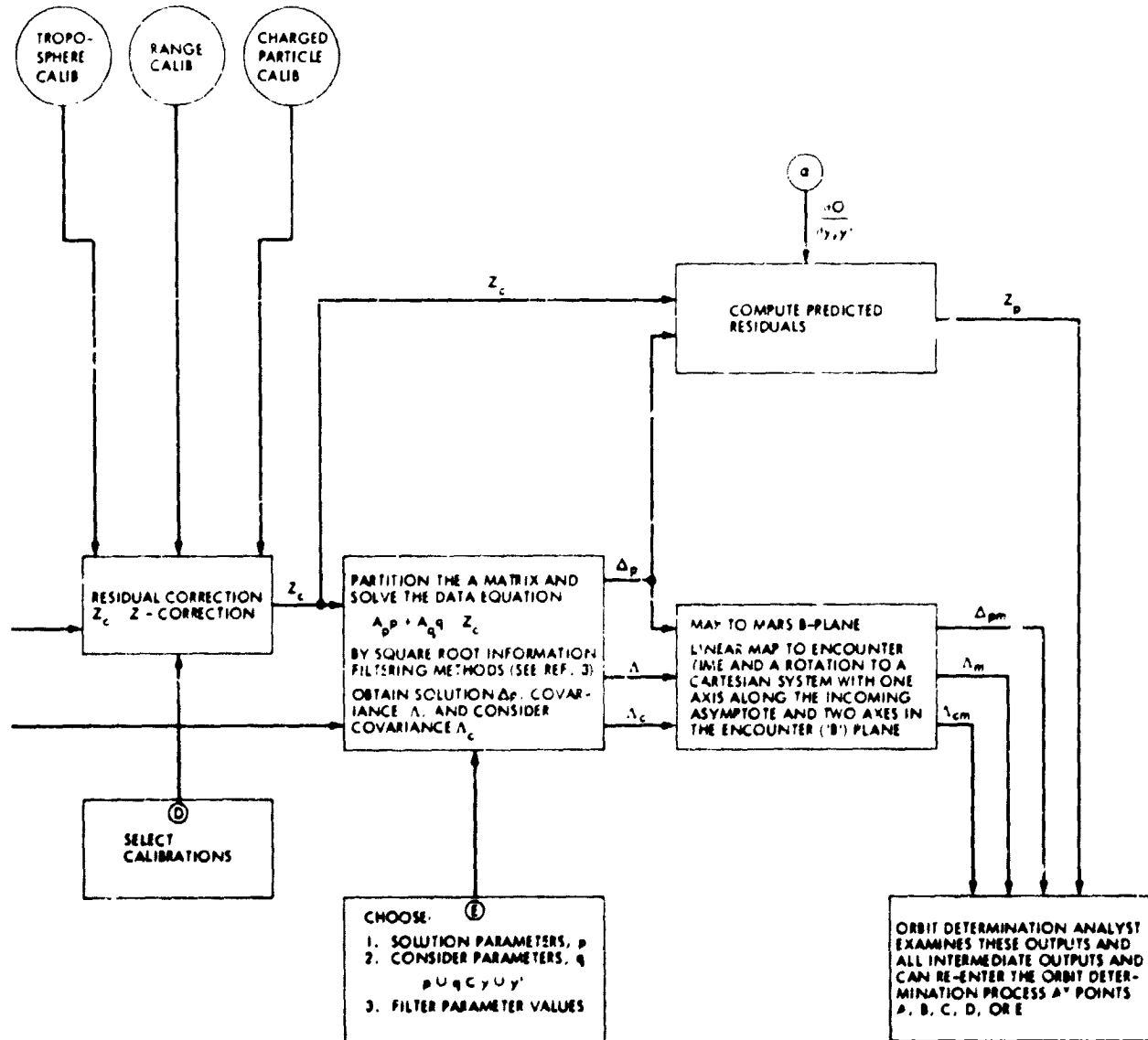


Fig. 2 (contd)

H. Orbit Determination Errors

The error in an orbit estimate results from an accumulation of a large number of identified error sources. Each error influences the estimation accuracy to a different extent depending on the mission phase, observation set, and estimation process. Although a large comprehensive error model was used during flight for error analysis, relatively few errors are really significant in their ultimate influence on orbit determination accuracy. These errors are listed in Table 3. Each major error is identified, its one-sigma level is given, and the corresponding orbit determination error is indicated. Two error levels have been indicated for the optical observations. The larger is the conservative value adopted before flight to allow for some performance variations in the optical measurements system. The smaller values are consistent with the values observed during flight.

IV. Orbit Determination Software System

The basic functions of the orbit determination process are described in this section in terms of their implementation in the Viking orbit determination software system including the ODP, OMSET, and ONP. These programs are actually systems of subprograms or links that perform individual orbit determination functions, e.g., trajectory integration, solution genera-

tion, and tracking data plotting and printing. These links generally communicate by UNIVAC 1108 mass storage files.

The primary task of the software system was to generate trajectory estimates based on radio data and optical data. The four types of solutions generated were radio solutions, optical solutions, radio plus optical solutions, and optical plus radio a priori solutions. The software interfaces used in generating these solutions are shown in Fig. 3. A detailed summary of the software inputs and outputs is given in Tables 4 and 5. For definitions of the programs and intermediate data files see Table 6.

For the ODP and the ONP, the large number of intermediate data files and solution files were systematically and efficiently stored on and retrieved from magnetic tape by the "FARMER," an automated file management system. Mass storage data files remained on the computer system for approximately 24 h before they were transferred to magnetic tape. For the ODP, the solution information was automatically extracted from the Salient Information File and stored in a data base at the time of transfer.

The operation of the orbit determination software system was typically controlled by the use of computer demand terminals. During the encounter phases, at least three com-

Table 3. Orbit determination system error model

Observation type	Error type/1σ error	Description	Major estimate error	
Radio: doppler and range	Equivalent station location error (ESLE) Distance from Earth's spin axis: 15m Height off equator: 15m Longitude: 3m	Errors in the radio measurements due to either physical uncertainties in tracking station locations or location like effects due to errors in time, polar motion or transmission media calibrations	300 to 500 km at E - 10 days	
	Solar radiation Reflectivity per axis: 5%	--	1000 to 1500 km at launch	
	Nongravitational acceleration Constant acceleration: 1.2×10^{-12} km/s ² Stochastic acceleration: 0.4×10^{-12} km/s ²	Errors due to gas leaks and A/C imbalance	100 km at E - 10 days	
	Planetary ephemeris Earth's relative error: 50 km	--	50 km	
	Data noise Doppler: 1 mm/s, 60-s count Range: 15m	-- --	50 to 100 km at E - 10 days	
	Optical	Data noise Line: 1 to 0.5 pixels Pixel: 1 to 0.5 pixels	Errors due to random center location, pointing determination, and telemetry error	60 to 30 km at E - 10 days
		Center finding bias (Mars obs.) Line: 2 to 1% of target radius Pixel: 2 to 1% of target radius	Irreducible bias in determining center from limb observations	70 to 35 km
		Satellite ephemeris	50 to 15 km	50 to 15 km

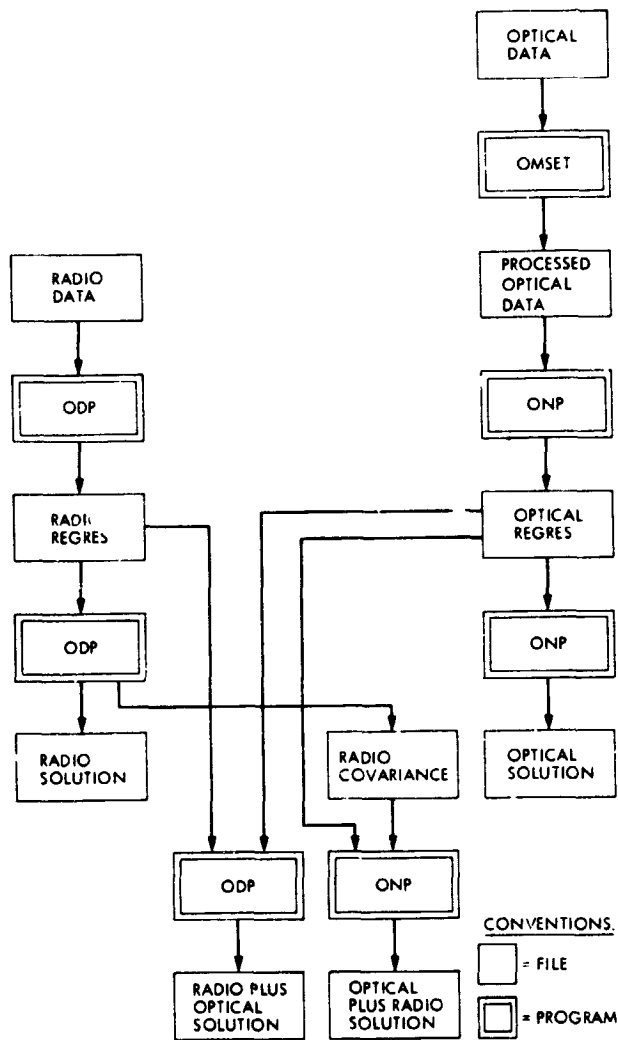


Fig. 3. Orbit determination software interfaces

puter demand terminals were used on the UNIVAC 1108 to operate the ODP, OMSET, and the ONP concurrently. A typical operational sequence for the encounter phase is given in Table 7.

V. Orbit Determination Strategy

A. Radio and Optical Orbit Determination

The Viking mission was designed requiring only radio orbit determination. The Project requirements on interplanetary orbit determination reflect this as shown in Table 8. Requirements on B-plane accuracy are given for the midcourse maneuvers at Earth departure, Mars approach, and for the Mars orbit insertion maneuver. The requirements are based on

Table 4. OD software inputs

	ODP	OMSET	ONP
Planetary ephemeris file	E	E	E
PV file	I	I	I
Card images of user optional inputs	I	I	I
Program control card file	I	I	I
Optical regres file	I		I
Lock files of nominal values	I		
Planetary ephemeris partials file	E		E
Radio data file	E		
Radio regres file	I		
Star catalog file		E	E
Pointing related engineering telemetry		F	
Optical data file		E	
Picture data hardcopy		E	
Satellite ephemeris parameters		I	
Picture sequence file containing geometry data		I	
Optical working file of nominal values			I
Edited optical data file			I
Radio covariance file			I

Note: E indicates an external input and I indicates an internal input to the OD software system

the need to ensure that the Viking prelanding Mars orbits were acquired with sufficient accuracy within specific propellant allotments. The table includes associated radio accuracies assuming the nominal Viking error model (Table 3). In each case, the major error affecting the capability at that time is identified. The accuracies and capabilities are shown in Fig. 4. The radio capabilities satisfy the requirements on a 99% basis.

In 1972, following the successful engineering demonstration of spacecraft-based optical navigation by Mariner 9, Viking adopted optical navigation as a backup to enhance navigation reliability. This was not done because of specific concern over radio orbit determination, a function which had performed without difficulty in previous interplanetary flights. Instead, optical orbit determination was adopted as a relatively inexpensive means for complementing radio orbit determination which, for Viking, would be operating under demanding circumstances, including stringent navigation requirements vs a rather unfavorable radio navigation geometry. Furthermore, it was recognized that the optical capability provided the opportunity to greatly improve navigational accuracy. This improvement would provide the attendant benefits of simpli-

Table 5. OD software outputs

	ODP	OMSET	ONP
User selected files of intermediate calculations	X	X	X
Radio regres file	X		
PV file	X		
Radio solution, covariance and residuals hardcopy	X		
Radio covariance file	X		
Plots of image geometry		X	X
Updated optical observation model		X	
Processed optical data file		X	
Line and pixel residuals		X	X
Updated satellite ephemeris parameters			X
Picture sequence file			X
Optical regres file			X
Optical solution, covariance and residuals hardcopy			X

Note: Residuals and solutions were often summarized as plots

Table 6. OD software glossary

Farmer	A system of programs used for automatically cataloging, storing, and retrieving mass storage files on magnetic tape
ODP	Orbit determination program Processes radio metric observations and ONP-processed optical observations to generate radio-based and radio-plus-optical orbit estimates
OMSET	Optical measurements set Processes raw optical observation data to generate processed optical observables
ONP	Optical navigation program Processes optical observables to generate optical-based orbit estimates
PV file	Contains probe ephemeris plus variational partials as sum and difference arrays
Radio covariance file	Contains radio covariance and state vector used as a priori by the ONP for optical-based solutions
Regres file	Contains computed observables, residuals, and data partials
Salient information file	Contains a record of the major computations made by each ODP link during a run

Table 7. Typical operations sequence

Generate radio solutions
Generate PV file for ODP, OMSET, and ONP
Get radio data and calibrations
Generate radio regres with ODP
Analyze radio data residuals
Iterate PV/regres if necessary
Generate radio solution with ODP
Deliver radio covariance file to ONP
Generate multiple radio solutions
Process optical data
Get PV file from ODP
Get optical data and hardcopy
Do video image extraction
Do image center finding
Do pointing error calibration
Analyze optical data residuals
Deliver OMSET data file to ONP
Generate optical solutions
Get PV file from ODP
Get processed optical observations from OMSET
Generate optical regres with ONP
Deliver optical regres to ODP
Generate optical solution with ONP
Analyze optical data residuals
Get radio covariance file from ODP
Generate multiple optical solutions
Generate radio plus optical solutions
Get PV file from ODP
Get radio regres from ODP
Get optical regres from ONP
Generate radio plus optical solution with ODP
Generate new PV file, deliver best estimate
Evaluate above solutions against short- and long-arc solutions
Select best solution
Generate new PV file with ODP
Deliver new PV file to all users

Note: Multiple solutions are generated by varying the data set, parameter list or weights, or filter options

Table 8. Mission requirements and radio capability

Parameter	Planned target			Requirement			Radio capability				Major error
	B, km	θ , deg	TCA	$ \Delta B $, km	$ \Delta \theta $, deg	$ \Delta TCA $, s	SMAA, km	SMIA, km	θ_{SMAA} , deg	$\sigma_{1-\sigma}$	
Viking 1											
Departure M/C	9,737	47	16:24:45	5,000	Circular	900	1,200	300	129	260	Solar radiation pressure model
Approach M/C				700	5	900	250	60	77	55	1 SLI
MOI				500	3	15	145	10	70	5	1 SLI
Viking 2											
Departure M/C	11,959	15	11:51:41	5,000	Circular	900	1,500	300	160	240	Solar radiation pressure model
Approach M/C	9,421*	-13.6*	11:51:41*	500	7	900	485	40	95	215	FSLI
MOI				350	5	15	250	5	91	5	ESLI

*Planned target at time of Departure M/C. Final target was modified slightly on approach.

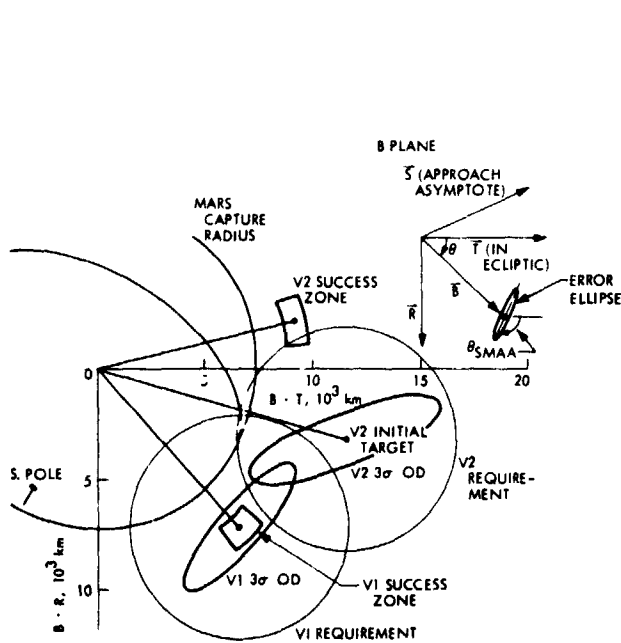


Fig. 4a. Mission requirements and radio capability: departure

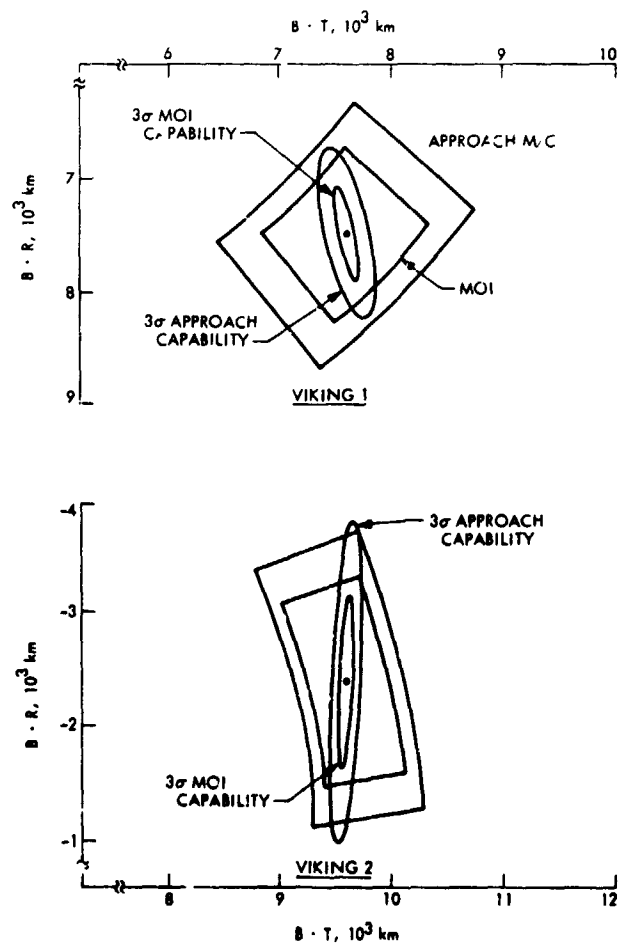


Fig. 4b. Mission requirements and radio capability: approach

ORIGINAL PAGE IS
OF POOR QUALITY

fied mission operations and increased fuel reserves, which ultimately enhance science return.

The detailed mechanics of the Viking optical observations are given in Section III. The specific geometric configuration of the optical observations during approach is shown in Fig. 5. The standard conceptualization of the optical observable is given by

$$\phi = \frac{X}{R}$$

(see Fig. 6). The angle measurement ϕ applies to either the line or pixel effective angle observation. The position measurement X is the corresponding B-plane displacement. For Viking, the line and pixel B-plane displacement correspondence is, to a fair degree of accuracy, represented by

$$\text{Line: } -B \cdot T$$

$$\text{Pixel: } B \cdot R$$

(see Fig. 5). An extension of the optical model proved very helpful:

$$\phi = \frac{X - \dot{X}T}{\dot{R}T} = \left(\frac{X}{\dot{R}} \right) \frac{1}{T} - \frac{\dot{X}}{\dot{R}}$$

where T = time to go. For an approaching spacecraft, $\dot{R} = V_{\infty}$, the planet-centered hyperbolic excess velocity.

This extension describes the way spacecraft normal velocity and B-plane displacement influence the observation. The velocity produces a bias, while the B-plane displacement produces a $1/T$ signature. If observations are taken at two times, T_1 and T_2 , X and \dot{X} are determined unambiguously. The expression for the accuracy in "estimating" X is given by

$$\sigma_X = \sigma_{\phi} V_{\infty} T_2 \left(\frac{\sqrt{2}}{1 - \frac{T_2}{T_1}} \right)$$

See Fig. 7 and observe the importance of increasing observation arc length ($\Delta T = T_1 - T_2$).

This illustrates the important fact that the optical observable permits separation of the trajectory displacement from either optical bias or velocity errors, provided that observations are obtained over a sufficiently long data arc. For this reason, long optical data arcs were planned for Mars approach.

This did in fact allow orbit estimates based on only the optical data. As indicated in Section X, the "optical-only" estimates generally agreed well with the radio only and the radio plus optical estimates. The agreement between the basically independent means for determining the approach orbit greatly enhanced the confidence placed in the final orbit determination results.

B. Approach Observation Schedules

Figure 8 displays the approach observation schedules planned and executed for the Viking 1 and Viking 2 missions. Each schedule covers the 40-day period before each encounter (termed the "planetary operations phase," during which the most intense preorbit insertion preparations took place).

During this time, the Earth-based doppler and range tracking coverage was virtually continuous. The optical observations included the star-Mars-star triads and star-Deimos single frames discussed in Section IX. A total of 35 triad observations was scheduled for each Viking delivery. The observations were concentrated at the end points of the 20-day arc preceding the "final" ($E-10$ day) M/C. That distribution was optimal with respect to the strength of the observations. The Viking 2 schedule included a data set midway between the endpoints to permit a preliminary optical-only determination. The number of observations was considerably larger than necessary for accuracy. The redundancy was included to allow for the possibility of lost observations and to provide sufficient data for residuals analysis.

Following the approach midcourse maneuvers, additional triads were planned to allow rapid orbit redetermination capability as well as a means for postmaneuver camera pointing validation. After the final triads, the sequence of Deimos-star observations was scheduled to support orbit insertion. These observations were carefully planned to provide good coverage of the satellite orbital motion, permitting separation of satellite ephemeris errors from spacecraft trajectory errors in the estimation process.

C. Orbit Estimation Strategies

There exists a large degree of flexibility in obtaining interplanetary orbit estimates, and the process of arriving at a final best estimate supporting a critical midcourse maneuver is by no means straightforward. The procedure generally consists of obtaining a large variety of solutions based on varying treatments of the available data sets. A summary of the more important data treatments is presented in Table 9. A performance analysis of some of these treatments is given in Section X. During flight, thorough analysis of these results then identifies, and hopefully resolves, any problems with particular

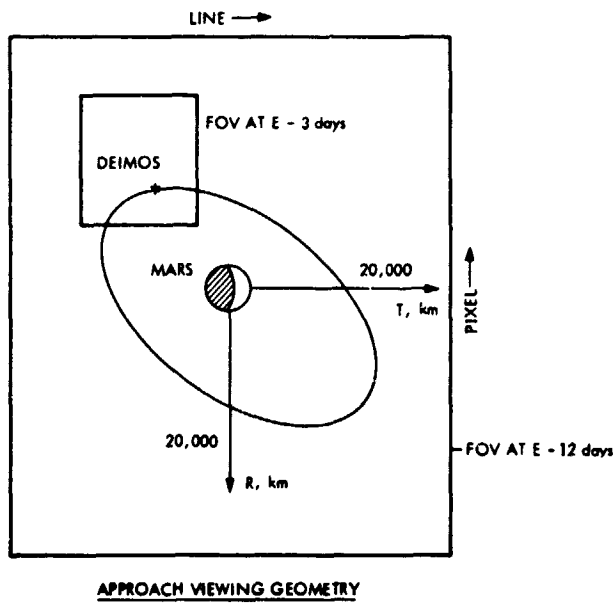
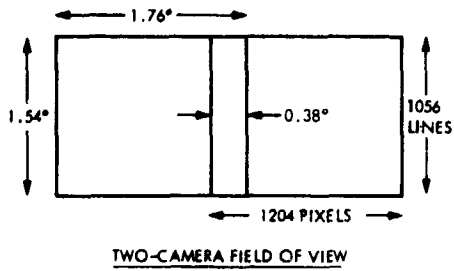


Fig. 5. Optical observations

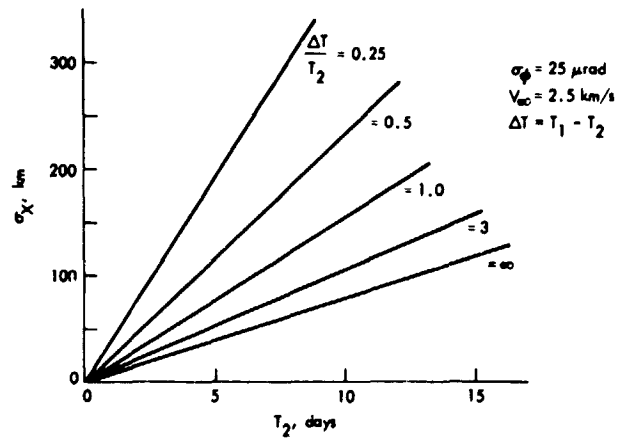


Fig. 7. Optical accuracy

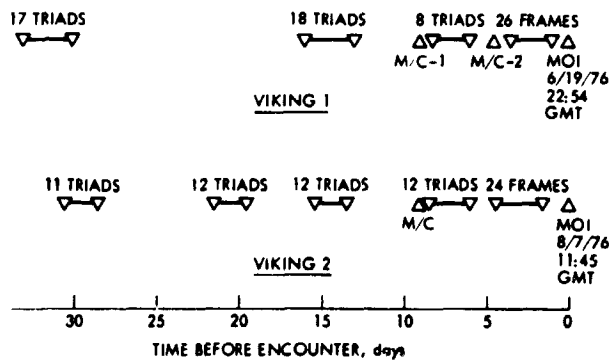


Fig. 8. Optical observation schedules

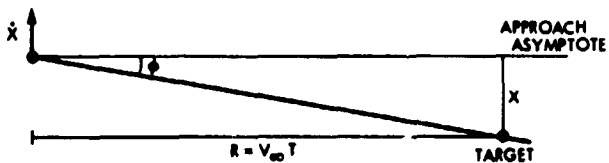


Fig. 6. Optical observable

Table 9. Data treatment

Observation sets
Short arc radio (21 days)
Doppler plus range
Doppler only
Range only
Doppler plus range with DRVID calibrations
Long arc radio (selection of all previous data)
Doppler plus range
Range only
Radio plus optical
Optical
Orbit determination filter
Sequential filter
Weighted least squares
Solution vector
S/C (state)
State, solar pressure (SP)
State, Deep Space Station (DSS) locations
State, SP, DSS
State, range biases
Data weighting
1-mm/s doppler, 1 pixel optical (nominal)
3-mm/s doppler, 0.5 pixel optical (account for charged particle corrupted doppler, good optical measurements, performance)
Radio and optical data combination
Direct radio plus optical
Radio <i>consider</i> covariance and estimate plus optical

data sets and ultimately leads to the selection of the final best estimate.

Special consideration was given to the particular character of the radio and optical orbit estimate accuracies. Generally, the radio estimates proved to be very accurate in $B \cdot T$ (~10-km errors) and relatively inaccurate in $B \cdot R$ (~200- to 400-km errors). The optical-only errors were equally distributed in $B \cdot T$ and $B \cdot R$ and generally much more accurate than the radio solutions in $B \cdot R$. The optical solutions were very inaccurate in TCA, however. These factors provided the following set of criteria that proved very successful in obtaining accurate and reliable final estimates:

- (1) Final $B \cdot R$ is consistent with the optical-only $B \cdot R$.
- (2) Final $B \cdot T$ is consistent with the radio $B \cdot T$.
- (3) Final TCA, accounting for the radio correspondence of $B \cdot R$ and TCA variations, should agree with the radio TCA.

This is not to suggest that the final estimates were constructed ad hoc, or by hand. Instead, data weighting and filtering specifications were modified, usually slightly, to produce radio plus optical solutions that satisfied the above criteria.

VI. Orbit Determination Results

A. Launch/Earth Departure Phase

The launch/Earth departure phase of the mission extended from launch to the first trajectory correction maneuvers, which were made 7 days and 10 days after launch, on Viking 1 and 2, respectively. The purpose of the maneuvers was to remove the nominal planetary quarantine bias and the launch error.

Viking 1 was launched on August 20, 1975, with Trans-Mars Injection (TMI) occurring at 21:52:48 GMT. Viking 2 was launched on September 9, 1975, with TMI occurring at 19:12:28 GMT. Figures 9 and 10 show for each spacecraft the Mars B-plane with the injection aim points and the launch (or injection) dispersion ellipses. The sequence is also shown of orbit determination solutions from 1 hour past up to several days past TMI. These solutions are summarized in Table 10 for both spacecraft along with the one-sigma uncertainties mapped to the Mars B-plane. Note that during the first few hours past injection, angle data (ground tracking antenna hour angle and declination) were used. As the spacecraft-station range increases, the angle data are no longer useful and were not used again.

The major error source contributing to the uncertainties shown in Table 8 is nongravitational acceleration uncertainty, in the form of solar pressure uncertainty. It is not possible to estimate solar pressure effects in the early launch/Earth departure phase because the inverse distance squared signature of a solar pressure acceleration error cannot be distinguished from a possible constant gas leak. Thus, a high reliance must be placed on the nominal solar pressure model. The first few estimates also have a significant uncertainty due to the uncertainty in the assumed Earth gravitational constant. Finally, as the spacecraft-station distance increases, the sensitivity of orbit estimates to station location errors tends to increase.

B. Cruise Phase

This portion of the interplanetary flight followed the departure correction maneuver, and terminated at start of planetary operations, 40 days before actual encounter. The basic activities during this phase are the provision of:

- (1) Ongoing updates and assessments of the spacecraft orbits for the primary purpose of predicting tracking antenna pointing and transmitter frequency.
- (2) Best-estimate trajectories to support planning and calculations for the Mars approach maneuvers following.
- (3) Evaluation of the overall accuracy level of the orbit determination system.

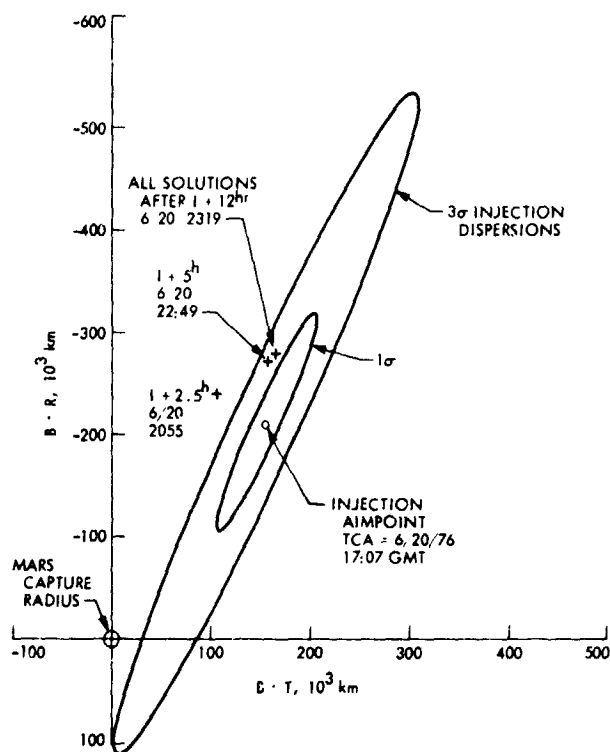


Fig. 9. Viking 1 launch phase solutions

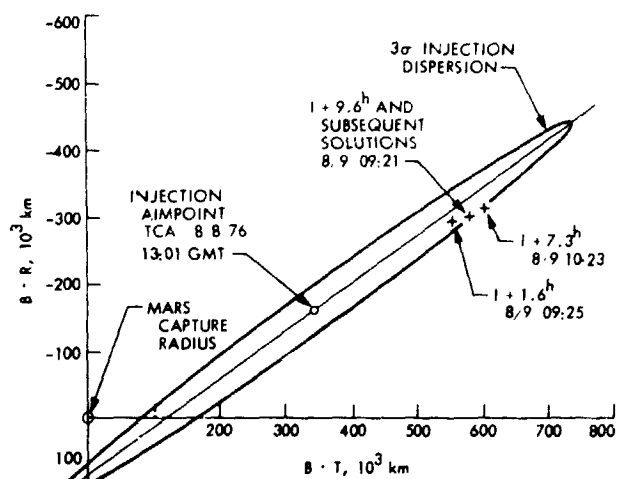


Fig. 10. Viking 2 launch phase solutions

Table 10. Launch departure solutions

Data span, from injection	DSS	Data	B · R, km	B · T, km	TCA	SMAA, km	SMIA, km	θ , deg	σ_T
					6/20/76				
Viking 1 nominal			-210,270	162,760	17:07				
1 h	42	Doppler, angle	-240,500	105,960	20:55	28,270	4,710	127	1 ^h 57 ^m
3.5 h	42, 44	Doppler, angle	-272,040	157,930	22:50	14,100	515	121	1 ^h 5 ^m
6 h	42, 61	Doppler	-277,470	164,500	23:19	9,180	420	125	39 ^m
9 h	42, 61	Doppler, range	-275,740	163,360	23:12	1,610	260	130	7 ^m
6 days	43, 61, 11	Doppler, range	-277,200	164,500	23:19	1,137 ^a	250 ^a	135 ^a	5 ^m
					8/9				
Viking 2 nominal			-163,290	339,730	13:01 ^b				
1.6 h	42	Doppler, angle	-299,550	555,650	09:25	22,370	1,680	155	58 ^m
7.3 h	42, 61	Doppler	-311,600	602,400	10:23	44,020	350	153	2 ^h 2 ^m
9.6 h	42, 61	Doppler, range	-301,560	581,580	09:18	1,670	275	161	4 ^m
5 days	11, 12, 42, 43, 61, 63	Doppler, range	-301,810	581,900	09:20	1,650 ^a	290 ^a	153 ^a	3.3 ^m
10 days	11, 12, 42, 61, 63	Doppler, range	-301,870	582,110	09:21	2,290 ^a	335 ^a	158 ^a	5.8 ^m

^aStation location uncertainties added to error model.

^bTCA date is 8/8 for this entry only

One of the tasks to be accomplished during cruise was to determine the nongravitational force environment of the spacecraft. Specifically, it was necessary to determine to an accurate level the solar pressure model for the spacecraft and simultaneously monitor the tracking data for any indication of a large attitude control gas leak or other acceleration anomaly. A large solar pressure modeling error of 5% will accumulate approximately 1000 km in position error by Mars encounter time. The goal was to increase the accuracy to perhaps 2% by the inflight processing of tracking data. For the Mars mission, months of tracking data were required to achieve this level of solar pressure model accuracy.

Typically, item 1 was satisfied on a weekly basis by processing a "short" data arc, which included the previous 3 weeks of two-way doppler and range data. The term "long arc" was applied to data spanning the entire cruise phase. Each arc length shows different characteristic sensitivity to possible error sources; treating the two data arcs separately provides a good measure of the overall orbit determination performance. Figures 11 and 12 show a partial history of short-arc solutions mapped to Mars for each spacecraft. A description of the long-arc processing follows in the next section.

VII. Long-Arc Radio Data Processing

This section presents a special description of the inflight and postflight processing of the Viking 1 and 2 radio data arcs spanning the entire interplanetary cruise. In summary, the orbit estimates using the long radio data arcs did not behave as well as expected on Viking 1. The Viking 1 B-plane estimate was in error by nearly two sigma, even allowing for the later application of ionosphere corrections to the tracking data. The Viking 2 estimate was quite accurate, however, owing to modifications to the long-arc strategy determined from analysis of the Viking 1 long arc post Viking 1 encounter.

A. Inflight Processing

The long-arc data processing was performed every 3 to 4 weeks and generally followed the outline of the short-arc processing activity. These data sets generally included all data (20-min doppler samples, 3 or 4 range points per pass) collected to date, from the near-Earth midcourse on but prior to any approach midcourse burns.

It had been expected that the processing of the long-arc data would produce stable and accurate radio-only trajectory estimates throughout the cruise phase and help verify the orbit solutions based on early approach optical data. The long data arcs provide more of a heliocentric trajectory determination, and as such are less sensitive to equivalent station location error (ESLE in Table 8) effects than the short arc counter-

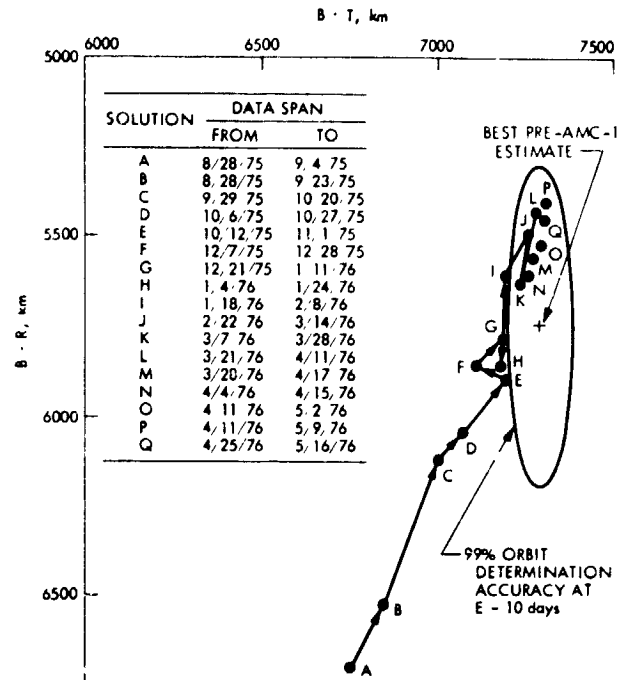


Fig. 11. Viking 1 cruise solutions

parts. Also, long arcs contain the slowly varying $1/R^2$ solar pressure acceleration signature, and can thus be most effectively used to evaluate the nominal solar pressure model. This last aspect is discussed further in Section VIII.

The actual inflight results from the long arc radio processing were mixed. The last few long-arc estimates were uniformly accurate in ecliptic $B \cdot T$ as was to be expected (see Section V) but not in $B \cdot R$ (see Fig. 13). The real-time solutions from the Viking 1 long arc data were in error by several hundred kilometers at the time of the approach maneuver. Figures 13 and 14 summarize the history of long arc solutions for each mission. Note that the final Viking 1 inflight estimate (point E in Fig. 13) was in error by ~ 250 km in $B \cdot R$ relative to the delivered "best" estimate obtained from short-arc radio and optical combined processing. This error constituted more than a "2.5 sigma" bias. See Section X for further discussion of the approach orbit determination results.

Based on analysis of the Viking 1 long-arc solutions following Viking 1 MOI, the Viking 2 long-arc solutions were improved by implementing the following strategies:

- (1) Adding Faraday calibrations for Earth ionospheric charged-particle effects (solution F of Fig. 14). This resulted in the removal of a 90-100 km bias in $B \cdot R$.
- (2) Introducing a constant nongravitational acceleration to absorb unmodeled error effects, and subsequently

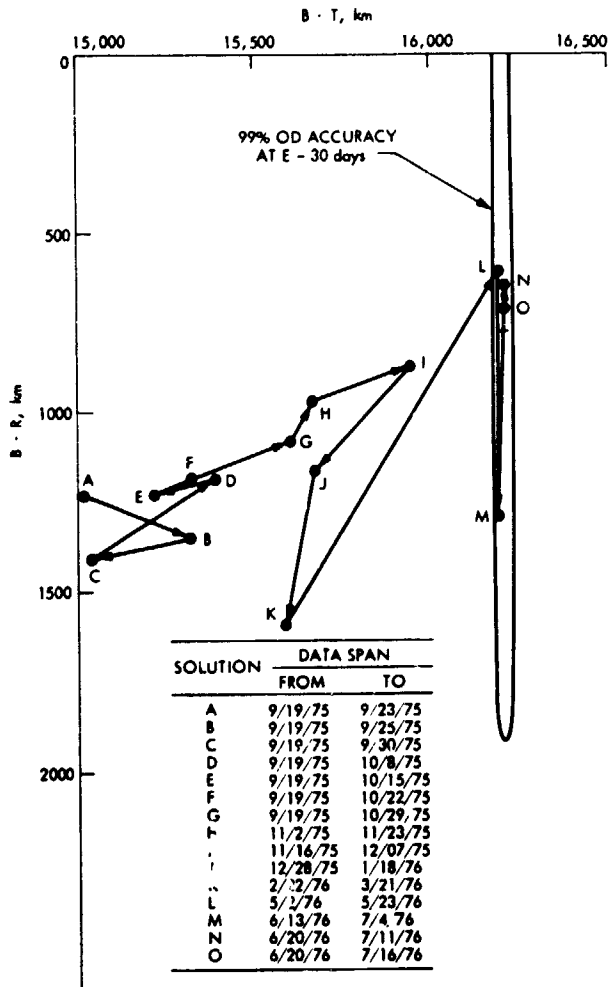


Fig. 12. Viking 2 cruise solutions

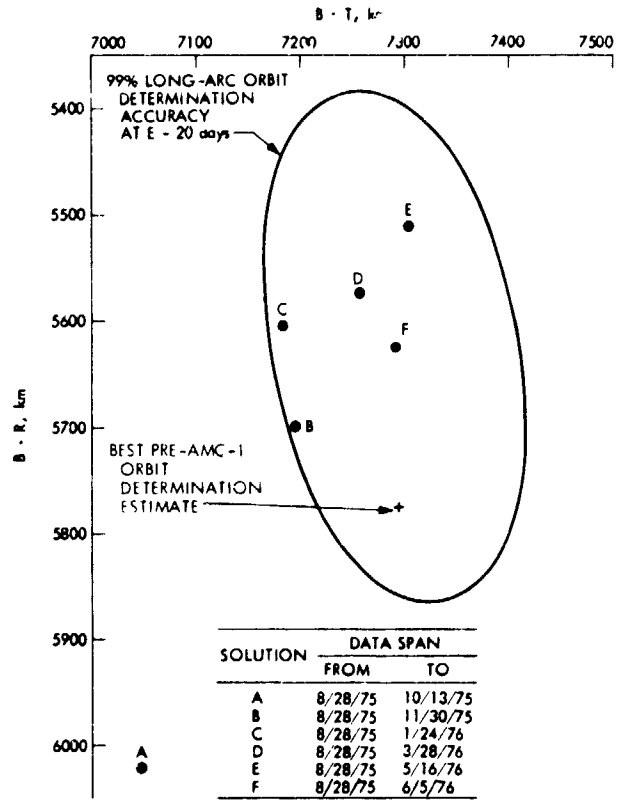


Fig. 13. Viking 1 long-arc solutions

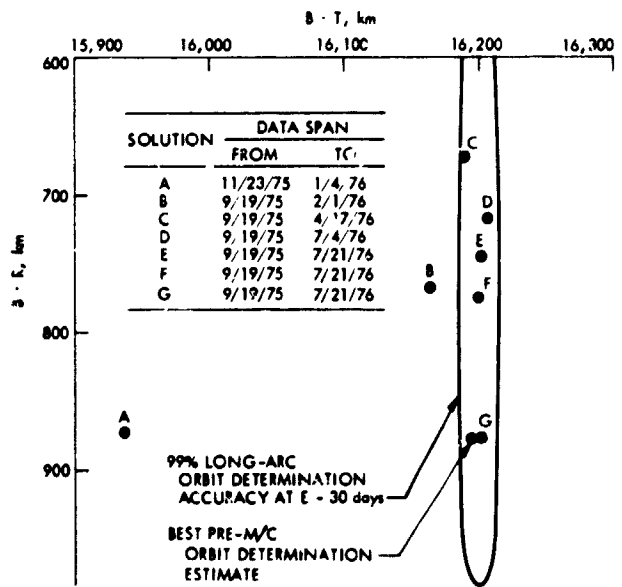


Fig. 14. Viking 2 long-arc solutions

converging the long arc trajectory using a sequential filter fit (solution G of Fig. 14).

In contrast to Viking 1, the resulting Viking 2 long-arc estimates were much improved, and in fact strongly supported the final best approach estimate. The sequential filter, state-only fit of the long data arc to the final data set 10 days from encounter was nearly coincident with the delivered short radio arc plus optical result.

B. Postflight Processing

As mentioned above, the accuracy of the inflight Viking 1 long-arc orbit determination was less than that expected initially, as measured against the near-Mars short-arc radio-plus-optical data solutions. Good solutions of $B \cdot T$ and TCA were obtained; however, the $B \cdot R$ solution, as mentioned earlier, was in error by approximately 250 km. The following remarks summarize the efforts made to rectify the Viking 1 long arc solution.

The dynamical environment for the interplanetary cruise is considered to be favorable for obtaining good radiometric-based heliocentric orbit determination. Between the Earth departure maneuver and the Mars-approach maneuvers, the spacecraft translational motion resulting from gravitational and solar pressure accelerations could be modeled in a straightforward fashion. The contribution to the translational dynamics from the attitude control system was minimal, owing to the use of coupled attitude thrusters. One notable but minor exception was the venting of atmospheric pressure from the lander during the Earth departure phase and later venting during planned checkout tests. (The events are discussed in more detail in the material to follow.)

Thus it was felt that with some further attention to detailed postflight processing, the long-arc solution could be made compatible with the very accurate near-Mars radio-plus-optical solution. Such a solution was finally obtained by accounting for the following phenomena:

1. The orbit solution was referenced to the improved planetary ephemeris DE-96. This ephemeris was available for use during real-time flight operations and was evaluated at that time using short data arcs. To accomplish the postflight reprocessing in a reasonable fashion, the doppler data was compressed to 2-h samples, from the 20-min inflight sample rate. A station location set compatible with DE-96 was obtained, and the trajectory recomputed based on DE-96. The first entry of Table 11 shows a change of +59 km in $B \cdot R$ and -9 km in $B \cdot T$ for the switch from ephemeris DE-84 to DE-96.

2. Two spacecraft outgassing events were identified from plots of the doppler and range residuals based on inflight

solutions. These events were verified postflight by the Viking spacecraft team, and the effective velocity increments resulting were accounted for. Figure 15 shows the nominal doppler residuals from the inflight data. Note the slight initial slope in the plot, indicating a somewhat constant, unmodeled spacecraft acceleration. Also note on the plot reference to the two jumps in the residuals, which occurred on 10/30/75 and 11/13/75. These jumps were traced postflight by the spacecraft operations team and were attributed to two planned events. The first jump, on 10/30/75, was attributed to a quick venting of atmospheric pressure from the GCMS instrument in an unknown direction. The second jump was due to venting of propellant pressure from the lander, also in an unknown direction as part of a planned lander checkout sequence. The two jumps are seen to have a fairly small magnitude, on the order of 5 mHz along the Earth line-of-sight direction, or about 0.3 mm/s, and thus, even if ignored, have only a small effect on the solution. Two impulsive velocity increments were introduced to account for the jumps, and as shown in the second entry of Table 11, the Mars B-plane coordinates changed by only -7 km and -13 km in $B \cdot R$ and $B \cdot T$ respectively. Figure 16 shows the final doppler residuals after including the effective velocity impulses. As a matter of interest, these same events also occurred for Viking 2, but in the opposite sequence. Figure 17 shows the lander checkout occurring on 11/21/75, when propellant was vented, and the GCMS venting occurring on 11/25/75. The larger slope in the initial doppler residuals in the figure is due to the lander bioshield venting, which was documented inflight. It was

Table 11. B-plane summary of Viking 1 postflight long-arc data processing

	B · R	B · T		
Final inflight solution (long-arc)	5,520 km	7,300 km		
Postflight long-arc improvements	$\Delta B \cdot R$	$\Delta B \cdot T$		
1. Orbit referenced to improved ephemeris DE-96	59 km	-9 km		
2. Estimate velocity increments due to spacecraft outgassing on 10/30/75 and 11/13/75	-7 km	-13 km		
3. Add calibrations to account for ionospheric effects	+31 km	+3 km		
4. Reestimate solar pressure coefficients using data set derived from items 1-3 above	+150 km	+14 km		
	B · R	B · T	TCA (UTC)	
Final postflight solution (long-arc)	5,752	7,295	6/19/76	16:31:21
Best inflight solution (radio + optical)	5,774	7,289	6/19/76	16:31:23

ORIGINAL PAGE IS
OF POOR QUALITY

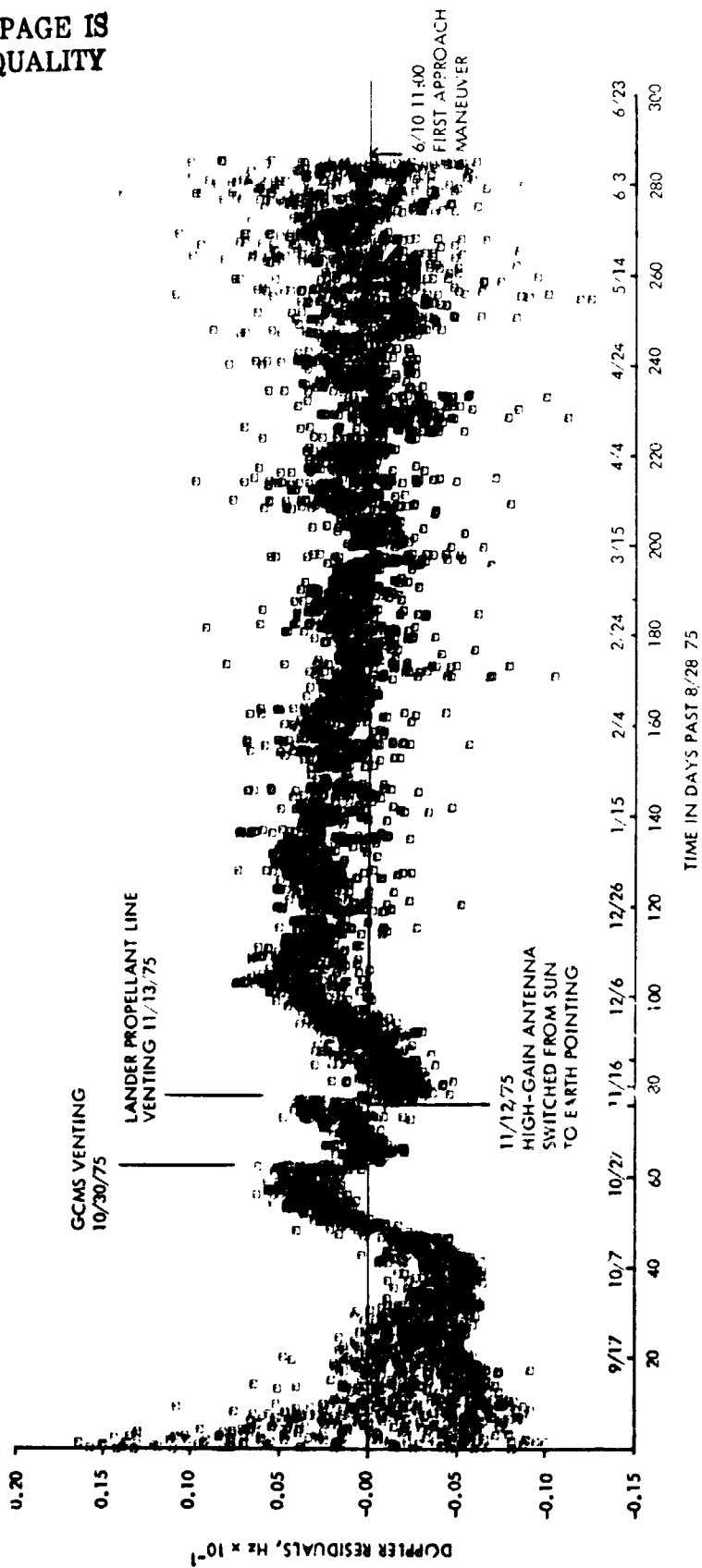


Fig. 15. Viking 1 long-arc inflight calibrated doppler residuals

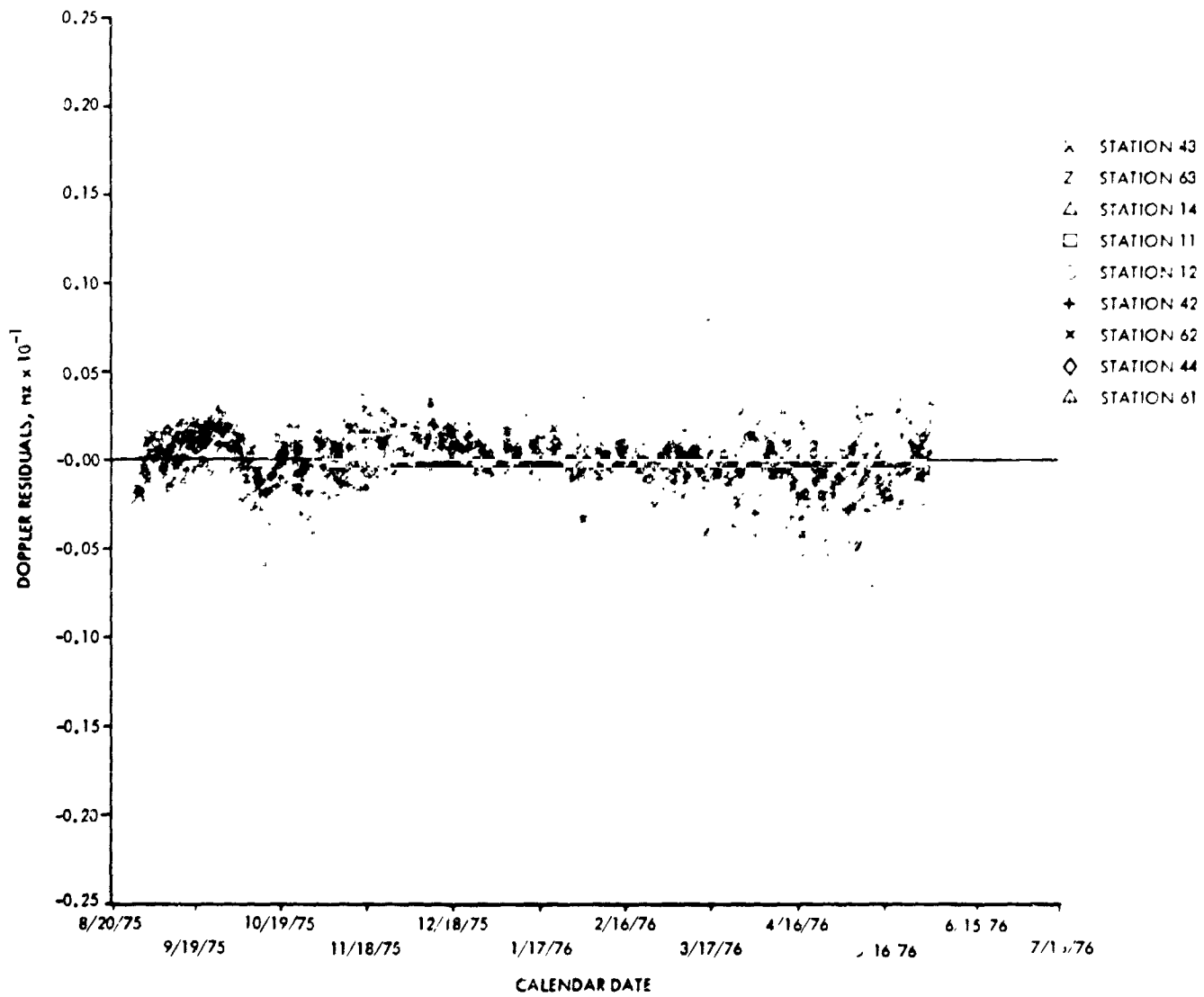


Fig. 16. Viking 1 long-arc postflight calibrated doppler residuals

ORIGINAL PAGE IS
OF POOR QUALITY

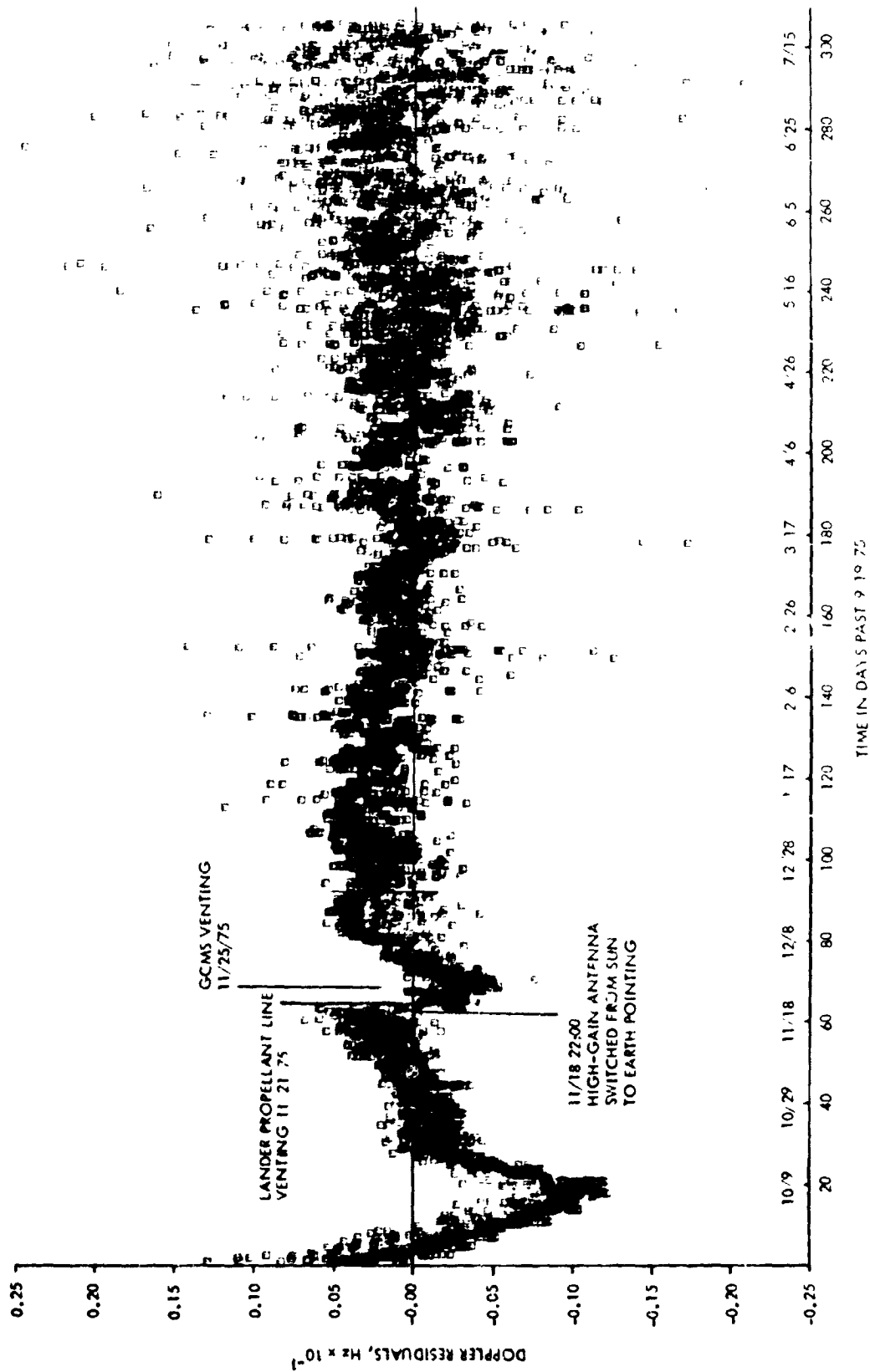


Fig. 17. Viking 2 long-arc inflight calibrated doppler residuals

confirmed postflight that the venting did cease at about the time shown in the figure.

3. Calibrations based on Faraday rotation data obtained from the DSN were introduced to account for ionospheric effects on the doppler and range data. Figures 18 and 19 show, respectively, the uncalibrated and calibrated doppler residuals. The calibrated residuals are much smoother in general; the larger level of apparent noise at the end of the data arc is probably due to space plasma effects, which were more pronounced during the approach phase and not removed by the Faraday correction. In the case of a long radiometric arc these effects can be assumed to be random and near-zero mean and were not explicitly accounted for in the long-arc processing. Figures 20 and 21 compare, respectively, the range residuals for the uncalibrated data and the calibrated data. Note that the difference is not strictly due to the correcting of the range data itself for ionosphere, which is on the order of 1-2 meters, but is due to the effect of the doppler calibrations on the orbit solution. The range residuals are from a combined doppler and range fit, where the effective doppler data weight dominated the range data weight. The third entry in Table 11 indicates that the application of ionospheric calibrations increments the B-plane position by +31 km in $B \cdot R$ and +3 km in $B \cdot T$.

4. After including the above adjustments and reconverging the trajectory, the solar pressure coefficients were reestimated. Table 12 compares the final inflight and postflight solutions. The final entry in Table 11 shows that the revised coefficients accounted for the largest B-plane change, +150 km in $B \cdot R$ and +14 km in $B \cdot T$. This procedure for trajectory convergence differed from the usual inflight procedure in that the solution used to converge consisted of the spacecraft state vector plus solar pressure coefficients from the final inflight solution.

In summary, several general conclusions regarding long arc radiometric data processing can be stated:

- (1) Careful attention should be paid to accurate representation of spacecraft-based dynamics, to both guard against real orbit effects, and effects which mainly corrupt the data, and reduce the overall solution confidence, as in the case of the early gas leaks on Vikings 1 and 2.
- (2) The orbit estimates should be converged as necessary to preserve the accuracy of the linear corrections made throughout cruise. In this regard, as a practical measure, the doppler compression rate should be on the order of several hours for continuous tracking missions to keep the data processing costs to a minimal level.
- (3) Ionospheric effects should be calibrated for inflight. These could be derived from either Faraday observa-

Table 12. Comparison of solutions for Viking 1 solar pressure parameters

Assumed constants		
Solar flux constant:	$1.01 \times 10^9 \frac{\text{kg} - \text{km}^3}{\text{m}^2 \text{s}^2}$	
Spacecraft bus area projection in X-Y plane:	26.607 m ² (includes solar panels, scan platform, lander, miscellaneous structure)	
Radius of high-gain antenna:	0.737 m	
Depth of high-gain antenna:	0.244 m	
	Final inflight solutions	Final postflight solutions
Spacecraft bus		
Z-axis coefficient (GR)	1.173	1.183
X-axis coefficient (GX)	0.060	0.0
Y-axis coefficient (GY)	0.036	0.01
Interior surface of high-gain antenna		
Specular reflectivity (MUF)	0.05	0.05
Diffuse reflectivity (NUF)	0.10	0.08

tions, in which case formal requirements for these data should be included in project planning, or from dual-frequency or DRVID tracking observables.

VIII. Solar Pressure Model Improvement

The major portion of the Viking spacecraft solar pressure acceleration was modeled by a constant-area flat plate reflectance representing the total cross-sectional area projected normal to the spacecraft-Sun line and the composite set of reflectance properties. A precise geometric model was separately defined for the parabolic Earth-pointing radio antenna since its projected cross-sectional area varied with time. The antenna contributed about 5% of the total solar pressure acceleration.

Solutions for the constant coefficients of the flat plate model and for the parabolic antenna were made throughout the cruise period, using both long and short data arcs. The final solutions, used for encounter OD and prediction, were made approximately two months before each encounter. Table 13 gives the nominal and final inflight adjusted values for the two vehicles. The values given in this table are essentially the composite values of $(1 + \gamma B)$ for the flat plate representation, where γ is the fraction of incident radiation which is reflected from the plate, and B is a factor depending on the diffuse and specular portions of the reflection. As the solar pressure coefficient determination was proceeding, an

C-2

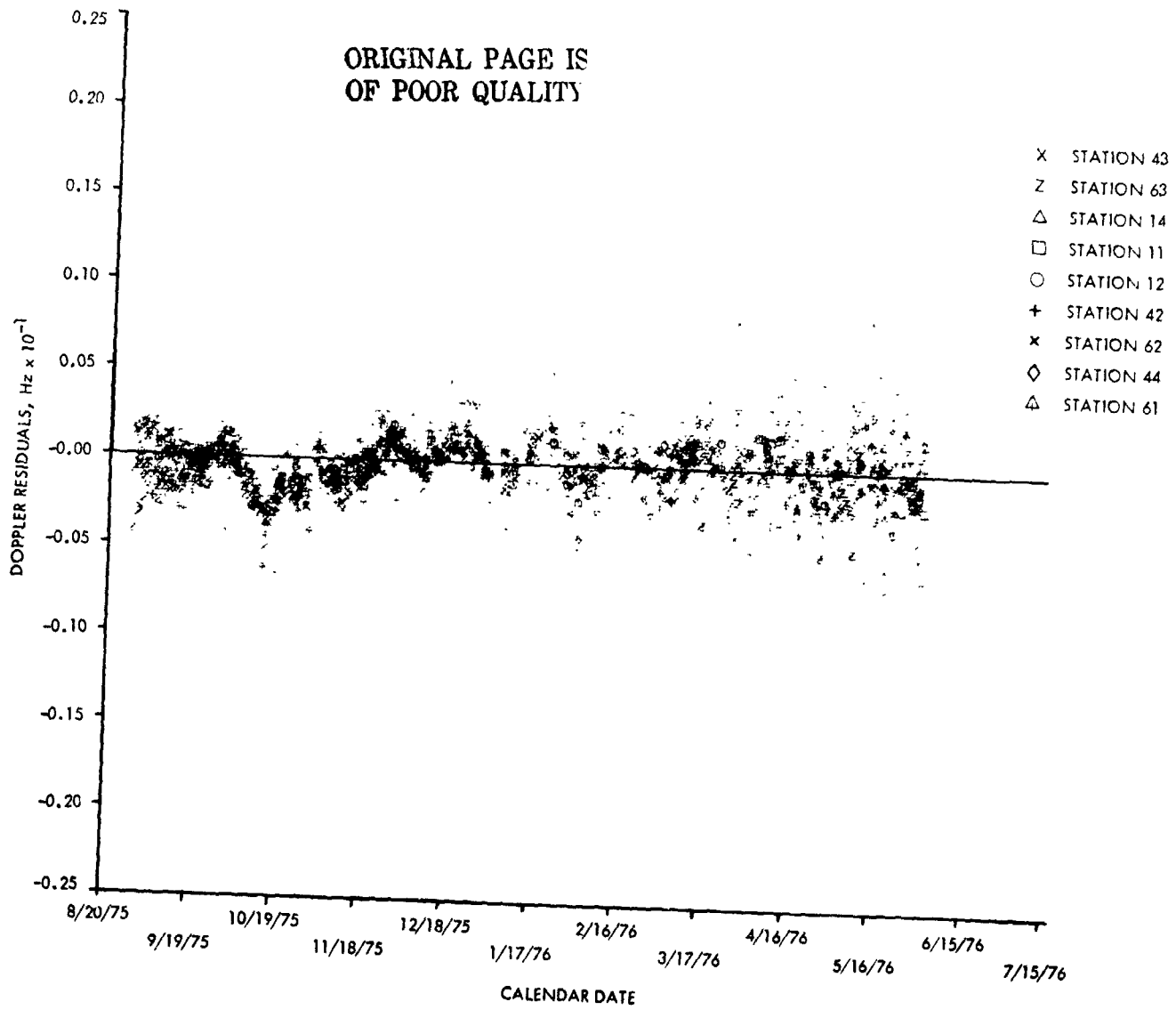


Fig. 18. Viking 1 long-arc postflight uncalibrated doppler residuals

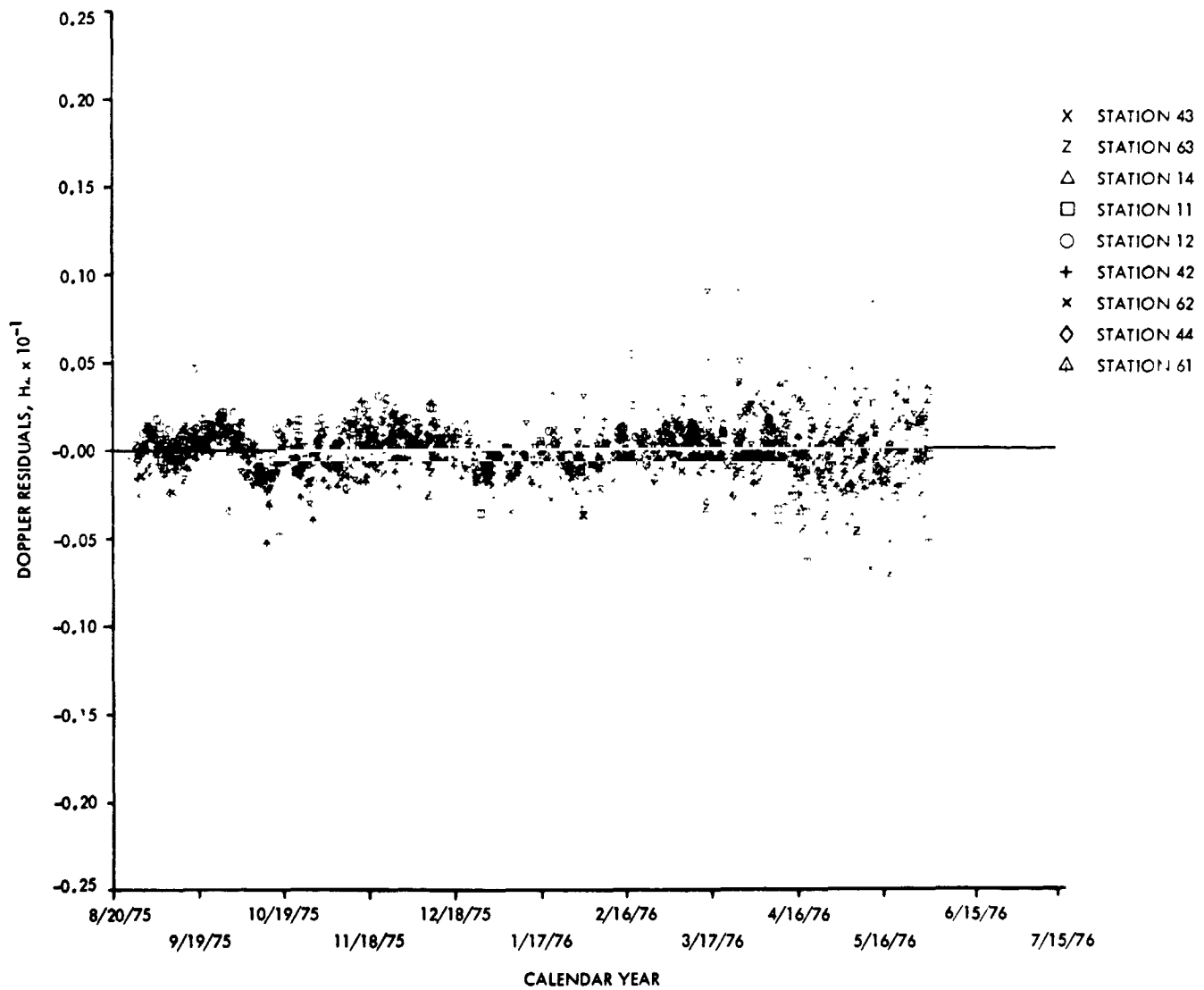


Fig. 19. Viking 1 long-arc postflight calibrated doppler residuals, doppler-only fit

ORIGINAL PAGE IS
OF POOR QUALITY

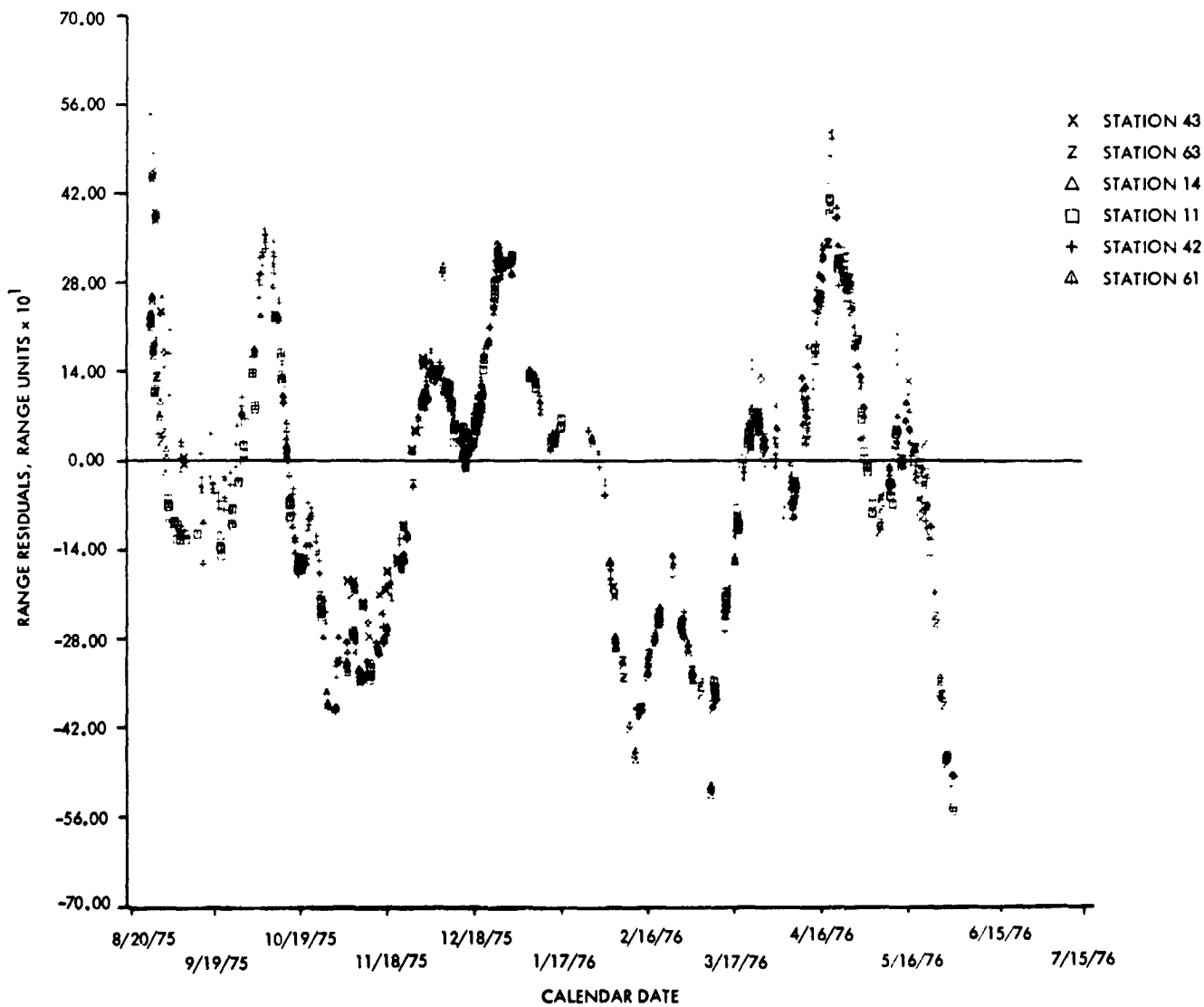


Fig. 20. Viking 1 long-arc postflight uncalibrated range residuals

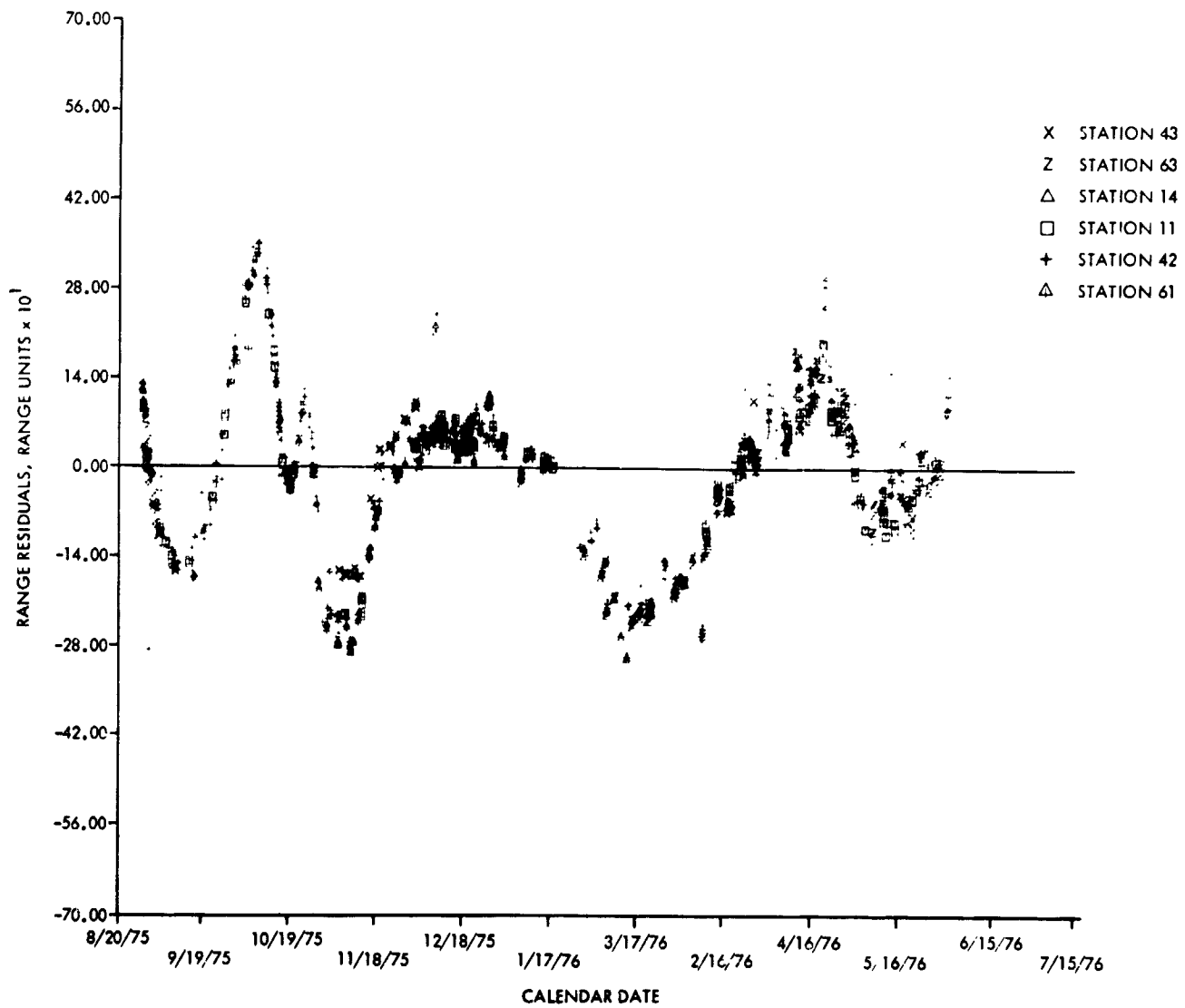


Fig. 21. Viking 1 long-arc postflight calibrated range residuals

Table 13. Comparison of inflight solutions for Viking 1 and Viking 2 solar pressure parameters

Parameter	Nominal values	Inflight solutions	
	Viking 1 and Viking 2	Viking 1	Viking 2
Spacecraft bus			
Z-axis coefficient (GR)	1.234	1.173	1.179
X-axis coefficient (GX)	0.0	0.060	0.037
Y-axis coefficient (GY)	0.0	0.036	0.025
Interior surface of high-gain antenna			
Specular reflectivity (MUF)	0.05	0.05	0.05
Diffuse reflectivity (NUF)	0.10	0.10	0.10

error was discovered in the specification of the nominal effective flat plate area and in the inclusion of reradiation effects in the nominal coefficients. This error was corrected by allowing the area to remain fixed and adjusting the nominal g_r coefficient from 1.320 to 1.234.

Note that most of the orbit solution migration shown in Fig. 11 is due to mapping the orbit solution to Mars with the uncorrected nominal solar pressure coefficients, through successively shorter times to encounter. The nominal parabolic antenna solar pressure coefficients are also shown in the table. Because of the small overall effect of the antenna, the nominal values could not be improved on.

IX. Optical Measurements Processing

A. Optical Measurement System

The optical measurements system of the Viking spacecraft consists of the Visual Imaging System (VIS), scan platform (S/P) and articulation control system, attitude control system (A/C) and the ground software required to combine their data to generate observations of the direction to Mars, or its satellites, with respect to the stars. The spacecraft subsystems involved are modeled in the software. These models are calibrated using preflight and inflight data so that they can be used to transform measurements into accurate navigation observations.

The VIS consists of two vidicon cameras with offset 1.54-deg by 1.76-deg fields of view (FOV), which overlap by 0.38-deg. They are sensitive enough to make detectable images of stars as dim as 9.5 visual magnitude with a 2.66-s exposure. The images are recorded, and then transmitted as 1056 lines of 1204 samples of intensity with 7-bit resolution. The cameras are shuttered and images recorded during alternate 4.48-s

frame times. The math model of the cameras relating image sample positions to directions relative to the S/P includes camera alignment, optical focal length, scan raster center, scale factor, rotation and nonorthogonality, and the geometric distortion in the vidicon.

The VIS is pointed in a desired direction by the scan platform articulation control system. The two orthogonal gimbals, clock and cone, are commandable in 0.25-deg increments and telemetered with 0.04-deg resolution. The math model of the scan platform includes the misalignments of the gimbal axes and instrument mounting surfaces and calibrations for the gimbal angles, null offset, scale factor, hysteresis, and harmonic errors.

The reference for the S/P pointing is the spacecraft attitude in space, which is controlled relative to the Sun and a reference star by the attitude control system. The nominal spacecraft attitude is defined by the directions to the Sun and reference star, but the actual attitude is defined by the error signals from sun sensors, star tracker, and/or gyros depending on the attitude control mode in use. The math model of the attitude deviations includes sensor null offsets, scale factors, and gyro drift rates.

The parameters of these math models were calibrated using VIS pictures of stars taken in flight. The VIS scan raster and geometric distortion parameters were estimated using images of a resseau grid marked on the vidicon face, with a posteriori image residuals of 0.25 pixel, 1σ . The VIS focal lengths and camera-to-camera alignment were estimated using successive VIS frames of a star field (the Pleiades) and of Mars and adjacent stars. The scan platform and attitude control parameters were estimated by comparing VIS pointing determined from angle telemetry with that determined from the stars appearing in the pictures.

B. Optical Observables

Two types of navigation observations were made using the VIS: stars-Mars-stars picture triads and satellite-star pictures. The triads are used when the Mars image is smaller than the FOV. Because of sensor dynamic range limitations, Mars and dim stars cannot be imaged accurately in the same picture. The two long-exposure star pictures are used to determine the pointing direction and rate of one camera. Using this, the pointing direction at the time of the Mars exposure is evaluated. The calibrated camera-to-camera alignment then is used to define the pointing direction of the camera taking the Mars picture. Because stars in the narrow FOV do not determine the rotation/twist of the S/P as accurately as the angle telemetry, the telemetry is used in the pointing estimation process. Accurate rotation is needed because of the

relatively large angular separation between Mars and the centroid of stars imaged in the other camera. A Mars limb model is then used to find the center of the Mars image on the frame. The camera pointing direction and the location of the center of the Mars image in the camera FOV combine to give a measure of the direction from the spacecraft to Mars.

The satellite-star pictures image a Martian satellite against a star background in a single picture and are used when the Mars image is larger than the FOV and the picture will not contain Mars. The long exposure required to see dim stars will not seriously overexpose small satellite images. For this type of navigation measurement, the angle telemetry is not as important since the satellite centroid-of-stars separation is smaller. Again, a center-finding technique on the satellite image, along with the pointing direction determined by the star background and the satellite center location, gives a measure of the direction from the spacecraft to the satellite.

C. Sequence Design and Pointing Optimization

The initial design of a navigation measurement sequence was chosen considering the time period to be covered, the frequency/number of measurements required to achieve the required accuracy, and the availability of suitable stars. Each picture/triad in this preliminary sequence was then repointed to optimize the data return. Special software was used to determine the pointing that guaranteed observation of Mars/satellite and maximized the probable number and brightness of stars, considering the range of S/P pointing errors and attitude control limit cycle. Also, in the early sequences, to optimize the probability of picture acquisition, the desired pointing was manually corrected for systematic S/P control offsets. The offsets were later automatically applied in the commanding process, making the manual operation no longer necessary.

The success of this optimization is demonstrated by the fact that not one picture/triad of the 142 planned was unusable because of missing the target or stars.

D. Data Flow and Management

Many Viking Flight Team organizations were involved in scheduling and processing navigation pictures. A large volume of pictures was processed, with relatively few problems, as a result of two important decisions:

- (1) Acquisition of optical navigation data was specially managed by the people processing the data.
- (2) Navigation pictures were given priority over all other concurrent picture processing requests.

The following events and times depict a typical processing sequence for a Mars observation triad played back at 8 kbits/s:

Triad recorded at spacecraft	T_0
Triad received at Mission Computing Center	$T_0 + 80^m$
Video reconstructed	$T_0 + 140^m$
Optical measurement processing complete	$T_0 + 200^m$

E. Telemetry Data Processing

The camera pointing at the shutter time of a picture was determined from the A/C and S/P angle telemetry. Three different sources of these data were used: the chain of data processing software used to generate pointing for science pictures, real-time monitoring of telemetry displays, and telemetry extracted from the engineering telemetry embedded in the recorded pictures.

Camera pointing, as derived from telemetry, was used to determine expected picture content: objects and their locations. These predicts were used to prepare input for OMSET to specify the areas of the picture to be extracted as arrays of intensity values. These areas would be offset by the difference between predicts and actual location once a known object (Mars or Deimos) had been located in the hard copy of the picture.

F. Picture Data Processing

The picture data (array of intensities) processing consisted of the determination of the locations in the image frame of four types of images: reseau, star, large body (Mars), and small body (Deimos). Generally, this consisted of either extracting an area around a small image and determining its center from the intensity profile or locating points on the limb of a large body and determining its center by fitting an ellipse to the set of limb points.

Reseau images were processed for camera distortion calibration. Areas around the known reseau locations were put in a file by OMSET. Because of the large number of reseau images to be processed, special software was used to determine the reseau location in each area and to write formatted location data for input to OMSET, which would do the calibration.

Star images were manually located from printout of the extracted area around the image and edited into the predicts file in place of predicted locations. The star location criterion used was eyeball interpolated peak intensity.

Mars limb points were found by OMSET using interpolated threshold crossings. Analysis of Mars pictures taken during Scan Cal II indicated that the best results were obtained for a threshold about 10 DN (~10% of peak signal) above the background. The limb fitting was done by OMSET at three different levels of data point editing with the operator selecting the one to be used and inserting that location into the predicts file.

Deimos images were too small to be located by their limb, but were generally larger and brighter than star images. The location criterion used for minimizing the effects of beam pulling, based on analysis of Mariner 9 data, was the center of a box circumscribed about the image, using tangency points just above the peak background level.

G. Optical Observables Generation

The residuals from processing of the star and target images and engineering telemetry were evaluated and each image was accepted, rejected, and/or reevaluated until a consistent set of data remained. Errors removed by this process include data transcription errors, mislocated stars (e.g., peak of background identified as dim star), bright stars biased by beam bending, dim stars not definitely located on the first attempt but found when star reference predicts were available, etc.

Processing of the Mars observations produced estimates of the VIS pointing and attitude control rates based on engineering telemetry and the star images in the first and third pictures. These values and the calibrated camera-to-camera alignment were used to determine the pointing of the camera imaging Mars. The VIS pointing angles, pointing covariance and expected image locations were updated based on this estimate. Residuals and their statistics were then computed. The same process, except for attitude control rates, was performed for the simpler, single-frame Deimos observations.

Each processed observation was added to a composite Optical Measurement File, which was used for orbit determination. This file contained picture time and best pointing based on star images, image identifications and distortion corrected locations, and their statistics.

H. Processing Results

1. **Pointing control and knowledge accuracy.** The spacecraft attitude control and scan platform pointing subsystems performance for control of camera pointing met or exceeded the ± 0.5 -deg control requirement as evidenced by no loss of data because of pointing error. The knowledge accuracy is indicated in Table 14, which gives the statistics of star residuals, the difference between observed star locations and

Table 14. Pointing knowledge accuracy (pixels)

Observation sequence	Viking 1				Viking 2			
	Line ^a		Pixel ^a		Line ^a		Pixel ^a	
	μ	σ	μ	σ	μ	σ	μ	σ
Mars 1	14	13	11	26	10	10	18	11
Mars 2	12	10	2	19	19	9	-1	16
Mars 3	-56	12	12	23	5	9	6	9
Mars 4	-	-	-	-	4	14	15	9
Deimos	-91	16	-7	18	5	16	8	13

^a1 line or pixel = 0.0015 deg.

the predicted locations, based on the calibrated model, and the angle telemetry.

The migration of the mean line residual on Viking 1 is due to platform offsets induced by stress during two midcourse maneuvers. Even with this offset, the knowledge accuracy was better than the ± 0.25 -deg (170 pixels) requirement.

2. **Mars and Deimos residuals.** Part of the measurement validation process was to maintain a plot of Mars/Deimos residuals after pointing correction. These plots are shown in Figs. 22 through 25. The reasonableness and consistency of these residuals indicated the performance level of center-finding. To make the plots nominally a straight line, residual line and pixel were plotted vs reciprocal time to encounter. Slope of a line of residuals is essentially proportional to B-plane miss and the intercept to measurement bias or cross velocity errors (see description in Section V).

3. **Detrended measurement accuracy.** A quantitative evaluation of the target residuals was obtained by estimating a target center-finding error (proportional to angular diameter) and a bias to remove the slope and intercept from the plotted residuals. The remaining error indicates the consistency or noise of the data. The Deimos residuals, which are affected by Deimos ephemeris, were corrected for observed ephemeris errors. The detrended standard deviations are given in Table 15 and indicate that the performance level achieved far exceeded expectations.

X. Approach Orbit Determination Evaluation

The output of the orbit determination process is a series of orbit estimates used in navigating the spacecraft. As indicated in Section V, these estimates are not the product of a single

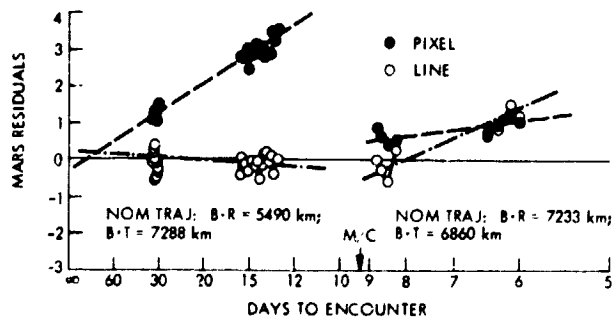


Fig. 22. Viking 1 Mars residuals

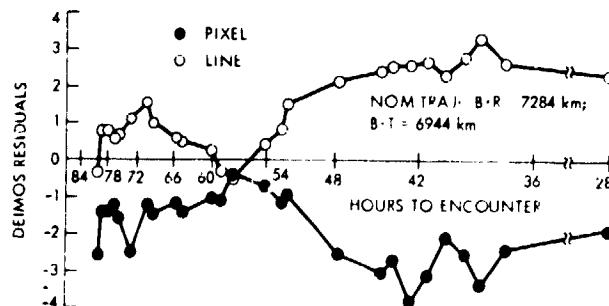


Fig. 24. Viking 1 Deimos residuals

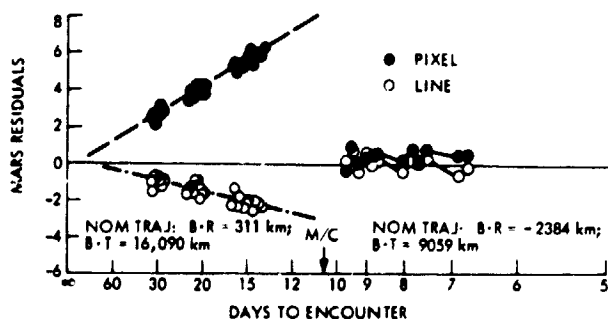


Fig. 23. Viking 2 Mars residuals

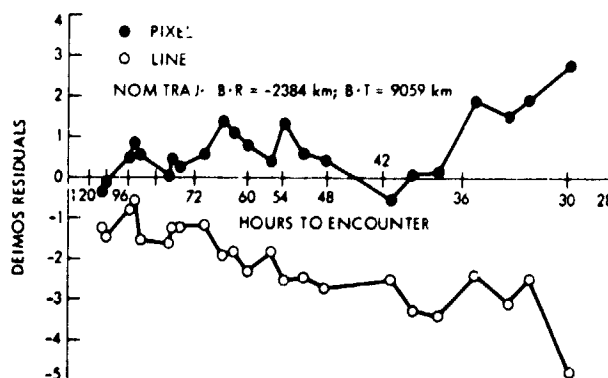


Fig. 25. Viking 2 Deimos residuals

Table 15. Detrended target residuals (pixels)

Observation sequence	Viking 1		Viking 2	
	σ line	σ pixel	σ line	σ pixel
Mars 1	0.36	0.28	0.27	0.26
Mars 2	0.22	0.28	0.33	0.29
Mars 3	0.34	0.20	0.32	0.45
Mars 4	-	-	0.41	0.39
Deimos	0.20	0.43	0.38	0.37

process, but are selected from a collection of orbit estimates, each obtained from a different treatment of the available relevant observation set. This section considers the general behavior of this set of solutions from which the best estimates

were selected. As would be expected, many more solutions were generated and analyzed during flight than can be presented here. Attention will be restricted to what is considered to be the set of most important solutions. More details on specific solutions can be obtained from the compilation in Section XI.

Variations of the solution values presented reveal the relative accuracy of various solution types, and some insight can also be gained into the selection process by which the best estimates were obtained. Analysis of relative solution variations did not provide the sole criterion, however. Consistency of observation residuals and evaluation of the expected or formal accuracy of the specific solutions provided criteria equally as important.

The absolute accuracy of the estimates can be evaluated only for the pre-MOI phase: that is, the estimates obtained

following the final approach midcourse. This evaluation can be made with respect to the reconstructed orbit estimate based on radio measurements made just before insertion. The near Mars data is sufficient in strength to allow determination of the encounter parameters to a high degree of accuracy, generally to within 10 km in $B \cdot R$ and $B \cdot T$ and less than 1 s in TCA. These estimates, although very accurate, are available far too late in the flight to assist in maneuver preparation. No such absolute reference is available for estimates prior to the approach midcourse maneuvers because of the relatively large uncertainty in the maneuver execution.

Table 16 presents the delivered orbit estimates including preliminary and final deliveries for each maneuver during the approach phase. The maneuver target values and associated execution uncertainties are given for the maneuver preceding the estimate. The relatively large execution errors predicted for the Viking 1 approach midcourse maneuvers were the result of the large (~ 50 m/s) maneuvers required to alleviate the Viking 1 propellant pressurant problem. Also presented in the table are the pre-MOI reconstructed estimates based on the near-Mars tracking data.

Figures 26 through 30 show actual orbit estimates obtained during flight. The solutions for $B \cdot R$ are plotted as a function of the time of the end of the observation set. The solution values are plotted with respect to the final best estimates for each approach phase, including the reconstructed estimates for pre-MOI estimates. The solutions are presented according to whether they were generated by the ODP (radio and radio plus optical) or the ONP (optical).

Solution values for TCA and $B \cdot T$ coordinates have not been included. The TCA coordinate is not critical for navigation analysis. The $B \cdot T$ coordinate was well determined by radio observations generally to within ± 10 km. This is because T lies in the ecliptic, in which most of the interplanetary spacecraft motion occurs. The effect is especially pronounced for Viking 2 owing to the near coincidence of the T direction and the line-of-sight from Earth. The relative precision in determining $B \cdot T$ was not shared by the optical-only solutions, yet in all cases these solutions agreed well with the radio and radio plus optical $B \cdot T$ solution values. The consistency of the optical-only solutions with the radio solutions in the $B \cdot T$ coordinate provided an extra margin of confidence in the optical-based results.

Observations and conclusions based on the presented data can be given as follows:

- (1) The radio only, uncalibrated solutions at times exhibit large variations. The variations are smaller and the solutions prove to be more accurate when the radio

data is calibrated for charged-particle effects. This, therefore, strongly indicates that the radio estimates were highly influenced by charged-particle activity and that the DRVID calibrations are effective in alleviating these errors. Note that the sequential filter performs well for Viking 1, but is very unstable for Viking 2 prior to the approach midcourse. This behavior is not uncommon to sequential filter processing when the data noise levels increase significantly. This was definitely the case for Viking 2 in comparison to Viking 1 as the result of increasing doppler errors due to space plasma activity.

- (2) The long-arc solutions (further discussed in Section VII) are stable, yet are not particularly accurate. The Viking 1 long-arc solutions in fact are in error beyond that predicted by covariance analysis. This proved to be a problem during the Viking 1 approach, and the long-arc estimates were largely discounted in selecting the final pre-AMC-1 best estimate. The Viking 2 pre-AMC estimates include long-arc solutions that behave interestingly like the Viking 1 long-arc solutions. An improved long-arc solution is shown, however, which includes modified processing strategies that resulted from after-the-fact analysis of the Viking 1 long-arc solutions post-Viking 1 MOI. Some description of this solution and the attendant modifications is given in Section VII. The improved solution nearly equals the delivered best estimate. However, agreement at this level should be taken as largely coincidental considering the expected accuracy of the long-arc solution.
- (3) Following each midcourse maneuver, solutions containing only postmaneuver observations were compared with solutions that included premaneuver data and solved for maneuver parameters. The through-maneuver solutions are seen to be superior to the postmaneuver solutions until considerable postmaneuver data has become available.
- (4) Generally the optical-based estimates performed extremely well, particularly once a sufficient optical data arc length was obtained. With respect to estimating $B \cdot R$, the optical data proved far superior to radio observations. Generally, the optical-only solutions, again given sufficient arc length, produced $B \cdot R$ estimates as accurate as any produced by radio plus optical solutions.
- (5) Prior to Viking 1 AMC-1, some difficulty was encountered initially when combining radio and optical data. This problem was partially the result of the early large dispersions in the radio solutions, and occurred in both the direct radio + optical and the radio a priori + optical processing procedures. The problems disappeared

Table 16. Orbit estimate deliveries

Parameter	B · R, km	B · T, km	TCA
Viking 1			
Pre-AMC-1			
Preliminary best estimate (delivered 5/21/76)	5,694	7,340	16:30:41
Final best estimate (delivered 6/6/76)	5,774	7,289	16:31:23
Pre-AMC-2			
Target value ^a	7,233	6,859	20:38
Execution error ^a	±450	±450	±10 s
Preliminary best estimate (delivered 6/13/76 20:00 GMT)	7,291	6,701	20:38:04
Final best estimate (delivered 6/14/76 04:00 GMT)	7,282	6,700	20:37:50
Pre-MOI			
Target value ^a	7,284	6,944	22:54
Execution error ^a	±225	±225	±5 s
Preliminary best estimate (delivered 6/17/76 14:20 GMT)	7,254	6,917	22:53:58
Final best estimate (delivered 6/18/76 14:50 GMT)	7,275	6,914	22:54:08
Reconstructed estimate	7,276	6,920	22:54:06
Viking 2			
Pre-AMC			
Preliminary best estimate (delivered 7/22/76)	887	16,197	12:20:49
Final best estimate (delivered 7/25/76)	870	16,195	12:21:13
Pre-MOI			
Target value ^a	-2,387	9,060	11:45
Execution error ^a	±70	±50	±20 s
Preliminary best estimate (delivered 8/1/76)	-2,387	9,052	11:44:44
Final best estimate (delivered 8/6/76 09:50 GMT)	-2,423	9,056	11:45:05
Reconstructed estimate	-2,424	9,058	11:45:19

^aFor maneuver preceding estimate.

ORIGINAL PAGE IS
OF POOR QUALITY

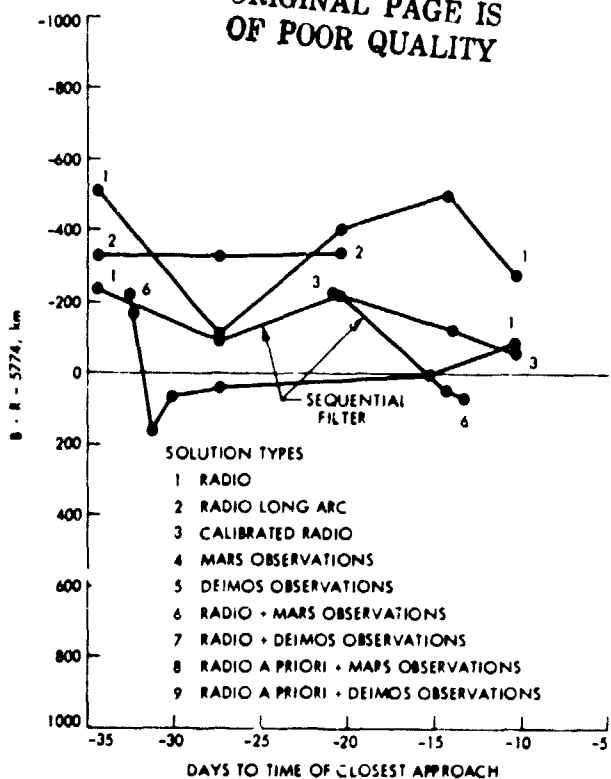


Fig. 26a. Viking 1 approach solution histories, pre-AMC 1: ODP

once a sufficient optical arc was obtained, allowing the optical data to govern the $B \cdot R$ determination.

- (6) The excellent performance of the optical solutions is considered to be the result of (a) better than expected precision of the optical observations themselves, and (b) availability of sufficiently long data arcs to permit unambiguous separation of trajectory miss ($B \cdot R$ and $B \cdot T$) from approach velocity and optical bias uncertainties. The Mars and Deimos observation types compared very well; the results of the Viking 2 post-M/C estimates indicate that optical center-finding uncertainty is small – most likely no larger than 1% of the Mars radius.

XI. Inflight Orbit Determination Solution Compilation

This section provides a compilation of inflight solutions beyond the launch phase, for each of Viking 1 and Viking 2 (launch phase solutions were given in Table 10). The solutions are presented in Tables 17 through 19 for Viking 1 and Tables 20 through 22 for Viking 2. These tables display the end result of the orbit determination program (ODP or ONP) execution: that is, the predicted spacecraft position in the B-plane at the

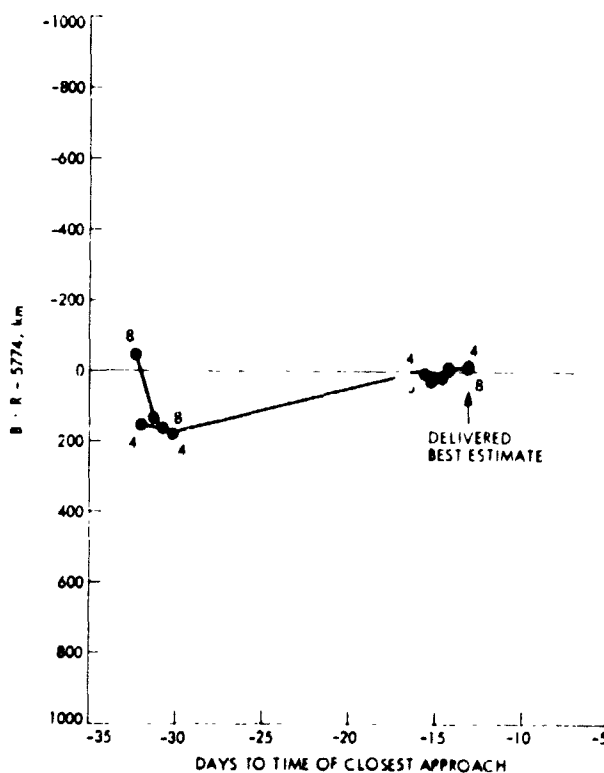


Fig. 26b. Viking 1 approach solution histories, pre-AMC 1: ONP

time of closest approach to Mars. Additional data describes pertinent facts about each solution, e.g., type of data used, the span of the data arc, etc. The variation within each table depending on the relevant and/or the availability of various data. The abbreviations used for describing the contents of the tables are as follows:

- (1) CASEID. This is a six character alphanumeric label which has been assigned to each orbit determination solution. Although of no immediate use to most readers, it is necessary to have this run identification in order to obtain additional detailed information from the archives regarding any particular solution.
- (2) EST. This column identifies the parameters, in a coded form, which were estimated in each run in addition to the spacecraft state. The lack of any entry means that only the spacecraft state vector was estimated. The following code words are abbreviations which identify the estimated parameters, other than the spacecraft state.

ATT constant nongravitational accelerations

EPHEM ephemeris parameters for either the Earth or Mars

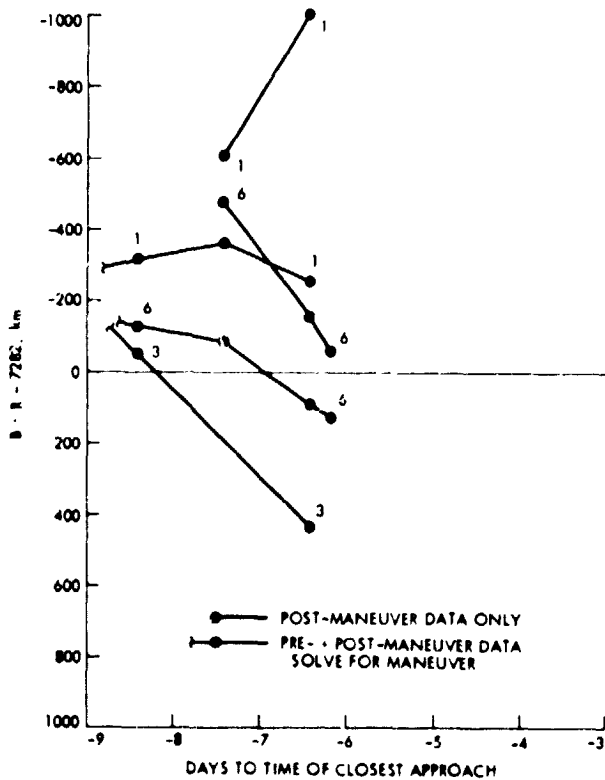


Fig. 27a. Viking 1 approach solution histories, pre-AMC 2: ODP

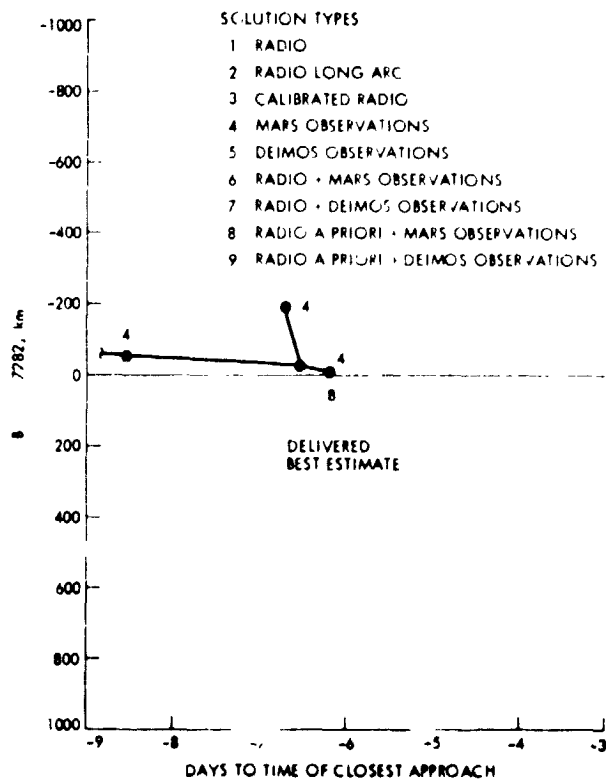


Fig. 27b. Viking 1 approach solution histories, pre-AMC 2: ONP

IM	impulsive maneuver burn parameters
RBIAS	range bias parameters
SEP	Mars satellite ephemeris parameters
SP	solar pressure acceleration coefficients
STA	DSN station locations
STOC	stochastic parameters were present

- (3) #F2. The number of two-way doppler points used in the solution
- (4) #PLOP. The number of PLOP range points used in the solution.
- (5) #MARS. The number of optical observations of the planet Mars used in the solution.
- (6) #DEIM. The number of optical observations of DEIMOS used in the solution.
- (7) SPAN. The length of the data arc processed, days.
- (8) LDPT. The calendar date of the last data point used in the solution. The entries give DATE, HR:MIN respectively.

- (9) TCA. The time of closest approach obtained for this solution.
- (10) $B \cdot R$. The estimated value of $B \cdot R$, km.
- (11) Sigma $B \cdot R$. The one-sigma uncertainty of the $B \cdot R$ estimate, km.
- (12) $B \cdot T$. The estimated value of $B \cdot T$, km.
- (13) Sigma $B \cdot T$. The one-sigma uncertainty of the $B \cdot T$ estimate, km.
- (14) Sigma TCA. The one-sigma uncertainty in the time of closest approach, s.

There are three tables each for both Viking 1 and Viking 2. For each spacecraft, the first table lists representative solutions obtained during the cruise phase; the second table lists solutions obtained during the approach phase using the ODP; the third table, covering the same time span as the second, contains solutions derived using the ONP.

XII. DSN Station Location Evaluation

The radic metric data and spacecraft-based optical data from the Mars encounters of the Viking spacecraft were used

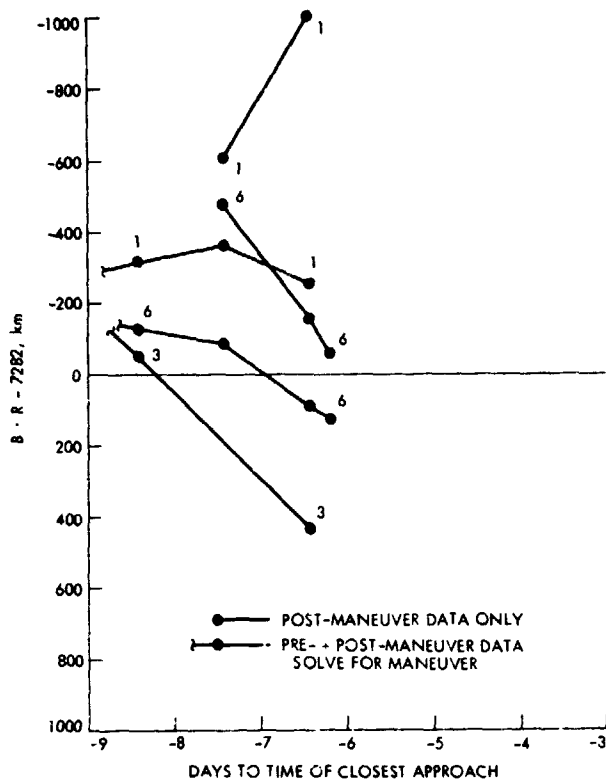


Fig. 28a. Viking 1 approach solution histories, pre-MOI: ODP

to evaluate the Deep Space Network station location set, LS 44. This set of station location estimates (Ref. 9) along with JPL Development Ephemeris 84 supported critical navigation operations in the vicinity of Mars. LS 44 is displayed in Table 23.

The evaluation was not intended to serve as the definition of an improved station location set. Such an update would normally be accomplished by combining in least squares fashion the Viking station location estimates with those from previous Mariner missions which had been incorporated in LS 44. Rather, the evaluation shows that LS 44 is consistent with the station location information inherent in the Viking encounter data and did meet the mission requirement on station location uncertainty.

A. Theoretical Background

The locations of the DSN stations are computed in a geocentric coordinate system whose axes are defined by the Earth's mean pole (axis of rotation), equator, and prime meridian of 1903.0. The cylindrical coordinates r_s , λ , and Z are the parameters used to locate a given station within this system where

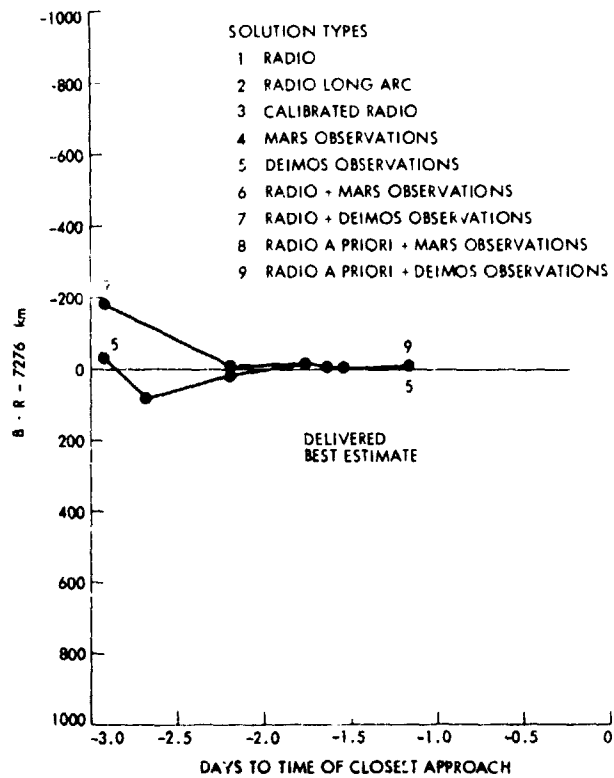


Fig. 28b. Viking 1 approach solution histories, p.e-MOI: ONP

r_s = distance from the axis of rotation, km

λ = longitude, measured east from the prime meridian, deg

Z = height above the equatorial plane, km.

Figure 31 shows the coordinate system and location parameters for a single station.

Using Earth-based data, it is apparent that uncertainties in a spacecraft's position are difficult to separate over a short arc from uncertainties in a station location. Consequently, the spacecraft orbit must be determined essentially independently from the station locations themselves. This is done in practice by using the radio metric data taken during the planetary approach phase. The probe's motion is heavily governed by the target planet's gravitational field, and its orbit can be well determined relative to the target body. A geocentric determination is obtained using the reference planetary ephemeris. Hence the station location estimates will reflect the accuracy of the reference ephemeris.

Based on this theoretical analysis and past experience processing radio metric data, some general guidelines can be established for determining the spin axis (r_s) and longitude (λ) estimates:

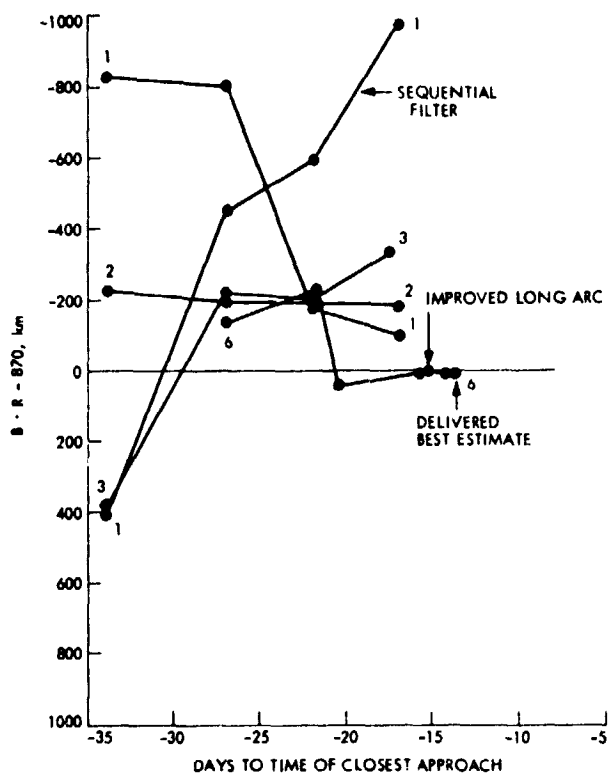


Fig. 29a. Viking 2 approach solution histories, pre-AMC: ODP

- (1) Define tracking arcs which reflect the planetary encounter geometry.
- (2) For each arc, obtain the best set of calibrations for ionospheric charged particle effects, tropospheric refraction, timing and polar motion which are currently available. To obtain accurate station spin axis and longitude estimates, the errors introduced by each of these sources must be minimized.
- (3) For each arc, obtain as accurate a spacecraft trajectory as possible.
- (4) Given the "best" trajectory, obtain estimates for the spacecraft state at the initial epoch of each arc and estimates for the DSN stations which participated in tracking the given spacecraft during the defined time period. In this regard, it is usually necessary to simultaneously estimate one or more other parameter types such as solar pressure, planetary oblateness, range biases, attitude control accelerations, planetary mass, etc.

These guidelines formed the basis for the actual procedures followed in the processing of planetary approach data.

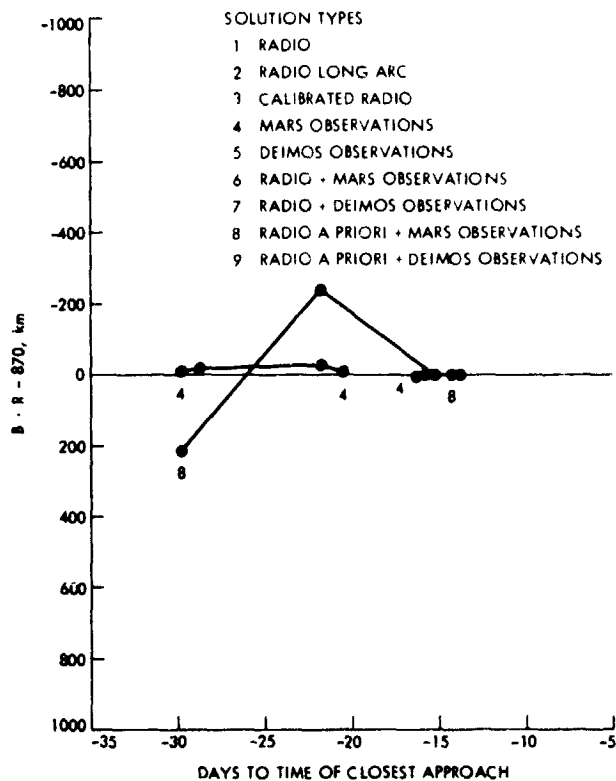


Fig. 29b. Viking 2 approach solution histories, pre-AMC: ONP

The data taken during the planetary approach phase of the mission did not provide accurate solutions for the Z-height component. This was expected. A study is currently ongoing to obtain accurate results on the relative Z-height differences between stations by processing near-simultaneous range data from the Viking orbiters. This work will not be discussed in this report.

B. Data Coverage and Calibrations

The data arc used to determine the encounter trajectory for Viking 1 extended from the first station pass after the approach maneuver on June 10 to the start of the orbit insertion turns on June 19. Another approach maneuver was performed four days from encounter, on June 15; the direction and magnitude of this maneuver were included in the final approach trajectory solution vector. The Viking 2 data arc was similar and extended from the approach maneuver on July 28 to the last preinsertion station pass on August 7. No intermediate maneuvers were performed on Viking 2.

The radio metric data coverage consisted of approximately 850 two-way doppler and 40 range measurements from each spacecraft. Optical observations, in the form of line and pixel measurement of Mars and Deimos, enhanced the radio metric

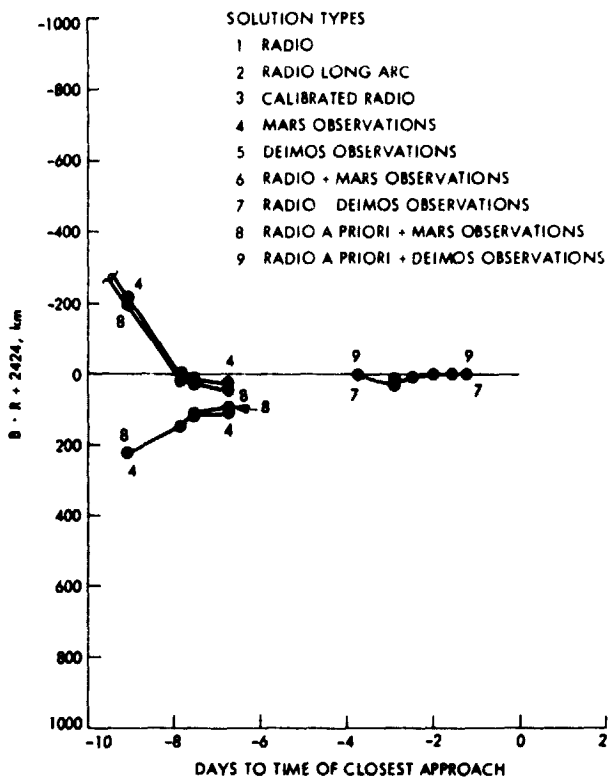


Fig. 30a Viking 2 approach solution histories, pre-MOI: ODP

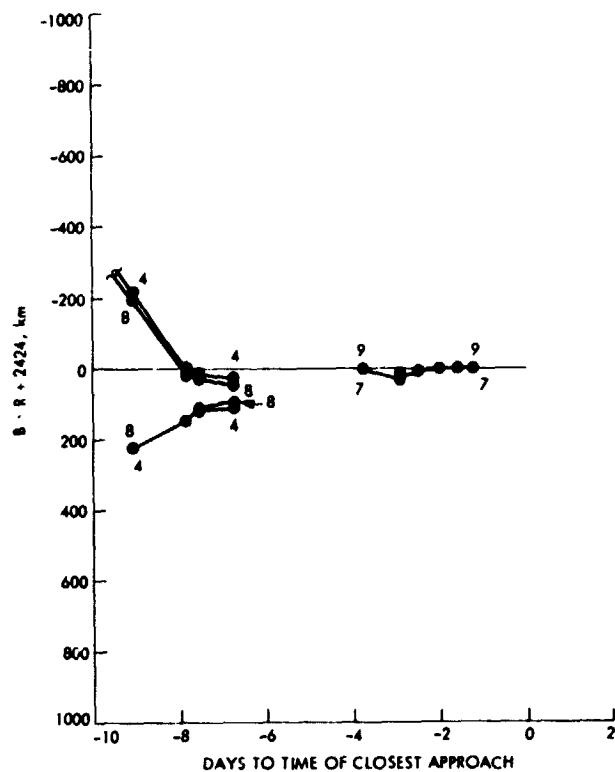


Fig. 30b. Viking 2 approach solution histories, pre-MOI: ONP

solutions for each spacecraft. Table 24 summarizes the encounter radio metric data sets that were used.

The uncalibrated doppler residuals measured against the best estimate trajectories are shown in Figs. 32 and 33. These residuals do not include any calibrations for charged particle effects on the computed doppler observables. Accurate calibrations significantly enhance the doppler observational models and contribute strongly to the accuracy of the station location estimates. Table 25 summarizes the charged particle calibration sets that were provided for each encounter data arc. Calibrated doppler residuals appear in Figs. 34 and 35.

C. Preliminary Solutions

Tables 26-29 show several sets of station location solutions for each encounter. Table 26 contains the Viking 1 solutions based on radio data only, and radio-plus-optical data, where the radio data is not calibrated for charged particles. Table 27 gives the same set of solutions, based on a calibrated radio data set. The solutions shown in Tables 26 and 27 were generated using a preliminary set of timing polynomials. The final set of timing polynomials for a particular data arc is not available until 4 to 5 weeks after the end of the radio data arc. Tables 28 and 29 show the uncalibrated and calibrated solution sets

for Viking 2, where the radio-plus-optical data set includes Mars pictures and Deimos pictures. For Viking 2, a finalized set of timing polynomials was used throughout. For each encounter, the radio-only solutions are consistent with the radio-plus-optical solution. Note that both spin axis and longitude corrections are quite large for all solutions using the uncalibrated radio data set.

D. Final Solutions

Table 30 gives the final corrections to LS 44 based on the Viking encounter data processing. The timing polynomial sets used for each encounter are listed in Table 30. The final Viking 1 solution is based on calibrated radio data plus Mars optical data. Note that the final timing polynomial set moved the station longitude corrections by approximately -1.5×10^{-5} deg. The final Viking 2 solution shown in Table 30 is based on the calibrated radio-only data set, although Table 29 shows that the solutions for the three calibrated data sets are very similar. Figure 36 displays the final spin axis and longitude corrections with $1-\sigma$ error bars.

The individual spacecraft solutions were then combined in least-squares fashion and the resulting corrections to LS 44 with $1-\sigma$ uncertainties are shown in Table 31. On the basis of

Table 17. Viking 1 cruise solution summary

CASEID	EST	# F2	# FLOP	# MARS	# DEIM	SPAN DAYS	L.DPT	TCA 6/19/76	B-R	b-R SIGMA	B-T	B-T SIGMA	TCA SIGMA
A03102		1039	229	0	0	22	12/28/75 13:30	16:30:41	5862	210	7107	271	36
A03305		766	122	0	0	20	1/24/76 10:23	16:31:14	5863	177	7176	156	39
A03708		883	24	0	0	22	3/14/76 11:51	16:29:41	5483	254	7259	104	83
A03811		812	117	0	0	22	3/28/76 12:41	16:31:01	5725	205	7214	72	68
A03905	SP STOC	219	0	0	0	213	3/28/76 12:41	16:30:03	5470	88	7236	60	23
A04204		712	128	0	0	22	5/02/76 12:40	16:29:50	5508	265	7292	42	88
A04506	BIAS STOC	996	92	0	0	22	5/19/76 12:39	16:29:46	5547	251	7297	37	86
A03319	SP STA STOC	3710	711	0	0	149	1/24/76 10:03	16:30:23	5604	78	7184	106	24
A04578	STA	4071	1562	0	0	262	5/16/76 12:39	16:29:30	5519	82	7298	41	28

ORIGINAL PAGE IS
OF POOR QUALITY

Table 18. Viking 1 approach phase solutions (ODP)

CASEID	EST LIST (BLANK = STATE)	FZ	PLOP	MARSDEM	SPAN DAYS	LOPT 1976	TCA 6/19/76	b.R	0.M SIGMA	0.T	B.T SIGMA	TCA SIGMA	
A04503		996	92	0	0	21.5062	5/16 12:39	16:28:12	5270.4	311.	7316.8	30.	98.9
A04506	RBIAS STOC	996	92	0	0	21.5062	5/16 12:39	16:29:46	5546.5	251.	7296.9	37.	86.2
A04576	RBIAS STOC	4071	1562	0	0	262.4903	5/16 12:39	16:29:09	5453.7	83.	7300.7	44.	29.3
A04519	RBIAS STOC	996	92	8	0	35.5419	5/18 6:00	16:29:51	5562.3	242.	7296.0	36.	82.8
A04522	RBIAS STOC	996	92	10	0	35.8751	5/18 14:00	16:30:09	5614.4	202.	7292.3	35.	69.8
A04529	RBIAS STOC	996	86	16	0	36.8752	5/19 14:00	16:31:56	5943.7	341.	7276.4	46.	115.2
A04539	RBIAS STOC	996	81	23	0	38.0418	5/20 18:00	16:31:26	5846.1	367.	7278.3	42.	125.7
A04603		1033	83	0	0	21.5111	5/23 12:32	16:30:49	5671.0	333.	7277.4	33.	107.3
A04606	RBIAS STOC	1033	83	0	0	21.5111	5/23 12:32	16:30:57	5696.9	172.	7275.1	34.	58.7
A04613	RBIAS STOC	1033	63	23	0	40.8134	5/23 12:32	16:31:17	5824.1	180.	7272.9	35.	61.8
A04676	RBIAS STOC	4497	1649	0	0	269.4854	5/23 12:32	16:29:10	5452.8	82.	7297.1	42.	29.7
A04703		1067	92	0	0	21.5285	5/30 12:46	16:29:18	5374.0	314.	7301.1	32.	99.4
A04709	RBIAS STOC	1067	92	0	0	21.5285	5/30 12:46	16:30:20	5544.6	173.	7292.7	34.	58.8
A04776	RBIAS STOC	4888	1668	0	0	276.4951	5/30 12:46	16:29:05	5443.1	82.	7302.8	37.	29.6
A04715	RBIAS STOC	1067	92	22	0	26.5805	6/4 14:00	16:31:33	5786.9	223.	7282.4	38.	79.9
A04722	EPHEM RBIAAS STOC	1067	92	22	0	26.5805	6/4 14:00	16:31:14	5792.0	225.	7310.5	81.	81.8
A04726	RBIAS STOC	1067	92	28	0	27.5804	6/5 14:00	16:31:46	5831.2	248.	7281.9	41.	89.0
A04730	RBIAS STOC	1067	92	14	0	28.5804	6/6 14:00	16:31:55	5851.1	253.	7277.7	37.	89.0
A04909		1067	77	0	0	21.5229	6/9 12:43	16:29:52	5505.6	267.	7321.0	36.	82.2
A04906	RBIAS STOC	1067	77	0	0	21.5229	6/9 12:43	16:29:51	5698.6	159.	7320.1	39.	58.4
DR4803	-	-	-	-	-	-	-	-	-	-	-	-	-
DR4808	-	-	-	-	-	-	-	-	-	-	-	-	-
DR4902	-	-	-	-	-	-	-	-	-	-	-	-	-

Table 18 (contd)

CASEID	EST LIST (BLANK = STATE)	F2	#	#	#	#	S'AN DAYS	LOFT	TCA 6/19/76	B.R SIGMA	B.T SIGMA	TCA SIGMA		
ARS102	IM RBIAS STOC	434	81	0	0	0	22.5331	6/11 12:47	20:37:46	7234.4	225.	6711.7	53.	74.2
A05155	IM	1331	81	0	0	0	23.5257	6/11 12:47	20:36:50	6968.9	702.	6683.3	42.	170.0
A05159	IM	1331	81	79	0	0	23.5257	6/11 12:47	20:37:51	7155.8	331.	6675.8	52.	58.5
A05202	IM	269	4	0	0	0	2.0108	6/12 12:36	20:36:18	6679.4	1973.	6616.9	114.	628.6
A05251	IM	1543	100	0	0	0	27.5146	6/12 12:36	20:36:37	6924.6	208.	6684.2	35.	61.8
A05253	IM	1543	100	39	0	0	27.5146	6/12 12:36	20:38:10	7199.9	105.	6668.0	36.	36.7
A05257	IM	270	8	4	0	0	2.0142	6/12 12:36	20:35:56	6908.7	1224.	6697.0	68.	391.6
A05302	IM	1591	106	0	0	0	28.5028	6/13 12:19	20:36:46	7031.6	422.	6713.7	48.	141.8
A05304	IM	1591	106	41	0	0	28.5028	6/13 12:19	20:38:27	7378.1	164.	6714.7	33.	61.1
A05305	IM	318	14	6	0	0	3.0024	6/13 12:19	20:37:06	7129.5	154.	6727.2	33.	53.1
A05357	IM	318	14	0	0	0	3.0024	6/13 12:19	20:32:03	6120.8	826.	6745.0	63.	247.6
DR5351	IM	666	97	0	0	0	28.0132	6/13 12:19	20:41:25	7727.8	502.	6653.7	52.	168.5
A05354	IM	1591	106	43	0	0	28.7402	6/13 18:00	20:38:37	7408.3	131.	6712.3	32.	50.9
A05355	IM	318	14	8	0	0	3.2398	6/13 18:00	20:37:40	7224.0	111.	6718.8	28.	39.6
A05665	IM SEP	224	6	0	7	1.4140	6/17 00:51	22:53:05	6989.1	364.	6897.6	31.	100.8	
A05674	IM SEP	224	6	0	9	1.6473	6/17 06:27	22:54:17	7267.3	134.	6904.5	28.	46.8	
DR5804	IM	142	12	0	0	0	2.2569	6/17 23:10	22:54:18	7284.5	623.	6908.4	88.	119.6
A05804	IM	276	12	0	0	0	2.3962	6/18 00:26	22:53:73	6937.4	390.	6854.7	63.	74.2
A05807	IM SEP	276	12	0	16	2.3962	6/18 00:26	22:54:17	7274.1	99.	6908.3	20.	29.8	
DR5951	IM	62	14	0	0	0	2.3993	6/18 02:35	22:54:10	7274.6	352.	6917.2	75.	60.2
A05855	IM SEP	276	12	0	19	2.5684	6/18 04:34	22:54:13	7258.9	48.	6906.8	19.	21.9	
A05952	IM	291	14	0	0	0	2.6781	6/18 07:12	22:53:38	7032.9	269.	6869.4	57.	47.5
AD5953	IM RBIAS SEP	291	14	0	19	2.6781	6/18 07:12	22:54:10	7251.3	22.	6911.9	8.	6.1	

Table 18 (contd)

CASEID	EST LIST (BLANK = STATE)	#	F2	#	PLOP	#	PARSEIM	SPAN DAYS	LOPT	TCA 6/19/76	B.R	B.N SIGMA	B.T SIGMA	TCA SIGMA
A0599	IM RB1AS SEP	291	14	0	22	2.4961	6/18 07:37	22:54:12	7266.0	18.	6919.1	7.	5.0	
A06002	IM	350	18	0	0	3.7656	6/19 09:23	22:54:10	7314.4	108.	6925.9	49.	4.0	
A06202		353	18	0	0	3.9205	6/19 13:11	22:54:20	6984.6	103.	6785.0	47.	4.0	
A06303		402	18	0	0	4.1354	6/19 18:15	22:54:10	7314.2	10.	6938.3	5.	.6	
A06904		431	18	0	0	4.2654	6/19 21:22	22:55:05	7276.8	1.	6919.2	.	.2	

Table 19. Viking 1 approach phase solutions (ONP)

CASEID	EST LIST (BLANK = STATE)	F2	PLOP	MARSDEIM	SPAN DAYS	LOPT	TCA 6/19/76	H.R	H.R SIGMA	B.T	B.T SIGMA	TCA SIGMA	
A1C238	-	-	-	4	0	-	5/18 14:01	16:30:39	5735.0	366.	7305.5	37.	117.2
A2C362	-	-	-	12	0	-	5/18 22:01	16:27:11	5931.2	210.	7166.4	341.	1619.4
A2C370	-	-	-	6	0	-	5/18 22:01	16:30:36	5754.1	233.	7320.2	69.	89.5
A1C478	-	-	-	10	0	-	5/19 14:01	16:31:33	5912.8	421.	7303.3	54.	137.7
A1C591	-	-	-	13	0	-	5/20 02:01	16:31:39	5941.6	429.	7307.2	61.	142.3
A2C794	-	-	-	15	0	-	5/20 14:01	16:32:18	5958.4	331.	7271.2	58.	104.8
A1C621	-	-	-	23	0	-	5/20 18:01	16:31:55	5957.7	175.	7251.1	395.	2287.3
A1C631	-	-	-	17	0	-	5/20 18:01	16:30:13	5897.2	168.	7331.3	94.	64.7
A3D127	-	-	-	20	0	-	6/4 06:00	16:31:07	5786.8	133.	7319.2	74.	63.6
A3D134	-	-	-	20	0	-	6/4 06:00	16:30:40	5785.6	123.	7334.7	158.	2266.1
A3D204	-	-	-	22	0	-	6/4 14:01	16:31:13	5808.9	113.	7319.8	75.	61.6
A3D210	-	-	-	22	0	-	6/4 14:01	16:30:37	5798.8	101.	7329.5	139.	2265.7
A3D221	-	-	-	22	0	-	6/4 14:01	16:30:24	5692.2	123.	7344.0	91.	63.9
A3D306	-	-	-	26	0	-	6/5 06:00	16:31:09	5801.4	96.	7321.2	77.	60.7
A3D413	-	-	-	28	0	-	6/5 14:01	16:30:27	5709.6	111.	7346.1	98.	67.0
A3D432	-	-	-	28	0	-	6/5 14:01	16:30:44	5771.9	79.	7330.1	80.	59.3
A4D450	-	-	-	28	0	-	6/5 14:01	16:29:25	5779.5	77.	7320.3	120.	2263.9
A3D620	-	-	-	35	0	-	6/6 18:00	16:30:57	5769.5	71.	7326.3	83.	61.1
A3D626	-	-	-	35	0	-	6/6 18:00	16:29:21	5773.6	66.	7300.7	112.	2257.5
A6E110 IM	-	-	-	39	U	-	6/11 10:01	20:36:00	7234.8	473.	6595.4	482.	3744.5
A7E209 IM	-	-	-	41	0	-	6/13 10:01	20:34:29	7264.7	137.	6697.5	154.	3723.5
A7E212	-	-	-	4	0	-	6/13 10:01	20:36:12	7261.0	141.	6752.8	189.	2304.0
A7E306 IM	-	-	-	43	0	-	6/13 18:01	20:36:59	7286.2	115.	6672.5	190.	3745.2

ORIGINAL PAGE IS
OF POOR QUALITY

Table 19 (contd)

CASEID	EST LIST (BLANK = STATE)	P2	PLOP	MARSDIEM	SPAN DAYS	LDPT	TCA 5/19/76	B.R	B.R SIGMA	B.T	B.T SIGMA	TCA SIGMA	
A7E311	-	-	-	8	0	-	6/13 18:01	20:34:19	7274.8	81.	6696.2	128.	2295.3
A1K206	-	-	-	0	7	-	6/17 00:52	22:53:26	7131.2	241.	6921.7	42.	84.4
A1K209	IM	-	-	8	7	-	6/17 00:52	22:49:00	7168.7	138.	6887.8	144.	1304.3
A1K212	-	-	-	0	7	-	6/17 00:52	22:51:26	7244.0	47.	6920.3	54.	274.1
A1K219	SEP	-	-	0	7	-	6/17 00:52	22:53:19	7091.7	144.	6917.1	22.	51.1
A1K311	IM	-	-	8	10	-	6/17 06:28	22:58:28	7275.7	201.	6901.7	139.	1403.6
A1K315	-	-	-	0	10	-	6/17 06:28	22:52:49	7359.7	364.	6963.0	273.	400.3
A1K417	IM	-	-	8	14	-	6/17 18:20	23:02:32	7321.8	180.	6995.3	181.	1111.9
A1K419	SEP	-	-	0	14	-	6/17 18:20	22:54:47	7270.3	51.	6918.7	47.	102.5
A1K421	-	-	-	0	14	-	6/17 18:20	22:55:34	7293.9	128.	6960.5	112.	184.4
A1K508	SLP	-	-	0	19	-	6/18 04:34	22:54:10	7259.4	19.	6912.6	11.	9.1
A1K519	SEP	-	-	0	19	-	6/18 04:34	22:54:43	7262.6	28.	6916.2	24.	115.8
A1K522	IM,SEP	-	-	8	19	-	6/18 04:34	22:54:59	7262.1	53.	6917.0	35.	382.5
A1K603	SLP	-	-	0	22	-	6/18 07:38	22:54:53	7275.9	17.	6914.8	18.	92.9
A1K606	IM,SEP	-	-	8	22	-	6/18 07:38	22:55:17	7276.1	26.	6915.3	18.	215.1
A1K612	SEP	-	-	0	22	-	6/18 07:38	22:54:13	7272.9	16.	6913.5	6.	4.5
A1K702	SLP	-	-	0	24	-	6/18 09:46	22:54:13	7274.6	17.	6913.6	6.	4.6
A1K705	SEP	-	-	0	24	-	6/18 09:46	22:54:25	7271.8	15.	6908.7	15.	75.7
A1K811	SEP	-	-	0	25	-	6/19 18:56	22:54:12	7266.7	11.	6912.6	5.	4.0

Table 20. Viking 2 cruise solution summary

CASEID	EST	θ P2	θ FLOR	θ MARS	θ DEIM	SPAN DAYS	LDPT	TCA 8/07/76	B-R	B-R SIGMA	B-T	B-T SIGMA	TCA SIGMA
B02504	SP STOC	1022	180	0	0	22	11/23/75	13:35	12:17:59	975	15532	942	210
B02906	STOC	861	184	0	0	22	01/18/76	10:41	12:21:44	1166	15662	439	52
B04307	REIAS STOC	1015	75	0	0	22	07/04/76	12:47	12:22:43	1287	16188	11	166
BR4402	REIAS STOC	497	103	0	0	21	07/11/76	12:39	12:20:15	654	16200	7.6	127
B03064		3220	814	0	0	135	02/01/76	14:00	12:20:14	765	16165	325	56
B04678	ATT	6144	1727	0	0	296	07/11/76	12:39	12:22:10	742	16206	3.8	71

Table 21. Vining 2 approach phase solutions (ODP)

CASEID	EST LIST (BLANK = STATE)	F ₂	PLOP ^B	PARSDEIM	SPAN DAYS	LOPT	TCA 8/07/76	M.R	B.R SIGMA	B.T SIGMA	TCA SIGMA	
B04382	RBIAS STOC	6062	1724	0	0	200.5110	7/04 12:27	12:20:20	653.5	131.16203.0	0.	40.5
B04307	RBIAS STOC	498	75	0	0	21.5271	7/04 12:47	12:22:47	1250.2	000.16100.0	14.	227.0
B04305		1092	75	0	0	21.5271	7/04 12:47	12:16:44	50.5	910.16205.6	13.	255.4
B04307	RBIAS STOC	1014	75	0	0	21.5271	7/04 12:47	12:22:43	1206.5	570.16100.0	11.	166.4
B04402	RBIAS STOC	497	103	0	0	21.4099	7/11 12:39	12:20:15	654.2	303.16199.6	0.	127.2
B04402	RBIAS STOC	1121	103	0	0	21.5097	7/11 12:40	12:19:00	430.6	279.16202.0	6.	95.4
B04408	RBIAS STOC	1121	103	10	0	21.5097	7/11 12:39	12:20:30	739.3	342.16197.5	0.	104.1
B04413		1121	105	0	0	21.5097	7/11 12:39	12:17:40	70.5	735.16208.5	12.	195.0
B04401	RBIAS STOC	6274	1734	0	0	295.5201	7/11 12:39	12:20:35	685.4	120.16202.7	4.	39.1
B04504	RBIAS STOC	616	128	0	0	26.3722	7/16 11:52	12:20:33	676.5	317.16197.3	7.	115.6
B04503		1344	128	0	0	24.5035	7/16 12:30	12:20:35	703.2	447.16198.6	13.	232.5
B04504	RBIAS STOC	1344	124	0	0	26.5035	7/16 12:30	12:18:28	289.6	267.16203.4	6.	95.0
B04508	RBIAS STOC	1364	128	14	0	24.7333	7/16 18:00	12:20:17	651.0	254.16198.6	6.	85.5
B04514	RBIAS STOC	1344	128	20	0	27.9433	7/18 0:0	12:21:37	921.1	250.16195.0	6.	95.0
B04603	RBIAS STOC	541	104	0	0	23.9360	7/20 24:0	12:20:03	545.2	270.16202.2	7.	104.3
B04603	RBIAS STOC	6392	1759	0	0	305.5076	7/21 12:21	12:21:11	698.6	137.16202.0	4.	41.0
B04602		1252	104	0	0	24.5153	7/21 12:41	12:21:03	778.9	791.16198.0	13.	225.0
B04603	RBIAS STOC	1252	104	0	0	24.5153	7/21 12:41	12:16:41	-91.9	200.16209.3	7.	103.4
B04616		1234	104	27	0	25.7374	7/22 18:00	12:21:34	487.1	102.16196.5	10.	84.4
B04619		1234	104	29	0	24.2375	7/23 6:01	12:21:32	081.4	95.16196.5	10.	80.2
B04622		1234	104	33	0	27.2375	7/24 6:01	12:21:33	000.4	06.16196.4	11.	95.6
B04627	RBIAS STOC	1236	104	15	0	27.7375	7/24 18:00	12:21:30	064.0	01.16196.3	11.	103.9
B04502 IM PRIAS		405	115	0	0	24.3451	8/02 9:17	11:44:55	2304.0	443. 9049.0	12.	203.5

Table 21 (contd)

CASEID	EST LIST (BLANK = STATE)	F2	PLOP	MARSDEIM	SPAN DAYS	LOPT	TCA 8/07/76	U.R	B.R SIGMA	B.T SIGMA	TCA SIGMA		
005002	IM MBIAS	1704	115	0	0	29.5014	8/02 12:32	11:39:8	-3504.7	648.	9067.5	12.	192.3
005011	IM MBIAS	46A	25	0	5	6.6732	8/03 18:00	11:45:33	-2428.3	155.	9057.7	8.	98.9
005103	IM MBIAS	8AA	126	0	0	31.8319	8/04 20:58	11:45:19	-2230.2	370.	9048.9	9.	112.7
005104	MBIAS	3A3	36	0	0	7.7889	8/04 20:58	11:45:16	-2293.0	785.	9051.1	15.	226.7
005103	IM MBIAS	1631	126	0	0	31.8528	8/04 20:58	11:41:59	-2860.0	367.	9056.8	9.	107.5
005104	MBIAS	595	36	0	0	7.7962	8/04 20:58	11:39:18	-3541.2	722.	9069.6	14.	202.6
005154	CBIAS MBIAS	595	36	0	9	7.7962	8/04 20:58	11:44:30	-2390.9	35.	9051.3	6.	61.1
005202	IM MBIAS	146A	131	0	0	12.5083	8/05 12:42	11:45:3	-2284.7	177.	9049.1	7.	65.1
005203	MBIAS	630	41	0	0	8.4517	8/05 12:42	11:45:52	-2135.4	214.	9048.1	7.	54.6
005302	IM MBIAS	1047	132	0	0	32.8639	8/05 21:44	11:45:36	-2229.8	191.	9050.4	9.	50.8
005303	MBIAS	422	42	0	0	8.8208	8/05 21:44	11:45:47	-2236.7	205.	9051.4	7.	46.9
005302	IM MBIAS	184A	132	0	0	32.8847	8/05 21:44	11:45:42	-2134.1	176.	9047.5	8.	42.7
005303	MBIAS	450	42	0	0	8.8281	8/05 21:44	11:46:36	-2703.8	197.	9046.8	7.	42.6
005353	CBIAS MBIAS	450	42	0	19	8.8536	8/05 22:20	11:45:24	-2422.7	16.	9058.2	4.	45.6
005356	CBIAS MBIAS SEP	450	42	0	19	8.8536	8/05 22:20	11:45:44	-2425.7	7.	9059.5	3.	34.6
005402	MBIAS	451	44	0	0	9.8035	8/06 21:19	11:45:18	-2420.3	17.	9057.6	1.	46
005402	MBIAS	702	44	0	0	9.8247	8/06 21:49	11:44:50	-2354.6	211.	9051.6	8.	19.0
005408	CBIAS MBIAS SEP	702	44	0	23	9.8247	8/06 21:49	11:44:55	-2423.7	5.	9055.2	2.	13.3
005502	MBIAS	707	43	0	0	10.0920	8/07 05:13	11:45:22	-2202.1	177.	9049.2	8.	4.0
005505	CBIAS MBIAS SEP	707	43	0	23	10.0920	8/07 05:13	11:45:17	-2420.1	4.	9057.9	1.	2.1
005602	MBIAS	707	43	0	0	10.0920	8/07 10:22	11:45:15	-2202.1	177.	9049.2	8.	4.0
005702	MBIAS	495	43	0	0	10.3118	8/07 10:29	11:45:19	-2424.1	15.	9057.7	1.	46

Table 22. Viking 2 approach phase solutions (ONP)

CASEID	EST LIST (BLANK = STATE)	°	'	"	PLOP	"	"	"	SPAN MARSUCIMOS DAYS	LOPT	TCA 8/9/76	H.R	B.R SIGMA	B.T	B.T SIGMA	TCA SIGMA
02C205	-	-	-	7	-	-	0	0	0	-	7/08 18:01	12:21:24	1000.2	419. 16109.5	9. 133.3	
03C223	-	-	-	13	-	-	0	0	0	-	7/08 18:01	12:12:04	665.6	152. 16108.3	205. 1540.8	
03C326	-	-	-	17	-	-	0	0	0	-	7/09 18:01	12:11:35	856.6	140. 16033.3	192. 1540.7	
03C334	-	-	-	11	-	-	0	0	0	-	7/09 18:01	12:20:36	855.2	181. 16200.6	9. 58.0	
04C410	-	-	-	15	-	-	0	0	0	-	7/16 18:01	12:20:27	849.9	280. 16205.3	291. 2710.1	
04C418	-	-	-	15	-	-	0	0	0	-	7/16 18:01	12:20:54	844.6	175. 16201.3	5. 62.7	
04C430	-	-	-	15	-	-	0	0	0	-	7/16 18:01	12:20:04	638.6	203. 16198.0	12. 117.7	
04C511	-	-	-	20	-	-	0	0	0	-	7/18 0:0	12:20:57	854.8	166. 16201.2	5. 73.6	
04C516	-	-	-	20	-	-	0	0	0	-	7/1 0	12:20:29	869.6	197. 16151.7	209. 2710.1	
05D107	-	-	-	25	-	-	0	0	0	-	7/ 0:0	12:21:15	879.2	136. 16157.6	149. 3571.4	
05D213	-	-	-	27	-	-	0	0	0	-	7/22 18:01	12:20:38	875.7	117. 16170.2	132. 3562.9	
05D224	-	-	-	27	-	-	0	0	0	-	7/22 18:01	12:21:47	879.7	54. 16194.1	26. 267.6	
05D234	-	-	-	27	-	-	0	0	0	-	7/22 18:01	12:21:00	861.5	146. 16201.2	5. 89.5	
05D309	-	-	-	29	-	-	0	0	0	-	7/23 6:01	12:21:08	875.2	66. 16194.4	24. 240.8	
05D404	-	-	-	33	-	-	0	0	0	-	7/24 6:01	12:21:07	880.9	46. 16194.0	28. 284.2	
05D416	-	-	-	33	-	-	0	0	0	-	7/24 6:01	12:19:58	878.5	88. 16180.7	107. 3535.9	
05D509	-	-	-	35	-	-	0	0	0	-	7/24 18:01	12:21:07	878.0	45. 16194.2	28. 288.7	
05D511	-	-	-	35	-	-	0	0	0	-	7/24 18:01	12:15:05	876.2	44. 16151.1	75. 2984.1	
05D516	-	-	-	35	-	-	0	0	0	-	7/24 18:01	12:21:05	872.8	90. 16200.3	4. 323.9	
06E109 IM	-	-	-	39	-	-	0	0	0	-	7/29 10:01	11:45:13	-2639.2	392. 8920.4	454. 4832.6	
06E120 IM	-	-	-	39	-	-	0	0	0	-	7/29 10:01	11:43:43	-2622.7	122. 9056.2	25. 316.5	
06E121 IM	-	-	-	4	-	-	0	0	0	-	7/29 10:01	11:46:35	-2209.7	335. 9054.4	27. 307.7	
06E207 IM	-	-	-	43	-	-	0	0	0	-	7/30 15:01	11:44:40	-2413.7	64. 9052.7	27. 311.6	

Table 22 (cont'd)

CASEID	EST LIST (BLANK = STATE)	R ²	PLOP	MARSDEIM	SPAM DAYS	LOFT	TCA 8/01/76	A.R	B.R SIGMA	B.T SIGMA	TCA SIGMA	
06E208	IM	-	-	0	0	-	7/30 15:01	11:46:11 -2279.0	91.	9056.4	34.	397.3
06E216	IM	-	-	43	0	-	7/30 15:01	12:08:50 -2423.2	67.	9048.7	145.	4046.9
06E217	-	-	-	0	0	-	7/30 15:01	11:44:49 -2278.6	90.	9045.2	114.	3490.9
06E309	IM	-	-	45	0	-	7/30 23:01	11:46:45 -2401.5	54.	9052.6	27.	317.0
06E306	IM	-	-	10	0	-	7/30 23:01	11:46:12 -2313.6	70.	9057.2	38.	433.0
06E311	IM	-	-	45	0	-	7/30 23:01	12:10:39 -2412.3	58.	9076.9	134.	3899.5
06E313	-	-	-	10	0	-	7/30 23:01	11:45:29 -2312.0	75.	9062.5	123.	4130.6
06E405	IM	-	-	47	0	-	7/31 18:01	12:21:51 -2398.4	50.	9148.8	95.	2215.0
06E413	-	-	-	12	0	-	7/31 18:01	12:28:54 -2314.9	60.	9101.4	102.	3394.2
06E421	IP	-	-	47	0	-	7/31 18:01	11:45:49 -2380.9	46.	9052.0	27.	326.0
06E423	IM	-	-	12	0	-	7/31 18:01	11:45:51 -2328.6	53.	9055.8	40.	470.2
07K138	IM	-	-	0	5	-	7/31 18:01	11:44:21 -2420.4	143.	9052.0	6.	70.7
07K209	-	-	-	0	9	-	8/04 14:11	11:46:01 -2405.3	53.	9045.6	45.	125.4
07K225	-	-	-	0	9	-	8/04 14:11	11:45:20 -2394.5	40.	9056.3	6.	83.0
07K227	SLP	-	-	0	9	-	8/04 14:11	11:45:14 -2394.7	29.	9056.0	4.	47.1
07K305	-	-	-	0	12	-	8/05 0:0	11:46:11 -2415.0	30.	9053.0	30.	76.2
08E407	-	-	-	0	16	-	8/05 11:41	11 51:45 -2423.0	21.	9051.6	16.	55.0
08E409	SLP	-	-	0	16	-	8/05 11:41	11:45:52 -2419.5	10.	9044.3	10.	38.2
08E504	-	-	-	0	19	-	8/05 22:21	11:44:04 -2418.8	15.	9070.4	12.	73.4
08E506	SLP	-	-	0	19	-	8/05 22:21	11:45:11 -2421.9	7.	9043.7	8.	31.0
08E507	SLP	-	-	0	19	-	8/05 22:21	11:45:34 -2422.9	6.	9058.3	2.	20.3
09E516	-	-	-	0	19	-	8/05 22:21	11:45:01 -2420.0	16.	9056.5	5.	60.2
09E607	SLP	-	-	0	23	-	9/06 06:16	11:45:30 -2419.0	5.	9043.2	7.	21.0
09E618	SLP	-	-	0	23	-	9/06 06:16	11:45:19 -2421.9	5.	9057.5	2.	11.8

Table 23. Location set 44^a

DSS	r_s^b	λ^c	z^d
11	5206.340852	243.1505848	3573.765
12	5212.052472	243.1945123	3665.629
13	5215.485322	243.2051121	3660.957
14	5203.997735	243.1104678	3677.053
41	5450.203703	136.8874855	-3302.189
42	5205.352165	148.9812708	-3674.589
43	5205.251697	148.9812726	-3674.756
44	5193.986790	148.9778162	-3691.410
51	5742.940160	27.6854256	-2768.744
61	4152.608849	355.7509710	4114.879
62	4860.818670	355.6321631	4116.902
63	4862.451845	355.7519840	4115.105

^aDevelopment ephemeris 84; 1903.0 pole; BIH: UT1 and pole motion.

^bDistance off Earth's spin axis, km.

^cGeocentric longitude, deg. east.

^dHeight from equatorial plane, km.

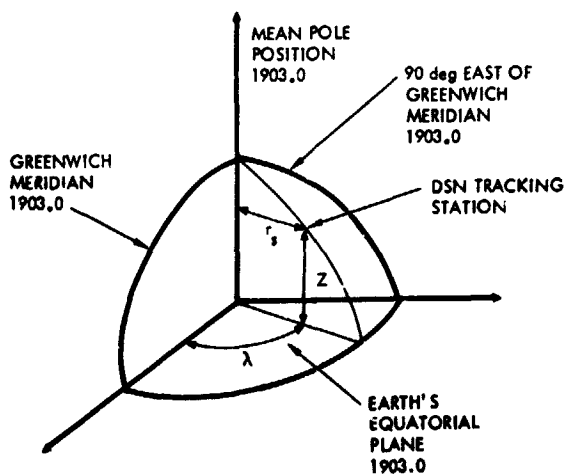


Fig. 31. A cylindrical coordinate system for a DSN station

Table 24. Summary of Viking 1 and 2 radio metric data sets

Participating DSS	Number of 2-way doppler measurements		Number of range measurements	
	Viking 1	Viking 2	Viking 1	Viking 2
11	48	55	12	14
14	180	98	0	0
42	0	88	0	14
43	139	115	14	3
61	42	71	5	12
63	232	5	12	0

Table 25. Summary of charged particle calibration sets

Participating DSS	Type of calibration ^a	Viking 1			
		From		To	
11	DRVID	6/11 19:10	6/18 00:40		
14	S/X	6/18 19:40	6/19 02:00		
		6/19 18:30	6/19 20:50		
43	DRVID	6/11 06:30	6/19 08:20		
61	DRVID	6/10 13:50	6/14 17:10		
63	DRVID	6/11 11:20	6/18 16:30		
	S/X	6/19 10:50	6/19 18:10		
Participating DSS	Type of calibration ^a	Viking 2			
		From		To	
11	DRVID	7/28 20:00	8/6 00:30		
14	DRVID	8/3 19:00	8/4 03:00		
	S/X	8/3 17:50	8/3 18:50		
		8/6 17:30	8/7 00:10		
42	DRVID	7/29 04:00	8/5 07:30		
43	DRVID	7/28 02:00	7/28 08:00		
		8/6 00:50	8/6 07:50		
	S/X	7/28 08:00	7/28 09:00		
		8/7 02:30	8/7 09:30		
61	DRVID	7/28 10:00	8/6 14:30		

^aAll data not calibrated by either DRVID or S/X was deleted.

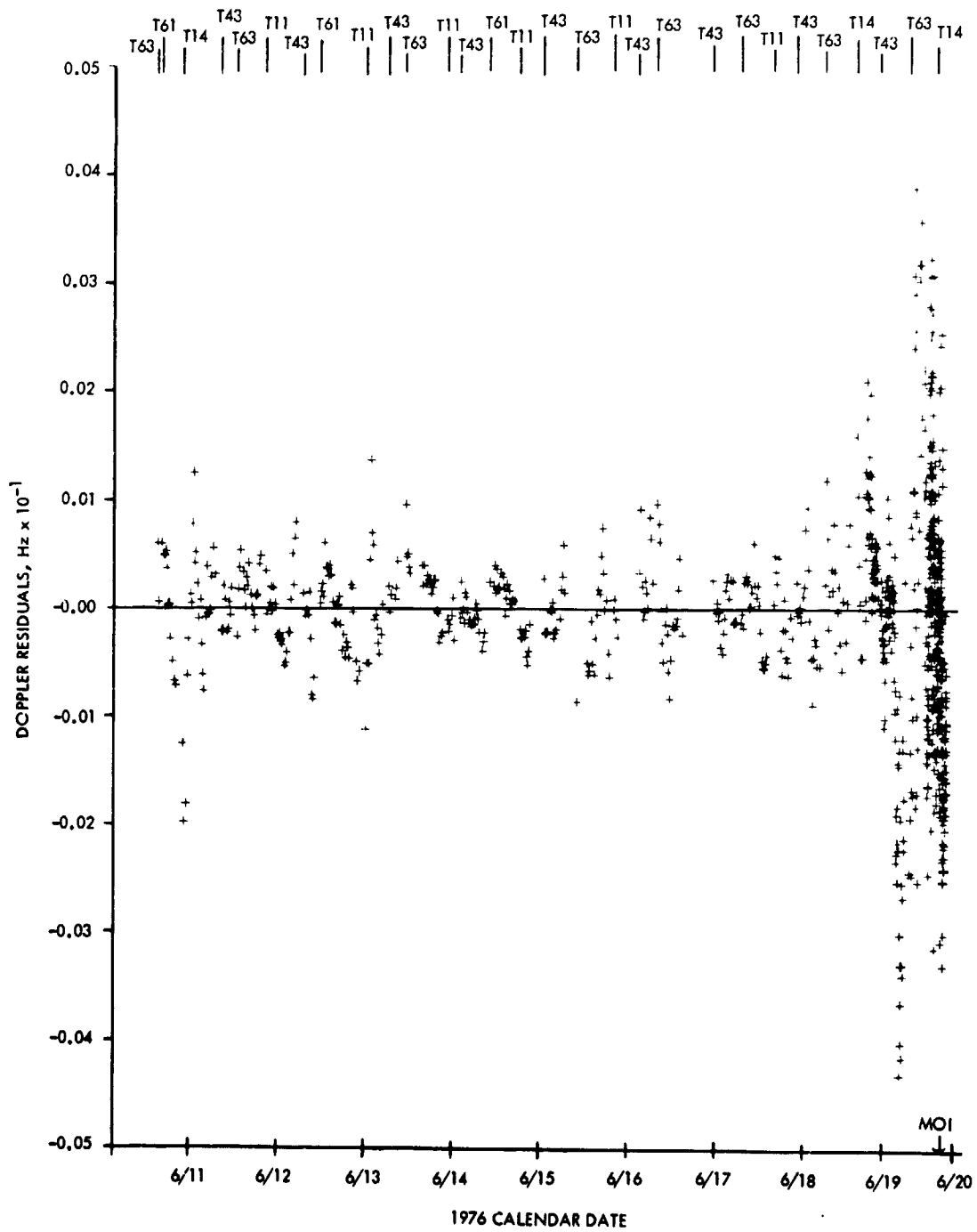


Fig. 32. Viking 1 uncalibrated doppler residuals

ORIGINAL PAGE IS
OF POOR QUALITY

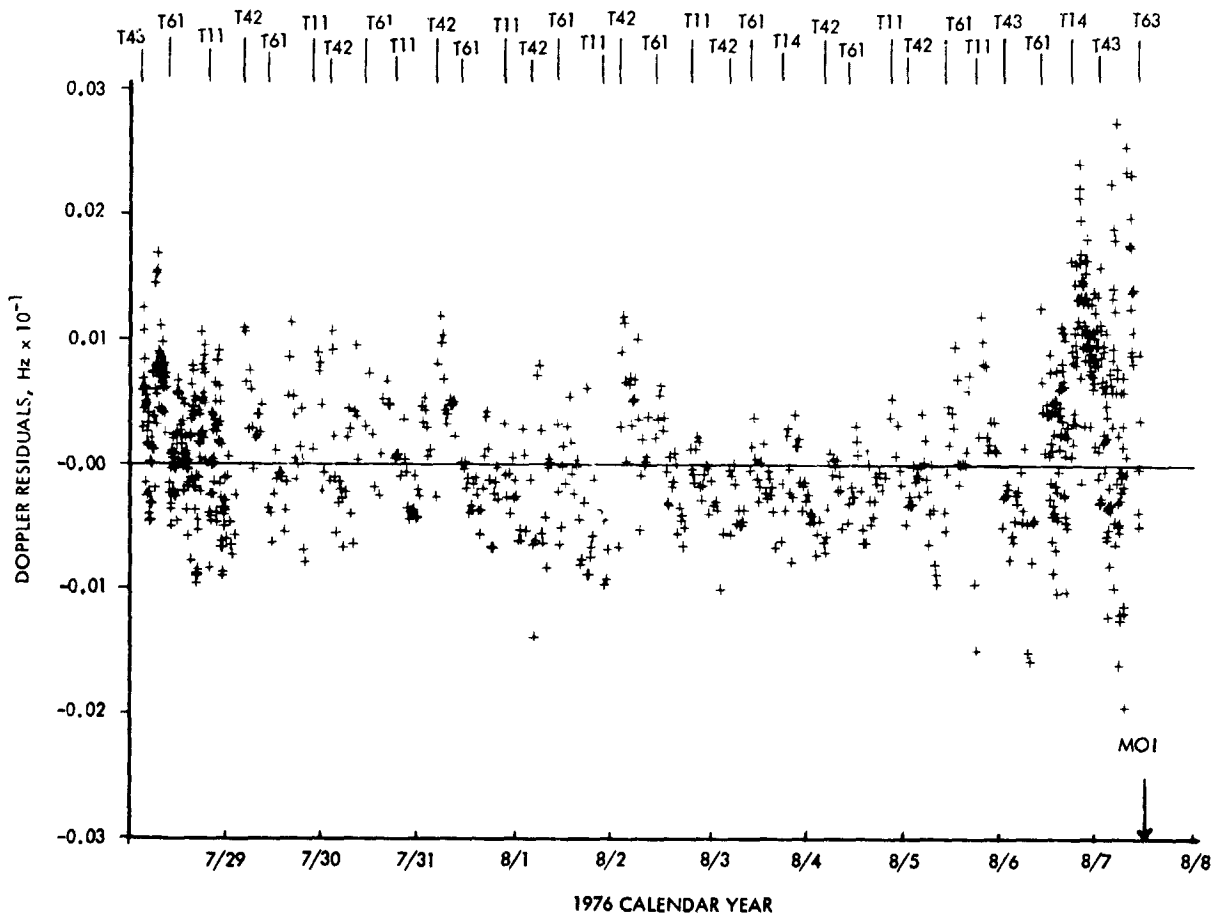


Fig. 33. Viking 2 uncalibrated doppler residuals

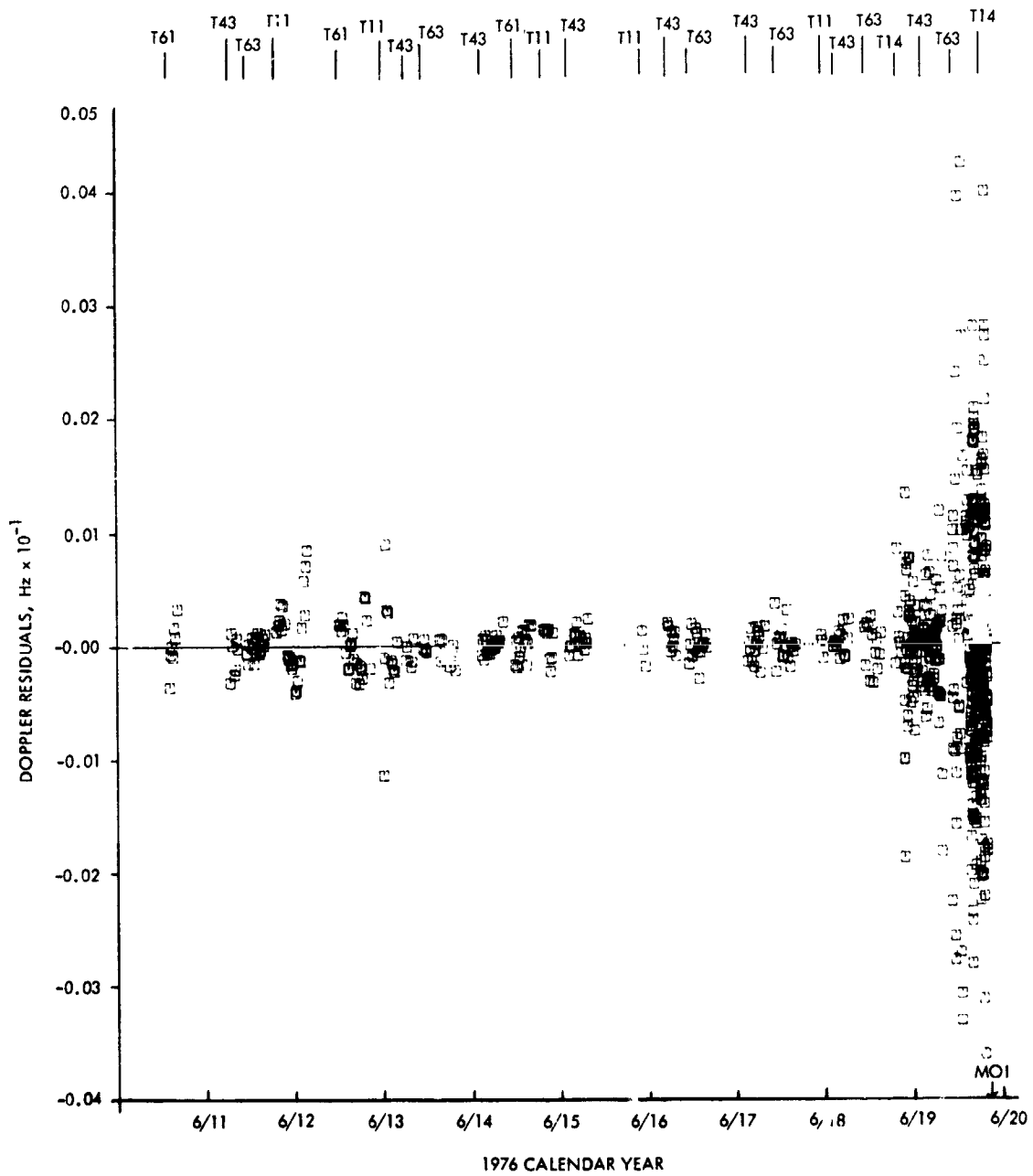


Fig. 34. Viking 1 calibrated doppler residuals

ORIGINAL PAGE IS
OF POOR QUALITY

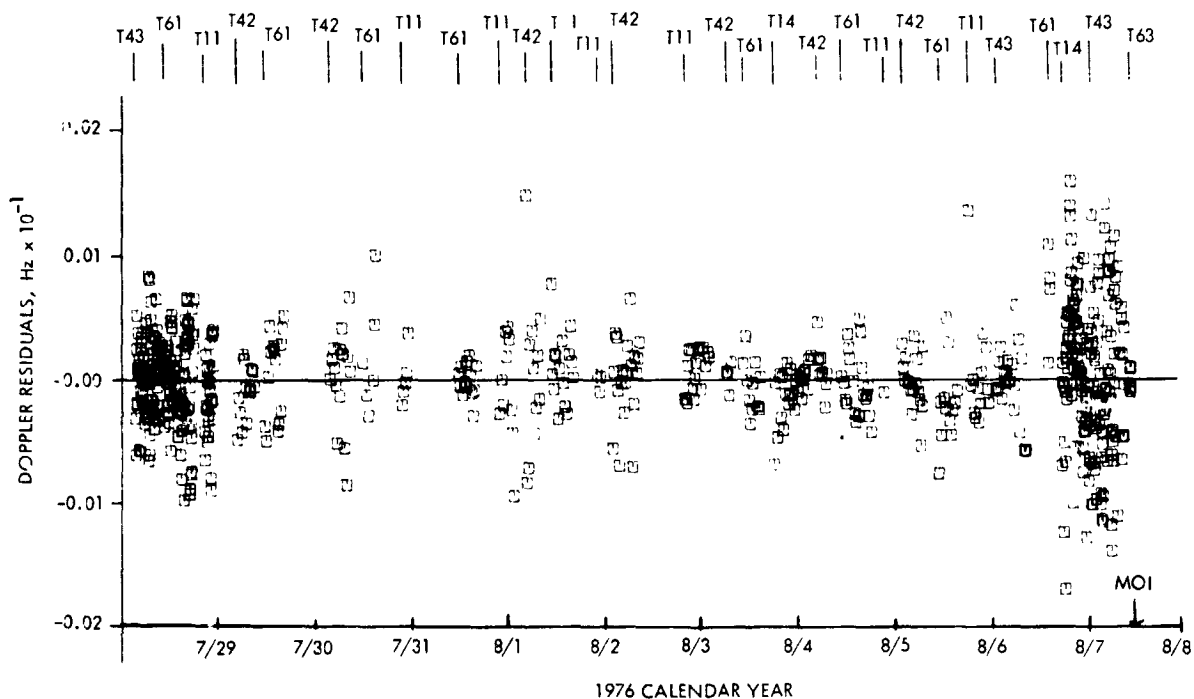


Fig. 35. Viking 2 calibrated doppler residuals

Table 26. Viking 1 uncalibrated corrections to LS44

	Participating DSS	Radio data	Radio data plus Mars pictures	1-sigma error ^a
Spin axis, m	11	-0.041	0.547	0.798
	14	1.18	1.96	0.709
	43	-3.29	-3.02	0.665
	61	-4.41	-3.76	0.835
	63	-2.10	-0.94	0.524
Longitude, 10 ⁻⁵ deg	11	-1.21	-0.747	1.15
	14	3.51	4.07	1.29
	43	-1.22	-0.712	1.10
	61	0.0	0.352	1.23
	63	1.41	1.74	1.16

^aFor radio data

Table 27. Viking 1 calibrated corrections to LS44

	Participating DSS	Radio data	Radio data plus Mars pictures	1-sigma error ^a
Spin axis, m	11	1.21	0.787	1.03
	14	1.58	1.66	1.60
	43	-0.509	-0.682	0.921
	61	-0.302	-0.675	0.121
	63	-0.213	-0.332	0.802
Longitude, 10 ⁻⁵ deg	11	0.798	0.496	1.45
	14	1.19	1.00	1.70
	43	-0.200	-0.479	1.33
	61	1.25	1.00	1.51
	63	2.12	1.89	1.42

^aFor radio data

Table 28. Viking 2 uncalibrated corrections to LS44

	Participating DSS	Radio data	Radio data plus Mars pictures	Radio data plus Deimos pictures	1-sigma error
Spin axis, m	11	-2.18	-2.23	-2.23	0.60
	14	-3.71	-3.91	-3.95	0.83
	42	-1.08	-1.03	-1.01	0.56
	43	-0.35	0.16	0.44	0.82
	61	-1.81	-1.81	-1.80	0.38
Longitude, 10^{-5} deg	11	0.12	0.28	0.35	0.95
	14	3.46	3.61	3.55	1.14
	42	2.20	2.34	2.41	0.94
	43	-2.88	-2.74	-2.79	1.14
	61	0.52	0.68	0.75	0.96

Table 29. Viking 2 calibrated corrections to LS44

	Participating DSS	Radio Data	Radio data plus Mars pictures	Radio data plus Deimos pictures	1-sigma error
Spin axis, m	11	-1.19	-1.11	-1.16	1.00
	14	-1.35	-1.28	-1.38	0.85
	42	0.20	0.18	0.32	0.80
	43	0.51	0.19	0.45	0.86
	61	0.48	0.42	0.47	0.64
Longitude, 10^{-5} deg	11	0.82	0.75	1.01	1.05
	14	2.00	1.95	2.14	1.20
	42	0.01	0.01	0.30	1.00
	43	-1.92	-2.05	-1.61	1.22
	61	0.94	0.83	1.65	1.03

Table 30. Final Viking corrections to LS44

	Participating DSS	Viking 1 ^a		Viking 2 ^b	
		Δ	1-sigma error	Δ	1-sigma error
Spin axis, m	11	0.38	0.85	-1.19	1.01
	14	0.67	1.58	-1.35	0.86
	42	-	-	0.20	0.80
	43	-0.34	0.88	0.51	0.86
	61	-0.23	1.00	0.48	0.64
Longitude, 10^{-5} deg	63	0.19	0.76	-	-
	11	-0.94	1.38	0.82	1.04
	14	-0.17	1.70	2.00	1.22
	42	-	-	0.01	1.00
	43	-1.70	1.28	-1.92	1.23
	61	-0.51	1.46	0.94	1.04
	63	-0.13	1.36	-	-

^aTiming polynomial set LD761004/PT761106.

^bTiming polynomial set LD761018/PT761116.

Table 31. Combined Viking 1 and 2 station location solutions

DSS	Δr_s^a , m	Computed 1- σ , m	$\Delta\lambda^a$, 10^{-5} deg	Computed 1- σ , 10^{-5} deg
11	-0.31	0.64	0.45	0.63
14	-0.92	0.75	1.52	0.81
42	0.22	0.79	-0.05	0.64
43	0.09	0.61	-1.27	0.68
61	0.31	0.53	0.67	0.64
63	-0.07	0.68	0.79	0.85

^a $\Delta r_s \equiv r_s$ (Viking) - r_s (LS 44); $\Delta\lambda \equiv \lambda$ (Viking) - λ (LS 44).

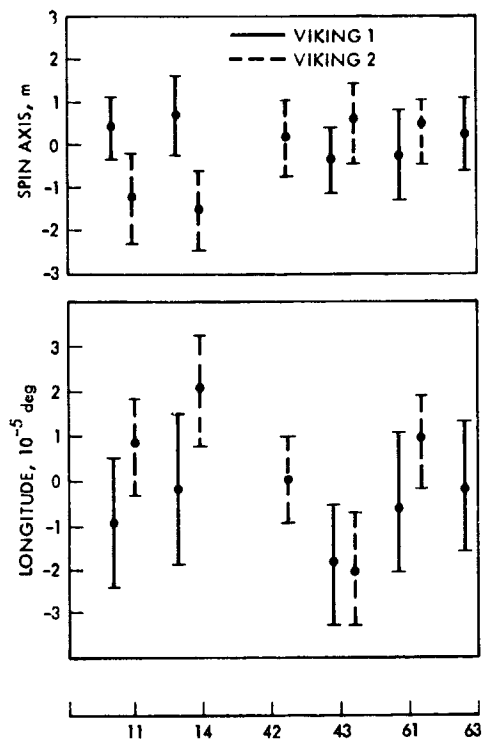


Fig. 36. Final Viking spin axis and longitude corrections to LS44

these results, it can be concluded that if Viking data were combined with the Mariner spacecraft data incorporated in LS 44, the perturbation to LS 44 would be well within the Viking mission requirement of 0.6 m in spin axis and 2.0×10^{-5} deg (~ 2 m) in longitude on station location accuracy.

XIII. Satellite Ephemeris Evaluation

This section records results of the analysis conducted to evaluate and update the Mars satellite ephemeris model, using Viking optical navigation data, i.e., photographs of Deimos against a star background. The improvement in the satellite ephemeris is an important by-product of the orbit determination activity using the optical data. The data available consisted of a total of 25 pictures spanning a 2.1-day data arc from VO-1 and 23 pictures over 3.3 days from VO-2.

A. Wilkins' Angles

The motion of the natural satellite in its orbit around the planet is obtained based on the analytical ephemeris theory developed by H. Struve and described in Ref. 10. Wilkins' orbital elements (Ref. 11) are used to define the coordinate system (Fig. 37). In this theory the orbital plane of the satellite is approximated to be inclined at a constant angle to a

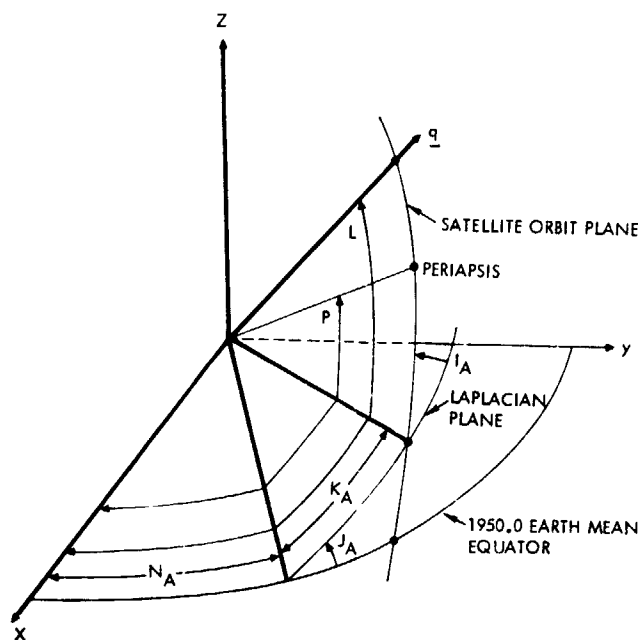


Fig. 37. Wilkins' angles

fixed plane, called the Laplacian plane, upon which the ascending node of the satellite orbital plane regresses. Short-period variations in the orbit are ignored. The angles shown in Fig. 37 are defined below:

N_A = longitude of node of fixed Laplacian plane on standard equator (1950.0 Earth equator).

J_A = inclination of fixed Laplacian plane to standard equator

K_A = the argument of the ascending node of the orbital plane on the fixed Laplacian plane

I_A = inclination of the satellite orbital plane to the fixed Laplacian plane

L = the mean longitude of the satellite measured along the standard equator, the Laplacian plane and the satellite plane

P = the longitude of pericenter of the orbit of the satellite, measured along the standard equator, the Laplacian plane and the satellite plane.

As mentioned earlier, I_A is held a constant in the theory. The angles N_A , J_A , K_A , L and P are modeled as linear functions of time given by

$$\left. \begin{aligned} N_A &= N_Z + N_R t \\ J_A &= J_Z + J_R t \\ K_A &= K_Z + K_R t \\ L &= L_Z + L_R t \end{aligned} \right\}$$

and

$$P = P_Z + P_R t$$

where the elements $(\cdot)_Z$ are the values of the angles $(\cdot)_A$ at a specified epoch and the elements $(\cdot)_R$ are their rates; the time t is measured in days past the epoch.

Table 32 gives the assumed a priori values and uncertainties for the Deimos ephemeris.

B. Analysis of Approach Optical Data for Ephemeris Determination

In this subsection we discuss the satellite ephemeris update, using the Viking 1 data for the analysis.

1. **Satellite ephemeris parameter set selection.** A preliminary analysis was conducted to establish the parameter set to be updated. Table 33 lists the results of six different parameter sets estimated using the Deimos optical data and the radio best estimate available in real-time, along with its associated covariance, as a priori. In each case the parameters estimated, in

Table 32. Viking nominal Deimos ephemeris

Parameter	Value	1-sigma uncertainty
N_A	46°.211	0°.1
J_A	36°.716	0°.1
K_Z	210°.266	1°.0
K_R	-0°.01813	0°.0003
I	1°.81	0°.02
L_Z	273°.587	0°.1
L_N	285°.16180	0°.0001
P_Z	126°.097	5°.0
P_R	0°.01813	0°.003
a	23458.89 km	0.1 km
e	0.00052	0.001

addition to the spacecraft state, are as indicated in the table. For the A1KX04 case the semimajor axis A , the mean motion LN and the angular rates for K and P were also estimated.

For the update parameter set selection it was decided to drop I (the inclination of the satellite orbit to the Laplacian plane) and to include the parameters N_A , J_A related to the orientation of the Martian pole; the latter are not as well known as is I , which is in fact modeled as a fixed constant in the satellite theory. The mean longitude L the eccentricity E and the longitude of pericenter P were included; also included was the node of the Laplacian plane K , which is not very well known.

Thus the update parameter set is: E, L, K, P, N_A, J_A .

2. **Data strategy selection.** Table 34 lists the results from estimating the satellite ephemeris parameter set described above, using four different data strategies. These are respectively:

- (1) The post-AMC2 radio data available during the real-time processing as a priori.
- (2) Optical data only.
- (3) The radio a priori resulting from processing all the radio data available from AMC1 until encounter.

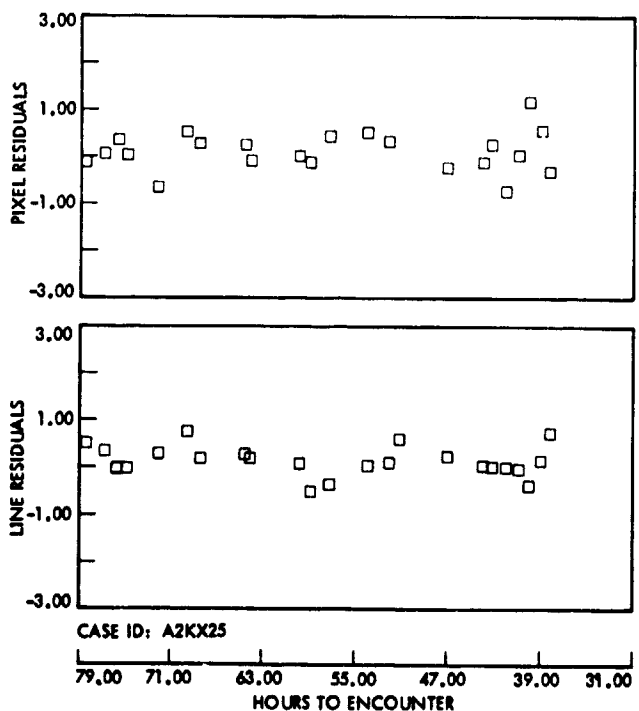


Fig. 38. VO-1 postfit Deimos residuals

Table 33. Parameter set selection for satellite ephemeris

RUNID	B·R, km	B·T, km	SMAA, km	ΔE	ΔL , deg	ΔI , deg	ΔK , deg	ΔP , deg	ΔN_A , deg	ΔJ_A , deg
A1KX04	7265.9	6912.6	10.3	-0.270-3	0.215-1	0.115-2	0.1215	-0.114+1	-0.313-1	-0.832-2
A1KX05	7265.9	6912.6	10.3	-0.270-3	0.219-1		0.1235	-0.114+1	-0.321-1	-0.935-2
A1KX06	7265.9	6912.6	10.3	-0.270-3	0.208-1			-0.114+1	-0.378-1	-0.748-2
A1KX08	7266.7	6912.6	10.8	-0.265-3	0.267-1	0.119-1	0.412	-0.112+1		
A1KX09	7265.9	6912.6	10.3	-0.270-3	0.220-1	0.115-2	0.121	-0.114+1	-0.314-1	-0.832-2
A1KX10	7271.8	6915.8	21.2		0.219-1					

Table 34. Data strategy selection for satellite ephemeris

Strategy	RUNID	B·R, km	B·T, km	SMAA, km	ΔE	ΔL , deg	ΔI , deg	ΔK , deg	ΔP , deg	ΔN_A , deg	ΔJ_A , deg
(1)	A1KX05	7265.9	6912.6	10.3	-0.270-3	0.291-1		0.1235	-0.114+1	-0.321-1	-0.935-2
(2)	A2KX25	7263.9	6907.9	10.8	0.250-5	0.241-1		0.105	-0.824	-0.303-1	-0.138-1
(3)	A3KX83	7275	6920	1.92	-0.178-3	0.257-1		0.146	0.450+1	-0.373-1	-0.724-2
(4)	A3KX87	7275	6920	1.89	-0.175-3	0.256-1		0.145	0.426+1	-0.370-1	-0.734-2

Table 35. Effect of degrading a priori uncertainty on satellite ephemeris

RUNID	B·R, km	B·T, km	SMAA, km	ΔE	ΔL , deg	ΔI , deg	ΔK , deg	ΔP , deg	ΔN_A , deg	ΔJ_A , deg
A2KX25	7263.9	6907.9	10.8	0.250-5	0.241-1		0.105	-0.824	-0.303-1	-0.138-1
A3KX94	7257	6899	15.97	0.111-4	0.257-1		0.121	-0.275+2	-0.308-1	-0.130-1

(4) The a priori resulting from processing the data in (3) plus the star-Mars-star optical data arc from AMC1 to AMC2.

Strategy (2) was considered the best for updating the satellite ephemeris parameters, i.e., using the Deimos optical data only. This process should yield the best determination of the parameters with no corruption from any external error sources. Figure 38 gives the post-fit residuals for this strategy.

3. Loosening a priori satellite parameter variances. Table 35 shows a comparison of the nominal navigation plan parameter uncertainties used as a priori with those degraded by an order of magnitude to allow the parameters greater freedom to move. Figure 39 gives the resulting post-fit residuals. The results were consistent with other solutions. However, the solution had large correlations between the parameters, the B-plane solution was further from the current best estimate (CBE), and the longitude of periapsis moved by a large amount. Since there was confidence in the nominal satellite parameters and their associated statistics as determined from

MM'71 data, this solution was not considered to be suitable for use as an update. There is not sufficient strength in the data to be able to make a definite determination regarding the periapsis shift; this will have to await the in-orbit optical results.

4. Evaluation of measurement biases. An analysis was conducted to evaluate measurement biases in the optical data. The focus was on the determination of any relative shifts in the measurement biases between the star-Mars-star triads and the Deimos-star data types. Biases were solved for in the latter using the strategies listed below:

- (1) Using the Deimos optical data only.
- (2) Using the a priori resulting from processing the radio data from AMC1 to encounter, including the post-AMC1 Mars data assuming zero biases, followed by the post-AMC2 Deimos data solving for biases.
- (3) Using the a priori resulting from processing all the radio and optical data between AMC1 and AMC2 and the post-AMC2 radio data, including the Deimos data solving for biases.

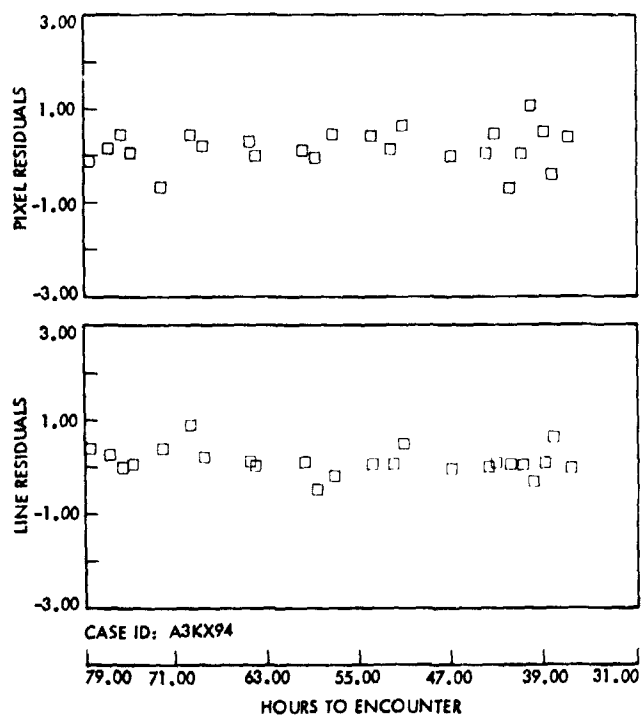


Fig. 39. VO-1 postfit Deimos residuals; loose a priori

- (4) Simultaneous processing of all the post-AMC1 radio and optical data, assuming zero biases for the Mars data.
- (5) Using the a priori as in (2), including only the post-AMC2 Deimos data, solving for biases.

Results are listed in Table 36. Biases do exist in the Deimos data at the level of approximately 1 pixel in the pixel direction and 1/3 pixel in the line direction. These types of biases are not surprising owing to the known difficulties in extracting precise image center from the intentionally overexposed Deimos image.

5. Evaluation of satellite parameter update. The values of the satellite parameters updated are listed in Table 37. They reflect a change in the inertial position (from the pre-updated Deimos orbit) of a minimum of 11 km and a maximum of 17.5 km, depending on the location in its orbit. Of this the down-track error is about 10 km.

To examine the effect of using the updated satellite ephemeris, a solution was made using the radio data available during the real-time processing along with the optical data, but not solving for the satellite ephemeris. The results, along with the current best estimate are shown in Table 38.

Table 36. Optical measurement biases

RUNID	BIASM ^a , × 10 ⁻³ deg		BIASN ^a , × 10 ⁻³ deg	
	Delta	Sigma	Delta	Sigma
A1KX76	-0.003	1.5	-0.028	1.5
A3KX01	-1.5	0.48	-0.41	0.55
A3KX91	-1.44	0.52	-0.42	0.60
A06524	-1.53	0.50	-0.40	0.60
A3KX35	-1.42	0.52	-0.42	0.60

^a1 pixel = 1.5 × 10⁻³ deg

Table 37. Deimos ephemeris parameter updates

Parameter	Value
<i>E</i>	0.5225 × 10 ⁻³
<i>L</i> , deg	273.61114
<i>K</i> , deg	210.37176
<i>P</i> , deg	125.27263
<i>N_A</i> , deg	46.180634
<i>J_A</i> , deg	36.702119

Table 38. Deimos ephemeris update evaluation

Run	B·R	B·T
Before update A1KX05	7266	6913
After update A1KX68	7269	6916
Current best estimate	7276	6920

Figures 40 and 41 show the pre-update and post-update Deimos residuals against the best postflight spacecraft trajectory. Figure 42 shows the same, using the satellite ephemeris corrections from case (4) in subsection 4, where biases were also solved for. An examination of Figs. 41 and 42 shows that similar biases are present in both sets of residuals; i.e., in the optical-only case biases are indistinguishable from spacecraft velocity errors. Also evident in both are spacecraft position offset signatures. The Fig. 41 residuals appear to be slightly flatter.

C. Satellite Ephemeris from VO-1 and VO-2

The results of applying the data and solution strategies discussed above are shown in Table 39. For both Viking 1 and 2, the changes of the parameter values from the nominal are displayed. The associated 1-σ uncertainties are also given in the table.

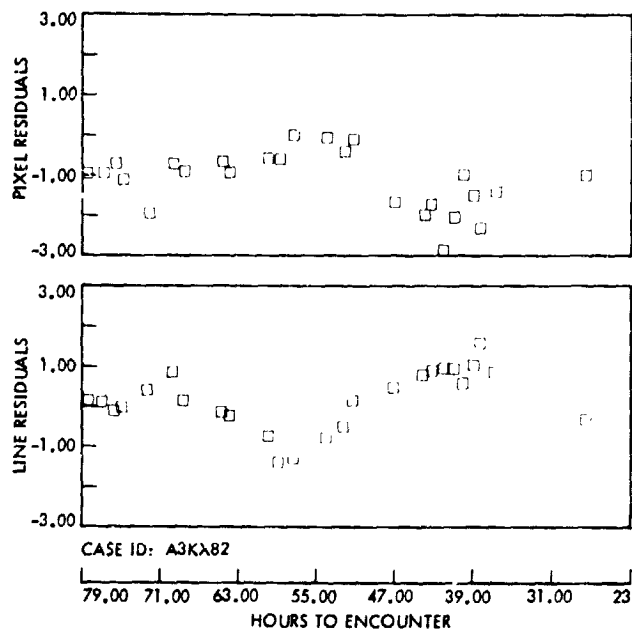


Fig. 40. VO-1 pre-update Deimos residuals

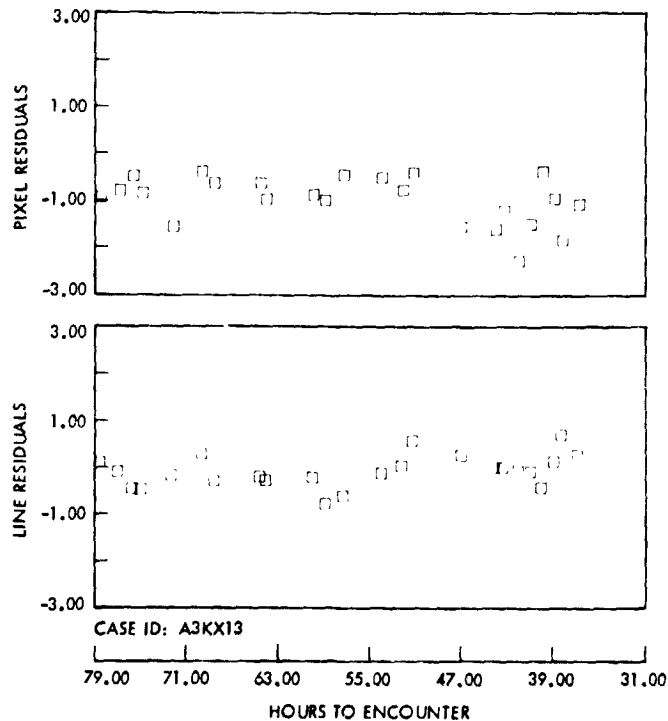


Fig. 41 VO-1 post-update Deimos residuals

Table 39. Deimos ephemeris using Viking approach optical data

Parameter	VO-1		VO-2	
	Δ	1 sigma	Δ	1 sigma
E	0.25×10^{-5}	0.27×10^{-3}	0.19×10^{-4}	0.17×10^{-3}
L , deg	0.024	0.020	0.045	0.010
K , deg	0.11	0.89	0.01	0.89
P , deg	-0.82	4.95	-1.62	4.83
N_A , deg	-0.030	0.050	-0.016	0.045
J_A , deg	-0.014	0.026	-0.020	0.015

As can be observed from the table, the major significant change from the a priori value is in the mean longitude L . Moreover, the change appears to be inconsistent between the results of VO-1 and VO-2 by a statistically large difference of approximately 8 km. This apparent discrepancy can be explained, however, by an examination of the short-period terms omitted in Wilkins' theory.

In Deimos down-track variations, the dominant perturbations in down-track position due to solar effects during the interval from VO-1 approach to VO-2 approach are given by (Ref. 12)

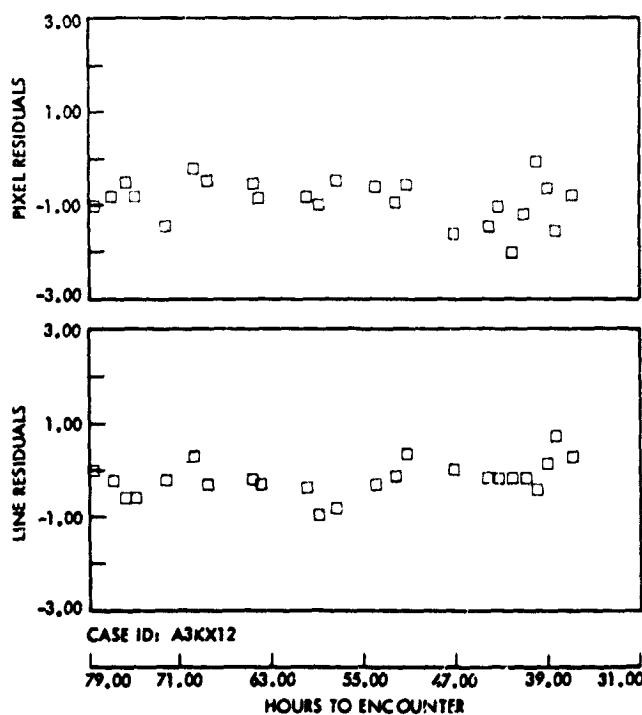


Fig. 42. VO-1 post-update Deimos residuals, biases solved for

$$\begin{aligned} \delta DT(\text{km}) = & -8.6 \sin l' - 0.6 \sin 2 l' \\ & - 5.5 \sin (2 l' + 2 g') \\ & - 1.1 \sin (3 l' + 2 g') \\ & + 0.7 \sin (2 l' + 2 g' - h + h') \end{aligned}$$

where

$$\begin{aligned} l' &= \text{mean anomaly of Sun} \\ &= 204.5^\circ + 0.5240207666 (\text{JD} - 2414800.5) \\ g' &= \text{argument of periapse of Sun} \\ &= 249.7^\circ \\ h' &= \text{node of Sun} \\ &= 180^\circ \\ h &= \text{node of Deimos} \\ &= K - 43.7^\circ \end{aligned}$$

The periods of these solar perturbations range from 229 to 687 days. The effect is to advance Deimos by 6.6 km in the down-track position at the time of the VO-2 approach observations, and by 0.6 km at the time of VO-1 approach, giving a net longitude difference of 6 km.

In addition to the above effects there is another short-period (65-h) term neglected in Wilkins' theory. The 65-h downtrack position variation, due to J_{22} , is given by

$$\delta DT(\text{km}) = - 5.1 \sin \theta$$

where

$$\frac{\theta}{2} = L + 136.0^\circ - 350.892017 (\text{JD} - 2442778.5)$$

This term, which has a period of the order of the data spans, would in general have different effects on VO-1 and VO-2 data. However, it may average out and would not therefore be expected to introduce any significant inaccuracy. After the short-period terms are accounted for, the VO-2 satellite ephemeris results are in very good agreement with VO-1 results.

In summary:

- (1) There appears to be very good agreement between the results of VO-1 and VO-2 after the short-periodic terms are taken into account.
- (2) The prediction error from Mariner 9 to Viking has been less than 15 km. This constitutes a verification of the long-period-variation term due to Born (Ref. 8); it is

the combined effect of the direct solar perturbation and an interaction perturbation induced by the variation in inclination of the satellite orbit relative to the planet equator due to solar perturbation. This effect would have yielded 80 km in the mapping from Mariner 9 to Viking.

- (3) The approach optical data had limited strength; verification and/or improvement of the Deimos ephemeris will have to await results from the in-orbit and extended mission close-encounter pictures.

XIV. Conclusions

The success of the interplanetary orbit determination effort is best measured by the accuracy of its delivered estimates:

- (1) Viking 1 trajectory was delivered to within 25 km of its intended target despite the difficulties brought on by the pressurant problem. Although this error includes execution uncertainty, it still indicates a very accurate estimate of the premidcourse orbit.
- (2) Viking 1 final pre-MOI orbit estimate, which was used to generate the MOI maneuver, was in error by 6 km. The accuracy of this estimate coupled with the precision of the orbit insertion maneuver permitted Viking 1 to fly a virtually nominal flight path to the initially prescribed lander separation orbit.
- (3) Viking 2 was delivered to within 37 km of its intended target.
- (4) Viking 2 MOI maneuver was based on an early, encounter minus 6-day, estimate. This estimate was in error by 37 km.
- (5) Viking 2 E-24 orbit was in error by 2 km.

There are a number of general conclusions resulting from the Viking inflight experience that should be of value to future interplanetary orbit determination efforts. These conclusions are summarized below:

- (1) Accurate postlaunch estimates are obtainable using just minutes of spacecraft tracking following launch. Early accurate estimates require moderate accuracy antenna angle observations.
- (2) Long-arc estimates prior to approach M/C, although stable, were not as accurate as expected. The long-arc technique has the potential for very accurate orbit estimation; however, it is computationally expensive, unwieldy to implement for Viking, and it is relatively difficult to establish the confidence in the resultant estimates. For these reasons, further development is

required if long-arc solutions are to be fully relied on in future applications.

- (3) Effect of charged-particle density variations in the interplanetary medium strongly influenced the Earth-based doppler measurements. The effects were somewhat larger than predicted, and introduced relatively large variations in the approach estimates. The doppler calibrations using DRVID successfully removed these effects and brought the radio-only solution accuracies to within their expected levels.
- (4) Optical measurements and the resultant optical-based solutions performed excellently. The limb measurement technique proved to be very precise and center-finding errors proved to be small, most likely within 1% of the Mars radius (i.e., ~35 km). The two-camera observation technique achieved the most optimistic accuracy levels.
- (5) Success of the optical orbit determination resulted from the concerted efforts in several areas, including: (a) use of long optical observation arcs, which essentially gave the optical-only solutions a stand-alone capability in determining the spacecraft orbit; (b) careful planning, design, and execution of the onboard optical observation sequences; (c) extensive participation in, and use of data from, inflight camera and S/P checkout and calibration activity; (d) use of spacecraft telemetry to improve two-camera observation accuracy; and (e) careful design of the radio-plus-optical processing techniques that obtained the relative advantages of the radio and optical data types. The optical orbit determination success in addition drew heavily from the development provided by the Mariner 9 demonstration, including the general technology and software development (ONP and OMSET were derived from Mariner 9 versions) and the Deimos satellite ephemeris determination.

References

1. Duxbury, T. C., Born, G. H., and Jerath, N., "Viewing Phobos and Deimos for Navigating Mariner 9," *Journal of Spacecraft and Rockets*, Vol. 11, No. 4, pp. 215-222, Apr. 1974.
2. Jerath, N., and Ohtakay, H., "Mariner IX Optical Navigation Using Mars Lit Limb," *Journal of Spacecraft and Rockets*, Vol. 11, No. 7, July 1974.
3. Born, G. H., et al., *Mariner Mars 1971 Optical Navigation Demonstration Final Report*, Technical Memorandum 33-683, Jet Propulsion Laboratory, Pasadena, Calif., Apr. 15, 1974.
4. Moyer, T. D., *Mathematical Formulation of the Double-Precision Orbit Determination Program (DPODP)*, Technical Report 32-1527, Jet Propulsion Laboratory, Pasadena, Calif., May 15, 1971.
5. Bierman, G. J., *Filtering and Smoothing for the Viking Filter*, Technical Memorandum 391-414, Jet Propulsion Laboratory, Pasadena, Calif., Feb. 28, 1973.
6. Rourke, K. H., and Jordan, J. F., "Application of Sequential Filtering to Estimation of the Interplanetary Orbit of Mariner 9," *Journal of Spacecraft and Rockets*, Vol. 10, No. 12, pp. 773-778, Dec. 1973.
7. Christensen, C. S., *Performance of the Square Root Information Filter for Navigation of the Mariner 10 Spacecraft*, Technical Memorandum 33-757, Jet Propulsion Laboratory, Pasadena, Calif., Jan. 15, 1976.
8. Born, G. H., and Duxbury, T. C., "The Motions of Phobos and Deimos from Mariner 9 TV Data," *Celestial Mechanics*, 12, pp. 77-88, 1975.
9. Koble, H. M., Pease, G. E., and Yip, K. W., "LS 44 - An Improved Deep Space Network Location Set for Viking Navigation," in *The Deep Space Network Progress Report 42-35*, pp. 79-88, Jet Propulsion Laboratory, Pasadena, Calif., Oct. 15, 1976.
10. *Explanatory Supplement to the Astronomical Ephemeris and the American Ephemeris and Nautical Almanac*, Her Majesty's Stationery Office, London, 1961.
11. Wilkins, G. A., "The Analysis of the Observations of the Satellites of Mars," *Modern Questions in Celestial Mechanics*, G. Colombo ed., Edizione Cremonese, Rome, 1967.
12. Hildebrand, C. E., personal communication.

Satellite Orbit Determination

C. E. Hildebrand, E. J. Christensen, D. H. Boggs, G. H. Born,
B. G. Williams, and Z. Shippony

I. Introduction

The satellite phases of Viking 1 and Viking 2 began on June 19, and August 7, 1976, when the respective spacecraft were inserted into orbit about Mars. Each spacecraft consisted of an orbiter-lander combination. The orbiters, which had their own complements of science instruments, also served as communication relays for the landers in their search for Martian life.

The Mariner 9 Mission to Mars served as the precursor to Viking and was instrumental in guiding the development of mathematical models and procedures used for Viking orbit determination (OD). For example, the gravity field of Mars developed with Mariner 9 data was found to be well within its predicted uncertainty for Viking applications. In addition, the ephemerides of the Martian satellites Phobos and Deimos as determined by Mariner 9 television data aided precise navigation of the Viking spacecraft on Mars approach (Ref. 1).

The orbital elements for the Viking spacecraft subsequent to Mars orbit insertion (MOI) and each major orbit adjust throughout the nominal 90-day mission are shown in Tables 1 and 2. As seen from these tables the Viking spacecraft were in a wide range of orbits. Generally the orbits were near synchronous with the Mars rotational period (24.6 h) as contrasted

with Mariner 9's orbital period of approximately 12 h. Other significant differences between Viking and Mariner 9 are in the orbit inclination and location of periapsis (64.5° and 22°S for Mariner 9 (Refs. 2 and 3)).

This part of the report relates the experiences of the Viking Satellite Orbit Determination Team in determining the Mars-centered ephemerides of the Viking Orbiters and positions of the landers from two-way doppler and range data. In Section II an overview of mission satellite OD functions and methods is given. Section III relates postmaneuver orbit convergence experiences, while Section IV discusses local orbit knowledge accuracies, including the effects of interplanetary media, use of constrained solutions and solving through trim burns. A very significant aspect of any planetary orbiter mission is rapid identification of the planet gravity field; the relevant procedures and results are given in Section V. Viking lander position determination is discussed in Section VI. While this chapter is primarily concerned with activities during the nominal mission, several interesting activities associated with the extended mission are also included. Specifically, results relative to sensing Mars' gravity field during the extended mission are included in Section V; Section VII contains a discussion of the Phobos Flyby Experiment conducted during February 1977.

Table 1. Areocentric orbital elements of Viking 1

	MOI	MOT-1	MOT-5	MOT-6	SKT-2	MOT-7	MOT-8	MOT-9
Date of maneuver	6/19/76	6/21/76	7/9/76	7/14/76	8/3/76	9/11/76	9/20/76	9/24/76
Semimajor axis, km	a 29325.5	20448.9	20512.0	20443.4	20435.9	18879.4	19081.1	20440.1
Eccentricity	e 0.8327	0.7600	0.7608	0.7602	0.7603	0.7412	0.7439	0.7598
Mean period, h	P 42.352	24.661	24.776	24.651	24.638	21.877	22.229	24.645
Longitude of ascending node, deg	Ω 129.80	129.68	124.77	124.20	121.78	116.99	115.72	115.08
Argument of periapsis, deg	ω 39.76	39.94	44.89	45.82	49.31	56.03	57.99	59.77
Inclination, deg	I 37.87	37.88	37.69	37.70	37.90	38.13	38.31	38.16
Height above surface at periapsis, km	h_p 1513.2	1513.1	1512.9	1508.5	1504.8	1491.2	1491.9	1515.4
Latitude of sub-periapsis passage, deg	ϕ_p 23.12	23.21	25.56	26.01	27.76	30.80	31.71	32.26

Keplerian elements referenced to Mars true equator of date. Mean radius of Mars = 3394 km.

Table 2. Areocentric orbital elements of Viking 2

	MOI	MOT-1	MOT-2	MOT-3	MOT-4	MOT-5
Date of maneuver	8/7/76	8/9/76	8/14/76	8/25/76	8/27/76	9/30/76
Semimajor axis, km	a 22054.8	21889.5	21943.0	21513.4	20472.2	21611.2
Eccentricity	e 0.775	0.7765	0.7769	0.7603	0.7610	0.7732
Mean period, h	P 27.623	27.313	27.413	24.040	24.622	26.794
Longitude of ascending node, deg	Ω 36.37	36.07	35.72	34.78	34.40	54.60
Argument of periapsis, deg	ω 69.32	69.77	70.02	72.66	73.65	68.34
Inclination, deg	I 55.17	55.20	55.21	55.65	55.39	74.90
Height above surface at periapsis, km	h_p 1518.2	1499.0	1501.0	1424.3	1489.0	1508.3
Latitude of sub-periapsis passage, deg	ϕ_p 50.17	50.40	50.51	52.00	52.16	63.80

Keplerian elements referenced to Mars true equator of date. Mean radius of Mars = 3394 km.

The Viking Navigation Plan (Ref. 4) extensively covers pre-flight models, procedures and error analysis for all Viking navigation functions from launch through landing. Consequently, preflight analysis will be discussed here only insofar as necessary to explain in-flight results.

II. Overview of Viking Satellite OD Activities

A. Support Activities

Viking satellite phase events requiring extensive navigation support are shown chronologically in Fig. 1. Prior to Viking Lander (VL) separation, orbit phase navigation activities were directed toward

- (1) Acquiring imaging and other scientific observations of candidate landing sites.
- (2) Achieving an orbit from which a safe landing could be effected.
- (3) Designing the VL deorbit burn, entry trajectory, and descent guidance and control sequences.

Postlanding activities during the primary mission shifted to VL/VO relay link design and maintenance, VO Science and

Radio Science support, and, between VL-1 landing and VL-2 descent design, analysis of the VL-1 descent performance. Specific areas requiring direct orbit determination support are described below.

1. **Mars orbit trim (MOT) design.** Orbit trim maneuvers were performed to achieve orbits such that

- (1) Landing site reconnaissance could be performed.
- (2) VL descent and landing could be safely executed.
- (3) The VL/VO relay link was of sufficient duration.
- (4) VO Science objectives could be met.

MOT design employed estimates of VO state at the time of the maneuver and at the target point (VL separation, for example). Estimates were typically provided at three different stages of the design process, ranging in time from several days prior to a maneuver to as late as 20 hours before a trim. Providing for "late updates" to the maneuver time employing the most recent estimates of orbit timing resulted in elimination of the major contribution of the orbit determination error to the orbit control error.

2. **Science sequence design.** VO position estimates accurate to 13 km at periapse were required for targeting the scan

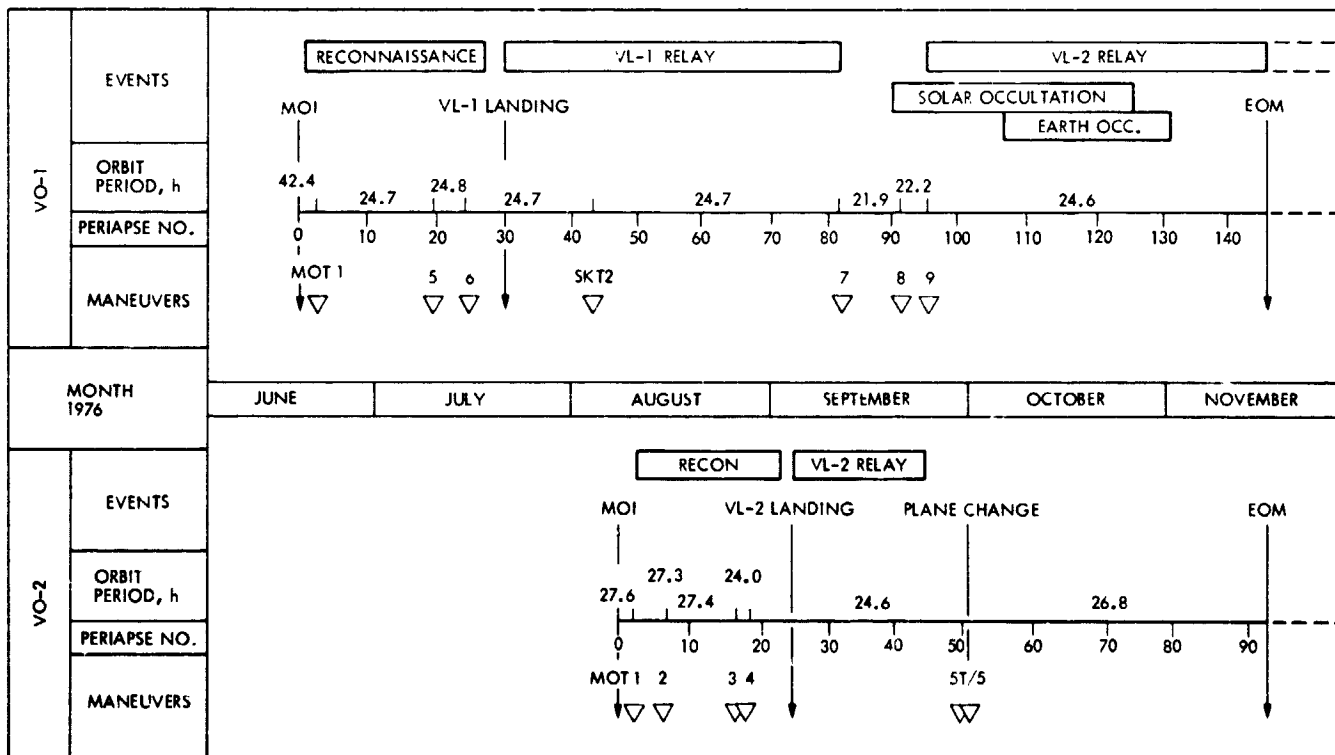


Fig. 1. Viking orbit phase navigation related events

platform instruments. Orbit determination support of this function was relatively intensive because

- (1) Science sequences were performed nearly every orbit during the prime mission.
- (2) Accuracy and lead time requirements limited the useful interval of prediction of a given solution.
- (3) Frequent orbit trims shortened the useful prediction intervals and often necessitated quick redetermination of the post-trim orbit so that science sequences could be updated to compensate for maneuver execution errors.

3. VL descent design. VO state estimates at VL separation provided initial conditions for the descent trajectory. Again, descent design employed VO state estimates at several stages of the design process. Provision was made for utilizing estimates becoming available as late as 26 hours before separation to update the time of initiation of the descent sequence.

4. VL/VO radio tracking. Predictions of round trip light times to the Viking orbiters and landers are routinely prepared to support the tracking activities of the NASA Deep Space Network (DSN). The DSN employs this information in selecting tracking frequencies and in monitoring data quality. Frequent orbit trims significantly impact the complexity of this task.

5. Pseudoresidual generation. Frequency-independent doppler observable predictions are routinely provided to the Mission Control and Computing Center (MCCC) at JPL. The predicted and actual doppler measurements are differenced by MCCC in real-time, and the resulting pseudoresiduals are displayed via closed circuit TV. The navigation group uses pseudoresiduals to monitor trajectory events (trims, VL separation, etc.), monitor orbit prediction accuracies, detect doppler data or orbit anomalies, and to edit the doppler data.

6. VL/VO relay link design. Lander science and engineering data is returned to Earth via a low-data-rate S-band direct link or a high-rate VL-to-VO UHF relay link. Orbit determination support of the relay link design activities consists of providing predicted VO trajectories and estimates of VL position, which are then used to determine the time of initiation and duration of each relay period. The VO trajectories typically provide predictions of time of periapse accurate to much better than 30 s 10 orbits in advance.

7. Radio Science. Local orbit estimates and pseudo Earth-to-Mars range measurements (normal points) are periodically prepared in support of Radio Science activities. The normal points, which are obtained by processing VO ranging data, are

used in the relativity/ephemeris experiment (Ref. 5). VO position estimates are also provided in support of the S/X occultation experiment.

B. Methods

The basic techniques for determining the state of a Mars orbiter were well established during the Mariner 9 mission (Ref. 3). The strategy involves processing a single revolution of two-way doppler to determine the local orbit. Accurate prediction is achieved by using data arcs spanning several revolutions to obtain improvement in the estimate of a spherical harmonic coefficient model of the Mars gravity field. The Mariner 9 spacecraft remained in essentially the same orbit from the first trim at two days after insertion until the end of the mission. The orbit periapses made a complete circuit of the planet at nearly constant latitude in a resonance cycle of 38 revolutions. Thus, gravity models generated with four to six orbits of data from one resonance cycle could be used in predicting over the same region on the next cycle. During the Viking Prime Mission, a technique designed to deal with a variety of orbits was employed. Basically, gravity models associated with a given orbit were developed by first processing two to four orbits of data estimating harmonic coefficients through sixth degree and order, and then selected "local" models were combined into an ensemble field.

A task which required relatively little attention during Mariner 9 was that of redetermining the orbit after a maneuver in support of Science Sequence Design and DSN tracking (only two trim maneuvers were performed during the Mariner mission, compared to three for VO-1 and four for VO-2 prior to lander separation). Possible approaches involve

- (1) Processing short arcs of post-maneuver doppler data.
- (2) For orbit trims, processing pre- and post-trim data and estimating trim ΔV components (and possibly gravity coefficients) in addition to VO state.

A problem encountered with the former technique is that ill-conditioning may lead to slow convergence, or even divergence unless a numerical method such as the Partial Step Algorithm (Ref. 6) is employed. This problem may be especially critical in the process of converging to the initial orbit after Mars orbit insertion. If an accurate orbit is available prior to the trim, the solution can be constrained with an a priori covariance matrix. This question is addressed in detail in Section IV. In any case, for rapid redetermination, the problem of assessing the estimate accuracy arises. In general, this can be satisfactorily done by processing several intermediate arcs and monitoring the evolution of the estimates of selected orbit parameters.

Viking lander position determination involved estimating both the cylindrical coordinates of the VL relative to a Mars fixed reference frame and the inertial direction of the Mars spin axis from short arcs of two-way doppler data and a few two-way range points. Accurate VL position estimates were required five days after landing. Potential errors resulting from an incorrect value of the Earth-to-Mars range were eliminated by making use of VO range residuals, as discussed in Section VI.

III. Initial Orbit Convergence

A. The Convergence Problem for Short Data Arcs

As a result of the excellent encounter phase orbit determination (OD) and Mars orbit insertion (MOI) maneuver design and execution, the differences between the actual post-MOI orbits achieved and the desired target orbits were within predicted 1σ levels. Thus, for example, the period component of the error in the a priori state used in the initial fit after insertion was 20.25 min for VO-1 and -5.98 min for VO-2 (using as reference the periods that resulted from processing full orbits of data, Section III-C). In general the determination of a postinsertion solution becomes more difficult as the total error in the a priori state increases: the overall accuracy of the Viking orbit insertion process allowed convergence to the (approximate) initial state of both orbiters without undue difficulty, using only the first several hours of post-MOI data.

Under less fortunate circumstances the initial determination of the post-insertion state could have been more troublesome, particularly a few hours after MOI when only short data arcs were available for fitting. Indeed, if the a priori state error had had a significant component in an unfavorable direction, and had the iterative differential-correction process using the classical Gaussian least-squares solution offered by the DPODP been used, a suitable solution might not have been obtained. The standard linear batch data filter, which is entirely adequate for interplanetary OD, has in fact been shown to lead to divergent results over a wide class of orbital configurations — even for relatively small initial state errors (Ref. 6).

Such a convergence problem arises from the coupled effects of nonlinearity and "ill-conditionedness," and was recognized some time before the Viking mission (Refs. 3, 4, 6). Nonlinearity here refers to the inability to accurately relate finite deviations in the data to deviations in the spacecraft state with first-order partial derivatives, and ill-conditionedness is related to the numerical difficulty inherent in computing the full-rank solution for a set of parameters — state in this case — which for a given data set is highly correlated statistically. A short

data arc, i.e., one spanning less than an orbital period, typically yields deleterious conditioning. As the amount of data used in a least-squares fit decreases from a full orbit to, say, a four-hour arc (i.e., 1/6 of a revolution) following perapsis, the process of inverting the linear system becomes increasingly dominated by numerical error.

A closely related, but distinct, problem associated with classical batch data filtering of ill-conditioned data sets is the inherent loss of precision in the formation of the "normal matrix" $A^T A$, where $A = \partial z / \partial x$ is the matrix of partial derivatives of observables (z) with respect to estimated parameters (x). This degradation intensifies the ill effects of nonlinearities in a solution attempt, but even when conventional techniques are adequate for convergence, the accuracy of the orbit determination process is enhanced by the square-root approach to the least-squares problem. The DPODP's square-root batch data filter (Ref. 7) eliminates the numerical error and instability that arise in the normal equations formulation. Most of the routine single- and multiple-revolution fits performed throughout the mission were devoid of convergence problems and were therefore accomplished using this full-rank, square-root solution technique.

Mission requirements dictated that the spacecraft postinsertion state be estimated as quickly as possible, namely, four to six hours after burn termination. It is perhaps ironic that during the orbit phase it was necessary to compute these crucial early state solutions using a small and thus poorly conditioned data set at the very time when the a priori error in the spacecraft orbit — and therefore the nonlinearity effect — was maximal. The partial-step algorithm (PSA) (Refs. 3, 4, 6, 8) was developed and implemented in the DPODP to deal with this post-MOI initial convergence problem, and also to produce an essential safeguard against an anomalous (larger than expected) orbit error due to an insertion burn irregularity. The fact that nine PSA iterations were necessary to obtain the first (data arc length: 4 hours) post-MOI state solution for VO-1 (see Section III-C) — despite the accuracy of the orbit insertion — underscores the utility of the PSA for orbiter state convergence.

The PSA is a sub-rank (i.e., partial-step) method that uses an a priori estimate error covariance ellipsoid to judiciously constrain the classical full-rank solution vector computed for each iteration of a least-squares process. The basis of the method is a spectral decomposition of A from which a similar representation of the pseudo-inverse (Refs. 9, 10) of A is computed. Specifically, components of the solution step in the normal-matrix eigenvector coordinate system are individually constrained to lie within the expected error ellipsoid. The possibility of taking a solution step leading to divergence is thereby greatly reduced.

B. Preflight Simulation Analysis

An important aspect of the DPODP's batch data-filtering process is that the PSA and square-root full-rank techniques give identical converged state solutions for fit cases that lie within the limitations of the latter: no penalty is paid for the margin of safety gained by using the PSA for a state fit that the full-rank method could perform equally well. On the other hand, due to the inherent nature of the nonlinear convergence problem, the power of the PSA is not unlimited. Thus the region of convergence, i.e., the largest initial spacecraft state error allowing convergence with the PSA, determined by preflight simulations will be described here. Such a region was determined for -- and centered about -- the nominal post-MOI orbit configuration for both VO-1 and VO-2. These nominal orbits were based upon best-estimate Mars encounter trajectories and associated insertion maneuver parameters updated a few weeks before the respective MOIs.

To compare convergence capability against the expected post-MOI total spacecraft state error, it was necessary to assess the a priori encounter-phase OD and maneuver execution errors. Encounter OD errors for both approaches were determined assuming the baseline physical model error levels quoted in Section 7 of Ref. 4 with doppler tracking (with 1σ noise = 1 mm/s) of the spacecraft from Encounter-40 days to Encounter-1 h (attitude maneuvers in preparation for MOI ignition occurred during the hour preceding MOI). The resulting orbit determination error, when mapped to MOI maneuver termination, was found to have 1σ cartesian components bounded by 5 km in position and 5 m/s in velocity for both VO-1 and VO-2.

The covariance matrices representing the dispersion in the maneuver system executions were computed by Monte Carlo techniques with program MOIOP (Ref. 4) based upon best-estimate approach trajectories. The RSS of these maneuver uncertainties and the approach OD errors -- the two processes were assumed to be uncorrelated -- yielded the total a priori state errors. The resulting 1σ values for position and velocity in the mean-Earth-equator of 1950.0 system are given in Table 3. The a priori maneuver execution error was the major component of the total uncertainty in the postinsertion state for both orbiters.

Although errors in all state-space directions led to convergence provided they lay within the PSA convergence region, some directions were more favorable than others. A worst direction for post-MOI state errors was found: the convergence boundary for this direction yielded the most conservative limit for the capabilities of the partial-step method. To gain an intuitive notion of the worst direction for an initial state error, the doppler time history for one orbit of a planetary satellite

Table 3. Post-MOI initial state uncertainties

VO-1	σ_x	9 km	$\sigma_{\dot{x}}$	15 m/s
	σ_y	25	$\sigma_{\dot{y}}$	10
	σ_z	12	$\sigma_{\dot{z}}$	8
	σ_{RSS}	29.2	σ_{RSS}	19.7
VO-2	σ_x	15	$\sigma_{\dot{x}}$	10
	σ_y	20	$\sigma_{\dot{y}}$	6
	σ_z	11	$\sigma_{\dot{z}}$	10
	σ_{RSS}	27.3	σ_{RSS}	15.4

as shown in Fig. 2 must be considered. Letting the solid line represent the real data and the broken line the predicted data based on an a priori post-MOI state, then t_0 and t_1 are the first and second periapsis times of the true trajectory, i.e., the generator of the real data. The following convergence characteristics were observed in all PSA test cases, where t represents the end of the data span included in the fit (for all cases, $t \leq$ the predicted orbital period):

- (1) If the second periapsis of the true trajectory was not included in the real data, i.e., if $t < t_1$, then convergence was obtained.
- (2) If the second periapsis was included in the real data, i.e., if $t \geq t_1$, then convergence was not obtained.

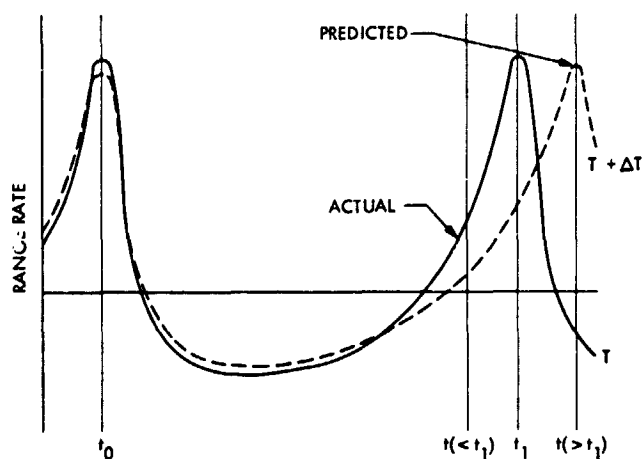


Fig. 2. Range-rate time history for different values of orbital period

These observations led to the conclusion that the presence of an unexpected periapsis in the data interval is the most significant condition that can occur with regard to limiting the convergence of the PSA. Thus, the worst initial direction error (where error Δ real minus predicted) is that which results in the predicted period being maximally larger than the actual period for a given error magnitude.

A worst-direction analysis, however, must be conditioned on the a priori probabilities associated with the direction of the initial error. Examination of Fig. 3, which heuristically depicts position-velocity space, might suggest that the worst direction is given by the vector *A*, the shortest distance to the boundary of the nonconvergence region. However, if the a priori initial error dispersion is represented by the ellipse centered at the origin, then the probable worst direction will lie more in the direction of the vector *B*. This worst direction can be found analytically by minimizing the scalar function

$$J(w) = gw + \lambda(w^T \Gamma_X^{-1} w - 1) \quad (1)$$

where

w = worst-direction error vector (to be computed)

$g = \partial a / \partial X$ (row-vector gradient of semimajor axis)

Γ_X = post-MOI state covariance matrix

λ = scalar Lagrange multiplier

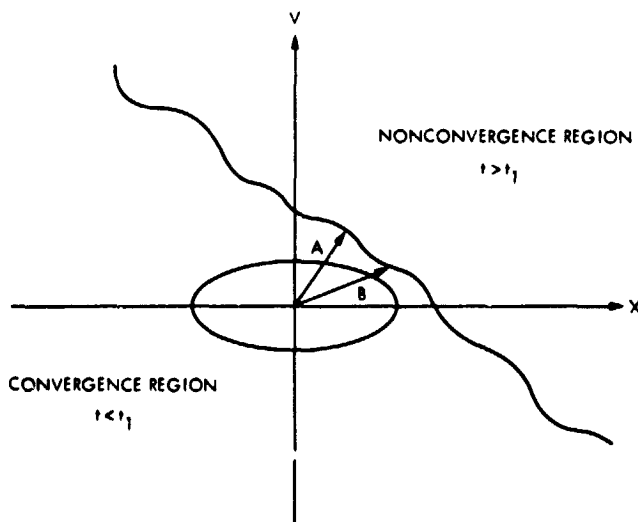


Fig. 3. Worst-direction diagram in phase space

The solution to the minimization of J in (1) is

$$w = - \frac{\Gamma_X g^T}{\sqrt{g \Gamma_X g^T}} \quad (2)$$

Evaluations of Expression (2) showed that the worst direction fell within a dispersion in position opposite the post-MOI position vector and a dispersion in velocity opposite the post-MOI velocity vector. Table 4 gives the worst-direction vectors determined by evaluating (2) for the a priori best-estimate post-MOI orbits.

A simplified state-only orbit determination program incorporating the PSA was used to obtain the preflight initial convergence results. The program approximates the spacecraft orbit about Mars with a conic path and the movement of a point-mass Earth with respect to Mars by linear motion. All accelerations other than two-body are ignored, and light is assumed to have infinite velocity. The simulated results duplicate the state-convergence properties of the full-modeled DPODP to within approximately one percent; thus the convergence regions to be given are realizable to within a similar margin. Media effects, while significantly influencing the accuracy of short-arc solutions, have little bearing on convergence characteristics and were therefore not included in the simulations.

Convergence profiles determined for large post-MOI state knowledge errors in individual orbital elements are summarized here. Worst-direction error capability limits found by testing multiples of the worst-direction vectors given in Table 4 are then given. Solution epochs used in these convergence cases were initial periapsis after MOI for VO-1 and MOI maneuver motor-off time (true anomaly ≈ 68 deg) for VO-2. The various data spans used for the fits all began 30 min after the respective epochs; thus VO-1 spans started ~ 40 min after

Table 4. Post-MOI convergence worst-direction error

Coordinate ^a	Viking 1	Viking 2
Δx	0.3769 km	0.9167
Δy	-0.8778	0.1867
Δz	-0.2956	-0.3532
$\Delta \dot{x}$	0.1383 m/s	1.1837
$\Delta \dot{y}$	1.0169	0.4473
$\Delta \dot{z}$	-0.3561	0.3704

^aVectors have been scaled so that $(\Delta x)^2 + (\Delta y)^2 + (\Delta z)^2 = 1$.

the nominal motor-burn termination. While convergence boundaries were seen to be only secondarily influenced by data-start times, the start times used gave optimal results. The presence of loose a priori information on the state and nominal data noise also had little influence on convergence characteristics.

Results are presented showing convergence and nonconvergence regions in terms of post-MOI position-error convergence limits vs tracking data span used. The position error is the magnitude $(\Delta x^2 + \Delta y^2 + \Delta z^2)^{1/2}$ of the position deviation in cartesian coordinates corresponding to an orbital element or worst-direction perturbation. OD accuracies are also included on each plot in the form of epoch RSS position uncertainties $(\sigma_x^2 + \sigma_y^2 + \sigma_z^2)^{1/2}$ as a function of the data interval. These accuracies were computed by the DPODP with state-only fits assuming baseline errors (R:f. 4) in gravitational harmonics and doppler data.

Figure 4 illustrates convergence properties for perturbations in the VO-1 post-MOI eccentricity. For example, for a 4-h VO-1 data interval, convergence is obtained for errors up to 0.11 in eccentricity, or equivalently, 2300 km in position-error magnitude. The maximum convergent position error drops to 430 km as the data interval is extended over nearly the entire

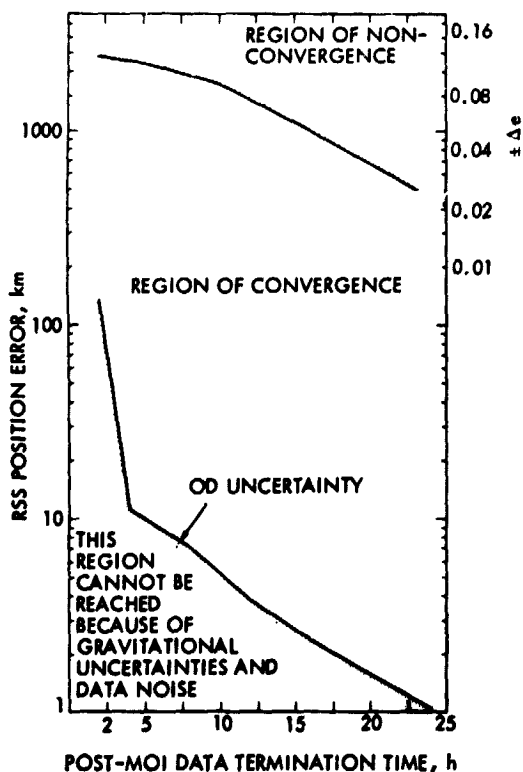


Fig. 4. Viking 1 eccentricity convergence profile

nominal 24.7-h orbit. The VO-2 eccentricity profile is similar; in both cases the convergence regions extend far above the OD uncertainty for all data spans. In addition, the region boundaries lie far above the 1σ RSS predicted position errors given in Table 3. The eccentricity convergence regions are found to be independent of the sign of the error.

Similar results are given in Fig. 5 for perturbations in the plane-of-sky node (see Section IV) for VO-2. The convergence limits are not dependent upon the sign of the Ω_{pos} error. Figure 6 illustrates the convergence region for a VO-1 state error in semimajor axis. For this parameter the sign of the perturbation does influence the region boundaries: a negative perturbation in semimajor axis exhibits more pessimistic convergence characteristics than a positive perturbation. The convergence properties associated with errors in the remaining Kepler elements are similar to those shown; each exhibits maximum convergent RSS position errors of over 1000 km.

Figures 7 and 8 summarize the PSA worst-direction capabilities found for VO-1 and VO-2, with the observed boundaries (solid lines) compared against the analytically determined boundaries (broken lines). The latter boundary divides the $t < t_1$ region from the $t > t_1$ region (cf., Fig. 2). The observed and analytic boundaries are seen to lie close together except

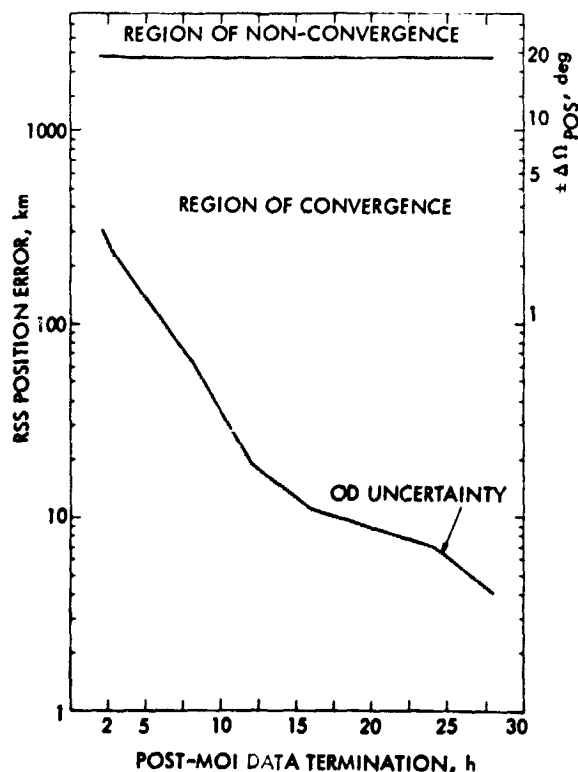


Fig. 5. Viking 2 Ω_{pos} convergence profile

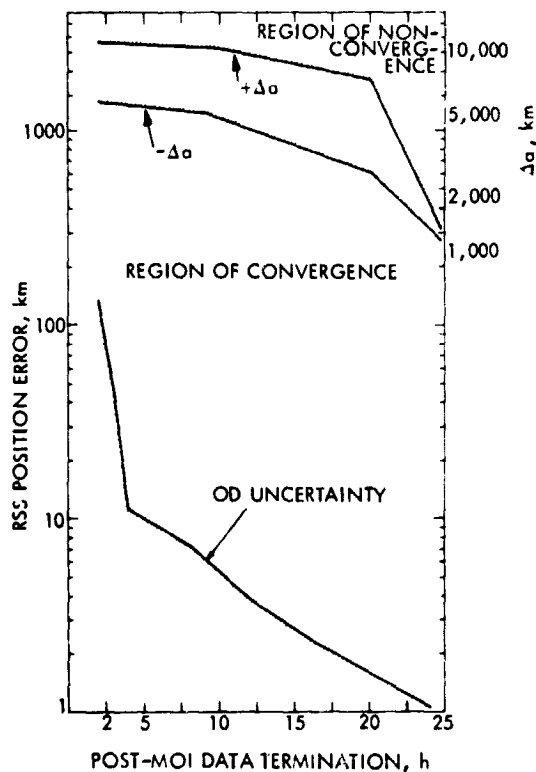


Fig. 6. Viking 1 semi-major axis convergence profile

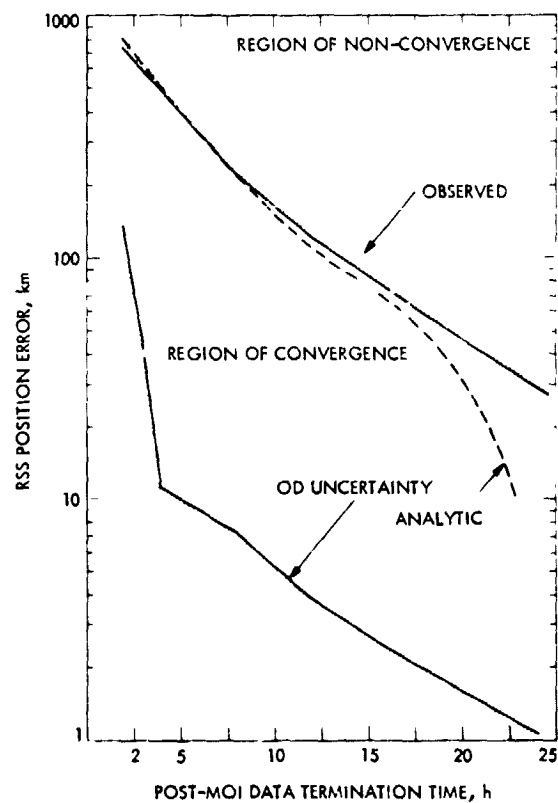


Fig. 7. Viking 1 worst-direction convergence profile

when t (data span end-time) approaches a full revolution of the nominal orbit, and in the case of VO-2, when $t \leq 6$ h. It is evident that a good margin of safety existed for the convergence problem; e.g., fitting 2 h of post-MOI VO-1 data would allow convergence for RSS position errors of up to 725 km and corresponding RSS velocity errors of up to 788 m/s. Similarly, a 4-h fit of VO-2 data would yield convergence for errors up to 400 km and 527 m/s.

The post-MOI convergence strategy was clear: upon preliminary convergence with say a 4-h data arc, finer "tuning," i.e., convergence to a more accurate solution, would be performed with successively longer data arcs. After finding the initial 4-h solution, most remaining error would lie in Ω_{pos} , and as seen in Fig. 5, this direction is quite favorable to convergence. Thus, convergence boundaries as a function of increased data span length were even more optimistic than those suggested by Figs. 7 and 8.

Naturally, as the error in the initial state increases, convergence becomes more difficult: the penalty for starting with a poorer a priori solution is an increased number of PSA iterations required. For example, during testing, a certain ill-directed VO-1 error with magnitude $\sim 3.3\sigma$ in position (100 km) and $\sim 5\sigma$ in velocity (100 m/s) was found to require 26 iterations for convergence with a two-hour data arc.

C. Viking 1 and 2 Initial Orbit Convergence

The first real-time operation of the Satellite OD Team was to obtain a spacecraft state solution from tracking data acquired during the early part of the first revolution of VO-1 following MOI. Mission anomalies that occurred during the days preceding encounter dictated that the first orbit about Mars would have a period of about 42.5 h instead of the nominally planned 24.7 h. Last-minute simulations with this and several other neighboring potential orbits showed no substantive changes in the initial convergence characteristics given in the previous subsection. Only the a priori maneuver error varied somewhat.

Initial convergence and refinement during the first VO-1 orbit were performed in the following manner. The data processed was two-way 1- and 10-min compressed doppler, which began soon after tracking station reacquisition following the MOI unwind attitude maneuver. Thus the processed data started 61 min after the initial periapsis, which was chosen to be the epoch for all fit cases done during this first orbit. The first fit used a data arc that ended about 4 h after periapsis; succeeding fits had data extending to 6, 9, 11, 12, 14, 20, 24, 30, 33 and 41 h (full-rev case) after periapsis. Each successive

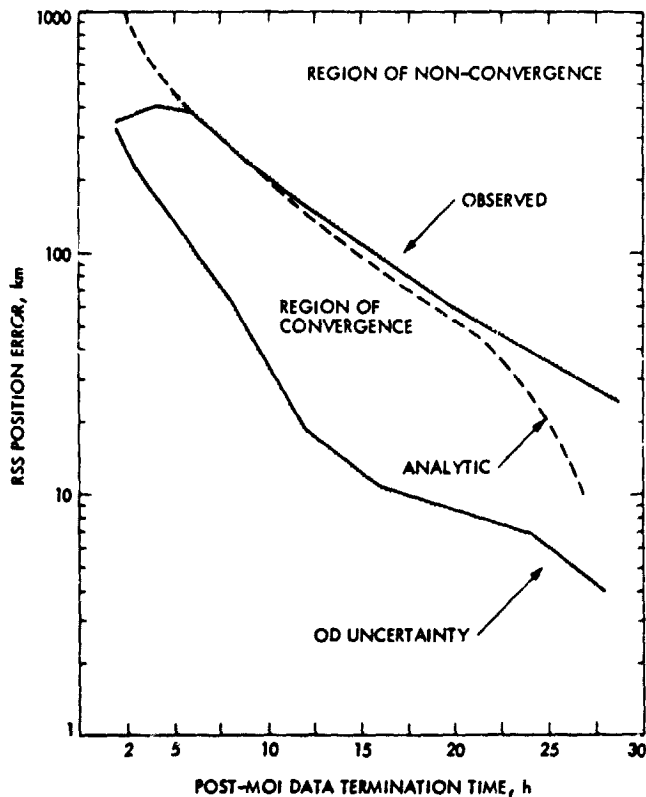


Fig. 8. Viking 2 worst-direction convergence profile

solution was used as a priori for the subsequent case, which then improved upon this state estimate. In a strict sense, this improvement was limited to a monotonic decrease in the computed uncertainties on the solution as data was added. As shall be seen, corresponding improvement in the solutions themselves did not always occur.

Nine PSA iterations were required to converge to the 4-h solution. Table 5 summarizes the solution states (Mars-centered, mean-Earth-equator of 1950.0) resulting from this and all succeeding short-arc fits performed throughout the first orbit. The last two columns give the orbital period and Ω_{pos} evaluated at the apoapsis following the epoch of the corresponding states. These are the important measures of the local accuracy of the estimates as they are the two major components of the VO state error (cf., Section IV). The first entry in Table 5 is the a priori state used to start the 4-h convergence process; this state was at the time the best estimate of the post-MOI orbit. The last entry is the final full-revolution solution that resulted from fitting the 40.4-h data arc obtained by deleting an hour of near-periapsis data at each end of the 42.4-h orbit. This solution is presumed to have the smallest error and is therefore a convenient reference against which to compare the short-arc fits.

The initial 4-h fit was an interesting example of the PSA's utility. Table 5 shows that this convergence yielded a solution requiring a sizeable net RSS move of 394 km and 0.280 km/s from the a priori state. In addition, the three hours of data yielded a system matrix with condition number (ratio of largest to smallest singular value) $\approx 0.15 \times 10^{11}$. Had a full-rank step resulting from this rather ill-conditioned system been taken for any of the first few of nine iterations, divergence would surely have resulted. In fact, taking the full-rank step (185 km, 560 km, -717 km, 0.397 km/s, 0.305 km/s, 0.433 km/s) computed for the first iterate leads rapidly to a divergent process. For comparison, the PSA first step was (-2 km, 63 km, -61 km, 0.030 km/s, 0.034 km/s, 0.039 km/s). After the fourth iteration the full-rank and PSA solution steps coincided as the remaining corrections moved within the linearity region. After more data accumulated, the 6-h arc was fitted with the DPODP by correcting the preceding solution. The small total adjustment required (cf., Table 5) enabled the DPODP to take full-rank steps for each iteration. As the data arc lengthened, subsequent DPODP solutions were obtained in the same manner.

The evolution of the orbit period error resulting from these short-arc state solutions is given in Fig. 9. For each fit, the absolute value of the difference between the full-rev period and the short-arc period given in Table 5 is shown. The broken-line curve is the corresponding formal statistical error in the period due to a 1σ (1 mm/s) doppler noise level. Figure 10

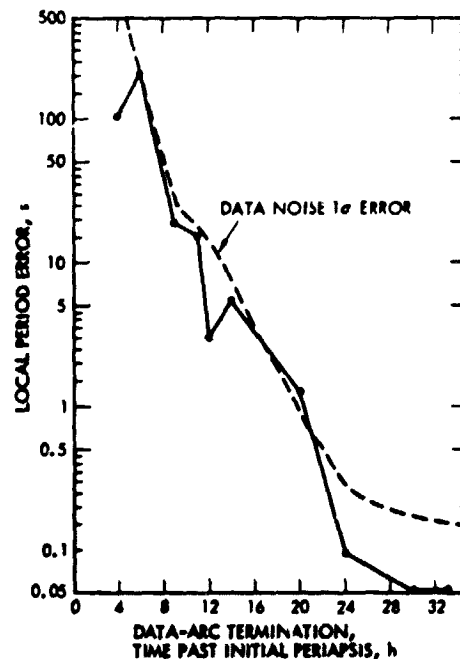


Fig. 9. Viking 1 first orbit period estimate evolution

Table 5. VO-1 first orbit convergence history

Data arc, h past periapsis	Epoch ^a cartesian state		Ω_{pos} , deg	Local period, h, min, s
	pos, km	vel, km/s		
A priori	2389.75	-2.4293	108.23	42 41 24
	3036.31	-1.0729		
	3027.17	2.9909		
4	2459.80	-2.2563	108.27	42 19 21
	3268.03	-0.9346		
	2710.22	3.1682		
6	2457.47	-2.2542	108.12	42 24 43
	3274.10	-0.9307		
	2704.65	3.1713		
9	2455.70	-2.2672	108.54	42 20 50.2
	3254.81	-0.9434		
	2730.34	3.1578		
11	2455.81	-2.2667	108.53	42 20 53.1
	3255.42	-0.9430		
	2729.48	3.1582		
12			108.47	42 21 5.9
14			108.43	42 21 14.4
20			108.47	42 21 7.6
24			108.443	42 21 8.740
30			108.438	42 21 8.784
33			108.436	42 21 8.784
41 (full-rev)	2456.5793	-2.2636113	108.435	42 21 8.836
	3254.6630	-0.9401376		
	2723.4073	3.1614176		

^aEpoch is initial periapsis ~ 76/6/19 23^h7^m7^s (ephemeris time).

gives the same history for the Ω_{pos} error. The performance of the initial short-arc estimates was evidently consistent with the predicted errors for both period and Ω_{pos} . The irregularity observed for the 20-h solution may result from nonstochastic errors in the doppler data due to the media (charged particle) effects.

Initial convergence and refinement during the first 27.6-h VO-2 orbit followed the same scheme as for VO-1. Data again started soon after completion of the MOI unwind attitude maneuvers. However, since the VO-2 MOI burn terminated after the initial periapsis, the first usable data started about 100 min after periapsis. The first fit used a data arc with length 130 min terminating again about 4 h after periapsis. Succeeding fits had arcs terminating 6, 8, 10, 12, 16, 18, and 26.5 h (full-rev case) past periapsis.

Table 6 shows that the initial convergence pattern for VO-2 differed substantially from VO-1 since the a priori estimate was much closer to the final solution. Thus the 4-h solution required only four DPODP full-rank iterations for conver-

gence. This first estimate is pathologically close to the final solution when compared against succeeding fits and the predicted error due to data noise as shown in Figs. 11 and 12. Later fits appeared to be significantly affected by nonrandom media contributions to the doppler noise as evidenced by the rather large changes in Ω_{pos} . Except for the 18-h case, bounds for these solution errors were nonetheless predicted reasonably well by the formal statistics shown. The more erratic behavior for VO-2 may be explained by its later arrival at Mars - the effect of solar plasma charged particle activity on the doppler noise became more pronounced as the Earth-spacecraft system moved closer toward superior conjunction with the Sun.

Contrary to the VO-1 experience, several of the VO-2 intermediate short-arc fits required the PSA - as well as a considerable number of iterations - for convergence. For example, 12 PSA iterations, the first seven of which involved constrained steps, were necessary to converge for the 6-h arc. The large variations observed in the early solutions are contained mostly in Ω_{pos} and are characteristic of media-induced systematic errors in such short data arcs.

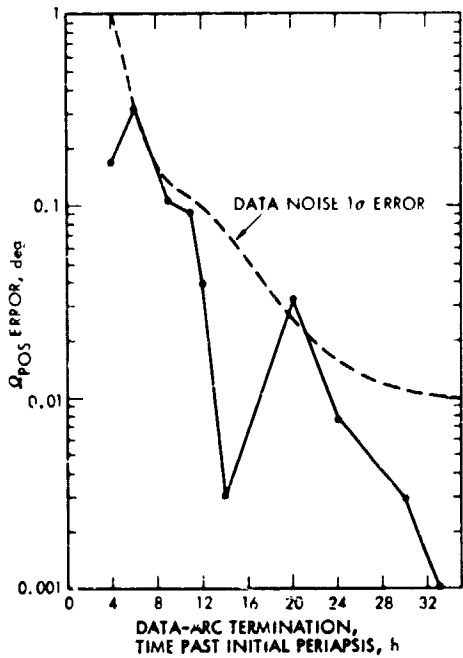


Fig. 10. Viking 1 first orbit Ω_{pos} estimate evolution

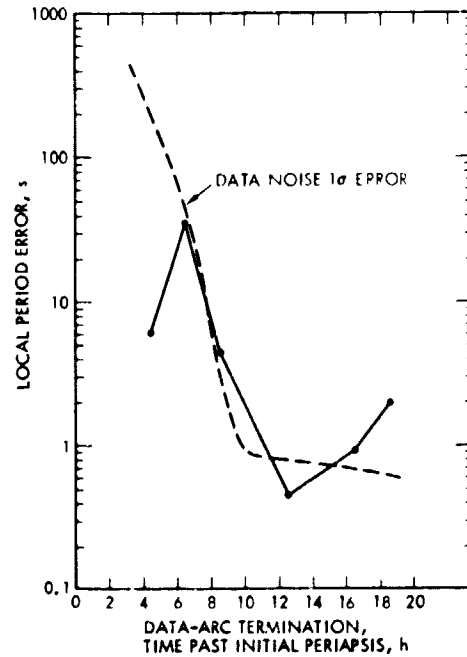


Fig. 11. Viking 2 first orbit period estimate evolution

Table 6. VO-2 first orbit convergence history

Data arc, h past epoch	Epoch ^a cartesian state,		Ω_{pos} , deg	Local period, h, min, s
	pos, km	vel, km/s		
A priori	1581	-2.209	146.79	27 31 23
	3286	2.076		
	5606	1.295		
4	1578.61	-2.2089	146.94	27 37 16
	3281.34	2.0746		
	5611.04	1.2962		
6	1512.33	-2.2137	152.25	27 37 57
	2745.14	1.9682		
	5909.63	1.4451		
8	1604.93	-2.2085	144.27	27 37 17
	3543.46	2.1215		
	5444.88	1.2168		
10	1587.04	-2.2089	146.03	27 37 21.7
	3372.60	2.0907		
	5556.21	1.2690		
12			146.51	27 37 22.1
16			146.68	27 37 22.56
18			146.42	27 37 23.60
27 (full-rev)	1579.8804	-2.2089724	146.764	27 37 21.605
	3299.2084	2.0775846		
	5601.0612	1.2908556		

^aEpoch ~ 76/8/7 12^h10^m14^s (ephemeris time) is initial periapsis +30.3 min.

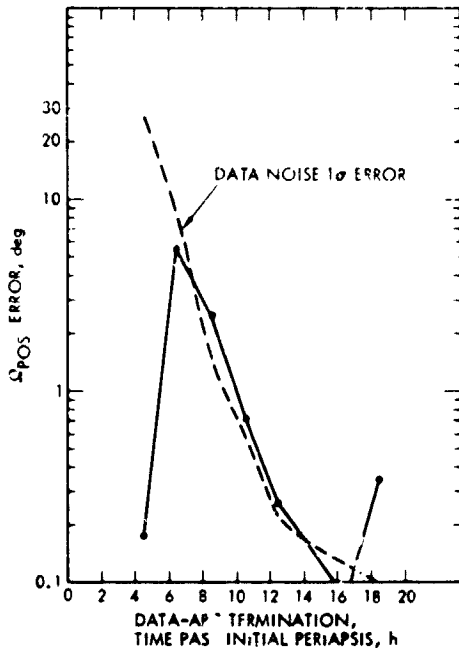


Fig. 12. Viking 2 first orbit Ω_{pos} estimate evolution

Support of the numerous Mars orbit trim maneuvers performed for both VO-1 and VO-2 typically required a determination of the post-trim orbit within a few hours following the maneuver (see Section IV). Thus short-arc fits of post-trim doppler were frequently a necessity, even if only for corroboration with a concurrent estimation-of-maneuver fit of pre- and post-trim data. Since these maneuvers were much smaller than the orbit insertion burns, the smaller attendant maneuver errors made reconvergence simpler than it was following MOI. Nonetheless, ill-conditioning due to the minimal information contained in the short data arcs would have led to divergence for some of these cases if full-rank unconstrained steps had been taken. The PSA provided a systematic technique for routinely converging to these short-arc solutions in the real-time mission environment.

IV. Short Arc Orbit Determination

A. Preflight Analysis

With a single exception, the Viking Prime Mission orbits had periods in the range 22.2 to 27.6 h, high eccentricities (0.76), and periapse altitudes of approximately 1500 km (see Tables 1 and 2). Preflight analyses demonstrated that the Mariner 9 strategy of estimating the spacecraft state by batch filtering a single orbit of two-way doppler (deleting near-periapse data) is also an optimal strategy for the Viking orbits.

In addition, the studies showed that the accuracy of local orbit estimates would be limited by gravity model errors until an in-flight gravity model update was performed. The preflight model of the Mars gravity field was a fourth degree and order set of spherical harmonic coefficients constructed from an ensemble of Mariner 9 harmonic coefficient models (Ref. 11). Preflight predictions of local accuracies (Ref. 4) may be characterized as follows:

- (1) Standard deviations of 0.02 to 0.04 s in orbit period and time-of-periapse passage.
- (2) Orbit orientation errors due almost entirely to errors of approximately 0.02 deg (1 σ) in the orbit node on the Earth plane-of-sky, Ω_{pos} , (the plane perpendicular to the Earth-spacecraft line)
- (3) Errors in the spacecraft position (Z_{pos}) along the Earth-spacecraft line with standard deviations of 15 to 25 m (0.1 to 0.2 μ s).

The major contributor to the total spacecraft position error is the error in Ω_{pos} . An error of 0.01 deg in Ω_{pos} produces position errors as large as 1 km at periapse and 6 km at apoapse.

B. Inflight Results

An indication of inflight accuracy levels can be obtained by examining the consistency of Ω_{pos} and Z_{pos} estimates from different solutions. Figures 13 and 14 present typical deviations of local estimates of these parameters from their values on selected reference trajectories. Since the magnitudes of the errors in the reference trajectories are not known, only the "scatter" of the estimates has significance. Generally, the RMS residuals in Ω_{pos} and Z_{pos} are consistent with preflight predictions for the first three months of the orbital mission. Some unexpectedly large excursions do occur, however, probably as a result of doppler signatures induced by interplanetary charged particles. Media effects, which are discussed in Section IV-C, were not treated in preflight studies, but their influence on the "post-fit" doppler residuals was quite evident. Plasma activity along the line-of-sight increased as the Sun-Earth-Mars angle approached the minimum of 0.26 deg on November 25. The increase combined with a decrease in tracking coverage is responsible for the large scatter in VO-2 Z_{pos} estimates during October (Fig. 14b).

It might be expected that the error in Z_{pos} determinations would be observed by passing the doppler-determined orbits through the VO range data. Figure 15 is a plot of these "pass-thru" range residuals, which are the data used to con-

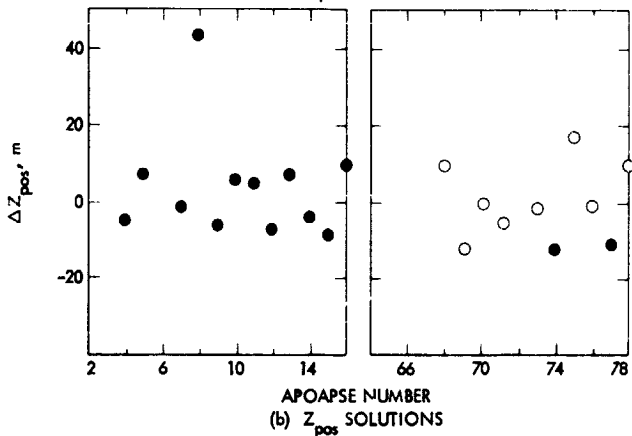
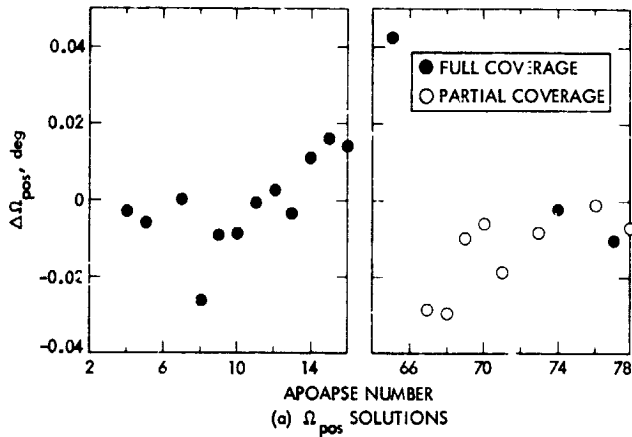


Fig. 13. Viking 1 orbit knowledge accuracy

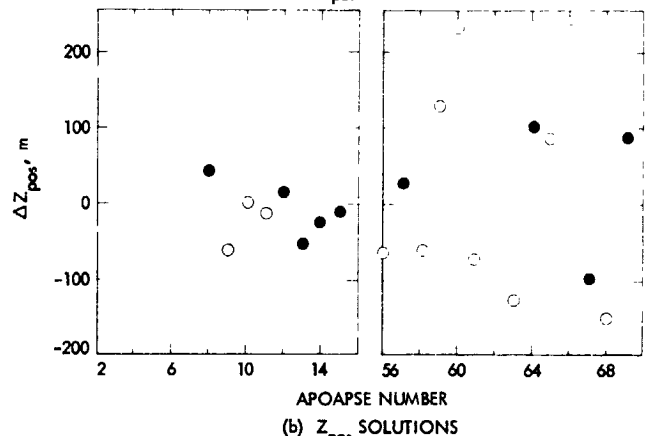
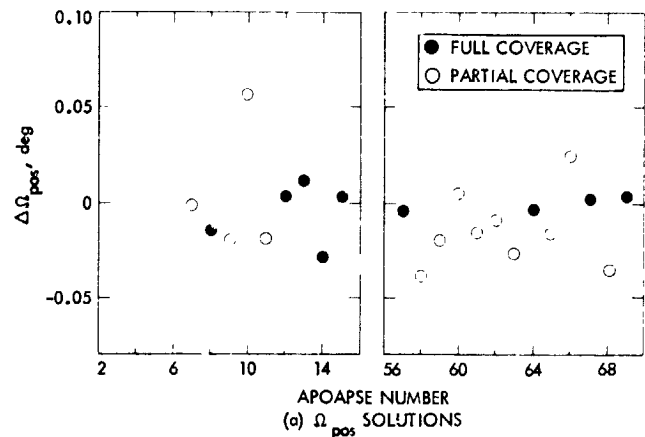


Fig. 14. Viking 2 orbit knowledge accuracy

struct the relativity/ephemeris normal points. The residuals contain contributions from several sources:

- (1) Range measurement error ($<0.1 \mu s$).
- (2) VO Z_{pos} error.
- (3) Earth/Mars range error ($\approx 7 \mu s$).
- (4) General relativistic time delay error ($\approx 1 \mu s$).
- (5) Charged particle effects.

For the first six weeks a sinusoidal variation with an amplitude of $0.3 \mu s$ and a period of approximately 28 days is apparent. This is induced by a pre-Mariner 9 value of the Earth/Moon mass ratio in the DF84 ephemeris (Ref. 4). The scatter relative to the sinusoid during this period is consistent with the predicted uncertainty of 0.1 to $0.2 \mu s$ (1σ) in Z_{pos} .

In addition to local orbit error levels, the accuracy with which future VO states may be predicted is of extreme impor-

tance to orbit phase navigation. Prediction accuracies prior to an inflight gravity model update as determined from preflight studies are shown for a Viking-1 synchronous orbit in Fig. 16. Indications of the significance of various prediction error levels are also given. The monotonic increase of position error at periaapse with increasing prediction intervals result from orbit resonance with the Mars gravity field induced by the nearly one-to-one commensurability of the spacecraft orbit period and the Mars rotation period (the details are given in Section V). The actual prediction performance of the Mariner 9 ensemble field during the initial phases of Viking-1 is also presented. As will be seen in Section V, inflight updating of the gravity model yielded significant improvements in prediction accuracy.

The remainder of this section discusses strategies for performing late updates of the Viking orbiter trajectories in support of postmaneuver activities and spacecraft sequences. Procedures which are discussed include unconstrained and constrained short arc OD combined with use of PVRA. A discussion of media-induced effects on OD also is included.

ORIGINAL PAGE IS
OF POOR QUALITY

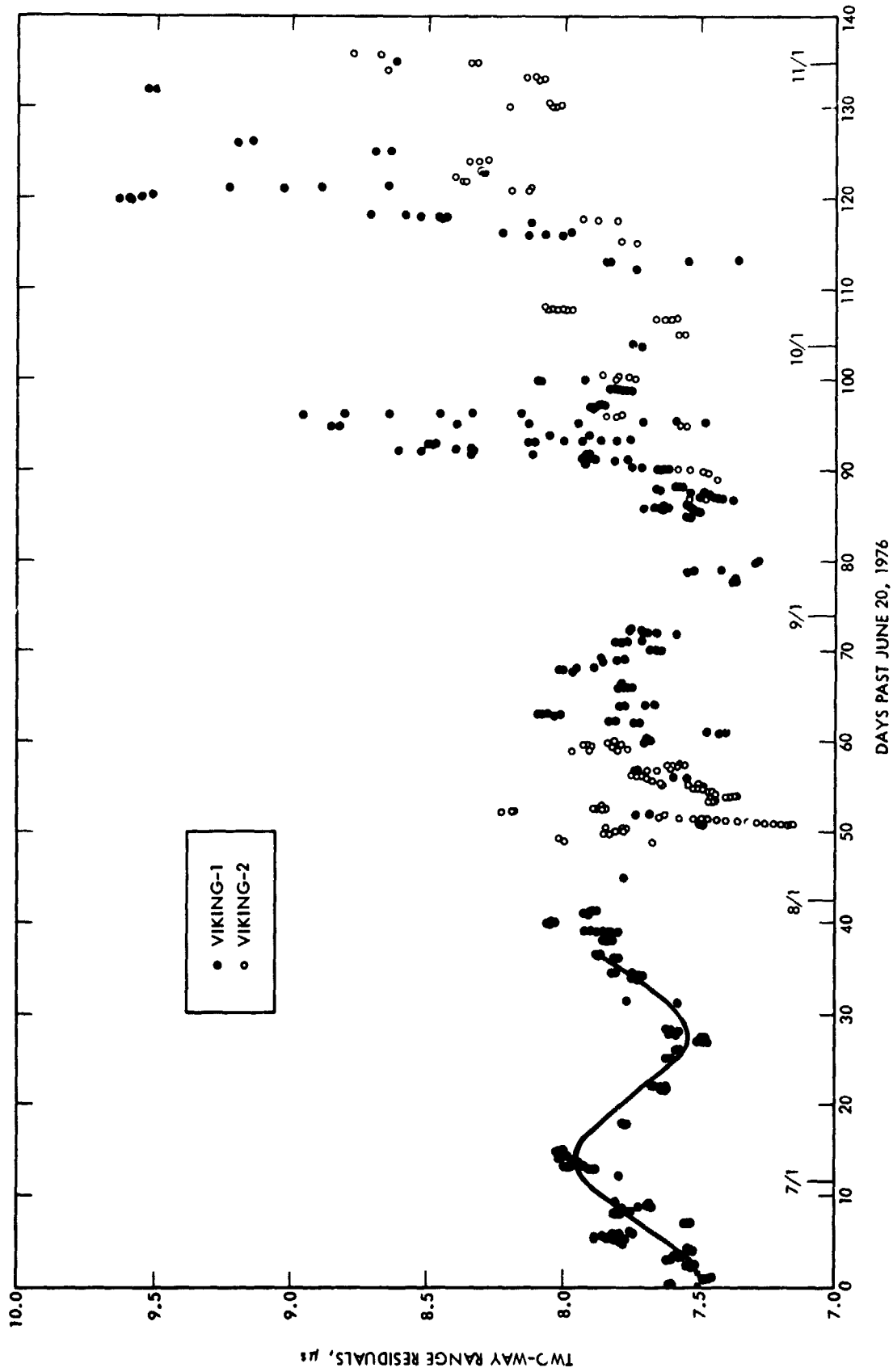


Fig. 15. Viking 1 and 2 two-way range residuals using DE84

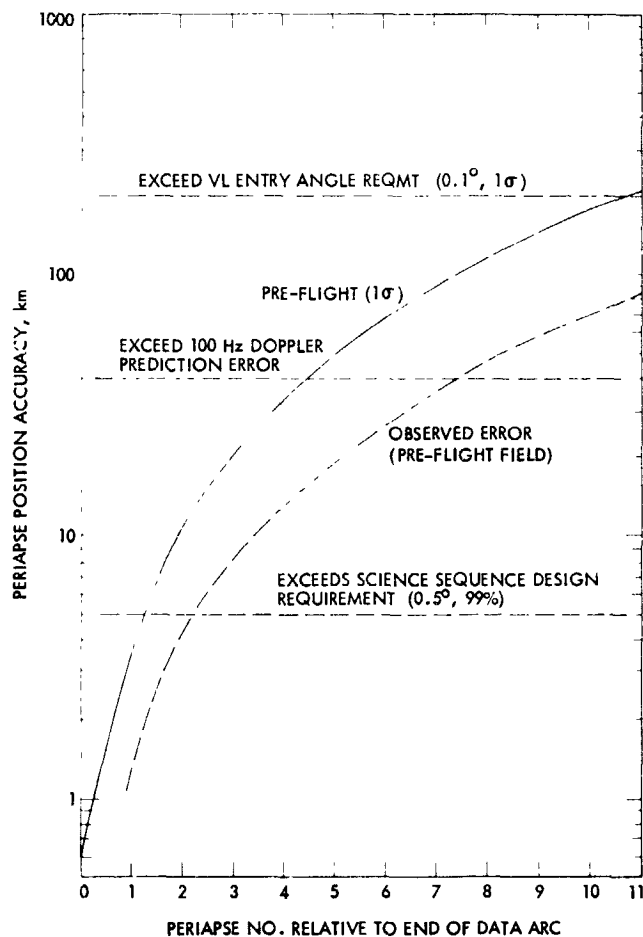


Fig. 16. Preflight and actual Viking 1 periapse position prediction accuracy

C. Late Update Strategies

Nominal mission planning called for VO science sequences in support of landing site selection and certification to be performed at nearly every periapsis prior to VL separation, including periapses following orbit trim maneuvers. Since the accuracy requirement on time-of-periapse passage knowledge imposed by imaging considerations (1.3 s, 1σ) was generally more stringent than the orbit control accuracy requirement, provision was made to update the sequence initiation time and initial camera pointing directions based on orbit knowledge derived from postmaneuver tracking.

Two orbit determination strategies for late updates were investigated preflight (Ref. 4, Section 8.6.5.7). The first strategy involved processing post-trim data only to estimate VO state. With the second, pre- and post-trim data were employed to estimate VO state and trim ΔV components. Both methods were used in Viking operations, with the first being preferred.

Solutions-through-trims were performed primarily to assess the viability of this technique. The advantages and disadvantages of these methods are discussed below, and the inflight performance is described.

1. Post maneuver processing. With this approach, VO state is estimated by processing short arcs of doppler data acquired after an orbit trim maneuver. As implemented a priori knowledge of the possible dispersions of the post-trim orbit was not used to constrain the solutions. As a result, estimate errors were expected to be almost entirely due to noise on the data until the arc encompassed nearly a full orbit. The short arc method has the advantages that (1) the DPODP link PVRA may be used, so that processing can be performed very rapidly (see Section IV-E), and (2) the solution accuracy may be evaluated both by generating formal covariance matrices and by monitoring the evolution of the estimates as the length of the data arc increases. Figs. 9 through 12 provide an example of the information used in the accuracy evaluation. The disadvantages are (1) many iterations may be required for convergence due to the poor observability of the orbit node on the plane-of-sky, somewhat offsetting the advantage of processing speed provided by PVRA, and (2) several hours of post-trim data may be required simply to achieve the same level of orbit knowledge as is available by propagating the pretrim orbit through the design maneuver (this criticism applies more to knowledge of orbit orientation than to orbit period).

2. Solve-through-trim. In this method, a full orbit of data prior to the maneuver is processed in conjunction with a short arc of post-trim data. Both VO cartesian state and three components of the trim ΔV are estimated. A priori knowledge of possible dispersions in ΔV direction or magnitude is not utilized to constrain the solutions due to the difficulty of determining the validity of such a procedure in the presence of errors in the model of the gravity field of Mars. Solving through the trim effectively utilizes knowledge of the orientation of the post-trim orbit to supplement the orientation information in the post-trim data. Thus the estimate errors for a given amount of post-trim tracking may be expected to be smaller than those achieved with the short arc method. However, since the data arc employed typically includes a periapse, estimate errors arise not only from data noise but also from an imperfect gravity model. The difficulty of generating a reliable estimate of solution accuracy is one of the limitations of this method. A more serious disadvantage, however, is the processing time required. One iteration of a solve-through-trim case requires significantly longer running time than a short arc case because:

- (1) PVRA cannot be employed.
- (2) ΔV partials must be generated, and an integration restart occurs at the time of the maneuver.

(3) The orbit of data prior to the maneuver must be processed.

3. Inflight experience. The results achieved in real-time operations by applying the previous strategies are presented in Figs. 17 and 18. The errors in the orbit node in the plane-of-sky and in the orbit period are shown as functions of the length of the post-trim data arc. Late update processing results are given for the maneuvers listed in Table 7.

Note that the solve-through-trim errors are typically an order of magnitude smaller than those realized by processing post-trim data only. In fact, when compared to covariance analysis results of Ref. 4, the solve-through-trim errors are surprisingly small. The probable explanation is that the gravity fields employed were developed by sensing the field in the vicinity of the "included" periaapse, and thus were more accurate than had been assumed in the analysis.

4. Constrained orbit determination. Neither of the late update strategies described to this point is without its limitations. Processing only postmaneuver data results in poor orbit convergence and somewhat unsatisfactory solution accuracy. Solving-through-trims requires excessive computation time and provides no convenient method for accuracy assessment. It was repeatedly observed that orbit orientation (Ω_{pos}) control accuracy for the trim maneuvers was better than the Ω_{pos} knowledge accuracy. The inverse is true with regard to orbit period. Thus, the convergence problem encountered when processing post-trim data alone may be largely eliminated by employing a priori constraints on the orbit orientation (0.05 deg, 1σ would generally have been conservative for Viking applications). For most cases, it would also have been acceptable to constrain the anomalistic or mean orbit period to the 99% maneuver execution level. A strategy of applying appropriate a priori constraints would yield accurate solutions with rapid convergence and short processing times. The question which arises is that of how the appropriate a priori covariance matrix is constructed. It is desired to constrain the "mean" values of the orientation angles and orbit period, but the DPODP accepts an a priori covariance matrix on VO state

Table 7. Trim maneuver description

Spacecraft	Trim	ΔV , m/s	Time from periaapse, h, min
VO-1	MOT1	80.1	+0:02
	MOT5	25.7	-3:04
	MOT6	2.7	-1:00
VO-2	MOT1	4.1	-1:38
	MOT2	1.8	+0:20

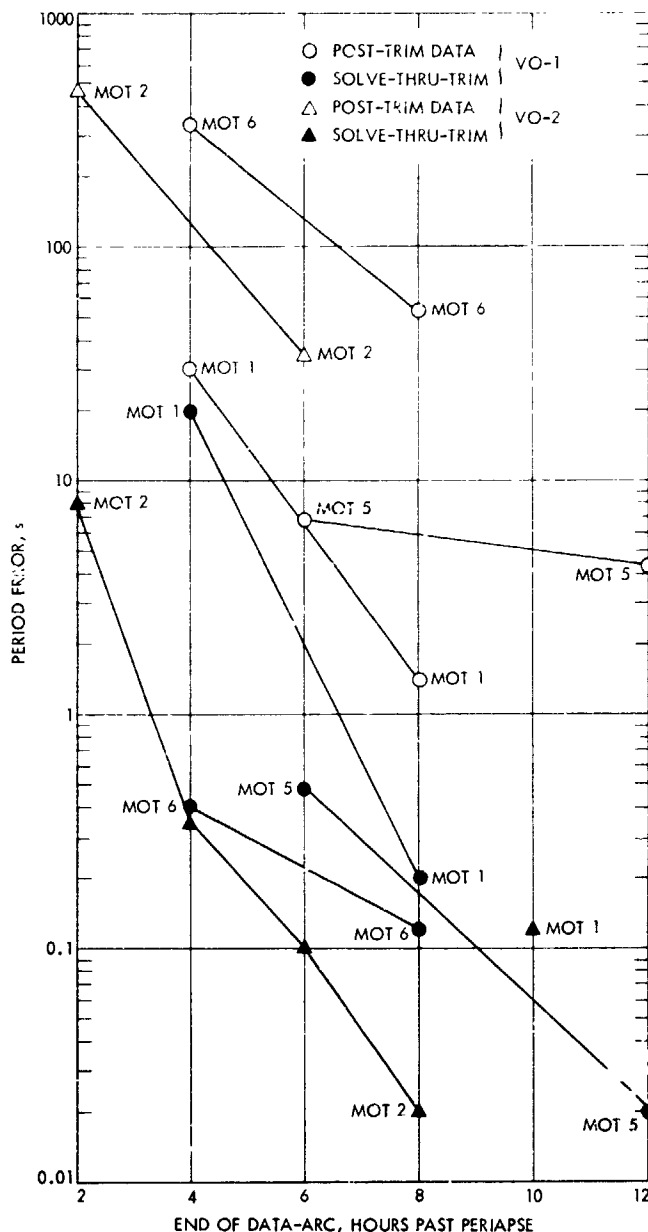


Fig. 17. Late update orbit period errors

only in terms of EME50 cartesian position and velocity at epoch. For the high-eccentricity Viking orbits, a suggested procedure is:

- (1) Construct a diagonal covariance matrix on "mean" Viking modified classical orbital elements (VMCOE) at apoapse, preferably referenced to the plane-of-sky.
- (2) Transform the VMCOE covariance matrix to a covariance on VO EME50 cartesian state at apoapse.

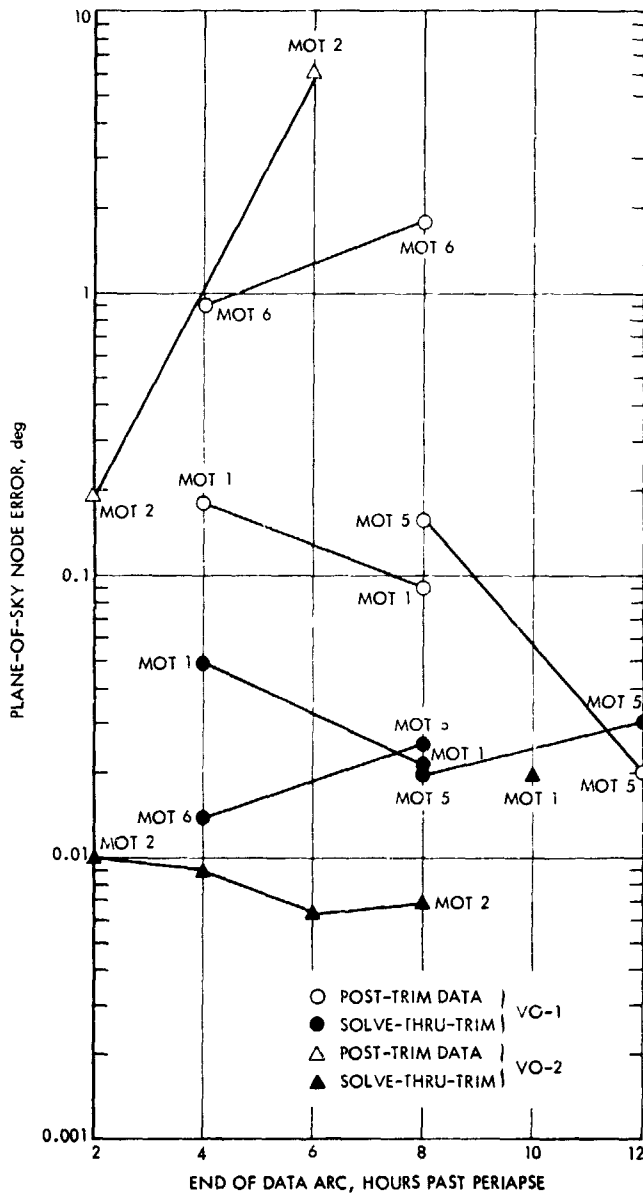


Fig. 18. Late update plane-of-sky node errors

- (3) With the DPODP links MAPGEN and MAPSEM, map the cartesian covariance from apoapse to the desired epoch (usually periapse), considering model errors such as Mars' harmonics.

The constrained orbit determination method proposed here has not been tested. However, an analogous technique which has been employed for processing short arcs during the Viking Extended Mission is reported in Section IV-D.

D. Constrained State Estimates During Extended Mission

Due to DSN scheduling restrictions, full-rev doppler tracking coverage for the Viking orbiters has not always been provided during events of scientific interest. Such events include the Radio Science Team occultation and VLBI experiments, which require the best possible knowledge of the spacecraft trajectory over a short time interval. Usually, these experiments provided doppler coverage only during the time-span of interest (3-4 hours), and it has been shown in Section III that state-only fits over short data arcs of this length are divergent for both full and subrank estimates. In order to utilize these short arcs of data, a constrained state estimate strategy was developed and implemented by the SATOD Team.

Navigation experience during the Viking orbit phases indicated that timing errors in orbit prediction are highly dependent on modeling errors (specifically Mars gravity), but orientation errors remain essentially constant throughout predictions from a state-only fit. In fact, the uncertainty in orbit timing can be likened to an uncertainty in the time of periapse passage. This suggests that constraints could be most easily applied to a suitable set of orbital elements $\vec{\beta}$, which includes orbital period and time from periapsis along with the classical elements $e, i, \Omega,$ and ω . Since the DPODP operates in cartesian state-space, the transformation of the diagonal a priori covariance takes the following form:

$$\Gamma_x = \left(\frac{\partial \vec{x}}{\partial \vec{\beta}} \right) \Gamma_{\beta} \left(\frac{\partial \vec{x}}{\partial \vec{\beta}} \right)^T$$

where Γ_{β} is the constraint on the $\vec{\beta}$ elements, \vec{x} is the set of cartesian components, and Γ_x is the constraint on the cartesian state.

Next, the proper strategy for implementing this constraint on the estimation process was considered. In order to insure that the estimate was actually being constrained to the true mean predicted orbit, the starting epoch was chosen at a point in the orbit where the rates of change of the osculating elements were small. Tests indicated that an epoch 2 hours removed from periapsis was sufficient to exclude the effects of short-period gravity perturbations. In addition, a scheme was devised for assigning values to the elements of the diagonal Γ_{β} matrix corresponding to a given prediction by comparing that prediction to nearby full-rank solutions. The deviations of these solutions around the predicted values provided sample statistics for the standard deviation of each element of β .

Error analyses were conducted to determine the effect of various angular constraints on the orbit timing errors. It was

found that the uncertainty in the orbit period determination for short data arcs (<10 h) could be reduced by as much as 2 orders of magnitude over an unconstrained estimate by assigning a standard deviation of 0.1 deg to the orientation angles. Reducing this constraint to 0.01 deg makes practically no difference in the period uncertainties (Fig. 19), but it does reduce the uncertainty in periapse timing by about half over a wide range of data arc lengths (Fig. 20). Further, the error analysis indicated the computed uncertainties in the estimated orientation angles were always less than their a priori constraint for data arcs longer than 2 hours.

The effects of various a priori timing sigmas were also considered in the error analysis; the period and time from periapse were constrained initially with a priori standard deviations of 5 and 30 s, respectively. Later, the constraint was tightened by using $\sigma_p = 1$ s and $\sigma_{tp} = 6$ s. It was found, for a given orientation constraint, that both sets of timing constraints gave essentially the same results for data arcs longer than 6 hours (see Fig. 20). Also, it is important to note that computed uncertainties in both period and time from periapse are always less than the a priori standard deviation for data arcs longer than 2 hours; a further decrease of an order of magnitude in the timing uncertainties occurred for partial data arcs greater than 10 hours in length. Recall that all these results were obtained with data taken after an epoch 2 hours removed from periapse.

Another a priori constraint technique was considered for short data arcs within 2 hours of periapse. These short arcs of radiometric tracking were obtained to support the Radio Science Team's solar occultation experiments, which require highly accurate determinations of the spacecraft position during the occultation events that are within an hour of periapse. In these cases, the rates of change of the osculating elements and the uncertainty in the gravity modeling are too great to constrain the estimate to the proper orbit as before, so in addition to estimating the six constrained orbit parameters, the coefficients of a 6 degree and order gravity model are also estimated. This results in a good fit of the data over short data spans near periapse, which results in a highly localized trajectory estimate and associated localized gravity model.

The usefulness of the constrained state estimate has been demonstrated under flight and postflight conditions for many situations which require accurate spacecraft position estimates from a limited data span. For example, postmaneuver state estimates with 10-12 hour data arcs have been successful using the first constraint technique discussed. The second technique has been used with many otherwise ill-conditioned short arcs of data to supply highly localized position estimates for experiments.

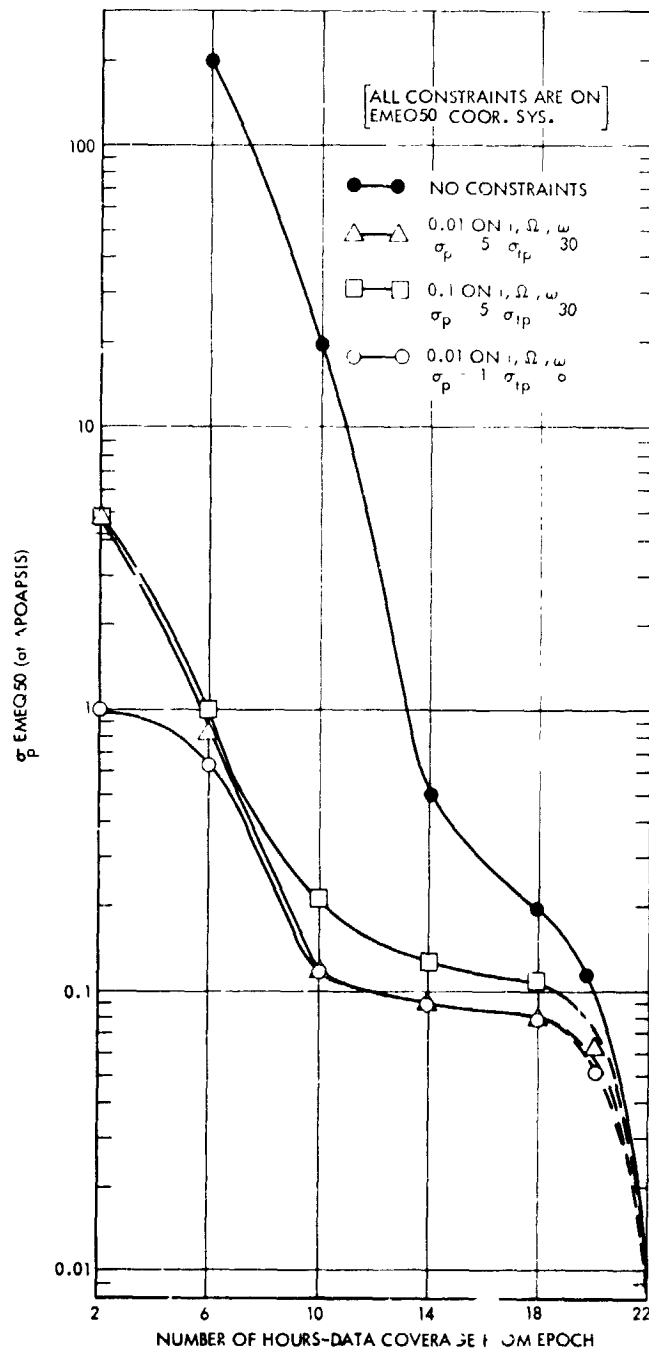


Fig. 19. Effect of a priori constraints on orbital period uncertainty

E. PVRA: Efficient Spacecraft State Estimation in Orbit Phase

As described in Sections III and IV-C, post-MOI orbit determination frequently involves processing full or partial orbits of two-way doppler data to obtain estimates of VO local position and velocity. Often, as in orbit redetermination fol-

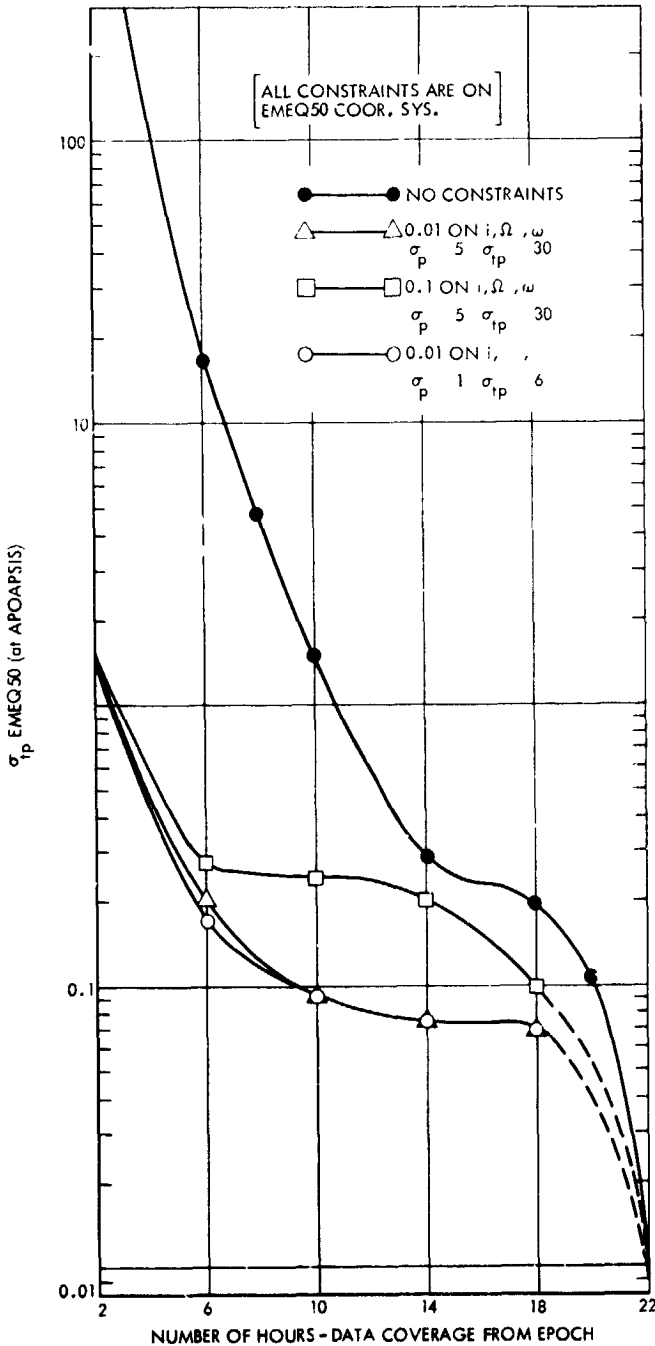


Fig. 20. Effect of a priori constraints on time periaapsis passage

lowing a maneuver, this processing must be performed on constrained timelines in order to provide early orbit updates for science sequence design and DSN station predicts. Thus, Viking ODP development included implementation of a new link specifically designed to efficiently perform the state-only data processing task.

This addition to the ODP software system, hereafter referred to as PVRA, performs those functions of links PV, REGRES, and ACCUM (Ref. 4) which are routinely required in orbit phase. To minimize the programming and program checkout efforts, PVRA was constructed from the building blocks of the links it replaces. Efficiency was achieved by reducing total program size and quantity of I/O performed. Significant reductions in number of instructions and amount of data storage required were effected by (1) restricting variational parameters to spacecraft epoch state (2) restricting trajectory models to central body gravity (including harmonics), third body gravity, and flat-plate solar pressure, and (3) eliminating sequential filtering capability. The combining of links PV, REGRES, and ACCUM2 into a single link led to I/O savings, since it was no longer necessary to both write and read a PV file (probe ephemeris and variational partials) and a REGRFS file (residuals and data partials).

A measure of the efficiency achieved by PVRA is given by a comparison of SUP values (1108 accounting units). Generating an ACCUM file for a single Viking orbit with links PV, REGRES, and ACCUM2 requires 8-9 SUP — the same file may be obtained with PVRA for approximately 2 SUP. Since dollar cost of running the ODP is proportional to SUP, these figures represent a cost saving of at least 75%. The overall savings for a typical three-iteration orbit determination run amounts to better than 40%. Comparisons of wall clock time required to complete a run on a dedicated machine reveal comparable savings in running time.

F. Media Effects on OD Accuracy

Radio metric data is affected in two ways as it passes through the Earth's troposphere, ionosphere and through whatever solar plasma may be present in interplanetary space along the signal's path from a tracking station to the spacecraft and back. The troposphere, which is nearly static, causes a decrease in apparent velocity of signal propagation: the primary effect on doppler data is due to the change in tropospheric path length along the line-of-sight as the spacecraft elevation changes during a pass. Range corrections for this effect, which have a typical variation of 25 m over a station pass (Ref. 4), were made for all Viking radio data with a spacecraft elevation-angle model that has a seasonal dependence.

The other media effect on radio data is due to the charged particle content of the ionosphere and the interplanetary plasma clouds emanating outward from the Sun. The ionospheric effect — an increase in phase velocity and an equal decrease in group velocity — also has an elevation dependence, a large diurnal dependence, and occasional large changes due to solar activity. Solar plasma effects, which are usually less

important, become quite significant at times of high solar activity or at small Sun-Earth-Probe (SEP) angles. Typical variations of range corrections over a pass are 5 m for the ionosphere, whereas solar plasma corrections can vary from 0 to 50 m or more in a pass. The potential for corruption of orbit estimate accuracy by unmodeled plasma effects is readily seen: a constant-rate range change of 50 m over an 8-h pass is equivalent to a doppler bias of about 3.4 mm/s - a (nonstochastic) contribution considerably larger than the assumed baseline doppler data 1σ noise level.

As the SEP angle approached a minimum on November 25, 1976, plasma activity increasingly degraded satellite OD accuracy, particularly noticeable for short data arcs. Figure 21 shows the effective one-way range error induced by the media charged-particle content during a pass of VO-1 data taken by DSS 63 on October 15, 1976. The line-of-sight phase change in meters derived from dual-frequency S/X doppler calibration data is given as a function of GMT. The near-constant rate of range variation seen to have occurred starting at 1124 GMT is approximately equivalent to a 2-way doppler bias of 0.08 Hz for the ensuing 4.5 hours of data, assuming equal uplink and downlink effects. This degree of activity was not unusual; occasional bursts of media-induced doppler signatures at levels of 0.2 Hz and higher were observed weeks before superior conjunction.

The contribution to the doppler signature due to the charged-particle effect can be eliminated with varying degrees

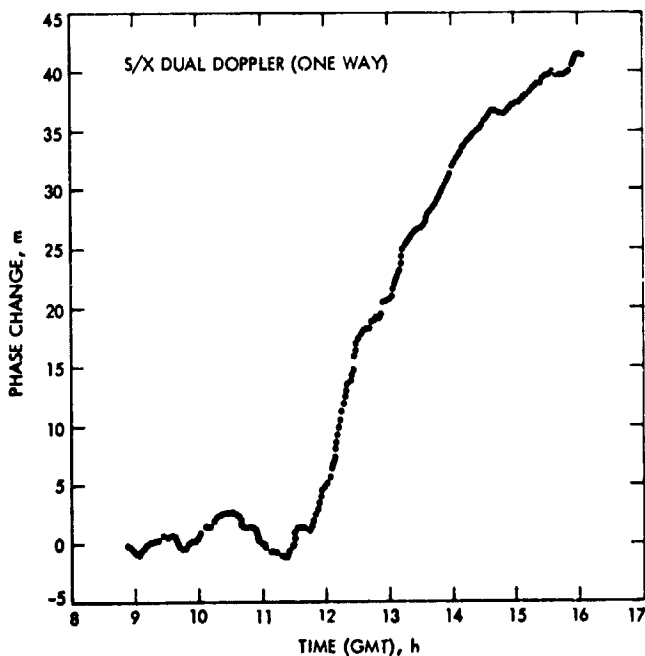


Fig. 21. Phase change for VO-1 DSS 63 10/15/76 pass

of success depending upon the availability of S/X and DRVID data. Calibration polynomials derived from S/X or DRVID were obtainable from the TSAC team program MEDIA (Ref. 4) for any station pass which had coverage with either data type (since X-band transmission occurs only on the downlink, the uplink contribution to S/X calibration must be estimated from the downlink). However, since DRVID coverage was rare and S/X availability was irregular throughout orbit phase, there was no opportunity to mitigate the effects of plasma on OD accuracy by calibrating the doppler on a regular operational basis. While mission accuracy requirements were met without performing such calibrations, activities such as quick-look orbit reestimation following the numerous trim maneuvers that took place during the weeks preceding conjunction would probably have been performed with less disquiet had the plasma contribution to the short-arc OD error been reduced by any significant amount.

Since no commitment had been made for providing S/X calibration support during in-orbit operations, the TSAC software was not designed to be compatible with constrained operational timelines. As a result, calibrations were not used for real-time navigation support even when S- and X-band data were available.

1. Worst-case errors. An accurate assessment of estimation error resulting from charged-particle activity requires some knowledge of the structure of the doppler error signal due to this source. Since such structure was not generally known in advance, a worst-case approach was taken to at least allow a priori OD error upper bounds to be established. Thus simulated doppler errors of a given magnitude were assigned a signature which maximized the resulting error in individual estimated state parameters. The impact of expected plasma effects on short-arc local period and Ω_{pos} accuracies, for example, could then be conservatively predicted before a mission event.

The method used for worst-case computations is easily developed by letting the vector ϵ denote the lumped error in a set of linearized doppler observations Z : the observation equation $Z = A\hat{x} + \epsilon$ yields for the error Δx in the weighted least-squares estimate of x

$$\Delta\hat{x} = F\epsilon \quad (3)$$

where

$$F = (A^T W A)^{-1} A^T W \quad (4)$$

W being the usual data-weight matrix. Thus

$$\Delta \hat{x}_i = \sum_j f_{ij} \epsilon_j \quad (5)$$

gives the component-wise OD error due to a not necessarily random doppler error sequence $\{\epsilon_j\}$. For unknown $\{\epsilon_j\}$, a meaningful bound for $\Delta \hat{x}_i$ can be computed by letting

$$\bar{\epsilon} = \max_j |\epsilon_j| \quad (6)$$

be the assumed doppler error level. $\Delta \hat{x}_i$ is then maximized by choosing

$$\epsilon_j = \bar{\epsilon} \operatorname{sgn}(f_{ij}) \quad (7)$$

for each i . Thus for a fixed-magnitude doppler disturbance at the $\bar{\epsilon}$ level

$$\Delta \hat{x}_{i \max} = \bar{\epsilon} \sum_j |f_{ij}| \quad (8)$$

Equation (8) was used to evaluate the possible effects of plasma activity for numerous short-arc fits. Figures 22 and 23 show worst-case period and Ω_{pos} results for the first VO-2 orbit following MOI; the upper curves are the OD errors due to an assumed media activity level of $\bar{\epsilon} = 0.015$ Hz as a function of the data-arc length. For comparison, the computed 1σ errors due to random data noise and the actual errors incurred in the succession of fits summarized in Table 6 are also given.

The Ω_{pos} plasma curve is evidently an order of magnitude higher than the data noise curve throughout most of the arc-length range. This result appears to be overly conservative, however, since the actual errors for this case are consistently close to those predicted by 0.015-Hz 1σ data noise. The curves for the period are also roughly separated by an order of magnitude until the 16-h point, at which time the data noise error drops off rapidly. Both curves flatten out at about 10 h, but perhaps the most striking feature is the apparent persistence of plasma period error for arc-lengths approaching a full orbit — 2 s for 24 hours of data. While this too may be unrealistically high, it is interesting to note that the interval between 16 and 22 h, where the plasma error remains essentially constant while the data noise curve falls, is the only region where the actual period errors were significantly larger than those predicted by random data noise alone.

2. S/X calibration of a multirevolution fit. While the quality of a short-arc fit was measured in terms of local orbit

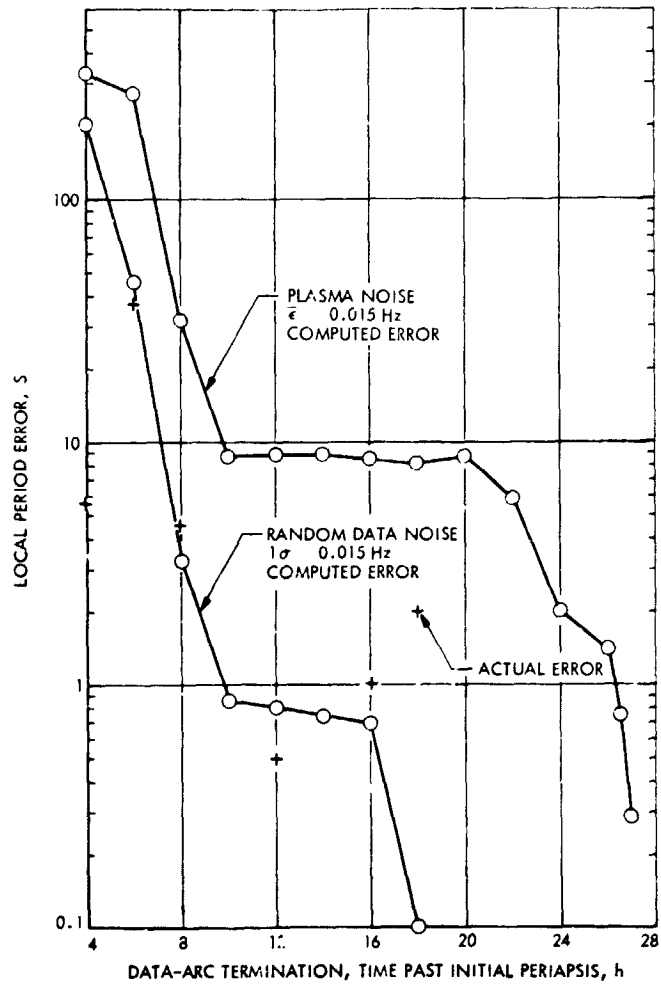


Fig. 22. VO-2 first orbit worst-case media-induced period error

accuracies, the more important single- and multirevolution fits were assessed by how well they predicted period and orientation several orbits beyond the end of the processed data. Although the prediction ability of the longer-arc fits was sufficient to satisfy operational demands, plasma activity became increasingly troublesome as solar conjunction was approached. Plasma noise and data outages would at times combine to degrade the most current single-revolution fit to the degree that more accurate states could be predicted using an estimate based upon data several days older, even though the prediction interval would thereby be longer. The prediction capability of multirevolution gravity sensing estimates was also adversely affected by increasing plasma activity, and aggregate gravity field determinations were, at the very least, inhibited by the growth in the plasma-induced error (see Section V).

The worst-case approach was not extended to the longer arcs because the effects of gravity uncertainties, which become

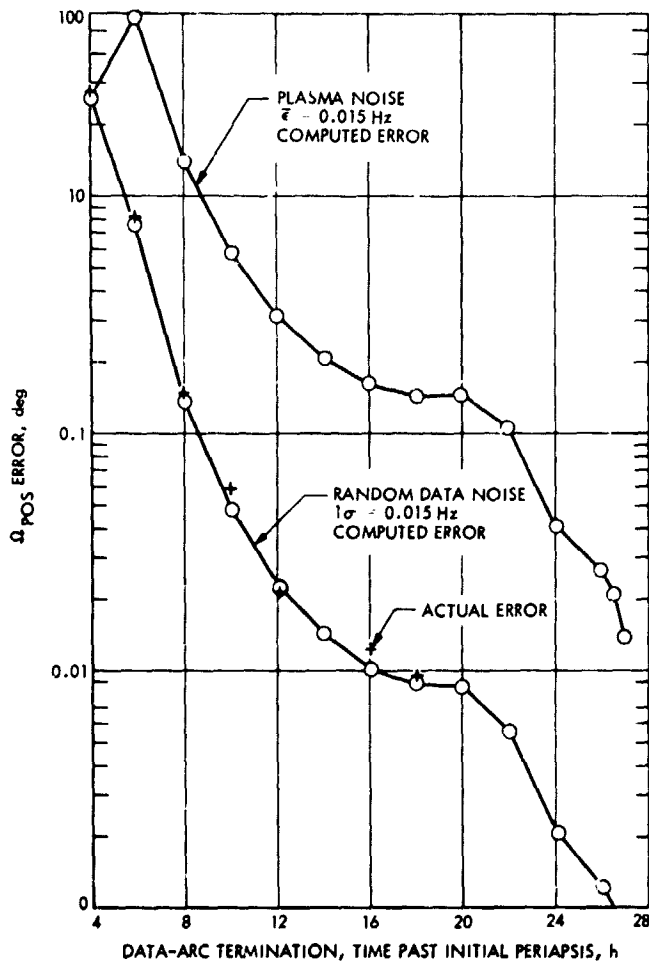


Fig. 23. VO-2 first orbit worst-case media-induced Ω_{pos} error

significant as the processed data arc length approaches a full revolution, could not be readily accounted for in the simulation of media-induced doppler error. Therefore, in an effort to assess both the effects of plasma activity and the potential of S/X calibration data for diminishing such effects on longer-arc fits, a three-revolution 6×6 gravity field estimate was performed. The data arc chosen began at P_{116} for VO-1, the interval with nearly the highest percentage coverage (~34%) of S/X data over all such intervals for both orbiters. Even though only 1/3 of the doppler could be calibrated, it was believed that inclusion of this data in the estimate would result in a noticeable effect on prediction accuracies since the arc occurred during a period of substantial plasma activity (October 15-18, 1976).

The gravity sensing was done both with and without the available S/X calibration corrections added to the data. Figures 24 and 25 give the comparative results in terms of errors in the predicted values of time of periaapsis t_p and Ω_{pos} that

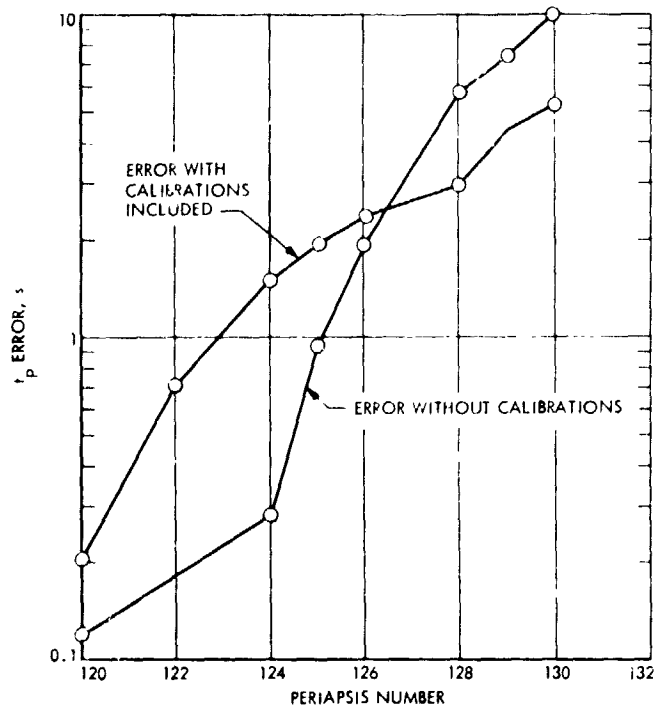


Fig. 24. Errors in predicted times of periaapsis (t_p) incurred using a 6×6 gravity field estimated using three revolutions (P_{116} - P_{119}) of partially calibrated S/X data

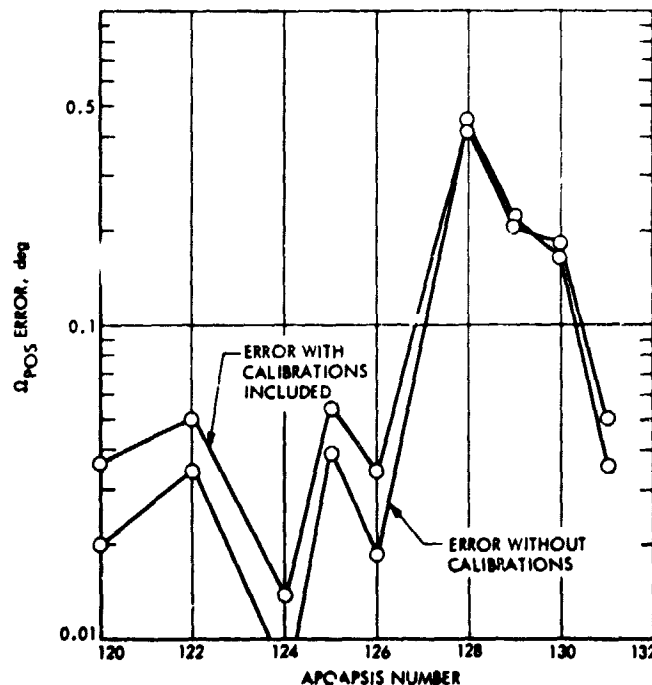


Fig. 25. Errors in predicted Ω_{pos} incurred using a 6×6 gravity field estimated using three revolutions (P_{116} - P_{119}) of partially calibrated S/X data

result from the two solutions. Shown is the magnitude of deviations from reference local single-revolution estimates for prediction intervals beyond periapsis 119. It is evident that results were, at best, inconclusive: the no-calibration solution performed better in predicting t_p until periapsis 126, beyond which point inclusion of the calibration data did reduce the prediction error somewhat. Similarly, calibrations improved Ω_{pos} predictions only for longer prediction intervals and then only slightly. The consistent pattern of Ω_{pos} errors may be an indication that significant errors existed in the reference Ω_{pos} values due to charged-particle noise.

No firm conclusions can be drawn from this trial case regarding the utility of S/X calibrations in improving the performance of multirevolution fits. A conclusive test would require full calibration of the data arc, and may also demand more accurate up-link calibration than was employed in the present study.

V. Modeling Gravitational Accelerations

A. Preflight Analysis

As pointed out earlier, the limiting error source on the period estimate is shared by modeling errors and data noise within a one-revolution fit, and dominated by gravity modeling errors for the predicted orbits that follow. Conceptually, the period experiences a change (ΔP) upon each periapsis crossing due to gravitational perturbations, as shown schematically in Fig. 26. For a synchronous orbiter the error in ΔP propagates in much the same manner as ΔP itself, so that the predicted error in the time of periapsis (t_p) grows as $\frac{1}{2}n(n+1)\epsilon_{\Delta P}$, where n is the number of predicted orbits. The error in ΔP may alter sign and magnitude for different periapsis crossings on an asynchronous orbit so that the error in t_p does not grow geometrically but instead goes as

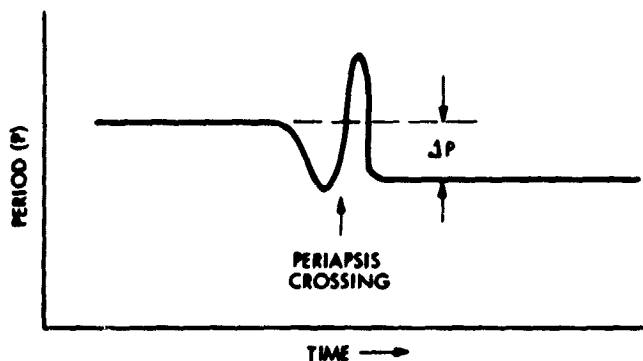


Fig. 26. Schematic representation of the change in period (ΔP) through periapsis

$$\epsilon_{t_p} = \sum_{i=0}^{n-1} (n-i) \epsilon_{\Delta P_i} \quad (9)$$

In this case the predicted orbit may experience the benefit of compensating errors which keep the errors in t_p smaller than might be expected. For this reason, and also since the critical phases of the mission were synchronous, most of the preflight (as well as in-flight) analysis was confined to synchronous orbiters.

An analytical expression for ΔP as a function of the orbital elements and a given gravity field (in the form of spherical harmonics) can be obtained using Kaula's expression for the disturbing function (Ref. 12).

$$\dot{P} = 6\pi \sum_{\ell m} \left(\frac{R}{a}\right)^\ell J_{\ell m} \sum_{pq} F_{\ell m p}(I) G_{\ell p q}(e) \times (\ell - 2p + q) \begin{cases} -\sin & \ell - m \text{ even} \\ \cos & \ell - m \text{ odd} \end{cases} \phi_{\ell m p q} \quad (10)$$

$$\phi_{\ell m p q} = (\ell - 2p) \omega + (\ell - 2p + q) M + m(\beta - \lambda_{\ell m}) \quad (11)$$

where

$J_{\ell m}$ = harmonic coefficients

$F_{\ell m p}(I)$ = inclination function

$G_{\ell p q}(e)$ = eccentricity expansion

ω = argument of periapsis

M = mean anomaly

The graphic node (β) is defined as $\beta = \Omega - \theta$, where θ is the hour angle and Ω is the ascending node (see Fig. 27). Under the condition of resonance

$$(\ell - 2p + q)M + m\beta = 0 \quad (12)$$

so terms corresponding to $\ell - 2p + q = m$, ($m \neq 0$) result in $M + \beta \approx \text{constant}$ and $\dot{P} \approx \text{constant}$. It is convenient to evaluate $M + \beta$ at the time of spacecraft periapsis, and in all future reference to β it is understood to be evaluated at periapsis.

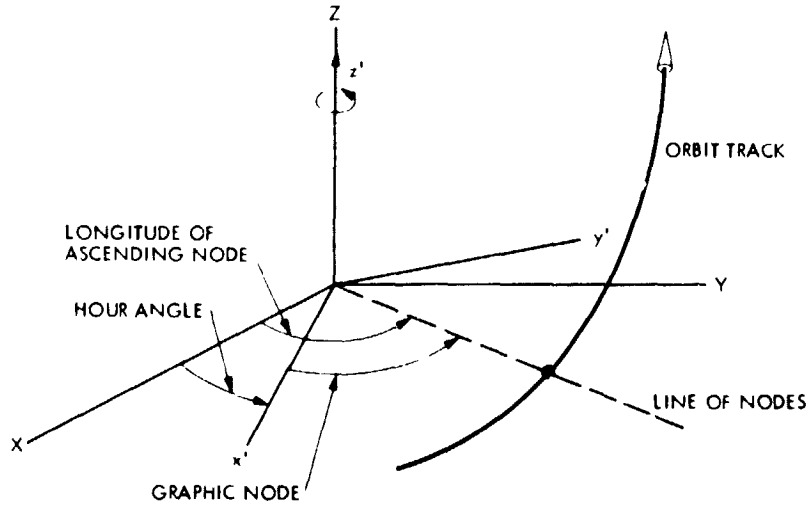


Fig. 27. Definition of the graphic node β

Thus ΔP can be easily expressed as a function of β for a synchronous orbit (Ref. 4). This analytical tool is convenient for a ready comparison of the prediction characteristics of different gravity models. Also, the uncertainty in ΔP for a given field with covariance Γ_C can be obtained as a function of β by

$$\sigma_{\Delta P}^2 = \left(\frac{\partial \Delta P}{\partial C} \right) \Gamma_C \left(\frac{\partial \Delta P}{\partial C} \right)^T \quad (13)$$

Error analysis indicates that a large reduction in the error of time of periaapsis passage can be expected once a gravity field is sensed over but two revolutions of a Viking synchronous orbit. The RSS position error based on a covariance analysis of the preflight nominal (Mariner 9 ensemble) field (Ref. 11) is represented in Fig. 28. Here, the initial error of 0.7 km at periaapsis is due to the error in the node in the plane-of-sky, which is essentially the same at each periaapsis, and the remainder of the error growth is due primarily to an in-track error resulting from an error in the time of periaapsis. The timing error can be approximated by dividing the residual position error by the velocity at periaapsis (~ 4 km/s). As indicated, the error is substantially reduced after gravity sensing by about an order of magnitude.

A number of simulations were performed to test the results of covariance analysis as well as gain some preflight experience. The specific purpose for these simulations was to examine the effects of data span and a priori on period and parameter estimation. Data close to periaapsis ($\sim \pm 1.0$ h) is particularly sensitive to unmodeled accelerations and may require high-order gravity terms to accurately represent them.

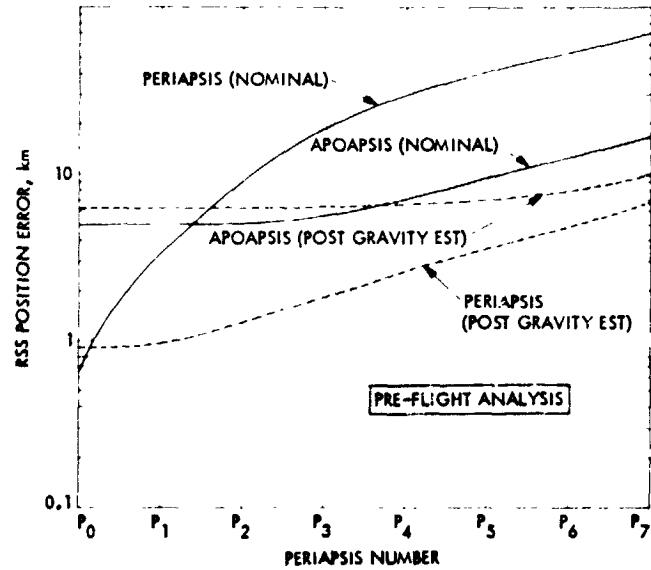


Fig. 28. RSS position error before and after gravity sensing over two revolutions of Viking 1. The figure represents a typical case from a preflight covariance analysis where errors in gravity, station locations, ephemeris and mass of Mars were considered

Since computational limitations may not permit sufficiently large-order parameter estimates to account for these effects, it is important to develop strategies which minimize their corrupting influence on the estimator. Based on the results of error analysis and simulation, the adopted procedure consisted of two revolution fits estimating a sixth order and degree field while deleting data within one hour of periaapsis. An appropriate a priori covariance was used to constrain the filter to the nominal field. It was felt that this strategy would permit fair

recovery of the "true" field while substantially reducing the error in ΔP .

In reality, most Viking orbits were slightly asynchronous and also experienced a small regression of the ascending node. Thus, the graphic node (β) is not constant so $\Delta P(\beta)$ is not absolutely constant. As a result, new information is gained on each periapsis crossing which permits gravity sensing over a fairly broad groundtrack. In order to obtain a single gravity model which retains all of the information contained in the individual short arc fields, selected models determined over short arcs were combined in a linear sense. A description of the method used to accomplish this follows.

B. A Linear Piecewise Batch Estimator

Gravity estimation techniques using combinations of short arc solutions have been applied successfully to Mariner 9 data in the past (Refs. 13, 14). The advantages sought here are to reduce the time and cost usually required to process long arcs of data in a single batch as well as provide a convenient means for combining gravity information from multiple spacecraft. As applied here, an a priori Mariner 9 field (C_0) with covariance (Γ_0) is combined with estimates obtained using short arcs (two to four revolutions) of data from VO-1 and VO-2 synchronous and walk phase orbits. Each short arc solution with its associated covariance will be referred to as \hat{C}_i and Γ_i respectively.

Rather directly then, consider the quantities

$$\hat{C}_i = \hat{C}_i - \Gamma_i \Gamma_0^{-1} (C_0 - \hat{C}_i) \quad (14)$$

as data and

$$\Gamma_i^{-1} = \Gamma_i^{-1} + \Gamma_0^{-1} \quad (15)$$

as the data weight applied to a least squares estimator

$$\hat{C} = \left(\sum_i \Gamma_i^{-1} + \Gamma_0^{-1} \right)^{-1} \left[\sum_i \Gamma_i^{-1} \hat{C}_i + \Gamma_0^{-1} C_0 \right] \quad (16)$$

where \hat{C} is to be taken as the best estimate of the field given the ensemble of all available data. Note that \hat{C}_i and Γ_i are the estimates and associated covariances obtained if no a priori knowledge is assumed. It must be pointed out, however, that the gravity information pertaining to the long-term behavior of

the orbit is not included in this estimator since the states at the beginning of each short arc are not connected dynamically (i.e., they are determined independently). It was found that this shortcoming does not seriously degrade the validity of the field. A similar result was previously demonstrated in Refs. 13 and 14.

The matrix inversions required here are performed using a square root algorithm, following the methods used in the DPODP (Ref. 9), in order to preserve precision. Cholesky decomposition is used to transform a positive-definite symmetric matrix Γ into an upper-triangular square root matrix Λ so that $\Gamma = \Lambda^T \Lambda$. Once Λ is obtained, it follows that $\Gamma^{-1} = \Lambda^{-1} \Lambda^{-T}$, where Λ^{-1} is computed using a backward substitution scheme. This algorithm has been shown to produce a more accurate inverse than conventional techniques and also insures that Γ^{-1} is symmetric.

Use of the square root method outlined here results in a more precise inverse due to the fact that the condition number (ratio of the largest to the smallest eigenvalue) of Λ is the square root of the condition number for Γ . This concept can be carried further by defining an upper triangular matrix Θ such that $\Lambda = \Theta^2$, i.e., a second square root. Θ is obtained from

$$\theta_{ii} = \sqrt{\lambda_{ii}}, i = 1, 2, \dots, n$$

$$\theta_{i-\ell, i} = (\theta_{i-\ell, i-\ell} + \theta_{ii})^{-1}$$

$$\times \left(\lambda_{i-\ell, i} - \sum_{j=1}^{\ell-1} \theta_{i-\ell, i-j} \theta_{i-j, i} \right); \begin{cases} i = 1, 2, \dots, n \\ \ell = 1, 2, \dots, i-1 \end{cases}$$

$$\theta_{ij} = 0; i > j \quad (17)$$

Then, $\Lambda^{-1} = \Theta^{-2}$. The process can be continued where Θ plays the role of Λ , etc., to obtain as many square roots as desired. At most, two square roots proved to be adequate for the combination of gravity fields prescribed by Eqs. (14-16).

C. VO-1 Experience

The synchronous phase of VO-1 began at the periapsis designated P_2 , approximately 42 h and 21 min after MOI on June 19, 1976. A number of maneuvers were performed to prepare for the July 20 landing, resulting in slight asynchronous phases (walk phases) of the mission. This may be seen by noting the period of rotation for Mars (approximately

24.6228 h) and the period of the orbit after each maneuver as given in Table 1. The change in period due to gravity perturbations for these phases of the mission ranged from +10.0 to -8.0 s on each periaapsis crossing, as shown in Fig. 29. This figure was obtained using the gravity model resulting from the combination of short arc estimates covering the span from P_2 to P_{46} , by applying the method previously described (Eq. 16). The practical advantage of this technique is evident in that this long arc of data could be reduced without requisite knowledge of the maneuvers. As indicated, this sixth order and degree model was sampled over only thirty degrees of the planet's longitude so its validity outside this region should be regarded with caution. The applied a priori constraint does not allow us to totally disclaim the global nature of this Viking sense model however.

The error in ΔP was reduced to ± 0.02 s for this interval using the new field, whereas the error would have been as large as 0.65 s had the nominal field been retained (see Fig. 30). As shown in Fig. 31, the expected error in ΔP for the nominal field was approximately 0.8 s in this region. This uncertainty was substantially reduced in the neighborhood of a two-revolution gravity fit crossing P_4 . The formal uncertainty was reduced over an even broader range of longitudes once the combined estimate was obtained, as might be expected (see Fig. 32).

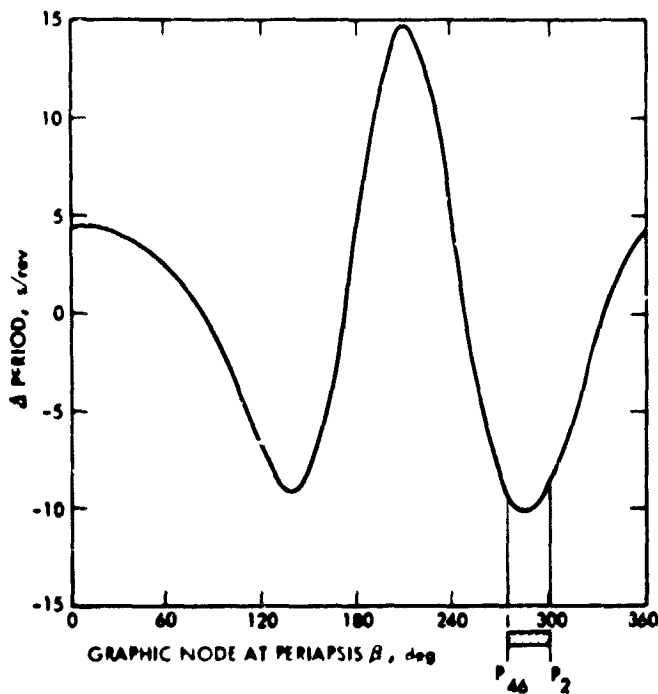


Fig. 29. Change in period as a function of graphic node at periaapsis based on a 6x6 VO-1 combined field determined over P_2 - P_{46}

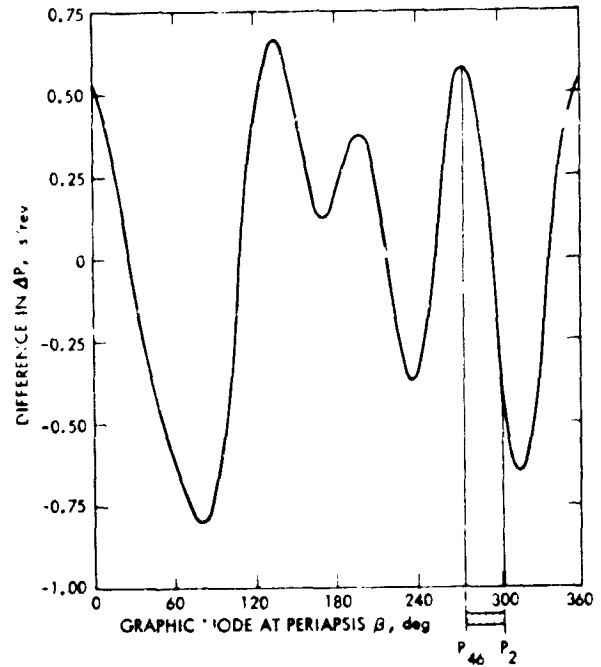


Fig. 30. Difference in the change in period (VO-1 6x6 combined field—nominal) as a function of graphic node at periaapsis

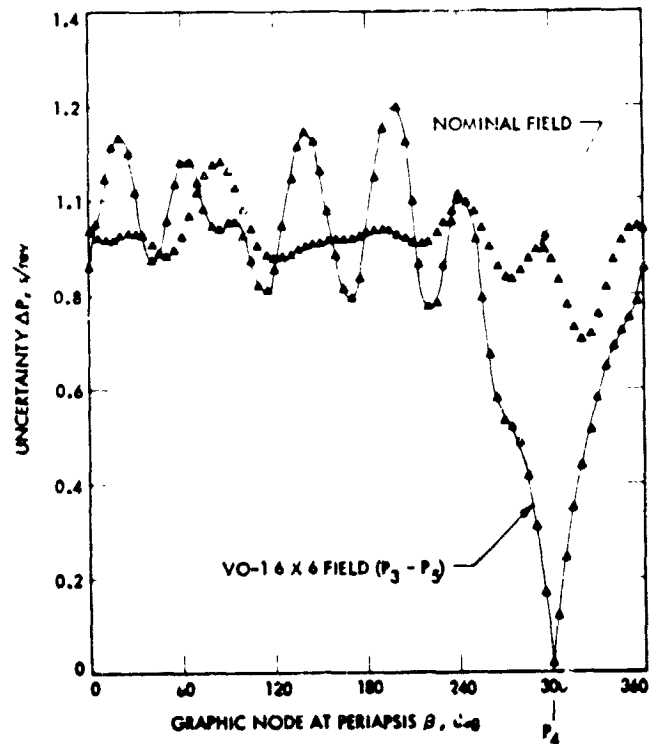


Fig. 31. Uncertainty in the change in period as a function of graphic node at periaapsis based on the nominal field and a VO-1 6x6 field determined over P_3 - P_5

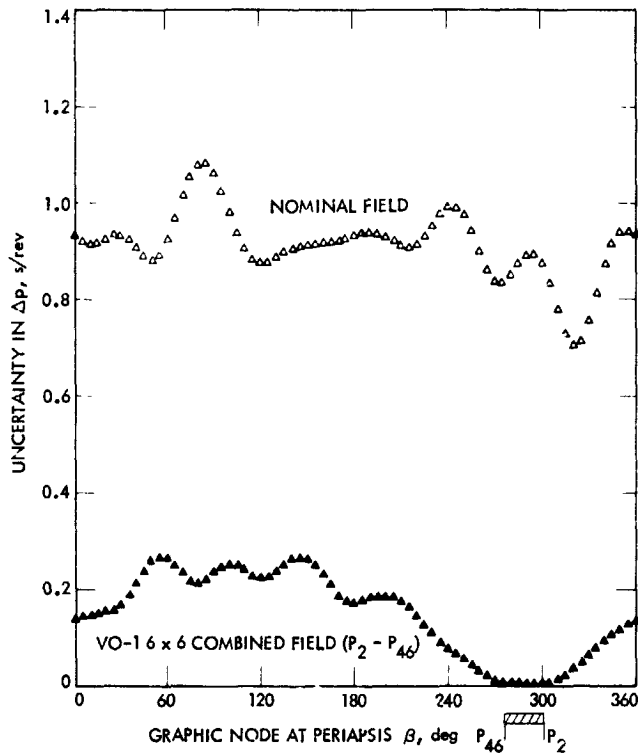


Fig. 32. Uncertainty in the change in period as a function of graphic node at periaapsis based on the nominal field and a 6x6 VO-1 combined field determined over P_2 - P_{46}

Comparisons between the observed ΔP and those predicted by various models are typified in Fig. 33. The sixth order and degree field obtained over $P_3 - P_5$ tracks the actual ΔP history remarkably well, as does the long arc combined field. It must be noted that all short arc models did not perform as well as that shown; thus the predictability of the $P_3 - P_5$ field may be deemed fortuitous. A fourth order and degree model obtained over the span $P_2 - P_4$ performed well locally but could not recover the information necessary to maintain accuracy for many orbits into the future. The early recovery of an accurate gravity model permitted prediction of the times of periaapsis to within 1.0 s 10 days in advance, while the nominal field would have produced errors on the order of tens of seconds.

Improvement of a global model continued once data was processed over the early walk phase of VO-2. Beginning the middle of August 1976, errors in the estimated period as large as 0.2 s were experienced due to increased solar plasma coupled with reduction in the VO-1 tracking coverage. Thus, data

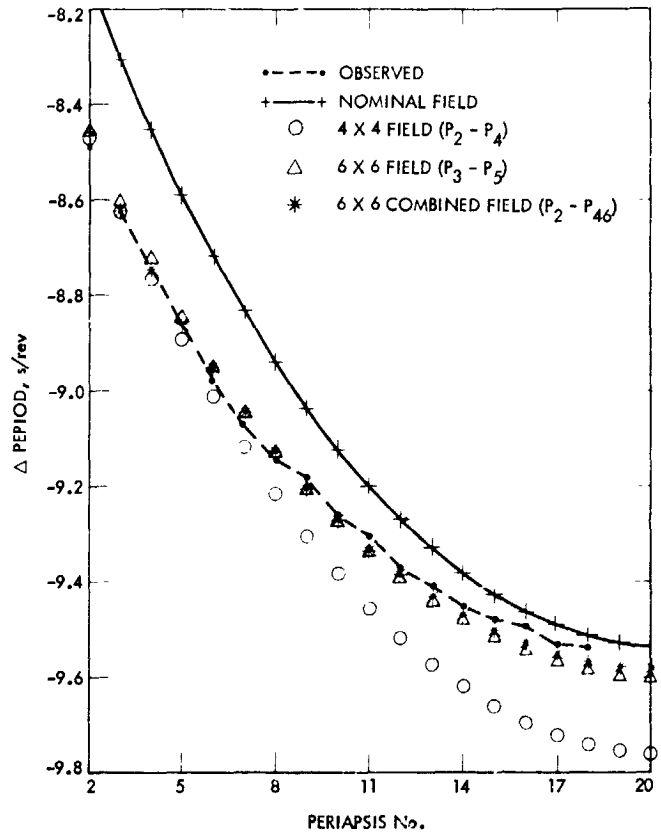


Fig. 33. Change in period as a function of periaapsis passage based on nominal and VO-1 determined gravity fields and observations for the first 20 days

taken during this phase was rendered useless for gravity determination purposes. Fortunately, this problem did not become serious until after the VO-2 subperiaapsis point had completed one circulation about the planet. This permitted sampling of the gravity field for all longitudes of periaapsis.

D. VO-2 Experience

Unlike the early phases of VO-1, VO-2 was initially on a markedly asynchronous orbit as indicated in Table 1. Coverage of the planet was completed after the first 10 revolutions (with maneuver interrupts at P_2 and P_6), during which time the solar plasma effects were still small enough to permit gravity estimation. The data noise level became intolerable (for further gravity sensing) after this time, including data taken after the plane change; thus no valuable gravity information was available after August 18, 1976.

Short arc gravity estimates were obtained over the orbits $P_0 - P_2$, $P_2 - P_6$, and $P_7 - P_{10}$ to ensure circumplanetary coverage by the subperiapsis point. These were then used to form a VO-2 ensemble field. This model was combined with the VO-1 field ($P_2 - P_{46}$) to yield the Model-V field (see table 8). The prediction accuracy of the combined VO-1/VO-2 field was found to be comparable to that of the individual ensemble fields. Consequently, the dual spacecraft gravity estimate was adopted for navigation purposes. Unlike a synchronous orbit, an asynchronous orbit exhibits an error in ΔP which may vary sharply in magnitude and sign upon each periapsis passage. Fig. 34 shows the error in ΔP and the resulting error in t_p based on a prediction starting at P_7 and extending through P_{14} , using the nominal gravity field. The error in ΔP was as large as ± 0.65 , but the error in t_p did not grow above 0.5 s during this interval of prediction due to compensatory period errors. After gravity sensing, the error in ΔP was held to ± 0.2 s; however, the error in t_p still grew as large as 0.68 s, indicating that compensating period errors are extremely model-dependent (see Fig. 35). Once VO-2 was synchronized prior to the landing sequence, the error in ΔP introduced by Model-V was observed to be less than 0.04 s, thus permitting much the same precision for the separation

Table 8. Normalized spherical harmonic coefficients for Mars $\times 10^5$ (this model is based on preconjunction Viking data for both orbiters with a Mariner 9 field (Ref. 11) included as a priori)

l	m	$C_{lm} \times 10^5$	$S_{lm} \times 10^5$
2	0	-87.64	0.00
2	1	0.00	0.00
2	2	-8.56	4.85
3	0	-0.81	0.00
3	1	0.63	2.58
3	2	-1.76	0.68
3	3	3.43	2.45
4	0	0.36	0.00
4	1	-0.01	0.24
4	2	-0.17	-0.81
4	3	0.66	0.65
4	4	-0.43	-1.66
5	0	-0.07	0.00
5	1	0.42	0.28
5	2	-0.54	0.00
5	3	-0.13	-0.56
5	4	-0.69	0.22
5	5	-0.37	0.55
6	0	0.18	0.00
6	1	0.68	-0.39
6	2	0.11	-0.31
6	3	0.61	1.35
6	4	0.46	0.00
6	5	0.26	0.33
6	6	0.12	0.03

design as realized in VO-1. It must be noted, however, that the solar plasma activity made it difficult to recognize gravity errors apart from local orbit determination errors at this time.

The validity of the Model-V became even more apparent once VO-1 was synchronized over the VL-2 site on September 24, 1976. The VO-1 only field differed by approximately 0.2 s in ΔP from Model-V for this phase, and it was found that the error in ΔP using Model-V was less than 0.04 s. Formal statistics, though usually optimistic, show extremely small uncertainties in ΔP for all values of β due to circumplanetary gravity sensing using VO-2 walk data (see Fig. 36). Qualitatively at least, this has been borne out, since the errors in ΔP due to Model-V did not exceed 0.4 s for the VO-2 walk orbit

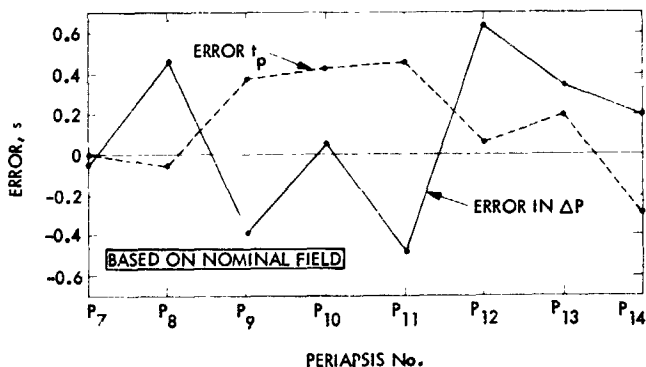


Fig. 34. Errors in predicted times of periapsis t_p and predicted changes in period ΔP incurred using the nominal gravity field on VO-2 (prediction started at P_7)

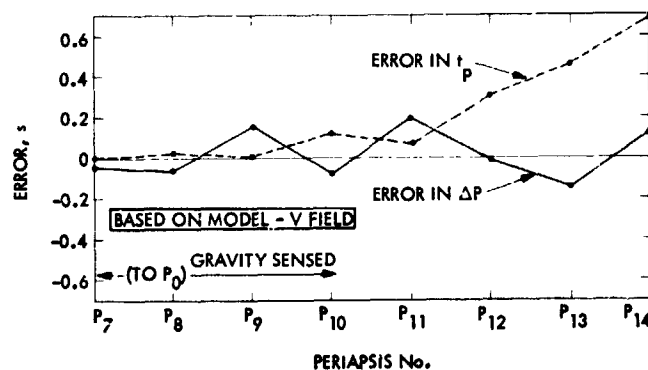


Fig. 35. Errors in predicted times of periapsis t_p and predicted changes in period ΔP incurred using the 6x6 VO-1 and VO-2 combined field on VO-2 (prediction started at P_7)

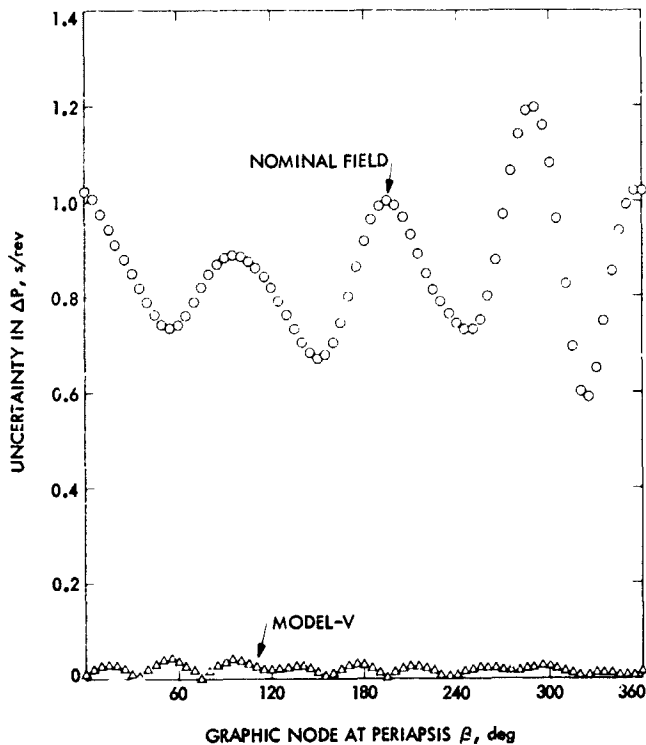


Fig. 36. Uncertainty in the change in period as a function of graphic node at periaapsis based on the nominal field and the 6x6 VO-1 and VO-2 combined field

and 0.04 s for the VO-1 synchronous orbit during the time period beginning the middle of September 1976 toward solar conjunction in the middle of November 1976.

It should be kept in mind that the VO-1 and VO-2 combined field (Model-V) also contains Mariner 9 data through the applied a priori nominal field. A comparison between this Viking sensed model and certain independently determined Mariner 9 models can be made using Fig. 37. Here, the change in period as a function of graphic node for each field is compared to the preflight field (see Eqs. 9-12), all evaluated for the first VO-1 synchronous phase. Model-V can be taken to be fairly accurate globally and strictly correct in the region covered by the early phases of VO-1 (P_2 to P_{46}). With little exception, all fields predict a $\Delta P(\beta)$ within one standard deviation of the preflight ($\sim \pm 1.0$ s). It is of interest to note that all fields (except Model-M) exhibit the same sinusoidal behavior in the neighborhood of $\beta = 300^\circ$, which leads to ΔP errors less than 0.3 s over the region P_2 to P_{46} in all cases. The fields tend to be less congruous for the more westerly longitudes, however, with differences as large as 1.0 s occurring. Clearly, none of these fields would have introduced gravity modeling errors significantly larger than those expected.

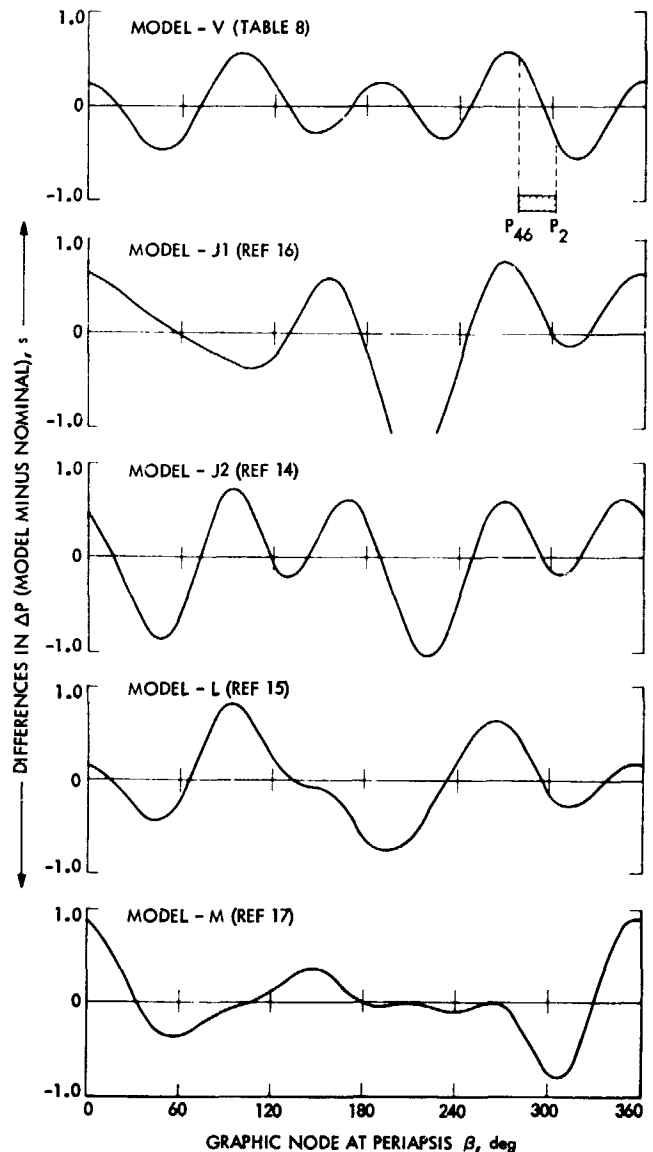


Fig. 37. Comparison of $\Delta P(\beta)$ between various gravity fields and the nominal gravity field evaluated for the first VO-1 synchronous phase

E. Gravity Estimation in Extended Mission

The orbital elements for the Viking spacecraft subsequent to solar conjunction are given in Table 9. All trajectories for this phase of the mission were virtually asynchronous in support of Mars, Phobos, and Deimos imaging, Phobos mass determination experiment, and lander relay links. As in the primary mission, knowledge of the gravity field was essential to the success of navigation and science sequences. Actually, prediction accuracy became more important owing to the long-range planning and reduced tracking schedule peculiar to the Viking extended mission.

Table 9. Areocentric orbital elements of Viking 1 and Viking 2

		Viking 1				
		MOT-10	MOT-11	MOT-12	MOT-13	MOT-14
Parameter		Date of maneuver, 1977				
		1/22	2/5	2/12	3/11	3/24
Semimajor axis, km	a	19538.5	19513.6	19498.4	18903.4	19804.6
Eccentricity	e	.7508	.7504	.7498	.8047	.8133
Mean period, h	P	23.033	22.989	22.962	21.919	23.505
Longitude of ascending node, deg	Ω	100.56	99.19	97.99	90.10	87.06
Argument of periapsis, deg	ω	78.25	80.18	81.64	90.00	93.96
Inclination, deg	I	39.11	39.26	39.30	39.23	39.30
Height above surface at periapsis, km	h_p	1474.9	1477.8	1485.4	299.1	303.1
Latitude of sub-periapsis point, deg	ϕ_p	38.14	38.58	38.80	39.23	39.19
		Viking 2				
		MOT-8	MOT-9	MOT-10		
Parameter		Date of maneuver, 1977				
		1/22	3/02	4/18		
Semimajor axis, km	a	21452.0	20488.5	19365.1		
Eccentricity	e	.8051	.7977	.7860		
Mean period, h	P	26.498	24.733	22.727		
Longitude of ascending node, deg	Ω	57.53	54.76	52.93		
Argument of periapsis, deg	ω	60.33	55.68	51.49		
Inclination, deg	I	79.01	80.18	80.51		
Height above surface at periapsis, km	h_p	787.2	750.9	722.9		
Latitude of sub-periapsis point, deg	ϕ_p	58.53	54.47	50.52		

No gravity model improvement was attempted during the solar conjunction phase because of inadequacies in the data. Data limitations at this time were primarily due to (1) high solar induced noise from mid-November 1976 to late January 1977, (2) lack of contiguous orbits with continuous coverage, and (3) lack of new information in the data. As a result, navigation throughout the conjunction phase had to rely on Model-V. Orbit determinations early in February 1977 indicated that Model-V was producing errors in ΔP on the order of 0.5 s for the low-altitude (800-km) VO-2 orbit and approximately 0.25 s for VO-1. Since accurate predictions were needed to support the VO-1/Phobos encounter phase, beginning February 12, 1977, and the VO-1 low-altitude (300-km) phase, beginning March 12, 1977, an early improvement in the gravity model was necessary. The new model (COMBIX) consists of the linear ensemble of all fields which comprise Model-V plus a number of short arc fields obtained after conjunction. The new short arc fields were reduced from 8 revolutions of VO-2 data and 5 revolutions of VO-1 data taken early in February. The merits of COMBIX as applied to the Phobos encounter phase are discussed in Section VII. An analysis of the low-altitude phase of VO-1 based on COMBIX follows.

Errors: analyses of the post MOT-13 low-altitude phase of VO-1 have been compared to the actual navigation experience for that period. In an attempt to bound the expected prediction errors, two somewhat subjective covariance matrices for the COMBIX gravity model were considered. COMBIX/NEW is the computed covariance which results from the least squares combination of the constituent fields that comprise COMBIX. The other covariance, COMBIX/AVE, was based on sample statistics derived from the deviations of the constituent fields from their mean.

These two covariance matrices were used to predict the evolution of orbit position errors over one planetary circulation (9 revolutions). The expected errors were found by mapping the state covariance obtained from a one-revolution fit. As usual, it was assumed that the corrupting influence of the short-period gravity effects could be eliminated by deleting data within one hour of each periapsis. The nominal orbit used for this low-altitude covariance mapping is defined by the orbit elements following MOT-13 as shown in Table 9.

The corresponding evolution of timing uncertainties predicted by the COMBIX/AVE covariance matrix is presented in Fig. 38. The trends for σ_P and $\sigma_{\dot{P}}$ obtained from COMBIX/NEW are 10^{-2} times the corresponding values computed using COMBIX/AVE. Such a small error is unrealistic, so COMBIX/NEW was not considered further in this study. The maximum timing error predicted by the COMBIX/AVE covariance is

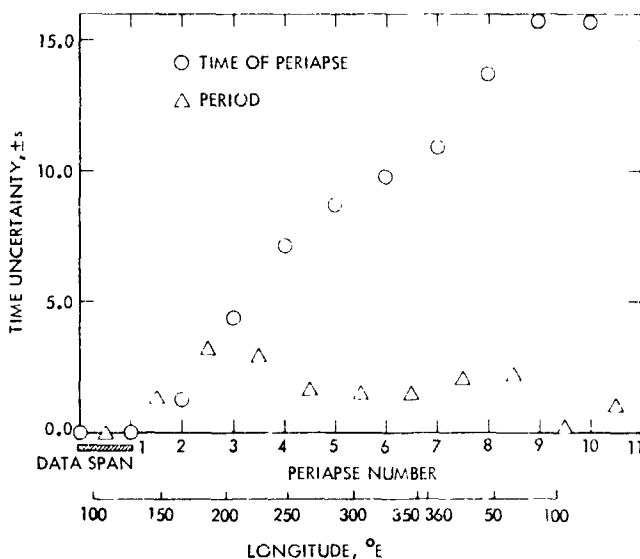


Fig. 38. Timing uncertainty mapped for $H_p = 300$ km, VO-1, using COMBIX/AVE covariance

15 s after 9 revolutions. Navigation experience indicates that the errors predicted by COMBIX/AVE bounded the actual timing errors, which were observed to be typically 5-6 s after 9 revolutions of prediction.

As expected, the observed errors in the change in period (ΔP) were generally larger for the post MOT-13 orbit than they were for the previous 1500-km altitude orbit. However, the random signs of the ΔP errors contribute to widely varying timing errors over a planetary circulation depending on the epoch of prediction.

Assuming that the observed error in ΔP history for the first low-altitude circulation of Mars (revolutions 264-273) is repeated on successive circulations, the predicted timing errors which would result from any given state-only fit can be estimated using Eq. (9). This relation was used to compute expected timing errors after 9, 14, and 18 revolutions of prediction, starting with each of the 9 orbits comprising the first low-altitude Mars circulation. The results are presented in Fig. 39. Notice that the error associated with any particular fit is roughly proportional to the number of orbits predicted. Further, the accumulated error in prediction depends highly on where the prediction starts. As noted earlier, the error in time of periapsis after 9 revolutions can be as large as 5-6 s.

It is concluded that analyses using two independent covariance matrices for COMBIX have at best bounded the observed timing errors. In particular, the computed covariance for COMBIX predicts timing errors that are small by nearly 2 orders of magnitude. This suggests that data noise covariances

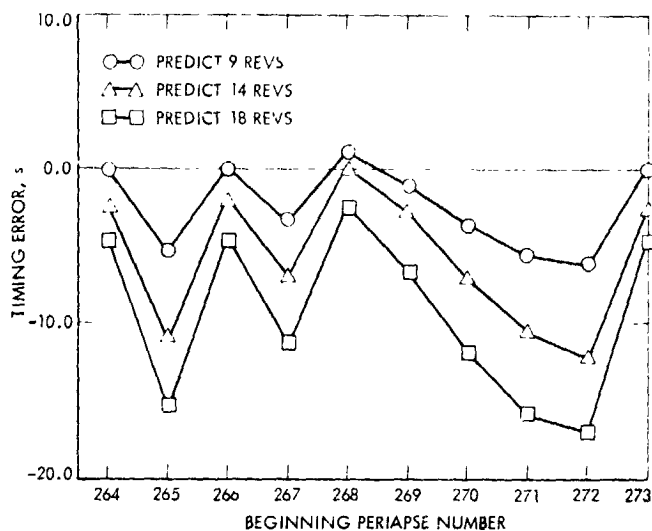


Fig. 39. Error in timing predictions based on observed errors in delta period (Revs. 264-273)

for gravity models are extremely optimistic and therefore do not reflect the true timing errors. Further it is difficult to assign or even properly bound the effect of modeling errors on the predicted times of periapsis associated with an arbitrary walk-phase state-only fit. However, the sample covariance matrix (COMBIX/AVE) does tend to properly bound the observed error in ΔP . This was concluded by noting that the observed errors in ΔP over the longitudes of 60°E to 260°E were on the order of one second, very close to the predicted uncertainties (see Fig. 38).

In summary, analyses tend to bound the error in ΔP as a function of longitude but have little value in bounding predicted timing errors. This is due to the fact that the magnitude of $\epsilon_{\Delta P}$ can be predicted but not its sign. Thus a given gravity model can best be evaluated by observing errors in predicted ΔP rather than predicted t_P for the asynchronous phases of the mission.

With this in mind, the $\epsilon_{\Delta P}$ history was examined for the VO-1 low-altitude fast-walk phase following MOT-13. During this phase, the orbit period was about 22 hours which resulted in subperiapse points successively spaced approximately 40° eastward in Mars longitude. After MOT-14 was executed on March 28, 1977, the orbit period changed to 23.5 hours and the walk-rate decreased to about 15° per VO-1 revolution. The errors in delta period throughout both low-altitude phases were monitored and are presented as a function of longitude of periapsis in Fig. 40. Note the COMBIX gravity model predicted delta periods within ± 0.8 s (1σ) for most of these low-altitude orbits, but some large errors were still evident for

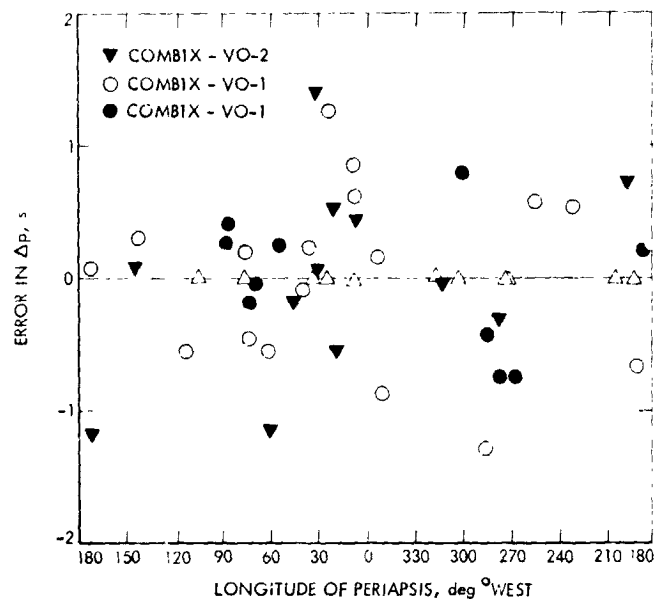


Fig. 40. Comparison of ΔP errors

orbits whose subperiapse points occurred at about 30° west longitude.

In order to reduce longitudinal deficiencies of COMBIX, a new 6th degree and order gravity field called COMB3X was estimated by including four new short-arc fields determined during the $40^\circ/\text{rev}$ fast-walk of VO-1 and seven new fields determined using the $15^\circ/\text{rev}$ slow-walk of VO-1. No new VO-2 data was included. This gravity model predicts ΔP to within ± 0.5 s (1σ) for all subsequently observed VO-1 revolutions. Further, the apparent error in COMBIX at 30° west longitude is not evident in COMB3X, which indicates that it should predict better than COMBIX in a global sense. The errors in ΔP observed for VO-2 while using COMBIX are also presented in Fig. 40, and since the period of the 800-km altitude VO-2 orbit was being predicted adequately with COMBIX, the decision was made not to use COMB3X for VO-2 but to continue using COMBIX for navigation purposes. Future development will be confined to obtaining a gravity model tailored to the low-altitude phases of the mission only.

F. Conclusions

A number of conclusions drawn from the VO-1 and VO-2 experience are particularly pertinent to synchronous orbits. At least for the high-altitude (~ 1500 -km), high-eccentricity (~ 0.76) Viking orbiters, the error in ΔP can be reduced to a few hundredths of a second by estimating a sixth order and degree gravity model over two revolutions while deleting data within an hour of periapsis. Further, if the orbit is slightly

asynchronous, a gravity model derived from a linear combination of short arc estimates retains the inherent local accuracy of its constituent fields. Improvement may be possible should higher-order terms be included but an error of ~ 0.02 s is very close to the limit imposed by data noise. This is clearly not the case for walk orbits where the error in ΔP was only reduced to 0.2 s within the fit. The solar induced noise became fairly high during the time VO-2 walk phase data was processed, which could explain a 0.2-s error, but this contradicts the excellent performance demonstrated by Model-V on the later synchronous phases. Perhaps a sixth order and degree field is inadequate to properly account for all perturbations experienced on a walk orbit, but such a conclusion requires further study.

During the low-altitude phase of VO-1 ($h_p \approx 300$ km) and VO-2 ($h_p \approx 800$ km) in the extended mission, a tailored sixth degree and order gravity field predicted period changes of the orbiters accurate to ± 0.5 s. Work is currently underway to develop higher degree and order tailored fields, which are necessary to reduce ΔP errors in these orbits to a level comparable to that of the nominal mission.

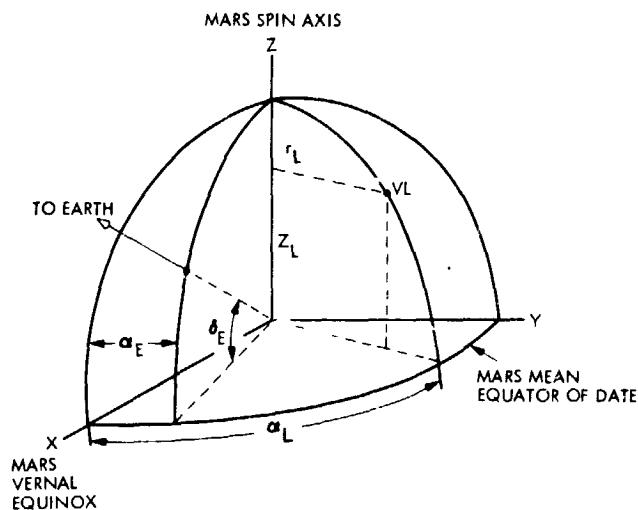
VI. Viking Lander Position Determination

A. Information Content of VL Radio Tracking Data

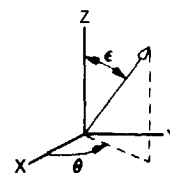
The VL radio tracking geometry is illustrated in Fig. 41. The lander and the Earth are referenced to a nominal Mars-centered equatorial-equinox coordinate frame (Ref. 17). The cylindrical coordinates of the VL relative to this frame are r_L (distance from the spin axis), Z_L (height above the equatorial plane), and α_L (areocentric right ascension). The lander rotates about the Mars spin axis with angular velocity ω (the rotation period is approximately 24.6 h). The areocentric right ascension α_E and declination δ_E of Earth define the Mars-to-Earth direction. The orientation of the true spin axis of Mars relative to the nominal is specified by the clock angle θ and cone angle ϵ (the latter is assumed to be small).

Doppler signatures induced by the VL rotational motion and by a Mars pole offset are shown in Fig. 42 (a,b). In each case, the doppler signature is a sinusoid with the period of Mars' rotation. The amplitudes are functions of either r_L or ϵ , and the phases depend upon either the right ascension of the VL relative to the Earth or on the clock angle of the true pole. The doppler signature induced by the third lander coordinate Z_L is illustrated in Fig. 42 (c). Examination of these signatures leads to the following conclusions:

- (1) Motion of the Earth in areocentric right ascension is necessary to provide separation of errors in Mars' pole direction from errors in r_L and α_L .



a) VL POSITION AND DIRECTION TO EARTH



b) MARS POLE ORIENTATION

Fig. 41. Viking lander tracking geometry

- (2) Doppler provides a relatively weak determination of Z_L (because the rate of change of Earth declination δ_E is small compared to the Mars rotation rate ω).

The insensitivity of VL doppler data to errors in Z_L was noted in numerical studies reported by Tolson et al. (Ref. 18), and a method of employing ranging data to determine this component of lander position was proposed. The drawback of VL ranging data is that it contains a bias that is equal to the ephemeris error in the distance from Earth to Mars. With estimates of r_L , α_L , ϵ , and θ from doppler data, the error in Z_L is approximately related to a range bias through the equation

$$\Delta Z_L \approx -\csc \delta_E \Delta \rho \text{ (bias).}$$

Thus, the error in Z_L is at least 2.4 ($= \csc 25^\circ$) times as large as the ephemeris range error. Prior to Viking-1 insertion, the uncertainty in the Earth-to-Mars range from the Viking ephemeris (DE84) was on the order of 1 to 2 km during the interval of the Viking Prime Mission. It was pointed out in Section IV that the VO position relative to the center of Mars along the line of sight (Z_{pos}) was well determined from doppler data. Thus, passing doppler-determined orbits through

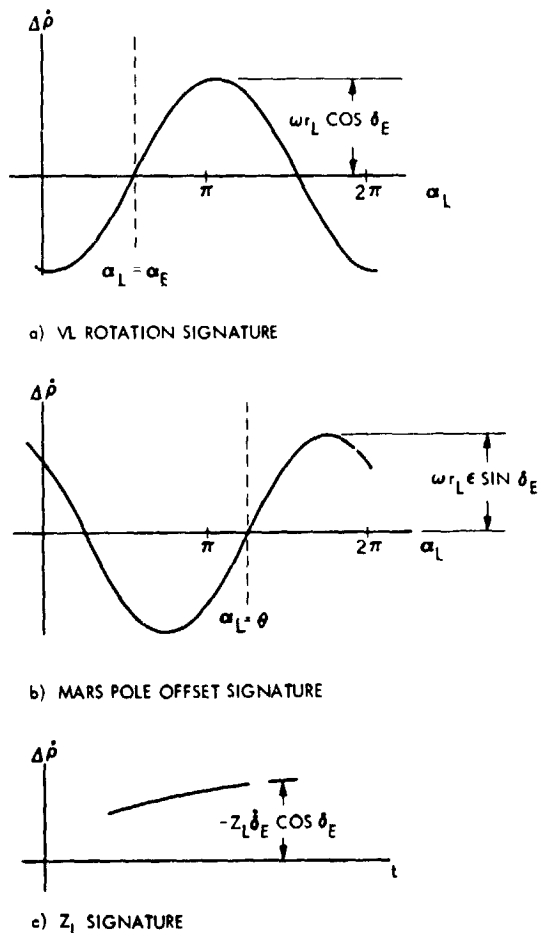


Fig. 42. Viking lander doppler signatures

VO range data was expected to give a measure of the ephemeris range error with an accuracy of 15 to 25 m. The method suggested in Ref. 18 involved using the VO range residuals to update the ephemeris range prior to processing the VL data. In practice, the VO range residuals are used to obtain an approximate ephemeris range error, which is then applied as an adjustment to the VL range measurement.

B. Preflight Analysis

Estimates of VL position accurate to 0.5 deg were required to be delivered within 5 days after touchdown, with the condition that at least one good VL range point had been acquired. The results of preflight studies (Ref. 4) employing up to 5 days of tracking are summarized in Fig. 43. The doppler arcs were centered at the time on each day that Earth crossed the VL meridian, and were of 30 to 90 min duration. The doppler sample rate was one point per minute. An "adjusted" range point was included on the third day. The parameters to be determined included the three components of VL

position and the direction of Mars spin axis (represented by the right ascension α and declination δ relative to the Earth mean equator and equinox of 1950.0). Although errors in tracking station locations were treated via the DPODP "consider" option (Ref. 7), the statistics primarily reflect the noise levels in the doppler and the VL range adjust. The dramatic improvement achieved with the second day of data is due to increased separability of VL position and Mars pole resulting from the change in the areocentric right ascension of Earth. The decrease in Z_L uncertainty from the second to the third day is evidence of the utility of VL ranging.

Note the strength of the pole orientation determination relative to that achieved with Mariner 9 data (Ref. 4). The lower precision of the pole right ascension estimate as compared to the declination estimate reflects a correlation between α and α_L produced by the tracking geometry.

C. Inflight Results

The initial VL-1 and VL-2 radio tracking is summarized in Fig. 44. The VL-1 coverage is relatively extensive as compared to that for VL-2. Not only were most of the VL-1 passes of longer duration, but they also span a greater range of tracking geometries. This is reflected in the formal statistics given in Fig. 45.

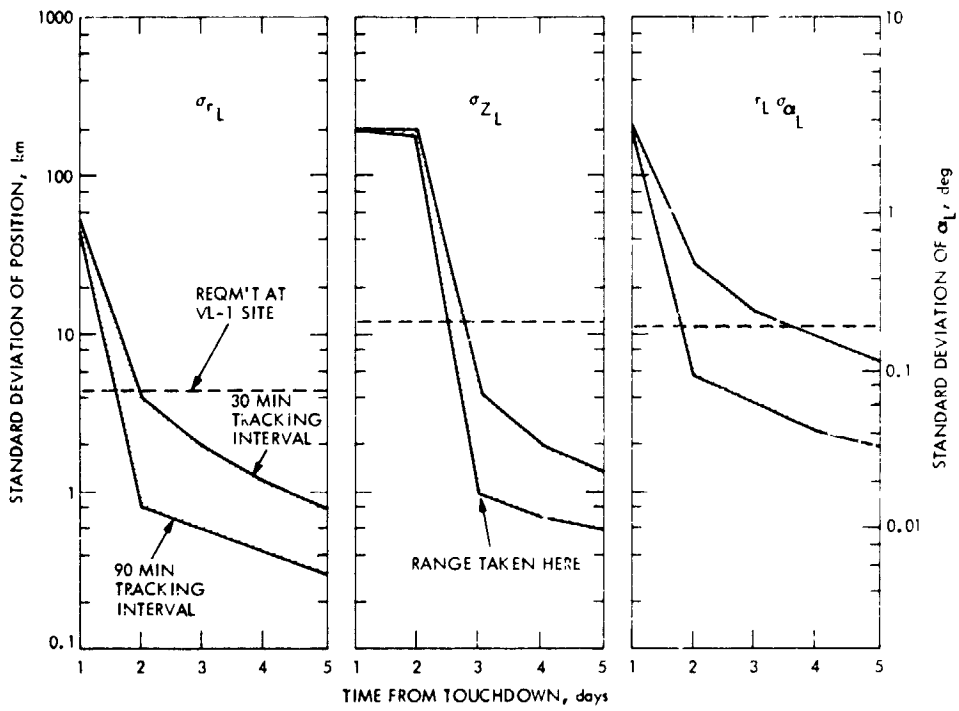
The poor VL-2 tracking coverage in combination with a higher level of space plasma activity observed in the VO after-the-fit residuals led to the decision to employ the pole as determined from VL-1 processing in estimating the position of VL-2. The final (5-day) position estimates and the pole estimate derived from initial VL-1 tracking data are given in Table 10. For verification purposes, landing site radii obtained

Table 10. VL position and Mars spin axis direction estimates at five days after touchdown

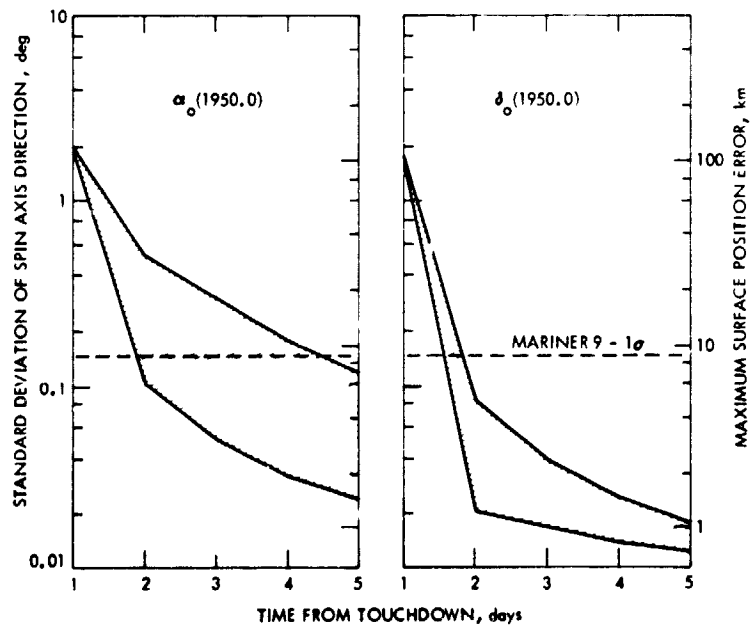
Parameter	Estimate	
	VL-1	VL-2
Radius, km	3389.4 ± 0.1	3381.4 ± 0.6
Topographic radius, ^a km	3388.9	3381.5
Areocentric latitude, deg	22.26 ± 0.01	47.66 ± 0.01
West longitude, ^b deg	48.01 ± 0.01	225.78 ± 0.01
α_0 (1950.0), deg	317.36 ± 0.02	-
δ_0 (1950.0), deg	52.708 ± 0.004	-

^a From reference 19.

^b West longitude λ is defined by $\lambda = 2\pi - (\alpha_L - V)$, where V is the hour angle of the prime meridian from Ref. 17 and α_L is measured in the equatorial/equinox frame relative to the estimated pole.



(a) VL POSITION



(b) MARS SPIN AXIS DIRECTION

Fig. 43. Standard deviations of Viking lander position and Mars spin axis direction from radic tracking (preflight)

ORIGINAL PAGE IS
OF POOR QUALITY

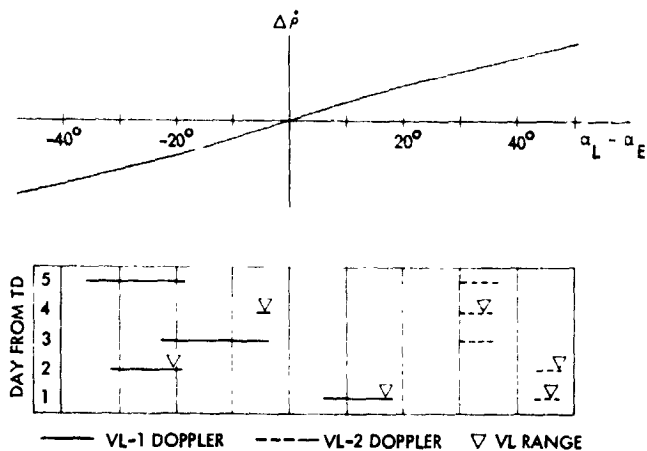


Fig. 44. VL radio tracking coverage for five days following touchdown

from studies of Mars topography (Ref. 19) are also presented. The VL-1 estimated pole is within 0.04 deg of the Viking preflight nominal adopted from Ref. 15.

VII. The Mass of Phobos from Viking Flybys

A. Introduction

On February 12, 1977, VO-1 was given a final precision trim in preparation for a number of close encounters with Phobos. The period of VO-1 (~22^h 57^m 30^s) was designed to be 3:1 commensurate with the period of the Martian moon such that encounters would occur on every third orbit of Phobos. In 12 of these encounters the closest spacecraft approach to the natural satellite was less than 200 km. The closest approach distance for the complete encounter sequence was 88 km on February 20, 1977.

The primary purposes for this experiment were to acquire close-up photography of the surface and to provide an opportunity to estimate the mass, and ultimately the density of Phobos — data which are relevant to a determination of the origin and evolutionary history of the satellite (Ref. 20). This section will discuss the real-time and postflight estimates of the mass of Phobos obtained by the SATOD Team.

B. Encounter Geometry

The spacecraft-Phobos encounter geometry is shown in Fig. 46 (excerpted from Ref. 20). Phobos is seen from the approaching spacecraft in a coordinate system with the T-axis parallel to the Mars equatorial plane. The direction to the Sun is about 16 deg above T and 37 deg into the paper while Mars is 63 deg below T and 50 deg out of the paper. The dots above

and to the right of Phobos indicate the points of closest flyby for each passage during the encounter period.

For comparison, the encounter sequence that would have occurred if Phobos had been massless is also shown. The difference between the encounter sequences is primarily due to the cumulative effect of the individual orbital period changes occurring at each encounter, which for this sequence all tend to increase the orbital period.

C. Preflight and Real-Time Estimates

The method of analysis used here requires knowledge of the mean period change (ΔP) of the orbiter induced by the Phobos encounter. When viewed relative to inertial space the effect of the mass of Phobos on the spacecraft velocity vector at encounter is to change its direction. The equations relating the spacecraft velocity change and the orbital period change are approximately given by (see Fig. 47).

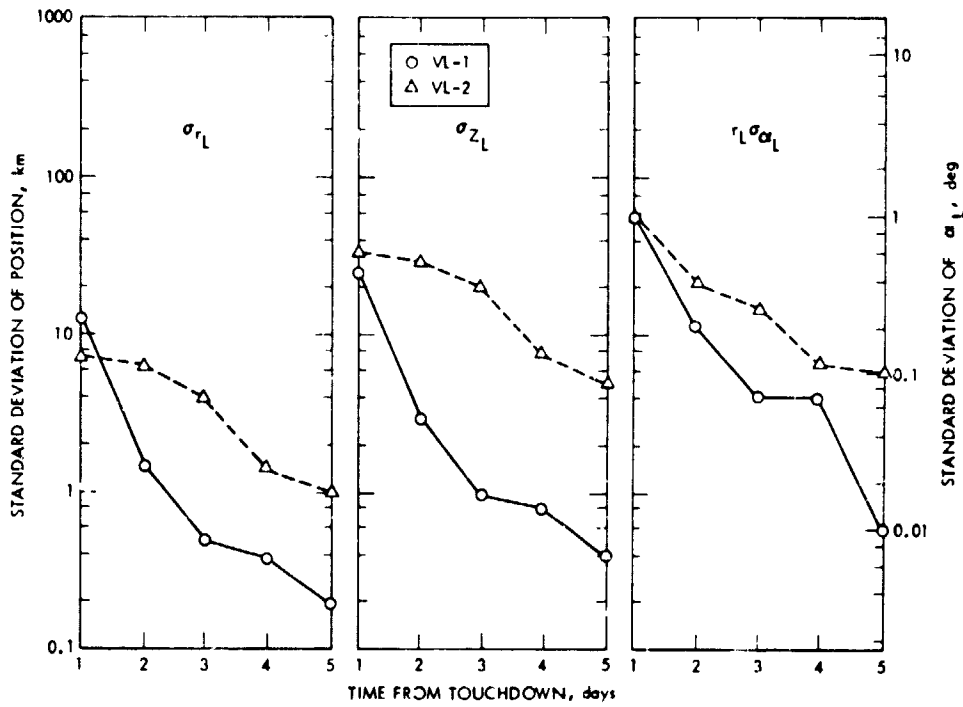
$$\Delta V = - (\Delta V_T) \cdot \hat{v} = - \frac{2\mu_P}{bV_R} (\hat{b} \cdot \hat{v}) \quad (18)$$

$$\Delta P = - \frac{6\mu_P a PV}{\mu_\delta b V_R} (\hat{b} \cdot \hat{v}) \quad (19)$$

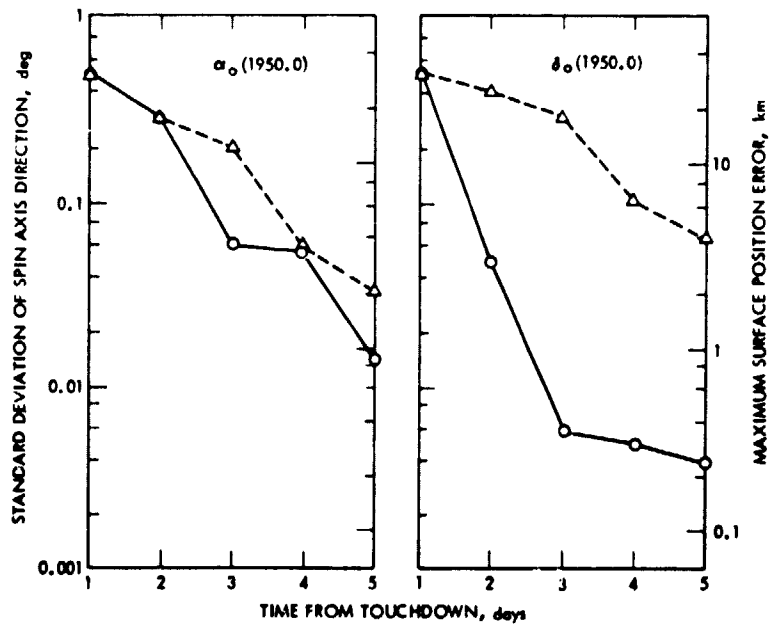
where

- \mathbf{V} Mars relative spacecraft velocity vector (in or out)
- $\Delta \mathbf{V}_T$ total change in spacecraft velocity
- ΔV component of $\Delta \mathbf{V}_T$ along the original velocity vector \mathbf{V}
- V_R spacecraft-Phobos relative velocity at closest approach
- μ_P GM of Phobos
- μ_δ GM of Mars
- b Phobos-spacecraft vector at closest approach
- a semimajor axis of spacecraft orbit relative to Mars
- P period of spacecraft orbit
- $(\hat{\quad})$ indicates unit vector

Equations (18) and (19) are accurate to within 1 or 2 percent. Figure 48 presents a change in the spacecraft orbital period as a function of the magnitude and direction of \mathbf{b} . Also



(a) VL POSITION



(b) MARS SPIN AXIS DIRECTION

Fig. 45. Standard deviations of Viking lander position and Mars spin axis direction from radio tracking (in-flight)

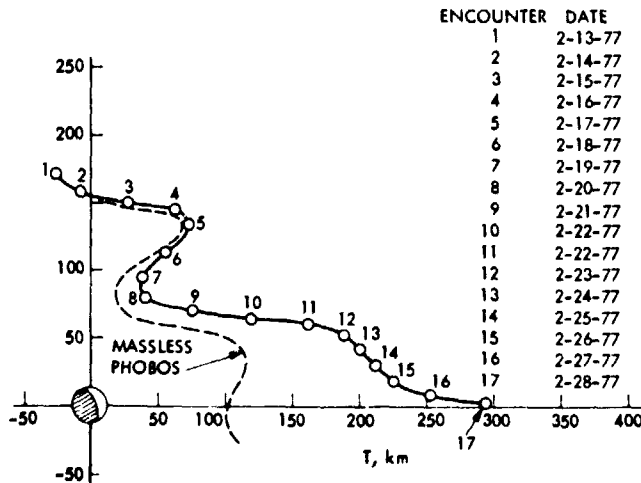


Fig. 48. Phobos encounters. The distance of VO-1 to Phobos is shown for each flyby (1 flyby/ -23h)

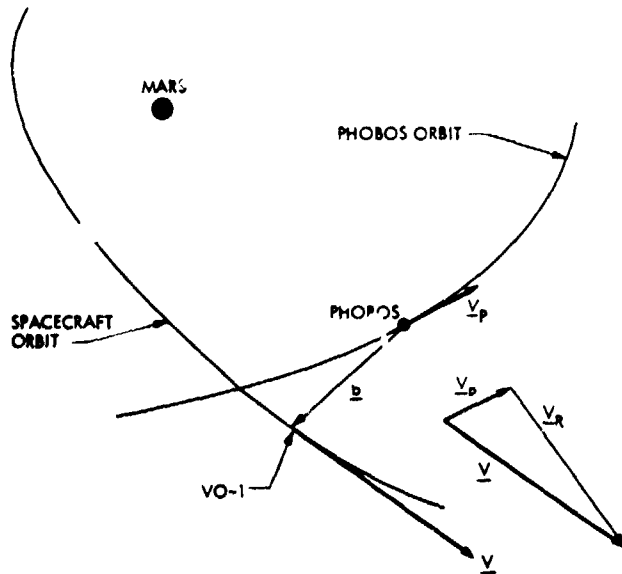


Fig. 47. VO-1 and Phobos encounter geometry

shown are the actual encounter points in the b-plane for the Viking encounter sequence for $\mu_p = 0.66 \times 10^{-4} \text{ km}^3/\text{s}^2$. As seen from this figure, the maximum period change for the Viking encounters was 1.2 s.

In addition to the direct effect just described there is also a period change due to the offset of Mars center of mass from the barycenter of the Mars-Phobos system. This is actually a resonance effect for the case at hand since the period of VO-1 is 3:1 commensurate with the period of Phobos. The spacecraft orbit period change is approximately described by

$$\dot{P} = -18\pi \frac{a_p}{a} \frac{\mu_p}{\mu_\delta} \left\{ F_{110}(I) G_{102}(e) \sin [\omega + 3M + (\Omega - \theta_p)] + F_{111}(I) G_{114}(e) \sin [-\omega + 3M + (\Omega - \theta_p)] \right\} \quad (20)$$

where $F(I)$ and $G(e)$ are the inclination and eccentricity functions described by Kaula (Ref. 12). Evaluating Eq. (20) yields

$$\dot{P} \approx -20 \frac{\mu_p}{\mu_\delta} \text{ s/rev}$$

which for $\mu_p = 6.6 \times 10^{-4} \text{ km}^3/\text{s}^2$ yields $\Delta P = -0.03 \text{ s/rev}$.

Perturbations due to the gravity field of Mars also produce changes in the mean period of VO-1 upon each periapsis passage. As a result, perturbations due to Phobos are not easily distinguished from Mars' gravity effects on the period evolution of VO-1. This may be qualified by noting that a component of the change in velocity (ΔV_T) incurred at encounter may be directly observable in the two-way doppler data. Figure 49 presents the magnitude of the doppler shift in a manner analogous to the ΔP information in Fig. 48. Such an observation would provide a uniquely separable signature which could lead to a ready mass estimate. Unfortunately, the maximum change in the VO-1 range-rate of 4 mm/s is largely obscured by the observed data noise level of 2 mm/s. The solar plasma contributes to the data noise as well as inducing systematic signatures into the data. However, the methods employed here are not sensitive to these effects.

The perturbation in the mean period of VO-1 due to the mass of Phobos can be considered large when compared to an estimated 0.1-s error in predicted ΔP due to uncertainties in the gravity field alone. The change in mean period from orbit to orbit can be determined from two-way doppler data to an accuracy of $\pm 0.03 \text{ s}$. Thus, any systematic deviation beyond $\pm 0.1 \text{ s}$ in the predicted ΔP can be attributed to an error in μ_p or in the distance of closest approach b . An error in b of 5 km resulting from Phobos and VO-1 ephemeris errors would produce a contribution to ΔP which would be less than 6% of the effect produced by the Phobos mass. By assuming that the difference between the observed and predicted values of ΔP on the first four encounters was due solely to an error in μ_p , it was concluded that the a priori GM of Phobos ($10^{-3} \text{ km}^3/\text{s}^2$) should be reduced to $5.5 \times 10^{-4} \text{ km}^3/\text{s}^2$. The observed period change on the fifth encounter was consistent with this value. This estimate permitted predictions of sufficient accuracy to

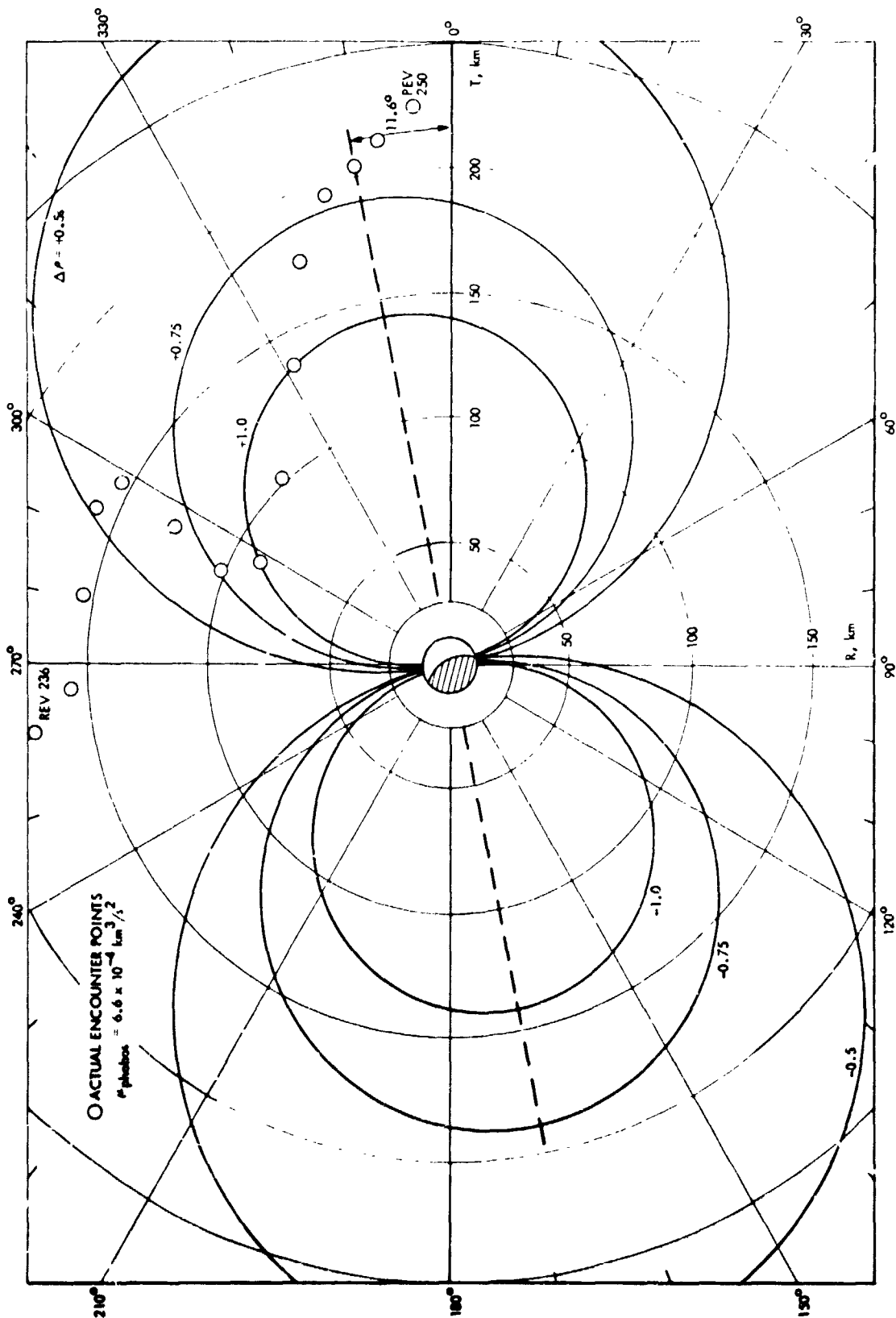


Fig. 48. Orbit period change vs B-plane encounter location

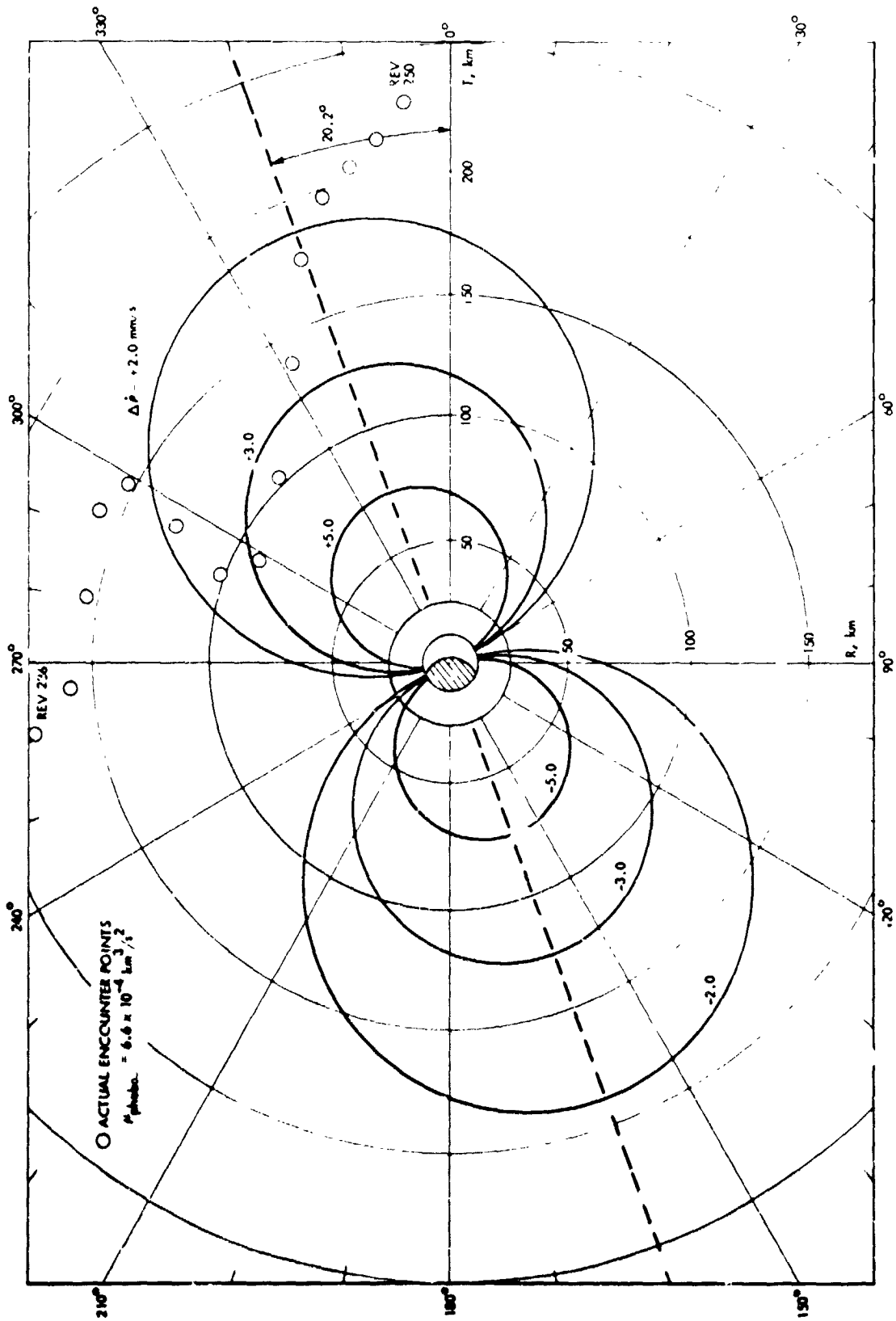


Fig. 48. Range-rate change vs B-plane encounter location

satisfy imaging requirements throughout the remaining encounter sequence.

D. Postflight Estimates

Most of the postflight analysis was confined to separating the Mars gravity effects from the perturbations of Phobos. Two rather distinct methods will be discussed. The first method uses the analytical expressions given by Eqs. (19) and (20) and is similar to that used for the real-time analysis. A correction is applied to the mass by assuming that the error in ΔP results solely from an error in μ_P , while the gravity errors contribute only in a random manner. Table 11 shows some of the salient parameters used in this calculation for 14 close encounters. Additional quantities which are essentially invariant between encounters are the semimajor axis ($a \approx 19,510$ km), spacecraft-Mars relative velocity ($V \approx 2.6$ km/s) and spacecraft-Phobos relative velocity at closest approach ($V_R \approx 2.20$ km/s).

The data ($\delta\Delta P$) is shown both before and after the fit, based on an a priori value of $\mu_P = 5.5 \times 10^{-4}$ km³/s². With an assumed systematic gravity error equivalent to $\delta\Delta P = 0.1$ s, the best estimate obtained by this method is $\mu_P = (6.63 \pm 0.8) \times 10^{-4}$ km³/s².

The second method, which is designed to minimize estimation errors arising from inaccuracies in the Mars gravity model, involves processing two consecutive revolutions of VO-1

doppler data using gravity coefficients tailored to the region beneath the included periapsis. This method was applied to periapsis number P242, which corresponded to an encounter with one of the largest Phobos-induced period perturbations. The procedure used to tailor the field was to estimate spherical harmonic coefficients based on two revolutions of data which were selected such that the Phobos perturbations were negligible and the central subperiapsis point coincided with that of P242. This opportunity occurred at periapsis number P257, over which a sixth degree and order gravity field for Mars was estimated. It was felt that this field would all but remove the gravity errors, thereby uncoupling the effects of the gravity of Mars and the mass of Phobos. Use of this local field resulted in an estimate of $\mu_P = (6.57 \pm 0.7) \times 10^{-4}$ km³/s², which is in excellent agreement with the results obtained via the analytical technique just described.

E. Concluding Remarks

The mass of Phobos has also been determined by Tolson, et al. (Ref. 22) by processing three revolutions of tracking data and solving for the spacecraft state and GM of Phobos. The result of their data analysis was an estimate of $(7.3 \pm 0.7) \times 10^{-4}$ km³/s² for GM of Phobos. It is significant that the results presented here are consistent with theirs within the quoted uncertainties, since different methods of analysis were used.

Table 11. Phobos encounter parameters

Periapsis number	b , km	$\hat{b} \cdot \hat{V}$	$\partial\Delta P/\partial\mu_P$, s ³ /km ³	$\delta\Delta P$, s ($\mu_P = 5.5 \times 10^{-4}$ km ³ /s ²)	$\delta\Delta P$, s ($\mu_P = 6.63 \times 10^{-4}$ km ³ /s ²)
236	174.5	-0.025	38.7	-0.2361	-0.2393
237	158.9	-0.110	185.7	0.0025	-0.0130
238	153.1	-0.283	496.0	-0.1576	-0.1990
239	156.9	-0.439	748.6	-0.0296	-0.0921
240	152.8	-0.499	873.3	0.0161	-0.0568
241	126.6	-0.470	995.4	-0.0683	-0.1514
242	102.8	-0.416	1087.7	-0.0250	-0.1158
243	88.9	-0.486	1470.7	0.2557	0.1329
244	103.8	-0.661	1709.9	0.2540	0.1112
245	136.8	-0.744	1455.5	0.0761	-0.0464
246	173.8	-0.767	1178.4	0.2480	0.1496
247	194.4	-0.774	1061.8	0.1010	0.0102
248	203.9	-0.775	1013.7	0.2264	0.1417
249	212.8	-0.773	949.9	0.2359	0.1566

VIII. Conclusions and Recommendations

The experiences of the SATOD Team have resulted in several observations and recommendations of interest to future orbital operations. These include:

- (1) Constrained OD techniques as discussed in Section IV appear to be a reliable means of obtaining rapid post-maneuver solutions and warrant further study. These techniques also are useful for routine OD solutions when limited tracking data exists such as often happened during the Viking Extended Mission.
- (2) Combination of short arc gravity solutions as discussed in Section V proved to be a reliable and relatively inexpensive (compared to a single long arc solution) means of obtaining a global gravity field.
- (3) Use of demand terminals, as opposed to batch loading used on Mariner 9, was essential for the timely performance of OD functions for the four Viking spacecraft.
- (4) If DRVID and S/X calibrations are to be used operationally, an automated option should exist in the OD software.
- (5) The procedure for producing normal points (Section IV) should be reevaluated and automated to a greater extent.
- (6) Period change and doppler shift plots for satellite flybys as discussed in Section VII are extremely useful for optimally choosing B-plane encounter conditions.

References

1. Rourke, K. H. et al., "The Determination of the Interplanetary Orbits of Viking 1 and 2," AIAA 15th Aerospace Sciences Meeting, Los Angeles, Calif., Jan. 1977.
2. Born, G. H. et al., "The Determination of the Satellite Orbit of Mariner 9," *Celestial Mechanics*, Vol. 9, pp. 395-414.
3. O'Neil, W. J. et al., *Mariner 9 Navigation*, Technical Report 32-1586, Jet Propulsion Laboratory, Pasadena, Calif., Nov. 13, 1973.
4. O'Neil, W. J. et al., "Viking 1975 Navigation Plan," Vol. I and Supplement I, Miller, J. K. (technical editor), Viking 75 Orbiter Control Document 612-32, Jet Propulsion Laboratory, Pasadena, Calif., May 1, 1975 (an internal document).
5. Jordan, J. F., Melbourne, W. G., and J. D. Anderson, "Testing Relativistic Gravity Theories Using Radio Tracking Data from Planetary Orbiting Spacecraft," COSPAR Space Research XIII, Akademie - Verlag, 1973.
6. Boggs, D. H., "A Partial-Step Algorithm for the Nonlinear Estimation Problem," *AIAA J.*, Vol. 10, No. 5, pp. 675-679, May 1972.
7. Moyer, T. D., *Mathematical Formulation of the Double-Precision Orbit Determination Program (DPODP)*, Technical Report 32-1527, Jet Propulsion Laboratory, Pasadena, Calif., May 1971.
8. Boggs, D. H., "The General Problem of Three Bodies: Periodic Orbits and Their Stability," Ph.D. Dissertation, UCLA, pp. 53-76, 1975.
9. Hanson, R. J., and Lawson, C. L., "Extensions and Applications of the Householder Algorithm for Solving Linear Least Squares Problems," *Mathematics of Computation*, Vol. 23, No. 108, pp. 787-812, Oct. 1969.
10. Greville, T. N. E., "The Pseudo-Inverse of a Rectangular Matrix and Its Applications to the Solution of Systems of Linear Equations," *SIAM Rev.*, Vol. 1, pp. 38-43, Jan. 1959.

11. Jordan, J. F., and Lorell, J., "Mariner 9. An Instrument of Dynamical Science," *Icarus*, Vol. 25, pp. 146-165, 1975.
12. Kaula, W. M., *Theory of Satellite Geodesy*, pp. 30-37. Blaisdell, Waltham, Mass., 1966.
13. Sjogren, W. L., and Lorell, J., "Mars Gravity Based on a Short-Arc Technique," *J. Geophys. Res.*, Vol. 80, No. 20, pp. 2899-2908, 1975.
14. Daniels, E. F., Tolson, R. H., and Gajcynski, J. P., "Spherical Harmonic Representation of the Gravity Field of Mars Using a Short-Arc Technique," *J. Spacecraft Rockets* (in press).
15. Born, G. H., "Mars Physical Parameters as Determined from Mariner 9 Observations of the Natural Satellites and Doppler Tracking," *J. Geophys. Res.*, Vol. 79, No. 32, pp. 4837-4844, 1974.
16. Reasenbergl, R. D., Shapiro, I. I., and White, R. D., "The Gravity Field of Mars," *Geophys. Res. Letters*, Vol. 2, No. 3, pp. 89-93, 1975.
17. deVaucouleurs, G., Davies, M. E., and Sturms, F. M., Jr., "Mariner 9 Areographic Coordinate System," *J. Geophys. Res.*, Vol. 78, No. 20, July 10, 1973.
18. Tolson, R. H., Blackshear, W. T., and Anderson, S. G., "Orbit and Position Determination for Mars Orbiters and Landers," *J. Spacecraft Rockets*, Vol. 13, No. 9, pp. 1095-1100, Sept. 1970.
19. Christensen, E. J., "Martian Topography Derived from Occultation, Radar, Spectral, and Optical Measurements," *J. Geophys. Res.*, Vol. 80, No. 20, July 10, 1975.
20. Tolson, R. H., et al., "Viking First Encounter of Phobos: Preliminary Results," *Science*, (in publication).
21. Kaula, W. M., *Theory of Satellite Geodesy*, Blaisdell, Waltham, Mass., 1966.
22. Tolson, R. H., et al., "The Mass of Phobos," *Geophys. Res. Letters*, Vol. 4, No. 12, Dec. 1977.

Maneuver Analysis

R. T. Mitchell, D. L. Farless, J. K. Miller, G. R. Hintz,
M. J. Adams, N. P. Dwivedi, and D. L. Gray

I. Interplanetary Maneuvers

At launch both Viking spacecraft were targeted to aim-points at Mars which were biased away from the final desired encounters to insure that the first maneuver on each vehicle would exceed a required minimum ΔV (applicable only to the first burn on each spacecraft), have a favorable attitude for communications during the first burn, and satisfy the planetary quarantine (PQ) constraint. As a result, it was virtually guaranteed that each vehicle would need at least one mid-course maneuver; and because of the tight trajectory control requirements at encounter, there was a high probability that Viking would be the first mission to Mars requiring more than one interplanetary maneuver.

The design of the required encounter trajectories for Viking was uniquely complex owing to the manner in which these trajectories were dependent on the landing site coordinates, specified sun elevation angle (SEA) at landing, and number of revs in Mars orbit from insertion to landing. Consequently, although the midcourse software targeted only to the classical B-plane parameters, the total problem to be solved at each maneuver was one of targeting to a final orbit from which separation could occur. Details of this process are covered in depth under Mars Orbit Insertion later in this chapter.

A. Choice of Maneuver Dates

For planning purposes, a maneuver strategy was developed which allowed for a maximum of two earth departure and two approach maneuvers for each spacecraft. As it turned out, only one of each was needed (with one exception due to a spacecraft malfunction) due to the near nominal performance of both the spacecraft and the orbit determination process. One of the significant early tasks was to specify nominal dates for the maneuvers. Since a wide spread of launch dates and encounter dates was considered, near-Earth maneuver dates were stated relative to launch date L , and near-Mars maneuver dates were stated relative to encounter date E . A chart of the dates chosen is shown in Table 1.

1. **Near-Earth maneuvers.** Several factors were considered in choosing dates for near-Earth maneuvers, the most important of which were:

- (1) The guidance singularity resulting from the type II trajectories.
- (2) Possible propellant tank overpressure due to solar heating.
- (3) Mission rules on spacing of activities.

Table 1. Prelaunch plan for midcourse maneuver locations

Spacecraft	Near-Earth		Near-Mars	
	Midcourse-1	Midcourse-2	Midcourse-3	Midcourse-4
Viking 1	L+7	L+35	E-30	E-10
Viking 2	L+13	L+42	E-30	E-10

The primary motivation for planning the first maneuver on Viking 1 prior to the launch of Viking 2 was to observe the propulsion system performance in space and have the opportunity to make any modifications that might be indicated on the second vehicle before its launch. A second consideration was to simplify the operational timelines by having the first vehicle's near-launch activities essentially complete by the time the second was launched. A third consideration, although of little importance here because of the slowly changing sensitivities, was that early maneuvers generally require a smaller propellant expenditure. The earliest possible maneuver date was constrained by the time needed for fuel and oxidizer tank warmup prior to first pressurization. Since perihelion occurred after launch, significantly higher tank temperatures could develop, and if the tanks were already pressurized, with the small initial tank ullage, an overpressure condition could develop with possible overpressure diaphragm rupture, venting of pressurant gas, and lowered reliability for subsequent pressure control. Small resistance heaters were provided to raise the tank temperatures and maintain them at a steady design value, prior to pressurization, but these heaters required many days after launch to heat the tanks to a safe temperature that would limit the expected overpressure. The resulting first maneuver dates listed in Table 1 are different for Vikings 1 and 2, due partly to the difference in expected initial ullage.

A second near-Earth maneuver date was also scheduled, in case it should be needed to compensate for delivery errors from the first maneuver or to remove a first maneuver PQ bias. The date for the second maneuver was set late enough to guarantee that, for any of the trajectories under consideration, the guidance singularity would occur before the second maneuver and not so near as to more than double the propellant required (based on the cost of the same maneuver a few days after the first maneuver). An additional benefit of the late second maneuver date was the expected availability of the 33-1/3 bps telemetry channel (guaranteed after day $L+20$).

2. Near-Mars maneuvers. The following factors affected the choice of near-Mars maneuver dates:

- (1) Maneuver capability decreases approximately linearly as encounter approaches.
- (2) It was desired to postpone repressurizing the propulsion system as late as possible prior to MOI.

- (3) Orbit knowledge improves as encounter approaches, especially if optical data are available.

- (4) There was a minimum turnaround time constraint between the last midcourse maneuver and insertion into Mars orbit (MOI).

The decrease in maneuver capability as encounter approaches dictates that a near-encounter midcourse be performed early in this phase if there are large known errors to correct. However, the desire to leave the propulsion system pressurized after this maneuver limited the date to within a few weeks of encounter. $E-30$ days was chosen as a compromise between these two factors. As it happened, there were no errors large enough to require an early approach maneuver, and the $E-30$ day opportunity was never used.

Since the orbit determination accuracy improves as encounter approaches, the trajectory control error is minimized by waiting as long as possible to do the maneuver. The limiting factor is the minimum turnaround time required after the maneuver to redetermine the orbit solution, finalize the design of the MOI maneuver, and prepare the necessary commands for the spacecraft. The nominal time of the last maneuver was set to $E-10$ days, which allowed for an emergency "recovery" maneuver at $E-5$ days.

B. Launch

Viking 1 was launched on August 20, 1975, and targeted to arrive at Mars on June 20, 1976. The launch vehicle injection accuracy was well within the 99% dispersion ellipse as shown in Fig. 1, and the launch+7-day Midcourse Correction Requirement (MCR) to the targeted aimpoint at launch was 3.5 m/s.

Viking 2 was launched on September 9, 1975, and targeted to arrive on August 8, 1976. The injection accuracy is shown in Fig. 2, and the launch+7-day MCR was 5.1 m/s.

C. Emergency Early Maneuver Strategy

Contingency planning was done to define a set of alternate (reduced) missions in case of an anomalous spacecraft injection. These plans involved using a portion of the spacecraft propellant to correct the spacecraft trajectory, in general not back to nominal, but to an optimum energy and asymptote direction combination that gave a trajectory passing near Mars up to perhaps several days different in arrival time from nominal. The propellant remaining would then determine the alternate mission, ranging from a reduced capability for Mars orbit trims all the way down to a simple flyby of Mars by the orbiter only. As part of this contingency planning, an

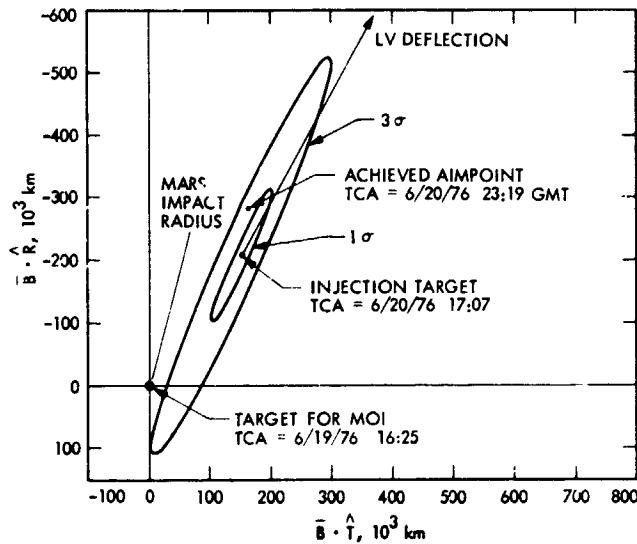


Fig. 1. Viking 1 injection dispersions

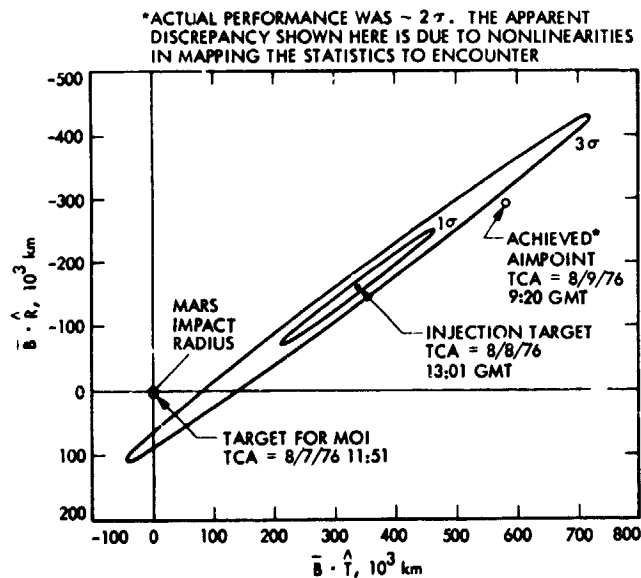


Fig. 2. Viking 2 injection dispersions

operational Emergency Early Maneuver (EEM) strategy was developed.

Since the mission would have been constrained by limited propellant under such contingency conditions, the maneuver would have had to be done at the most efficient time possible. The following considerations made injection plus 4 hours ($t+4$ h) the time chosen for an EEM maneuver:

- (1) The most likely launch vehicle anomaly correctable with the spacecraft propulsion system is an underburn or overburn with correct thrust pointing.

- (2) For a simple injection underburn or overburn, sufficiently accurate spacecraft turns for a corrective maneuver can be determined before launch for a given launch date and encounter date.
- (3) With spacecraft command files for both the underburn and overburn cases available prelaunch and only the ΔV magnitude command to be determined after launch, the earliest the maneuver can be performed is 4 hours after injection. This includes the time required both for the ΔV determination and for spacecraft personnel to generate and transmit the appropriate commands to the spacecraft.
- (4) For an injection under/over burn, a maneuver at $t+4$ hours saves about 15% of the cost of performing the same correction several days after injection.

Figure 3 shows a representative launch energy plot demonstrating how the decision would have been made on whether or not to execute an EEM. Achieved injection energy is shown as a function of time from the start of the Centaur second burn, starting at about $-60 \text{ km}^2/\text{s}^2$ in the parking orbit and reaching $0 \text{ km}^2/\text{s}^2$ (parabolic escape) in about 270 seconds. The next 50 seconds was the key time for evaluating the Centaur performance. In region 1, a near-nominal mission could be achieved with a maneuver at the normal first mid-course time, although at the low end of this interval there would have been little or no propellant left for site retargeting or for any extended mission activities. In region 2, the propellant savings resulting from the early maneuver would be needed in order to land from orbit. In region 3, it would not be possible to get the lander into orbit in any event; and a

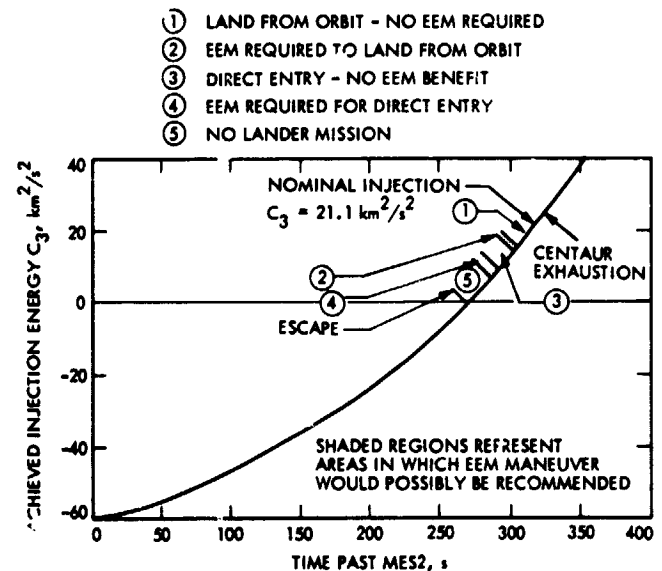


Fig. 3. Viking 1 EEM energy envelopes

direct entry from the approach hyperbola, followed by insertion of the orbiter alone did not require the ΔV savings of an EEM. In the fourth interval, however, the EEM savings were required to do a direct entry. If the Centaur left the spacecraft in region 5, it would not have been possible to get the lander to Mars. Regions 2 and 4 then represent energy deficiencies where an EEM would have been of significant benefit to the mission. A Centaur burn to depletion in this case would have been included in region 1, but could have duplicated at least regions 2 and 3 for some trajectories with lower injection energies.

Operationally, for each candidate launch date, an average thrust pointing direction for a total of four subsequent launch dates over the range of possible correctable energy deficiencies was determined, and corresponding turn sets were delivered to spacecraft personnel in preflight preparation for implementing

the emergency maneuver. In actual flight, both launches were executed normally and no contingency measures were required.

D. Summary of Maneuvers Performed

Three interplanetary maneuvers were performed by Viking 1 and two by Viking 2. A summary of all the targeted and achieved aimpoints is given in Table 2, and plotted in Figs. 4-6. Data on the maneuver parameters, both ideal and commandable, are given in Table 3. In Table 3 the spacecraft cone and clock angles of the Earth are shown only for the burn (i.e., end-of-turns) orientation. The traces of the Sun and Earth in spacecraft cone and clock coordinates during the turns for the first maneuver on Viking 1 are shown in Fig. 7 as representative of the type of data provided for turn constraint analysis.

Table 2. Targeted and achieved encounter conditions

Parameter	B.R. km	B.T. km	/B/, km	θ , deg	Date 1976	Closest approach time, GM F, (h:min)	ΔV , m/s
Viking 1							
Injection							
Targeted	-210270	152720	259880	-54.0	6/20	17:07	
Achieved	-277130	164490	322270	-59.3	6/20	23:19	
1st midcourse							
Targeted	7119	6643	9737	47.0	6/19	16:24	4.684
Postmaneuver estimate	6122	6996	9296	41.2	6/19	16:28	
Pre-encounter estimate	5774	7289	9299	38.4	6/19	16:31	
AM/C1							
Targeted	7232	6861	9969	46.5	6/19	20:38	50.540
Achieved	7291	6700	9902	47.4	6/19	20:38	
AM/C2							
Targeted	7292	6945	10070	46.4	6/19	22:54	60.142
Achieved	7277	6919	10041	46.4	6/19	22:54	
Guidance success							
99% required			± 700	± 5		± 15 min	
Viking 2							
Injection							
Targeted	-163290	339730	376940	-25.7	8/08	13:01	
Achieved	-301780	581980	655570	-27.4	8/09	9:20	
1st midcourse							
Targeted	3100	11550	11959	15.0	8/07	11:52	8.108
Postmaneuver estimate	1086	15560	15598	4	8/07	12:18	
Pre-encounter estimate	870	16199	16222	3.1	8/07	12:22	
AM/C							
Targeted	-2384	9062	9370	-14.7	8/07	11:45	9.223
Achieved	-2424	9058	9377	-15.0	8/07	11:45	
Guidance success							
99% required			± 500	± 7		± 15 min	

Table 3. Maneuver data

Maneuver	Ignition epoch, Time/GMT	RY turns, Ideal/implemented	ΔV , Ideal/implemented	Burn orientation, Cone/clock
Viking 1				
1st midcourse	8/27/75	-226.658, -79.500	4.6949	51.84
	18:30	-226.773, -79.538	4.6844	284.76
AM/C1	6/10/76	104.054, -97.160	50.5291	117.92
	11:00	104.038, -97.085	50.5396	22.17
AM/C2	6/15/76	106.386, -97.038	60.1234	118.02
	14:00	106.358, -97.088	60.1424	23.63
Viking 2				
1st midcourse	9/19/75	102.594, -53.243	8.1125	28.59
	16:30	102.713, -53.223	8.1085	239.55
AM/C1	7/28/76	-85.262, -40.145	9.2261	31.97
	01:00	-85.303, -40.019	9.2226	80.96

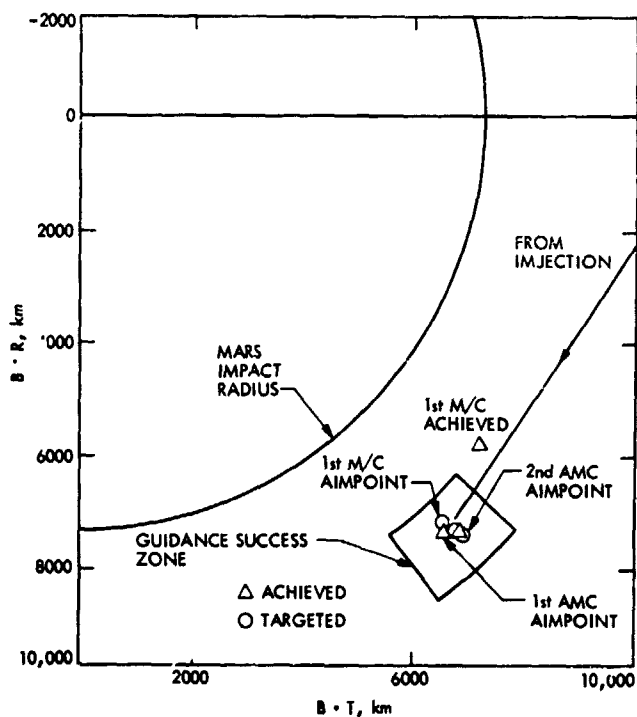


Fig. 4. Viking 1 midcourse aimpoints

The final target encounter parameters for each spacecraft were determined such that the post-insertion requirements on the orbital elements could be achieved with near minimum ΔV expenditure at insertion. A guidance success region was then defined about the nominal encounter point such that, for any delivery within this region, the nominal mission could be completed within the 99% ΔV budget available. Figures 4, 5,

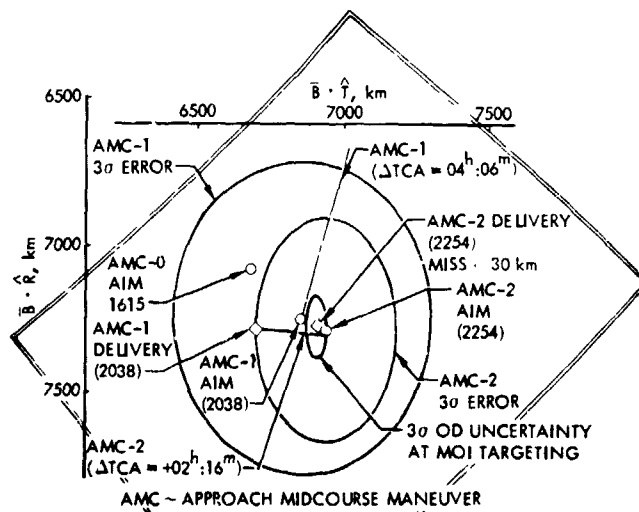


Fig. 5. Viking 1 midcourse aimpoints, detail

and 6 show this guidance success region for each mission, as well as targeted and actual encounter conditions. The boundary of this region is also indicated in Table 2.

1. Near-Earth midcourse maneuvers. Only one near-Earth maneuver was required for each spacecraft, and was performed in each case on the first scheduled maneuver date. For Viking 1 this maneuver was targeted directly to the nominal Mars encounter conditions. The planetary quarantine allocation was easily met without biasing, and no significant mission benefits would have resulted from biasing the first maneuver aimpoint. Reconstruction estimates of the maneuver actually executed indicated a pointing error of 0.8σ of the a priori expected error and a magnitude error of only 0.03σ . The

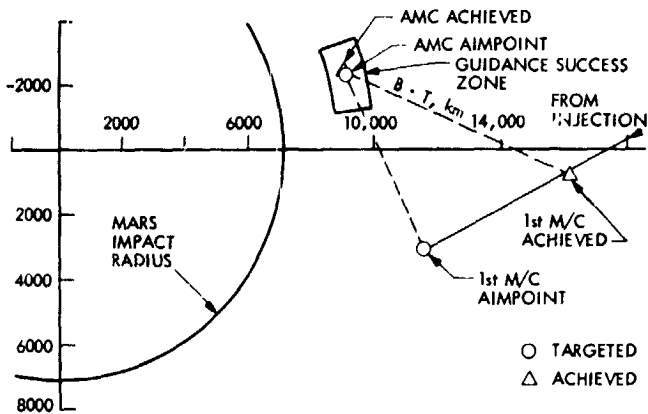


Fig. 6. Viking 2 midcourse aimpoints

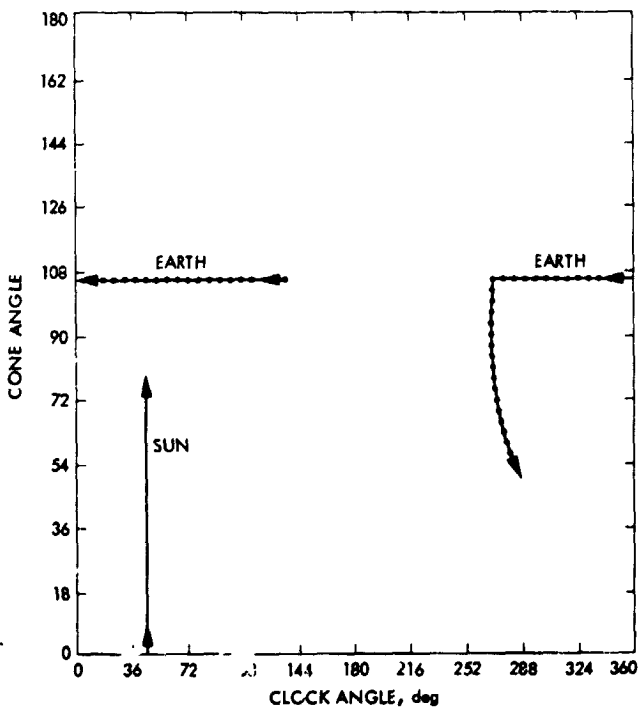


Fig. 7. Viking 1 first midcourse Earth/Sun cone and clock angles during turns

targeted and achieved aimpoints are shown in Figs. 4 and 5. The expected delivery accuracy is broken down into the maneuver execution component and the orbit determination component in Fig. 8.

For Viking 2, the planetary quarantine requirement could have been met by targeting the first maneuver directly to the final aimpoint only because of the very high reliability of the spacecraft propulsion system. This would have led to expected post-maneuver control dispersions as shown in Fig. 9 and a

20% probability of ending up on an impacting trajectory. Such an event would have been satisfactory as far as meeting the formal requirements of the planetary quarantine constraint. However, it would have been sufficiently unsettling to leave the spacecraft on an impact trajectory for the better part of a year, that in all likelihood a second near-Earth maneuver would be performed to get off such a trajectory. On the other hand, at least one near-encounter maneuver was almost certainly going to be required whether the first maneuver was biased or not. Also, there was only a very low probability that a second near-Earth maneuver would be required for any reason other than to take the spacecraft off of an impacting trajectory. It was, therefore, decided to bias the first maneuver aimpoint such that the probability of an impacting trajectory resulting from the control dispersions would be less than 1%.

Other criteria for selecting a biased aimpoint, in addition to the 1% probability of impact figure mentioned above, were to minimize the additional propellant expenditure because of the bias, to insure an attitude for the near-encounter maneuver that would be favorable for communications during the burn, and to have most, if not all, delivery dispersions be such that MOI would be possible, albeit far from nominal, without performing another midcourse should this become necessary for whatever reason. For a significant portion of the delivery dispersions about the *unbiased* aimpoint, this "MOI protection" was *not* available due to the excessive ΔV requirements to achieve a suitably high periapsis altitude on those cases where the hyperbola would impact. Figure 10 shows the final biased aimpoint selected and the control dispersions. Only about 2% of the population, those cases with B out around 20,000 km or more, posed ΔV problems for achieving some kind of orbit insertion. Although not apparent in Fig. 10, the maximum ΔV penalty for biasing was about 5 m/s. Also, an approach maneuver to the final aimpoint from any trajectory dispersed within 3σ from the biased aimpoint would have an Earth cone angle in the burn attitude of less than 117 deg, permitting use of the high-gain antenna without having to put it in the flipped position.

2. Near-Mars maneuvers. During the planning stages of the Viking mission, the option was maintained to schedule two near-encounter maneuvers for each vehicle, one at $E-30$ days and one at $E-10$ days. The earlier maneuver was to correct any large navigation errors or to do any retargeting that would require large ΔV 's, resulting in unacceptable control accuracy for the "last" pre-encounter maneuver. The 10-day maneuver was to be a precision correction based on the latest trajectory estimate available at that time.

The near-Earth maneuver for Viking 1 was executed well within the expected control errors, but the execution errors, in conjunction with unmodeled nongravitational accelerations

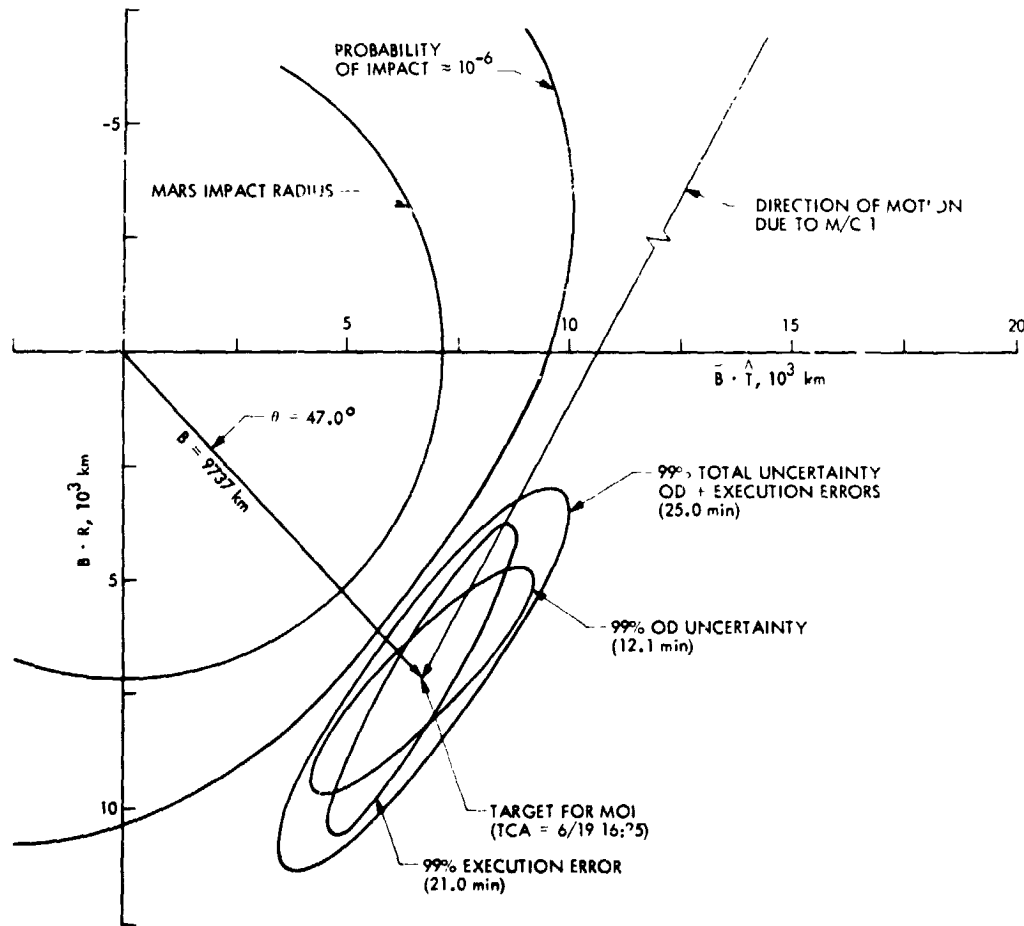


Fig. 8. Viking 1 midcourse 1 dispersions

during the subsequent interplanetary flight, gave an encounter trajectory well outside the defined guidance success region as shown in Fig. 4. A maneuver at $E-10$ days to correct the trajectory to the nominal encounter point and arrival time required just under 4 m/s. The plan was to do the maneuver at this time, eliminating a maneuver at $E-30$ days. However, when the propulsion system was pressurized prior to this planned maneuver, a leak in the pressure regulator was noted that would have built up pressure in the fuel and oxidizer tanks to an unacceptable level prior to the MOI burn. For spacecraft reliability reasons, it was decided not to reclose the pressurant line, but rather to perform a large motor burn (50 m/s) that would assure opening the pressure regulator in the hope that it would reseal properly and not leak. By designing this maneuver to change primarily the arrival time, the impact on the mission would be minimized. The post-insertion timing problem could be compensated for by altering the target orbital period at insertion, and by reducing the orbital energy (i.e., approach speed) with this maneuver. About 50% of the propellant

expended in this large maneuver would be saved by the reduced velocity requirement for MOI.

Such a maneuver was designed and implemented at $E-9.5$ days. The pressure regulator continued to leak at about the same rate after this maneuver, and the pressure buildup prior to MOI was still going to be unacceptable. Accordingly, a second maneuver similar to the first was designed, this time not in hope of eliminating the leak, but rather to create enough ullage space to keep the pressure buildup prior to MOI down to an acceptable level.

At $E-4.5$ days, a maneuver of about 60 m/s was executed and was successful in its objective of providing sufficient ullage volume, and no spacecraft problems were experienced due to excessive pressurization prior to MOI. The B -plane target conditions for these two near-encounter maneuvers were altered from the nominal in order to optimize the MOI for the reduced approach velocity and higher period in the post-MOI

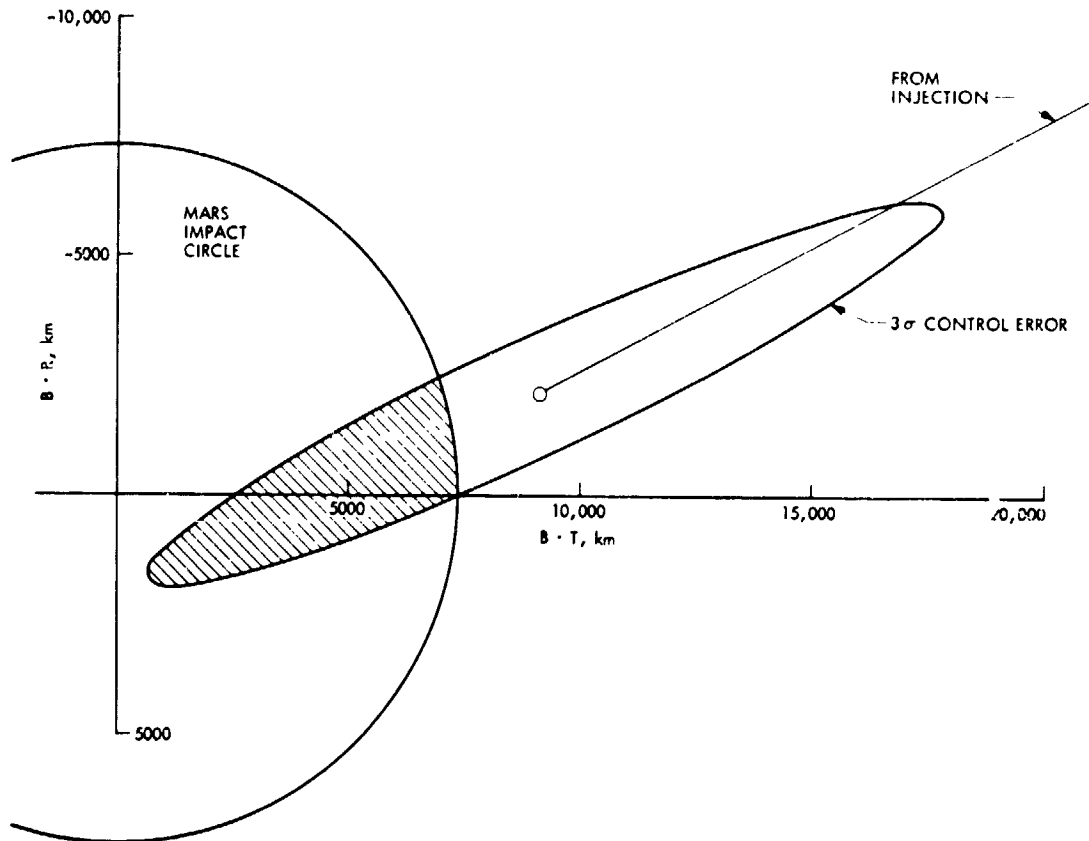


Fig. 9. Viking 2 unbiased first maneuver

orbit. The targets and achieved conditions are shown in Table 2.

For Viking 2, the trajectory change required with the near-encounter maneuver was relatively large, owing to the intentional bias of the near-Earth maneuver. In addition, there was a shift in the estimated encounter conditions due to unmodeled nongravitational accelerations during cruise and a change in the final required encounter conditions as a result of changing the planned latitude of the landing site by about two degrees. However, the ΔV requirement of about 10 m/s for this maneuver at $E-10$ days was still small enough that the orbit control accuracy that could be achieved would be satisfactory and there was no need for a maneuver at $E-30$ days. Figure 6 indicates the final, premaneuver encounter, the target for the maneuver, and the final achieved encounter. This maneuver was performed in the blowdown mode to avoid repressurizing the propellant feed system and risking a repeat of the regulator problem experienced on Viking 1. Data relative to this maneuver may be found in Tables 2 and 3.

E. Maneuver Mechanization

The Viking spacecraft implemented velocity changes by first performing turns about the vehicle roll and yaw axes, and then thrusting in the desired attitude until the specified ΔV had been sensed by counting accelerometer pulses. In general, the desired control could not be commanded exactly because both turns and accelerations were measured in discrete values. However, the effects of this quantization can be minimized in terms of their effect on the resulting trajectory, whereas ignoring them in the case of small maneuvers with high sensitivities could result in significant control errors relative to normally occurring statistical control dispersions.

For the interplanetary maneuvers on Viking, the primary accuracy requirement was on the control in the B -plane. Arrival time variations of the magnitude caused by the quantization of the maneuver commandable quantities were of no concern. For this reason, the ΔV magnitude quantization was always handled by adding or subtracting a velocity component

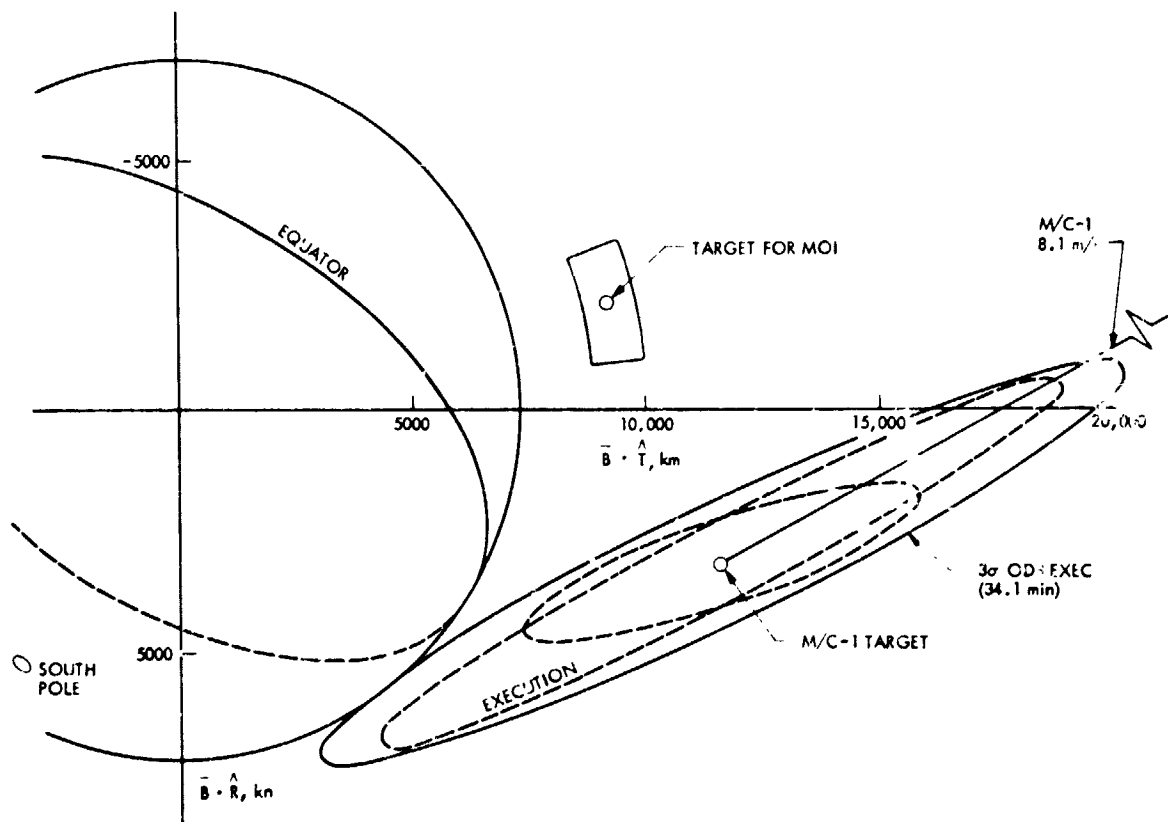


Fig. 10. Viking 2 biased first maneuver

to the maneuver ΔV perpendicular to the critical plane. An example of this for the first maneuver on Viking 2 is shown in Fig. 11. A velocity increment of 0.0134 m/s was subtracted from the noncritical component, reducing the total ΔV by about 0.004 m/s to reach the next lower ΔV quantum value. In this case, the ideal and commandable ΔV 's were very close; in general their difference can be as large as 0.015 m/s.

The technique for determining the turn quantization is graphical; two examples are shown in Fig. 12. The four achievable turn sets (resulting from rounding either way in both roll and yaw) are shown around the desired encounter point. The turn selection is then made, not necessarily to the nearest point, but rather to that point giving errors of the least consequence. Another consideration may be to compensate for a shift in the orbit determination estimate between the time of the original turns design and the quantization. It is readily seen from Fig. 12 that an indiscriminate quantizing of the turns could have led to a bias in the encounter parameters of up to 1000 km. In those cases where a second roll turn was used for communications, the turn was simply quantized to the nearest pulse, since this turn only affected the spacecraft roll attitude and had virtually no effect on the thrust pointing.

The targeting errors accepted in this process could possibly have been further reduced by quantizing the turns and the magnitude jointly rather than independently. However, the magnitude quantization affects the ideal turns, and this would have led to an interface complication between navigation and spacecraft personnel that was not warranted.

A major consideration in the selection of a turn set to achieve a specified thrust pointing is the apparent path the Sun and Earth will follow over the spacecraft during the turns. As an aid to this selection process, plots are generated showing these traces in a cone-clock system. (Fig. 7 showed such a plot for the turn set chosen for the first maneuver on Viking 1.) The quantization described above is negligible as far as affecting that selection.

II. Orbit Insertion

The orbit insertion problem for Viking consisted of two basic parts: one being to determine the optimum conditions for the approach hyperbola in order to effect the transfer, the other being to determine the required maneuver to transfer

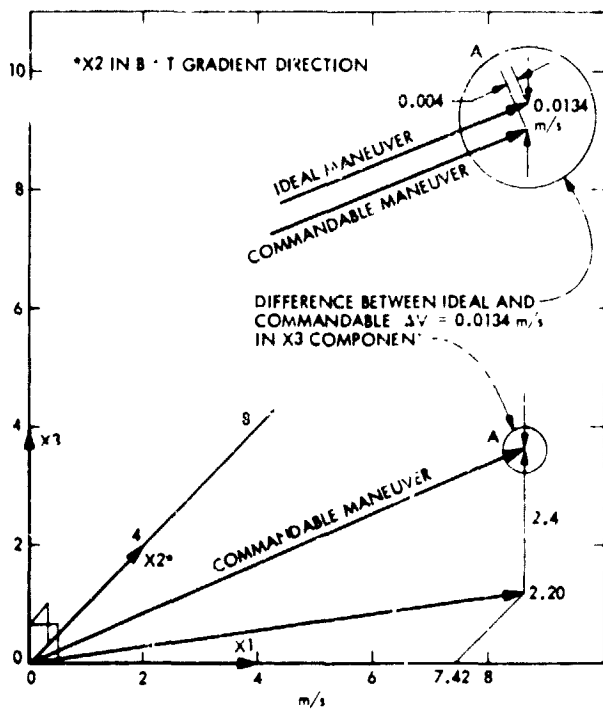


Fig. 11. Viking 2 first maneuver velocity in critical plane coordinates

from the actual achieved approach trajectory, generally dispersed from the nominal, to the required postinsertion orbit. The nominal orbit plane is approximately established by the fact that it must contain the τ vector (incoming hyperbolic asymptote) passing through the center of Mars, which is uniquely established by the launch and encounter dates, and it must at least, nearly contain the point of landing which is located in inertial space by specifying the site latitude and the sun elevation angle (SEA) at landing. The lack of precision in this definition of the approach orbit plane comes about from the fact that when a large amount of apsidal rotation is required at Mars orbit insertion to achieve the required relationship between orbit periapsis and the landing site, it requires less ΔV at MOI to do both in-plane and out-of-plane rotations than it does to do a strictly planar transfer. Once the orbit orientation is established, the hyperbolic radius of closest approach is determined to give a minimum velocity transfer to the required postinsertion orbit, and the time of closest approach is selected to properly time the postinsertion events as required for site reconnaissance and landing. Expected dispersions in postinsertion orbital period are also a key factor in selecting arrival time. In actual flight, the approach trajectory is generally dispersed from the planned nominal as a result of control errors at the time of the last interplanetary maneuver. Based on these estimated control errors and on knowledge statistics the problem to be solved at this point is to deter-

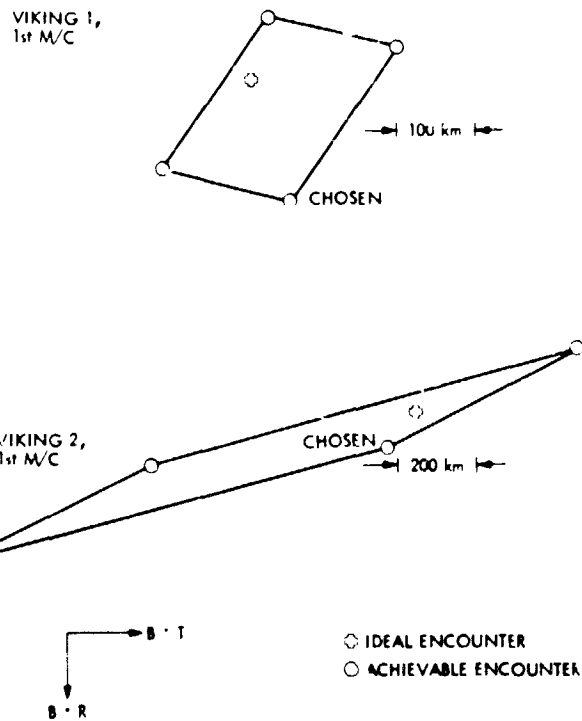


Fig. 12. Examples of B-plane turns quantization

mine what postinsertion requirements should be targeted to at insertion vs those which should be, or must necessarily be, corrected with in-orbit maneuvers where parameter correction capabilities and knowledge statistics are significantly different from those available at MOI. Figures 13 and 14 show the general orbit geometry for the two orbit insertions.

A. Viking 1

The orbit insertion strategy for Viking 1 was to target to a Mars synchronous period and nominally require no trim maneuvers prior to landing. This of course was changed when the two large approach maneuvers were made, delaying the arrival time by about 6 hours. At this point there were two options available to restore the nominal timeline. One was to target the period at insertion 3 hours subsynchronous, thus causing the second periapsis (P2) to occur at the normal time, and synchronizing the orbit at this point. The other was to target about 18.5 hours supersynchronous (Mars synchronous minus the 6-h shift), causing the first periapsis to occur at the time that P2 would normally have occurred, and then synchronize. The proper phasing and timing had to be achieved by P2 in order to allow time for site certification to take place prior to the nominal landing date. Of these two options, the latter was implemented, primarily based on ΔV considerations. Figure 15 shows the nominal planned timeline as well as the two

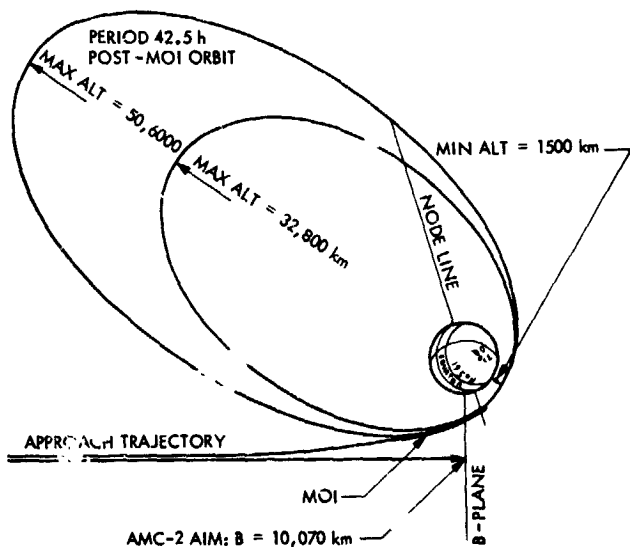


Fig. 13. Viking 1 orbit geometry

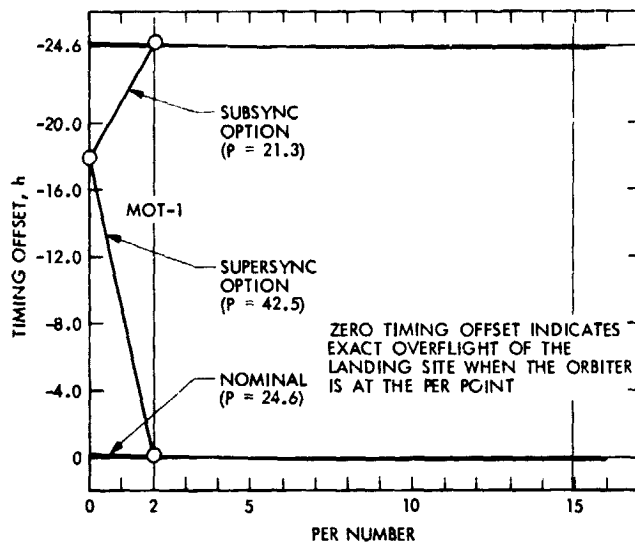


Fig. 15. Viking 1 insertion timing strategy

options. In the presence of delivery dispersions on the approach hyperbola, the plan was to target directly to the specified SEA and LATPER on the separation orbit, nominally leaving no orbit orientation biases to be removed either by orbit trims or by the lander during descent. Figure 16 indicates the feasibility of this plan, where it is seen that the expected delivery errors in θ (the orientation of the B -vector in the B -plane), even with radio only OD, were relatively small. More importantly, knowledge errors in orientation θ at the time of the calculation of the insertion parameters were small. This was not the case for Viking 2, and the considerably different strategy developed for that case will be discussed later. For

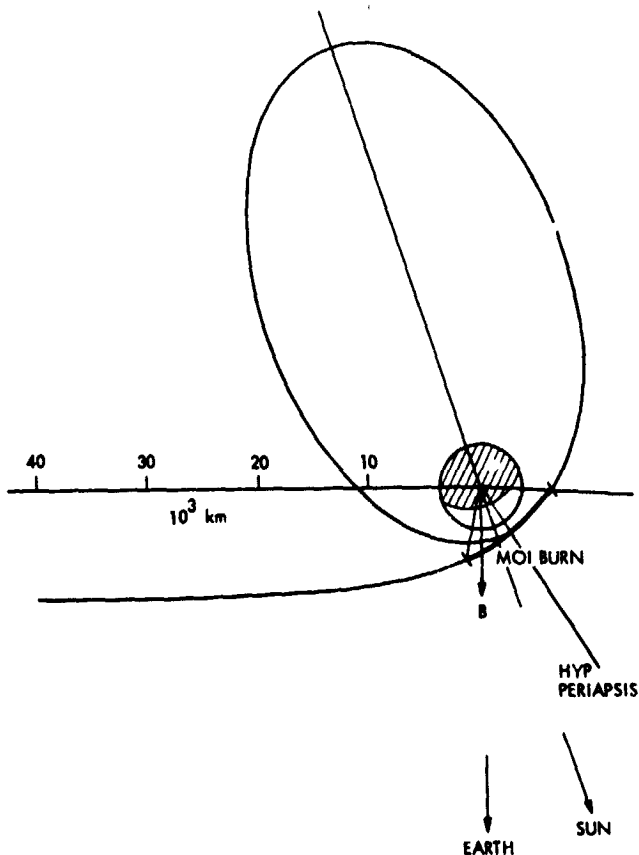


Fig. 14. Viking 2 MOI geometry

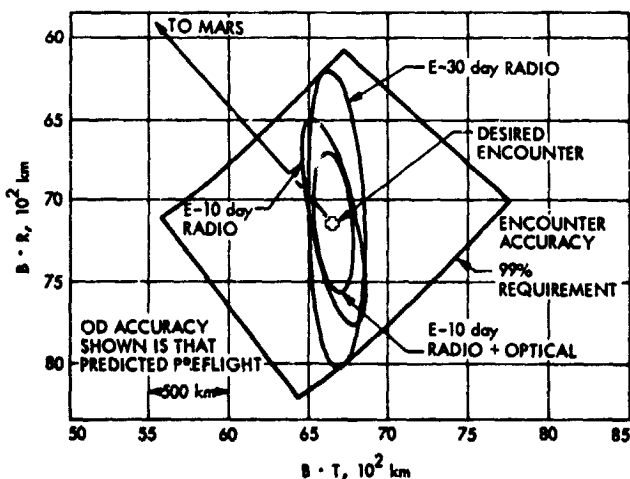


Fig. 16. Viking 1 approach midcourse B-plane delivery

C-3

delivery errors in B -magnitude, the situation was quite different. If the achieved B -magnitude was too large, then the periapsis altitude h_p targeted to at insertion had to be larger than the nominal 1500 km, because an ellipse of 1500 km h_p would not intersect the hyperbola without introducing unwanted apsidal rotation. On the other hand, if B -magnitude was too small, then the option existed to raise h_p part way or all of the way up to 1500 km at insertion, at a cost of more ΔV at insertion and reduced period control. Figures 17, 18, and 19 show the ΔV cost to correct B -plane errors for orientation θ delivery errors of 0, +2, and -2 deg, and B errors from 0 to -700 km for correcting any amount of B error with any combination of corrections between insertion and in-orbit trims. As an example, in reading these figures, consider Fig. 17, with no orientation correction to be made at insertion, and assume a ΔB of -700 km. Then a minimum ΔV transfer would require about 1200 m/s and give an h_p of 1030 km. Raising h_p to 1100 km at insertion would cost 1230 m/s and could be corrected to 1500 with an in-orbit trim of 35 m/s for a total of about 1265 m/s. Correcting to 1500 km at insertion would require 1410 m/s.

The ΔV vector control for orbit insertion was better in magnitude than in pointing — at the 99% level about 3 m/s and 20 m/s, respectively. Period was the most important parameter to control accurately at insertion, as well as the parameter most sensitive to errors. Since at a fixed radius the velocity determines the period, it was necessary to control the spacecraft velocity at burnout as precisely as possible. This is best done by having the insertion ΔV nearly aligned with the orbiter velocity at burnout, thus seeing only the 3 m/s magnitude error and very little projection of the 20-m/s perpendicular (pointing) error. Generally, any correction of orientation or altitude at insertion necessitates moving the ΔV vector away

from the velocity vector, thus increasing the pointing error component on the spacecraft velocity and degrading the period control. Figure 20 indicates the period control as a function of the orientation and altitude corrections made at insertion. The effects of knowledge errors based on optical tracking data are included. Although both positive and negative orientation errors are not shown for each value of ΔB , the results are approximately the same for errors on either side of the nominal.

A consideration in planning which delivery errors would be corrected at insertion was the fact that the spacecraft team was concerned that the final maneuver parameters not vary significantly from a nominal set specified well before encounter so as to not disrupt the sequencing work done for this

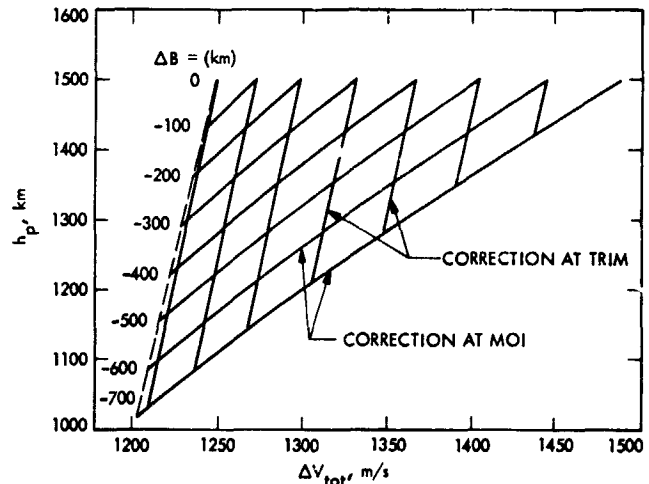


Fig. 18. ΔV trades for h_p correction at MOI/trim, $\Delta\theta = 2$ deg

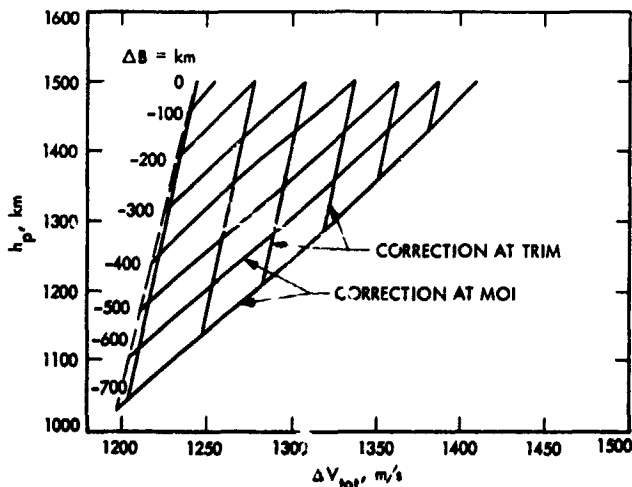


Fig. 17. ΔV trades for h_p correction at MOI/trim, $\Delta\theta = 0$ deg

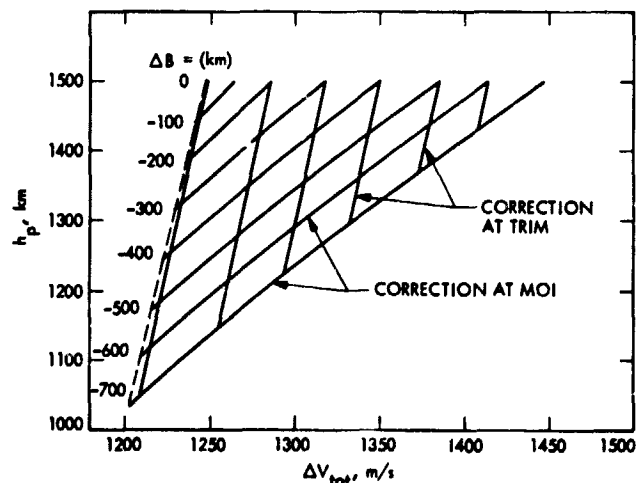


Fig. 19. ΔV trades for h_p correction at MOI/trim, $\Delta\theta = -2$ deg

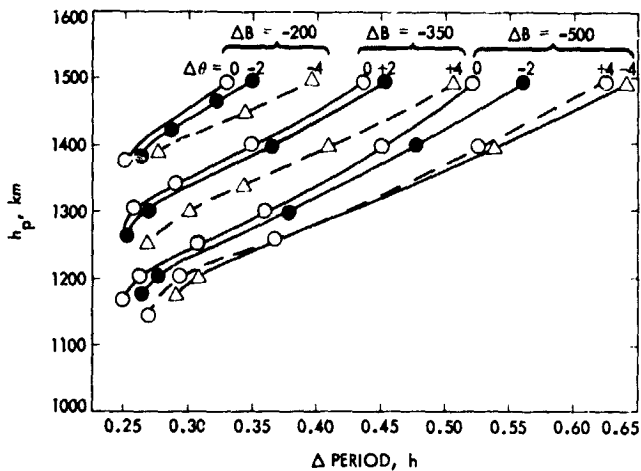


Fig. 20. Viking 1 post-MOI period dispersion

period of the mission. To this end, the effects of correcting various delivery errors on the commandable quantities were investigated with the results as shown in Figs. 21 and 22. Figure 21 shows the roll and yaw turns required on a grid of delivery points covering the required approach delivery accuracy zone for targeting to a synchronous period, the nominal SEA and LATPER, and a minimum ΔV transfer which determines h_p . The results show that all of the delivery zone can be covered by turns within ± 10 deg of nominal, and in fact that ± 10 deg was quite conservative, since it was known well before encounter that the final delivery was virtually guaranteed to be well within the zone shown. Raising altitude for low deliveries was not considered here, but could have been a limiting factor, along with degraded period control and increased ΔV costs, in determining the amount of h_p to be restored at insertion. Figure 22 shows the change in ignition time as a function of altitude restored at MOI. The maximum ignition time delta shown is 12 min, which was within the allowable range. The range of ΔV 's at insertion was not a problem because, with an acceleration of about 0.5 m/s^2 at burnout, the maximum range conceivable would only amount to a very few minutes in total burn duration.

A set of orbit insertion commands was sent to Viking 1 soon after the second approach maneuver (AMC-2) was implemented, based on the nominal encounter trajectory targeted to at AMC-2. This was done as a hedge against the possibility that it might become impossible to uplink commands at a later time. (There was no reason to suspect that such a failure would occur — this was simply a precaution to increase the likelihood of success for this critical event.) Furthermore, it was known that this maneuver, when applied to any trajectory that could result within the 99% delivery statistics of AMC-2, would yield a postinsertion orbit that could be trimmed to a

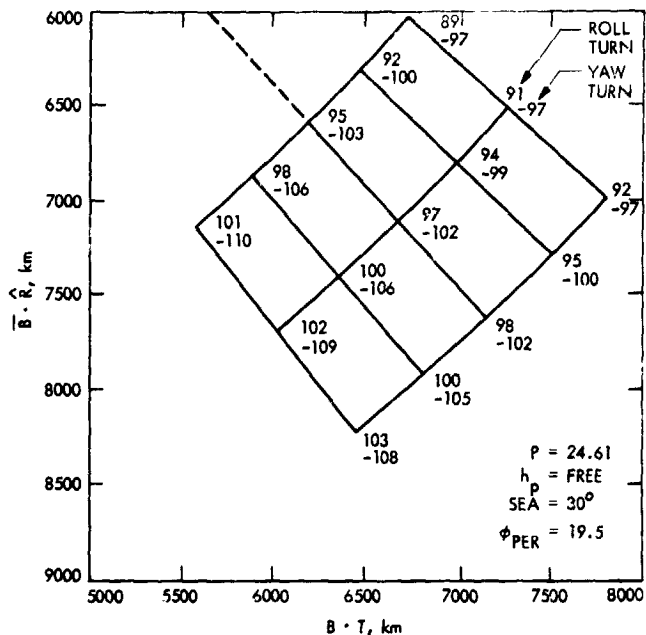


Fig. 21. Roll-yaw turn variations for Viking 1 MOI

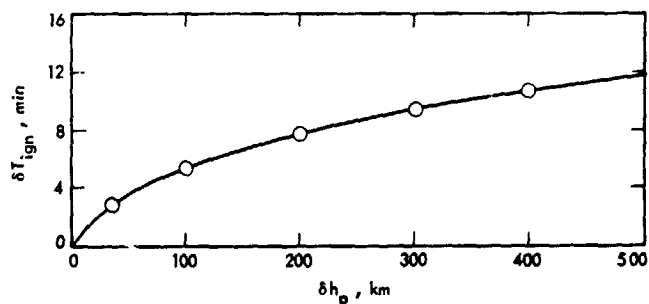


Fig. 22. Ignition time sensitivity to h_p error

satisfactory landing orbit within the ΔV available. A key decision to be made after the results of AMC-2 were known was whether or not to update the command load onboard the spacecraft. Figure 23 and Tables 4 and 5 indicate some of the navigation tradeoffs for each case. The decision made was to do the update, based partly on the reduced ΔV costs (Table 5) but also on the fact that the geometry for obtaining site reconnaissance early in the period from insertion to landing was much improved.

Turn constraints for the Viking 1 insertion proved to be quite restrictive, nearly to the point of forcing the maneuver to be biased somewhat from nominal. The final turn sets under consideration, those based on a nominal AMC-2 and those for the update, fortunately were able to satisfy the constraints.

Table 4. Viking 1 MOI command update site acquisition tradeoffs

Parameter	Onboard			Update		
	Nominal	0.99		Nominal	0.99	
			Post-MOI			
PERIOD, h	44.1	-1.8, 1.3	42.3, 45.4	42.5	-1.8, 2.0	40.7, 44.5
HP, km	1399.	-67, 68	1332, 1467	1511	-61, 68	1450, 1579
			Separation Orbit			
INCL, deg	37.7	-0.3, 0.3	37.4, 38.0	37.7	-0.3, 0.3	37.4, 38.0
ϕ_{PER} , deg	20.0	-0.7, 0.5	19.3, 20.5	19.5	-0.5, 0.5	19.0, 20.0
ΔDR , deg	0	-0.2, 0.2	-0.2, 0.2	0	-0.1, 0.1	-0.1, 0.1
ΔXR , deg	0.6	-0.8, 0.6	-0.2, 1.2	0	-0.5, 0.5	-0.5, 0.5
SEA, deg	29.5	-0.9, 0.9	28.6, 30.4	30.1	-0.8, 1.0	29.3, 31.1

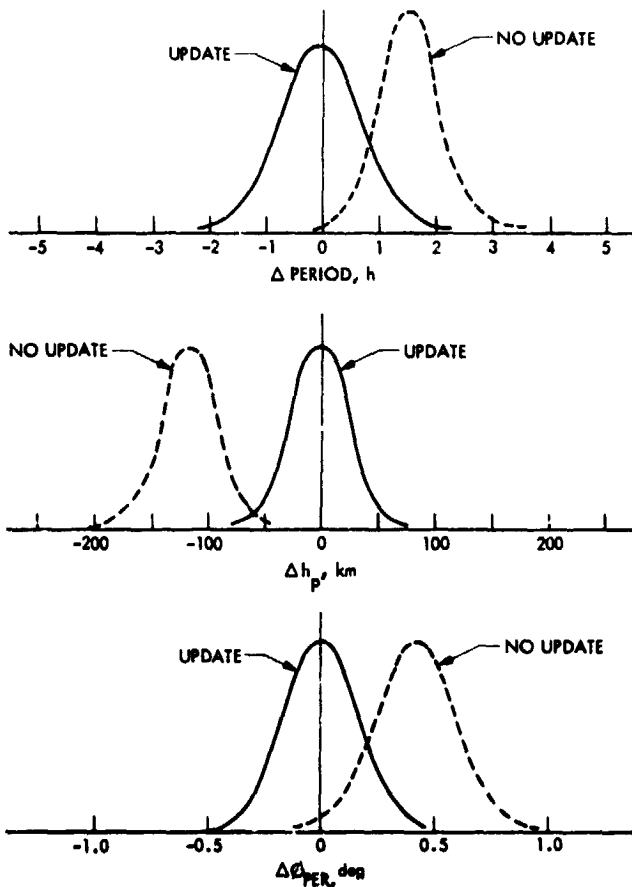


Fig. 23. Effect on post-MOI orbit dispersions of updating MOI parameters based on post-AMC-2 orbit knowledge

Table 5. Viking 1 MOI command update ΔV budget tradeoffs

Parameter	Onboard		Update	
	Nominal	0.99	Nominal	0.99
1 ΔV_{MOI}	1107.9		1097.3	
2 ΔV_{TRIM}	98	116	81	102
3 SUBTOTAL (1+2)	1206	1224	1178	1199
4 $\Delta V_{TOTAL AVAILABLE}$	1350			
5 $\Delta V_{AVAIL POST-TD (4-3)}$	144	126	172	151
6 $\Delta V_{REQ'D POST-TD}$	16			
7 Margin	128	110	156	135
8 50% Margin	132		156	
9 Desires	100 for extended mission + 25 for $A_1 - A_2$			

Table 6. Final MOI parameters and related data for Vikings 1 and 2

Parameter	Viking 1	Viking 2
Roll, deg	100.36	134.66
Yaw, deg	-97.57	-110.91
Roll, deg	156.47	141.96
ΔV , m/s	1097.27	1100.81
Ignition time, GMT	19 Jun 22:20:43	7 Aug 11:29:52
Burn duration, s	2269.	2375.
True anomaly ignition, deg	-67.2	-44.1
burnout, deg	-21.5	67.3
Earth cone, burn attitude	115.70	130.48
Earth clock, burn attitude	178.49	180.00
OWLTL at ignition, s	1048.	1183.

Table 7. Trajectory data — Viking 1 insertion

Parameter	Approach hyperbola	Post insertion	
		Target	Achieved
$B \cdot R$ } Leliptic	7277	-	-
$B \cdot T$ }	6919	-	-
Time of periaapsis (P_0) (GMT)	19 Jun 22:54:06	(P_2) 21 Jun 17:39	(P_2) 21 Jun 17:27
Altitude of periaapsis, km	2168	1511	1514
a , km	-6280	29595	29325
e	1.886	0.834	0.833
i	38.0	37.7	37.9
ω } MEQ	15.4	39.5	39.8
Ω }	129.9	130.0	129.8
Period, h	-	42.5	42.35
$\Delta\psi$, deg	-	24.3	24.3

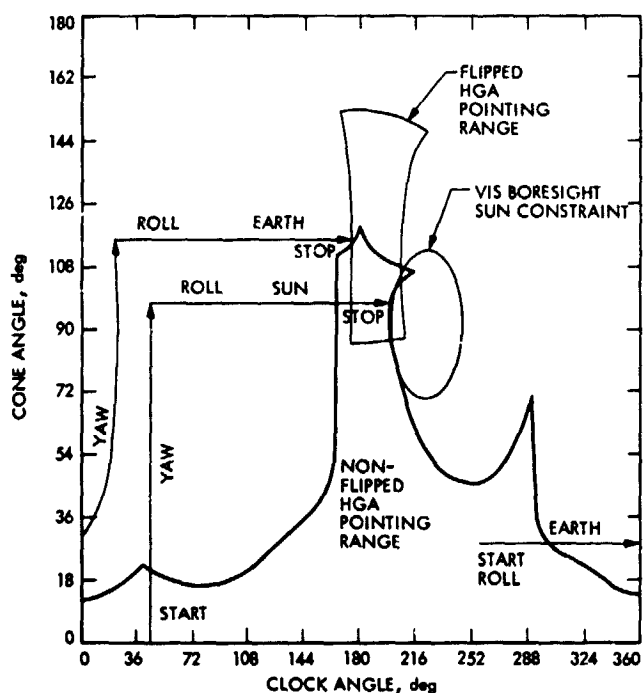


Fig. 24. Viking 1 Earth/Sun traces for MOI

The problem, as illustrated in Fig. 24, was to have the Earth within the accessible region of the high-gain antenna while keeping the Sun out of the field of view of the instruments.

The actual implementation of this maneuver went essentially as planned, with performances well within the a priori statistics. Tables 6 and 7 show the relevant maneuver and trajectory parameters related to the planned and achieved maneuver. A reconstruction of the actual maneuver performed based on postflight tracking data indicates an actual pointing error of 8.47 mrad, or about 1.2 σ , and a magnitude error of 0.415 m/s overburn, or about 0.4 σ .

B. Viking 2

The strategy for targeting the orbit insertion for Viking 2 was quite different from that of Viking 1 in two respects, although the final objective of reaching the separation orbit with a near-Mars synchronous period and a specified SEA and LATPER was the same. First, the nominal arrival time was determined to allow for a supersynchronous post-insertion period such that the spacecraft would overfly three different specific longitude zones in the region of 46° N latitude for the purpose of site reconnaissance before making the decision to synchronize over one of them. This timing relationship is indicated in Fig. 25 with the three longitude regions of interest indicated on the right. The primary landing site candidate at the time of MOI was at 10° W longitude, in the region indicated as B1. To reach this site, the plan was to target to a period of 27.4 h at insertion and do a nominal trim to synchronize to 24.6 h on rev 19 for a landing on rev 25. Alternate maneuver locations and phasing combinations for synchronizing over B2 or B3 are shown. Although both ascending and descending crossings of 46° latitude are shown to indicate site reconnaissance opportunities, only the ascending crossing is available for landing.

The second aspect of the Viking 2 strategy that was distinct from Viking 1 was the targeting of the post-insertion orbit orientation. The approach control and knowledge errors (Fig. 26) show quite good control and knowledge in B-magnitude, but rather poor in orientation, especially for the case of radio-only data. Primarily as a result of this characteristic of the knowledge data, the plan was to always perform a planar

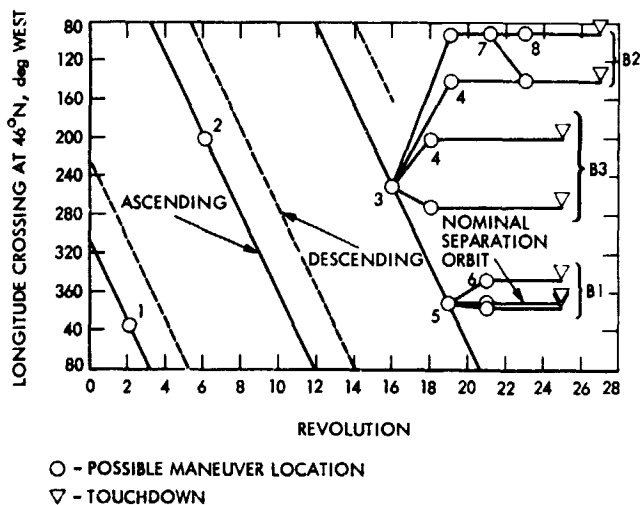


Fig. 25. Viking 2 nominal post-insertion orbit timing

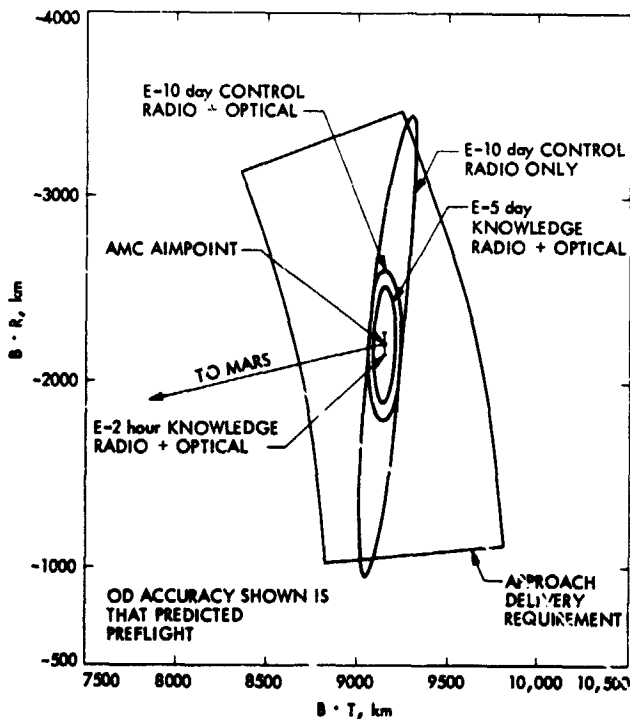


Fig. 26. Viking 2 approach control and knowledge

insertion and target to the proper in-plane orientation. An in-orbit trim where the orbit knowledge was essentially perfect was then to be performed at the true anomaly of the vertical impact point. This trim would perform an orbit rotation and would have nearly the same effect as an orientation correction on the approach hyperbola. The clear advantage of performing this correction in orbit is that the risk of making an overcorrection or a change in the wrong direction at MOI is elimi-

nated. In fact, even if an attempt were made to correct any out-of-plane errors at MOI, a priori statistical studies indicated a significant probability that an in-orbit orientation trim would still have been required.

The relatively nominal performance of the approach mid-course and the resulting orbit determination estimate of a very small error at the time of the post-AMC update calculations for the insertion parameters, coupled with the fact there was some question about the desired landing coordinates at this time, resulted in this strategy having virtually no effect on the MOI targeting.

A set of MOI commands was generated and sent to the spacecraft about one week prior to the implementation of the AMC, based on the nominal trajectory targeted to with this maneuver. About four days prior to the MOI, an updated set of parameters was calculated based on the OD solution at that time, which indicated AMC execution errors of about 8 km in B -magnitude, essentially no error in θ , and about -19 s error in arrival time. This was the command load that was eventually executed for the orbit insertion. The final encounter solution differed from the one used for the final command generation as shown in Fig. 27. A history of predicted and final key orbital elements post-MOI is given in Table 8, and the nominal and updated insertion maneuver parameters are shown in Table 9.

As with Viking 1, the post-insertion orbital period control was very important in order to do the site certification observations as scheduled. An arrival time error is equivalent to an ignition time error, and thus can significantly affect the post-insertion period, especially when TCA occurs early. This relationship is shown in Fig. 28, where all insertion parameters are fixed except for ignition time. As was shown in Fig. 27, the

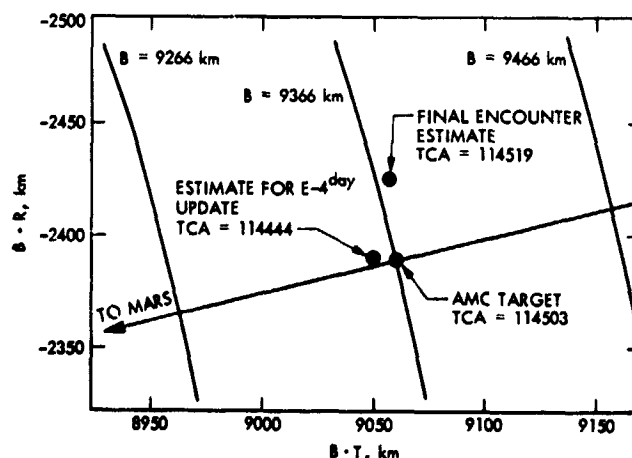


Fig. 27. Viking 2 approach trajectory history

ORIGINAL PAGE IS
OF POOR QUALITY

Table 8. Viking 2 post-MOI orbital parameters

Parameter	Nominal design value	Post-AMC based on pre-AMC MOI load	Last pre-MOI based on E-4 day update to insertion parameters	Actual
P , h	27.414	27.772	27.490	27.623
h_p , km	1500	1468	1521	1519
i , deg	55.0	55.1	55.2	55.2
LATPER, deg	45.3	44.7	45.6	45.5
SEA, deg	119.6	120.8	119.7	119.2

Table 9. Viking 2 orbit insertion parameters

Parameter	Pre-AMC nominals	E-4 day update
Roll turn 1, deg	+134.725	+134.663
Yaw turn, deg	-112.009	-110.913
Roll turn 2, deg	+142.072	+141.957
ΔV , m/s	1102.1	1100.8
TIGN, 8/07/76 (GMT)	11:30:39	11:29:52
Earth cone, deg	131.6	130.5
Earth clock, deg	180.0	180.0

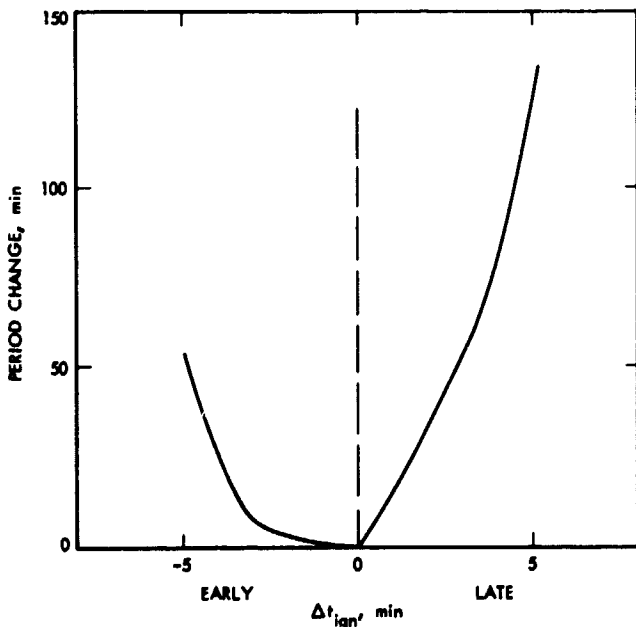


Fig. 28. Viking 2 period change vs ignition time error

final estimate of the encounter time differs from the estimate made at the time of the update calculations by 35 s, and in a direction such as to make the ignition time appear to be early. This was fortuitous, as can be seen in Fig. 28, and evidently had little impact on the resulting orbit period.

The question of correcting periapsis altitude on Viking 2 was of less concern than on Viking 1 because of the improved control accuracy. Nevertheless there was still the possibility of needing to correct for low B -magnitude deliveries. A plot of the cost for doing this is shown in Fig. 29. Orientation is not a parameter here because of the targeting strategy discussed earlier.

The problem of satisfying turn constraints was straightforward on Viking 2 as opposed to the situation described previously on Viking 1 because the Earth-Sun relationship posed no problem. However, as expected, it was necessary to use the flipped position of the high-gain antenna to get communications as illustrated in Fig. 30.

The maneuver implementation was near nominal, as indicated by the trajectory data of Table 8. Figure 31 shows the predicted doppler shift during the burn with actual values superimposed. A postflight reconstruction of the maneuver indicated a pointing error of 0.36° , or 1.1σ , and a magnitude error of only 0.05 m/s, or about 0.03σ .

III. Orbit Trim Maneuvers

The most exciting maneuver analysis challenge, following the insertion of each Viking spacecraft into orbit about Mars, was that of providing the proper orbit geometries for site certification and landing. After the landings, station-keeping

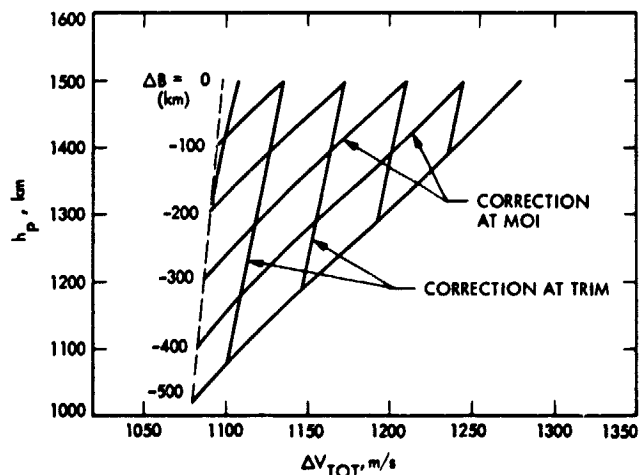


Fig. 29. ΔV cost for correcting periapsis altitude errors at MOI vs in orbit for Viking 2

maneuvers were made to maintain acceptable relay-link telecommunications performance between the orbiters and landers. The activities after landing also included orbiter excursions away from the vicinity of touchdown, e.g., a longitudinal walk for global water vapor mapping by the MAWD. In addition, a large plane-change maneuver was performed by the Viking 2 Orbiter to move to a high inclination for polar observations.

The maneuver design for Viking was accomplished in two phases. First, there was the preflight design and strategy development that was dictated by mission objectives and requirements. Orbit determination and maneuver execution accuracy statistics were used, together with propellant budget considerations, to determine specific maneuver requirements and strategies to ensure a high probability of meeting the mission requirements. This phase, which had to account for all candidate launch and arrival data combinations, is discussed in Refs. 1 and 2.

The second phase of the maneuver design occurred in flight. This section describes the maneuver analyses that were performed in flight, the software that was employed, and the actual inflight results for the entire orbital phase of the nominal Viking Mission. The first subsection concentrates on the prelanding objectives and geometry considerations. The maneuver strategies discussed here evolved during the preflight

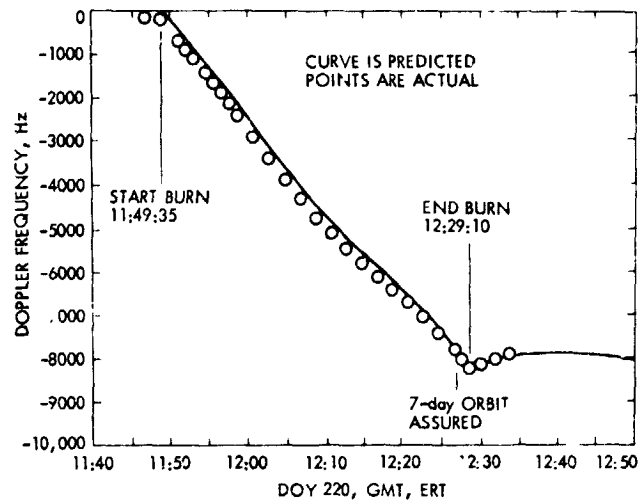


Fig. 31. Viking 2 MOI burn tracking data residuals

and interplanetary portions of the mission. The last two subsections consider the actual adaptive design and implementation of the maneuvers as the mission progressed. This design process included the minimization of both propellant usage and the effects of maneuver execution errors, while complying with several mechanization constraints. The actual inflight results are given in these subsections.

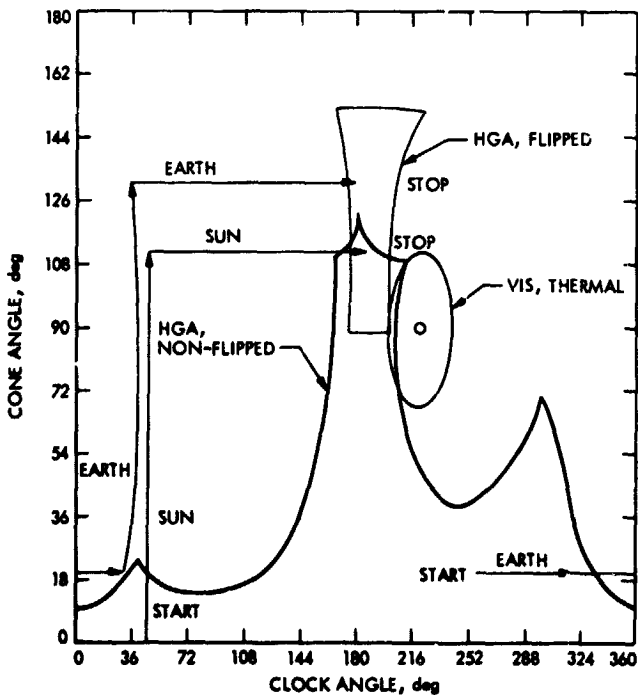


Fig. 30. Viking 2 Earth/Sun traces for MOI

A. Prelanding Maneuver Strategies

1. Maneuver requirements. The orbit trim problem is to attain certain mission-, spacecraft-, and operations-dependent objectives, while coping with delivery, satellite orbit determination and maneuver execution errors. The objectives of the prelanding orbit trim strategies for Viking were:

- (1) *To satisfy the requirements for landing.* The orbit of the spacecraft had to be controlled to within prescribed geometrical bounds. These bounds were governed by the need to acquire the landing site and to position the spacecraft orbit within a specified space-time region from which the lander could maneuver to the desired landing site without violating any of its design constraints. Primary lander design constraints were those which required the lander to operate within and near its maximum deorbit ΔV capability, within its maximum separation-to-entry coast time capability of 5 h, within prescribed entry angle corridor limits, and within the relay-link geometry constraints. The required target orbit for the sequence of prelanding trims was specified for that spacecraft revolution during which the Viking lander was to separate from the orbiter.

- (2) To provide near-periapsis site reconnaissance as soon as possible following the orbit insertion maneuver. Early reconnaissance of the site was required to permit adequate time for site certification prior to landing. To obtain an acceptable site reconnaissance sequence of a point of interest on the planet, it was necessary for the spacecraft to observe this point at acceptable viewing angles and range.
- (3) To satisfy the operational maneuver spacing constraints. At least 20 h had to be allowed between the orbit insertion maneuver and the first trim and 48 h between successive trims in order to provide adequate orbit determination and command generation time. These time intervals also were to ensure having sufficient propellant communication time. If propellant (liquid) separated or settled at the upper end of the tank during or following engine cutoff, then a small communication channel would slowly transfer the liquid from the forward end to the aft end. In a worst-case situation, the time required would have been 28 h (see Ref. 3). The time required following a motor burn to obtain thermal equilibrium (acceptable temperature distributions in the system) and to do propulsion subsystem performance analyses did not levy additional constraints because the time needed for these activities was considerably less than 28 h. Also, at least four spacecraft revolutions had to be allowed between the last prelanding trim and lander touchdown in order to provide adequate orbit determination and deorbit command generation and validation time.
- (4) To make efficient use of propellant capability. The definitions of some of the separation orbit control parameters depend on the PER angle, which is the true anomaly of the point in the orbit that is nominally placed directly above the landing site. The PER point is the sub-spacecraft point at the PER angle on the actual orbit. Four of the orbit parameters that had to be controlled are shown in Fig. 32: namely, the downrange (DR) and crossrange (XR) of the PER point with respect to the desired landing site, the orbital period P , and the periapsis altitude h_p above the Martian surface.

To satisfy landing requirements it was also necessary to control the lander downrange azimuth and sun elevation angle (SEA) at touchdown (TD). The VL azimuth dispersions were critical because the landing dispersion ellipse was very elongated in the downrange direction and, consequently, the total ensemble of landing dispersions was very sensitive to azimuth dispersions. The sun elevation angle (SEA) is defined as the angle between the local horizontal and the direction to the Sun at the point of interest. This angle is interpreted to be in the interval from 90 to 180 deg in the morning, with the

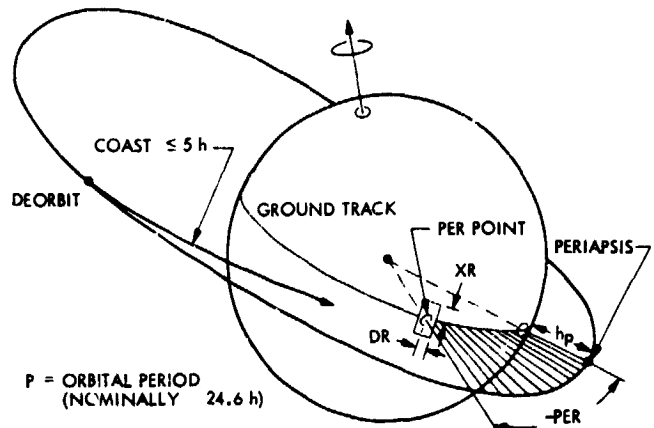


Fig. 32. Satellite orbit control for lander separation

morning terminator being at SEA = 180 deg, and in the interval from 0 to 90 deg in the afternoon, with the evening terminator occurring at SEA = 0 deg. The SEA requirement was actually a time constraint on the amount that the relay transmission window could be shifted without changing the initiation time of all other landed events. The allowable shift of 21 min mapped to an SEA requirement. The requirement on SEA also ensured satisfactory lighting conditions at the landing site for VO site certification imaging before landing. As for the other landing parameter constraints, the tolerances for azimuth and SEA were specified in terms of corresponding parameters on the separation orbit.

Timing was also a key target parameter. The timing delay ΔT is defined to be the time required for the VO to reach the PER point after the landing site has crossed the meridian of the PER point (see Fig. 33).

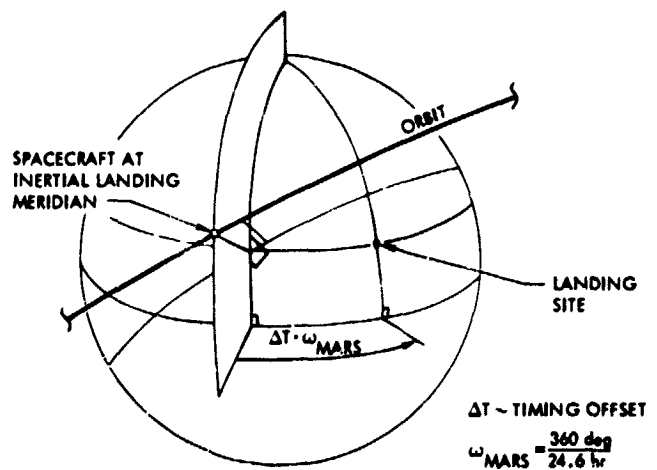


Fig. 33. Timing definitions

The timing strategy for the last prelanding trim maneuver was to optimally compensate for the residual DR and XR errors following the previous trims. The period of the separation orbit was adjusted by the last prelanding trim, controlling the timing offset such that the VL could be targeted to touch down at the landing site as the landing site crosses one diagonal of the DR x XR tolerance zone. That is, the separation orbit period was chosen so that the VL could touch down at the landing site by performing the amount of downranging and crossranging (DR and XR) indicated in Fig. 34. As discussed in *Lander Flight Path Analysis*, the DR tolerance was effectively set to zero, to maximize the probability of a successful VL entry and landing.

The target value for the timing offset parameter on the separation orbit was selected to reflect both these DR and XR geometrical errors and the fact that the VL leads the VO between the deorbit maneuver and touchdown. The VL/VO geometry at touchdown and PER passage is shown in Fig. 35.

To obtain an acceptable site reconnaissance sequence of a point of interest on the planet, it was necessary for the spacecraft to observe this point at an acceptable emission angle, incidence angle, and slant range. The emission angle (EMA) is defined as the angle between the local vertical at the point of interest on the surface of the planet and the vector from this point to the spacecraft; the incidence angle INA is the angle between the local vertical and the direction to the

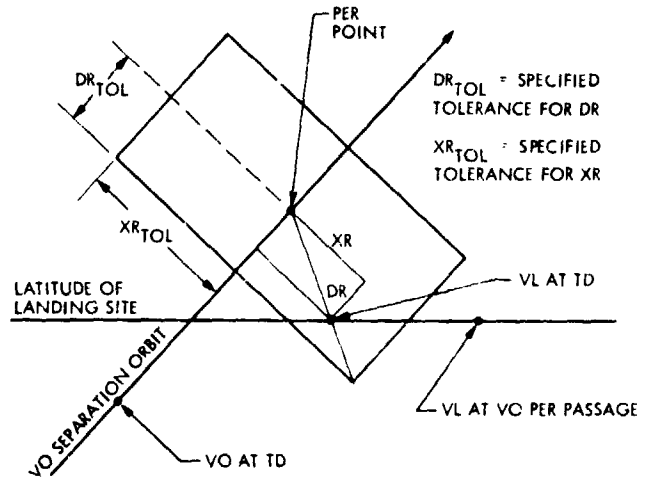


Fig. 35. VL/VO timing relationship

sun at the point of interest; and the slant range SR is the distance from the spacecraft to the point of interest (see Fig. 36). The sun elevation angle SFA is the complement of INA, except that SEA is defined to be in the interval from 90 to 180 deg in the morning. The constraints on these angles depended on the type of observation to be taken, e.g., stereo, oblique photopair, MAWD, and simple VIS. There was also a viewing angle constraint imposed by the site certification stereo analysis process that the tilt angle, shown in Fig. 37, be less than 9 deg. This requirement became the dominant one

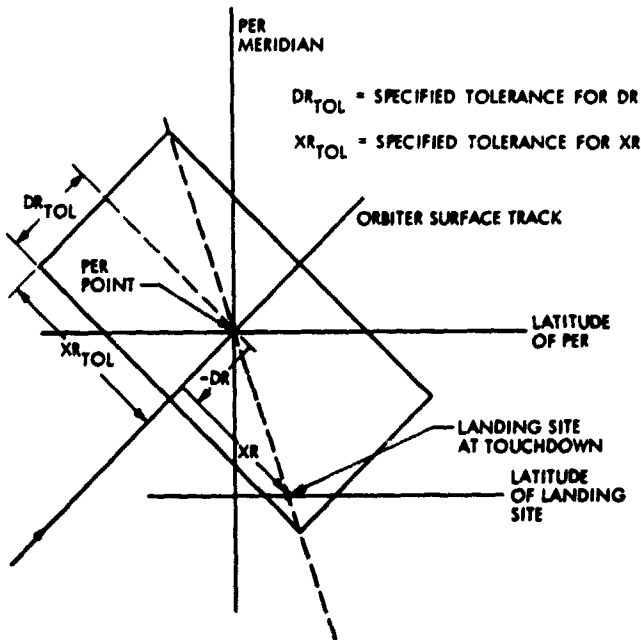


Fig. 34. Separation orbit time phasing

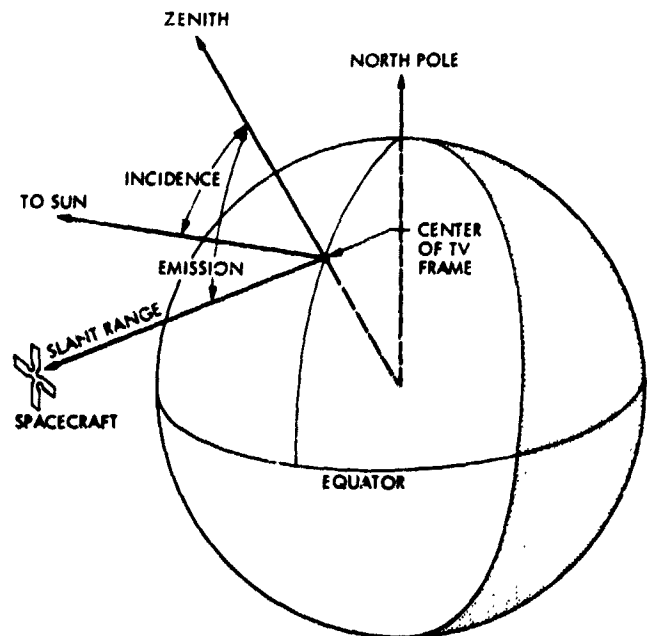


Fig. 36. Reconnaissance parameters

during flight operations, where it was considered in terms of the equivalent timing offset value.

There was also a strong desire to provide site reconnaissance on Viking 2 for both the primary and secondary sites on two separate spacecraft revolutions before synchronizing with respect to a site. Synchronizing with respect to a point on the planet refers to transferring the spacecraft to an orbit with period equal to the Mars rotational period so that the spacecraft will continue to overfly this point. This process requires two trims: one time-phasing maneuver to move the spacecraft over the point on the planet, followed by another to adjust the period to equal a Mars day (~24.6 h).

2. Maneuver capability. This subsection presents a method and the required design curves for analyzing an orbit trim maneuver on a given nominal spacecraft orbit. The method utilizes the orbit parameter gradients in the Flight Plane Velocity Space shown in Fig. 38. The flight plane coordinate system used is that formed by the nominal velocity direction \hat{V}_M , the normal to the orbit plane \hat{V}_N , and the direction orthogonal to these away from the planet \hat{V}_G . For a given nominal orbit the gradients of the orbit parameters with respect to these velocity directions are a function of the true anomaly of the trim maneuver only. The gradient vectors form the rows of a linear mapping matrix which maps velocity perturbations into perturbations in the orbit parameters as follows:

$$\begin{bmatrix} \Delta P \\ \Delta h_p \\ \Delta i \\ \Delta \Omega \\ \Delta \omega \\ \Delta t_{TP} \end{bmatrix} = \begin{bmatrix} \partial P / \partial V_M & 0 & 0 \\ \partial h_p / \partial V_M & \partial h_p / \partial V_G & 0 \\ 0 & 0 & \partial i / \partial V_N \\ 0 & 0 & \partial \Omega / \partial V_N \\ \partial \omega / \partial V_M & \partial \omega / \partial V_G & \partial \omega / \partial V_N \\ \partial t_{TP} / \partial V_M & \partial t_{TP} / \partial V_G & 0 \end{bmatrix} \begin{bmatrix} \Delta V_M \\ \Delta V_G \\ \Delta V_N \end{bmatrix}$$

Note that the gradients of P , h_p and t_{TP} lie in the flight plane, the gradients of i and Ω are normal to the flight plane, while the gradient of ω has components both in the flight plane and normal to it. These observations can be made by noting the locations of the zeros in the above mapping matrix.

Changes in the inclination i and argument of periaapsis ω produce changes in the latitude of the PER point (LATPER), according to the equation

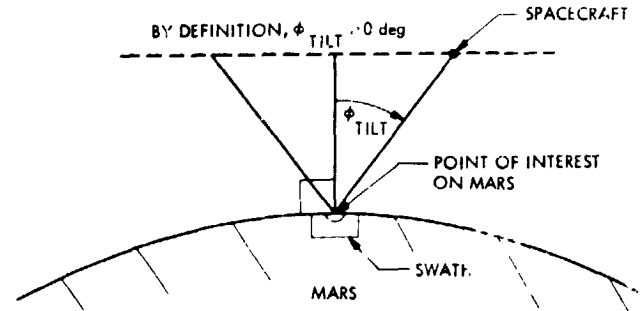


Fig. 37. Definition of tilt angle ϕ_{TILT}

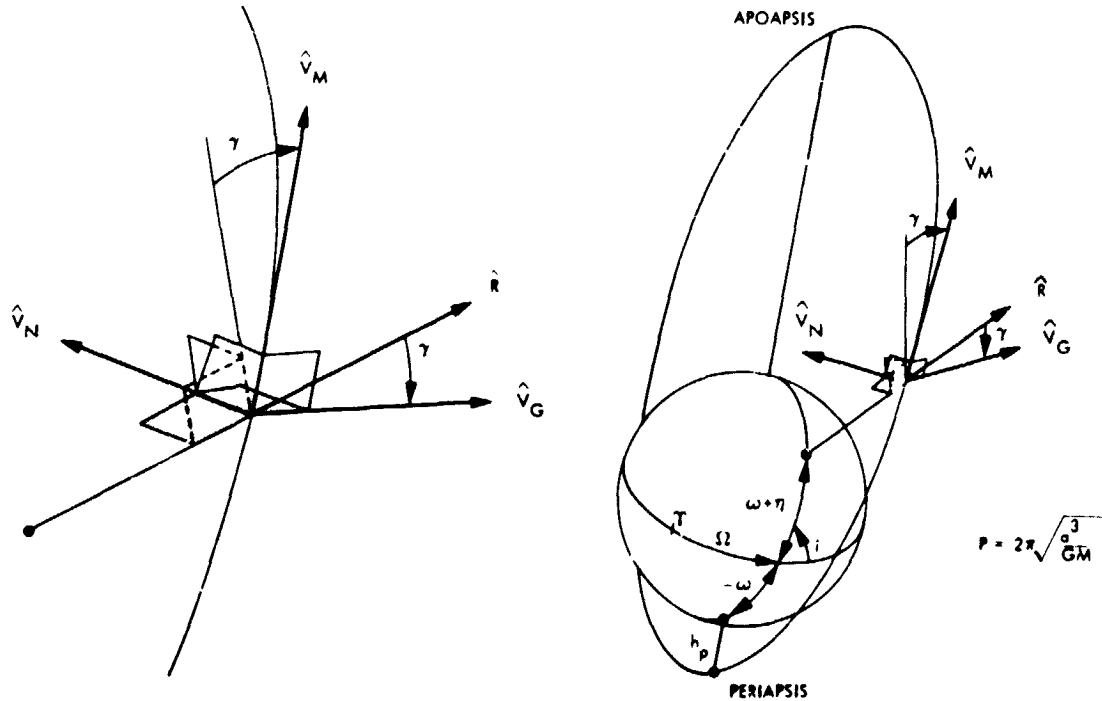
$$\sin(\text{LATPER}) = \sin i \sin(\omega + \text{PER})$$

This equation determines the sensitivity of LATPER to velocity changes. On the other hand, the sensitivity of the SEA at PER passage depends on all three orientation parameters: Ω , ω and i .

The gradient vectors for Viking 1 are given as functions of true anomaly in Figs. 39 through 45. Figures 46 through 52 exhibit the same data for Viking 2. In order to assess the effect of any given trim maneuver, the values of the gradients of the parameters of interest were inserted into the above mapping matrix, and the indicated matrix multiplication was performed. Thus the appropriate maneuver required to change the orbit parameters a given amount can be estimated by inspection. The information presented here was very useful in determining the maneuver capability and the effect of maneuver execution errors at various points around the orbit. It was also helpful in obtaining good initial guesses for use in high-precision numerical searches.

Figures 53 through 56 provide sensitivity data for sunline maneuvers. For example, Figure 53 gives the partial of period with respect to a velocity increment ΔV applied while the Viking 1 spacecraft is in the cruise orientation.

3. Maneuver strategies. Many prelaunch maneuver strategies were considered before launch to account for all possible launch and arrival date candidates. After launch, the design process was reduced to refining the strategies required for the two inflight missions. These strategies are described next to provide background for the maneuver sequences that were actually implemented. These descriptions also help to demonstrate the significance of the maneuver design changes that were required as the mission progressed. The orbit control capability and propellant costs for these strategies are described statistically in Ref. 4.



- FLIGHT PLANE VELOCITY SPACE
- P ~ ORBIT PERIOD
 - a ~ SEMIMAJOR AXIS
 - GM ~ GRAVITATIONAL CONSTANT
 - h_p ~ PERIAPSIS ALTITUDE
 - t_{TP} ~ TIME TO NEXT PERIAPSIS PASSAGE
 - γ ~ FLIGHT PATH ANGLE
 - η ~ TRUE ANOMALY
 - \hat{v}_M ~ UNIT VECTOR ALONG NOMINAL VELOCITY VECTOR
 - \hat{v}_G ~ UNIT VECTOR NORMAL TO NOMINAL VELOCITY VECTOR IN ORBIT PLANE DIRECTED AWAY FROM PLANET
 - \hat{v}_N ~ UNIT VECTOR NORMAL TO ORBIT PLANE IN ANGULAR MOMENTUM DIRECTION
 - i ~ INCLINATION
 - Ω ~ LONGITUDE OF ASCENDING NODE
 - ω ~ ARGUMENT OF PERIAPSIS

Fig. 38. Flight plane velocity space

ORIGINAL PAGE IS
OF POOR QUALITY

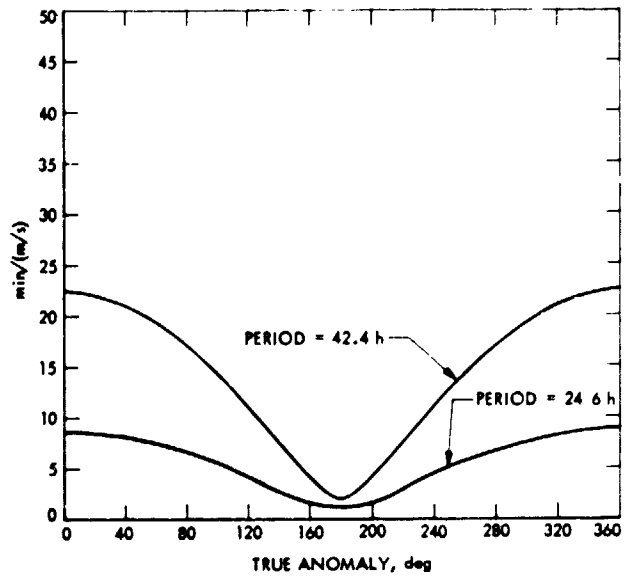


Fig. 39. Period gradients for Viking 1

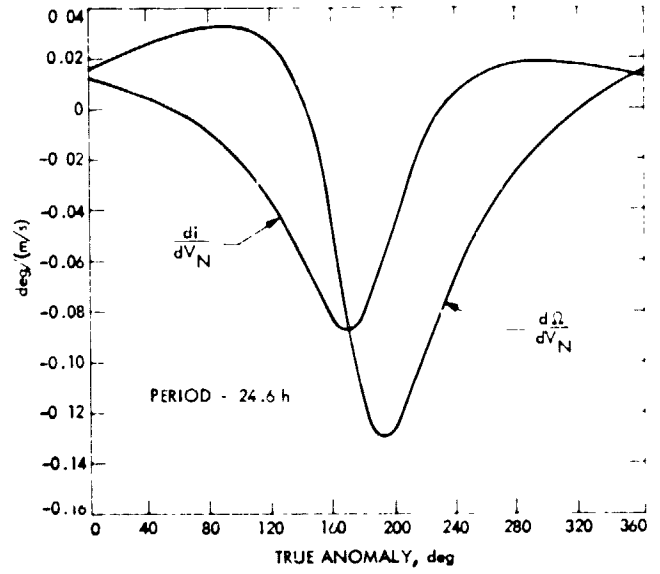


Fig. 41. Right ascension of ascending node and inclination gradients for Viking 1

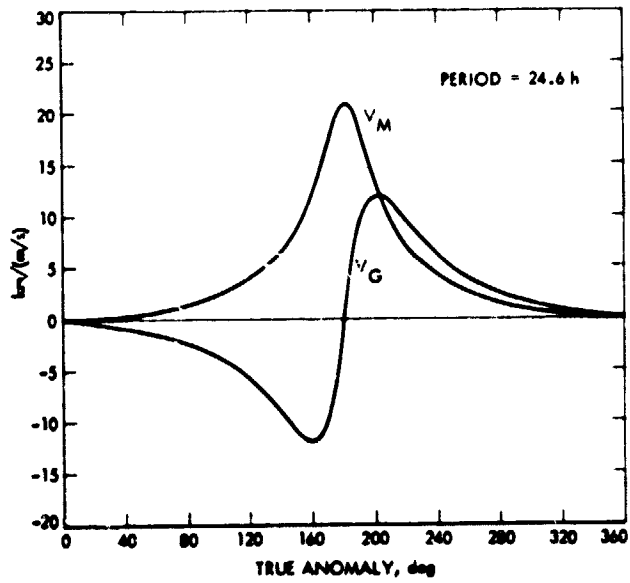


Fig. 40. Periapsis altitude gradients for Viking 1

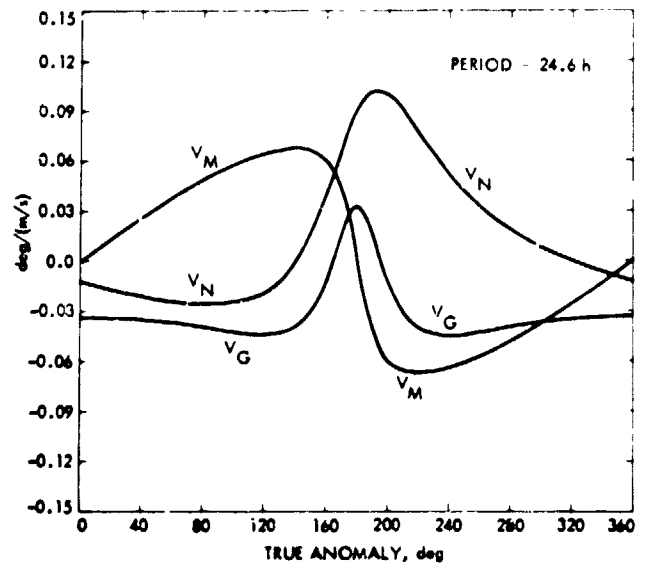


Fig. 42. Argument of periapsis gradients for Viking 1

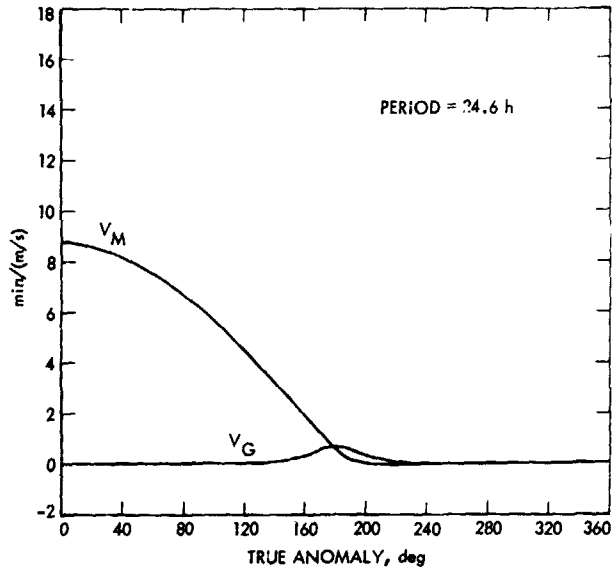


Fig. 43. Time to periapsis gradients for Viking 1

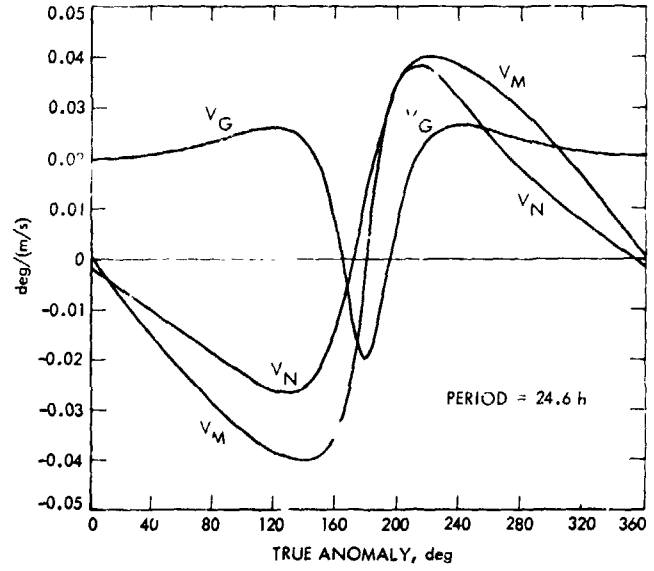


Fig. 45. Sun elevation angle gradients for Viking 1

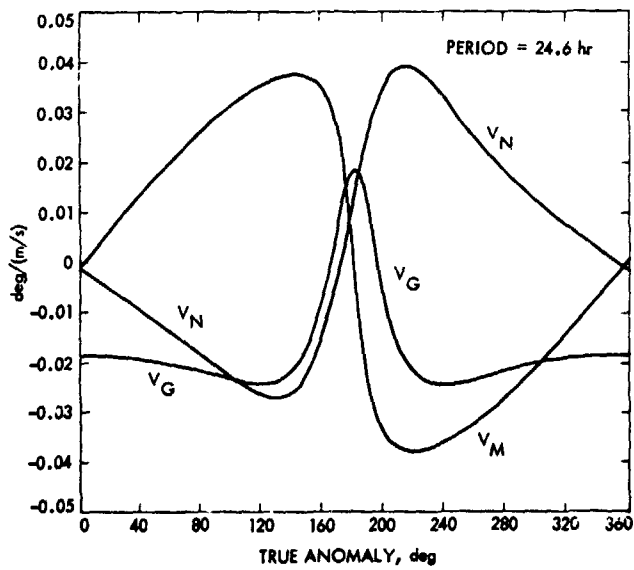


Fig. 44. LATPER gradients for Viking 1

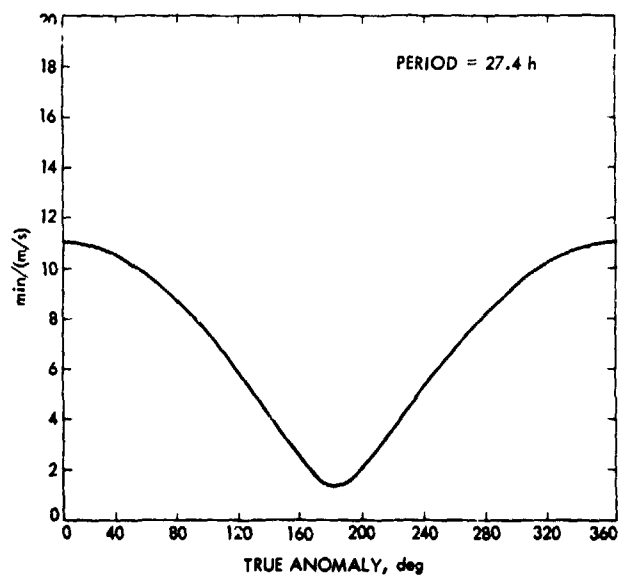


Fig. 46. Period gradients for Viking 2

ORIGINAL PAGE IS
OF POOR QUALITY

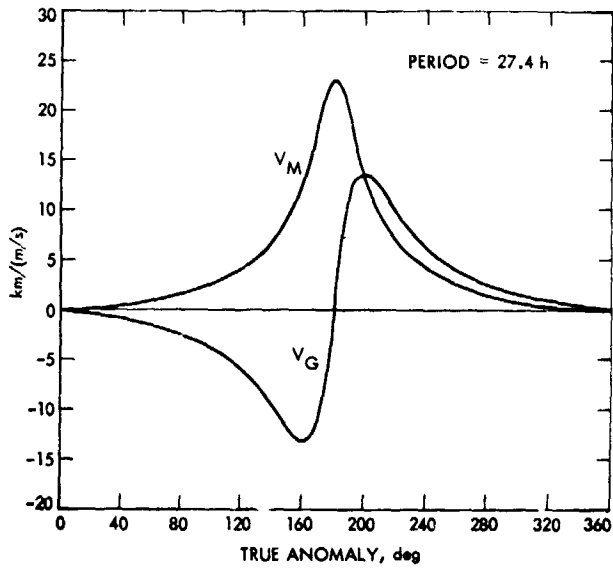


Fig. 47. Periapsis altitude gradients for Viking 2

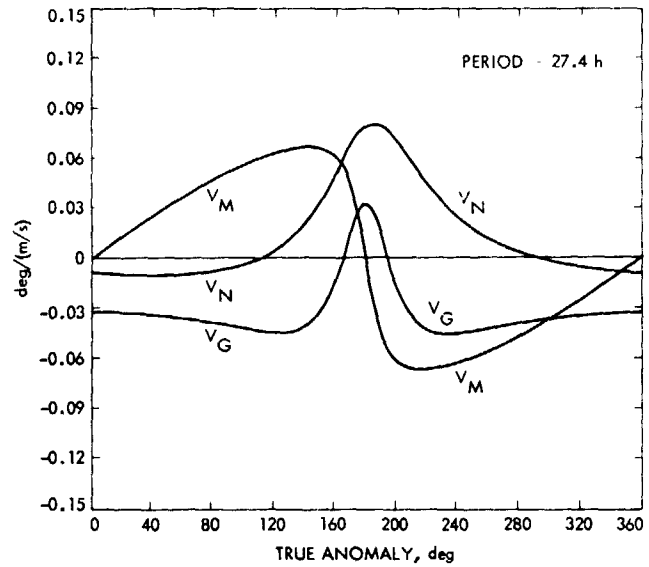


Fig. 49. Argument of periapsis gradients for Viking 2

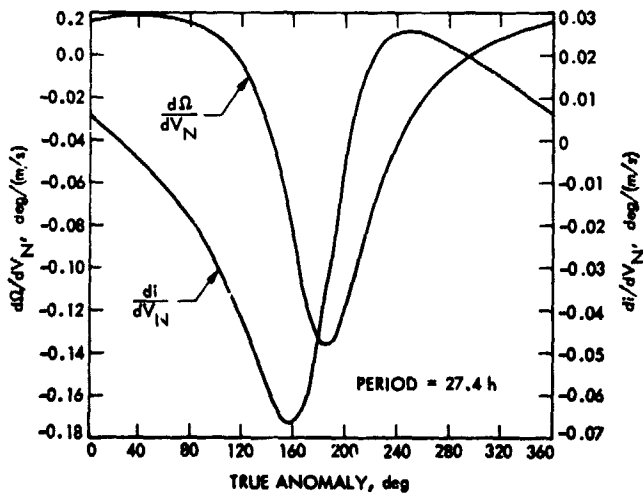


Fig. 48. Right ascension of node and inclination gradients for Viking 2

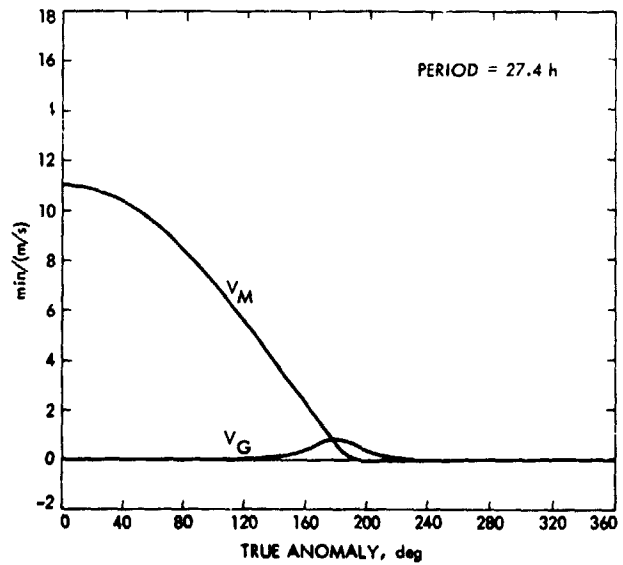


Fig. 50. Time to periapsis gradients for Viking 2

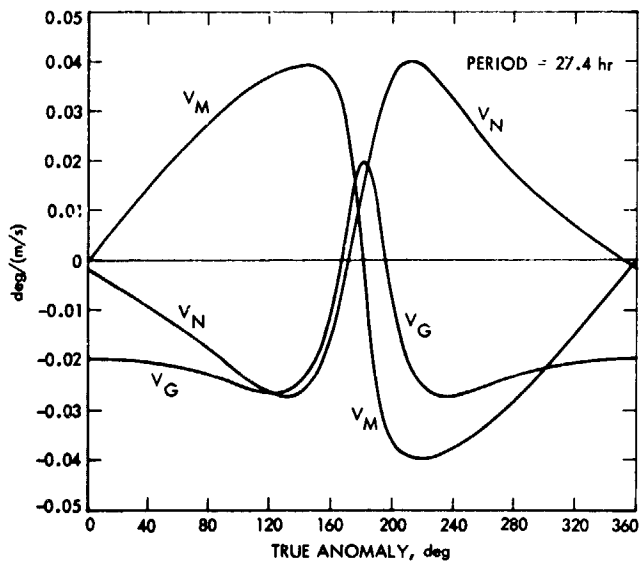


Fig. 51. LATPER gradients for Viking 2

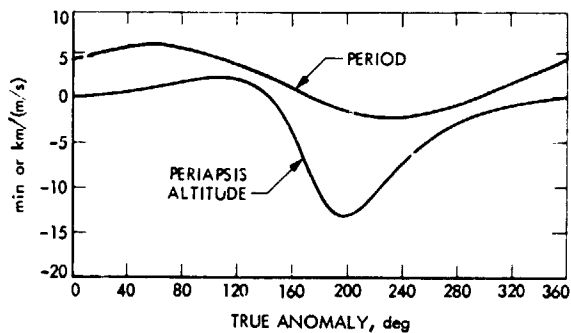


Fig. 53. Partial of period and periapsis altitude with respect to velocity for a sunline maneuver on Viking 1

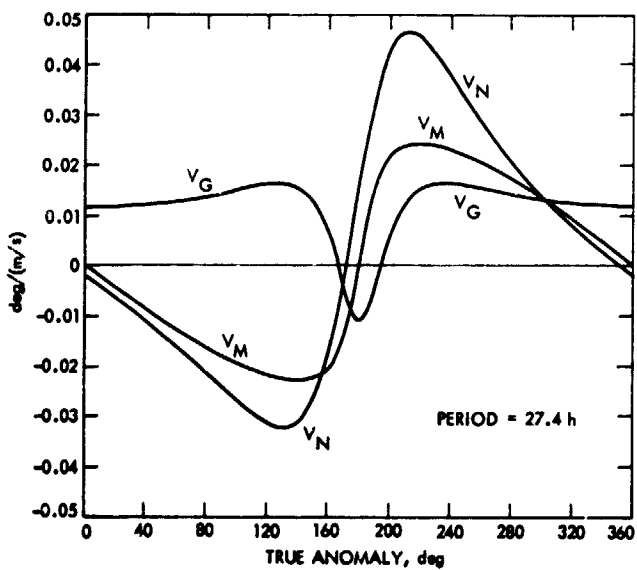


Fig. 52. Sun elevation angle gradients for Viking 2

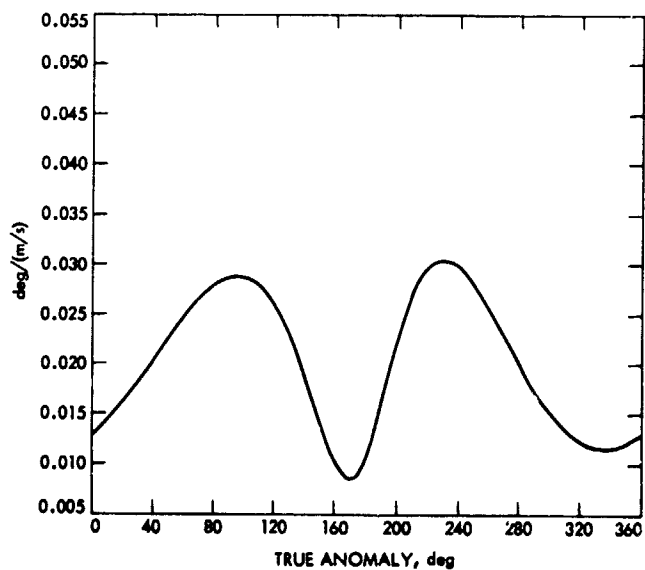


Fig. 54. Partial of LATPER with respect to velocity for a sunline maneuver on Viking 1

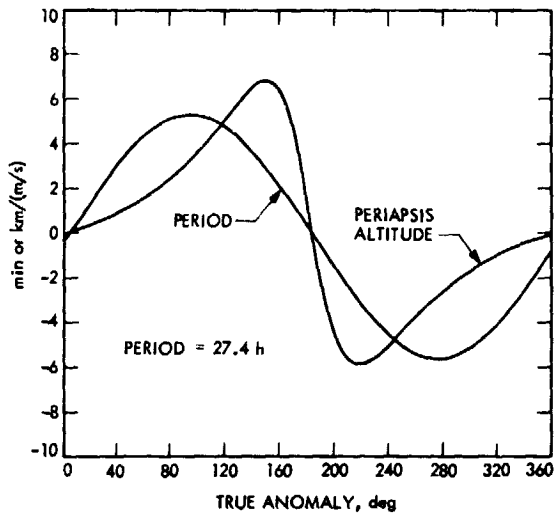


Fig. 55. Partial of period and periapsis altitude with respect to velocity for a sunline maneuver on Viking 2

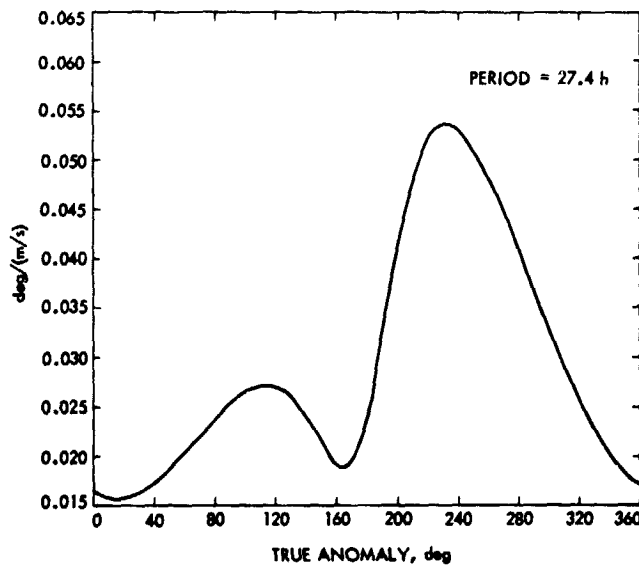


Fig. 56. Partial of LATPER with respect to velocity for a sunline maneuver on Viking 2

Following the insertion of each Viking spacecraft into orbit about Mars, a sequence of orbit trim maneuvers was to be performed according to a predetermined strategy to prepare for lander separation and to permit the taking of site certification reconnaissance data. These strategies were motivated by geometrical factors, expected MOI delivery errors, plus the need for operational flexibility and simplicity. The strategies were formulated as a fixed sequence of orbit parameter-correction maneuvers to be performed on specified spacecraft revolutions about the planet.

The planned Viking 1 maneuver timeline between MOI and lander touchdown is shown in Fig. 57. This phasing diagram shows the timing strategy incorporated in the maneuver strategy. The maneuver sequence consists of:

- (1) A time-phasing maneuver MOT-1 at the second periapsis P2 to nullify the landing site longitude offset at P5.
- (2) A time-phasing maneuver MOT-2 at P5 to produce a nearly synchronous orbit.
- (3) A ΔV -optimal LATPER-correction MOT-3 between P7 and P8 if necessary.
- (4) A combined h_p correction and time-phasing maneuver MOT-4 near the eleventh apoapsis (A11).

An important requirement for the Viking 1 strategy was to provide site reconnaissance as expeditiously as possible. Therefore, the spacecraft was to be inserted into a synchronous orbit with no time of arrival bias and the time-phasing and near-sync trims performed first. Since the h_p and orientation errors were expected to be acceptable for reconnaissance purposes, they were to be corrected later in the maneuver sequence.

Given the maneuver spacing constraints described earlier, the first trim could not be performed before A2. Since period changes are made most efficiently at periapsis, the MOT-1 was to be near P2. MOT-2 could be made near P4, but it was delayed to P5 because there was a very high probability of being able to take reconnaissance at P4 and because this delay would save some orbiter propellant.

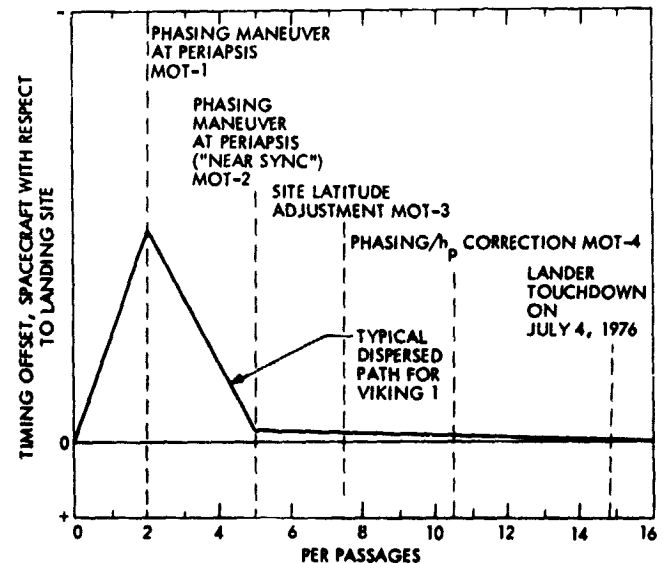


Fig. 57. Viking 1 timing strategy

The remaining trims now fill out the timeline. MOT-3 was scheduled, if necessary, about two revs after the second trim. The exact position and direction of this maneuver was to be determined by a numerical search which would minimize the orbiter ΔV cost. MOT-4 was scheduled near apoapsis since this is the most ΔV -efficient place to correct h_p . Since there had to be at least four revs between MOT-4 and lander touchdown, it could not be performed after the vicinity of A11. The trim was positioned near A11 to relax the operational implementation of the maneuver sequence as much as possible and to minimize the timing error buildup resulting from period errors incurred at MOT-4.

More information concerning the trim maneuvers is provided in Ref. 2. However, it is worthwhile at this point to discuss MOT-3 and MOT-4 in some detail. The purpose of MOT-3 is to correct the latitude of the orbiter PER point (LATPER) to within an acceptable latitude band determined by the target DR X XR tolerance zone centered at the PER point. Figure 58 illustrates the situation when LATPER is

dispersed north of the landing site latitude. A numerical search is used to determine the position and direction of the spacecraft maneuver which corrects LATPER, while minimizing the cost function

$$J = \Delta V_{MOT-3} + \Delta V_{MOT-4}$$

Eventually, statistical studies showed that the probability of needing MOT-3 was less than 1%, so it was eventually dropped from the maneuver timeline.

The last trim was to be performed at a true anomaly of about 164 deg near A11 in order to correct h_p to within tolerances and to nullify any remaining timing error on the separation orbit, while holding ω essentially fixed. The rationale for selecting a true anomaly of 164 deg for MOT-4 can be understood by referring to Figs. 39, 40, and 42. The timing error is corrected by changing the orbital period via a velocity increment in the V_M direction, which is along the spacecraft velocity vector. However, h_p can be corrected by changing the velocity in both the V_M and V_G (in-plane) directions. Therefore, in order to adjust the orbital period and h_p independently, a velocity component is added along V_M to change period and a component is added along V_G to adjust h_p . The component along V_G must take into account that the V_M increment would also change h_p . Now, the timing errors that MOT-4 had been designed to correct are only those introduced by execution and OD errors experienced by previous trims. So the V_M component would generally be much smaller than the V_G component. Reviewing Fig. 42 shows that the sensitivity of ω to V_G is zero at 164 deg. Also, note that this true anomaly is very close to the point ($\eta = 160$ deg) of maximum sensitivity of h_p to a change in V_G , which means that the maneuver point is a relatively efficient point to obtain a combined period and h_p change. Therefore, the 164-deg maneuver point was selected. Essentially the same result could be achieved at a true anomaly of about 196 deg on the same spacecraft revolution. Figure 40 shows that the sensitivity of h_p to V_G is also maximized near this point, although in the opposite direction. The final selection of the maneuver point at 164 deg or at 196 deg could be made based on operational considerations such as communication constraints.

The Viking 2 strategy was designed primarily to correct relatively large expected post-MOI orientation dispersions, to control lander azimuth and SEA at touchdown, and to provide site reconnaissance for both the primary and secondary sites on two separate spacecraft revolutions prior to synchronizing with respect to a site. It was also important to have 12 nearly synchronous revolutions prior to touchdown 25 revs after MOI for reconnaissance purposes. The maneuver timeline and phas-

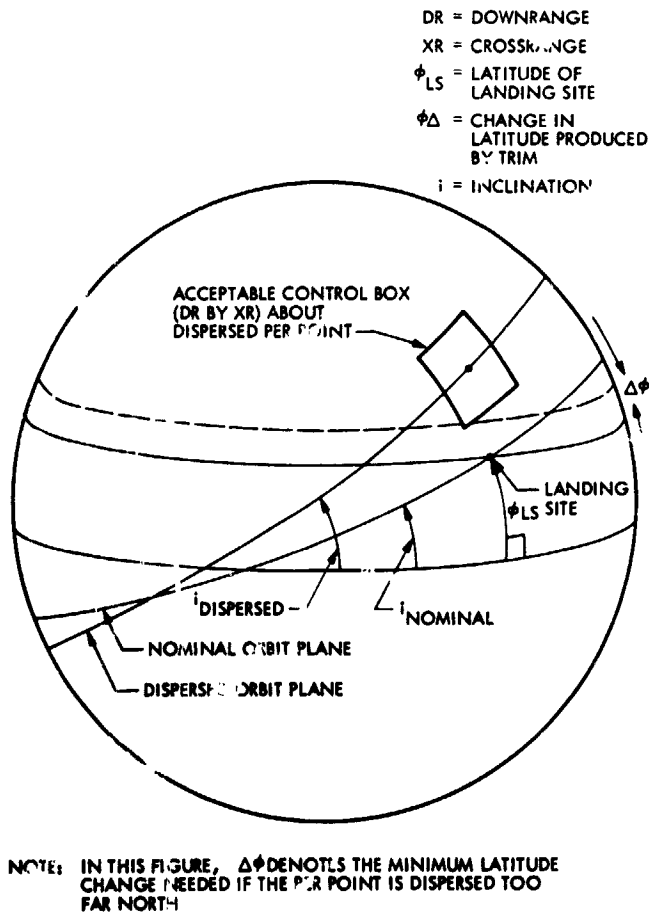


Fig. 58. Latitude correction trim

ing diagram is shown in Fig. 59. The maneuver sequence consisted of:

- (1) The first trim MOT-1, which was to be either a time-phasing maneuver performed near P2 or a combined LATPER-correction and time-phasing maneuver at the true anomaly of the vertical impact point (about 252 deg for Viking 2) between P1 and P2. In either event, the time-phasing would nullify the site longitude offset at P13.
- (2) A time-phasing maneuver MOT-2 at P13 which would produce a nearly synchronous orbit.
- (3) A combined h_p -correction and time-phasing maneuver MOT-3 near A21.

This strategy was to be combined with a MOI maneuver which would target to the nominal ellipse orientation angle ψ (see Fig. 60) regardless of the estimated approach trajectory (pre-MOI) inclination. MOT-1 could then be performed at the true anomaly of the vertical impact point (see Fig. 61) to rotate the orbit about this point to bring the PER point to within an acceptable band about the latitude of the landing site. The geometrical effects of MOT-1 are illustrated in Fig. 62. In this figure, point 1 is the expected location of PER following MOI using estimated approach trajectory data; point 2 is the actual post-MOI PER location; and point 3 is the post-MOT-1 PER location. Note that the angle from the vertical impact point to PER ($\psi + \text{PER angle}$) is invariant.

In addition to correcting geometrical errors, the maneuver strategy had to provide for observing both the primary site and

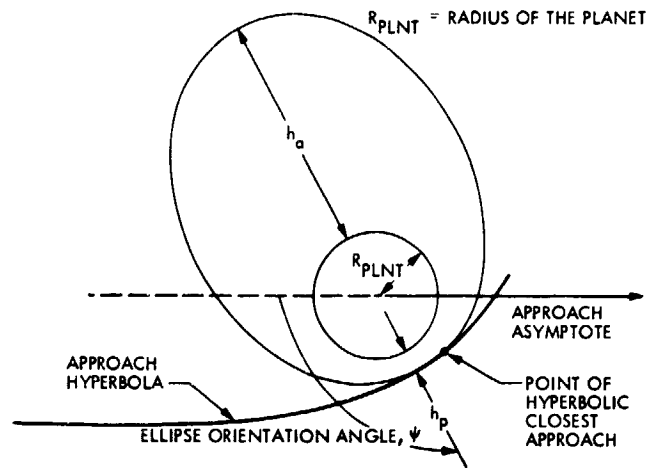


Fig. 60. Definition of ellipse orientation angle ψ

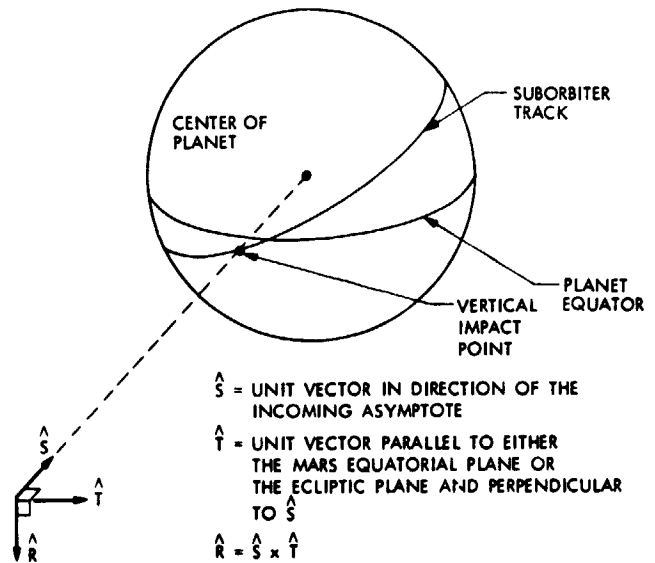


Fig. 61. Definition of vertical impact point

the secondary site at acceptable emission angles twice prior to synchronizing to the primary site, plus correcting in-plane orbit size and shape (P and h_p) errors. These requirements were to be satisfied by correcting period and orientation errors early, and leaving periapsis altitude errors to be removed by the last of the three pre-separation trims.

The nominal post-MOI period and timing offset were selected to provide near overflights of both sites twice prior to synchronization at the thirteenth periapsis P13. The first in-orbit trim is performed at the true anomaly of the vertical impact point between P1 and P2. This maneuver is equivalent to a rotation about the S-vector of the approach hyperbola and restores the orientation and SEA, adjusts period to nullify

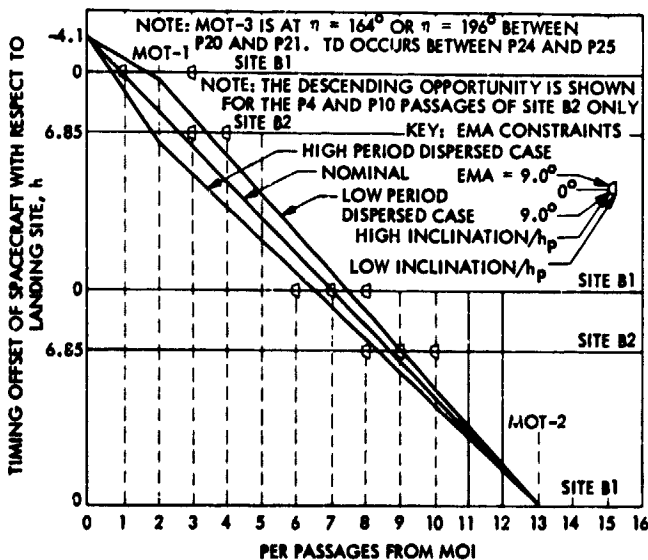


Fig. 59. Viking 2 timing strategy and reconnaissance opportunities for EMA < 9 deg

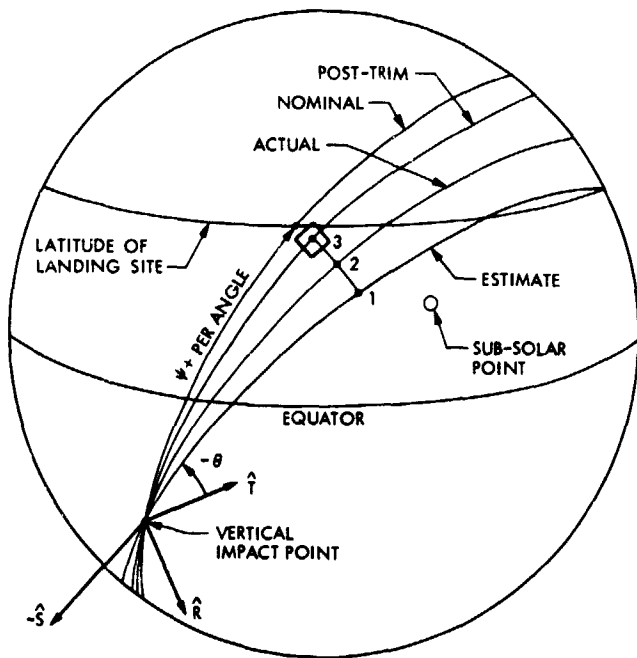


Fig. 62. Site acquisition geometry for Viking 2

the timing error at P13, and holds ψ essentially fixed. These constraints determine the velocity correction vector, which means that the periapsis altitude cannot in general be controlled independently with this maneuver and often is further dispersed by it. If the post-MOI orientation parameters were satisfactory, timing errors would be corrected at P2 and no orientation correction would be made.

The second trim MOT-2 is made at P13 so that there are 12 near-sync orbits prior to landing. This trim is nominally a synchronizing trim, but, in the presence of OD and execution errors experienced in MOT-1, it actually phases to the required timing offset on the separation orbit. This maneuver is performed at or near periapsis to minimize ΔV .

The third trim is performed at a true anomaly of about 164 deg (or equivalently 196 deg) between P20 and P21 in the same manner as the last trim for Viking 1. The placement of MOT-3 had to be properly balanced between P13 and P25. Location soon after P13 permits too much time for timing error growth by separation. Location too near P25 increases the size of the MOT-3 ΔV and increases the final period dispersions, which in turn increase the postlanding relay geometry (timing offset) dispersions. Selection of a point near A21 was determined to achieve the best balance among the various tradeoffs.

For this strategy, the nominal post-MOI orbit would provide a direct overflight of the site B1 on revolutions 1 and 7,

and a near direct overflight of site B2 on revolutions 3 and 9. The timing strategy involved for the nominal and 99% period-dispersed cases is shown in Fig. 59. The vertical lines indicate the range of timing offset that will allow reconnaissance with $EMA < 9.0$ deg. For each reconnaissance opportunity, two such vertical lines are shown: one for the 99% low inclination and h_p values and the other for the 99% high values. These parameter combinations are given because of the high correlations between i and h_p ($\rho_{ih_p} = 0.98$ for Viking 2 with radio only OD and $\rho_{ih_p} = 0.86$ for radio plus optical) on the post-MOI orbit and because of their effect on EMA. Reconnaissance probabilities which include the effects of altitude and orientation dispersions are given in Ref. 4.

Another significant feature of this strategy is that both period and orientation errors are corrected early to meet reconnaissance requirements. If the period errors were not corrected early, large timing dispersions would occur at the second reconnaissance opportunities for each site, greatly reducing the likelihood of viewing the sites. If the orientation errors were not corrected before the reconnaissance opportunities, large geometrical errors would produce unsatisfactory viewing angles.

B. Maneuver Mechanization

The planned maneuver sequence for the Viking spacecraft was a gyro warmup period followed by a roll turn, yaw turn, possibly a second roll, and finally the motor burn to achieve the desired ΔV . Turns could be made of either polarity and for durations exceeding a complete revolution about either (roll or yaw) axis. The duration of the turns was controlled by counting a specified number of pulses, each 1 s in length. Hence, the computed (ideal) turns to implement a correction had to be quantized to an integer number of seconds in duration and could not be mechanized precisely. With a turn rate of about 0.18 deg/s, the maximum resolution error was 0.09 deg about each of the axes. A similar situation existed for controlling the magnitude of the velocity correction. An accelerometer was used, which issued a pulse for each 0.03 m/s, corresponding to a maximum resolution error of 0.015 m/s. In addition, there was a requirement that each motor burn be at least 1 s (i.e., approximately 1/2 m/s for prelanding trims) in length.

There were two methods for reducing the effects of these resolution errors and the minimum burn duration constraint. One method was to alter the time of motor ignition, changing slightly the pointing and magnitude requirements. The second was to modify the direction of the maneuver in such a way that critical target parameters were unchanged and resolution errors were mapped into less important, and perhaps less sensitive, parameters.

In loading the maneuver into the spacecraft's onboard computer, the turns parameters had to be specified well in advance of implementing the maneuver. On the other hand, it was only necessary at this time to estimate the velocity increment magnitude ΔV (equivalently, the burn duration) and ignition time. Following this stage of the maneuver design process, the orbit determination process continued; i.e., additional tracking data were processed to predict the orbital parameters at the time of the trim maneuver. The ΔV and ignition time were then updated to account for late changes in the orbit estimate.

Execution errors associated with the mechanization of a maneuver may be classified as proportional (to the maneuver magnitude) and fixed (independent of the magnitude). The inflight a priori 99% execution errors in both magnitude and pointing are shown in Table 10 for both spacecraft.

Table 10. Inflight a priori execution errors (99%)

Maneuver	Pointing, mrad	Proportional magnitude, %	Fixed magnitude, m/s
Viking 1			
MOT-1	16	0.22	0.029
MOT-5	16	0.21	0.035
MOT-6	16	0.21	0.035
SKT-2	16	0.14	0.063
MOT-7	16	0.11	0.031
MOT-8	9.6	0.113	0.053
MOT-9	9	0.115	0.031
Viking 2			
MOT-1	8.5	0.244	0.028
MOT-2	9	0.241	0.028
MOT-3	8.5	0.244	0.028
MOT-4	8.5	0.239	0.028
MOT-5A	9.0	0.157	0.030
MOT-5	15.5	0.157	0.030

C. Maneuver Constraints

There were a number of constraints on the design of each of the maneuvers, primarily on the turns that could be performed and on the timing of the maneuvers. Two independent roll/yaw turn sets could achieve the desired thrusting direction, although the spacecraft orientation would usually be different after the implementation of each set. By varying the turn combinations, including turns of more than 180 deg, eight different turn sets can be found which yield the required thrust pointing direction. In general, turns constraints identified by the Orbiter Performance Analysis Group (OPAG) eliminated some of these sequences from further consideration.

Turns constraints were determined by the pointing requirements of certain onboard instruments. The violation of these constraints was checked by superimposing traces of the Sun and Earth during the turns on another figure which indicated the unacceptable regions in cone angle vs clock angle space (Fig. 63). Thus, an appropriate set of turns was determined from among the candidates. Specific instruments which imposed constraints were the VIS, IR, and the Canopus sensor sun shutter. The VIS and IR imposed constraints on the pointing of the scan platform. The constraint imposed by the Canopus sensor sun shutter to prevent its being pointed at the Sun was precautionary since the purpose of the shutter was to protect the Canopus sensor from light sources such as the Sun. The precaution was necessary because, if the shutter failed either in the open position and the sensor was damaged by being exposed to direct sunlight or in the closed position, the spacecraft would be unable to maintain its star reference.

It was also very desirable to maintain downlink communication during the motor burn. Communication constraints, which required that the low-gain antenna (LGA) be directed, with varying tolerances, to the Earth, were satisfied by vectorially adding a velocity increment to the maneuver in a noncritical direction.

Figure 63 shows the pointing region for the high-gain antenna (HGA) in either the unflipped ("normal") or flipped

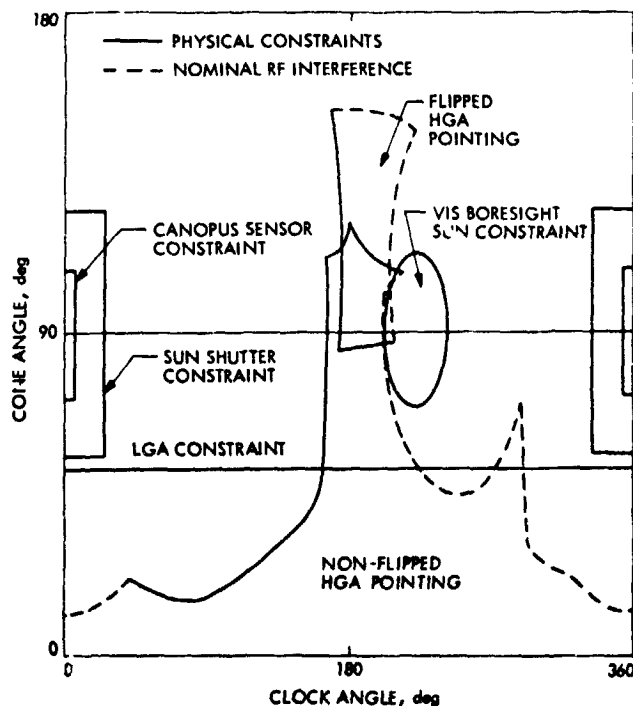


Fig. 63. Viking maneuver pointing constraints

positions. To communicate over the HGA during the burn, the turn set had to be selected to position the Earth vector in one of these regions. Recall that a second roll turn was introduced for MOI to communicate over this antenna in the flipped position. However, flipping the antenna was generally considered to be risky and was not done for any of the trims.

Maneuvers performed on orbits having significant solar occultations were further constrained to lie within a specified tolerance of the sun direction. This constraint limits the size of the yaw turn to avoid further depletion of the batteries. And, in fact, burns were performed in the cruise mode as sunline maneuvers whenever possible. Thus the turns were eliminated, greatly reducing operational complexity.

Timing constraints were imposed for certain trims. For example, some trims were prohibited from being performed within 1 1/2 hours of periapsis to permit the taking of relay-link data. One maneuver was constrained to be at least four hours after periapsis to allow sufficient time for the orbiter to take and playback relay data.

These and other constraints are considered in more detail in the discussions of the individual trims for each spacecraft given below in Subsections E and F.

D. Trim Maneuver Software

The Mars Orbit Trim Operations Program (MOTOP) was implemented for use by the Flight Path Analysis Group (FPAG) to calculate and analyze the VO orbit correction maneuvers required to acquire the landing site, to satisfy mission and science objectives and to station-keep over the lander. To meet these requirements, MOTOP was designed to perform the following functions:

- (1) *Trim maneuver strategy function.* Simulate selected maneuver strategies designed to acquire primary and secondary landing sites and to support postlanding VO operations, while satisfying mission constraints.
- (2) *High-precision trim maneuver computation junction.* Compute the precise velocity correction vector and time of ignition, given the best estimate of the spacecraft state, the required postmaneuver orbit parameters, and other mission, spacecraft and astronomical data.
- (3) *Maneuver post-processing function.* Given the velocity correction, compute the turn sequences required to achieve proper thrust pointing and generate the maneuver-commandable quantities based on spacecraft performance data. Data useful for the analysis of maneuver constraints is generated. The turn sequences

required to properly align the VO relay antenna bore-sight are computed.

- (4) *Statistical error analysis function.* For each maneuver of a maneuver strategy, perform an error analysis to generate expected velocity cost and postmaneuver control statistics, given maneuver execution and orbit determination uncertainties.
- (5) *Post-maneuver performance evaluation function.* Based on pre- and postmaneuver orbit determination, evaluate the performance of all orbit trim maneuvers after execution, including ΔV , and turns that were actually implemented.

For further details on MOTOP, see Refs. 5 and 6.

To perform the five MOTOP operational functions, a variety of subprograms could be executed. However, as the mission progressed, the typical mode of operation was to perform the strategy function by using just one of the MOTOP strategy algorithms. This algorithm targeted one trim to a maximum of four parameters in the following list: period, radius at periapsis, time for periapsis, right ascension of the ascending node, argument of periapsis, inclination, latitude of the PER point, and sun elevation angle. If less than four parameters were targeted, the remaining degrees of freedom were used to minimize ΔV . The high-precision analysis was then performed by using DPTRAJ in a man-in-the-loop iterative fashion.

E. Viking 1 Trim Maneuvers

This section and the following section treat the actual adaptive design and implementation of the maneuvers as the mission progressed, including the inflight results. Tables 11 and 12 give the commandable quantities for each trim, while Table 13 provides the resulting trajectory data.

1. **Prelanding trim maneuvers.** Figure 57 showed the original maneuver timeline and phasing strategy associated with a synchronous post-MOI target orbit. However, because of the propellant pressurant regulator leak discussed earlier, two large approach midcourse maneuvers were performed followed by insertion into a 42-h orbit. This large initial target orbit made it necessary to change the phasing strategy to that shown in Figure 64. This strategy maintained essentially the same maneuver timeline as that shown in Fig. 57, with phasing maneuvers at P2, P5 and A11. But MOI-1 was now a large period-change maneuver designed to return to the nominal timeline to permit the taking of reconnaissance data and to prepare for lander separation.

If the errors encountered at MOI were small, MOT-1 would be a syncing trim to decrease the orbiter period from 42 h to

Table 11. Design quantities: velocity increment and ignition time

Maneuver	Velocity increment ΔV , m/s	Ignition time GMT-OET (date, h:mn:s)
Viking 1		
MOT-1	80.053	6-21-76, 17:26:21
MOT-5	25.713	7-9-76, 00:40:00
MOT-6	2.736	7-14-76, 07:12:00
SKT-2	2.228	8-3-76, 03:00:00
MOT-7	21.327	9-11-76, 19:03:54
MOT-8	3.708	9-20-76, 22:15:29
MOT-9	22.926	9-24-76, 15:10:00
Viking 2		
MOT-1	4.077	8-9-76, 17:16:00
MOT-2	1.776	8-14-76, 08:31:15
MOT-3	42.728	8-25-76, 17:48:29
MOT-4	11.292	8-27-76, 20:25:38
MOT-5A	5.006	9-29-76, 04:33:20
MOT-5	342.551	9-30-76, 21:07:38

synchronous. If the errors experienced on this trim were also small, no further maneuvers would be needed to acquire the nominal landing site. However, in the presence of large execution errors at MOI, the P2 trim would phase to produce a tilt angle of less than 9 deg at P4 and P6. Note, for example, that a dispersed path having a large positive offset at P2 would be targeted for a negative offset at P5. This strategy improves the tilt angle (equivalently timing offset) at P4. A satisfactory tilt angle is then obtained at P6 by a phasing maneuver at P5. The last trim is performed at A11 to sync over the site in preparation for landing. The probability (pre-MOI) of achieving a 9 deg or less tilt angle at P4 and P6 with the Viking 1 execution and OD errors was about 98%.

The phasing diagram in Fig. 65 shows the timing offset between the Viking 1 spacecraft and the planned landing site at 19.5°N latitude and 34.0°W longitude. This figure gives the planned sequence of events at the time of MOT-1, when hope still remained for a July 4th landing. Even prior to implementing MOT-1, it was clear that the P5 trim, MOT-2, could be deleted from the maneuver timeline. Recall from the discussion above that MOT-2 was intended to phase to obtain satisfactory tilt angles for reconnaissance purposes in the event of large post-MOI orbit dispersions. However, the MOI was very accurate and did not introduce large dispersions. Note that the first periapsis passage P1 has been omitted in Figs. 64 and 65. This notation was adopted to maintain the correspondence between periapsis number and GMT reflected in extensive operational plans. As shown in Fig. 65, the probability was greater than 99% that the tilt angle requirement (tilt < 9 deg) would be satisfied for every rev before MOT-3; thus,

Table 12. Design quantities: turns

Maneuver	Roll reference	Turns, deg		
		Roll	Yaw	Roll
Viking 1				
MOT-1	Canopus	56.856	-126.850	0.0
MOT-5	Canopus	-153.329	-130.500	0.0
MOT-6	Canopus	46.270	-51.100	0.0
SKT-2	Canopus	101.506	-23.907	0.0
MOT-7	Sirius	125.177	-126.116	0.0
MOT-8	Sirius	0.0	0.0	0.0
MOT-9	Sirius	0.0	0.0	0.0
Viking 2				
MOT-1	Canopus	0.0	0.0	0.0
MOT-2	Canopus	0.0	0.0	0.0
MOT-3	Vega	0.0	0.0	0.0
MOT-4	Vega	0.0	0.0	0.0
MOT-5A	Vega	0.0	0.0	0.0
MOT-5	Vega	-141.351	-123.777	144.839

MOT-2 was cancelled. There was a small probability that execution errors experienced at MOT-1 would produce a period error that was large enough to require a phasing maneuver at MOT-3, but, in fact, the A1 site was almost perfectly acquired by MOT-1.

Site reconnaissance now proceeded as planned and soon showed that the A1 site was unsatisfactory for landing. As the search for a satisfactory nearby site continued, MOT-3 was designed to provide for significant landing site adjustments as late as possible. However, no satisfactory site was found in time to permit a landing on July 4th.

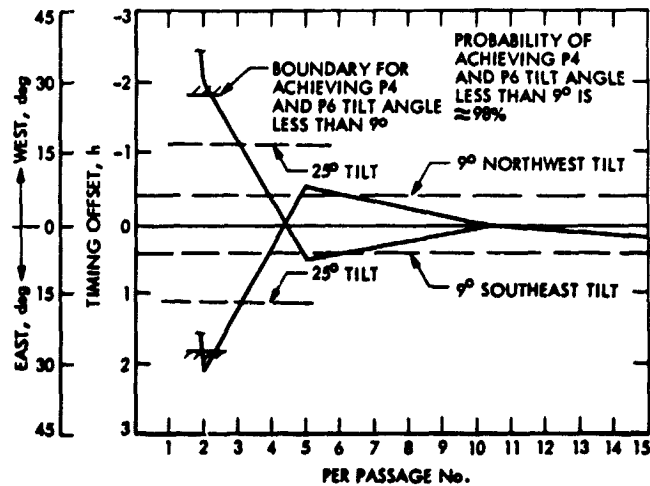


Fig. 64. MOT site acquisition strategies

Table 13. Trajectory data

	P, h:min:s	r_p , km	Parameters			Time (GMT, 1976)
			Ω , deg	ω , deg	i , deg	
Viking 1: MOT-1						
Premaneuver (A2)	42:21:07	4907.2	129.80	39.76	37.37	20:16:56 (6/20)
Postmaneuver (A3)	24:39:40	4907.1	129.68	39.94	37.88	05:47:19 (6/22)
Viking 1: MOT-5						
Premaneuver (A19)	24:37:13	4905.6	127.59	42.74	37.99	16:02:28 (7/8)
Postmaneuver (A20)	24:46:34	4906.9	124.77	44.89	37.69	16:43:52 (7/9)
Viking 1: MOT-6						
Premaneuver (A24)	24:45:51	4906.2	124.24	45.61	37.73	19:48:34 (7/13)
Postmaneuver (A25)	24:39:04	4902.5	124.20	45.82	37.70	20:31:03 (7/14)
Viking 1: SK1-2						
Premaneuver (A43)	24:36:21	4900.1	121.94	48.96	37.81	07:50:13 (8/2)
Postmaneuver (A44)	24:38:17	4898.8	121.78	49.31	37.90	08:28:06 (8/3)
Viking 1: MOT-7						
Premaneuver (A82)	24:32:08	4885.5	117.12	55.82	38.15	06:50:09 (9/11)
Postmaneuver (A83)	21:52:37	4885.2	116.99	56.03	38.13	06:02:33 (9/12)
Viking 1: MOT-8						
Premaneuver (A92)	21:52:38	4882.4	115.78	57.63	38.10	10:56:42 (9/20)
Postmaneuver (A93)	22:13:45	4885.9	115.72	57.99	38.31	08:59:57 (9/21)
Viking 1: MOT-9						
Premaneuver (A96)	22:13:55	4885.2	115.25	58.51	38.10	03:41:26 (9/24)
Postmaneuver (A97)	24:38:42	4909.4	115.08	59.77	38.16	03:08:11 (9/25)
Viking 2: MOT-1						
Premaneuver (A2)	27:37:12	4912.4	36.28	69.36	55.18	05:05:11 (8/9)
Postmaneuver (A3)	27:18:47	4893.0	36.07	69.77	55.20	08:33:16 (8/10)
Viking 2: MOT-2						
Premaneuver (A6)	27:19:16	4892.8	35.80	69.90	55.21	18:30:49 (8/13)
Postmaneuver (A7)	27:24:47	4895.0	35.72	70.02	55.21	21:52:53 (8/14)

Table 13 (contd)

	Parameters					Time (GMT, 1976)
	P, h:min:s	r_p , km	Ω , deg	ω , deg	i , deg	
Viking 2 MOT-3						
Premaneuver (A16)	27:24:47	4896.0	34.85	70.52	55.19	04:38:23 (8/25)
Postmaneuver (A17)	24:02:24	4818.3	34.78	72.66	55.65	06:22:43 (8/26)
Viking 2: MOT-4						
Premaneuver (A18)	24:02:31	4818.6	34.70	72.71	55.65	06:25:12 (8/27)
Postmaneuver (A19)	24:37:19	4883.0	34.40	73.65	55.39	06:45:15 (8/28)
Viking 2: MOT-5A						
Premaneuver (A50)	24:38:28	4897.0	31.71	75.53	55.38	02:16:44 (9/29)
Postmaneuver (A51)	24:38:35	4925.5	31.27	75.89	55.34	02:57:44 (9/30)
Viking 2: MOT-5						
Premaneuver (A51)	24:38:35	4925.5	31.27	75.89	55.34	02:57:44 (9/30)
Postmaneuver (A52)	26:47:38	4902.3	54.61	68.34	74.90	04:56:43 (10/1)

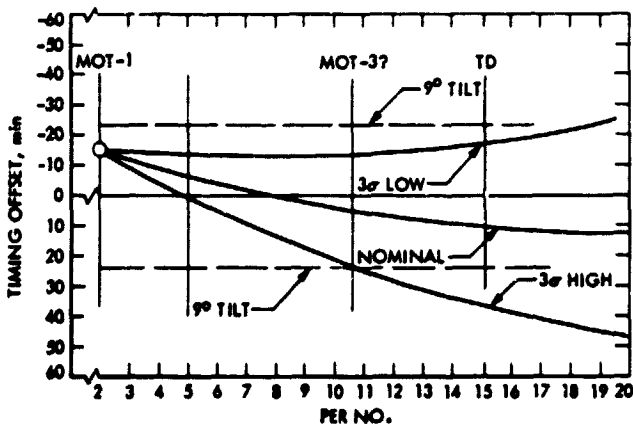


Fig. 65. Site acquisition for July 4, 1976, landing

Since no site was found in the immediate neighborhood of A1, MOT-3 and MOT-4 were cancelled and a maneuver strategy comprised of MOT-5 and MOT-6 was designed to walk to an area northwest of the original site. Following the implementation of MOT-5, the spacecraft began to walk to a candidate site in the northwest region. In this walk, still another candidate was found. MOT-6 synchronized to this site at 22.5°N and 47.4°W . Final adjustments in the site coordinates were made and landing occurred on 20 July 1976 (GMT). Each of the trims is considered in turn in the following discussion.

The post-MOI orbit parameters are given in Table 13 and the orbit geometry is shown in Fig. 66. MOT-1 was designed to return the spacecraft to the nominal timeline to permit the taking of reconnaissance data and to prepare for lander separation. The landing site rendezvous problem is illustrated in Fig. 67.

MOT-1 was designed to remove all downrange (DR) error at P15 and to perform no correction of the latitude of the PER point (LATPER). The remaining error, XR, would then be taken out by the VL at deorbit to conserve propellant on the orbiter. Also, since the landing site was subject to adjustment, it was possible that the current LATPER might be better than the nominal one. Therefore, LATPER was left to precess to a value of 19.65°N at P15. This meant that VL1 would have to crossrange 0.3 deg to move to 19.5°N or as much as 3.0 deg to reach candidate sites further south. Deleting the correction of LATPER also maximized the probability of needing only one trim by minimizing the execution errors. In fact, the probability of satisfying the entry angle requirements for the nominal site was shown to be 86%. The A1 site acquisition probability density function is given in Fig. 68. This figure shows the probability of success as a function of the VL entry angle and crossranging.

Given the above maneuver criteria, MOT-1 reduces to a period-change maneuver where the target period must provide

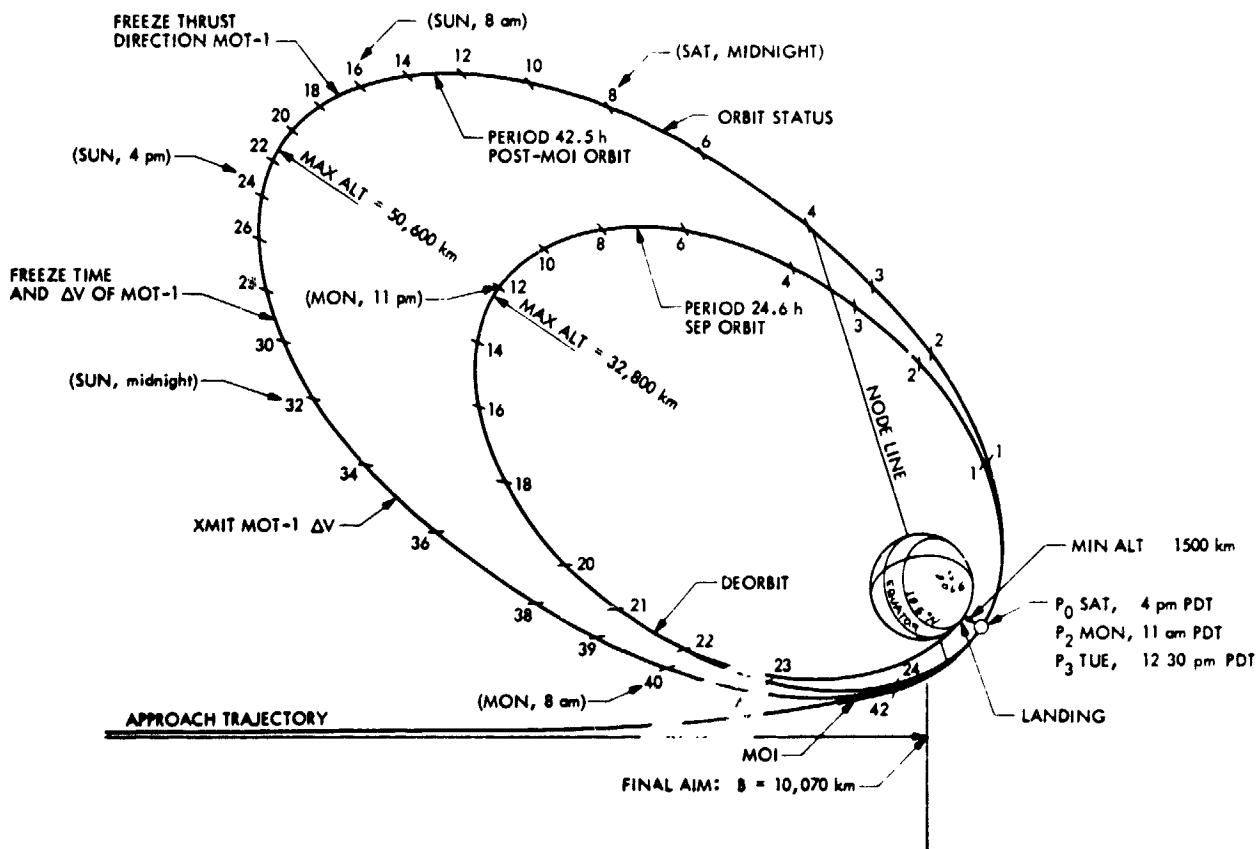


Fig. 66. Viking 1 orbit geometry

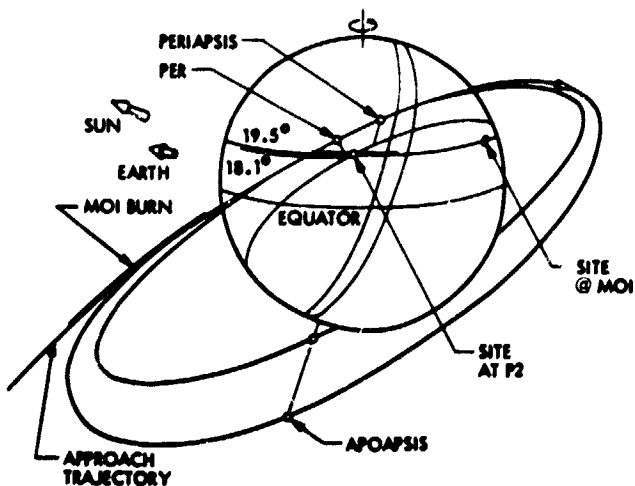


Fig. 67. Landing site rendezvous

DR = 0 at P15. To minimize ΔV , the trim was performed at perapsis, the most ΔV -efficient place for such a maneuver. The maneuver was made in the direction of $-V_M$. Being tangential to the spacecraft velocity vector essentially nullified

the effects of pointing errors and, in fact, the 99% accuracy for period was predicted to be 1.8 min for the 80.053 m/s burn.

The MOT-1 design was subject to a constraint on the maneuver execution time. The motor burn had to occur between 13:16 GMT and 22:16 GMT on June 21, 1976. This block of time in the onboard computer CCS was reserved for the maneuver commands. Commands for activities other than the propulsive maneuver were loaded into the CCS for times outside of this window. The boundaries of the window were computed by FPAG prior to MOI, using expected 99% dispersions for MOI. This maneuver constraint was easily met.

For MOT-1, the angle between the LGA and the Earth exceeded 50 deg so the burn was performed in the blind. The commandable quantities are given in Tables 11 and 12, trajectory data in Table 13.

Following the execution of MOT-1, site reconnaissance proceeded as planned and soon showed that the A1 site was unsatisfactory for landing. As the search for a satisfactory site continued, MOT-3 was designed to provide for significant

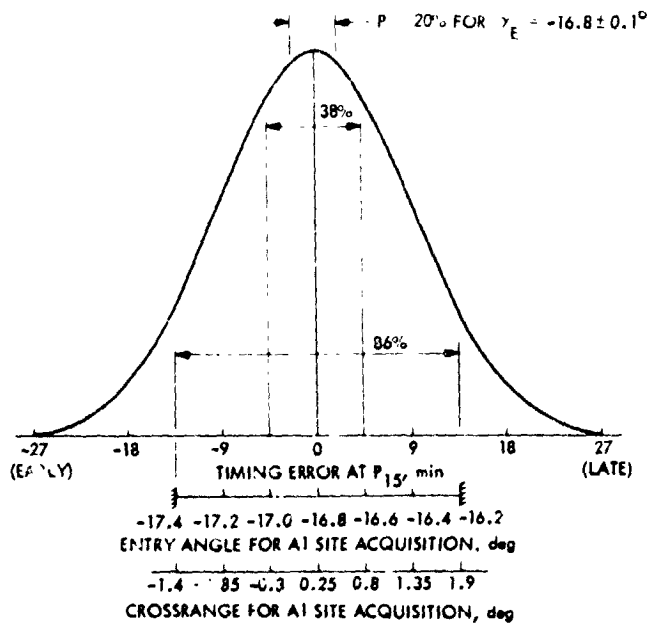


Fig. 68. A-1 site acquisition probability

landing site adjustments as late as possible in support of a July 4th landing. Initially, it was not known whether the new site would be east or west of the original one, or how far in either direction. So ΔV -cost and accuracy analyses were performed for changing the orbital period ± 1 min while keeping h_p fixed and satisfying the communication constraint (angle between the Earth and the LGA < 50 deg). Once the new site was selected, the required period change to walk to this location could be determined and the results for ± 1 min scaled to this new value.

The problem was then considered in flight plane velocity space, using the gradient values given in Figs. 39 and 40. The magnitude of the ΔV_M component is determined by the period change, while the ΔV_U component cancels the h_p change introduced by the ΔV_M component. A third component is required along $\Delta \hat{P}_N$ to satisfy the communication requirement. Figure 69 shows the magnitude of the resulting inplane velocity increment ΔV_p and the 3-dimensional vector ΔV for the period decreasing case $\Delta P = -1$ min. Finally, the expected 99% accuracy for period is determined, using the execution error statistics listed in Table 10, the sensitivity of period to ΔV_M , and the angle between ΔV and $\Delta \hat{P}_M$.

A new candidate landing site was selected at 19.35°N and 32.5°W for targeting purposes. Even though the landing site selection team had not determined that there was a satisfactory lander footprint about this point, the decision was made to proceed with the maneuver design process for MOT-3 so that maneuver parameters would be available if needed. Since

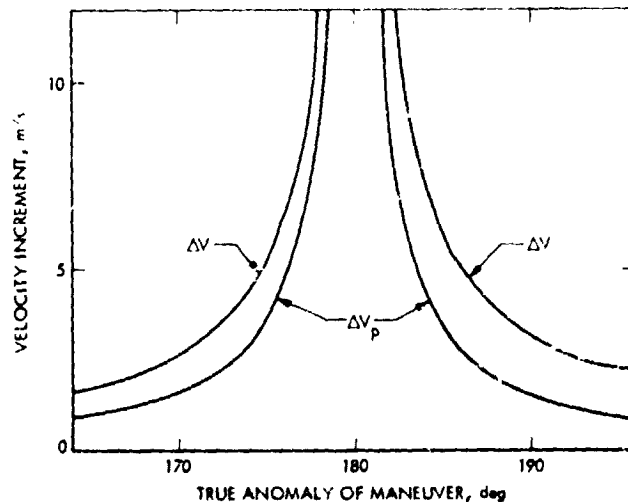


Fig. 69. MOT-3 velocity cost analysis for Viking 1. $\Delta p = -1$ min

the site was to the east of the original one, the orbital period had to be reduced.

MOT-1 had obtained an orbit that would place the PER point at 19.5°N and 34°W . Figure 70 shows the resulting VL accessible area, which consists of those sites that the lander could reach by crossranging 3 deg or less and by targeting to an entry angle γ_E between -17.4 and -16.2 deg. This figure also shows the 99% landing dispersion ellipse if MOT-3 were deleted and the lander performed $+1.20$ deg of crossranging while targeting to $\gamma_E = -16.51$ deg. The benefit of using MOT-3 for the new candidate (19.35°N , 32.50°W) was thus seen to be questionable. But this candidate had not yet been shown to be acceptable for landing. If this site should be rejected, the late update capability and the VL crossranging capability could be used to attain another site in this eastern region. However, since no satisfactory site was found in the eastern region, MOT-3 was cancelled.

A new candidate site (AINW) was specified northwest of A1 at 23.4°N , 43.4°W . Therefore, it was necessary to change both the latitude and longitude of the PER point. A three-trim strategy (Fig. 71) was designed consisting of phase and sync maneuvers (to correct the longitude) and a LATPER change maneuver. However, subsequently, the first of these maneuvers, known as MOT-4, was omitted by combining the phase and LATPER changes in MOT-5. The only penalty for deleting this maneuver was that the tilt angle would exceed 9 deg at P20 for targets northwest of 23.5°N and 43.0°W .

The revised strategy is shown in Fig. 72. The design criteria for this revised AINW acquisition strategy may be stated briefly as follows:

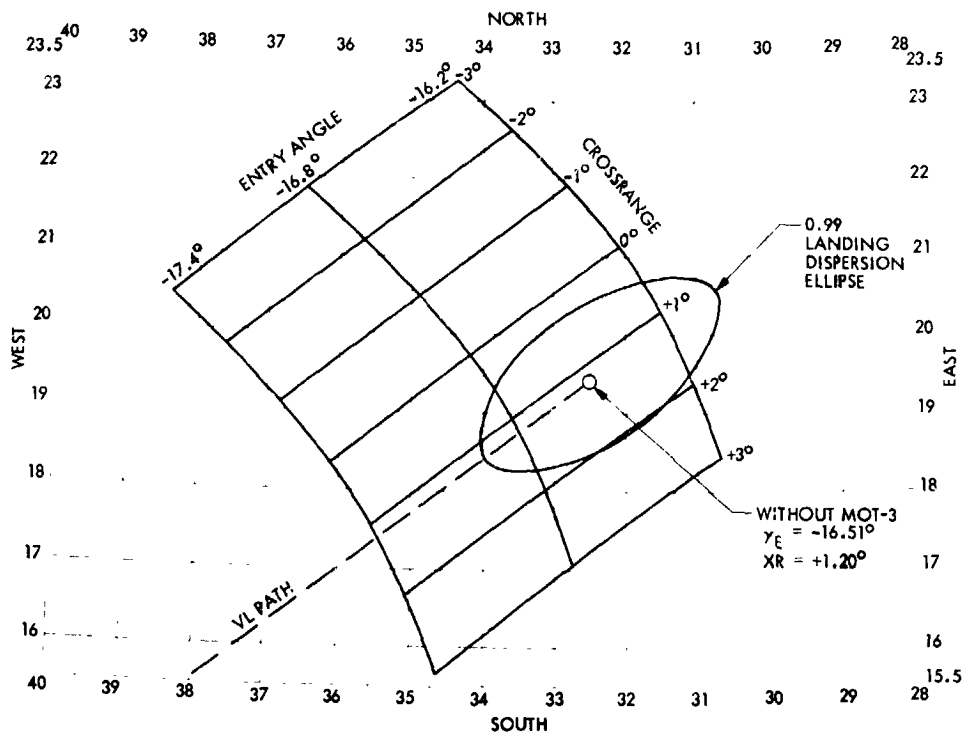


Fig. 70. VL accessible area and landing dispersion ellipse with MOT-3

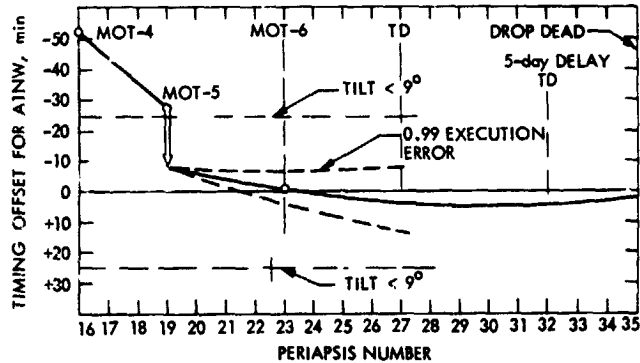


Fig. 71. A1NW acquisition with MOT-4, $LATPER_{TD} = 23^\circ N$

- (1) The orbiter will time-phase to the optimum entry flight path angle $\gamma_E = -16.8$ deg.
- (2) The lander will crossrange $XR = -3.0$ deg to reach the northernmost site at $24.0^\circ N$ latitude.
- (3) The VL will land near periapsis P27.
- (4) The orbit will minimize the drift following P27 if the landing is delayed by five days.

The maneuver software discussed earlier was used to compute MOT-5 to phase (adjust period) and correct orientation

(LATPER) for minimum ΔV while holding h_p fixed. The resulting tilt angle expected at P20 and the VL accessible area are shown in Fig. 73. Tilt angles for viewing the given latitude and longitude are shown in the range from 0 to 20 deg. For example, the tilt angle in the P20 coverage for a site at $24^\circ N$ latitude and $39.6^\circ W$ longitude is 8 deg. The VL accessible area shows those sites that the lander could reach by crossranging 3 deg or less and by targeting to γ_E between -17.4 and -16.2 deg.

An analysis was performed to determine the latitude and longitude changes that could be accommodated with the late

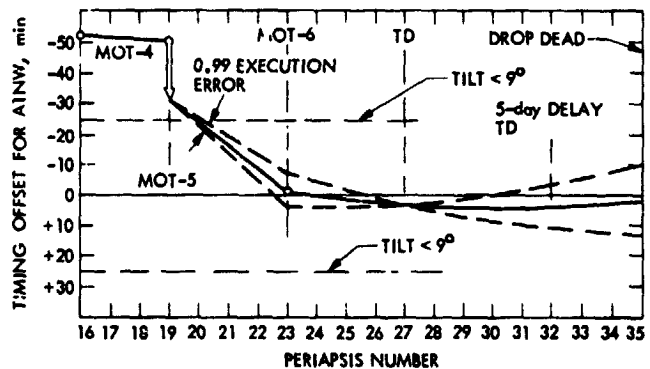


Fig. 72. A1NW acquisition without MOT-4

ORIGINAL PAGE IS
OF POOR QUALITY

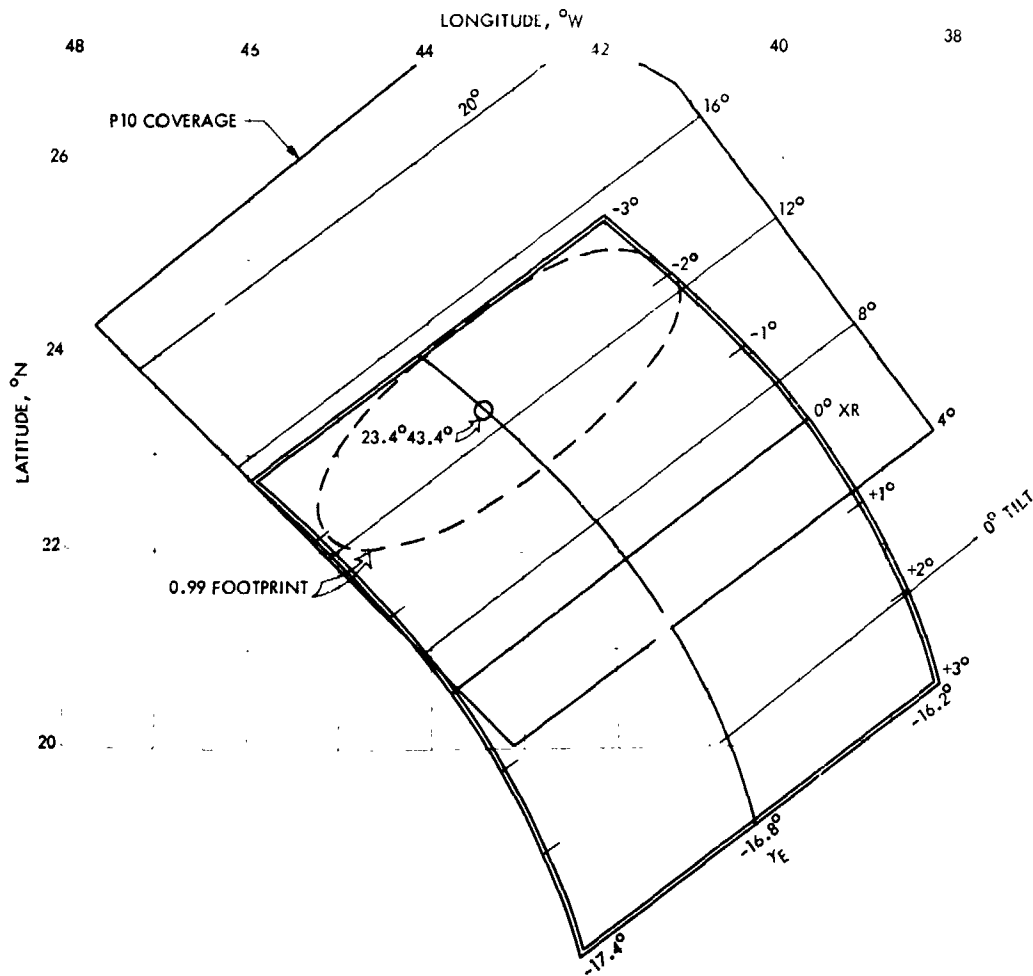


Fig. 73. P20 tilt and VL accessible area

update. (Recall that late updates involved changes in ΔV and t_{ign} , while the turns remained fixed.) The band of equivalent latitude and longitude adjustments that could be obtained by such an update are shown in Fig. 74. The solid line marked $\Delta\Delta V = 0.0$ m/s shows site changes that could be made by adjusting only the ignition time. Other lines running parallel to this one show sites that could be obtained by also adjusting ΔV . The band is shown for changes of only ± 30 min in t_{ign} because this was approximately the maximum adjustment capability at the time of the final maneuver design.

This information concerning site targeting adjustment capability was of great interest at this point in the mission since the very intense search for the final landing site was still in progress. In fact, prior to implementing MOT-5, another site was selected at 23.5°N latitude and 51.0°W longitude: This new site became known as A1WNW. Table 14 can be used as a reference for keeping track of the site changes.

As discussed above, some latitude and longitude adjustments could be made while using the thrust directions specified for A1NW. However, to walk to this new site, the wait time between MOT-5 and MOT-6 was increased according to the phasing strategy shown in Fig. 75. MOT-5 would still perform the LATPER-change and phasing; MOT-6 would be performed near P26 to sync. The phasing was to target for the

Table 14. Viking 1 landing site targeting adjustments

Parameter	A1	A1R	A1NW	A1WNW	A1WNWSE	Final target ^a
Latitude, °N	19.5	19.35	23.4	23.5	22.5	22.4
Longitude, °W	34.0	32.5	43.4	51.0	47.4	47.5
SEA at TD, deg	29.8	30.8	38.0	39.0	38.1	38.2

^aViking 1 landed at 22.46°N latitude and 48.01°W longitude.

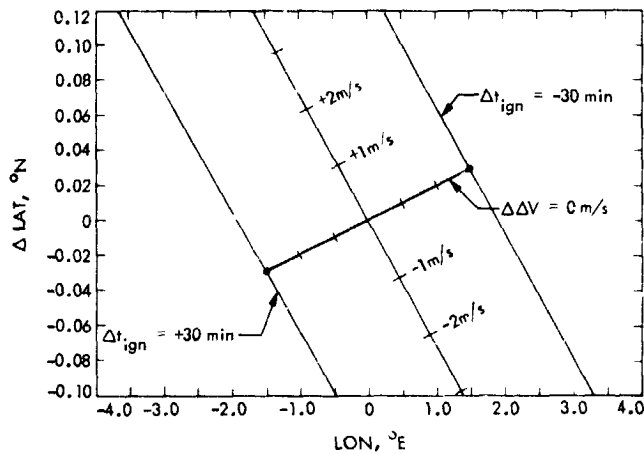


Fig. 74. MOT PER update for Viking 1

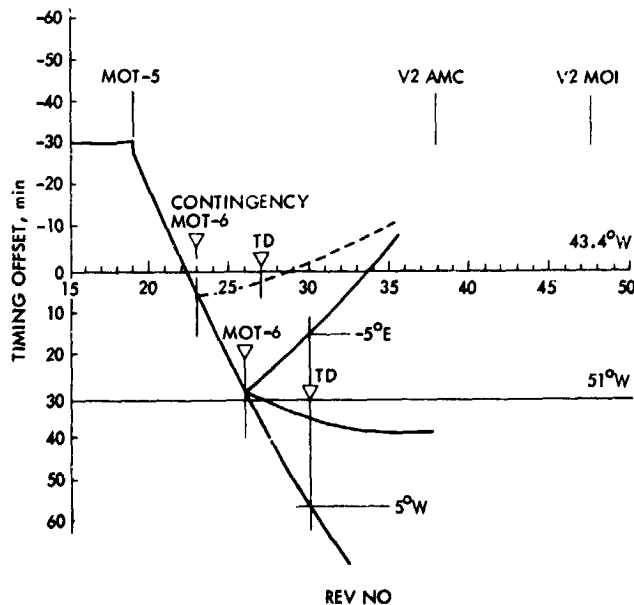


Fig. 75. Site acquisition for Viking 1

optimal γ_E of -16.8 deg at P30 (or, if delayed, at P35). The fan of paths at the MOT-6 maneuver shows the results of changing the longitude targeting requirements by ± 5 deg after MOT-5 has been executed. A contingency plan is also shown in the figure. If, following the taking of additional reconnaissance data, the decision were made to return to A1NW, MOT-6 would be executed at P23 for the optimal $\gamma_E = -16.8$ deg to touchdown at 23.4°N , 43.4°W near P27.

When the commandable quantities were determined for targeting to A1NW, the GMT ignition window was specified as 23 h: 35 min on July 8 to 00 h: 40 min on July 9. Moving to a

site farther to the west required increasing the period. Hence, it was necessary to delay the maneuver. Because of the constraint to remain within the ignition window, the maneuver was performed at the latest allowable time at a slight ΔV penalty. The required ΔV was 25.713 m/s.

Only the final (updated) commandable quantities are shown in Tables 11 and 12. Table 13 shows the trajectory data. The P30 value of LATPER was changed from 21.1 deg to 22.0 deg by MOT-5.

Still another candidate site, known as A1WNWSE (22.5°N , 47.4°W) was located by using reconnaissance data obtained during the walk begun by MOT-5. MOT-6 was designed to time-phase to $\gamma_E = -16.8$ deg at this site, while minimizing the postmaneuver asynchronism. The latter was needed to give more time to select a landing ellipse if the proposed area was very rough. These objectives put a heavy demand on the period accuracy.

The design of the maneuver involved a tradeoff of several factors:

- (1) The need for optimal period control.
- (2) Timing constraints at P30 and P35.
- (3) A favorable geometry for communications.
- (4) No change in h_p .

This is a 4-dimensional optimization problem. To simplify the analysis, the requirement to fix h_p was ignored at first and the problem was considered in flight plane velocity space. A ΔV_M component was needed to decrease the period by 6 min 40 s to time-phase. A normal component ΔV_N was needed to satisfy the 50 deg constraint on the angle between the Earth vector and the LGA. We know from the gradient curves that the required magnitudes of ΔV_M and ΔV_N are functions of the true anomaly. The period sensitivity to ΔV_M is symmetric about the true anomaly $\eta = 180$ deg, but maneuver locations with $\eta > 180$ deg were more favorable for communications. So only this region ($\eta > 180$ deg) was considered. Figures 76 and 77 show the 99% period control and ΔV cost, respectively. A maneuver at apoapsis would provide the best period accuracy, but would have changed h_p by 120 km. Also, the ΔV cost is largest here because of the relative insensitivity of period to velocity changes. For example, if the maneuver at $\eta = 220$ deg were to maintain h_p fixed, the 99% period accuracy would have increased to 12 s.

As a tradeoff, the maneuver at $\eta = 262.5$ deg was selected. Calculations using high-precision (DPTRAJ) trajectory data and LTOP target data refined the maneuver design to $\Delta V =$

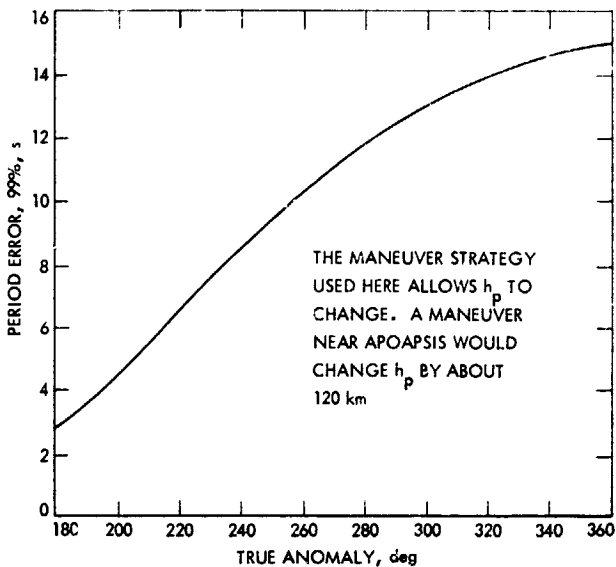


Fig. 76. MOT-6 period control vs true anomaly

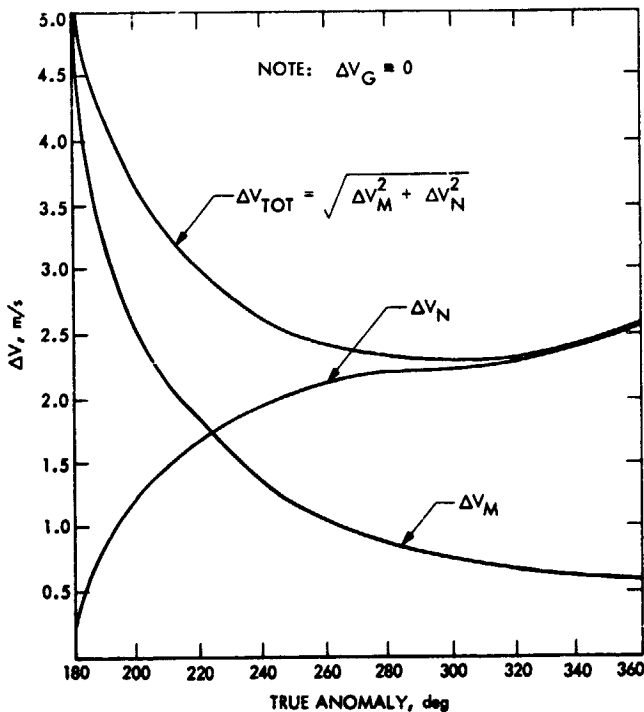


Fig. 77. MOT-6 ΔV -cost vs true anomaly

2.7 m/s ($\Delta V_M = 1.2$ m/s, $\Delta V_N = 2.5$ m/s) and a 99% period accuracy of 11 s. The timing offset history is shown in Fig. 78.

The landing site specification was finalized at 22.4°N latitude and 47.5°W longitude. Figure 79 shows the VL parameters for revs 30 and 35 that resulted from the execution of

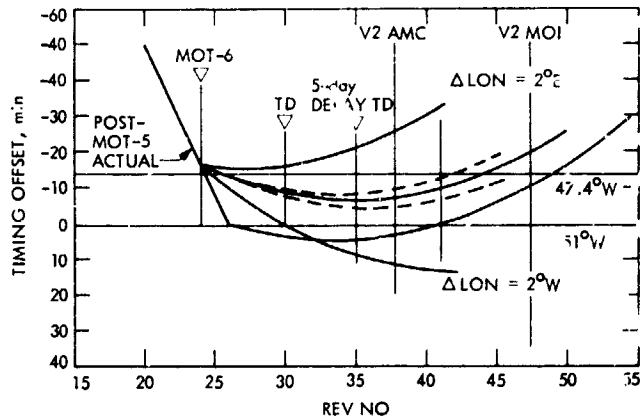


Fig. 78. Site acquisition strategy following MOT-5

MOT-6, where the dashed curves at $\gamma_E = -16.9$ and $\gamma_L = -15.7$ deg indicate desired VL operating limits. Thus, MOT-6 had adequately completed the final landing site acquisition preparatory to lander separation.

2. Station-keeping trim. The mission design designated certain SOLs as station-keeping maneuver opportunities. That is, station-keeping trims (SKT) could only be performed on SOL 5, SOL 13 and SOL 26. SOL 5 was reserved for an early SKT to adjust the relay geometry in the event that the lander attained an unfavorable orientation. After the landing, the orientation was found to be favorable for the relay so this maneuver was cancelled. In fact, only the SKT at SOL 13 was performed for Viking 1.

The maneuver design was greatly influenced by a malfunction that occurred on VL-1 following landing. The lander relay to the orbiter had been mechanized to operate in a 1-, 10- or 30-W mode. Instead of operating in the 30-W mode as programmed, the lander used the 1-W mode on SOLs 1 and 2. On SOL 3, VL-1 began using the 30-W capability. Since the reason for this relay link malfunction was not known, there was concern that the VL-1 might switch back unexpectedly to the 1-W mode. Therefore, the trim was designed to maintain the VO-VL relay which would provide maximum 1-W relay performance.

Figure 80 shows the longitude offset history for the orbiter with respect to the landing site. The dashed curve shows the offset if the SKT-2 had not been performed. This path would have moved the VO to a geometry which provided better (longer) 30-W performance. However, an SKT would have been required before the EOM in any event. Another reason for performing the station-keeping at this SOL rather than a later one was that Viking 2 was still in interplanetary cruise, whereas a later opportunity would have been during the busy time of Viking 2 landing site selection. The solid path was

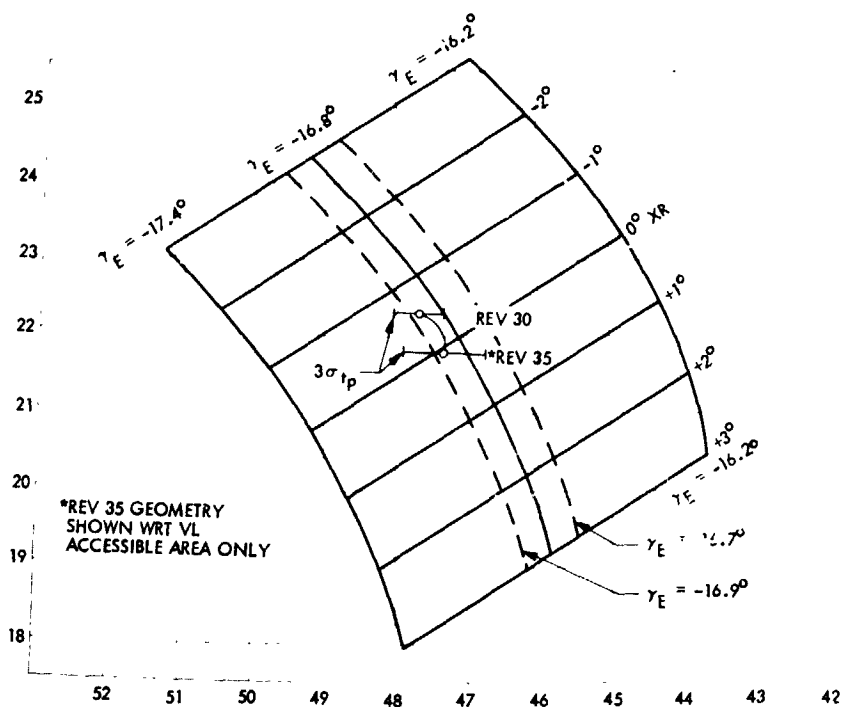


Fig. 79. VL parameters R30-R35

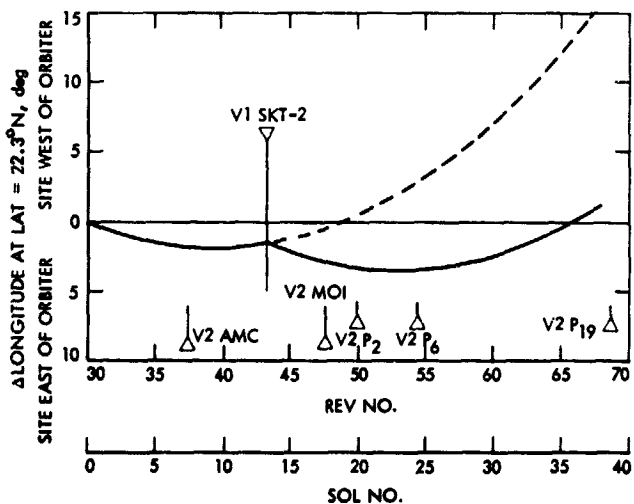


Fig. 80. Station-keeping strategy for Viking 1

chosen to keep the VO in the area of good 1-W performance through about SOL 40. This would allow about 25 more SOLs to observe and analyze the relay link mode selection. Another SKT could have been performed later to again adjust the offset to remain within the good 1-W region if necessary. However, this additional trim was not needed.

To introduce the longitude shift discussed above, it was necessary to increase the orbital period of the VO by 2 min 13 s. It was also necessary to keep h_p fixed and to perform the maneuver at least four hours after periapsis. This ignition constraint allowed sufficient time for the VO to receive and play back relay data from the lander. The minimum ΔV maneuver that would target to the increased period and fixed h_p , subject to the execution time constraint, was located at the beginning of the ignition window, i.e., at a true anomaly of 162 deg. This maneuver was an in-plane maneuver of 1.9 m/s and orthogonal to the h_p gradient.

To reduce the effect of execution errors on the orbital period, an out-of-plane component ΔV_N was added to the velocity vector as shown in Fig. 81. Figure 82 shows the effect on period control as the angle between ΔV_M and ΔV is increased, while the component along ΔV_M is fixed. When ΔV points directly along ΔV_M , i.e., the angle is zero, the fixed magnitude execution error is the dominate error source pointing in the direction of maximum sensitivity to orbit period. As the angle increases, the sensitivity to the fixed error decreases. For large angles, the pointing error begins to dominate and the period error rises.

Finally, it was desirable to maintain communications during the maneuver. At the time of the SKT, the communications

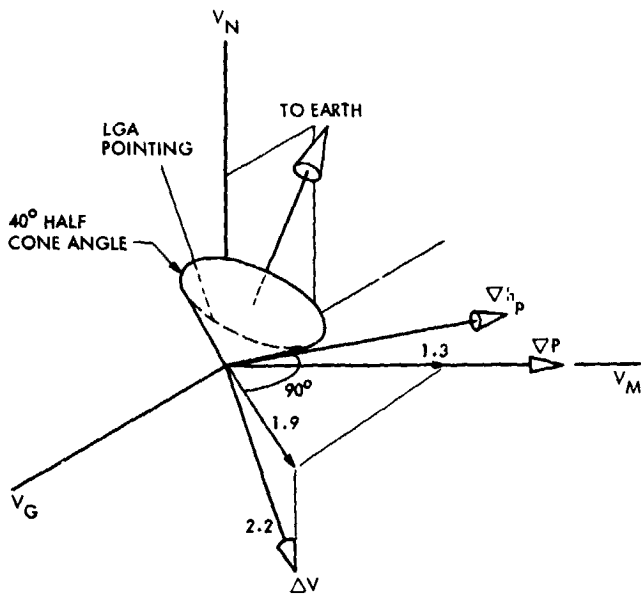


Fig. 81. SKT-2 ΔV geometry for Viking 1

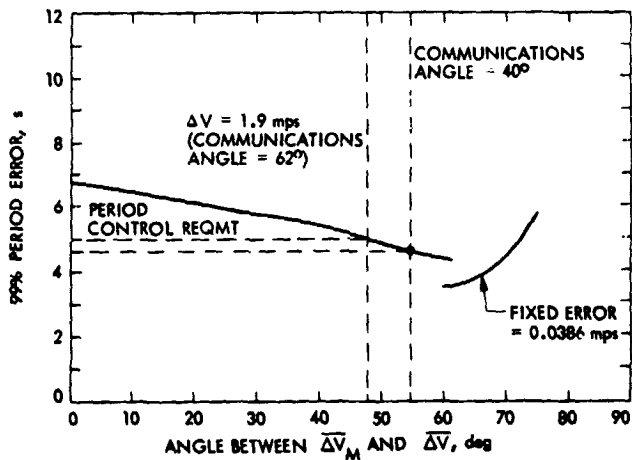


Fig. 82. SKT-2 accuracy analysis

angle constraint was that the angle between the LGA and the earth not exceed 40 deg. Since this communications constraint could be satisfied with acceptable period control (5 s 99%) at a ΔV penalty of only 0.3 m/s, the maneuver shown in Figure 81 was performed. The commandable quantities are given in Tables 11 and 12. Trajectory data are given in Table 13.

3. VO excursion maneuvers. Three trims were performed to "walk" VO-1 to VL-2. The walk was designed so that VO-1 could support VL-2 science data return in an optimum manner during the VO-2 plane change and resync walk period, September 29 to October 17, 1976. Resynchronizing the VO-1 orbit

east of the VL-2 landing site would afford the optimum VL-2/VO-1 relay link windows. Hence, a walk/resync maneuver sequence was designed to position the VO-1 orbit track 11 deg east of the VL-2 longitude at the time of VL-1 latitude (22.4 deg) overfly. Figure 83 shows the geometric relationships.

In addition to providing the relay geometry discussed above, the maneuver sequence was required to walk around as much of the planet as possible by periastris P88 for site reconnaissance purposes. Figure 84 shows how much longitude would not be overflowed as a function of the targeted longitude at P93. This figure also shows the required walk rate in deg/rev for the interval from P80 to P88 to achieve the targeted site longitude and the corresponding ΔV cost. For example, a

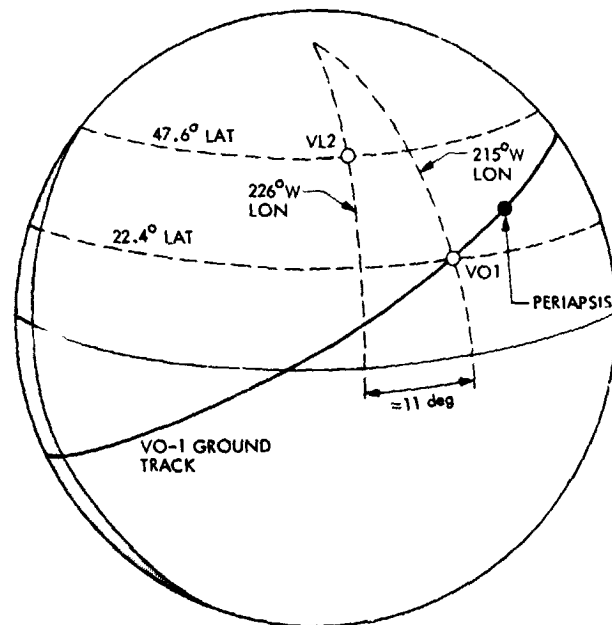


Fig. 83. VL-2/VO-1 relay geometry

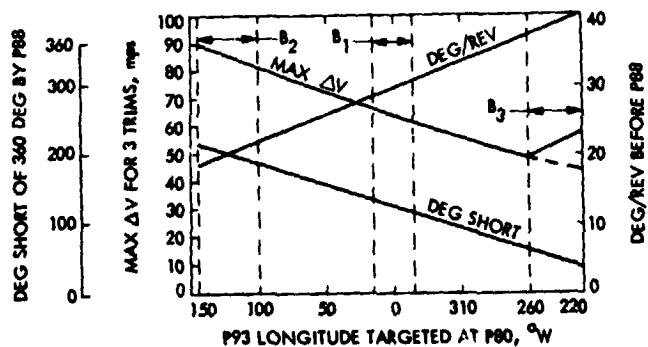


Fig. 84. Viking 1 walk analysis

desynchronizing trim performed at P80 to produce a 40-deg/rev walk rate would cause the spacecraft to overfly all but 30 deg of longitude by P88, while the ΔV cost would be less than 60 m/s.

Ultimately a decision was made to land VL-2 at B_3 . However, by this time, the orbiter science long-range planning had begun working to a 40-deg/rev walk. To avoid redoing this sequence design work, it was required that the first phasing maneuver target to this walk rate. Following a decision to delay each of the planned maneuvers for two revolutions, the final walk design characteristics were: (1) to provide a 14-rev subsync walk beginning on rev 82 and ending on rev 96, (2) to

begin the walk at 40 deg/rev, and (3) to resync, providing maximum duration VL-2 to VO-1 relay links, i.e., to provide the geometric relationship shown in Fig. 83.

These objectives were achieved via a sequence of three trims:

- (1) MOT-7 near P82 to begin a 40-deg/rev walk,
- (2) MOT-8 on rev 92 to phase to the Viking 2 site on rev 96.
- (3) MOT-9 on rev 96 to sync 11 deg east of the Viking 2 site.

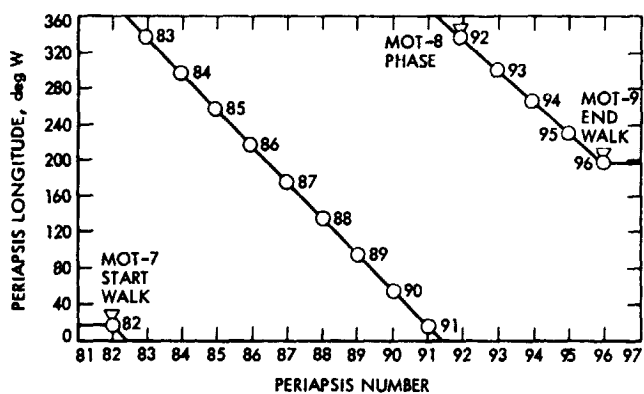


Fig. 85. VO-1 walk timeline

Since VO-1 was now moving into a period of solar occultations which would result in a significant drain of the VO-1 batteries, a turns constraint was imposed on MOT-8 and MOT-9. If the yaw maneuver were to move the solar panels too far off the Sun, the power system would switch to a share mode in which the spacecraft would get some of its power from the Sun and the rest from the batteries. MOT-8 and MOT-9 were constrained to a yaw of less than 40 deg to avoid the use of this share mode and thus avoid further depletion of the batteries.

MOT-7 was to be performed on rev 82 to begin a 10-rev subsync walk of 40 deg/rev as shown in Fig. 85. (A subsync walk was chosen to walk around the planet as rapidly as possible.) Therefore, it was necessary to reduce the orbital period by 2.7 hours. To minimize the ΔV cost, the maneuver

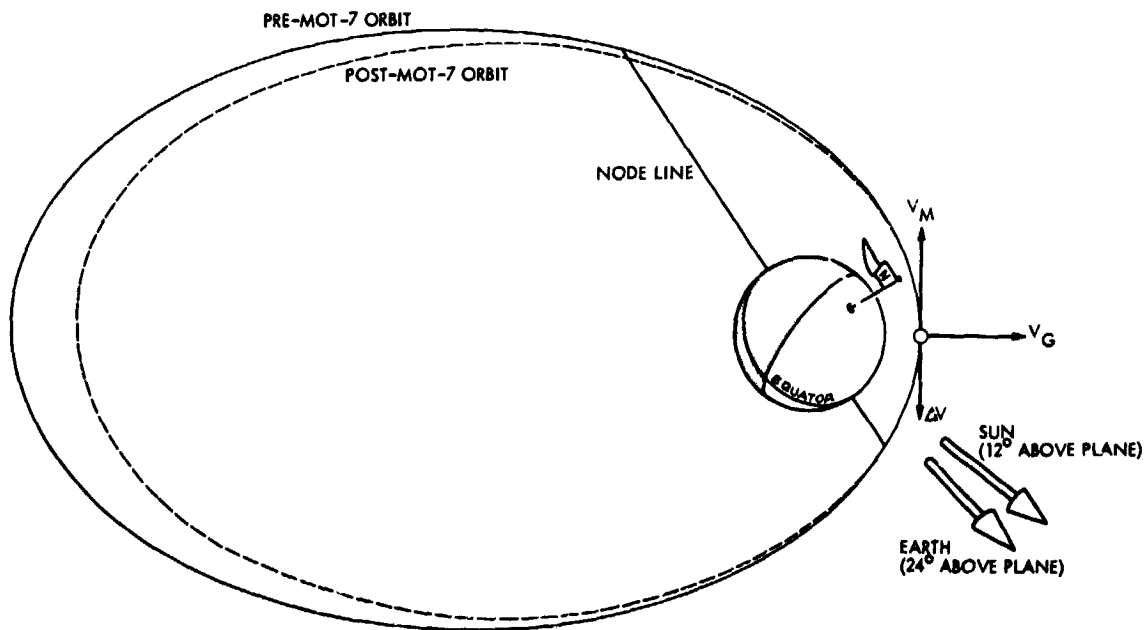


Fig. 86. MOT-7 geometry for Viking 1

was performed at periapsis as a retromaneuver opposite the spacecraft velocity vector (Fig. 86).

The accuracy of the maneuver was considered acceptable because the period could be controlled to within 20 s to 99% probability. Performing the maneuver along the velocity vector essentially nullified the effects of pointing errors. The 20 s was essentially due to magnitude errors only. Recall that the execution accuracy was improved for the SKT by adding a component normal to the orbit plane. Such a strategy could not be used here. In fact, adding such a component would have degraded the accuracy by increasing the effect of the (proportional) pointing error.

Finally, the cost of maintaining communications during the motor burn of 19 m/s was deemed to be too great, so this maneuver was performed "in the blind." Figure 86 shows the geometry of the maneuver. Recall that the LGA points in the $-\Delta V$ direction so that the 40-deg communication constraint was violated. Figure 87 shows the graph of the expected change in frequency (in Hz) during the MOT-7 turns that was used for monitoring the maneuver. Since communications over the LGA are not lost by the roll turn, a hold was built in following this turn to allow time to verify that it was performed correctly. After this verification, the spacecraft proceeded to perform the yaw. Approximately 4 min after beginning this turn, the downlink was lost. The maneuver was completed in the blind and was accurate to within 10 s in period. The commandable quantities are given in Tables 11 and 12; the trajectory and performance data are given in Table 13.

MOT-8 phased VO-1 for VL-2 relay at rev 96. It was only necessary to reduce the walk rate from 40 to 35 deg/rev by increasing the orbital period by 0.3 h. This maneuver would

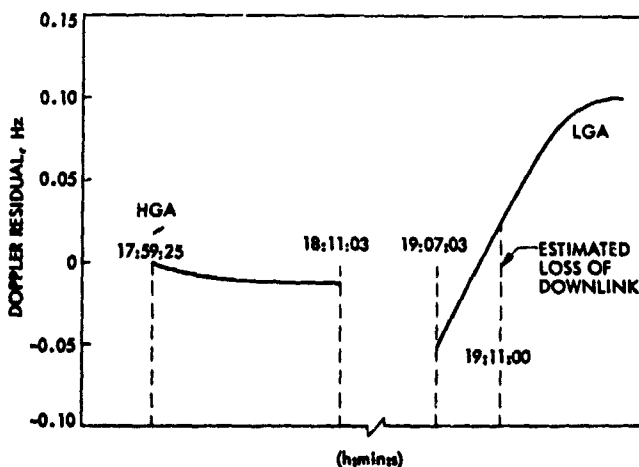


Fig. 87. MOT-7 turns doppler for Viking 1

not have been needed if it were not for the 40-deg/rev walk requirement following MOT-7. That is, the phasing could have been accomplished by one trim instead of two.

After several strategies were considered, the minimum ΔV sunline maneuver was performed at a true anomaly of 54 deg. Performing a sunline maneuver greatly reduced the operational complexity by eliminating the need for turns and also provided communications during the motor burn by remaining in the cruise attitude. Figure 88 shows the geometry. Thirdly, this orientation also avoided further depletion of the batteries begun by the solar occultations by keeping the solar panels pointed toward the Sun. The 99% period accuracy was shown to be 12 s, which was acceptable. Therefore, the 3.7 m/sec maneuver was performed on September 20, 1976. Performance data are given in Table 13.

The post-MOT-8 timeline shown in Fig. 89 made it necessary to redesign MOT-9. As discussed above, this maneuver had been intended to complete the walk/resync maneuver sequence by syncing VO-1 11 deg east of VL-2. Before MOT-8 was implemented, a high-precision (DPTRAJ) trajectory run provided a list of the expected periapsis passage times through P110, assuming nominal MOT-8 and MOT-9 trims. Before MOT-8 was implemented, orbiter science viewing and relay link times were computed based on these expected postmaneuver data. Execution errors experienced at MOT-8 introduced a somewhat different periapsis history. Therefore, the target period for MOT-9 was adjusted to correct the future periapsis timeline, while sacrificing the requirement to resync at 11 deg east of VL-2. Given this tradeoff, a perfect MOT-9 would now produce the expected periapsis passage times through P110 to within 1 min and obtain an orbit that is 1.1 min super-synchronous.

This maneuver was also performed along the sunline for the same reasons as was MOT-8. The ΔV penalty for performing the maneuver along the sunline was only 4 m/s, which was considered acceptable. The orbital geometry characteristics were the same as those for MOT-8 since the maneuver was again performed at the minimum ΔV sunline maneuver location. The VO-1/VL-2 offset history following MOT-9 is shown in Fig. 90. Performance data are in Table 13.

Note that this maneuver sequence increased the height at periapsis to 1516 km. One of the alternate strategies that was considered would have kept h_p fixed by performing MOT-8 at about 139 deg. Such a MOT-8 maneuver would have lowered h_p in anticipation of raising it again at MOT-9. However, it was decided that fixing h_p was not worth an increase in ΔV cost of 4 m/s.

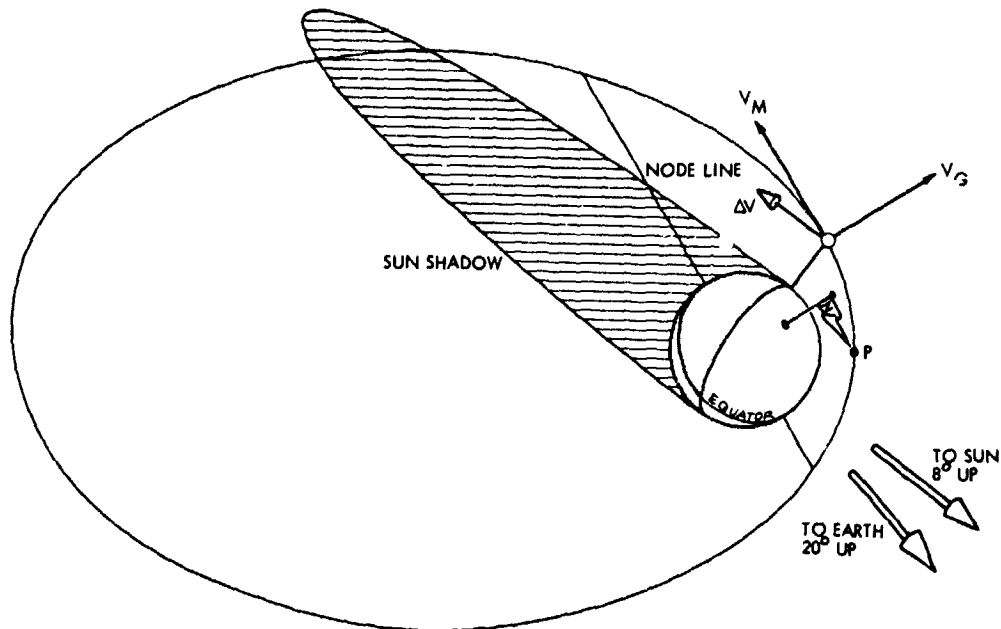


Fig. 88. MOT-8/9 geometry for Viking 1

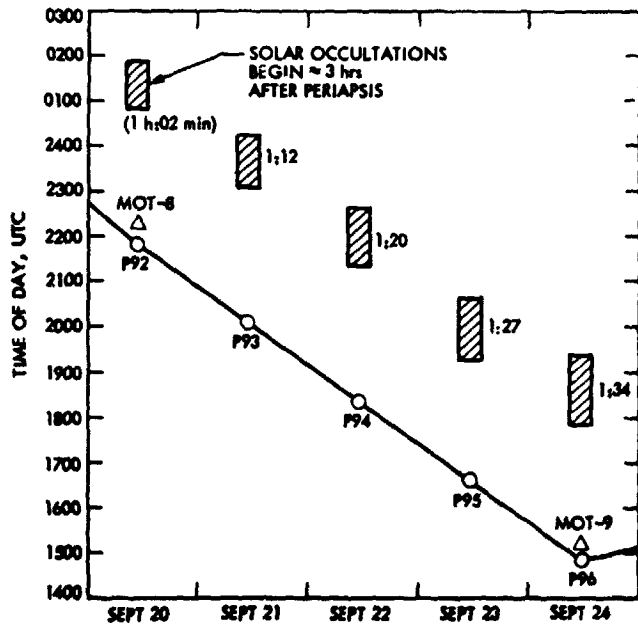


Fig. 89. Viking 1 timeline

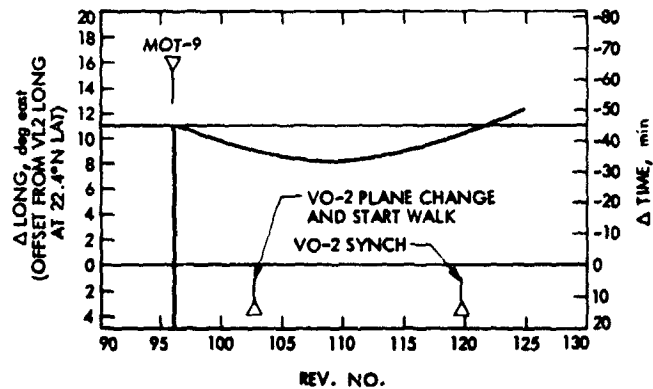


Fig. 90. VL-2/VO-1 offset

walk was performed to look at site B1 in Cydonia, B2 in Alba Patera, and B3 in Utopia Planitia. Furthermore, each of these sites was only specified as lying within the latitude and longitude bands shown in Table 15. However, a candidate in the B1 band at 46.0°N and 10.0°W was used as the nominal site for the initial design phase.

F. Viking 2 Trim Maneuvers

1. **Prelanding trim maneuvers.** Since Viking 1 had shown how difficult it can be to obtain a satisfactory landing site on Mars, the Viking 2 site certification and acquisition process was designed to look at three candidate sites before the spacecraft was synchronized over any one of them. A site selection

The MOI maneuver was targeted to a period of 27.4 h to introduce a walk rate of 40 deg/rev (+2.8 h of asynchronism). Therefore, the spacecraft could, in the absence of MOI dispersions, acquire the nominal site with a single trim at P19 after a walk of more than 720 deg. Following the P19 trim, the spacecraft would be in a synchronous orbit in preparation for the landing to occur during rev 25. Figure 91 shows this

ORIGINAL PAGE IS
OF POOR QUALITY

Table 15. Candidate Viking 2 landing sites

Site	Longitude range	Best estimate longitude before MOI	Latitude range
B1	345°W to 15°W	0°W	40°N to 50°N
B2	90°W to 140°W	110°W	42°N to 50°N
B3	200°W to 270°W	257°W	40°N to 50°N

nominal maneuver timeline, together with the reconnaissance (VIS) and IR schedules. Note that these activities would be performed for B2 on revs 4, 7 and 8, and for B3 on revs 9, 10 and 11. IR data would be obtained for B1 on revs 12, 13 and 14. The rev 4 observations were to be taken near the ascending crossing of the candidate site latitude, while all of the others would be near the descending crossing (dashed line on Fig. 91). VOI would obtain VIS data for B1.

Dispersions for the post-MOI orbit could introduce the need for up to two additional trims: MOT-1 at P2 and MOT-2

at P6. The 99% dispersions are shown as dashed lines in Fig. 91. MOT-1 would time-phase to the nominal B1 site at P19 if this would produce acceptable geometrical conditions on the reconnaissance and IR revs listed above. Reconnaissance demanded an EMA < 9 deg; IR needed a timing offset of less than 5 min. If these requirements were not met, MOT-1 would phase back to the nominal (solid) timeline at P6, where MOT-2 would phase to B1 at P19.

Other trims would be needed to cover all site selection alternatives. If B2 or B3 were selected, MOT-3 would be performed at P16 to move to the new site. Note that the walk rate following MOT-3 is determined by the longitude of this new site. The syncing maneuver MOT-4 would follow at P18 for B3 or P19 for B2. However, it was noted that proceeding to B2 in this fashion would be ΔV -expensive since it required moving to a subsynchronous orbit at P16 to walk eastward. An alternate plan would have delayed these two maneuvers to P21 and P23 (maneuvers MOT-7 and MOT-8 in the figure). This plan would move the spacecraft westward at least to P23,

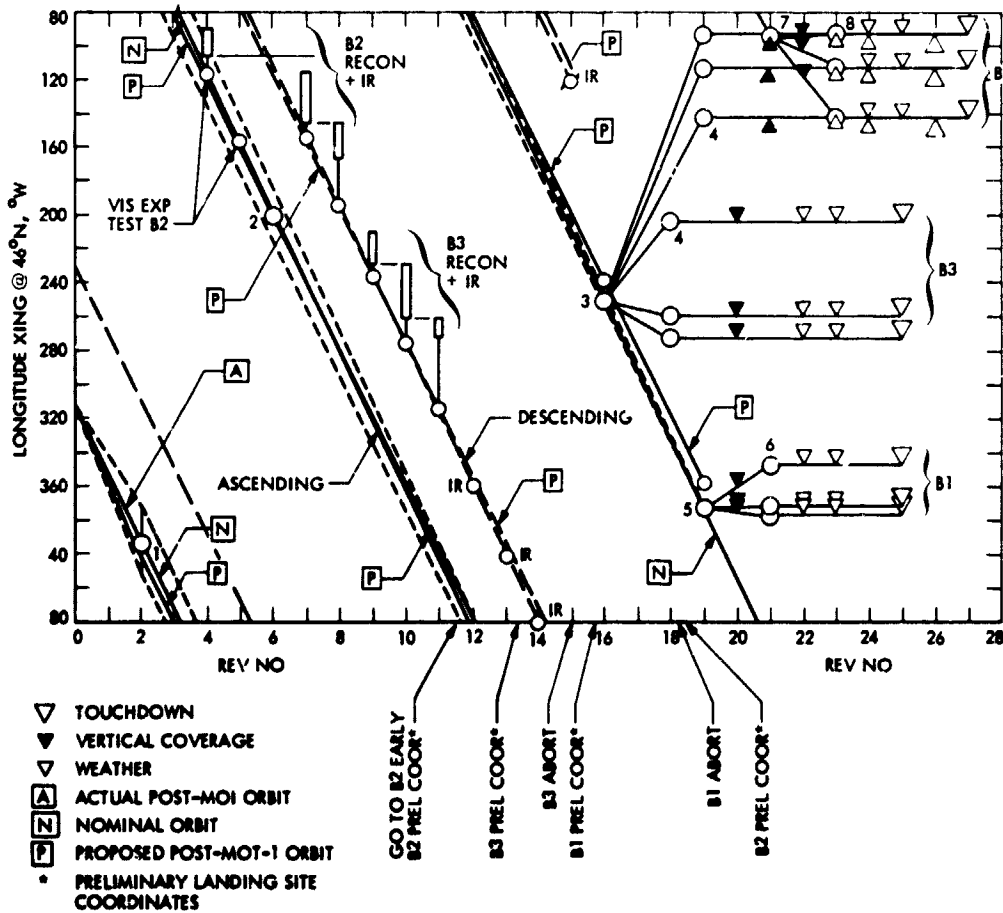


Fig. 91. Viking 2 site certification/acquisition

saving almost 50 m/s but would also delay the landing to rev 27. If B1 were selected, MOT-5 and MOT-6 would provide the phasing and syncing respectively. Figure 91 shows three paths for each site. Two of these are for the endpoints of the longitude ranges. The intermediate one shows the path to the best estimate shown in Table 15 except for B1 where the path is to 10°W (the preflight nominal).

This maneuver strategy possesses several very desirable characteristics:

- (1) It requires as few as one trim.
- (2) All site-selection data are acquired at least five days before the selection maneuver (MOT-3 or MOT-5).
- (3) Information is acquired on all sites before the decision point at P16.
- (4) Maneuvers and observations are not required on the same rev.
- (5) All trims are on fixed revs with no multiple options.

The disadvantages are:

- (1) The strategy could require up to five trims.
- (2) The walk size cuts down IRTM diurnal capability.
- (3) The trims to B2 are costly or a delay in landing is incurred.

The four pre-landing trims that were actually performed are considered in turn below. The first two were the statistical trims MOT-1 and MOT-2. The others were the site selection trims MOT-3 and MOT-4, which acquired the final target landing site at 47.9°N areographic latitude and 225.8°W longitude in the B3 area. Maneuver data for all of the trims are given in Tables 11 and 12.

Two strategies were considered for the first trim, MOT-1. Figure 92 shows how the timing offset history for each of these strategies would differ from that of the pre-MOI design. Since the post-MOI period was 12 min too large, the spacecraft reached P2 24 min late, i.e., approximately 6 deg west of the

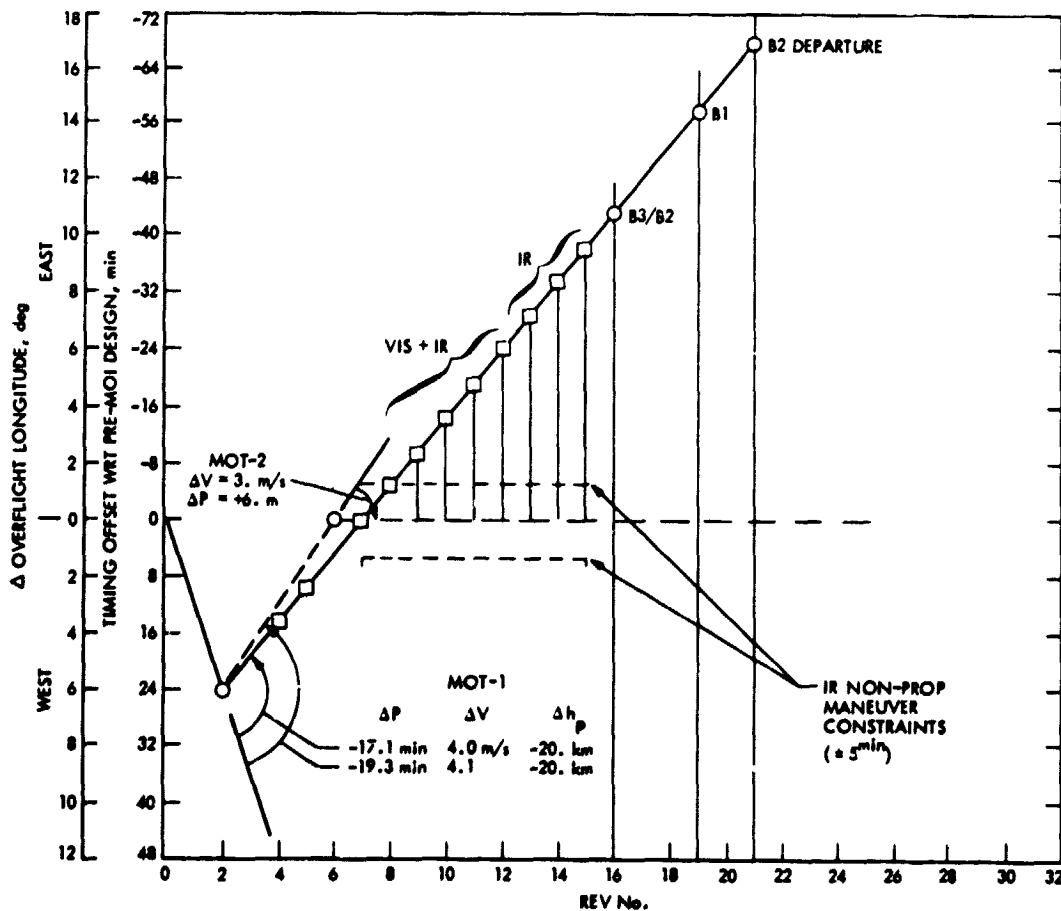


Fig. 92. Viking 2 orbit timing at MOT-1

desired longitude. One strategy would return the spacecraft to the nominal pre-MOI design by P6, where a second trim would obtain the nominal post-MOI period of 27.4 h. After P6, the spacecraft follows the nominal offset history shown in Fig. 91. Note that this path satisfies the ± 5 -min IR constraint for those revs on which the IR data are to be taken. The second strategy would cancel MOT-2 and target MOT-1 to achieve the pre-MOI design value for the time of periapsis passage at P7. Canceling MOT-2 would eliminate the need for late updates to the observation times for revs 5 through 15. These times would be known as soon as the post-MOT-1 orbit was determined and could be loaded into the onboard computer at that time. Eliminating the trim would also remove the risk involved in performing another maneuver. This MOT-1 targeting would (1) cause the spacecraft to overfly the midpoint of the B1 region at P19, (2) maintain the P7 observations exactly with respect to the plan, (3) enhance P8 through P11 reconnaissance observations in the B2 region, and (4) produce no expected degradation in the P12 through P15 IR observations. The timing offset history for this one-maneuver strategy is shown in Fig. 91 as the path labeled P.

The two-maneuver strategy was designed to decrease the period by 19.3 min at MOT-1, producing a period which is 6 min less than the nominal post-MOI value of 27.4 h. Thus the 24-min offset error at P2 is removed at the rate of 6 min per

rev for four revs to P6 (Fig. 92). The partial of period with respect to velocity, given in Fig. 55, shows that such a period-change can be accomplished by a 3.5-m/s sunline maneuver at the true anomaly $\eta = 275$ deg. However, by performing the maneuver at $\eta = 243$, it can also be used to remove the +18-km h_p error experienced at MOI for $\Delta V = 4.15$ m/s. Actually, MOT-1 was designed to overcorrect the h_p error by 2 km, anticipating the fact that MOT-2 would raise it again. A small ΔV penalty was accepted in favor of the sunline maneuver (Figs. 93 and 94) to (1) provide excellent communications, (2) avoid using power from the batteries, and (3) simplify the operational complexity involved in command generation. The 99% period accuracy of 8 s was also acceptable. The second trim (MOT-2) is then performed at P6 as a sunline maneuver to increase period by 6 min.

The MOT-1 of the alternate strategy was designed in a similar manner. This maneuver would have decreased period by only 17.1 min for 4.05 m/s.

The two-maneuver strategy was selected, with the maneuver being performed at 17 h: 16 min GMT on August 9, 1976. As for MOT-1 on Viking 1, this maneuver was subjected to a constraint on the execution time. That is, the motor burn had to occur within a window (between 15 h: 00 min GMT on August 9, 1976, and 04 h: 00 min GMT on August 10, 1976)

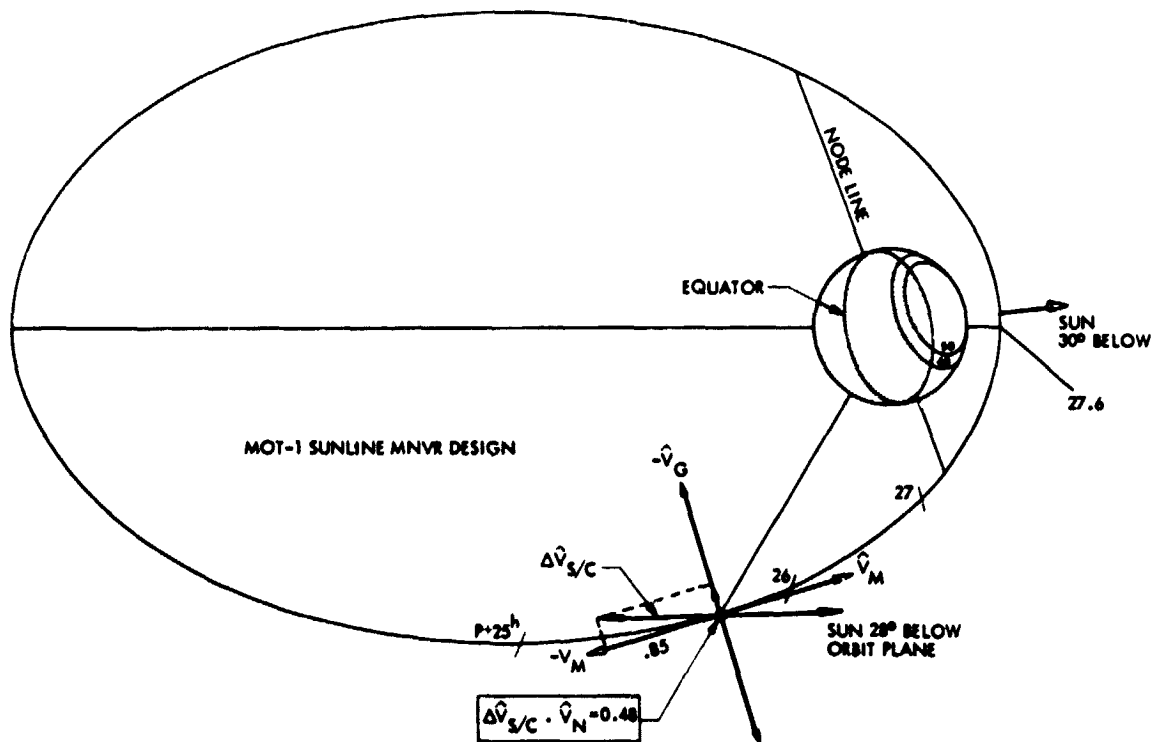


Fig. 93. Orbit plane for Viking 2

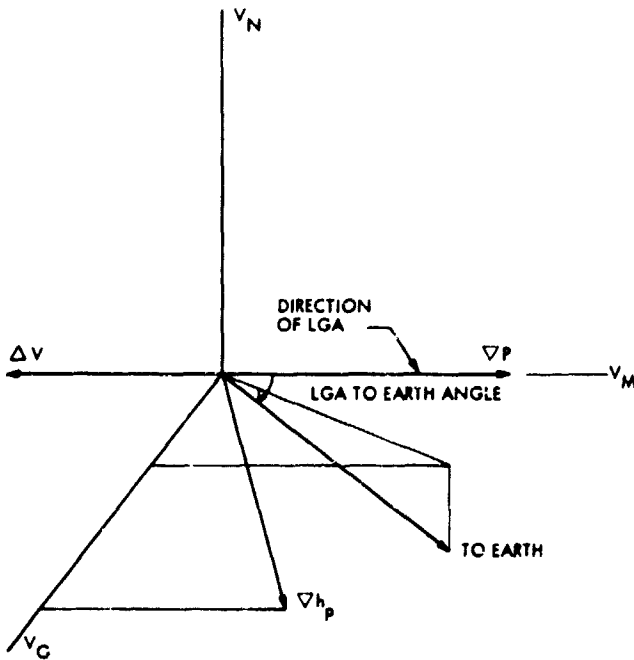


Fig. 94. MOT-1 ΔV geometry for Viking 2

that had been reserved in loading commands into the CCS. This constraint was easily met.

The period obtained by MOT-1 was 5.4 s too small due to execution errors. Figure 95 shows how the timing offset history would differ from the pre-MOI design if the MOT-2 maneuver computed before MOT-1 was performed. This path would have remained well within all constraint limits, but the maneuver was updated to produce the second path shown in the figure. Figure 55 shows that the required period increase of 6 min could have been obtained by a 1.2-m/s sunline maneuver at $\eta = 95$ deg. High precision (DPTRAJ) analysis obtained the preliminary commandable quantities: RT = 0.0 deg, YT = 0.0 deg, $\Delta V = 1.27$ m/s, $t_{ign} = 08$ h: 56 min on August 14, 1976. At the time of the delivery of this preliminary set, the ignition window was specified to be 08 h: 10 min to 10 h: 10 min, while the ΔV and time of ignition could still be updated.

The update capability was used principally to improve the period control accuracy following the trim. Figure 96 shows the ΔV cost and 99% period control accuracy for sunline maneuvers at different true anomalies. The discontinuities in the period control graph were caused by the fact that the 99% fixed magnitude error was given as 0.052 m/s for burn durations less than 3 s and only 0.028 m/s for longer burns. Therefore, the best period accuracy within the GMT window could be obtained by a maneuver at $\eta = 40$ deg. Using the latest orbit determination, the command update made $\Delta V =$

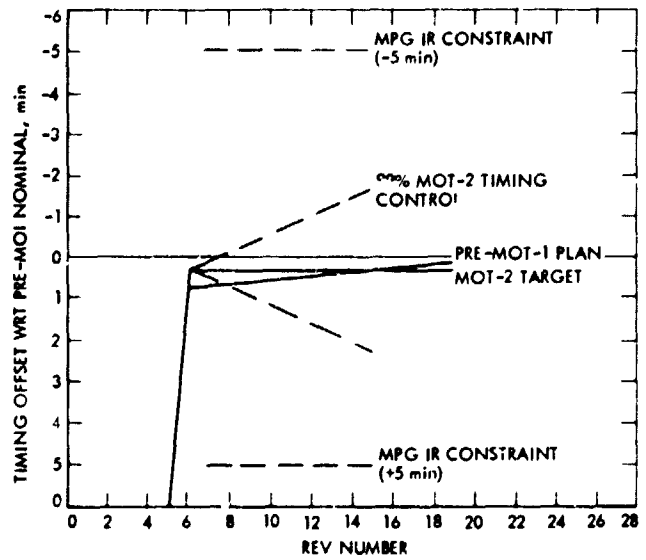


Fig. 95. Viking 2 orbit timing at MOT-2

1.8 m/s with motor ignition at 08 h: 31 min: 15 s GMT on August 14, 1976. The maneuver geometry is shown in Fig. 97.

Eventually, a candidate site was located in the B3 region. However, this site was only specified as $48.0^\circ N \pm 1.5^\circ$ areographic latitude and $226.0^\circ W \pm 2.0^\circ$ longitude (see Table 16). Trims MOT-3 and MOT-4 were then designed to:

- (1) Reach areographic latitudes from $46.5^\circ N$ to $49.5^\circ N$ with less than 3 deg of VL crossranging (XR).
- (2) Target timing to the optimum lanuer entry flight path angle

$$\gamma_E = -17.0 \text{ deg}$$

(PER = -9.9 deg).

- (3) Treat the point at $48.0^\circ N$ areographic latitude and $226.0^\circ W$ longitude as the nominal site.
- (4) Perform MOT-3 and MOT-4 near P16 and P18 respectively.
- (5) Land near P25.
- (6) Minimize the orbit drift for a 5-day delay in landing.
- (7) Provide communications during the burn if possible.

The two trims had to walk the spacecraft to the new site longitude and increase LATPER by 1.8 deg. Figure 98 shows the site acquisition timeline. To time-phase, MOT-3 must change the period from 27.4 to 24.05 h. This subynchronous

Table 16. Viking 2 landing site adjustments

	Specification for MOT-3 design	Specification for MOT-4 design	Achieved site
Areographic latitude, °N	48.0 ± 1.5	47.9 ± 1.5	47.97
Areocentric latitude, °N	47.7 ± 1.5	47.6 ± 1.5	47.67
Longitude, °W	226.0 ± 2.0	225.8 ± 2.0	225.67
Sun elevation angle, deg	130.0 ± 3.0	130.0 ± 3.0	

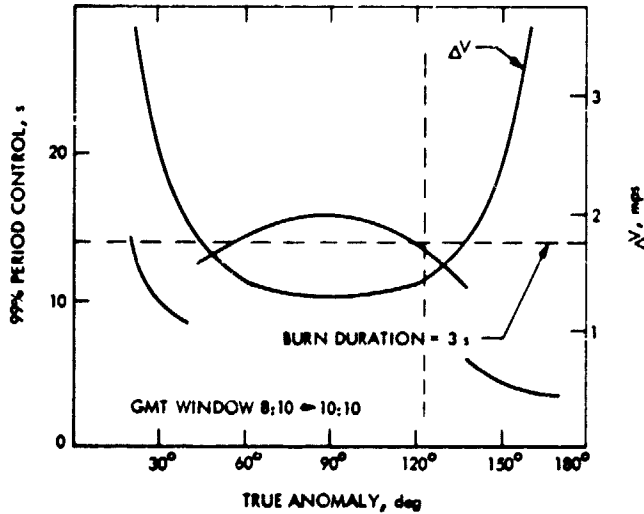


Fig. 98. Maneuver update analysis for Viking 2 MOT-2

orbit takes out the longitudinal offset at the rate of 9 deg per rev. MOT-4 then synchronizes the orbit. The timing offset jumps shown in Fig. 98 at P16 and P18 reflect the changes in the right ascension of the PER point produced by the trims. The amount of LATPER correction by each trim was selected by considering sunline maneuvers at various true anomalies. Since MOT-3 was required to increase LATPER and decrease period, it had to be performed before periapsis (Figs. 55 and 56). Therefore, sunline maneuvers were targeted at true anomalies before periapsis to change this period from 27.4 to 24.05 h. On the other hand, MOT-4 had to increase both period and LATPER, so sunline maneuvers were targeted at true anomalies after periapsis to move the spacecraft from the 24.05-h orbit to a synchronous one. This process determines the postmaneuver values for all orbital parameters. The results for the two trims were then inspected to find a combination of maneuvers that would increase LATPER by 1.8 deg and produce a final h_p value of 1500 km. Figures 99 through 102 give the ΔV cost and achieved h_p and LATPER changes. After the MOT-3 maneuver at $\eta = 290$ deg and MOT-4 at $\eta = 130$ deg had been selected, a high precision (DPTRAJ) analysis produced the trajectory changes shown in Table 17. Note that the inclination of the orbit is increased by each of these maneuvers, reducing the ΔV cost of the later plane change maneuver, which had to raise inclination to 75°.

Thus it was possible to design both trims as sunline maneuvers, providing excellent communication angles. Table 17 shows the planned trajectory changes for the preliminary

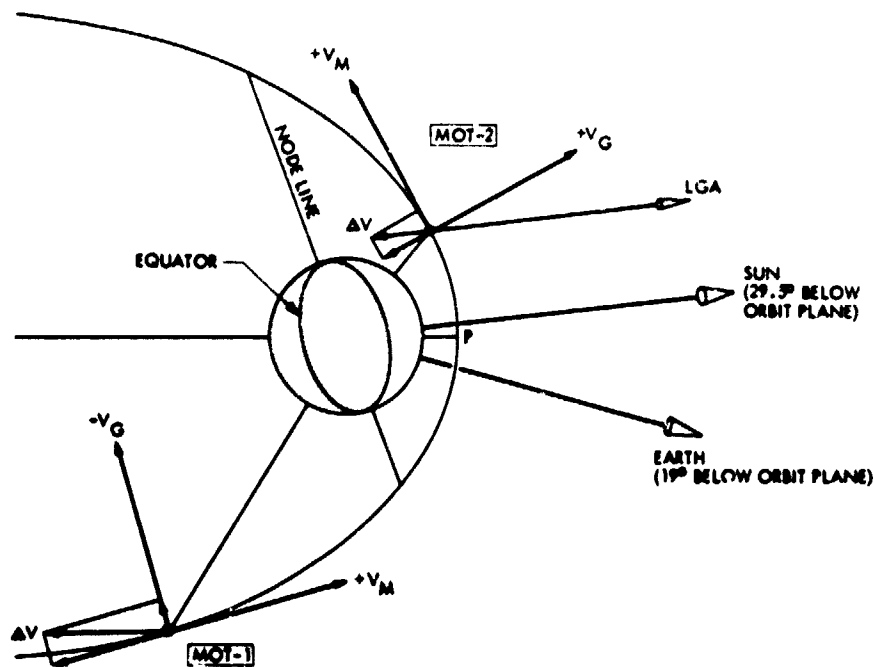


Fig. 97. MOT-2 geometry for Viking 2

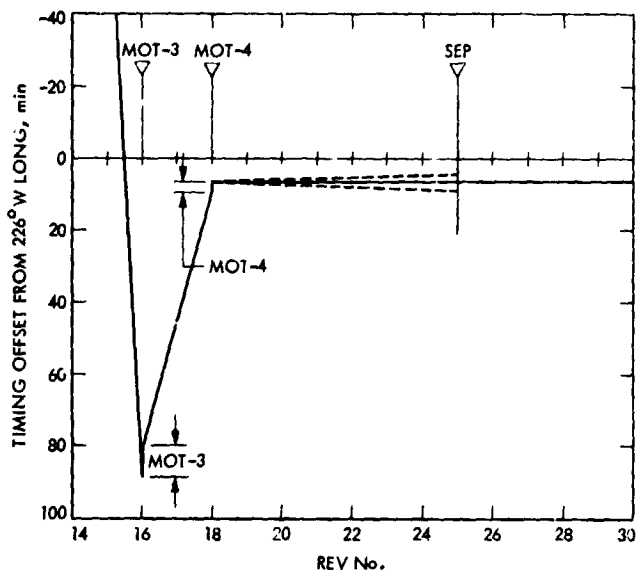


Fig. 98. Viking 2 site acquisition

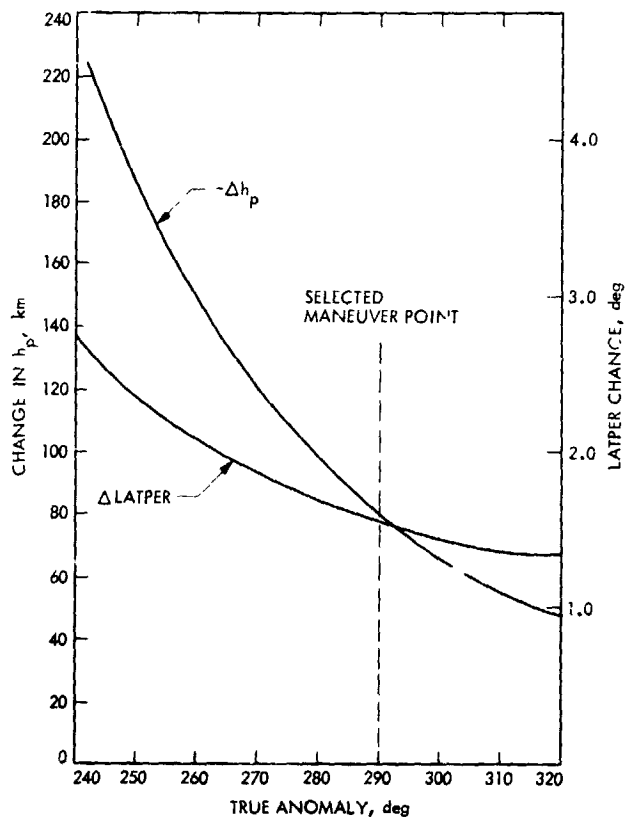


Fig. 100. MOT-3 h_p and LATPER changes for a sunline maneuver on Viking 2

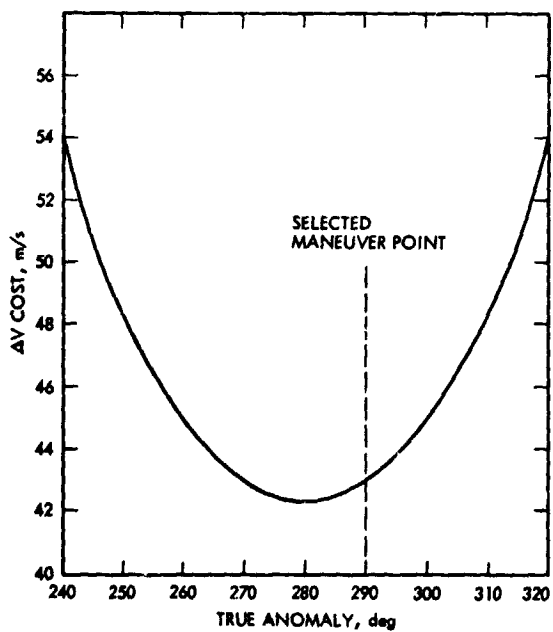


Fig. 99. MOT-3 ΔV cost analysis for a sunline maneuver on Viking 2

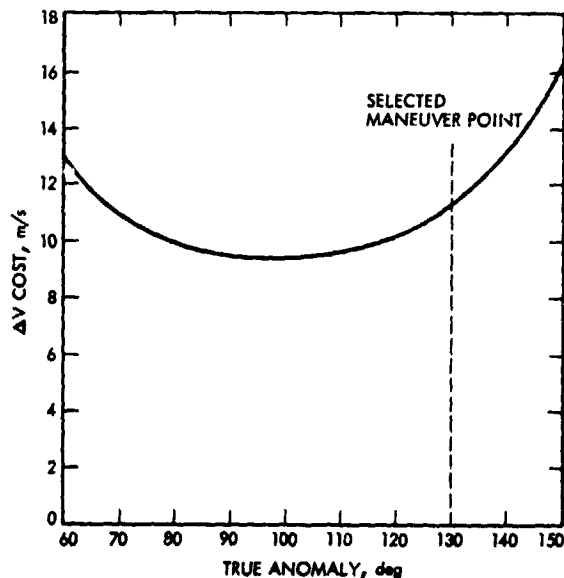


Fig. 101. MOT-4 ΔV cost analysis for a sunline maneuver on Viking 2

Table 17. MOT-3 and MOT-4 trajectory summary for Viking 2

Parameter	Pre-MOT-3 actual	Post-MOT-3		Post-MOT-4 target	SEP target
		Target	Achieved		
Period, h:min:s	27:24:45	24:02:56 ±103s (99%)	24:02:24	24:37:20 ±15s (99%)	24.37:20
Periapsis altitude, ^a km	1512	1433	1434	1497	1500
Aerographic LATPER, deg	46.0	47.5	47.5	47.9	48.1
SEAPER, ^b deg	—	—	—	—	128.9
Inclination, deg	55.2	55.6	55.6	55.4	55.4
Time of P25, GMT	249/0107	247/1823	247/1818	247/2249	247/2249 ±116s (99%)

^aThe periapsis altitude was computed using the value 3384 for the Mars radius at the landing site latitudes.

^bSEAPER is the sun elevation angle at PER passage on the touchdown orbit.

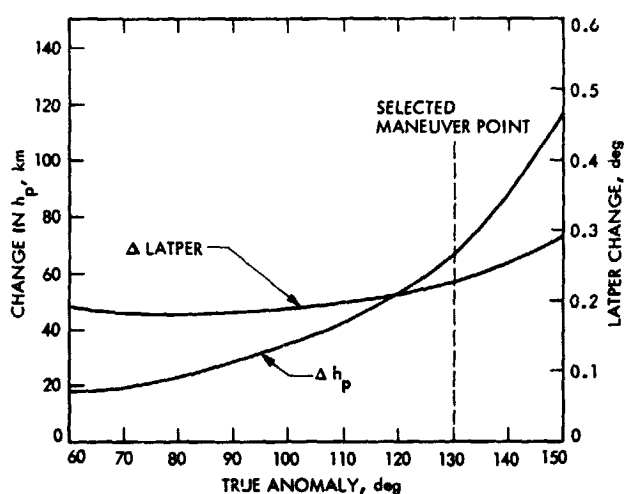


Fig. 102. MOT-4 h_p and LATPER changes for a sunline maneuver on Viking 2

command set. Note that the 67-km h_p overcorrection introduced by MOT-3 is to be restored by MOT-4. Also, the Sun elevation angle at PER passage on the separation orbit is essentially nominal. The maneuver geometries for both trims are shown in Fig. 103. The VL accessible area, shown in Fig. 104, covers almost all of the specified region (inside shaded portion) of candidate landing sites. Note that the 99% landing ellipse for zero lander crossranging and $\gamma_E = -17.0$ deg is centered at the nominal site (48.0° aerographic latitude, 226.0° W longitude). The ellipse for $+3.0$ deg of crossranging is also shown in this figure for comparison purposes.

Table 17 shows the orbit attained by MOT-3. LATPER was only $+0.003$ deg high while the period was 32 s too small. At this time, a slight adjustment was made in the nominal Viking 2 landing site, which was specified for MOT-4 design purposes as 47.9° N $\pm 1.5^\circ$ aerographic latitude and 225.8° W $\pm 2.0^\circ$ W longitude. MOT-4 was retargeted to the optimum $\gamma_E =$

-17.0 deg, obtaining the maneuver parameters given in Tables 11 and 12. This retargeting reduced ΔV by 0.4 m/s and made the time of motor ignition 18 min (4° in true anomaly) earlier than for the maneuver computed before MOT-3 was implemented. Figure 105, which gives the VL accessible area, shows that the new nominal could be obtained by $+0.3$ deg of crossranging and 0.0 deg of downranging by the lander. The 99% landing ellipse is also shown.

The post-MOT-4 orbit was perfectly acceptable. Landing occurred near P25 on September 3, 1976 (GMT).

2. Post landing trims. A sequence of three postlanding trims was planned for VO-2 to (1) increase the orbit inclination to 75 deg, (2) walk 480 deg around the planet in 16 revs, (3) resync the VL-2 to VO-2 relay near the descending overflight of the VL-2 latitude, and (4) provide a Sun elevation angle greater than or equal to 15 deg at VL-2 overflight following the resync.

The first of these maneuvers, MOT-5 on rev 51, was designed to accomplish the large inclination change and produce an acceptable SEA at the rev 67 (descending crossing) VL-2 overflight. It was also targeted to initiate the global walk. A statistical trim MOT-6 of less than 2 m/s (99%) was planned to follow on rev 56 to remove the effect of MOT-5 execution errors on the orbit period. Later, MOT-7 would terminate the global walk for a ΔV cost of about 14 m/s. However, after MOT-5 was performed, the other two trims were canceled, leaving the spacecraft in a 26.8-h orbit.

The failure of the primary VO-2 IRU at VL-2 separation raised concern about attitude control during MOT-5. When the primary IRU failed, the secondary one was brought on-line automatically. Since MOT-5 was the first major maneuver event to occur on the orbiter since separation, there was concern that the backup IRU would fail during the burn. Therefore, a short 5-m/s test burn MOT-5A was introduced before

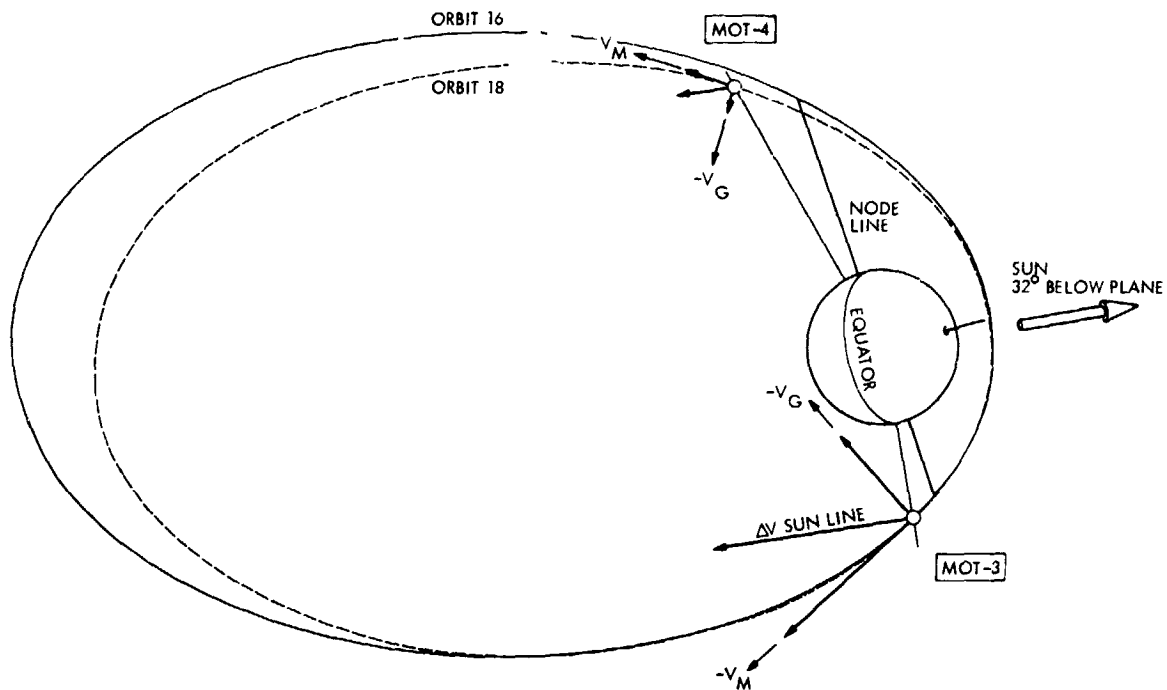


Fig. 103. MOT-3/MOT-4 geometries for Viking 2

the large plane change. Burning only 5 m/s without attitude control would not be catastrophic, whereas the 350 m/s for MOT-5 surely would be.

The test maneuver MOT-5A was designed to (1) be 5 m/s, (2) be performed at least 32 h before the large plane change maneuver MOT-5, (3) maintain the rev 50 and 51 (SOL 25 and 26) relay links, and (4) be performed in the sunline attitude if possible. In fact, MOT-5A was performed along the sunline 40 h before MOT-5. The exact ignition time was selected to avoid changing the orbit period, thus maintaining the rev 50 and 51 relay links as previously planned. Recall from the parameter sensitivity discussion that adding a velocity increment orthogonal to V_M does not change period. Figure 106 shows the sunline direction to be orthogonal to V_M at the true anomalies $\eta = 50$ and 185 deg. At the latter, 99% execution pointing errors maintain the time of P50 within 2 s and the time of P51 within 6 s. Since these errors would be considerably greater at $\eta = 50$ deg, the $\eta = 185$ deg point was selected. Note from the V_G curve in Fig. 106 and the test burn geometry shown in Fig. 107 that this maneuver had a large component along the $+V_G$ vector. Therefore, the maneuver would increase h_p by 31 km. The normal component would reduce inclination by 0.1 deg, which was a slight penalty since the plane change maneuver was intended to increase this parameter.

The test burn was executed at 04 h: 33 min: 20 s GMT on September 29, 1976, producing $\Delta V = 5.006$ m/s. The telemetry data received from this maneuver showed no anomalies and gave confidence that the spacecraft could satisfactorily implement the large maneuver to follow.

MOT-5 was designed as a ΔV optimal maneuver with three target parameters (inclination, periapsis altitude and period), subject to a constraint on the Sun elevation angle (SEA ≥ 15 deg) at the rev 67 descending crossing of the landing site latitude. An inclination of 75 deg was needed for polar observations. This increase of 20 deg required about 350 m/s. Given such a large velocity change along the normal (ΔV_N) direction, little additional ΔV was needed to achieve the period and h_p targets. But for this large a maneuver, the execution errors were necessarily large and h_p could only be controlled to within ± 54 km (99%). Since the requirement on h_p was that it be between 1400 and 1500 km after the maneuver, it was targeted for 1450 km to maximize the probability of satisfying this constraint. The period was targeted for 26.66 h, yielding a 30-deg/rev walk. Resyncing after 16 revs would provide a longitude timing that would achieve a 9-min offset east of the landing site when the spacecraft crossed the VL-2 latitude. This would maximize the relay link duration (see Fig. 108). Figure 109 shows the ΔV cost of targeting to these three parameters as a function of the target value for SEA. The ΔV optimal maneuver of 343.2 m/s was

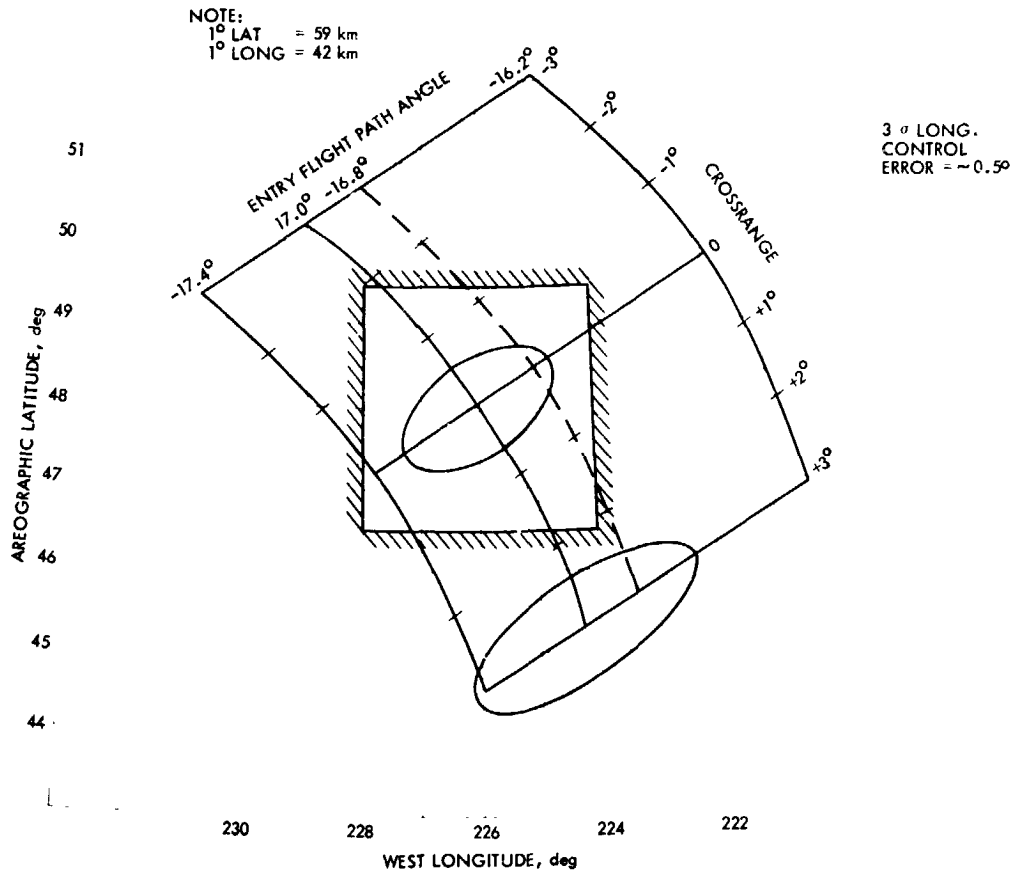


Fig. 104. Preliminary MOT-3/MOT-4 VL accessible area for Viking 2

selected, attaining an SEA of 22 deg. The maneuver and orbit geometry is shown in Figs. 107 and 110.

The maneuver attitude was achieved by a three-turns sequence: roll = -141.351 deg, yaw = -123.777 deg, and roll = -144.839 deg. The late update specified $\Delta V = 342.551$ m/s with ignition at 21 h: 07 min: 38 (GMT) on September 30, 1976. MOT-5 was satisfactorily executed achieving $h_p = 1528$ km, period = 26.78 h and $i = 75.1$ deg.

After implementation of MOT-5, and prior to the planned phasing maneuver on rev 56, the science activity plans for VO-1 were changed. The plan for a VO-1 walk for radio science was eliminated. As a result, VO-1, which had been timed to provide the VL-2 relay during the VO-2 walk, was left to continue the VL-2 relay. No further maneuvers were made on VO-2, leaving it in the $\sim 30^\circ$ /rev walk. VL-1 relay links were infrequent during this period, and were done with VO-2 when the relative timing permitted.

ORIGINAL PAGE IS
 OF POOR QUALITY

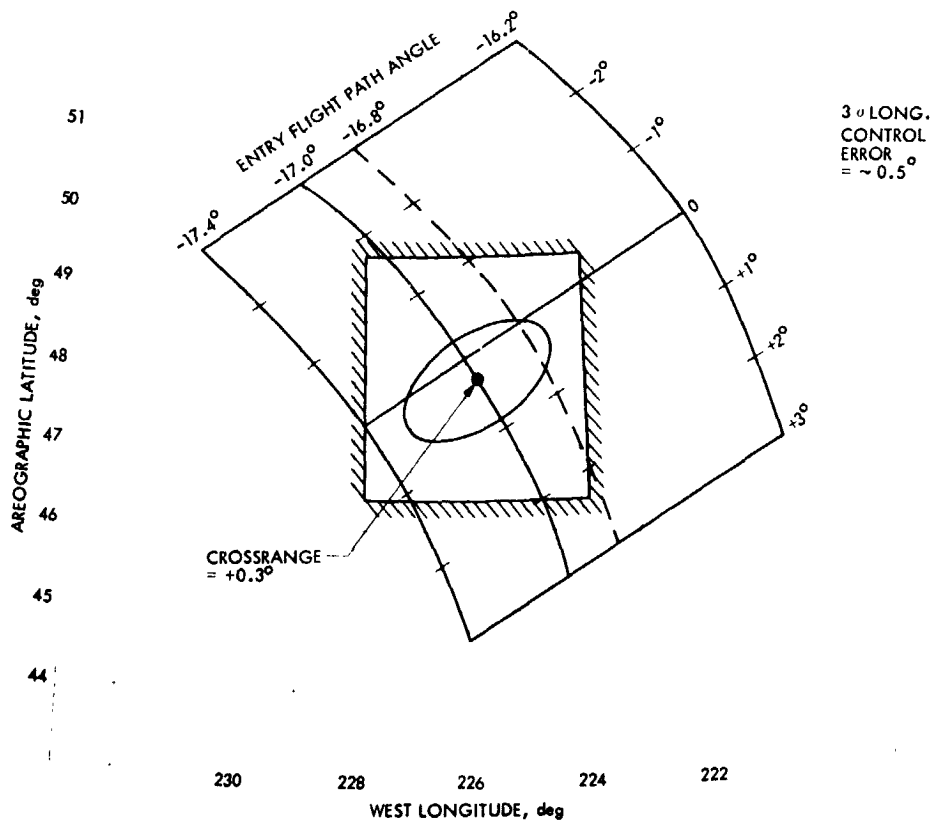


Fig. 105. Post-MOT-4 VL accessible area for Viking 2

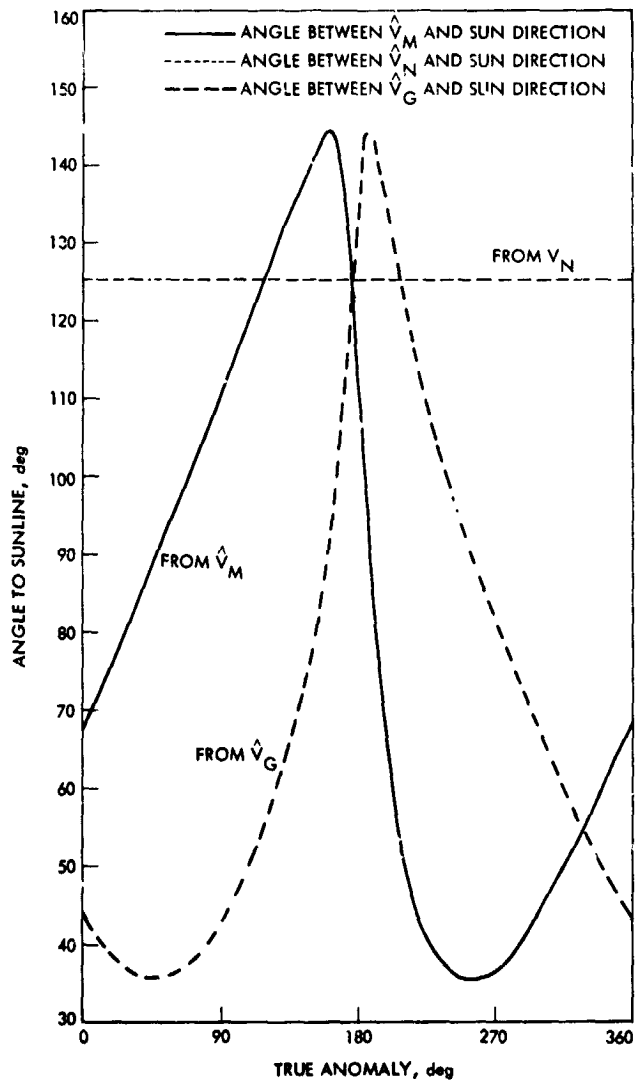


Fig. 106. Sun direction in velocity space

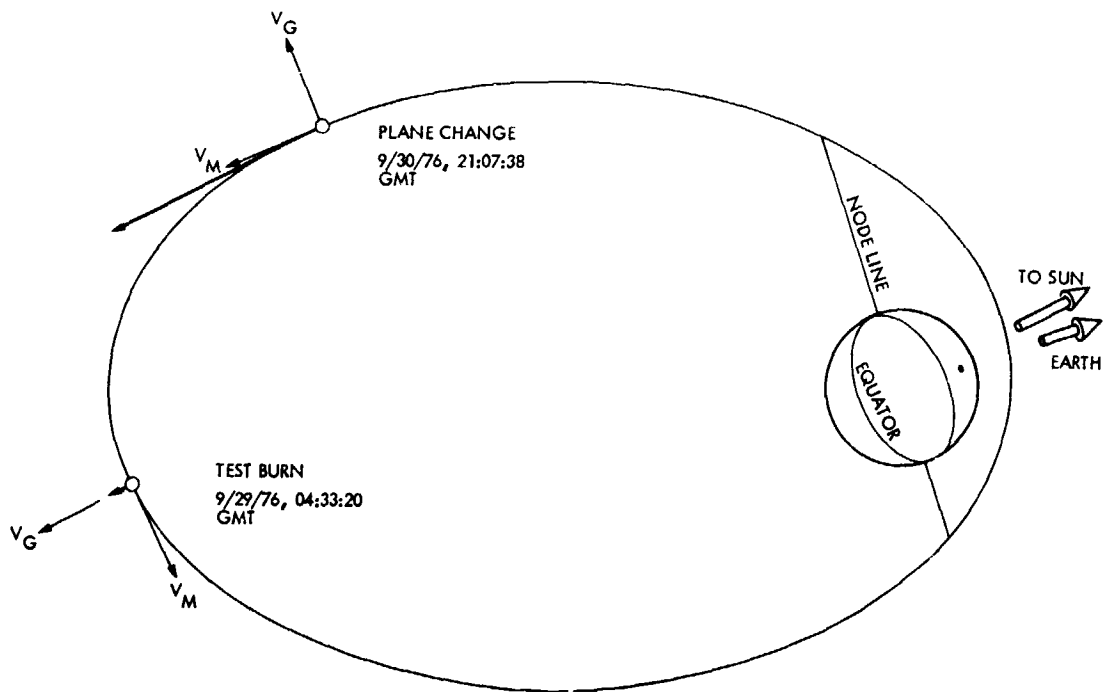


Fig. 107. Viking 2 plane geometry (MOT-5)

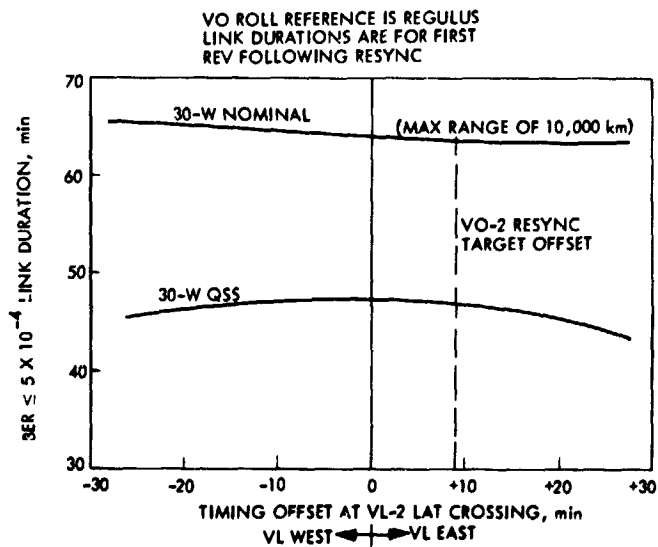


Fig. 108. VL-2/VO-2 relay sensitivity to timing offset

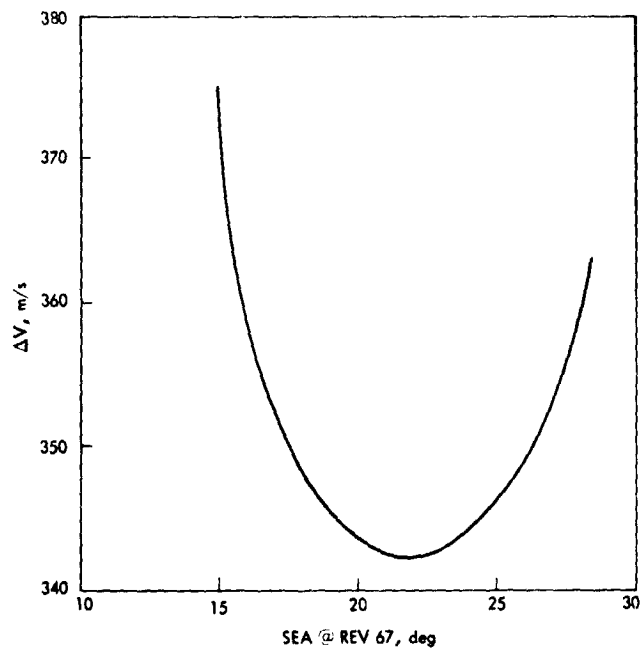


Fig. 109. Viking 2 plane change cost

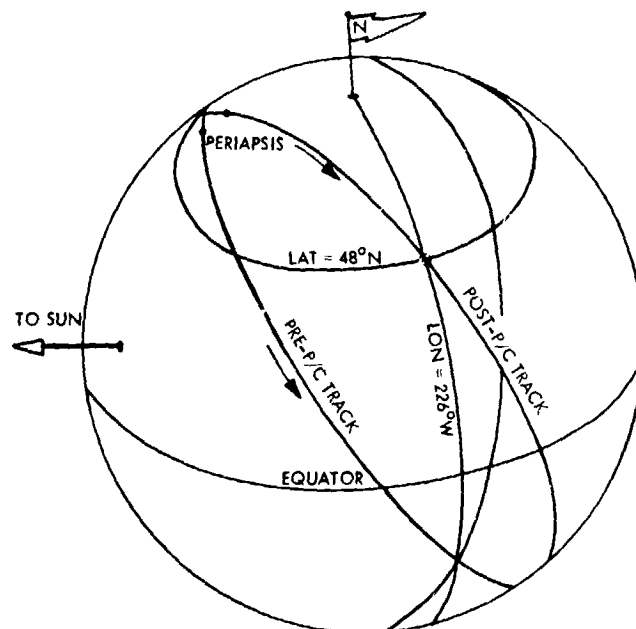


Fig. 110. Viking 2 plane change geometry

References

1. Hintz, Gerald R., "Orbit Trim Strategies for the 1975 Mars Viking Mission," *J. Spacecraft Rockets*, Vol. 11, No. 11, Nov. 1974.
2. O'Neil, W. J., et al., "Viking 1975 Navigation Plan," Document 612-32, Jet Propulsion Laboratory, Pasadena, Calif., May 1, 1975.
3. Dowdy, M. W., Hise, R. E., and Peterson, R. G., "Development and Qualification of the Propellant Management System for Viking 75 Orbiter," *J. Spacecraft Rockets*, Vol. 14, No. 3, March 1977.
4. Miller, J. K., et al., "Viking 1975 Navigation Plan Supplement 1," Document No. 612-32 (Supplement 1), Jet Propulsion Laboratory, Pasadena, Calif., May 20, 1976.
5. Hintz, Gerald R., and Pavlovitch, Theodore, "Viking 75 Project Software Requirements: Document for the Mars Orbit Trim Operations Program (MOTOP)," Document 620-5, Jet Propulsion Laboratory, Pasadena, Calif., July 1973.
6. Pavlovitch, Theodore, Hintz, Gerald R., and Rinderle, Edward A., Jr., "Viking '75 Project User's Guide for the Mars Orbit Trim Operations Program (MOTOP)," Document 620-405, April 20, 1976.

Lander Flight Path Analysis

E. A. Euler, G. L. Adams, and F. W. Hopper

I. Introduction

The primary functions of the Lander Flight Path Analysis Team (LFPAT) were to (1) design the Viking Lander (VL) descent trajectory and compute the descent guidance parameters for command transmission to the Viking Lander and Viking Orbiter (VO), (2) reconstruct the VL trajectory from separation to touchdown using data transmitted from the VL to Earth via the VO during descent, and (3) predict the VL/VO relay link system performance during descent and post touchdown.

Each of these primary functions is discussed in detail in subsequent sections. Sections II, III, and IV address item 1 above and discuss the preflight VL capability, the history of proposed descent trajectory designs as the site selection process evolved, and the final trajectory design and guidance parameters for each vehicle. Sections V, VI, and VII address the trajectory reconstruction process, including the overall reconstructed VL flight path summary and a detailed discussion of the entry trajectory and atmosphere reconstruction results. The postland relay link prediction function is discussed in Section VIII.

The following paragraphs contain an overall description of the LFPAT flight operations activities, key interfaces, proce-

dures, timelines, and the software used to perform the functions described above.

A. LFPAT Software

1. **LTOP - Lander Targeting Operations Program.** This program consisted of a number of different modes to generate and completely analyze proposed descent trajectories. The heart of the program was a detailed three-degree-of-freedom trajectory model. Although the onboard computer computations were not simulated in this program, all other applicable VL subsystems were modeled to the degree of sophistication necessary to maintain a flight path positional accuracy of about 10 km at touchdown. Given the parameters of the orbit on which separation was to occur, the program had the capability to construct deorbit maneuver parameters (time, pointing angles, ΔV) to achieve a variety of different desired target conditions, perform an error analysis on a given trajectory, predict the VL/VO relay link performance for descent, and most importantly, compute the onboard guidance parameters necessary to achieve the desired flight conditions. Additionally, the program operated in a postflight mode to make a weighted least squares estimate of the deorbit maneuver parameters and to generate the actual attitude profile prior to entry using telemetry received from the VL.

2. **LATS – Lander Trajectory Simulation.** This program was a non-real-time, high-fidelity, six-degree-of-freedom digital simulation of the descent trajectory. The onboard flight software computations were functionally simulated, and all other VL descent subsystems (i.e., radars, propulsion systems) were modeled in great detail to accurately simulate the detailed vehicle dynamics and onboard guidance, control, and navigation processes. This program was used primarily as a verification of the descent guidance parameters and trajectory design, but it was also useful as an analysis tool to investigate potential anomalies. During preflight test and training, the program was used to generate simulated onboard descent telemetry to test the lander trajectory reconstruction process.

3. **RLINK – Postland Relay Link Program.** RLINK modeled the VO orbital motion to predict the relative VL/VO geometry after landing and used VO and VL relay subsystem parameters to predict the overall link communications systems performance. The output of the program was used to monitor actual performance and to compute the relay data transmission start times and durations for uplink planning.

4. **PREPR – Preprocessor for Lander Trajectory and Atmosphere Reconstruction.** This program provided the data conditioning and editing functions necessary to prepare the data obtained from onboard telemetry during the entry to touchdown time period for the reconstruction software. The preliminary functions included editing and calibrating the accelerometer and gyroscope data and smoothing these data to produce a continuous time history of angular velocity and acceleration of the vehicle center of gravity at a desired frequency. Other subsystem data used for reconstruction (radars, pressure, temperature) was unaltered.

5. **LTARP – Lander Trajectory and Atmosphere Reconstruction Program.** LTARP was essentially a classical orbit determination program that employed a sequential Kalman-Schmidt filter. The six-degree-of-freedom trajectory was generated by integrating the sensed vehicle acceleration and angular velocity data along with gravitational accelerations. The observables were radar altimeter and terminal descent and landing radar data, ambient and stagnation temperature and pressure data, and externally supplied position or velocity fixes (e.g., landed position). The usage of the program is described in Subsection VI-A.

B. Operational Activities

Although a number of operational support tasks were performed beginning at about MOI-30 days (such as MOI/MOT support), the activity period leading directly to separation of the VL started about SEP-10 days. At this time the predicted separation orbit was well determined and a preliminary target

landing site was available, allowing for a realistic design of the descent trajectory to be flown and the associated flight computer load, along with an estimate of the key event times (separation, touchdown, etc.).

The preliminary data was used to do preliminary command and sequencing for both the VO and VL, and to perform descent validation runs in the VCSF in Denver. This early validation of descent was done to provide a "shakedown" of the system in Denver and to identify any potential problems with the proposed descent. In actuality, this early test proved valuable for VL-1 when ground hardware problems were discovered in the VCSF in the first test of the system, performed on June 25, 1976.

The descent validation process is shown schematically in Fig. 1. The VL trajectory was targeted and the VL descent guidance parameters were computed by the LFPAT using LTOP, and then verified by the OMATT using DPTRAJ. This check by the OMATT was performed independently to provide confidence that the proposed parameters were error-free prior to release by the FPAG. The LPAG then generated the necessary command load for the VL and prepared the predicted GCSC memory map at separation that was used to initialize the descent simulation to the VCSF. The separation state vector and attitude were sent from the FPAG to the LSO to complete the set of initialization data. The simulation of descent was performed by the LSO using the VCSF. Key trajectory and subsystem data was sent back to JPL by the LSO for comparison with simulation results from FPAG programs LTOP and LATS. In addition, each element of the flight team did other checks on the detailed output data in certain specialized areas.

During the time period from SEP-10 to SEP-5 days, two additional simulations were run that utilized worst-case environment and subsystem data along with 3σ trajectory perturbations to further validate the proposed load under stress conditions. This activity ended at SEP-5 days, at which time all of the data was reviewed by the SPFPAD and problems were identified and resolved.

This same process was repeated twice in the final three days before SEP, but on a much tighter schedule. Table 1 shows the operations timeline during this last critical time period prior to SEP. In addition to the activities described above to validate the descent load, the translation from engineering parameters to the 24-bit GCSC words and proper memory location was performed by the LFPAT manually and compared with both the predicted and actual memory maps. This provided an independent check on the command generation process for descent.

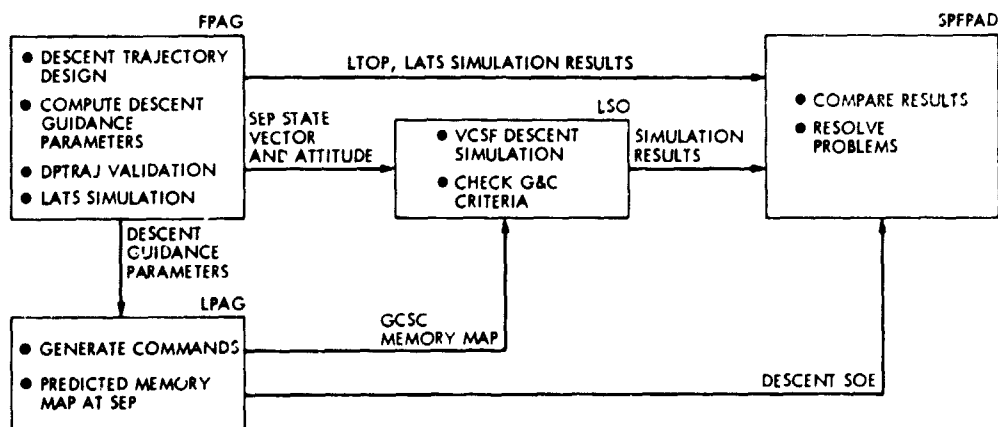


Fig. 1. Descent validation process

Because of the extremely short response time to anomalies during this time period, preparations were made for certain anomalies before the VL executed preseparation checkout. Specifically, an alternate deorbit roll attitude was selected and validated in case a lateral accelerometer failure was observed during the preseparation calibration. Also, trajectories were designed and analyzed for a separation on successive orbits after the nominal in case a *no-go* was encountered during the countdown to separation. The availability of this data could minimize the delay and aid in the rescheduling of separation.

The last prime VL navigation function prior to separation was the evaluation of the latest VO orbit prediction data to determine if a separation time update was necessary to remove

the timing error inherent in the orbit solution used to generate the onboard computer load. This change could be made as late as SEP-16 hours and would reduce the onboard navigator initial conditions error and landing site error due to this error source. For both missions the timing errors were small (<1 s) and separation time updates were not necessary.

One final verification of descent was performed between SEP-13 and SEP-5 hours that incorporated any VL commands sent in the SEP-9.5-hour update and the most recent estimate of the separation state vector. For instance, on Mission 2, the decision was made to lock out one beam of the TDLR due to an anomaly in the preseparation test. This was properly modeled in the final LATS and VCSF verification runs. The successful comparison of these simulations contributed to the final decision to "go" with only 3 beams used in the onboard navigation process.

Table 1. Preseparation timeline

SEP-84 hr	final site target coordinates
SEP-78	final orbit determination
SEP-77	preliminary descent maneuver conference
SEP-64	FPAG delivery of descent guidance parameters to LPAG
SEP-57	begin VCSF validation
SEP-49	final descent maneuver conference
SEP-45	descent validation complete
SEP-44	VL/VO command conference
SEP-43	VO uplink
SEP-39	VL uplink
SEP-33	VL preseparation <i>go/no go</i>
SEP-30	begin VL preseparation C/O
SEP-16	TSEP update conference
SEP-15.5	VL final C&S conference
SEP-13	begin final VCSF validation
SEP-11	final VL command conference
SEP-9.5	final VL uplink
SEP-6	VO uplink for TSEP
SEP-4	final descent validation complete
SEP-3.5	<i>go/no go</i>

During the actual descents the entry trajectory status was monitored and displayed by comparing the onboard estimate of altitude vs time with the preflight nominal and 3σ deviations. These plots are shown in Figs. 2 and 3. Although the VL-2 data was not obtained in real-time due to a VO-2 anomaly after separation, the plots were constructed during the playback of the descent data from the VO tape recorder the day after VL-2 descent.

After touchdown the emphasis shifted to the VL trajectory and atmosphere reconstruction (LTR) and relay link planning functions. Because of the large preflight uncertainty in vehicle performance and environmental data, the LTR function was scheduled to be complete within 10 days after touchdown of Mission 1 so that these results could be used in the design of the Mission 2 descent and influence the Mission 2 landing site selection. For Mission 1, all of the key parameters indicated a

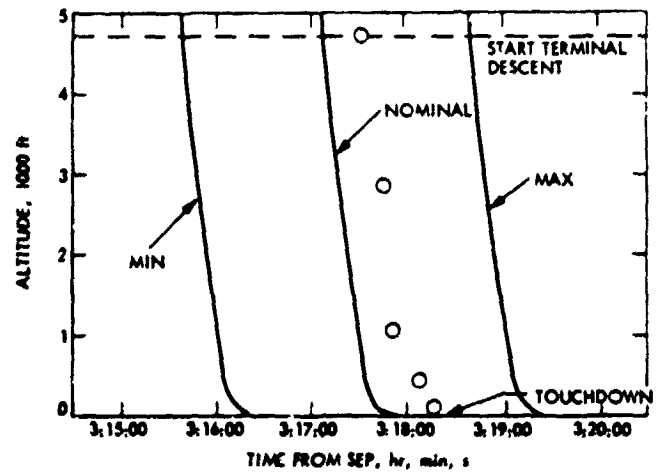
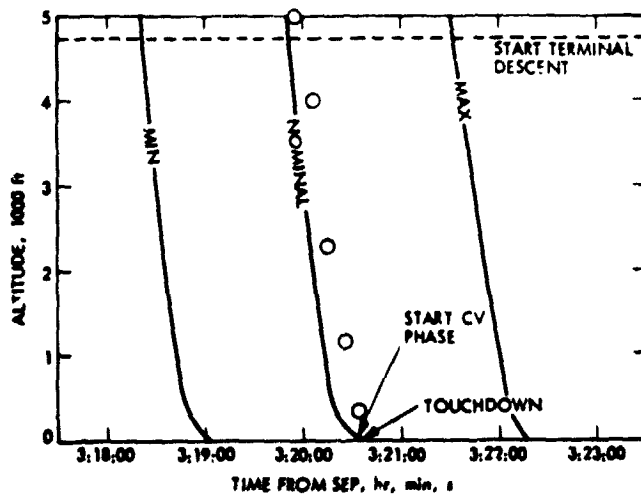
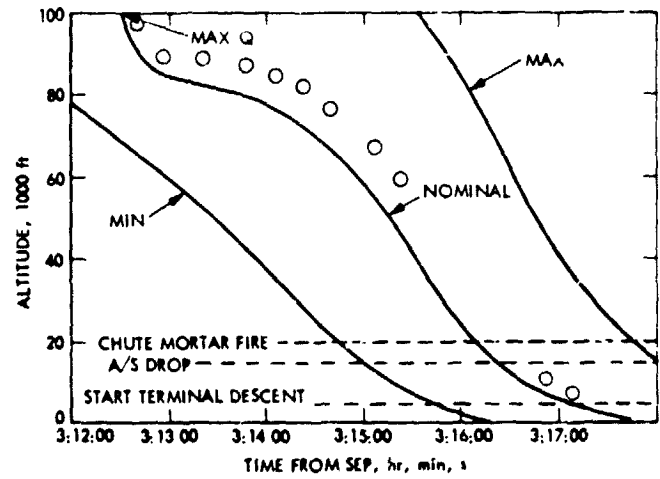
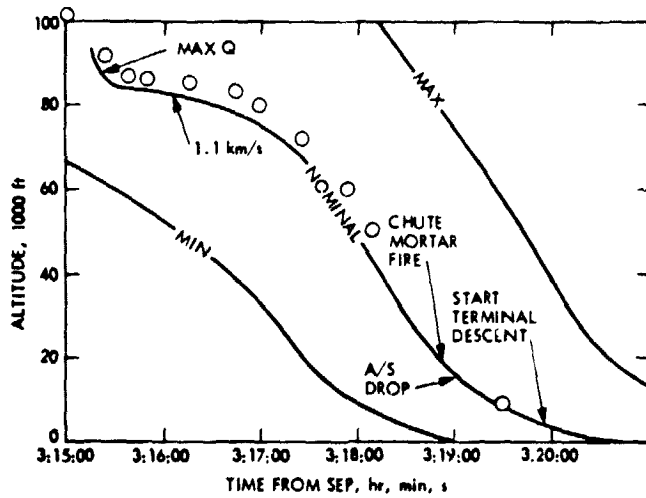
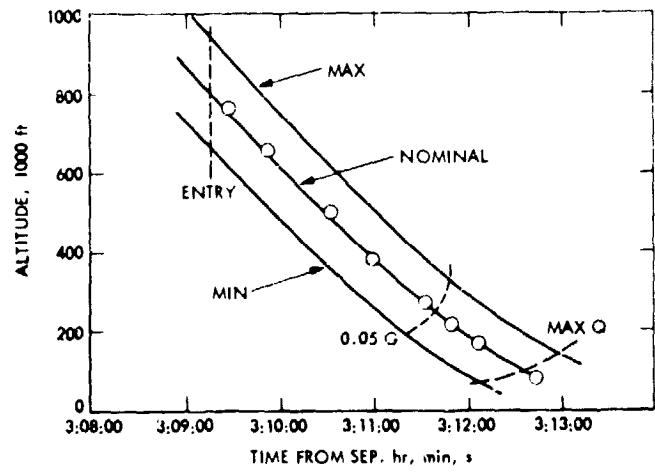
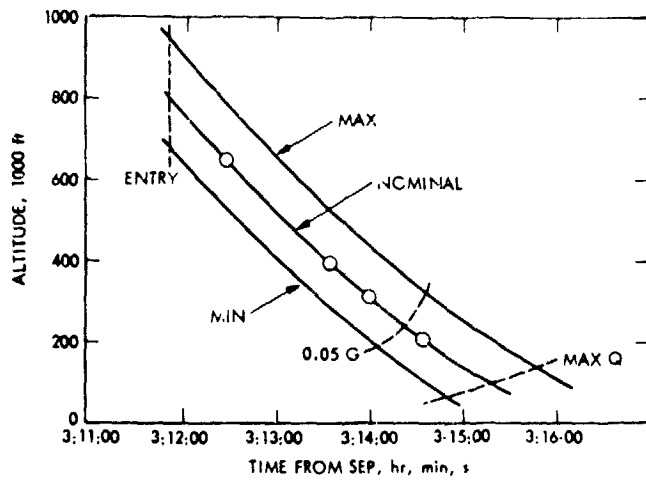


Fig. 2. VL-1 altitude vs time during entry phase

Fig. 3. VL-2 altitude vs time during entry phase

near-nominal descent and, in fact, when the results were completed, everything was so close to the predicted values that no changes were made to the Mission 2 trajectory design. A detailed comparison of the predicted and actual flight parameters is given in Section VI. The LTR process for Mission 1 did, however, take longer than expected. The estimates of systems performance and environmental quantities were not truly understood until about four weeks after landing. As a result of the experience gained in this first attempt in dealing with real entry data, the reconstruction of the Mission 2 descent went smoothly and was essentially complete about two weeks after landing.

The relay link planning functions and selection of final transmission times were tied closely to the overall mission operations strategy. At the beginning of each long-range planning cycle (20-25 days before commanding), the predicted link performance was used to specify link durations at required bit error rates. Prior to TD and early in the postland phase, these durations were quite conservative, being based on performance above the QSS (quasistatistical sum) of adverse tolerances. After a number of observations of actual relay performance were made and understood, the durations were based on observed performance.

Approximately two days prior to the preliminary command and sequencing activities for each cycle, the latest orbit predictions were used to select the final VL transmission and VO receiver start times. No change was made to the durations.

These activities required close coordination with the OMATT for design of VO orbit station-keeping maneuvers. Further discussion of the relay link activities is given in Section VIII.

II. Preflight VL Capability Estimate

The design of the VL trajectory, sequence of events, and associated onboard guidance parameters evolved over many years and changed frequently as the design of the Viking Lander matured. An extremely conservative approach was taken in the design of all descent mission phases. This conservatism was necessary owing to the lack of previous experience with a spacecraft of this type, the desire to provide maximum margin since the entire descent had to be accomplished without ground intervention, and the large degree of uncertainty in the Mars environment (atmosphere density profile, winds, terrain characteristics) that existed prior to the mission.

The relevant preflight system and mission constraints are shown in Table 2. Because of VL aeroshell structural limitations the maximum dynamic pressure q_{max} experienced by the VL during entry was not to exceed 144 lb/ft². The total

Table 2. Preflight system and mission constraints

Deorbit ΔV	$\Delta V = 156 \text{ m/s}$
Coast time	$t_c = 5 \text{ h}$
Maximum dynamic pressure	$q_{max} = 144 \text{ lb/ft}^2$
Total stagnation heat load	$Q = 1510 \text{ Btu/ft}^2$
Stagnation heating rate	$\dot{Q} = 26 \text{ Btu/ft}^2 \cdot \text{s}$
Parachute deployment dynamic pressure	$5.0 \text{ lb/ft}^2 < q_{DPP} < 8.6 \text{ lb/ft}^2$
Parachute deployment Mach number	$M_{DPP} < 2.1$
Descent relay communications system performance	Must exceed sum of adverse tolerances
Initial postland link duration	$\Delta t = 10.4 \text{ min}$

stagnation heat load Q during entry was not to exceed 1510 Btu/ft², while the stagnation heating rate \dot{Q} was not to exceed 26 Btu/ft²·s. At parachute deployment the dynamic pressure was to be between 5.0 and 8.6 lb/ft² and the Mach number to be less than 2.1. The maximum deorbit ΔV of 156 m/s was determined by propellant loaded, propellant margin, and VL mass. VL thermal and power constraints dictated that VL coast time from deorbit to entry not exceed 5 hours. Finally, in order to ensure that allowable bit error rates would not be exceeded during data transmission from the VL to the VO, the relative VL/VO geometry was to provide for relay communications system performance exceeding the sum of adverse tolerances throughout descent and at least 10.4 min after landing. In addition, it was desired to minimize the entry weight (or equivalently, use the maximum ΔV capability, thereby maximizing deorbit propellant usage within constraints) and select trajectories to minimize the landed dispersions.

All these constraints had to be satisfied under stacked worst-case conditions. Worst-case conditions were obtained by selecting each relevant statistical error source at its 3 σ magnitude and with its worst-case sign. Winds were selected at their 99% magnitude, as shown in Fig. 4, and in the worst-case selected from one of the five equally probable atmosphere models. The atmosphere models are illustrated in Figs. 75 and 76 of Section VII-A herein.

This is not the entire set of constraints that had to be satisfied. However, these constraints governed the design of the descent trajectory. Other constraints, which were satisfied by orienting the VL properly during descent, will be discussed in a subsequent paragraph.

One of the key concepts for expressing VL capability was *accessible area*. The accessible area was that region in inertial space within which the VL could land from the given separa-

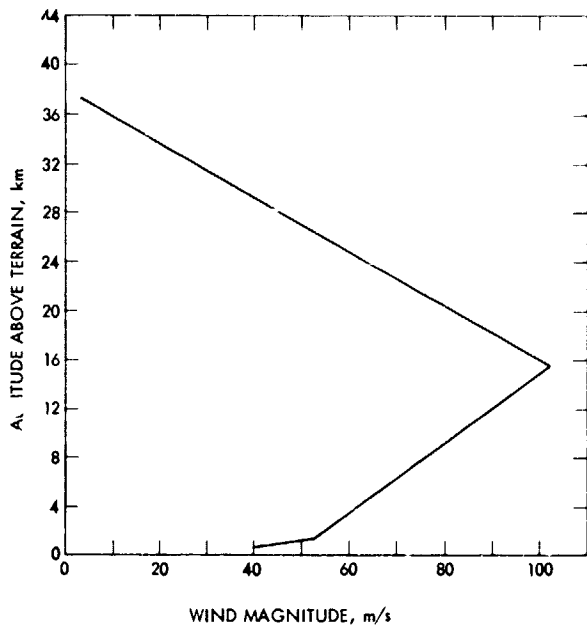


Fig. 4. 99% design wind magnitude profile

tion orbit without violating mission or system constraints. During VL trajectory design development, the accessible area became progressively reduced in size as new system requirements and desires became known. In the following discussion, the three major accessible area concepts will be presented.

The first accessible area is called the *maximum accessible area*. It is the region in which the VL could land if it were utilizing its maximum capabilities and if there were no trajectory dispersions. The second accessible area is called the *targeting region*, and reflects entry corridor (γ_E) dispersions and a more conservative utilization of VL capabilities. The third accessible area is called the *preferred targeting region*, which refers to a small entry flight path angle band of ± 0.1 deg centered about the optimal entry flight path angle. This region was employed in the targeting of the final VO site acquisition maneuvers and the final design of VL descent trajectories. It reflects a design objective introduced by project management during flight operations in order to maximize the probability of mission success. Each of these accessible areas will be discussed in more detail in subsequent paragraphs of this section.

A. Maximum Accessible Area

The procedure for constructing the maximum accessible area begins with a determination of the entry corridor, i.e., the γ_E region between the steepest and shallowest permissible entry flight path angles at fixed entry altitude. The entry corridor is determined by the entry phase constraints on q_{max} , Q , \dot{Q} , q_{DEP} , and M_{DEP} . These parameters are examined over a broad range of entry flight path angles, for all five

equally probable Martian atmospheres mentioned above, and with worst-case winds and VL aeroshell aerodynamic characteristics. The results of this process are shown in Figs. 5 through 8. Each figure shows the final set of environmental and VL characteristics which produced the maximum values of the relevant entry parameters. Figure 5, for example, shows that the maximum q_{max} was attained in the maximum ρ_s atmosphere with a 99% headwind, a 5% (3σ) low aeroshell C_D , and a 0.02 (3σ) low L/D. The steepest γ_E permitted under these conditions was $\gamma_E = -17.7$, since q_{max} equals the constraint value of 144 lb/ft² at this value of γ_E . Figures 6 and 7 show the same kind of information for \dot{Q} and Q , respectively. Examination of Fig. 6 shows that with steep γ_E restricted to -17.7 deg, the \dot{Q} constraint was also satisfied. Although the shallowest conceivable entry flight path angle is the worst-case skipout flight path angle, which for the VL was -13.5 deg, the shallowest permissible entry flight path angle for the VL was actually determined by the parachute deployment constraints. In order to maximize parachute performance (maximize speed reduction and minimize terminal descent propellant usage), it was desirable to deploy the parachute at the highest possible altitude. Figure 8 shows q_{DEP} and M_{DEP} vs altitude above the areoid (near the end of the aeroshell phase) for a range of entry flight path angles. The worst-case conditions which maximize q_{DEP} and M_{DEP} are listed on the figure. This figure suggests that γ_E could not be more shallow than -16 deg owing to the parachute deployment constraints of Mach number and dynamic pressure. An earlier design of parachute deployment altitude satisfied the constraints exactly for γ_E of -15.9 deg. Subsequent environmental model adjustments shifted the curves as shown in Fig. 8, causing a minor violation of the deployment dynamic pressure constraint for $\gamma_E = -15.9$ deg. This minor constraint violation was found acceptable owing to the extreme conservatism in stacking the error sources. Therefore, the parachute deployment altitude and the γ_E limit of -15.9 deg were preserved to avoid a redesign of

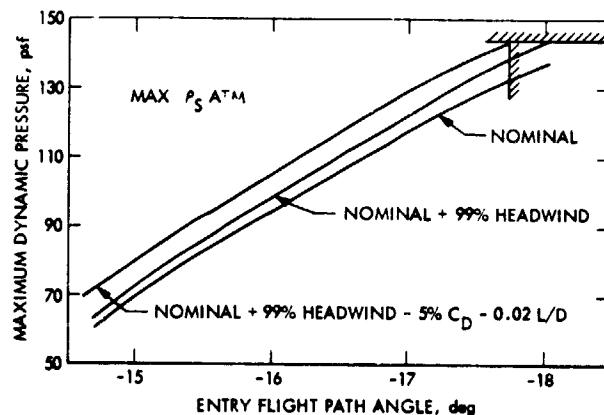


Fig. 5. Sensitivity of q_{max} to entry errors

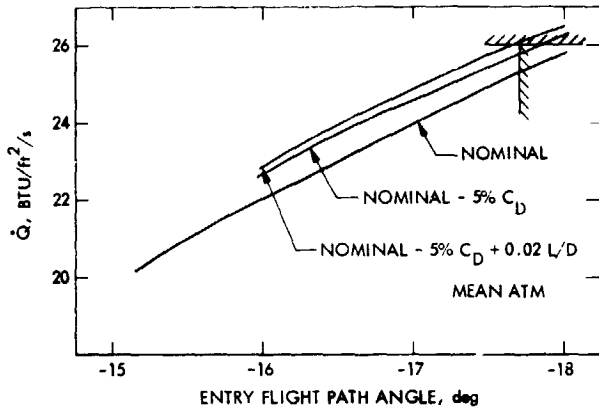


Fig. 6. Sensitivity of stagnation point heating rate to entry errors

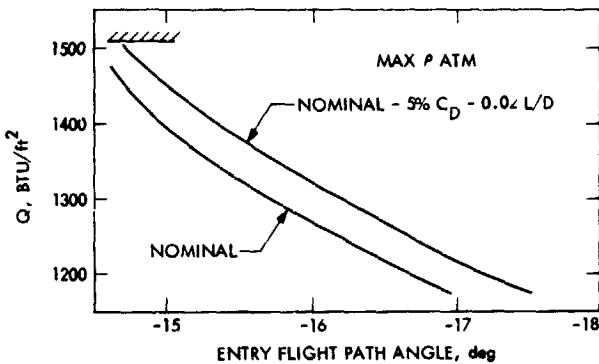


Fig. 7. Sensitivity of total stagnation heat load to entry errors

several other descent parameters. This figure is referred to later in the description of how the parachute deployment altitude above terrain was selected to provide maximum terrain height capability while still satisfying parachute deployment constraints. Thus, the VL entry corridor was bounded by a shallow γ_E of -15.9 deg and a steep γ_E of -17.7 deg. Note in Fig. 7 that the Q constraint was easily satisfied by this corridor.

It will be useful at this point to define relevant descent parameters to aid in the remaining discussion of the maximum accessible area. Figure 9 depicts the deorbit controls of ΔV_{VO} , CA, and CLA, entry lead angle λ_E , and touchdown PER and XR angles. Cone angle CA is the in-plane thrust pointing angle; clock angle CLA is the out-of-plane thrust pointing angle. Entry lead angle is defined as the angular separation between the VL and the VO when the VL arrives at the entry radius. A negative lead angle means the VL is leading the VO, and this is the normal situation. The PER angle is the

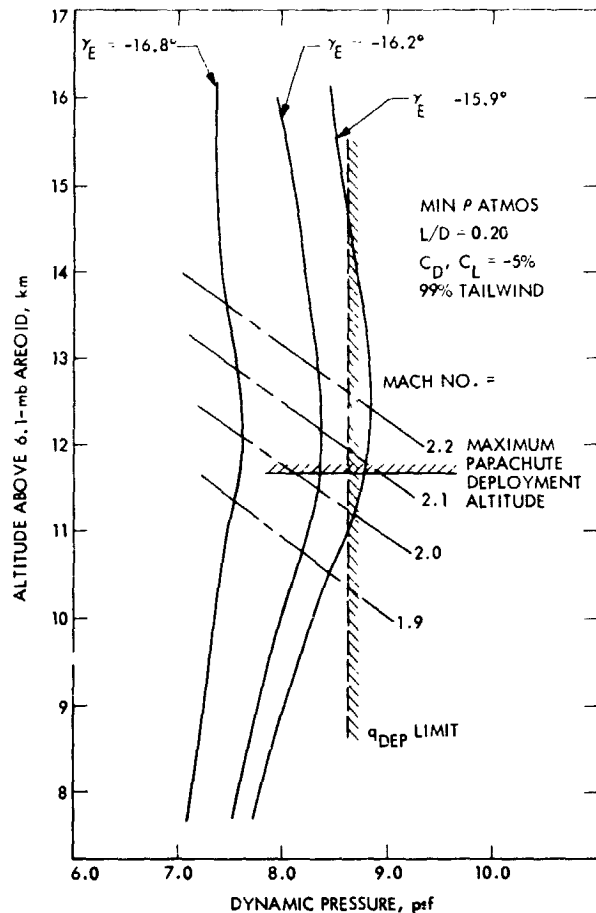
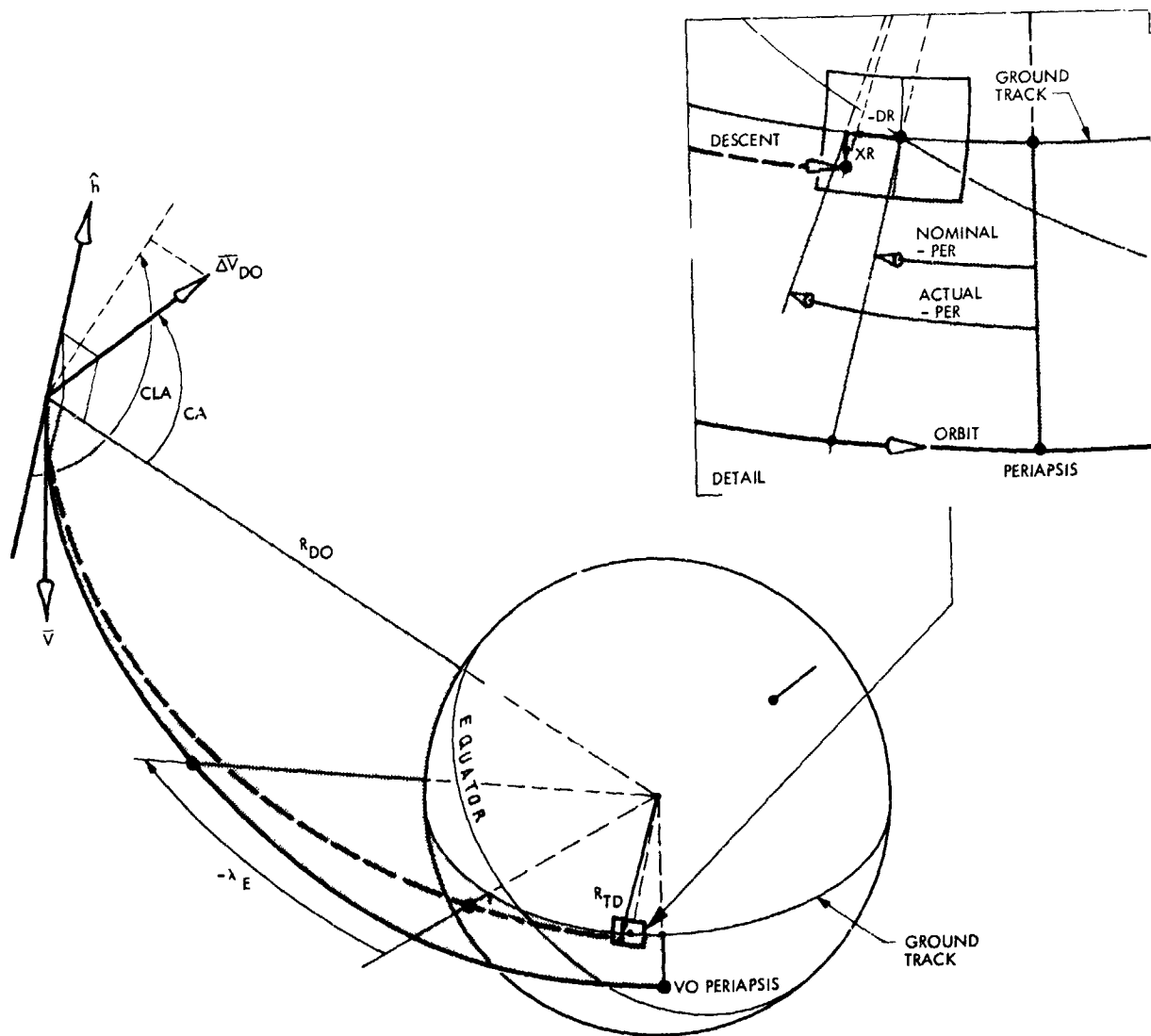


Fig. 8. Parachute phase dynamic pressure and Mach No. vs altitude

angle between VO periapsis and the VL at touchdown. The XR angle is the angular displacement of the VL out of the VO orbital plane at touchdown. Coast time t_c is measured from the beginning of the deorbit burn maneuver to entry.

The final step in constructing the VL maximum accessible area was to determine the XR capability for the entry corridor defined above. XR capability was determined primarily by ΔV_{max} and $t_{c/max}$. The maximum available deorbit propellant of 160.1 lb was determined by subtracting the ACS propellant and all propellant margins from the total propellant loaded in the tanks. This in turn, along with initial VL mass and deorbit propulsion system I_{SP} , determined a maximum available deorbit ΔV of 156 m/s. The maximum allowable coast time of 5 hours was based on worst-case power and thermal analysis for VL descent. Finally, analysis showed that for the entry corridor specified earlier, a lead angle of -20 deg would always permit satisfaction of the descent and initial postland relay link constraints. These three parameters —

ORIGINAL PAGE IS
OF POOR QUALITY



- R_{TD} RADIUS AT TOUCHDOWN
- R_E RADIUS AT VL ENTRY
- R_{DO} RADIUS AT DEORBIT
- h VL TRAJECTORY ANGULAR MOMENTUM
- CA CONE ANGLE (IN-PLANE POINTING)
- CLA CLOCK ANGLE (OUT-OF-PLANE POINTING)
- ΔV_{DO} DEORBIT DELTA V
- t_c COAST TIME
- λ_E LEAD ANGLE
- DR DOWN RANGE
- XR CROSS RANGE

Fig. 9. Descent trajectory geometry

ΔV_{max} of 156 m/s, $t_{c/max}$ of 5 hours, and λ_E of -20 deg and the entry corridor specified earlier completely defined the maximum accessible area shown in Figure 10. Each convex subregion in this figure corresponds to a specified entry flight path angle and was determined by the ΔV_{max} boundary and the $t_{c/max}$ boundary.

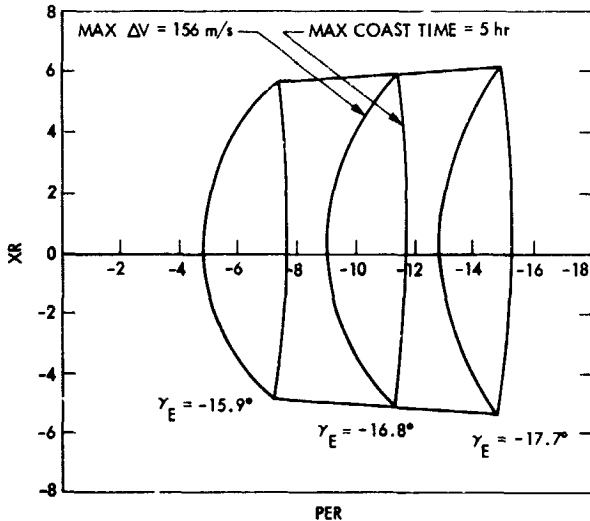


Fig. 10. Maximum accessible area

B. Targeting Region and Preferred Targeting Region

The targeting region is a subregion of the maximum accessible area and is obtained by acknowledging entry flight path angle dispersions due to orbit determination and deorbit execution errors and by utilizing VL capabilities in a more conservative fashion.

The prelanding predicted entry flight path angle dispersions (fixed altitude) over a region of the accessible area are shown in Figure 11. The statistical errors resulted from orbit determination and statistical deorbit execution errors, although orbit determination errors made only a very small contribution. The total errors were obtained by adding the accelerometer thermal bias shift effect to the statistical errors. The possibility of an accelerometer thermal bias shift was postulated during preflight analysis, when it was shown that moderately large temperature transients might occur in the accelerometers due to RCS firings during deorbit. Note, however, that the accelerometer thermal bias shift effect applied only to the shallow side of the entry flight path angle, not the steep side. The asymmetry of the plot is due to the effect of the rotating atmosphere. That is, to achieve zero XR the deorbit ΔV vector must be displaced out of the VO orbital plane in the direction of negative XR (see Figure 9), so that after the VL encounters

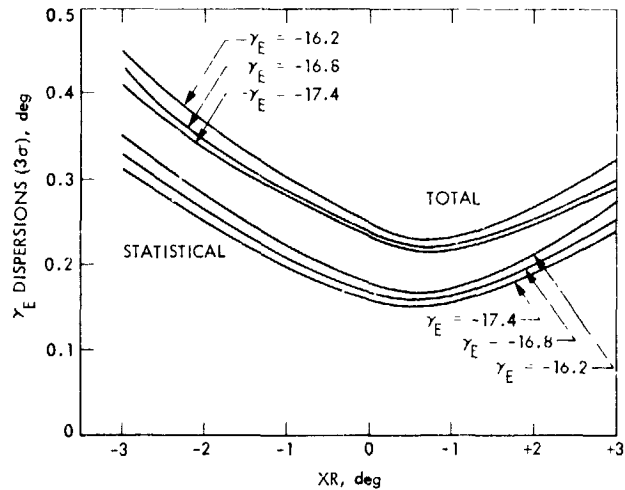


Fig. 11. Dispersions (3σ) over targeting region

the rotating atmosphere, the atmosphere will carry the VL back into the VO orbital plane. However, as the displacement of the deorbit ΔV vector out of the VO orbital plane increases, so does the contribution of out-of-plane pointing errors to γ_E errors.

To protect against entry flight path angle dispersions causing entry outside the entry corridor, it was necessary to constrict the entry corridor on both the shallow and steep boundaries by the expected $3\sigma_{\gamma_E}$ dispersions. These dispersions vary significantly with XR and, to a lesser extent, with γ_E , as is clearly shown in Figure 11. Cross-range targeting was limited to ± 3 deg in order to limit both entry flight path angle and touchdown location dispersions.

Finally, the deorbit ΔV was set at its maximum value of 156 m/s in order to minimize entry weight and coast time. This has the effect of eliminating the convex subregions for each γ_E in the maximum accessible area and reducing it to a single γ_E arc.

The targeting region obtained by constricting the entry corridor by the $3\sigma_{\gamma_E}$ dispersions and by fixing deorbit ΔV at its maximum value is shown in Figure 12. Also shown is the superimposed maximum accessible area, as well as the third accessible area concept mentioned earlier, namely, the preferred targeting region. This latter region was obtained from the targeting region by defining a mini-entry corridor of ± 0.1 deg about the optimal entry flight path angle, which for VL1 was -16.8 and for VL2 was -17.0 deg. After the optimal entry flight path angle was selected for the actual descent, the final VO site acquisition maneuver was designed to keep the selected landing site within this band.

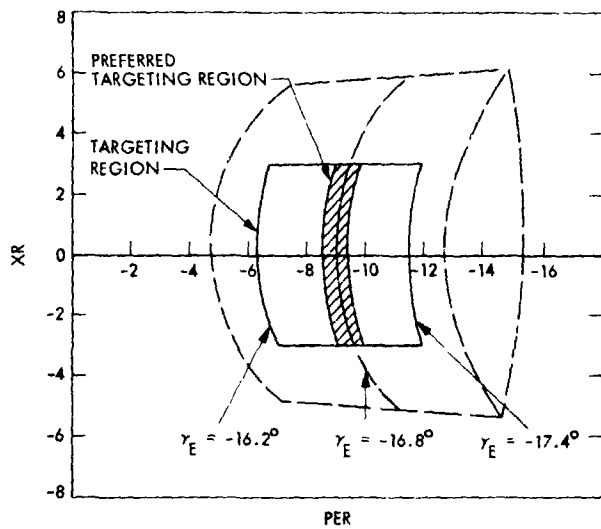


Fig. 12. Targeting regions

C. Landing Accuracy

If the landing site is selected to lie within the targeting region described earlier, a descent trajectory which satisfies all relevant system and mission constraints is assured. The measure of the VL capability to land close to a selected site is given by the touchdown dispersion ellipse. This 99% ellipse is centered at the nominal touchdown site and is defined by the downrange semimajor axis, SMA, and the crossrange semiminor axis, SMB.

Figure 13 shows the variation of SMA over the targeting region and the contribution of deorbit execution errors to the total. Figure 14 shows both the total SMA and SMB of the touchdown dispersion ellipse, as well as the contribution of each important error source to the total. Statistical components were RSS'd to obtain the total statistical error. The total error was obtained by adding the total statistical error to the algebraic sum of the nonstatistical errors. The trapezoidal bars represent the variation in each error source from $XR=0$ to $XR=3$ deg. It should be noted that SMA and SMB showed very little variation over the entry corridor, so that the results shown in Figure 14 were applicable to the entire targeting region.

Deorbit execution errors were analyzed in terms of errors in deorbit ΔV magnitude (due primarily to accelerometer bias), in-plane pointing, and out-of-plane pointing. Since very little cross-ranging was actually required for either VL, ΔV magnitude was the dominant contributor to γ_E errors and SMA, out-of-plane pointing was the dominant contributor to SMB, while in-plane pointing was an insignificant error source as far

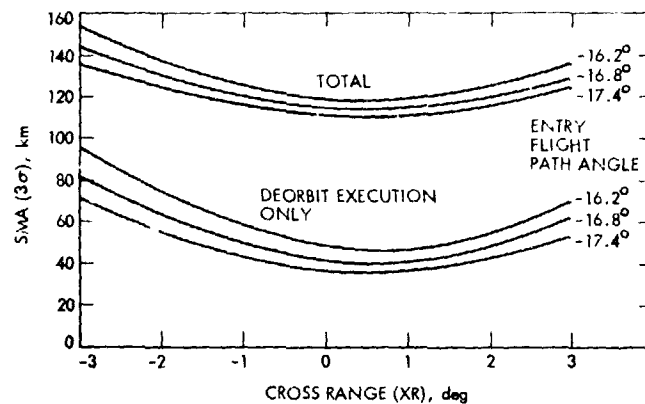


Fig. 13. SMA of the 0.99 landing dispersion ellipse over the targeting region

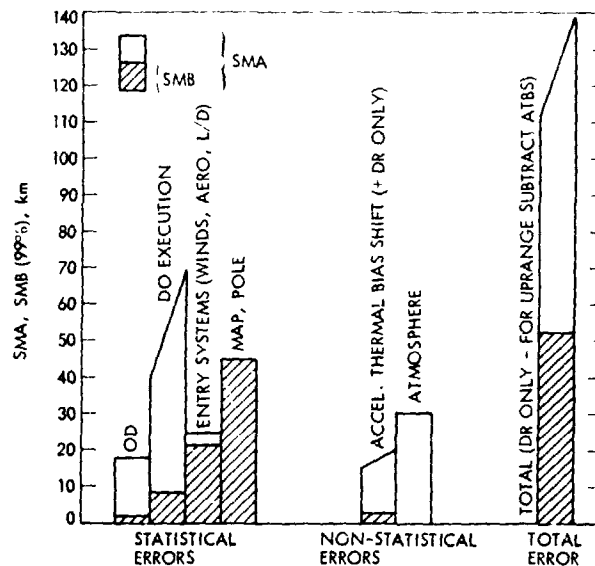


Fig. 14. Components of touchdown dispersion ellipse SMA and SMB over targeting region

as γ_E , SMA, and SMB were concerned. This situation can be understood by viewing each error component in terms of the energy and angular momentum errors it induces in the descent trajectory.

The three deorbit execution error components produce the vector $\delta \Delta V$ in the commanded deorbit ΔV . The energy error induced by $\delta \Delta V$ is proportional to $\bar{V}_{DO} \cdot \delta \Delta V$, where \bar{V}_{DO} is the velocity at deorbit start. The angular momentum error is proportional to $\bar{r}_{DO} \times \delta \Delta V$, where \bar{r}_{DO} is the radius vector at deorbit start. For both VLs, deorbit began when the true anomaly was about 217 deg, so that the radius was large, while

the velocity was relatively small. The consequence of this situation is that the error $\delta\Delta V$ does not induce a significant energy error in the VL descent trajectory, but can induce a significant angular momentum error if \bar{r}_{DO} and $\delta\Delta V$ are nearly perpendicular.

Thus, the entry errors (at fixed entry radius) and touchdown errors (SMA and SMB) produced by deorbit execution errors were due primarily to the deorbit angular momentum error. Furthermore, the angular momentum magnitude error maps into a γ_E error and SMA, while the angular momentum direction error maps into an entry heading angle error and SMB. For both VLs, the in-plane pointing angle CA was close to 90 deg. Examination of Fig. 9 shows that for CA close to 90 deg, a CA error will produce only negligible angular momentum errors. This explains why in-plane pointing was an insignificant error source for Viking. Contrariwise, again referring to Fig. 9, with CA close to 90 deg, a ΔV magnitude error maps directly into angular momentum magnitude error. And since for the VLs the out-of-plane pointing angle CLA was also close to 90 deg, which means the deorbit ΔV vector lay essentially in the orbital plane, a CLA error, while producing very little error in angular momentum magnitude, will produce a significant angular momentum direction error. This accounts for its importance with respect to SMB errors.

Entry systems errors were comprised of winds and errors in predicting VL aerodynamic characteristics. Each of these two sources made roughly equal contributions to SMA, while the SMB contribution was due primarily to winds. Since the direction of the wind was assumed to be random, winds made equal contributions of 19 km to both SMA and SMB. The errors in VL aerodynamics which contributed to SMA were L/D , C_L , and C_D errors. This should be apparent since these errors induce errors in the lift and drag vector magnitudes and in-plane directions. The only VL aerodynamic errors which contributed to SMB were the VL entry roll angle and lateral CG offset errors. These errors act by tilting the VL lift vector out of the entry plane.

Since the touchdown dispersion ellipse was very important in the selection of a suitable landing site (i.e., the ellipse could not include potentially hazardous surface features), the uncertainty in the location of a given point on the Martian surface must also be factored into the dispersion ellipse. The two error sources which produce errors in locating a point on the Martian surface were the Martian pole error and the map error. These error sources together made equal contributions of 45 km to both SMA and SMB.

The accelerometer thermal bias shift error, which was defined earlier, was a nonstatistical error. It induced entry and touchdown errors in much the same way as a deorbit ΔV

magnitude or pointing error; i.e., it produced a deorbit angular momentum error.

Five equally probable atmosphere models were assumed for preflight analyses. Since only one atmosphere can be used for targeting the actual descent trajectory, it is important to know how the touchdown point would be shifted if one of the other atmosphere models were encountered. For Viking, the mean atmosphere model was used for targeting. The maximum displacements of the touchdown point were induced by the min ρ and max ρ models. This should be expected since these were the models having the minimum and maximum upper atmosphere densities, respectively. Since each atmosphere was assumed to be equally probable, the conservative approach was to add this touchdown error algebraically to the total statistical error. The touchdown error due to atmospheres was totally an SMA error, with no contribution whatever to SMB.

The final values for SMA and SMB, as indicated in Fig. 14, were 112 km for SMA and 52 km for SMB. This value of SMA assumed negligible cross-ranging. If the actual targeted landing site had required the project-approved 3 deg of cross-ranging, SMA would have increased to 138 km.

D. Additional Design Considerations

There are certain VL capabilities which are not reflected by the accessible area and touchdown dispersion ellipse concepts discussed earlier. Since the flight program was designed to deploy the parachute on altitude above the local terrain, it was necessary to carefully select that parameter.

Given the highest permissible parachute deployment altitude above the areoid shown in Fig. 8, there existed a highest terrain height (also referenced to the areoid) at which the VL was capable of landing for stacked worst-case system and environmental conditions. The design Martian terrain height was 2.75 km, with an uncertainty of ± 3 km (3σ). Figure 15 shows the relationship of the maximum terrain height and the highest permissible parachute deployment altitude to the areoid. In order to provide the VL with the capability of landing at the maximum terrain height and at the same time keep the parachute deployment altitude independent of whatever landing site was selected, it was necessary to select the parachute deployment altitude as the difference between the highest permissible parachute deployment altitude above the areoid and the maximum terrain height above the areoid. This difference is shown to be 5.98 km (19,600 ft) in Fig. 15. (The actual deployment altitude was reduced by the onboard altitude sensing uncertainty of 0.18 km.)

There was a high probability that the VL could land at the maximum terrain height. However, with stacked worst-case

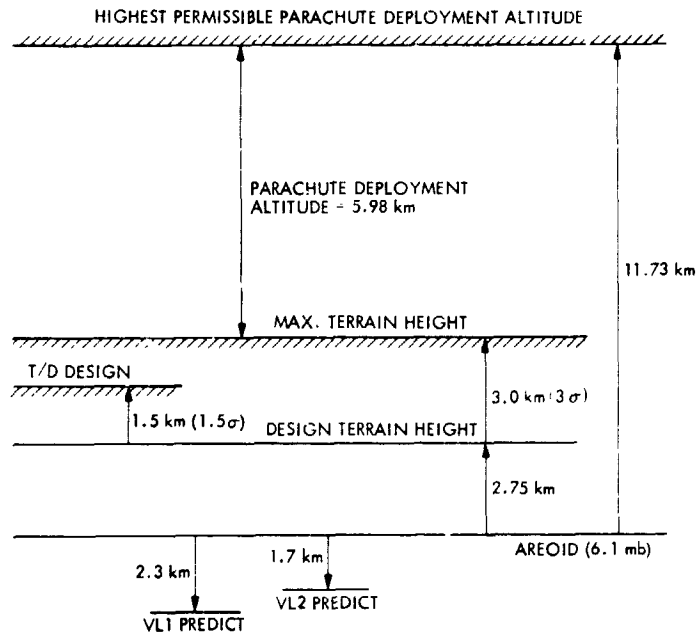


Fig. 15. VL terrain height capability

conditions for the terminal descent phase at the maximum achievable deceleration by the VL terminal descent system, sufficient propellant was not available to ensure a safe landing at this maximum terrain height. The terminal descent phase was governed by the terminal descent contours shown in Fig. 16. These contours and the corresponding terminal descent propulsion system ignition altitude were designed according to a stacked worst-case philosophy, with one exception. Because of higher VL velocities near the surface for descent through the min ρ_s atmosphere, this model was critical for the terminal phase design. These VL velocities were increased still further by the addition of worst-case winds. Finally, because of the fixed parachute deployment altitude above terrain discussion earlier, the higher the terrain, the higher the VL velocities at both parachute deployment and terminal descent ignition. Adding the maximum terrain height to the above stacked worst-case resulted in a terminal descent phase trajectory requiring more propellant than was available. For this reason a decision was made to use a 1.5σ terrain height uncertainty in the design of the terminal descent phase. Thus, in a stacked worst-case sense, the highest terrain at which the VL was capable of landing was the design terrain height $+1.5\sigma$. This relaxation regarding terrain height uncertainty was acceptable for two reasons. First, attainment of the aforementioned high velocities on the parachute prior to terminal descent ignition was quite improbable because of the stacking of several worst-case conditions. And second, as shown in Fig. 15, the nominal VL-1 and VL-2 sites were well below the maximum permissible terrain heights. This was also true of alternate VL-1 and

VL-2 sites. Although it was possible to adjust the parachute deployment altitude as a function of selected site terrain height, this parameter was held constant to provide additional deployment q and Mach number margins for the lower sites.

The final VL capability to be discussed is one that was discovered after the actual launches of the Viking spacecraft had occurred. During cruise, a concern developed over the use of the high-power mode of the relay transmitter (30 W) from parachute deployment to touchdown + 3 minutes because of potential VL thermal problems. An analysis was conducted to determine the acceptability of using the 10-watt mode instead during this phase of the mission, thereby avoiding VL thermal problems. The analysis was based on 0.99 uprange/downrange touchdown dispersions over the entire targeting region and on maximum VL pitch/yaw attitude dispersions from parachute deployment to touchdown.

For VL-1, analyses showed that a significant probability of data loss occurs only for the -3 deg XR region at parachute deployment and touchdown. If a data loss did occur at parachute deployment, it was very unlikely that it would have a duration exceeding 1 s. For the initial postland link, the worst relay performance degradation would be 1-2 dB below adverse tolerances, but could last for 2 min in the worst case. This performance degradation corresponds to a bit error rate of 2×10^{-2} and was acceptable for real-time imaging. On the basis of these results it was concluded that VL-1 had the capability to operate satisfactorily in the 10-W mode from parachute

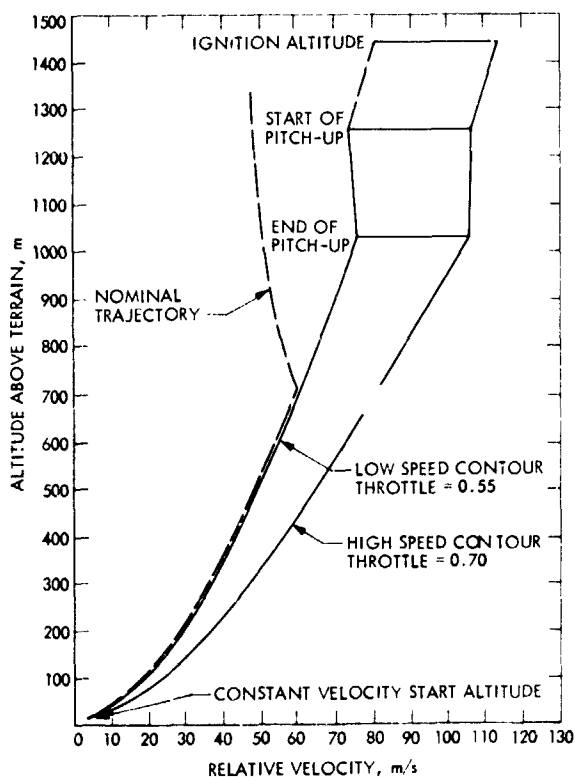


Fig. 16. Terminal descent contours

deployment to touchdown + 3 min, and, therefore, the 10-W mode was used for the actual VL-1 descent.

For VL-2 in the 10-W mode the probability of relay performance below the sum of adverse tolerances was significant over the whole targetable region of the accessible area at terminal descent start and touchdown, and also at parachute deployment for the -3-deg XR region. This analysis could not justify using the 10-W mode for VL-2. However, the excellent relay performance of the actual VL-1 descent and initial post-land links provided the rationale for using the 10-W mode on VL-2.

III. Preliminary VL Trajectory Design History and Validation

A. Preliminary VL-1 Trajectory Design History and Validation

This section documents the history of the VL-1 preliminary descent trajectory design in response to the unexpected problems encountered in the selection of candidate landing sites (LS's). This sequence of LS's developed when it became appar-

ent that the prime A1 site and subsequent sites were much rougher than expected.

Figure 17 depicts the sequence of LS's on a Mars grid as well as related actual and potential VL-1 targeting regions. The sequence of VL-1 LS's in the order in which they were selected is as follows: A1, A1-R, A1-NW, A1-WNW, and A1-WNWSE. The four corresponding targeting regions are shown and numbered in the order in which they were considered. A targeting region shown with solid lines denotes a targeting region for an actually achieved separation orbit. Those shown with dashed lines denote potential targeting regions which would have been achieved if other Mars orbit trim (MOT) maneuvers had been executed.

The separation orbit following MOT-1 for a VL-1 touchdown on July 4 produced targeting region No. 1. The prime landing site is denoted by A1 and corresponds to an entry at -16.8-deg flight path angle and essentially zero XR at TD. The prime site was dropped when VO observations indicated that it was quite rough. Attention was then turned to a revised A1 site, denoted by A1-R, which would have required a shallower entry with a moderate XR at TD. However, site A1-R was also dropped when VO observations indicated that it too was quite rough. It should be noted that preliminary descent trajectories were designed for both A1 and A1-R sites. Plans for landing on July 4 were then cancelled so that time would be available to explore a region known as "Northwest Territory." An MOT was designed (but not executed) to place the spacecraft over the Northwest Territory on July 16. The targeting region which would have existed if this MOT had been executed is labeled No. 2 and the candidate site is denoted A1-NW. This site could have been achieved with nominal -16.8-deg entry flight path angle, but with a substantial negative XR. It was quickly rejected, for the same reason as for earlier sites. The LFPAT did complete preliminary design for this site and landing date, but no validation or other Project work based on this data was done.

A MOT strategy (MOT-5/MOT-6) was then defined which would open up to observation a large region to the west of the first three sites. MOT-5 would induce a steady westward drift; MOT-6 would stop the drift when an acceptable landing site was finally selected. One of the considered options for MOT-6 would have produced targeting region No. 3, and the site considered within this region was denoted by A1-WNW. This site would have required an entry trajectory very similar to the previous site (A1-NW). However, this MOT-6 design was not implemented because evidence was mounting that region 3 would be less hospitable than the nearer region. Therefore, an MOT-6 was designed and eventually executed which produced targeting region 4. The selected site within this region was denoted A1-WNWSE, and this was the final VL-1 site. The

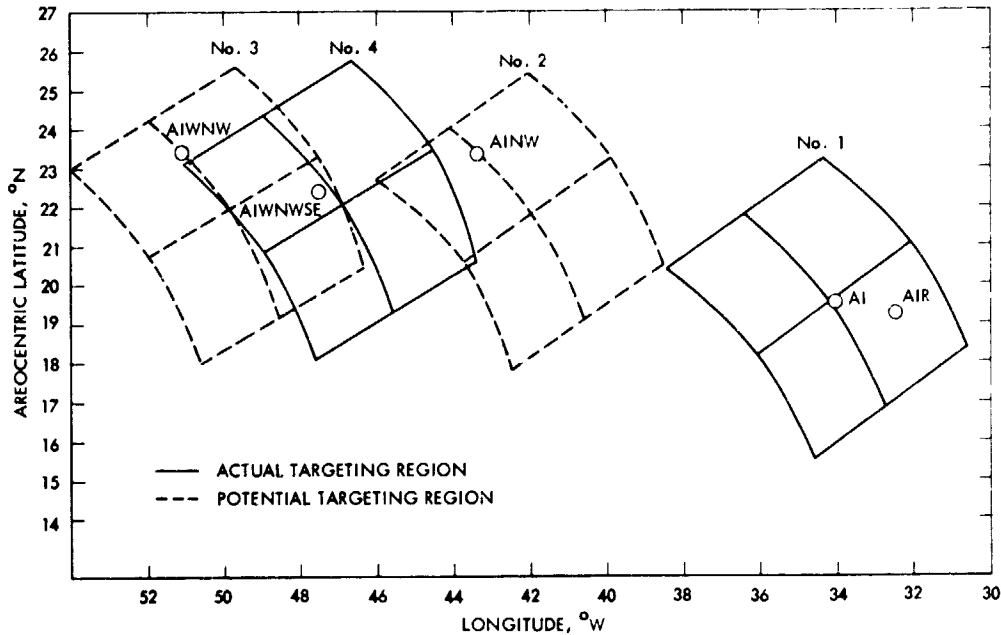


Fig. 17. VL-1 landing site and targeting region history

final targeting region is shown in Fig. 18 on an expanded scale, along with the 99% landing dispersion ellipse about the A1-WNWSE site. Preliminary descent trajectories were designed for both A1-WNW and A1-WNWSE sites. Table 3 presents a summary of key descent trajectory parameters for all VL-1 landing sites considered.

The first step in the descent validation process for sites A1 and A1-WNW consisted of an independent validation of the nominal descent trajectory and the inertial navigation reference frames by the OMATT using the DPTRAJ program. The separation epoch and commanded deorbit pointing computed by the LFPAT using LTOP served as the fundamental inputs to be used by the OMATT to verify that indeed the predicted entry condition and navigator IC's were obtained.

The second step involved the selection of 3σ dispersed entry state vectors which produced minimum and maximum time entry trajectories in conjunction with the following environmental and VL system conditions:

For minimum time entry trajectory

- Low aeroshell L/D ($L/D = 0.16$, $Z_{CG} = -0.139$ ft)
- Min ρ atmosphere
- 10,000-ft terrain height
- Nominal RA blackout
- Aeroshell C_L and C_D high by 5%
- Parachute C_L and C_D low by 12%

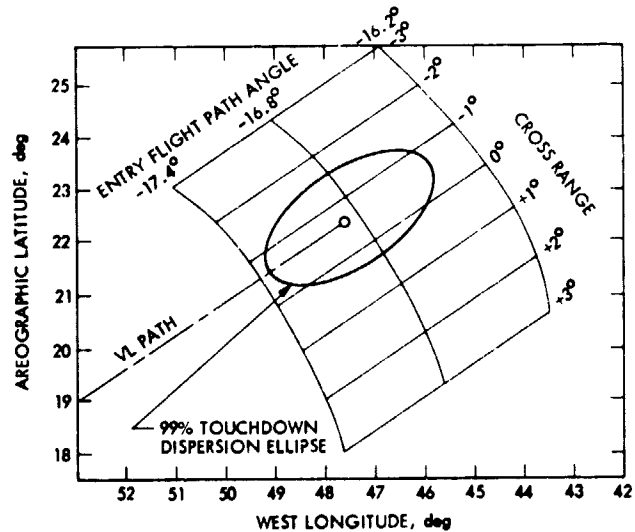


Fig. 18. Final VL-1 targeting region and landing site

Low RA lock altitude (inhibit RA lock for 36 s after blackout)

Entry attitude errors (roll, pitch, yaw)

Mission 1: $\phi_E = 0.8514$ deg, $\theta_E = -0.6192$ deg,
 $\psi_E = -0.7224$ deg)

Mission 2: $\phi_E = -0.7482$ deg, $\theta_E = -0.6192$ deg,
 $\psi_E = -0.8772$ deg)

Sense 0.05-g event at 0.07 g

99% tailwinds

Table 3. Summary of descent trajectory designs for candidate VL-1 LS's

Parameter	Site designation				
	A1	A1R	A1NW	A1WNW	A1WNWSI
Location					
Areocentric latitude, deg	19.5	19.35	23.4	23.5	22.4
Longitude, deg. W	34.0	32.5	43.4	51.0	47.5
Landing time					
UTC, hr:min	7/5/76 01:41	7/5/76 01:42	7/17/76 09:40	7/20/76 12:05	7/20/76 11:53
LLT, hr:min	16:48	16:55	16:15	16:11	16:13
Entry flight path angle, deg	-16.79	-16.51	-16.81	-16.80	-16.89
Coast time, hr	3.043	3.023	3.293	3.205	3.082
PER _{TD} , deg	-8.85	-7.61	-9.10	-9.05	-9.18
XR _{TD} , deg	+0.25	+1.20	-2.10	-1.77	-0.60
Comments	Used for preliminary LSO validation	Approved at MOT3 maneuver conference if site ok	Never used; cancelled before use	Used for preliminary LSO validation (repeat)	Final

LLT: local lander time from midnight at landing site.

PER_{TD}: angle from VO periapsis to the projection of the landing site into the orbit plane at touchdown.

XR_{TD}: central angle from the landing site at touchdown to the orbit plane.

For maximum time entry trajectory

High aeroshell L/D ($L/D = 0.2$, $Z_{CG} = -0.175$ ft)

Max ρ atmosphere

-26,000-ft terrain height

Aeroshell C_L and C_D low by 5%

Parachute C_L and C_D high by 12%

Entry attitude errors (roll, pitch, yaw)

Mission 1: $\phi_E = -0.8514$ deg, $\theta_E = 0.6192$ deg,

$\psi_E = 0.7224$ deg

Mission 2: $\phi_E = 0.7482$ deg, $\theta_E = 0.6192$ deg,

$\psi_E = 0.8772$ deg

Sense 0.05-g event at 0.03 g

No winds

The third step consisted of the simulation of the nominal SEP to TD descent trajectory and simulation of entry to TD trajectories for the minimum and maximum time dispersed cases by LTOP, LATS, and the VCSF (LSO). The final results were compared to validate the accuracy and consistency of the three trajectories. It should be noted that the LATS program

utilized the corresponding nominal descent flight load file generated by LTOP, while the VCSF used the corresponding predicted VL memory map generated by LPAG from this same descent flight load file. Thus, the simulation was more than just a validation of descent trajectory dynamics; it was also a validation of the *command load* required to produce the descent trajectory. This third step was the most important step in the entire descent validation process.

The fourth and final step involved only the use of LTOP to verify that the dispersed entry trajectories satisfied all design constraints when subjected to additional stress conditions. Four stress cases were required: (1) maximum aeroshell dynamic pressure, (2) maximum parachute deployment dynamic pressure and Mach number, (3) maximum terminal descent ignition velocity, and (4) minimum terminal descent ignition velocity. The detailed conditions producing these 4 stress cases are defined in FPAG Procedure SPF3-107.

One feature of the descent validation process requiring more discussion was the selection of the dispersed entry state

vectors. The selection process was based on the convenient fact that the two dominant eigenvectors contained the bulk of the entry dispersions in inertial flight path coordinates at fixed radius and were nearly coplanar with entry time/entry flight path angle space. This simplified the selection of dispersed samples to produce minimum and maximum flight time entry trajectories. The two dominant eigenvectors were first projected into entry time/entry flight path angle space. Two linear combinations of these eigenvectors were then formed to produce a low and steep sample (minimum time trajectory) and a high and shallow sample (maximum time trajectory). In addition, the effect of accelerometer thermal bias shift was added to the high and shallow sample since it tends to make entry time occur at a higher radius and a shallower flight path angle. In practice, this selection process produced error samples in inertial flight path coordinates which were greater than or equal to 3σ in all components, except for inertial entry velocity. Prior to transfer of these dispersed samples to the LSO, they were first transformed into equivalent samples in MEQ coordinates at fixed entry time.

The final descent validation was performed using the descent trajectory designed for the A1-WNW site, even though the final selected site, A1-WNWSE, differed substantially from the A1-WNW site. However, both sites required nearly the same entry flight path angle for site acquisition. In addition, the final site had a smaller cross-range at TD associated with it, so that entry dispersions would, in fact, be smaller than those actually used in the final descent validation process. Thus, adequate rationale existed for relying on the final descent validation results based on A1-WNW. Therefore, the final descent trajectory design was validated for nominal descent but not for the dispersed entry cases.

B. Preliminary VL-2 Trajectory Design History and Validation

The history of the VL-2 preliminary descent trajectory design was not complicated by a sequence of substantial LS selection changes as in the case of VL-1. Lessons learned during the VL-1 site certification and acquisition process were applied in defining the strategy for the corresponding VL-2 process. Three longitude bands (designated B1, B2, and B3) of potential VL-2 sites were selected. The insertion and trims were designed to produce a steady westward drift of the VO-2 orbit so that each longitude band could be examined in a more orderly fashion for an acceptable VL-2 landing site. When an acceptable site was found, the MOT-3/MOT-4 maneuver sequence could be designed to place the orbit over this landing site at the correct time. The final VL-2 site area was selected in the B3 band at a latitude of $48^{\circ}0$ N and a longitude of $226^{\circ}0$ W. Minor adjustments to this site were made on two subsequent occasions, with the final landing site coordinates defined to be $47^{\circ}89$ N and $225^{\circ}86$ W. The targeting region from the

final separation orbit for this site and the 99% landing dispersions are shown in Fig. 19. The key trajectory parameters for the related descent trajectory design are tabulated in Section IV (Table 4). There was no evolution of descent trajectory designs for VL-2 as there was for VL-1.

As can be seen in Fig. 19 the nominal VL-2 entry flight path angle was selected to be -17.0 deg, unlike the -16.8 deg angle for VL-1. There were two reasons for this. First, the fact that VL-1 had actually entered with a flight path angle of -17.0 deg and performed excellently provided a strong argument for doing the same thing with VL-2. Second, the B site nominal atmosphere extrapolated from the atmosphere reconstructed by LTARP from the actual VL-1 data showed that entry at an angle steeper than -16.8 deg was entirely satisfactory since the reconstructed atmosphere closely resembled the $\text{min} q_{\infty}$ atmosphere at high altitude, and thus a lower q_{max} would be encountered.

As can be seen in Fig. 19, the touchdown dispersion ellipse for VL-2 was smaller than the preflight ellipse used for VL-1. There were several reasons for this. First, analysis of actual VL-1 deorbit data showed that temperatures were stable during deorbit and no accelerometer thermal bias shift had occurred. It was for this reason that the accelerometer thermal bias shift was deleted as a VL-2 error source. Second, the actual VL-1 atmosphere reconstruction process, as expected, was able to reduce the degree of atmospheric uncertainty; consequently, the in-plane, nonstatistical touchdown dispersions due to the unknown atmosphere were reduced from ± 30 km for VL-1 to ± 12 km for VL-2. Third, as a result of landed VL-1 tracking, the pole component of the map/pole

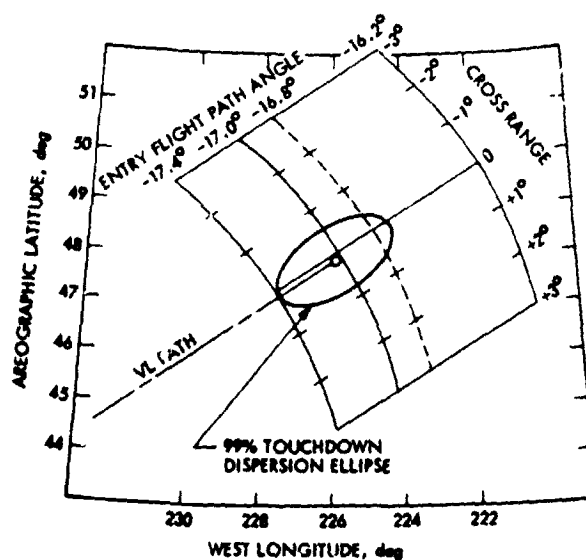


Fig. 19. Targeting region and landing site

dispersion was greatly reduced. This permitted the 45- X 45-km dispersion ellipse used for VL-1 to be reduced to a 30- X 30-km ellipse for VL-2, which essentially was the map error only.

The descent validation process for VL-2 followed the same steps as for VL-1. For VL-2, of course, there was only one descent validation.

IV. Final VL Trajectory Design and Descent Parameters

This section describes the final VL-1 and VL-2 trajectory designs and presents the basis for the selection of relevant descent parameters. The expected trajectory dispersions and descent relay performance will also be discussed.

A. Nominal VL Descent Trajectory Design

The final VL descent trajectory design process began with the specification of the final landing site and the current best estimate (CBE) of the separation orbit.

The final landing site for VL-1 was:

Areocentric latitude = 22°4 N (areographic latitude = 22°6 N)
 Longitude = 47°5 W

The final landing site for VL-2 was:

Areocentric latitude = 47°59 N (areographic latitude = 47°89 N)
 Longitude = 225°86 W

In addition to the landing site, two other targets were required for the targeting process. For both VL-1 and VL-2 these were:

Deorbit $\Delta V = 156$ m/s
 Entry lead angle = -20 deg

The selection of deorbit ΔV as a target is consistent with the decision discussed earlier to select the deorbit ΔV at its maximum value in order to minimize coast time and entry weight. Entry lead angle was selected as a target because the targeting region employed in landing site selection was based on a lead angle of -20 deg to ensure acceptable descent and initial postland relay link performance. Note that entry flight path angle γ_E was not a target since selection of the landing site within the targeting region automatically determined γ_E (observe the γ_E arcs in Figs. 18 and 19).

The orbital elements and epoch of the separation orbits which were used in the design of the nominal VL-1 and VL-2 descent trajectories are given below

VL-1	VL-2
$P = 88693.9459$ s	$P = 88638.0192$ s
$r_p = 4901.185$ km	$r_p = 4882.8472$ km
$i = 37.7302$ deg	$i = 55.384312$ deg
$\Omega = 123.5689$ deg	$\Omega = 33.924799$ deg
$\omega = 46.6924$ deg	$\omega = 73.985842$ deg
$t-t_p = 74088.242$ s	$t-t_p = 74953.478$ s
epoch = 1976 July 20/ 08 00.00 UTC	epoch = 1976 Sept. 3/ 19 00.00 UTC

The VL-1 separation orbit above corresponds to SATOD solution P24548, the VL-2 separation orbit corresponds to SATOD solution Q20524.

The resulting targeted descent trajectory is shown in Figure 20. To the scale shown in this figure, no discernible differences exist between the VL-1 and VL-2 descent trajectories. Major descent trajectory events are shown. The VL descent trajectories are essentially coplanar with the VO trajectory. The VL-1 out-of-plane thrusting angle of -7.4 deg produced only a relatively small out-of-plane displacement of the descent trajectory, as did the VL-2 out-of-plane thrusting angle of +1.9 deg. Important trajectory parameters for these descent trajectories are summarized in Table 4.

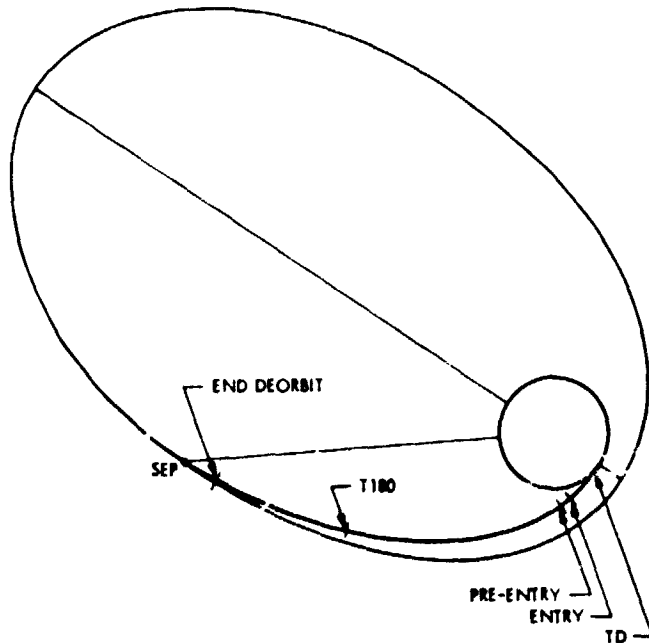


Fig. 20. Nominal VL descent trajectory

Table 4. VL descent trajectory design summary

Parameter	VL1	VL2
Separation to entry		
Separation time (UTC) ^a	202/08.32.15	247/19.19.29
Deorbit ΔV	156.0 m/s	156.0 m/s
Deorbit propellant consumption	162.4 lb	162.2 lb
Coast time	3.082 hr	3.038 hr
Entry conditions ^b		
Entry time (UTC)	202/11.44.08	247/22.28.46
Entry time from SEP	11513.0 s	11356.7 s
Inertial velocity	4.6105 km/s	4.6135 km/s
Inertial flight path angle	-16.89 deg	-17.03 deg
VL/VO lead angle	-20.0 deg	-20.0 deg
Entry mass	984.2 kg	982.9 kg
Entry to touchdown		
Maximum dynamic pressure	112.6 lb/ft ²	115.8 lb/ft ²
Parachute deployment (mortar arm)		
Altitude above terrain	5.857 km	5.856 km
Dynamic pressure	6.567 lb/ft ²	6.535 lb/ft ²
Mach number	1.014	1.041
Time from SEP	11931.6 s	11766.8 s
Terminal descent		
Engine ignition altitude	1.462 km	1.462 km
Time from SEP	11992.0 s	11826.0 s
Relative velocity at end of warmup		
Propellant consumption	51.5 m/s	52.7 m/s
	152.0 lb	152.0 lb
Touchdown		
Touchdown time (UTC)	202/11.52.50	247/22.37.18
Touchdown time from SEP	12034.9 s	11868.7 s
Areographic latitude	22° 59' N	47° 89' N
Longitude	47° 52' W	225° 85' W
PER angle	-9.18 deg	-10.0 deg
Cross-range angle	-0.60 deg	0.12 deg
Sun elevation angle at touchdown	38.3 deg	128.8 deg

^aDay of year/hr:min:sec.

^bEntry was defined as 800,000 ft above the areoid at touchdown.

B. Descent Flight Load Parameters

After the VL descent trajectory had been designed, a corresponding set of descent guidance parameters had to be computed. These constituted a set of commands which were up-linked to the spacecraft and which, when executed, produced the desired descent trajectory. The descent guidance parameters represented the culmination of the descent trajectory design process and guaranteed satisfaction of all trajectory-related constraints and requirements discussed earlier. They

also guaranteed satisfaction of certain constraints and requirements imposed on the VL attitude during descent.

Table 5 summarizes the actual uplinked descent guidance parameters for both VL-1 and VL-2. Definitions of the parameters are also presented in this table.

Certain VL descent flight load parameters are discussed in this section, along with their rationale, in the approximate order in which they were executed by the flight software. In particular, most VL attitude-related parameters and "manual" parameters will be discussed.

The VL attitude commands A(2) through A(6) were referenced to the VL attitude just prior to separation. This separation (or celestial lock) coordinate frame was defined by the ideal VO celestial lock orientation corrected for the predicted VO roll drift while the VO was on roll inertial hold from SEP-3 hr to SEP. For VO-1 the reference star was Canopus and the predicted VO roll drift angle was -0.082 deg. For VO-2 the reference star was Vega and the predicted VO roll drift angle was -0.470 deg.

The VL orientation during the deorbit burn was specified by attitude command A(2). This matrix defined the required pointing of the VL x-axis for the deorbit burn as determined by the targeting process. It also defined the VL roll orientation about the x-axis which would result in minimum sensitivity of entry flight path angle errors to deorbit pointing errors in the event of a VL z-axis accelerometer failure. The technique for selecting this roll angle is described in Section 10.2.6.2 of the Navigation Plan (Ref. 1). For VL-1 this roll orientation was 20 deg; for VL-2, 36 deg. The relative VL/VO attitude orientation geometry during the deorbit burn is shown in Fig. 21 for VL-1/VO-1 and in Fig. 22 for VL-2/VO-2.

Following the deorbit burn, the VL was reoriented to prepare for the long coast phase of the descent trajectory. In the case of VL-1 a roll maneuver about the x-axis (defined by matrix A(4)) was performed to position the VL z-axis perpendicular to the Sun direction. This maneuver, plus another 180-deg roll (defined by matrix A(5)) midway through the long coast at time T(180) prevented uneven heating of the IRU, which is located on the z-axis. In the case of VL-2, the reorientation after the deorbit burn involved a repositioning of the x-axis as well as a roll about the x-axis. The repositioning of the VL-2 x-axis was required to shield the RPA from the Sun during the long coast. This maneuver was defined so that the Sun vector was 120 deg from the VL-2 x-axis and in the x-y plane. Like VL-1, VL-2 performed a 180-deg roll midway through the long coast.

The preentry phase for VL-1 began at E-6 min (command T(6)), which required that the attitude maneuver for preentry

Table 5. Trajectory-related descent guidance parameters

Parameter	Definition	Units	VL1 Values	VL2 Values
H(STRT)	Terminal descent ignition altitude	m	47978406.472504+04	47978406.492504+04
H(MORT)	Parachute deployment altitude	m	19376231939533+05	19373347913735+05
H(CV)	Altitude for constant velocity descent start	m	55000000000000+02	55000000000000+02
T(1)	Deorbit attitude maneuver initiation time	s	24100000000000+03	24100000000000+03
T(2)	Deorbit burn initiation time	s	42100000000000+03	42100000000000+03
T(4)	Orbital descent initiation time	s	19370000000000+04	19370000000000+04
T(5)	Preentry attitude maneuver initiation time	s	10973000000000+05	10997000000000+05
T(6)	Preentry initiation time	s	11153000000000+05	11177000000000+05
T(7)	Entry initiation time	s	11513000000000+05	11357000000000+05
A(2)	Coordinate transformation from VL axes at SLP to VL axes at deorbit burn 1. Note that elements of this matrix and all subsequent matrices are ordered as follows: $a_{11}, a_{12}, a_{13}, a_{21}, a_{22}, a_{23}, a_{31}, a_{32}, a_{33}$		- 73323713887637+00 - 64070943159820+00 22771633992980+00 66078442039462+00 - 59240455954451+00 46089130490209+00 - 16039720928329+00 48841402732925+00 85774382748850+00	- 33354670650285+00 - 86553878353195+00 - 37361631296415+00 22393304513958-10 38892568230245+00 - 92099693446312+00 94246729383414+00 - 31556208239837+00 11034263634975+00
A(3)	Coordinate transformation from VL axes at SLP to VL axes at deorbit burn 2		- 73323713887637+00 - 64070943159820+00 22771633992980+00 66078442039462+00 - 59240455954451+00 46089130490209+00 - 16039720928329+00 48841402732925+00 85774382748850+00	- 33354670650285+00 - 86553878353195+00 - 37361631296415+00 22393304513958-01 38892568230245+00 - 92099693446312+00 94246729383414+00 - 31556208239837+00 11034263634975+00
A(4)	Coordinate transformation from VL axes at SLP to VL axes at orbital descent initiation		73323713271361+00 - 64070943159820+00 22771633992980+00 67997301947204+00 - 69089792252640+00 24555397255752+00 - 11942467313914-11 33489025800971+00 94225713851910+00	- 4990993084502+00 - 79511180443866+00 - 34321593926037+00 86602544371108+00 - 45905800100533+00 - 19815607844903+00 - 54581794756338-12 - 39631170832476+00 91811599899540+00
A(6)	Coordinate transformation from VL axes at SLP to VL axes at preentry		- 60554864843276+00 - 29449742785269+00 73931191356108+00 56557407807886+00 81283710992091+00 - 13924326043383+00 - 55987448232560+00 - 50256054135157+00 - 65876662907758+00	11687432054119+00 - 75817129938006+00 - 64149564822583+00 56700860459145+00 - 47936637898329+00 66985748658995+00 - 81537788844823+00 - 44202279974769+00 37386413059280+00
A(10)	Coordinate transformation from VL axes at SLP to local vertical axes at TD (for entry navigation)		- 53461754340999+00 - 22260179296535+00 81524997936300+00 - 56306874904968+00 81319407546387+00 - 14720388854768+00 - 63018860901449+00 - 53773956279883+00 - 56008792733380+00	30250041886948+00 - 68769688902108+00 - 69927261323582+00 55955115468320+00 - 47324487639062+00 68039813704721+00 - 77161873184202+00 - 59709967921818+00 21926282740361+00
C(0)	Deorbit velocity polynomial coefficients. $\Delta V = C(0) + C(1)x + C(2)x^2 + C(3)x^3 + C(4)x^4$	m/s	11768773060325+00	11768773060325+00
C(1)		m/s ²	48572641104301+00	48572641104301+00
C(2)		m/s ³	- 11959749037646-03	- 11959749037646-03
C(3)		m/s ⁴	42852972770049-07	42852972770049-07
C(4)		m/s ⁵	- 81106468877497-11	- 81106468877497-11

Table 5 (contd)

Parameter	Definition	Units	VL1 Values	VL2 Values
V(01)	Initial velocities for terminal descent on contours 1 and 2,	ft/s	36521197349423+03	36521197349423+03
V(02)	respectively	ft/s	25098446653991+03	25098446653991+03
V(CV)	Velocity for constant velocity descent	ft/s	.80000000000000+01	80000000000000+01
CNTUR1(1)	Terminal descent contour 1 coefficients	ft	51903708481594+02	51903708481594+02
CNTUR1(2)	$h = \text{CNTUR1}(1) + \text{CNTUR1}(2) \times V + \text{CNTUR1}(3) \times V^2$ $+ \text{CNTUR1}(4) \times V^3 + \text{CNTUR1}(5) \times V^4$	s	00000000000000	00000000000000
CNTUR1(3)		s^2/ft	49021868166001-01	49021868166001-01
CNTUR1(4)		s^3/ft^2	-80680562201667-04	-80680562201667-04
CNTUR1(5)		s^4/ft^3	48926667394356-07	48926667394356-07
CNTUR2(1)		Terminal descent contour 2 coefficients	ft	50428843099282+02
CNTUR2(2)		s	00000000000000	00000000000000
CNTUR2(3)		s^2/ft	72166099323428-01	72166099323428-01
CNTUR2(4)		s^3/ft^2	-93165337602190-04	-93165337602190-04
CNTUR2(5)		s^4/ft^3	55467986066320-07	55467986066320-07
V(C01)		Deorbit delta-V for 1st burn	ft/s	51181102362205+03
V(C02)	Deorbit delta-V for 2nd burn	ft/s	00000000000000	00000000000000
V(X1)	Inertial velocity at entry in local vertical at TD coordinates	ft/s	15116249894268+05	15132202739134+05
V(Y1)		ft/s	38774722789450+03	29037834500908+03
V(Z1)		ft/s	-42870531724524+03	-25106426610671+03
H(1)	Entry altitude above landing site	ft	80649084954711+06	80394306555191+06
R(P)	Planet radius at landing site	ft	11117349216188+08	11097978071929+08
A(1 1)	Entry pitch rate polynomial coefficients $\Delta\theta = A(1 1) \times t + A(1 2) \times t^2$	rad/s	-46650828266879-03	-56701155069293-03
A(1 2)		rad/s ²	-24098930026432-06	-23904143143198-06
phi(CL)	Parachute roll angle change	rad	-17165423606995+01	26638380727306+01
K(G)TD	Gravity gradient at TD	s ⁻²	-22014744572449-05	-22130223872909-05
K(G)I	Gravity gradient at entry	s ⁻²	-17843044878578-05	-17941807369155-05
G(O)	Acceleration of gravity at TD	ft/s ²	12237280165855+02	12280036963421+02
R(XE)	Inertial position at entry in local vertical at TD coordinates	ft	-37839557222424+07	-36735063678810+07
R(YE)		ft	-29139711932419-11	00000000000000
R(ZE)		ft	-11307503747749+08	-11320824957924+08
V(XS)	Landing site velocity at TD in local vertical at TD coordinates	ft/s	61684720202416+03	44396452737212+03
V(YS)		ft/s	38774722789450+03	29077834600908+03
V(ZS)		ft/s	71197930593091+01	39616245434857+01
H(DOT1)	Altitude rate at entry	ft/s	-43905011318684+04	-44317205519357+04
TU	Time from 6/24/76 GMT to SI P	s	22771350000000+07	62039690000000+07
RA	Right ascension of landing site on 6/24/76	rad	.37979792980543+01	68548924619507+00
A(1F)	Pitch change at entry	rad	.14643526285480+00	14643526285480+00
TT(1A)	Time between 1st and 2nd deorbit burns	s	.00000000000000	00000000000000
V(SI)	Velocity to deploy stagnation temperature sensor	ft/s	36089238649591+04	.36089238649591+04
T(CP)	Thermal pulsing time limit	s	70000000000000+02	70000000000000+02
T(180)	Time for coast roll maneuver	s	.64550000000000+04	64670000000000+04
A(5)	Coordinate transformation from VL axes at SI P to VL axes after coast roll maneuver	-	-73323713887637+00	-49999973272647+00
		-	-64070943159820+00	-79511159741106+00
		-	.22771633992980+00	-34321588942269+00
		-	-67997302518712+00	-86602510056962+00
		-	69089792252642+00	45905788147787+00
		-	-24555397255747+00	19815604967524+00
		-	.11580432793257-11	.49970748025596-12
		-	-33489025800967+00	39621160513495+00
		-	-94225713851911+00	-91811586567765+00
		-		
t(C01)	Backup time for deorbit burn 1	s	1791.	1782
t(C02)	Backup time for deorbit burn 2	s	0.	0.
t(05G)	Backup time for 0.05-g event	s	11690.	11530
t(PROBE)	Backup time for 1.1 km/s event	s	11813.	11657
H(05G)	Altitude for re-initialization at 0.05-g event	ft	259635.	257666
MMTI	Time from Sol 0 midnight at landing site to separation	s	46341	23444

ORIGINAL PAGE IS
OF POOR QUALITY

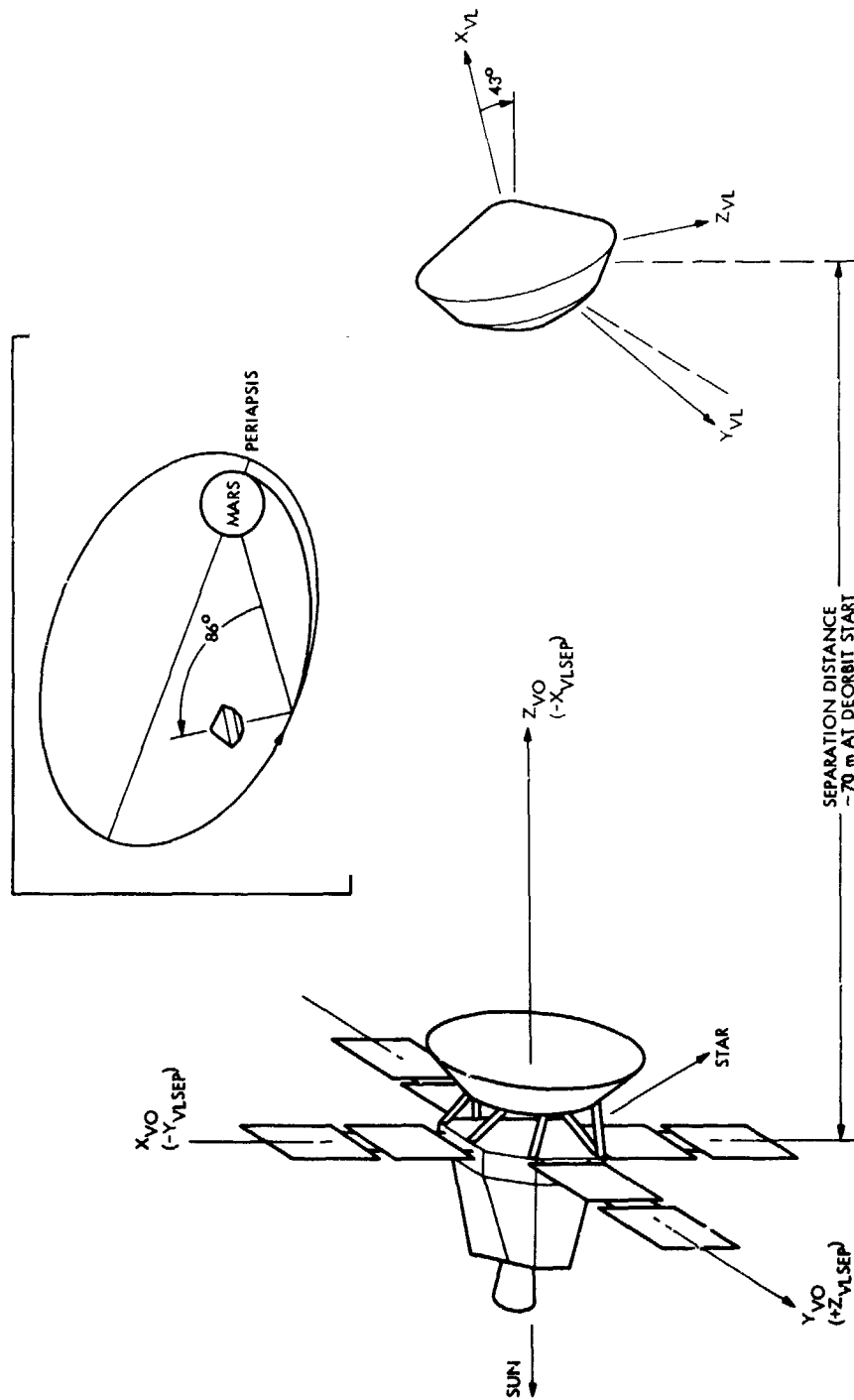


Fig. 21. VO-1/VL-1 relative geometry at deorbit

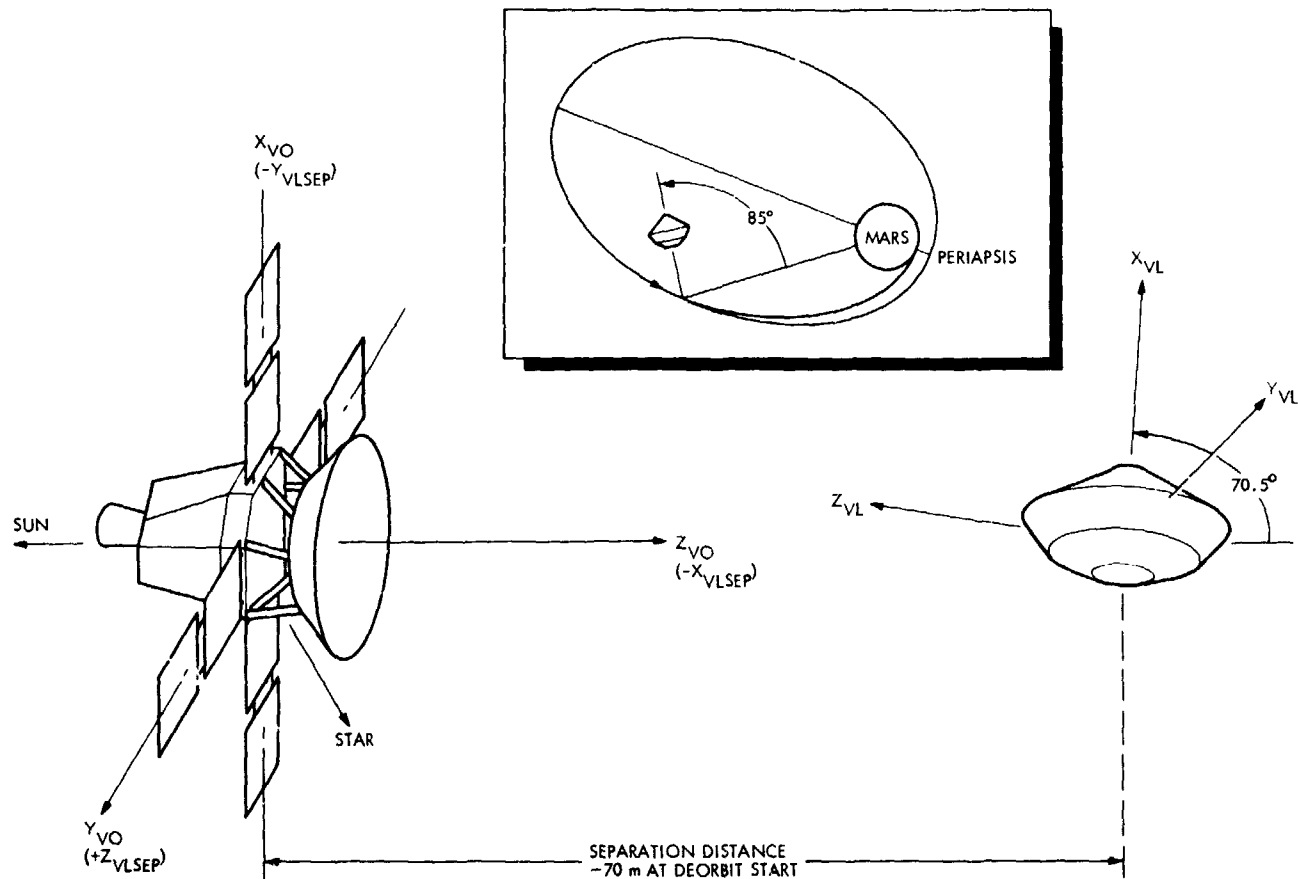


Fig. 22. VO-2/VL-2 relative geometry at deorbit

be initiated at E-9 min (command T(5)). The preentry phase for VL-2 was delayed until E-3 min in order to keep the Sun out of the RPA port while electron temperature measurements were being made. This required that the VL-2 attitude maneuver for preentry be initiated at E-6 min. The required VL attitude at the beginning of preentry was specified by matrix A(6). The VL began a slow pitch maneuver from this attitude in order to maintain the RPA port essentially parallel to the VL relative velocity vector until entry, i.e., until 800,000 ft above the areoid at touchdown. This pitch maneuver was a quadratic function of time (with respect to preentry start) defined by polynomial coefficients A(E1) and A(E2). The slow pitch was interrupted momentarily at entry by a step change in pitch (defined by A(1E)) to place the VL in the aerodynamically trimmed orientation. The slow pitch maneuver then maintained this trimmed orientation until aerodynamic moments took over at 0.05 g.

The parachute phase roll command $\phi(\text{CL})$ was designed to produce the required VL leg 1 azimuth at touchdown, which for VL-1 was 320 deg and for VL-2 was 210 deg.

The manual parameters presented in Table 5 will be discussed next. Deorbit burn cutoff backup time $t\text{CO1}$ was selected so that an overburn would still keep the VL from exceeding the steep entry angle constraint (-17.4 deg) of the entry corridor and not deplete propellant to such an extent that attitude control would be impossible during subsequent trajectory phases. For VL-1 the numerical value of $t\text{CO1}$ was obtained from $t\text{CO1} = 1757 + 6 + 28$ s, where 1757 s was the nominal cutoff, 6 s was the GCSC cutoff time error, and 28 s corresponded to an overburn which would change the entry flight path angle from the nominal -16.87 deg to the steep constraint of -17.4 deg. For VL-2 the overburn component of $t\text{CO1}$ was different: it was 19, not 28 s, since the VL-2 nominal entry flight path angle was -17.03 deg. Backup time $t\text{CO2}$ was set to 0, since the deorbit burn was a one-burn, not a two-burn.

The backup time $t(0.05 \text{ g})$ for the 0.05 g event was selected to ensure attitude stability in the worst-case entry situation. This worst-case entry situation would occur at a 3σ shallow entry in the min ρ atmosphere with 3σ low C_D and C_L , 3σ low

L/D, and 99% tailwind. For VL-1, $t(05\text{ g})$ was set at 177 s after entry; for VL-2, it was set at 173 s.

The backup time $t(\text{PROBE})$ for the 1.1 km/s event was selected to be greater than the worst-case situation producing the longest time interval between entry $T(7)$ and the 1.1 km/s event, yet soon enough to prevent interference with the parachute deployment event. The latest that the 1.1 km/s event could have occurred is 282 s after $T(7)$. This would occur for a 3σ shallow entry in the $\text{min}\rho$ atmosphere with 3σ low C_D and C_L , 3σ high L/D, and a 99% tailwind. The earliest that parachute deployment could occur is 337 s after $T(7)$. This would occur for a 3σ steep entry in the $\text{max}\rho$ atmosphere with 3σ high C_D , C_L , and L/D and a 99% headwind. Therefore a judicious selection of $t(\text{PROBE})$ for both VL-1 and VL-2 was $T(7) + 300$ s.

Parameter $H(05\text{ g})$, which was used to re-initialize the navigation computations for altitude at the 0.05-g event, was selected as the midpoint altitude between the extreme altitudes at which 0.05 g could occur in the entire set of atmosphere models. This approach minimized the maximum altitude error.

Parameter MMTI, the Mars mission time increment, was the time difference between SFP GMT and Sol 0 midnight GMT at the nominal landing site. For VL-1, SEP was commanded at 202/08:32:15 and Sol 0 midnight at the landing site was 201/19:39:54. For VL-2, SEP was commanded at 247/19:19:29 and Sol 0 midnight at the landing site was 247/12:48:45.

C. Descent Trajectory Dispersions

Trajectory dispersions were predicted for the nominal VL descent trajectory design in order to verify that the dispersed trajectory parameters would not violate constraints. The predicted entry and touchdown dispersions for the nominal VL-1 and VL-2 descent trajectory designs are summarized in Table 6.

Tables 7 and 8 present the constraints checklists for the final VL-1 and VL-2 descent designs, respectively. The rationale for the constraints themselves was presented earlier in Section II. Many of the minimum and/or maximum values appearing in this table were obtained by applying both the statistical and nonstatistical dispersions in Table 6 to the nominal VL descent parameters. The methods employed for obtaining the min/max values for parameters not appearing in Table 6 will be discussed next. The min/max values of the VL-Sun angle and the RPA/UAMS angle of attack were obtained by applying the maximum attitude limit cycle excursions expected during the appropriate descent trajectory phase. Required terminal descent propellant min/max values

were obtained by defining 3σ terminal descent ignition min/max velocity cases to produce min/max propellant consumption cases, respectively. The maximum ignition velocity case was defined by a 3σ shallow entry flight path angle, the $\text{min}\rho_s$ atmosphere, a 3σ high terrain height, a 99% tailwind, a 3σ high A/S L/D, and 3σ low A/S and parachute aerodynamic coefficients. The minimum ignition velocity case was defined by a 3σ steep entry flight path angle, the $\text{max}\rho_s$ atmosphere, a 3σ low terrain, no wind, nominal A/S L/D, and 3σ high A/S and parachute aerodynamic coefficients. The min/max values for terminal descent propellant remaining and the minimum planet-relative velocity at parachute release were obtained using methods described in the Navigation Plan (Ref. 1). Min/max leg 1 azimuths at touchdown were obtained by applying the maximum expected inertial roll hold attitude excursion during the parachute phase. And finally, the minimum postland relay link duration was obtained from Monte Carlo analyses conducted preflight.

D. Descent Relay Performance

The predicted nominal and adverse descent relay performances for VL-1 and VL-2 are shown in Figs. 23 and 24, respectively. The 1-W and 10-W mode phases of the descent trajectory are indicated in these figures. Note, however, that the 1- and 10-W modes were actually 1.7 and 10.26 W, respectively, for VL-1, and 1.4 and 9.68 W, respectively, for VL-2. The predicted performance assumed the reference star to be Canopus for VO-1 and Vega for VO-2. The predicted nominal and adverse initial postland link durations were 14.4 and 12.2 min, respectively, for VL-1, and 17.9 and 14.7 min, respectively, for VL-2.

V. Reconstructed VL Flight Path Summary

This section presents the CBE's of the VL descent trajectories. Detailed entry phase and atmosphere reconstruction is discussed in Sections VI and VII, respectively.

Table 9 summarizes the CBE's of pertinent VL-1 and VL-2 descent trajectory parameters from SEP to TD. The predicts in this table represent the best a priori predicts and so are not necessarily identical to the nominal descent trajectory designs. The reconstructed trajectory parameters in this table were actually the result of a 2-step process. The first step consisted of reconstructing the trajectory from entry to touchdown with LTARP, using the a priori entry state, the SATOD landing site fix, and entry phase IRU and measurement data. The second step consisted of reconstructing the separation-to-entry segment of the descent trajectory with the reconstruction mode of LTOP. This latter process employed a weighted least squares algorithm to process the CBE of the SEP state vector from SATOD and the entry state vector estimate generated by

Table 6. Predicted VL entry and touchdown dispersions

Parameter	VL-1			VL-2	
	3 σ statistical error	Nonstatistical atmosphere error	Nonstatistical ATBS error	3 σ statistical error	Nonstatistical atmosphere error
Fixed entry altitude errors					
V_I	0.628 m/s	NA	0.017	0.635 m/s	NA
γ_I	0.203 deg	NA	0.076	0.191 deg	NA
ψ_I	0.098 deg	NA	a	0.197 deg	NA
t	26.56 s	NA	3.57	29.55 sec	NA
LAT	0.307 deg	NA	a	0.299 deg	NA
LONG	0.309 deg	NA	a	0.343 deg	NA
Fixed entry time errors					
V_I	25.22 m/s	NA	a	28.35 m/s	NA
γ_I	0.849 deg	NA	a	0.969 deg	NA
ψ_I	0.342 deg	NA	a	1.126 deg	NA
h	35.55 km	NA	a	39.92 km	NA
LAT	1.107 deg	NA	a	1.533 deg	NA
LONG	1.576 deg	NA	a	1.897 deg	NA
Entry phase					
q_{max}	6.06 lb/ft ²	-23 → 6	-1.31	5.64 lb/ft ²	-23 → 6
q_{DEP}	0.51 lb/ft ²	-0.4 → 1.0	0	0.52 lb/ft ²	-0.4 → 1.0
M_{DEP}	0.042	-0.06 → 0.34	0	0.044	-0.06 → 0.34
Touchdown					
t	34.4 s	-15 → 40	6.8	35.4 s	-15 → 40
DR	70.0 km	±30	18.2	58.8 km	±12
XR	50.7 km	0	-0.3	37.6 km	0

^aNot significant.

Table 7. VL-1 descent constraints checklist

Parameter	Nominal value	Minimum/maximum value	Constraint
Inertial entry flight path angle	-16.89 deg	-17.09/-16.61	See Table 8
Inertial entry velocity	4.6105 km/s	NA/4.6112	See Table 8
Maximum dynamic pressure	112.6 lb/ft ²	NA/124.6	See Table 8
Deployment dynamic pressure	6.567 lb/ft ²	5.66/8.08	See Table 8
Deployment Mach number	1.014	NA/1.40	See Table 8
VL-Sun angle	137.2 deg	131.2/143.2	See Table 8
Coast time	3.082 h	NA/3.090	See Table 8
Terminal descent propellant required	152.0 lb	144/173	See Table 8
Terminal descent propellant remaining (per tank)	16.5 lb	6.5/23.9	See Table 8
Minimum planet-relative velocity at chute release	169 ft/s	115/NA	See Table 8
RPA/UAMS angle of attack at pre-entry	0.5 deg	NA/1.5	See Table 8
Leg 1 azimuth at touchdown	320. deg	310/330	$300 \leq A_z \leq 340$
Initial postland link duration	12.2 min	11.0/NA	See Table 8

Table 8. VL-2 descent constraints checklist

Parameter	Nominal value	Minimum/maximum value	Constraint
Inertial entry flight path angle	-17.03 deg	-17.23/-16.84	$-17.7 \leq \gamma_E \leq -15.9$
Inertial entry velocity	4.6135 km/s	NA/4.6141	$V_E \leq 4.625$
Maximum dynamic pressure	115.8 lb/ft ²	NA/127.4	$q_{max} \leq 144$
Deployment dynamic pressure	6.54 lb/ft ²	5.62/8.06	$5.0 \leq q_D \leq 8.6$
Deployment Mach number	1.041	NA/1.43	$M_D \leq 2.1$
VL-Sun angle	120. deg	114./126.	Sun angle ≥ 110
Coast time	3.038 h	NA/3.046	$t_c \leq 5.0$
Terminal descent propellant required	152. lb	144./173.	$W_T \leq 185.0$
Terminal descent propellant remaining (per tank)	16.5 lb	6.5/23.9	$W_R \leq 26.0$
Minimum planet-relative velocity at chute release	172.9 ft/s	118./NA	$V_R > 100$
RPA/UAMS angle of attack at pre entry	0.5 deg	NA/1.5	$\alpha \leq 20$
Leg 1 azimuth at touchdown	210. deg	200./220.	$190 < A_z < 230$
Initial postland link duration	14.7 min	12.5/NA	$\Delta t \geq 10.4$

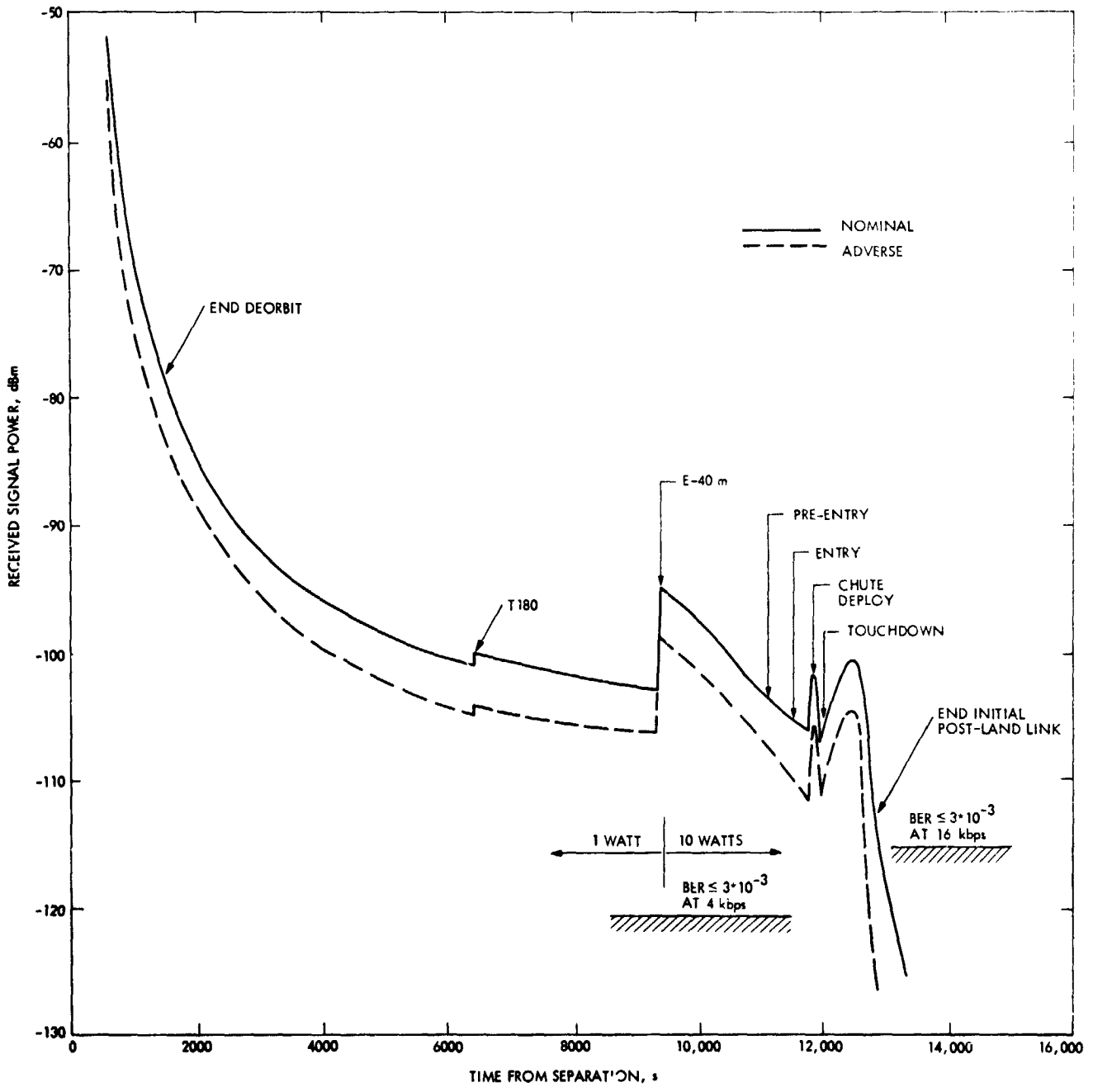


Fig. 23. Predicted VL-1 descent relay link performance

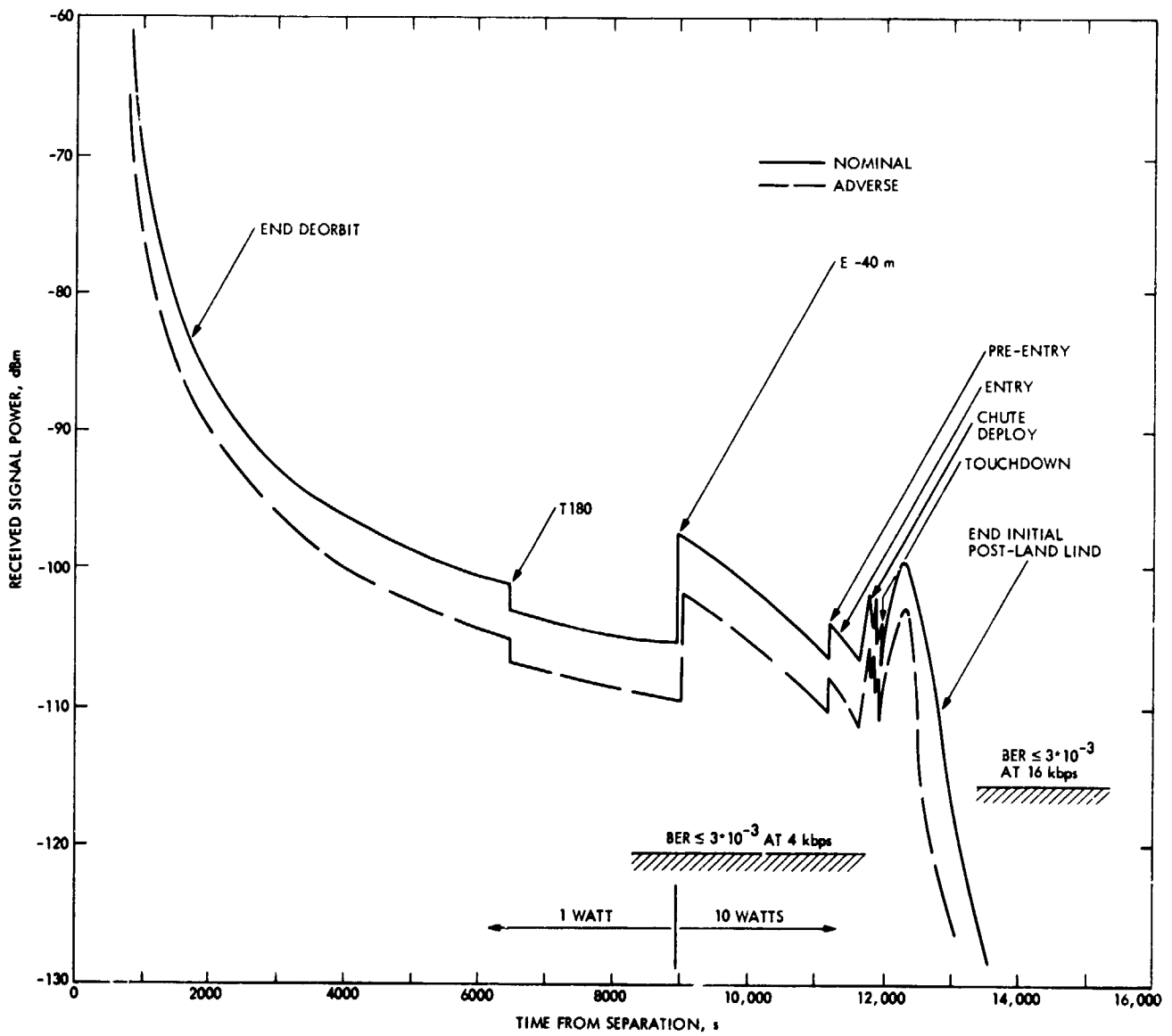


Fig. 24. Predicted VL-2 descent relay link performance

Table 9. Descent reconstruction summary

Parameter	VL-1			VL-2		
	Predict	Estimate	$\Delta(\sigma\text{-level})$	Predict	Estimate	$\Delta(\sigma\text{-level})$
Separation (MEQ SEP+0)						
X	15480.259 km	15480.340 km	0.08 km (.04)	12990.758 km	12990.932 km	0.17 km (.06)
Y	7617.091	7617.090	-0.001 (~0)	-4991.806	-4992.063	-0.26 (.15)
Z	-13234.228	-13234.296	0.068 (.07)	-16509.059	-16508.515	0.54 (.21)
\dot{X}	-1.160690 km/s	-1.160683 km/s	7.0E-6 (.11)	-.044430 km/s	-.044438 km/s	-8.E-6 km/s (~0)
\dot{Y}	0.410977	0.410977	~0 (~0)	.856233	.856244	1.10E-5 (.24)
\dot{Z}	0.572120	0.572117	-3.0E-6 (.02)	1.065381	1.065392	1.10E-5 (.14)
Deorbit						
ΔV	156.0 m/s	156.310 m/s	0.199% (1.26)	156.0 m/s	156.086 m/s	0.055% (.35)
CA	85.°914	86.°155	0.°241 (.84)	85.°106	85.°343	0.°237 (.82)
CLA	97.°384	97.°373	-0.°011 (.04)	91.°927	91.°765	-0.°162 (.56)
Coast						
i_{RPA} from T4 to T180	137.°5	127.°9/141.°9	9.°6	122.°1	114.°3/128.°2	7.°6
i_{RPA} from T180 to T5	129.°8	122.°5/135.°1	7.°3	114.°	109.0/120.2	6.°1
α_{VL} from E-6 ^m to E	-19.°5	-19.°9/-18.°9	0.°6	-19.°5	-19.7/-19.1	0.°4
α_{VL} from E to .05 g	-11.°1	-10.°9/-10.°4	0.°7	-11.°1	-11.2/-10.7	0.°4
i_{RPA} from E-6 ^m to E-0	110.°0 @ E-6 ^m 118.°6 @ E-0	109.°8/119.°5	NA	70.°0 @ E-3 ^m 74.°9 @ E-0	69.9/74.6	NA
Entry						
T7	11513.s	NA	NA	11357.s	NA	NA
V_I	4.61000 km/s	4.60989 km/s	-1.10E-4 (.01)	4.61430 km/s	4.61216	-2.14E-3 (.23)
γ_I	-16.°900	-16.995	-0.095 (.34)	-17.°005	-17.084	-0.079 (.25)
ψ_I	54.°173	54.145	-0.028 (.25)	44.°790	44.754	-0.036 (.10)
r	3635.57 km	3635.41	-0.16 (.01)	3626.96 km	3628.77	1.81 (.14)
LAT (areocentric)	12.°575	12.503	-0.072 (.20)	36.°586	36.476	-0.11 (.22)
LONG	62.°004W	62.151W	0.147 (.28)	243.°036W	243.131W	0.095W (.15)
Entry						
r	3635.57 km	NA	NA	3626.96 km	NA	NA
V_I	4.61000 km/s	4.60978	-2.2E-4 (1.05)	4.61430 km/s	4.6134	-9.0E-4 (4.25)*
γ_I	-16.°900	-16.999	-0.099 (1.46)	-17.°005	-17.042	-0.037 (.58)
ψ_I	54.°173	54.144	-0.029 (.89)	44.°790	44.802	0.012 (.18)
t	11513.0 s	11512.9	-0.1 (.01)	11357.0 s	11358.34	1.34 (.14)
LAT (areocentric)	12.°575	12.°498	-0.077 (.76)	36.°586	36.54	-0.05 (.46)
LONG	62.°004W	62.158W	0.154W (1.50)	243.°036W	243.049W	0.013W (.11)
Entry phase						
q_{max}	112.49 lb/ft ²	96.5	-15.99 (NA)	115.75 lb/ft ²	99.3	-16.45 (NA)
q_{deploy}	6.57 lb/ft ²	6.8	0.2 (NA)	6.536 lb/ft ²	6.3	-0.2 (NA)
$M\#_{deploy}$	1.014	1.1	0.1 (NA)	1.041	1.05	0.01 (NA)
Touchdown						
t	12035.6 s	12050.6	15.2 (NA)	11868.2 s	11900.9	32.7 (NA)
Terrain height	-2.3 km	-1.4	0.9 (0.9)	-1.7 km	-2.8	-1.1 (1.1)
LAT (areocentric)	22.°369	22.23	-0.14 (NA)	47.°596	47.646	0.050 (NA)
LONG	47.°535 W	47.°93W	0.40W (NA)	225.°845W	225.680W	-0.165W (NA)
Azimuth leg 1	320.°0	321.°6	1.6 (0.24)	210.°0	210.°1	0.1 (0.02)

* The entry state best estimates are the result of a backward integration of the final state near touchdown. The abnormally large fixed altitude velocity error is probably the result of small accumulated velocity errors obtained in the forward filtering process. All other indications are that the true velocity was much closer to the predict.

LTARP in the first step of this process to reconstruct the best separation-to-entry trajectory. In Table 9, Δ is defined as the difference between the reconstructed and predicted values, except for the coast phase, where Δ is defined as the maximum magnitude difference. Note that the estimates of the coast phase angles are given as the min/max values which were observed over the entire coast phase.

Table 10 compares the actual event-dependent VL sequence of events with the predicted SOE. All times are referenced to separation and are rounded to the nearest second.

Figures 25 and 26 depict the CBE's of the contributions of all error sources to the VL-1 and VL-2 landing site errors, respectively. The reconstructed error sources correspond to reconstructed entry state, atmosphere, winds, and aeroshell L/D characteristics. For VL-1, the dominant contributor to the landing site error was the deorbit execution error—more specifically, the deorbit ΔV magnitude error. The errors due to VL aerodynamics and winds were also important. Although the deorbit execution error was also important for VL-2, the dominant contributor to the VL-2 landing site error was the VL aerodynamics modeling error. A more detailed explanation of the VL aerodynamics modeling error can be found in Section VI, where the unusual observed trim angle of attack vs Mach number characteristics are discussed. The smaller contribution of the deorbit execution error to VL-2 was very likely due to the fact that the VL-2 axial accelerometer was of higher quality than the VL-1 axial accelerometer. During VL-2 pre-

**Table 10. Actual vs predict VL SOE
(all times in seconds from separation)**

Event	VL1		VL2	
	Predict	Actual	Predict	Actual
End of deorbit burn	1757.	1760.	1757.	11757.
Entry radius	11513.	11513	11357.	11358.
0.05 g	11665	11652.	11505	11495.
q_{max}	11713.	11707.	11553	11553
1.1 m/s	11761.	11760.	11600.	11606.
M/F	11933	11943.	11767	11792.
Terminal descent ignition (pyro fire)	11993	12005.	11826.	11856.
Constant velocity start	12029	12043	11861.	11893.
Touchdown	12036.	12051.	11868.	11901.

separation checkout the accelerometer bias stability data showed very little variability, unlike the relatively large variations which were observed during the VL-1 pre-separation checkout. Table 11 shows the landing error contributions due to each deorbit execution error. In the entry trajectory reconstruction process, the winds can only be estimated below about 25 km. For VL-1, analysis of the high-altitude attitude data indicated that the vehicle "cocked" slightly, producing a cross-range error. This cross-range error can be explained by an average wind of about 30 m/s from the east, which also corresponds to the estimated wind at 25 km altitude. This inferred

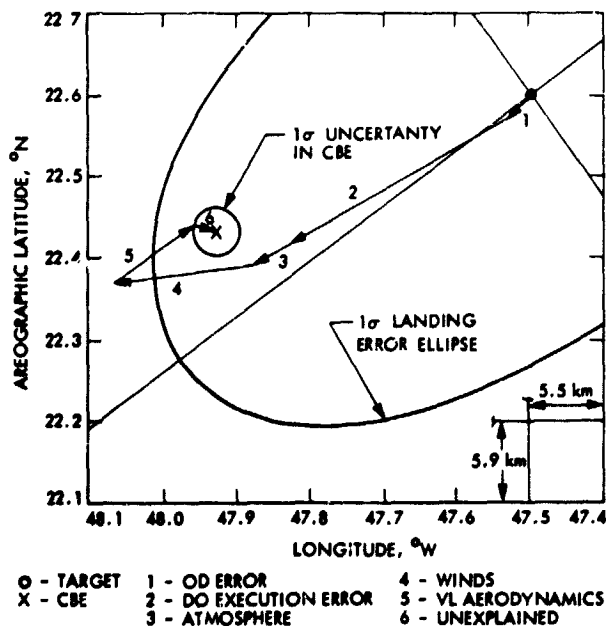


Fig. 25. VL-1 landing site error

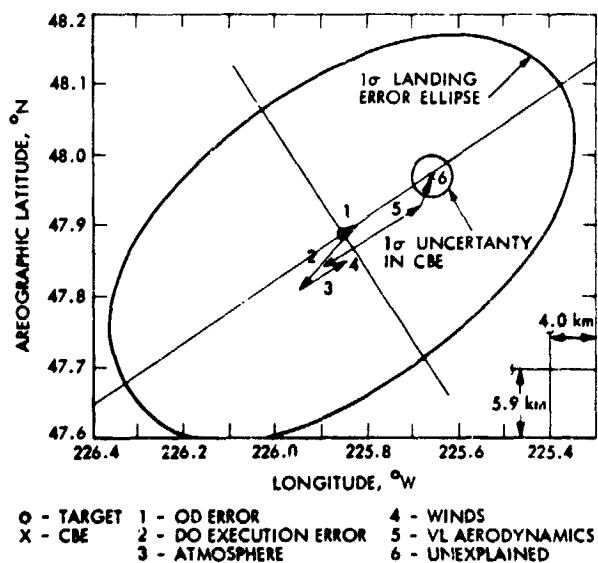


Fig. 26. VL-2 landing site error

Table 11. VL entry flight path angle and touchdown errors resulting from each deorbit control error

VL-1: Error due to				
	Δ magnitude error	In-plane pointing error	Out-of-plane pointing error	All deorbit control errors
γ_E error (fixed radius)	-0.070 deg	-0.009 deg	-0.001 deg	-0.080 deg
DR error at TD	-21.6 km	-2.1 km	-0.4 km	-24.1 km
XR error at TD	-0.59 km	-0.003 km	+0.12 km	-0.47 km
VL-2: Error due to				
γ_E error (fixed radius)	-0.019 deg	-0.007 deg	-0.008 deg	-0.034 deg
DR error at TD	-4.52 km	-0.85 km	-1.98 km	-7.35 km
XR error at TD	-0.02 km	-0.01 km	+1.47 km	+1.44 km

high-altitude wind has been included in the VL-1 wind contribution error. Two 1- σ dispersion ellipses are shown in Figs. 25 and 26. The large ellipse represents the a priori control dispersions which were predicted prior to separation. The small ellipse (a circle) represents the knowledge dispersions for the final estimate of the landing site from LTARP. It should be noted that the reconstructed trajectories which modeled the above reconstructed error sources also satisfied the observed VL entry sequence of events and q_{max} .

Plots of reconstructed and observed descent relay performance time histories are shown in Figs. 27 and 28 for VL-1 and VL-2, respectively. The reconstructed descent relay performance was computed using the best reconstructed descent trajectories and, in the case of mission 2, with an anomalous VO roll attitude of -22 deg off Vega, which was the final estimated attitude after stabilization.

VI. Entry Trajectory Reconstruction

This section documents the trajectory reconstruction results obtained by the Lander Flight Path Analysis Team following the landings of VL-1 and VL-2. Trajectory, atmosphere, and vehicle parameter estimates are presented, along with estimate uncertainties. In addition, characteristics of each reconstruction are discussed, with mention of difficulties encountered and resulting accuracy implications.

A. Description of Process

In order to facilitate understanding and correct interpretation of results, a brief description of the overall reconstruction process used is given, with pertinent details added in later sections as required.

Data used in the reconstruction were

- (1) Targeted entry state (position, velocity, and attitude) and covariance thereof.
- (2) Raw dynamic data file from DECSFT (tabulated gyro and accelerometer telemetry data, all properly scaled and time-tagged)
- (3) Measurement data file from DICST (tabulated RA, TDLR, pressure and temperature measurements, calibrated and time-tagged).
- (4) Post-touchdown measurements (ODP landed position fix, and pressure and temperature measurements from the meteorology experiment).

The dynamic data were preprocessed by the program PREPR, which (after data editing and filling any gaps present) yielded a file of smoothed time histories of angular velocity and acceleration for each vehicle axis. PREPR did nothing to the measurement data except to arrange the data into a file with time-sequencing corresponding to that of the dynamic data file (this could result in negligible time-tag shifts).

The actual reconstruction was done by the program LTARP. By means of a planetary model and the PREPR dynamic data file, LTARP propagated the targeted entry state forward in time in the manner of a strapped-down inertial navigator. In so doing, angular velocity data was integrated to keep track of vehicle attitude, and total acceleration (sensed from the PREPR dynamic data file plus computed gravitation) was integrated to provide velocity and position time-histories. At selected time points corrections were applied to the state thus computed by processing with a Kalman-Schmidt filter RA and TDLR measurements from the PREPR measurement data

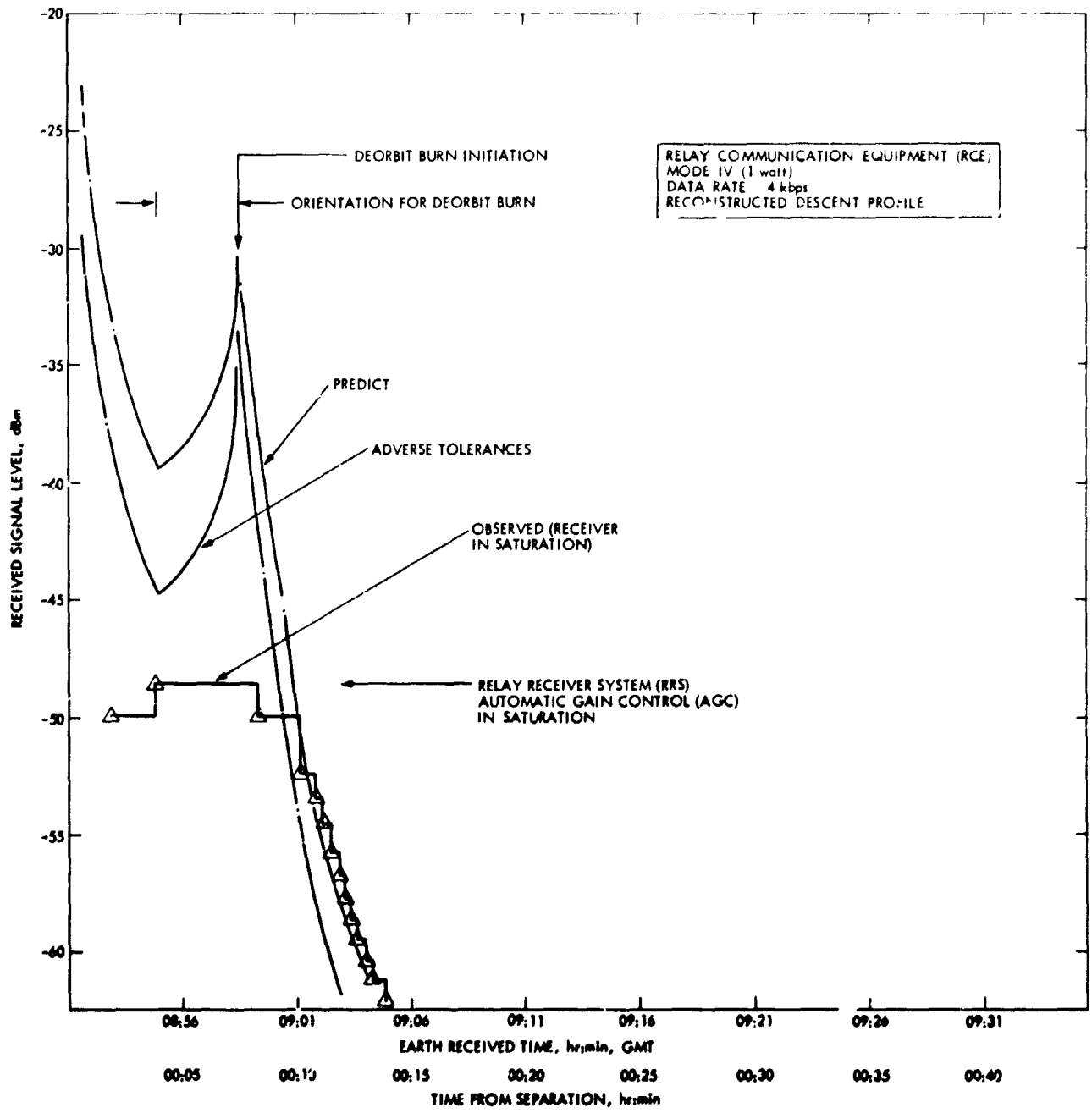


Fig. 27. Reconstructed and observed VL-1 descent relay performance

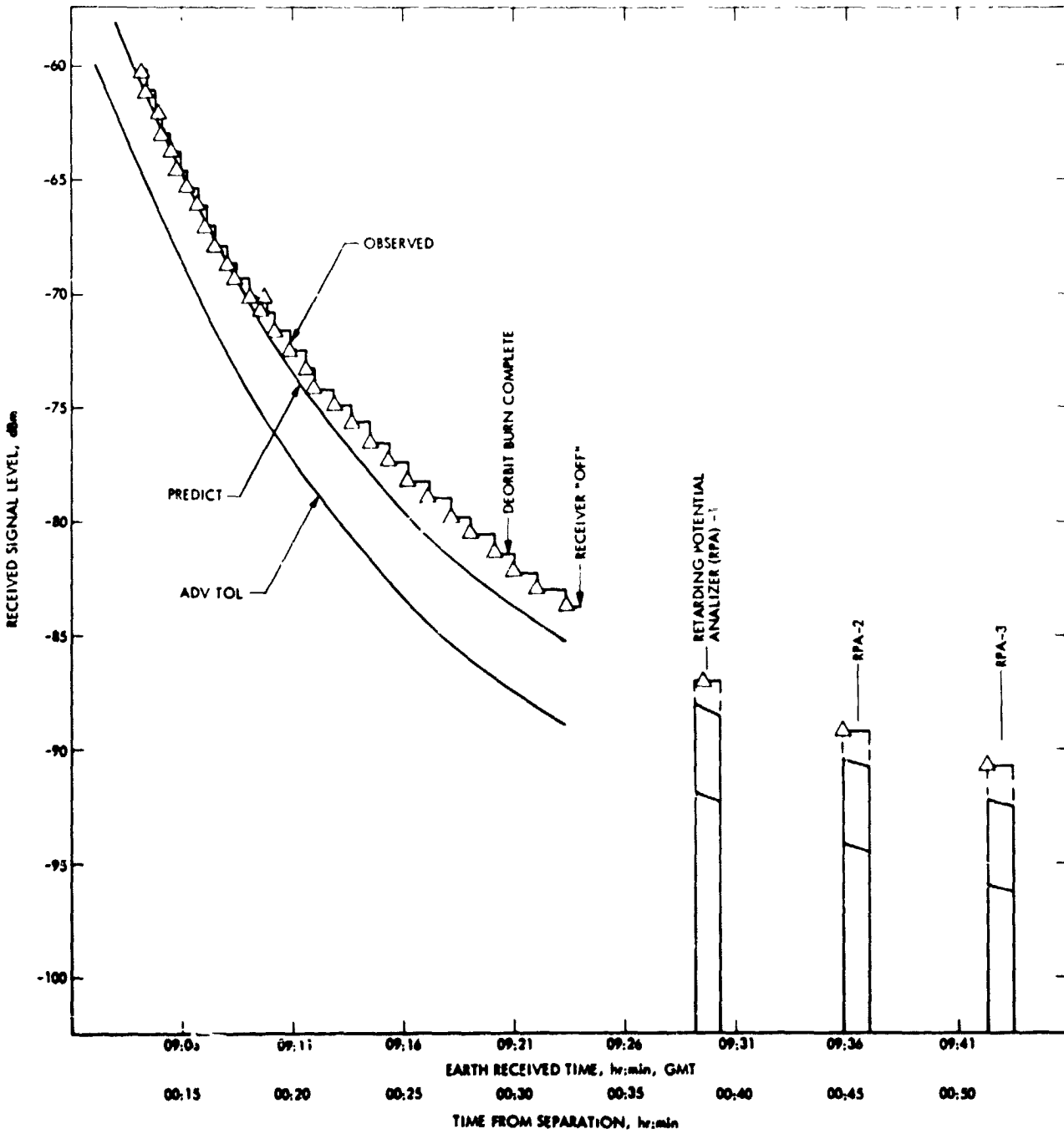


Fig. 27 (contd)

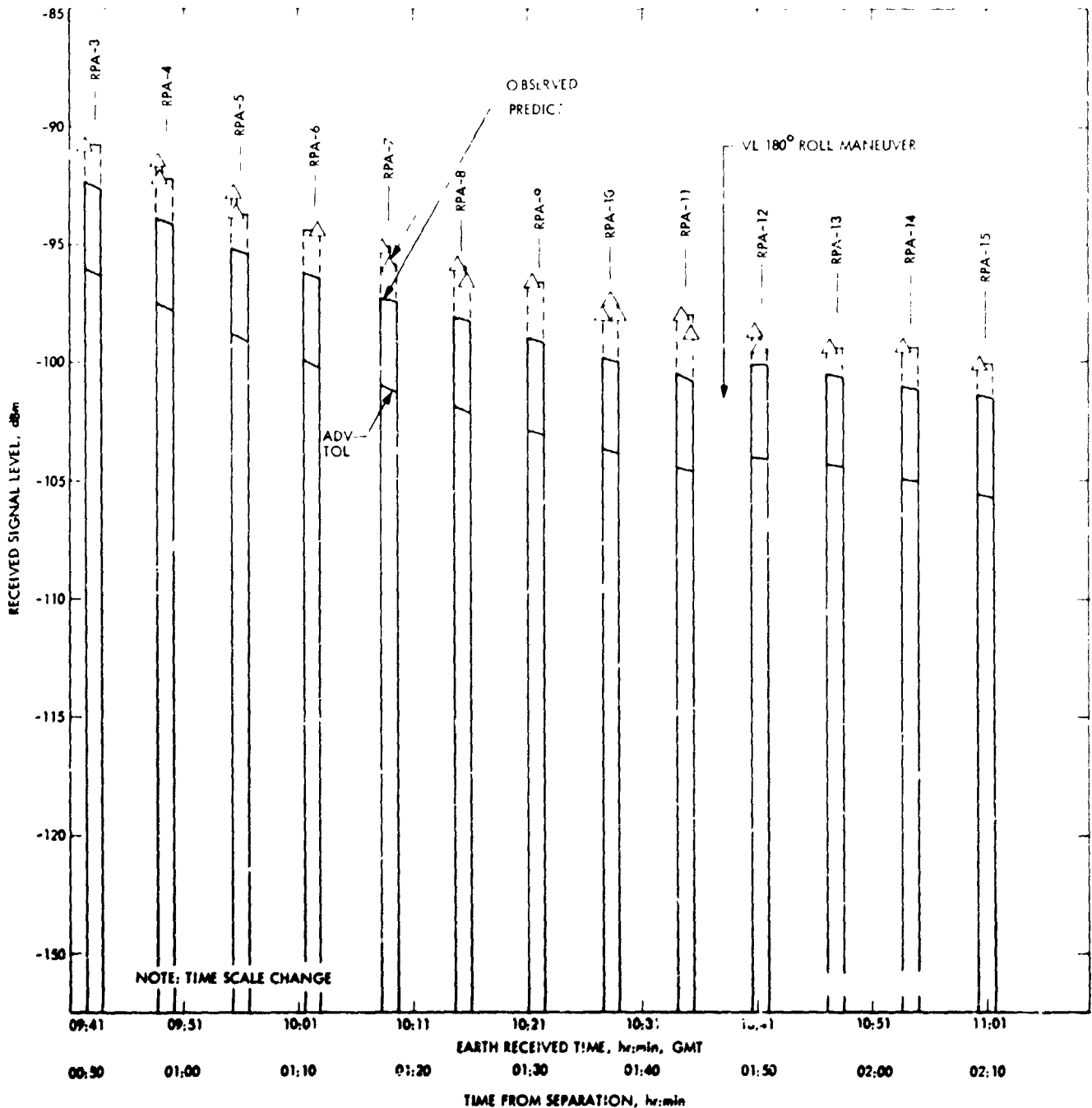


Fig. 27 (contd)

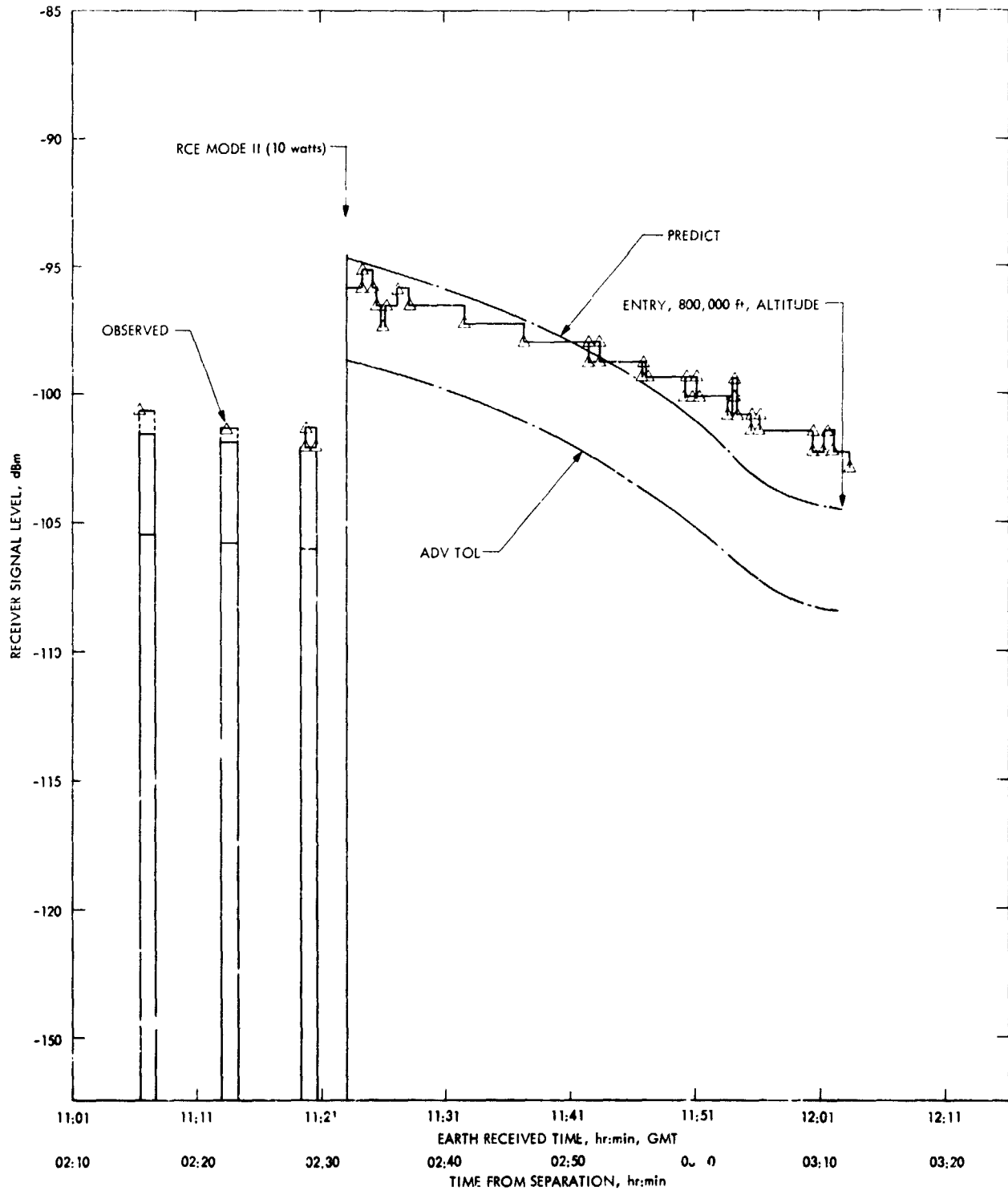


Fig. 27 (contd)

ORIGINAL PAGE IS
OF POOR QUALITY

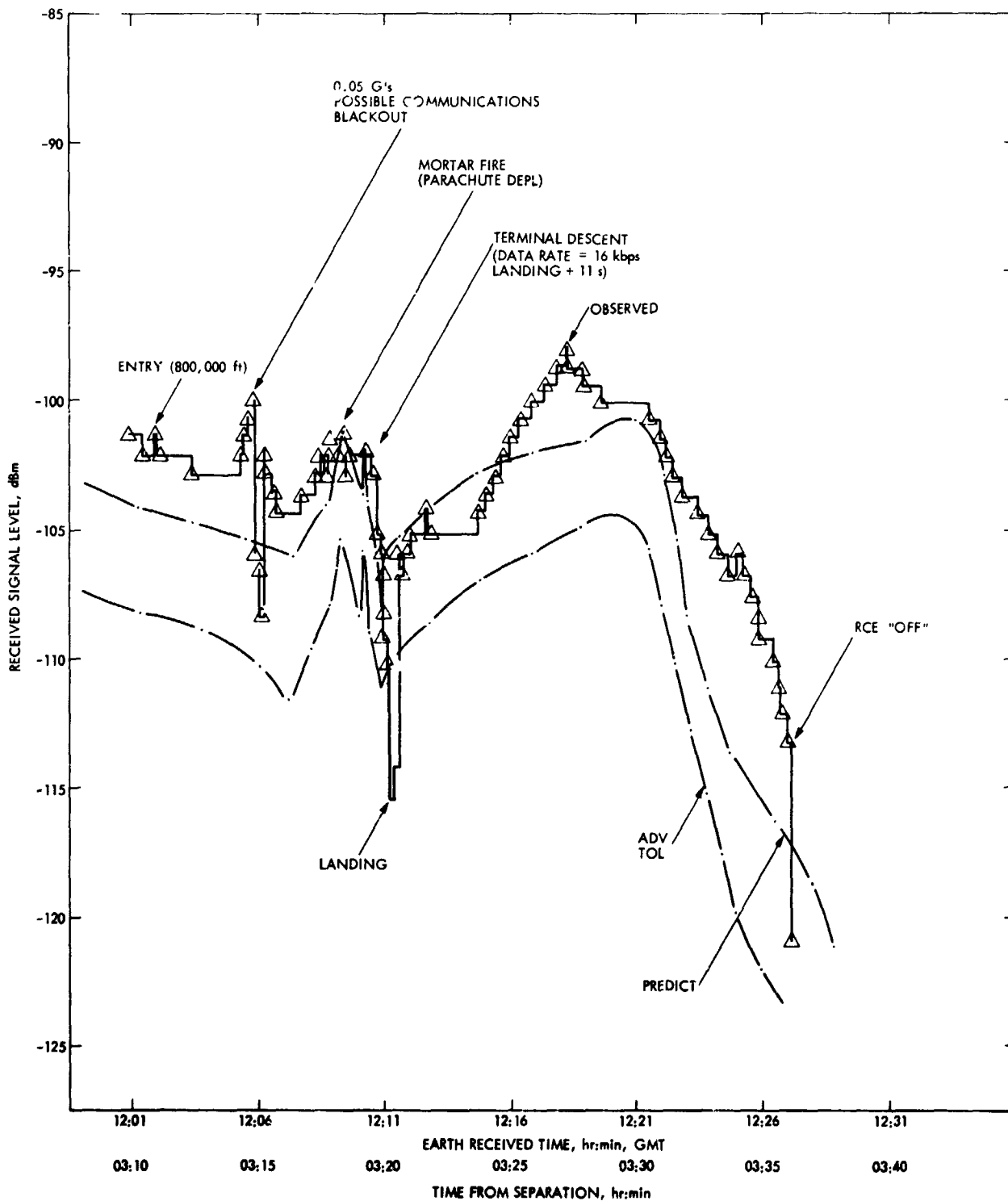


Fig. 27 (contd)

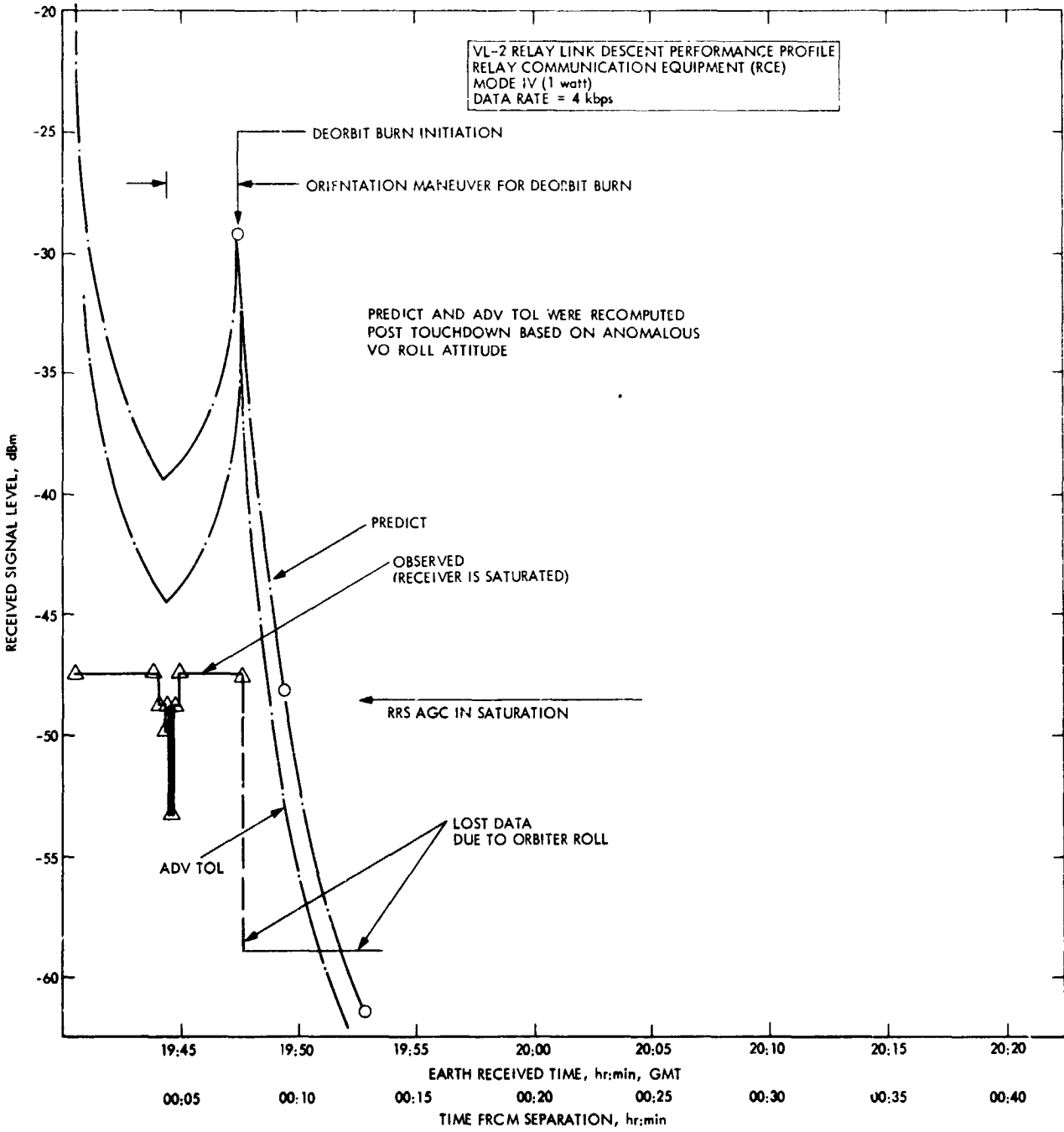


Fig. 28. Reconstructed and observed VL-2 descent relay performance

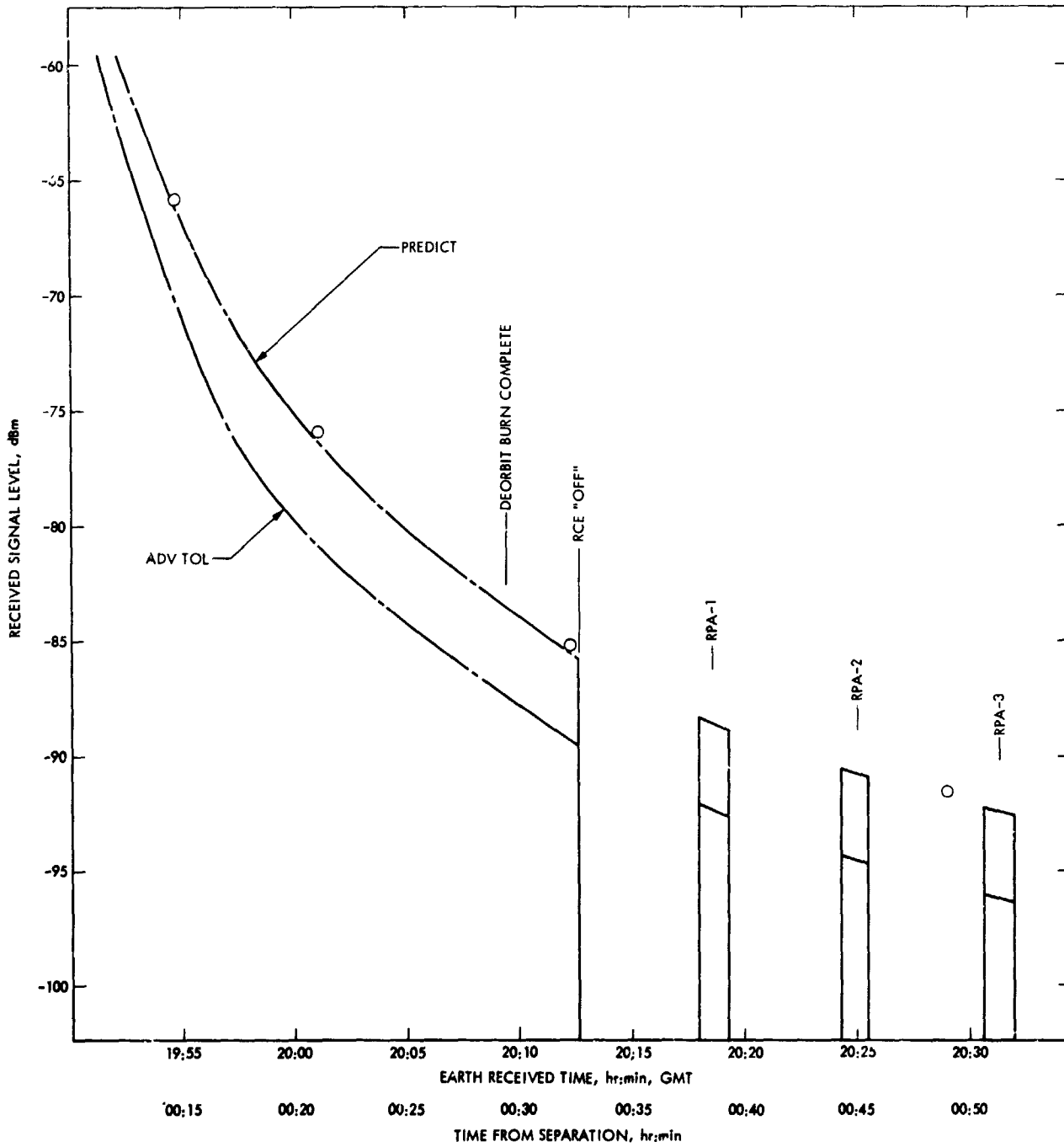


Fig. 28 (contd)

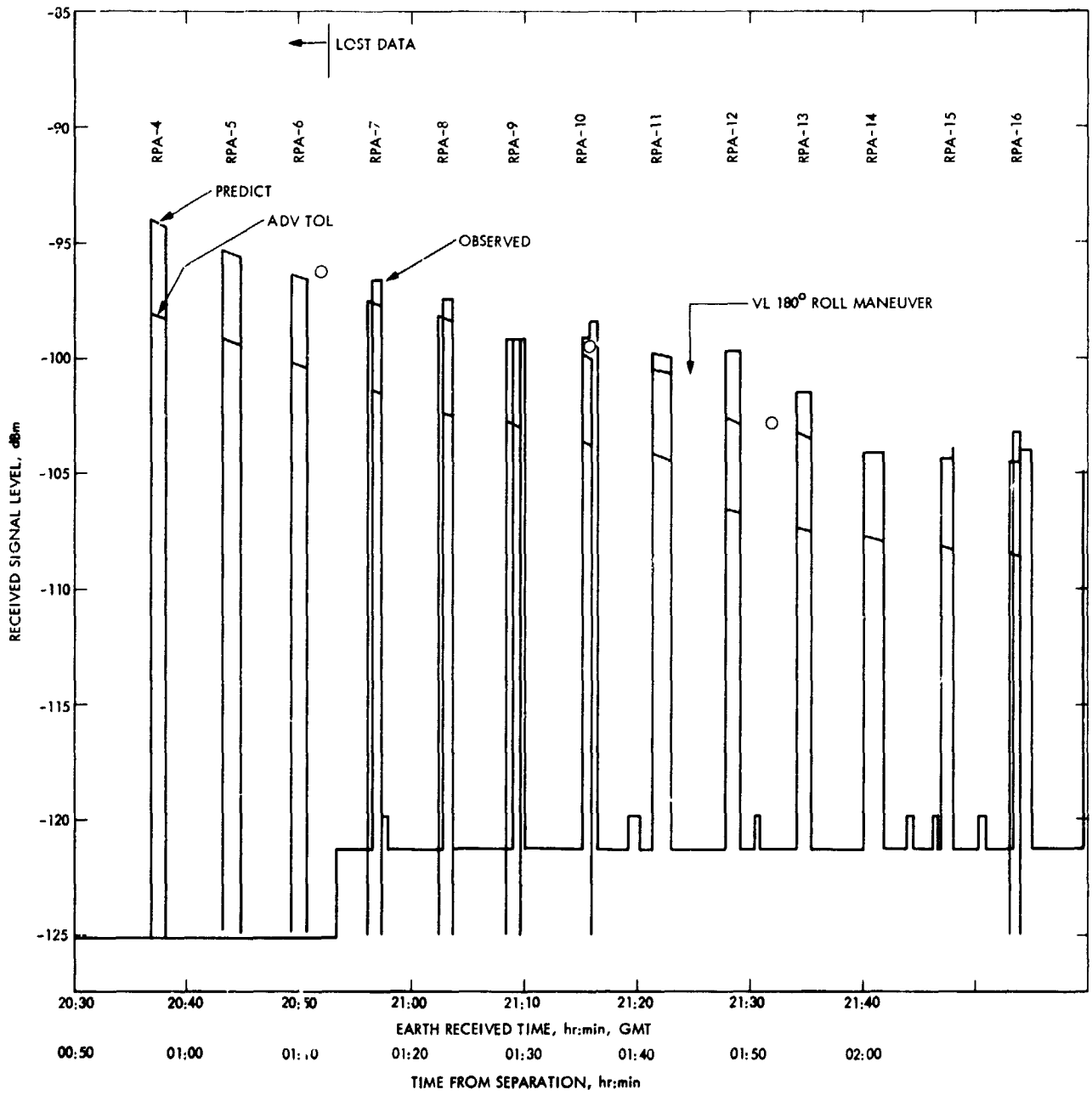


Fig. 28 (contd)

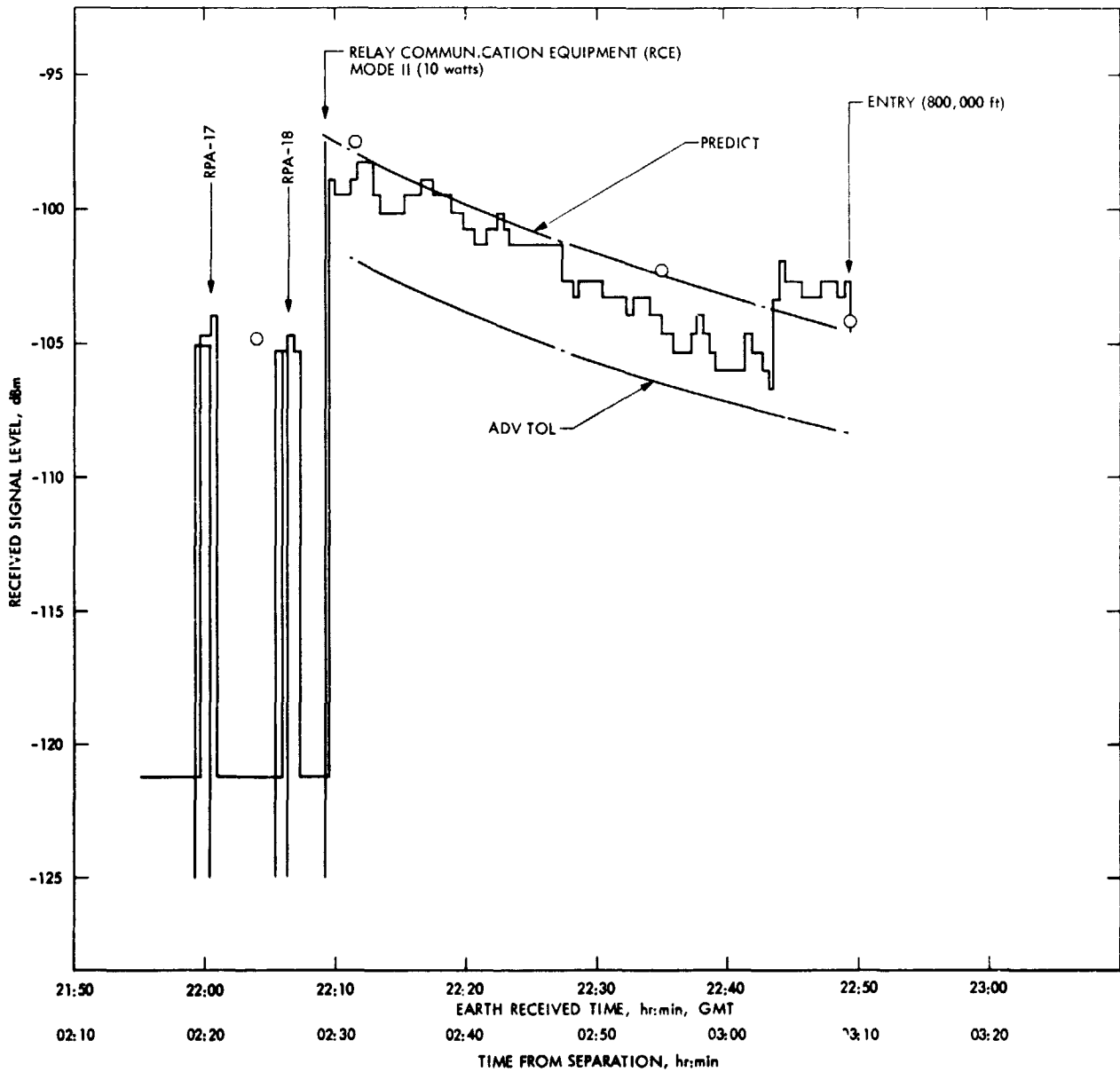


Fig. 28 (contd)

ORIGINAL PAGE IS
OF POOR QUALITY

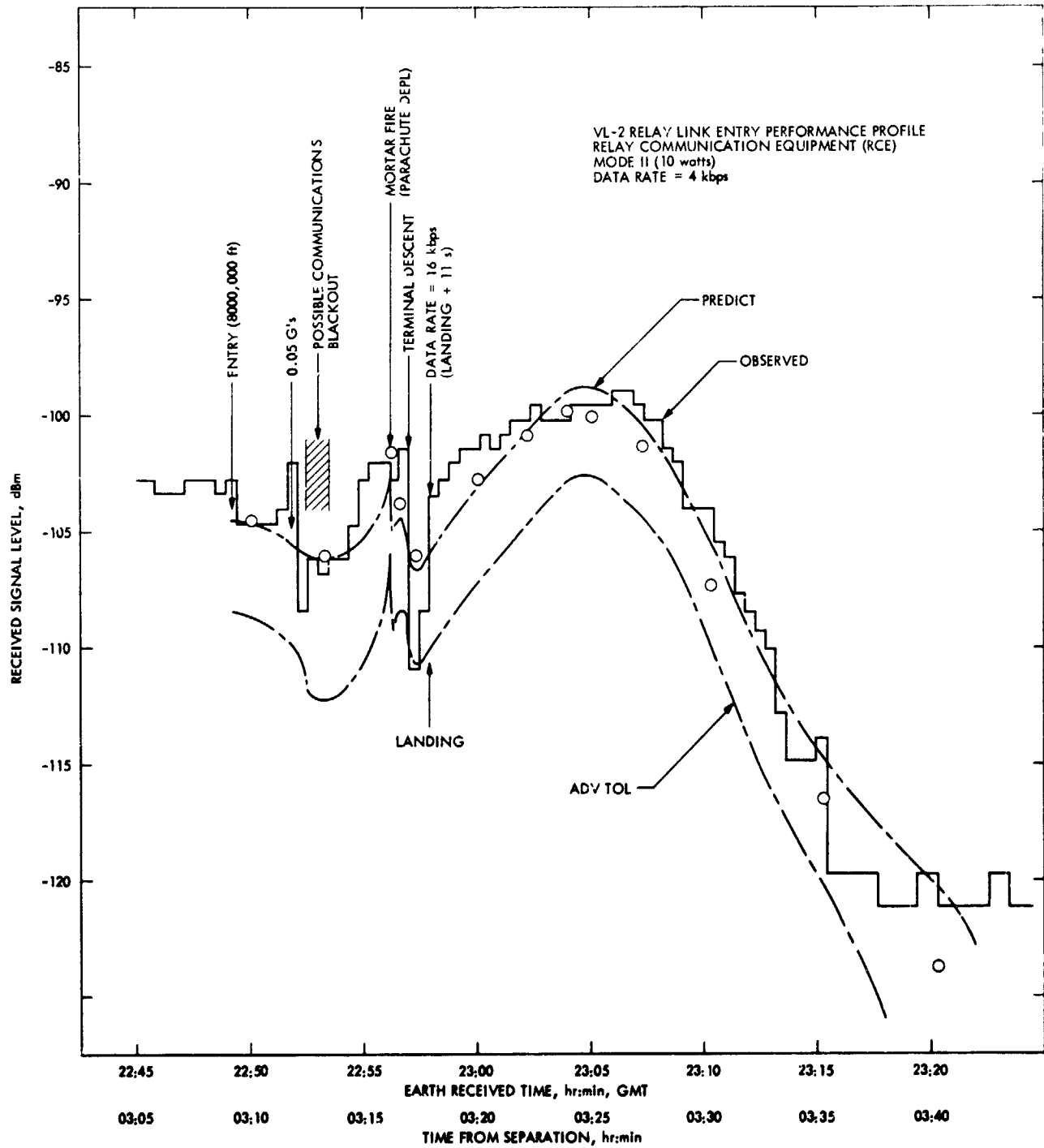


Fig. 28 (contd)

file. After similarly processing the position fix slightly before touchdown, the resulting final state was integrated back to entry to provide a continuous reconstructed trajectory.

This trajectory was then "frozen," and the atmosphere reconstructed thereon. Working from entry to touchdown, LTARP computed dynamic pressure from sensed acceleration, using a priori aerodynamic data. Density was computed from dynamic pressure, based on the velocity history from the frozen trajectory (modified by wind estimates). Pressure was computed by integration of density with respect to altitude in the hydrostatic equation. Temperature was then computed from density and pressure by means of the equation of state. Wind estimates were based on a comparison of a priori aerodynamic trim predictions with those computed for the frozen trajectory on a no-wind basis. Pressure and temperature measurements from the PREPR measurement data file were processed by the Kalman-Schmidt filter at selected times to provide atmospheric corrections. Finally, a continuous reconstructed atmosphere was obtained by means of a deterministic run of the frozen trajectory, incorporating a wind vs altitude table and other parameter estimates from previous filtering runs.

B. Data

The primary data used for the initialization of the reconstruction process is presented in this section. The a priori entry state and covariance for each mission are shown in Table 12. Also shown is the transformation from the MEQ coordinate system to the a priori direction of the body axes at entry. The a priori uncertainty in body attitude was 1 deg (1σ) in pitch, yaw, and roll. The uncertainties in system parameters are documented in the Navigation Plan.

The IRU data contained in the entry telemetry was converted to engineering units using the scale factors shown in Table 13. Known biases (determined in pre-separation check-out) were removed from the data and are also shown in Table 13. These biases were also used by the onboard software during each descent.

A radar altimeter scale factor of .9965 was applied to the decalibrated TM values to correct for terrain effects on signal return time. A bias of about 17 m was identified during instrument calibrations, but was not used in the reconstruction because of its variation with altitude and insignificance compared with terrain uncertainty.

Values of model parameters critical to the reconstruction are presented in Table 14. 1σ uncertainties are given where significant.

Owing to software modeling limitations, the (fourth-order) reference areoid was modeled as a spheroid with polar and equatorial radii shown in Table 14. This surface matched the radius of the reference areoid exactly at the targeted landing site and was very close in the general area of each site. The data contained in this report is with respect to this spheroidal surface. For statistical purposes it was regarded as an altitude reference with zero uncertainty. ODP landed position fixes together with 1σ uncertainties are presented in Table 15.

Nominal terrain height profiles were deduced for both landers from available contour maps and input to LTARP by means of tables. Plots of these profiles are included in Figs. 29 and 30. The 1σ uncertainty of each profile was regarded as ± 1 km.

Aerodynamic tables were constructed from data in Ref. 2, with 1σ uncertainties as follows.

Aeroshell phase axial force coefficient vs Mach number and total angle of attack, $\pm 1.7\%$.

Aeroshell phase trim angle of attack vs Mach number (for nominal CG offset of 1.83 in.), ± 0.5 deg.

Parachute phase drag coefficient vs Mach number, $\pm 4\%$.

C. Entry Trajectory Reconstruction Results

The VL-1 and VL-2 reconstructed trajectory variables are recorded at various times of interest in Tables 16 and 17, along with uncertainties in the estimates, Tables 18 and 19. These variables are plotted in Figs. 31 to 47 for VL-1 and Figs. 48 to 65 for VL-2, with significant events noted, and design limits included where applicable. Comparisons of estimates with predicted values were given earlier in Table 9.

1. Discussion of results. Were it not for a data gap problem, which will be discussed, both the VL-1 and VL-2 trajectory reconstructions would have been simple and straightforward, using LTARP and the procedures developed therefor (Ref. 3). Much of the development work leading to LTARP was aimed at providing the ability to cope with large (e.g., 3σ) entry dispersions, but for both vehicles the entry dispersions were about 1σ or less. The fear of a large radar blackout region and a resulting loss of reconstruction accuracy led to studies and development of special procedures, but both landers obtained near-continuous radar altimeter measurements below 130 km altitude. Similarly, the TLLR data was almost continuous where scheduled and of excellent quality. A great worry had been the anticipated poor quality of the dynamic data, and much work went into PREPR to provide the capability to edit out numerous wild points and to fill gaps in the raw data prior to smoothing. Surprisingly, the data was of

Table 12. A priori entry state and covariance

Entry state (MIO)						
Parameter			VL-1	VL-2		
GCSC time, s			11513.	11357		
\dot{X} , km/s			-1.00835	-4.08531		
\dot{Y} , km/s			-3.90904	-1.29505		
\dot{Z} , km/s			2.22757	1.71021		
X, km			-2633.44	1272.62		
Y, km			2375.78	2619.54		
Z, km			793.41	2161.78		
Hour angle of Mars prime meridian, rad			3.48898	5.36033		
Covariance \dot{X} , \dot{Y} , \dot{Z} , X, Y, Z (units of entry state)						
VL-1						
.454628E-3						
-399004E-3	.355271E-3					
-130670E-3	.118580E-3	.46862E-4				
-205089	.177043	.058938	95.656			
-748189	.660641	.216765	335.290	1235.277		
.423299	-.377960	-.134959	-190.734	-700.423	413.903	
VL-2						
.131407E-3						
.269558E-3	.580284E-3					
.227811E-3	.475459E-3	.402963E-3				
.472355	1.007282	.633365	1754.266			
.148690	.301740	.257541	530.109	169.071		
-.205232	-.428525	-.365593	-753.121	-232.558	333.894	
Attitude transformation, MEQ to body axes (at prepitch program initiation)						
VL-1						
	.095223		-.933758		.345006	
	-.538920		-.339754		-.770800	
	.836957		-.112*33		-.535573	
VL-2						
	-.851931		-.511782		.110874	
	-.482538		.684999		-.545833	
	.203399		-.518513		-.830526	

Table 13. Instrument bias and scale factors

Parameter	VL-1	VL-2
X-gyro bias, rad/s	-3.1282E-4	-9.353E-5
Y-gyro bias	-2.7633E-4	-1.9730E-4
Z-gyro bias	-4.340E-5	-2.5360E-4
X-gyro scale factor, deg/pulse	8.00422E-4	7.96527E-4
Y-gyro scale factor, deg/pulse	7.90358E-4	7.84698E-4
Z-gyro scale factor, deg/pulse	7.92614E-4	7.93027E-4
X-accelerometer bias, km/s ²	-1.0894E-5	-2.0129E-5
Y-accelerometer bias, km/s ²	1.1067E-5	-6.745E-6
Z-accelerometer bias, km/s ²	7.478E-6	1.0167E-5
X-accelerometer scale factor, km/s/pulse	1.27219E-5	1.27754E-5
Y-accelerometer scale factor, km/s/pulse	3.18267E-6	3.14868E-6
Z-accelerometer scale factor, km/s/pulse	3.18009E-6	3.19154E-6

Instrument bias added to the decalibrated TM value; scale factors applied to TM pulse counts by DECSFT.

Table 14. Model parameters and uncertainties

Parameter	Value	1 σ uncertainty
Mars gravitation constant μ	428284431.5 km ³ /s ²	
Harmonic J_2	.001965	
Mars rotation rate	7088219E-4 rad/s	
Universal gas constant	.00831434 km ² /K mol s ²	
Ratio of specific heats γ	1.38 ^a	1
Molecular weight of lower atmosphere	43.3 ^a	.1
Radius of reference spheroid		
	VL-1	VL-2
Equatorial radius, km	3393.470	3394.114
Polar radius, km	3375.654	3376.294
Lander mass		
Entry mass, kg	982.93	981.63
Mass after aeroshell drop, kg	789.25	787.95

^aRegarded as constant below 100 km.

Table 15. ODP landed position fixes, 1 σ uncertainties

Parameter	VL-1	VL-2
Radius, km	3389.4 \pm .13	3381.35 \pm 1.
Latitude (areocentric), deg	22.23 \pm .01	47.67 \pm .05
Longitude (west), deg	47.93 \pm .014	225.67 \pm .05

The numerical values in this Table differ from those in Table 10 of the *Satellite Orbit Determination* chapter because the above entries are with respect to the preflight (i.e., Mariner 9) Mars pole, whereas the other entries are with respect to the inflight "solved-for" pole.

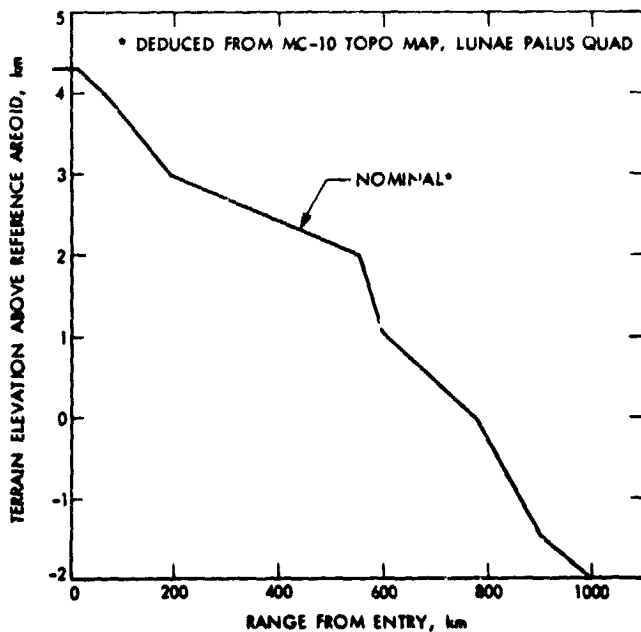


Fig. 29. VL-1 nominal terrain height profile

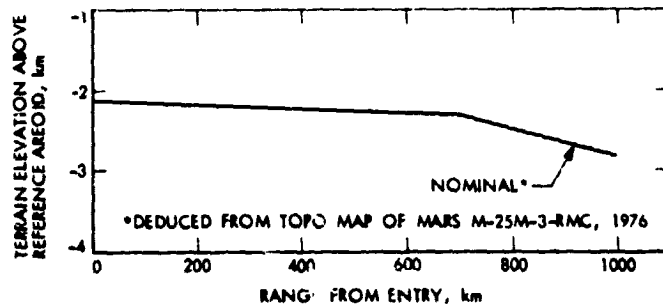


Fig. 30. VL-2 nominal terrain height profile

Table 16. Viking trajectory / atmosphere reconstruction summary: Viking 1 reconstruction

Variable	Entry	0.05 g	Max q	1.1 km/s	Mortar fire	Verner ignition	Touchdown
GCSC time, s	11513	11652	11707	11760	11943	12005	12050.8
V_R , km/s	4.4177	4.5388	3.2139	1.1032	0.2327	0.0532	0.0027
γ_R , deg	-17.758	-12.995	-7.962	-0.429	-53.392	-69.758	-
λ_R , deg	52.138	54.784	56.080	56.343	55.547	-34.151	-
Altitude above MSL, km	242.8	78.3	32.2	25.8	4.3	-0.09	-1.5
Latitude, deg	12.503	18.286	20.447	21.376	22.208	22.224	22.228
W longitude, deg	62.151	54.072	50.747	49.260	47.932	47.928	47.931
σ_R , deg	0.60	0.003	-0.31	-0.48	-0.60	-3.06	-
β_R , deg	0.09	0.12	-0.36	-0.52	-0.19	9.75	-
α_R , deg	-18.81	-11.19	-11.64	-12.49	-8.85	-13.40	-
Pressure, mb	-	.74E-3	.28	.54	4.42	7.20	7.62
Density, gm/cc	-	30E-8	.87E-6	.16E-5	.111E-4	.159E-4	.165E-4
Temperature, K	-	140.	165.	177.	214.	234.	241.
Mach no.	-	>20.	15.4	5.1	1.1	.21	-
Dynamic pressure, lb/ft ²	-	.6	96.5	22.0	6.8	.4	-
Range, km	0	574.1	799.6	898.5	986.5	988.1	988.4

Date: 9-5-76

Time: 250/00:25:00.

Data sources: PREPFXA00220, PREPFXA20277.

PREPR files ENTRYD1G, ENTRYD2G; LTARP runs JTFB50, JTFB56.

Table 17. Viking trajectory / atmosphere reconstruction summary: Viking 2 reconstruction

Variable	Entry	0.05 g	Max q	1.1 km/s	Mortar fire	Vernier ignition	Touchdown
GCSC time, s	11357	11495	11553	11606	11791.8	11756	11900.87
V_R , km/s	4.4756	4.595	3.148	1.1	.237	.9510	.0030
γ_R , deg	-17.6221	-12.949	-7.443	-.043	-50.80	-80.3	-
λ_R , deg	42.7813	49.597	53.027	54.641	55.28	120.2	-
Altitude above MSI., km	240.99	77.69	29.80	24.71	3.12	-1.23	-2.8
Latitude, deg	36.476	43.258	45.791	46.758	47.638	47.647	47.646
W longitude, deg	243.131	233.944	229.507	227.597	225.715	225.683	225.680
σ_R , deg	-.262	-.719	-.886	-.728	1.32	ϕ : -15.15	-51.61
β_R , deg	.132	-.121	-.059	.084	-2.53	ψ : -135.01	-89.01
α_R , deg	-19.262	-11.115	-12.088	-12.985	-9.15	θ : -87.34	-98.33
Pressure, mb	-	.00069	.30	.54	4.65	7.09	7.78
Density, gm/cc	-	27E-8	.95E-6	.156E-5	.11E-4	.16E-4	.178E-4
Temperature, K	-	126.	166.	179.	205.	229.	229.
Mach no.	-	>20	15.1	5.1	1.05	.20	-
Dynamic pressure, lb/ft ²	-	.65	99.3	20.3	6.3	.42	-
Range, km	0.	578.	817.	914.	1005.	1006.8	1007.0

Date: 9-22-76.

Time: 266/20:40.

Data sources: V75CDBB, PPFVL2LA3, PREPFXB00220.

A/S phase axial force coefficient ~ 0.7% > nominal.

Parachute phase drag coefficient ~ 7% > nominal.

Hypersonic α_{trim} variable, averaging -12.5 deg.

PREPR files: ED1VL2C, ED1VL2D, ED2VL2P; LTARP runs: FWHJ20, 22, 27, 28, 34

Table 18. Viking trajectory / atmosphere reconstruction summary: VL-1, 1 σ uncertainties in estimates

Variable	Entry	0.05 g	Max q	1.1 km/s	Mortar fire	Vernier ignition	Touchdown
GCSC time, s	11513	11652	11707	11760	11943	12005	12050.8
V_R , km/s	.001	.0008	.0007	.0006	.0002	.0002	.0002
γ_R , deg	.031	.020	.017	.017	.056	.36	4.5
λ_R , deg	.051	.038	.036	.093	.50	1.7	23.6
Altitude above MSL, km	.9	.44	.26	.22	.21	.2	.2
Latitude, deg	.069	.040	.033	.032	.032	.032	.032
W longitude, deg	.073	.043	.036	.035	.033	.035	.035
σ_R , deg	.41	.25	.20	.20	.41	ϕ : 1.4	3.8
β_R , deg	.054	.042	.039	.050	.29	ψ : 1.3	3.9
α_R , deg	.032	.020	.017	.017	.022	θ : .19	.19
Pressure, %		2.2	2.3	2.7	2.4	1.	.7
Density, %		2.3	2.6	3.7	2.7	1.7	.8
Temperature, %		2.7	2.2	4.	1.8	1.3	.5
Mach no., %			4	4.	3.	3.	
Dynamic pressure, %		2.	2.	2.	2.	4.	
Range, km	0.	.07	.1	.12	.2	.25	.27

Table 19. Viking trajectory / atmosphere reconstruction summary: VL-2, 1 σ uncertainties in estimates

Variable	Entry	0.05 g	Max q	1.1 km/s	Mortar fire	Vernier ignition	Touchdown
GCSC time, s	11357	11495	11553	11606	11791.8	11856	11900.87
V_R , km/s	.0011	.0011	.001	.001	.0003	.0002	.0002
γ_R , deg	.031	.020	.017	.017	.056	.36	4.5
λ_R , deg	.051	.038	.036	.093	.5	1.7	23.6
Altitude above MSL, km	1.	.83	.6	.5	.5	.5	.5
Latitude, deg	.069	.040	.033	.032	.032	.032	.032
W longitude, deg	.073	.043	.036	.035	.035	.035	.035
σ_R , deg	.41	.25	.20	.20	.41	ϕ : 1.4	3.8
β_R , deg	.054	.042	.039	.050	.29	ψ : 1.3	3.9
α_R , deg	.032	.020	.017	.017	.022	θ : .19	.19
Pressure, %	-	2.2	2.3	2.7	2.4	1.	.7
Density, %	-	2.3	2.6	3.7	2.7	1.7	.8
Temperature, %	-	2.7	2.2	4.	1.8	1.3	.5
Mach no., %	-	-	4.	4.	3.	3.	
Dynamic pressure, %	-	2.	2.	2.	2.	4.	
Range, km	0.	.07	.1	.12	.2	.25	.27

ORIGINAL PAGE IS
OF POOR QUALITY

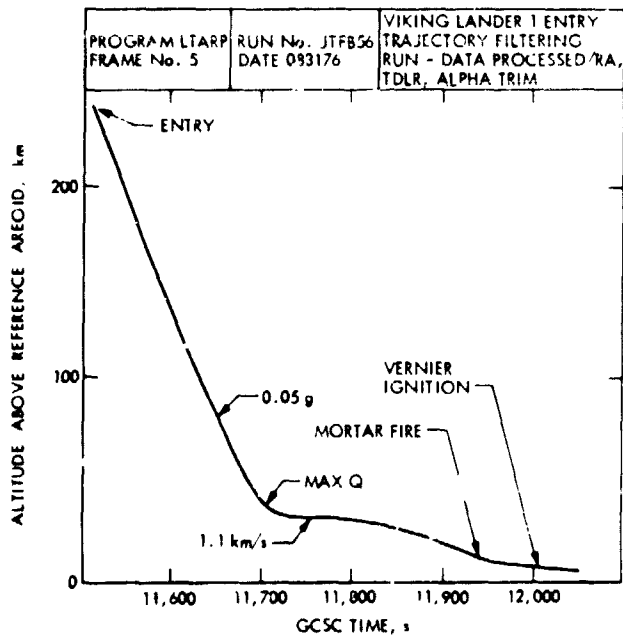


Fig. 31. VL-1 altitude above reference areoid vs time

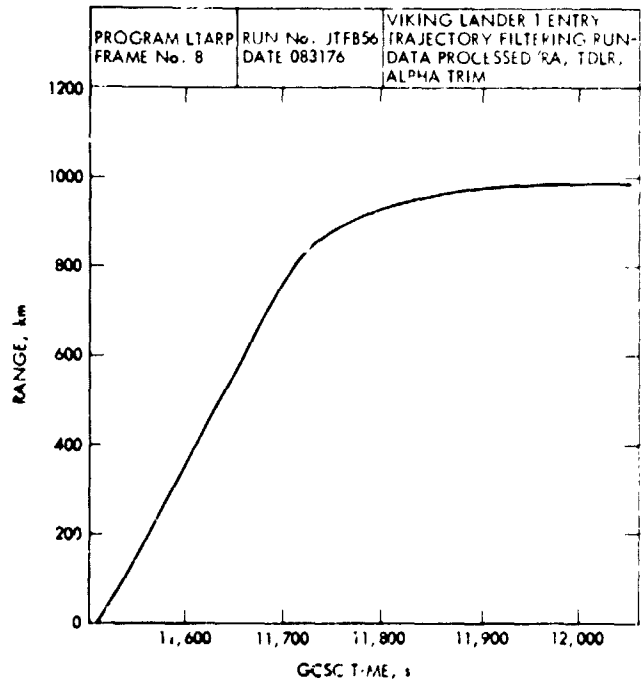


Fig. 33. VL-1 range from entry vs time

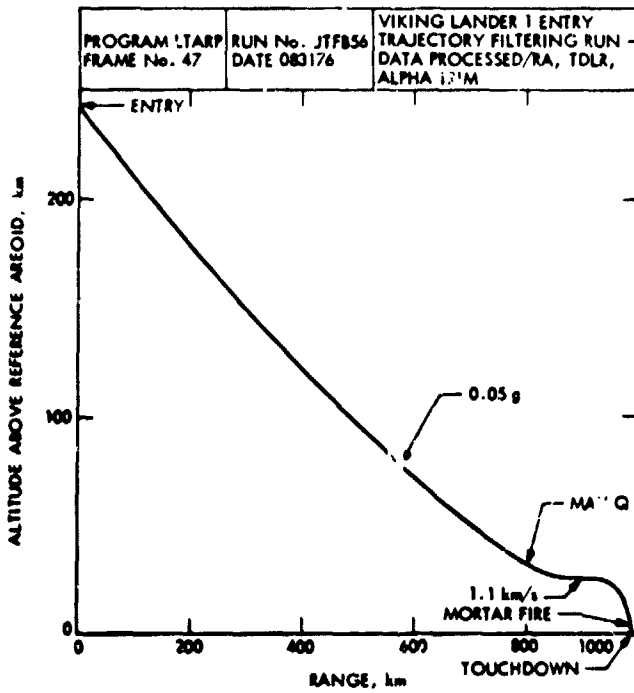


Fig. 32. VL-1 altitude above reference areoid vs range

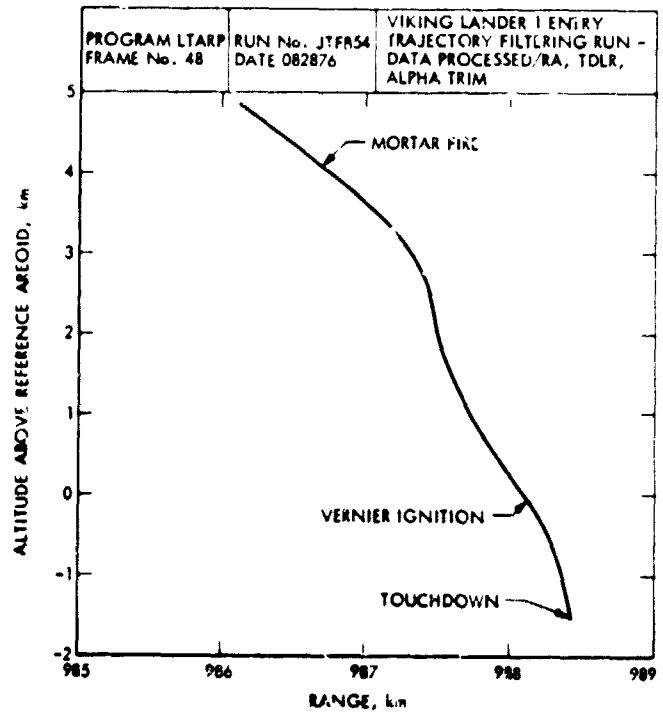


Fig. 34. VL-1 altitude above reference areoid vs range

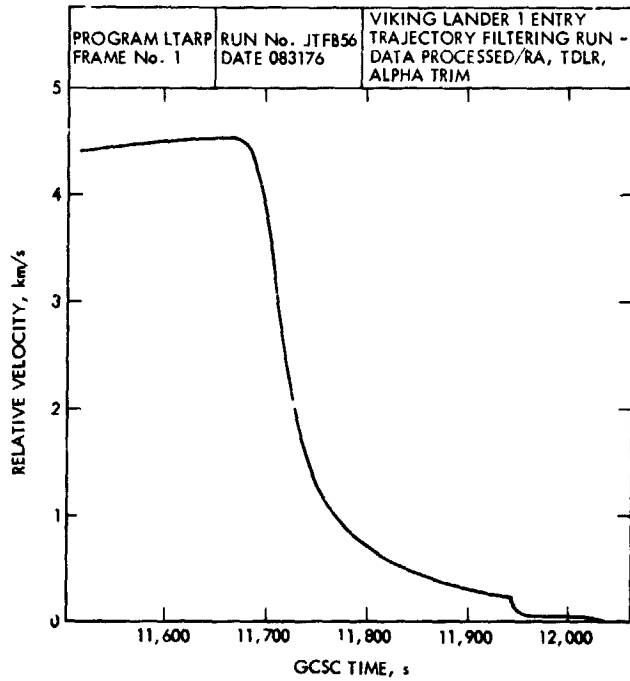


Fig. 35. VL-1 relative velocity vs time

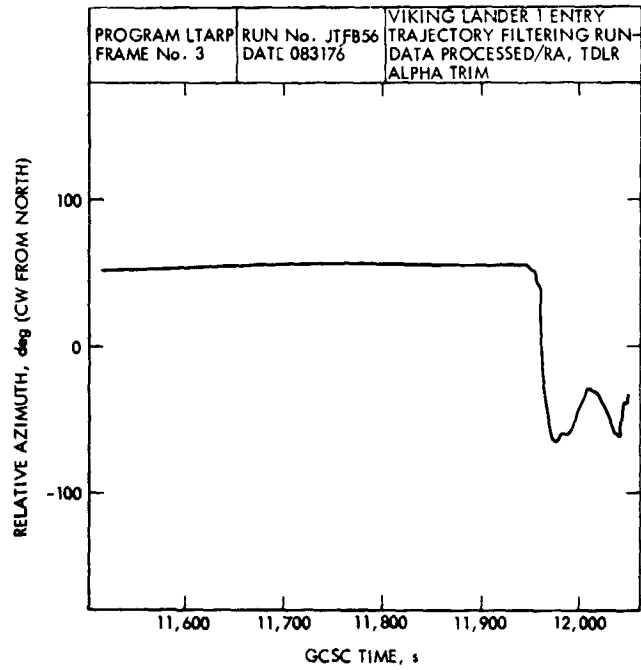


Fig. 37. VL-1 relative azimuth vs time

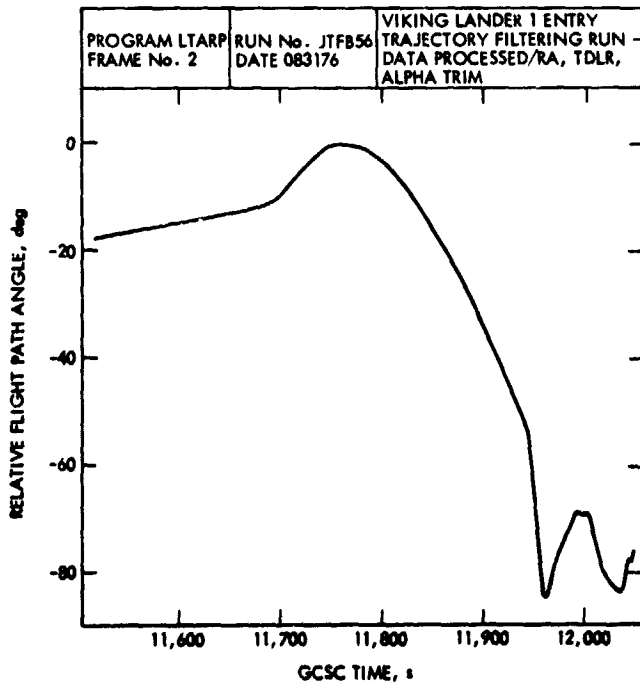


Fig. 36. VL-1 relative flight path angle vs time

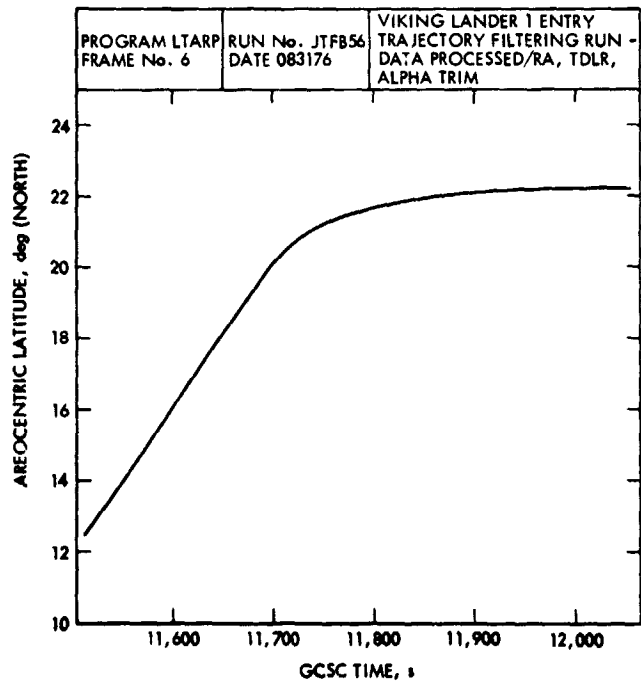


Fig. 38. VL-1 areocentric latitude vs time

CH

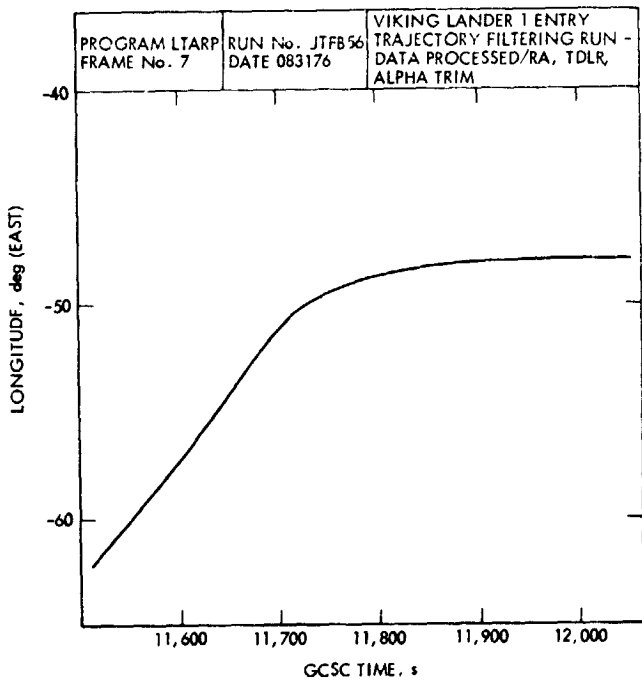


Fig. 39. VL-1 longitude vs time

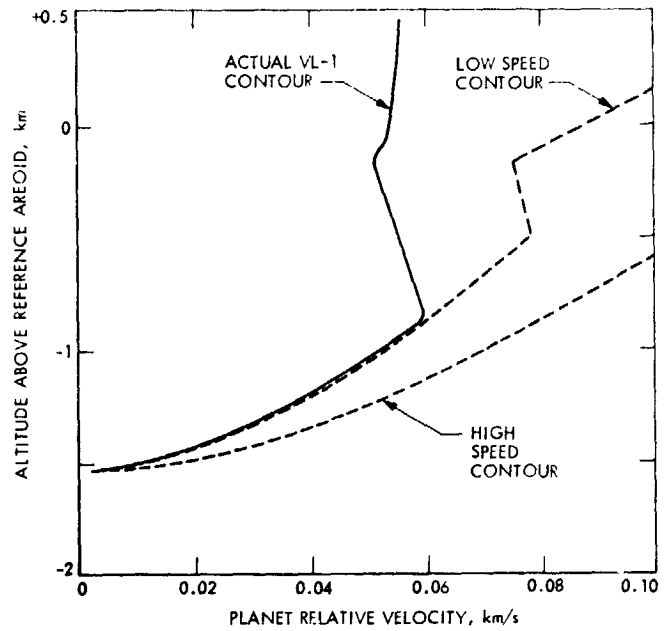


Fig. 41. VL-1 terminal descent performance

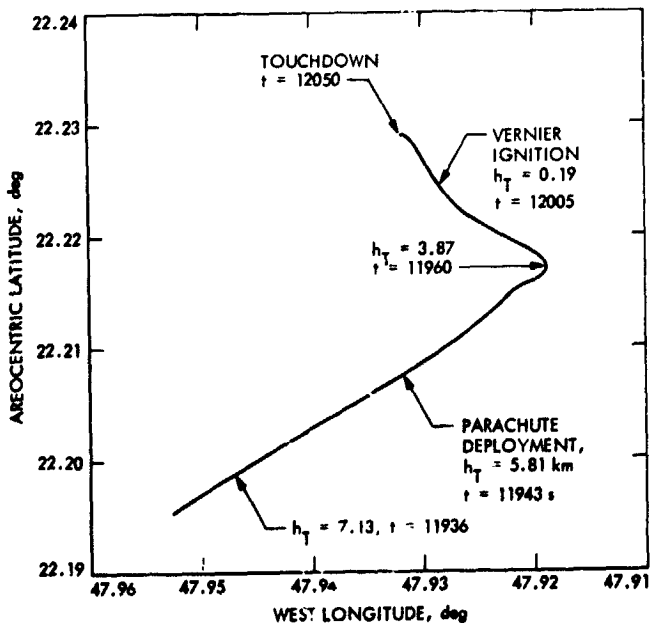


Fig. 40. VL-1 ground trace near touchdown

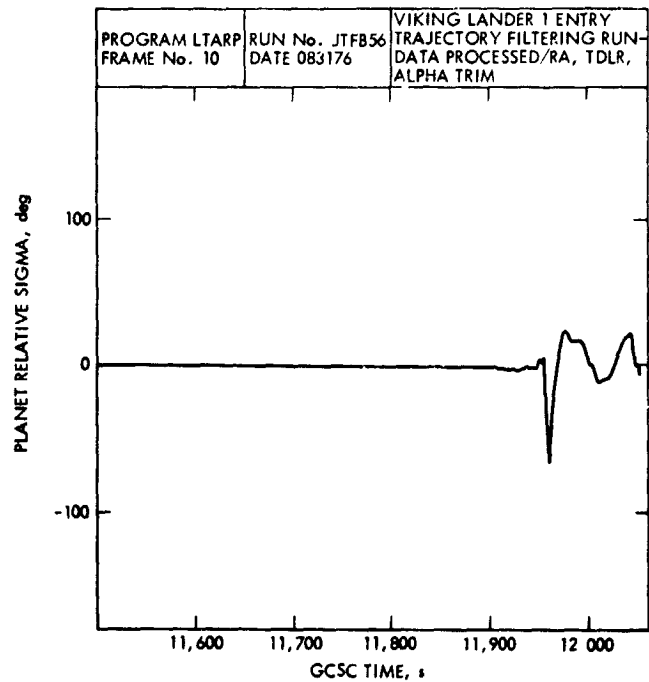


Fig. 42. VL-1 planet relative sigma vs time

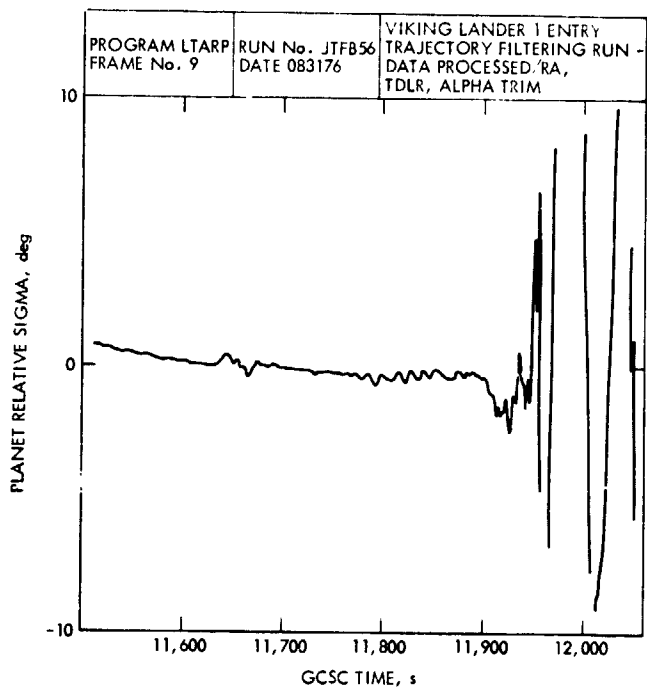


Fig. 43. VL-1 planet relative sigma vs time (detail)

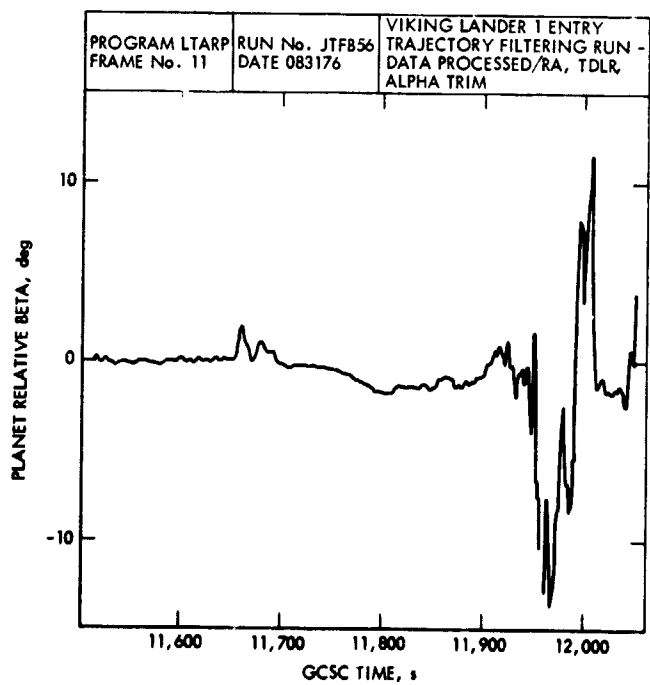


Fig. 44. VL-1 planet relative beta vs time

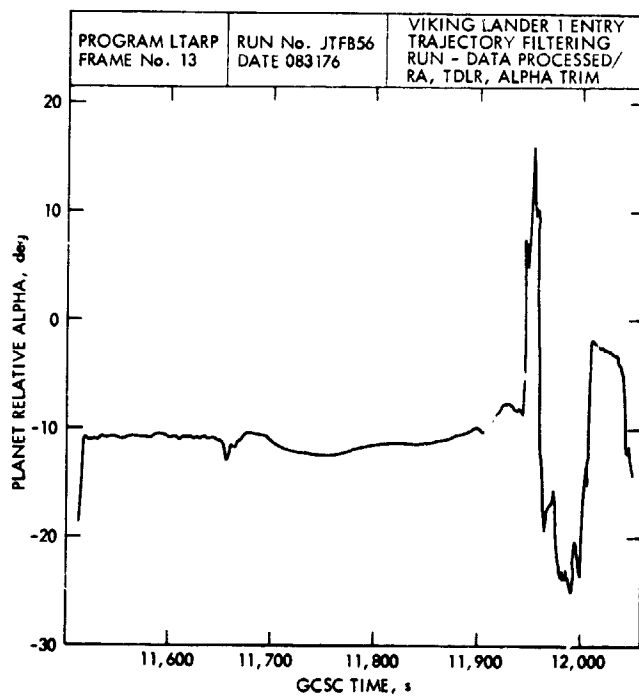


Fig. 45. VL-1 planet relative alpha vs time

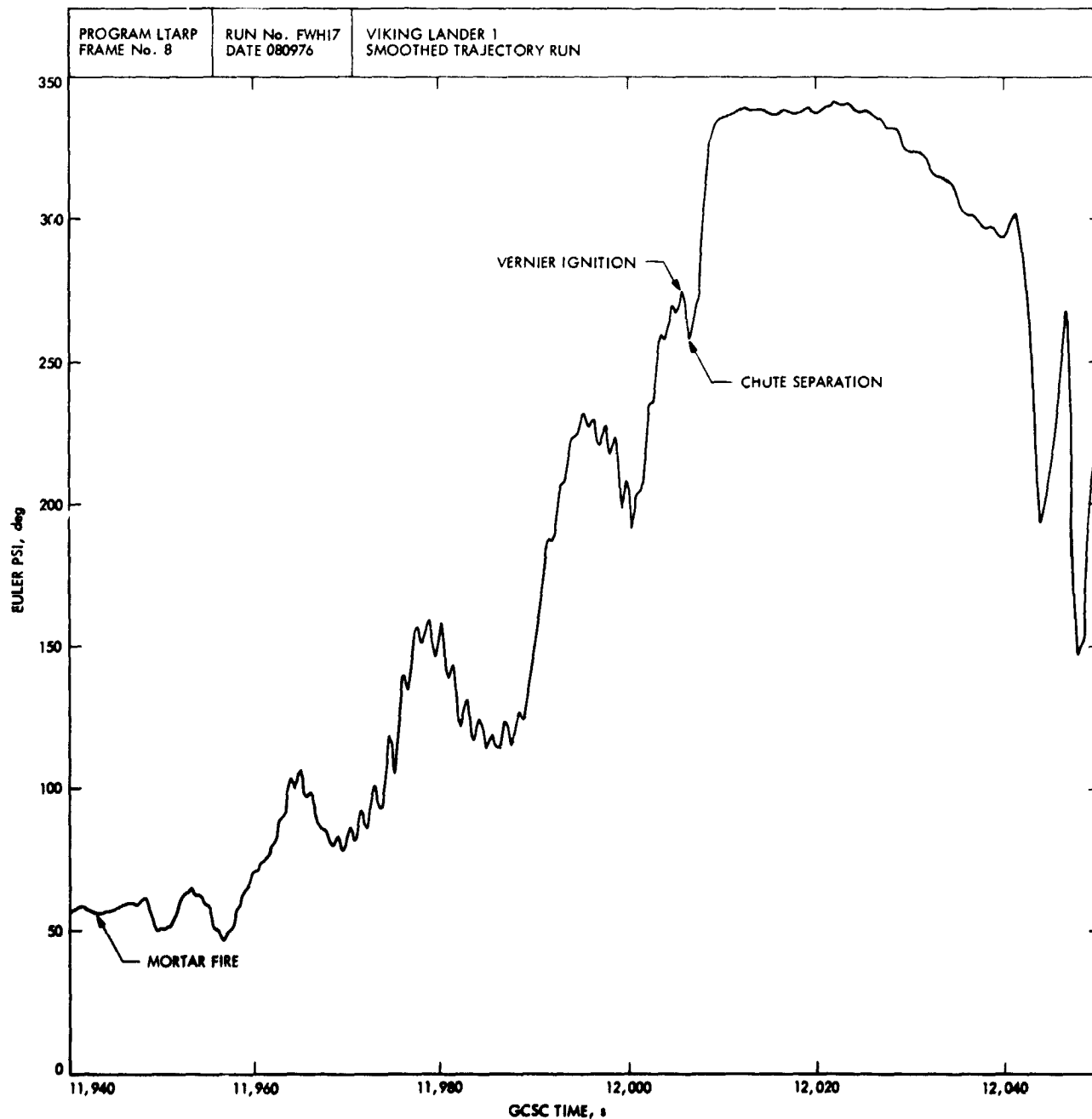


Fig. 46. VL-1 Euler PSI vs time

ORIGINAL PAGE IS
OF POOR QUALITY

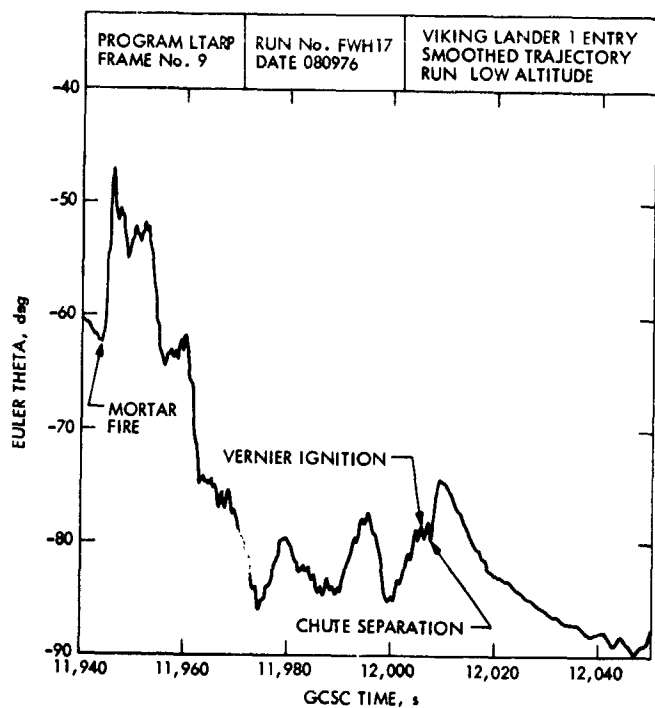


Fig. 47. VL-1 Euler theta vs time

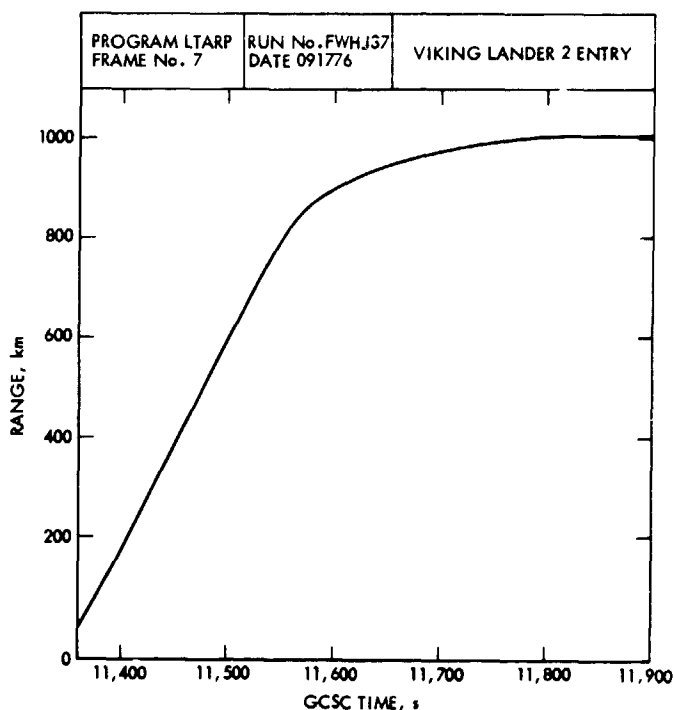


Fig. 49. VL-2 range from entry vs time

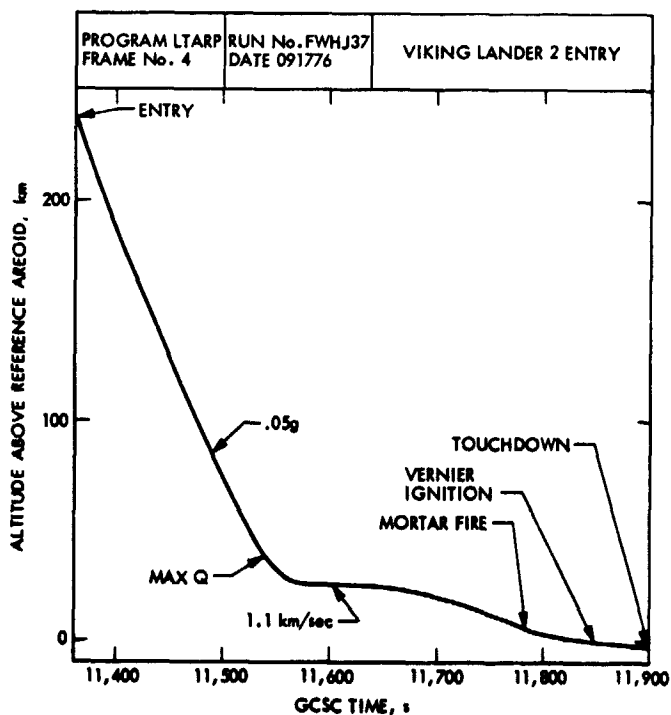


Fig. 48. VL-2 altitude above reference areoid vs time

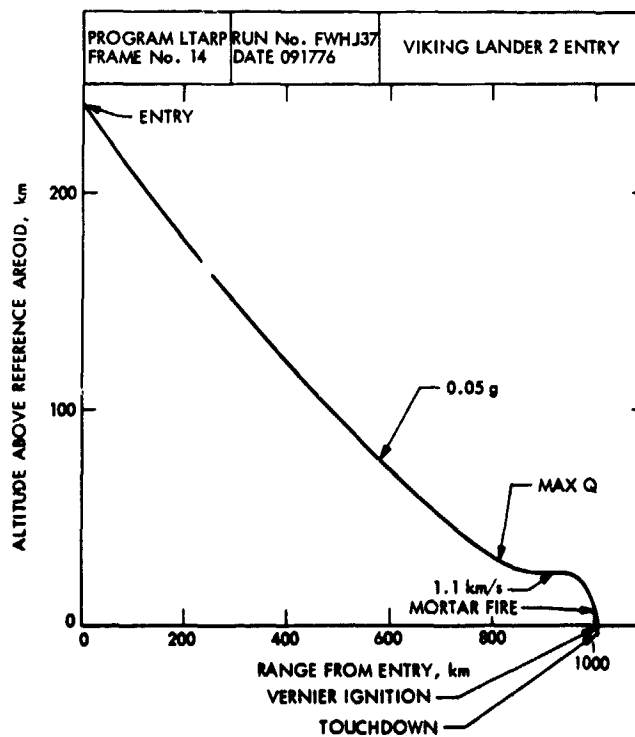


Fig. 50. VL-2 altitude above reference areoid vs range

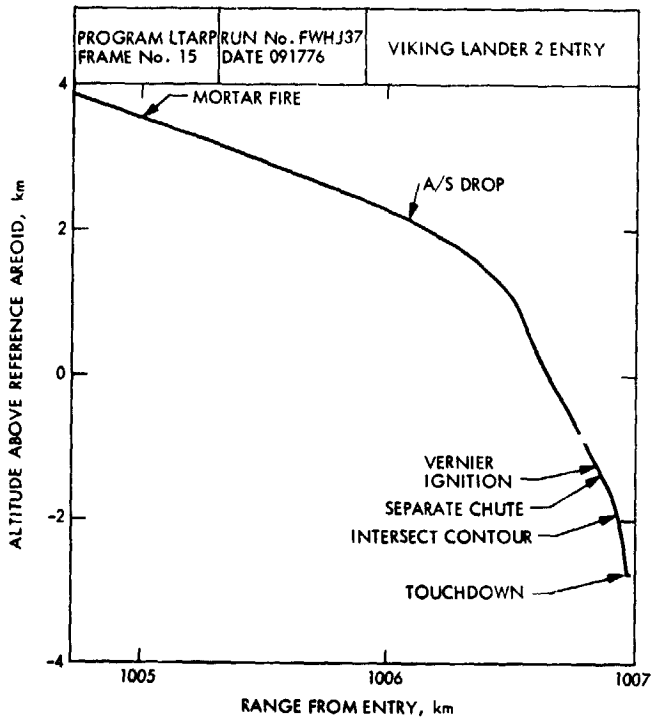


Fig. 51. VL-2 altitude above reference arcoid vs range

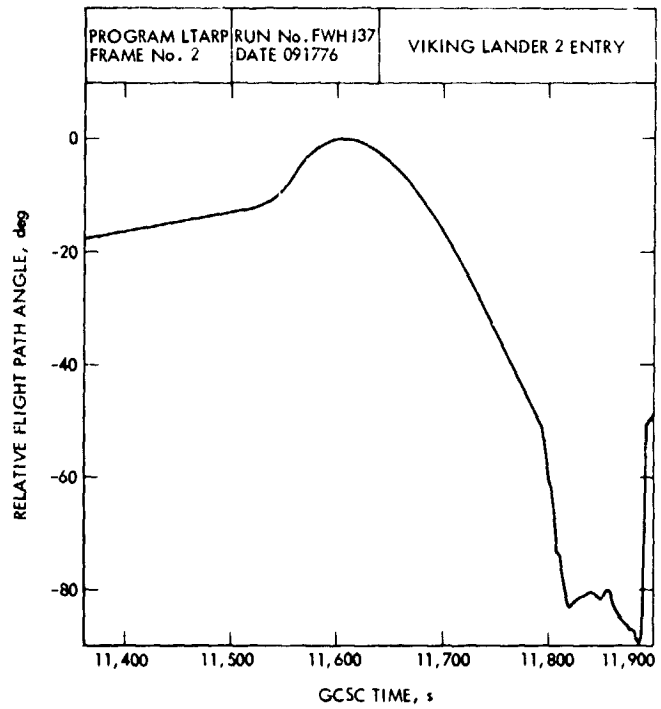


Fig. 53. VL-2 relative flight path angle vs time

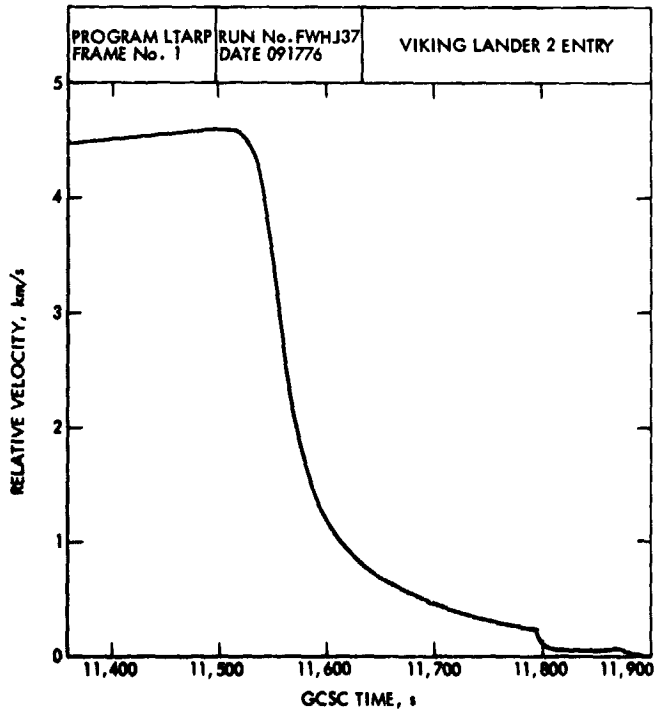


Fig. 52. VL-2 relative velocity vs time

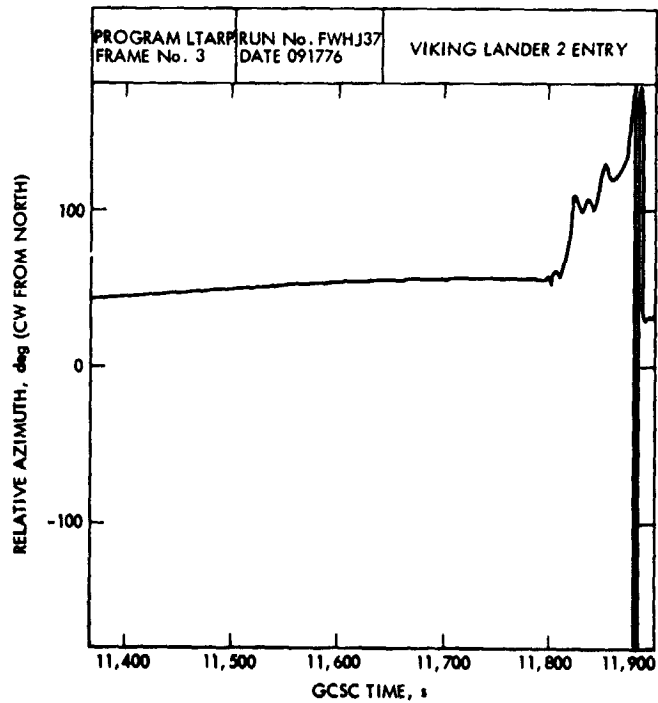


Fig. 54. VL-2 relative azimuth vs time

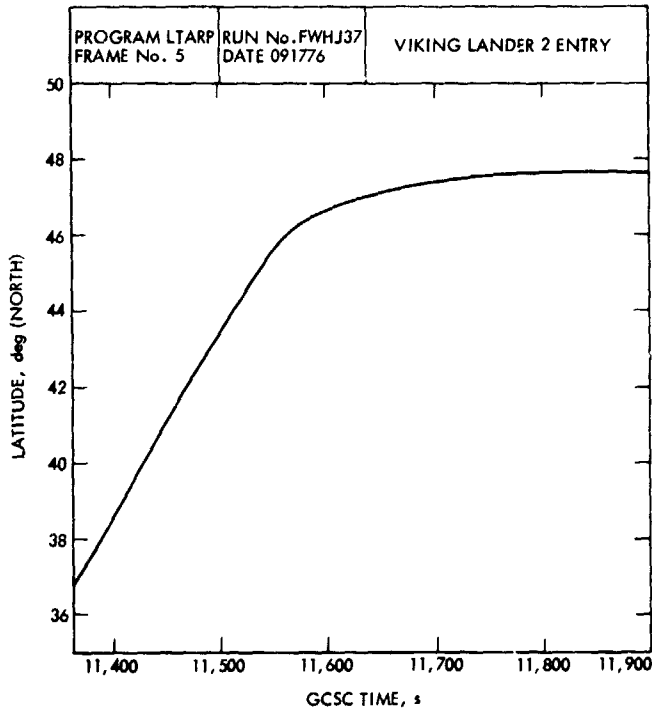


Fig. 55. VL-2 latitude vs time

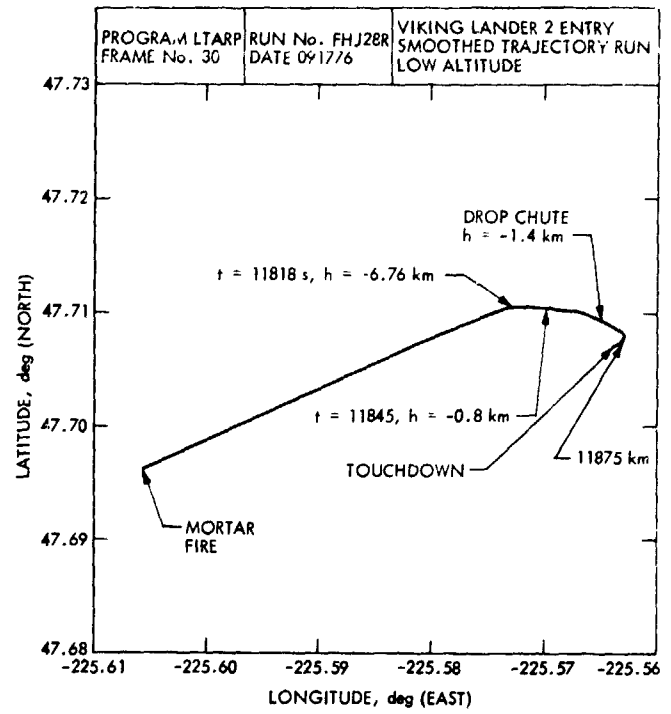


Fig. 57. VL-2 latitude vs longitude

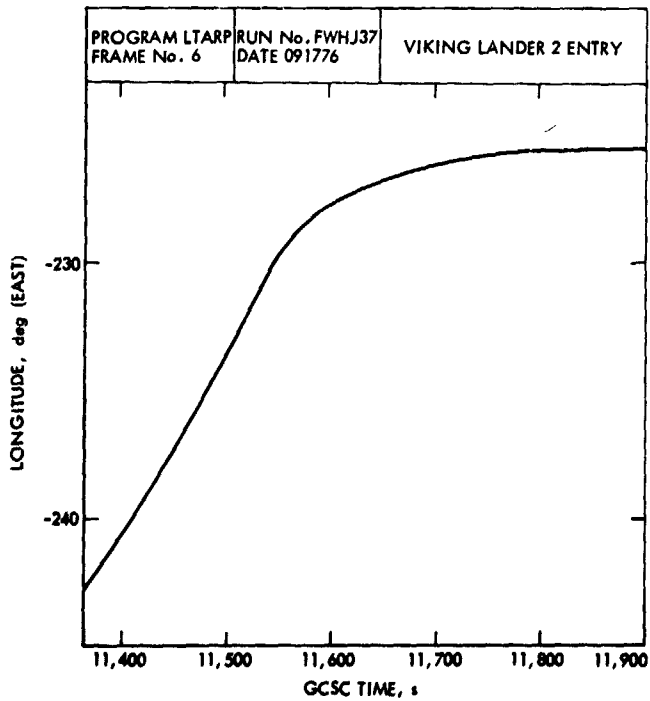


Fig. 56. VL-2 longitude vs time

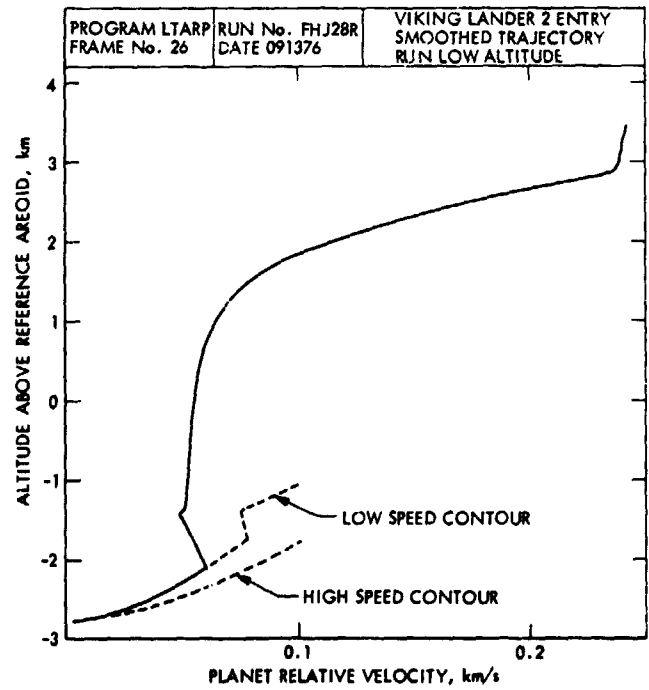


Fig. 58. VL-2 terminal descent performance

ORIGINAL PAGE IS
OF POOR QUALITY

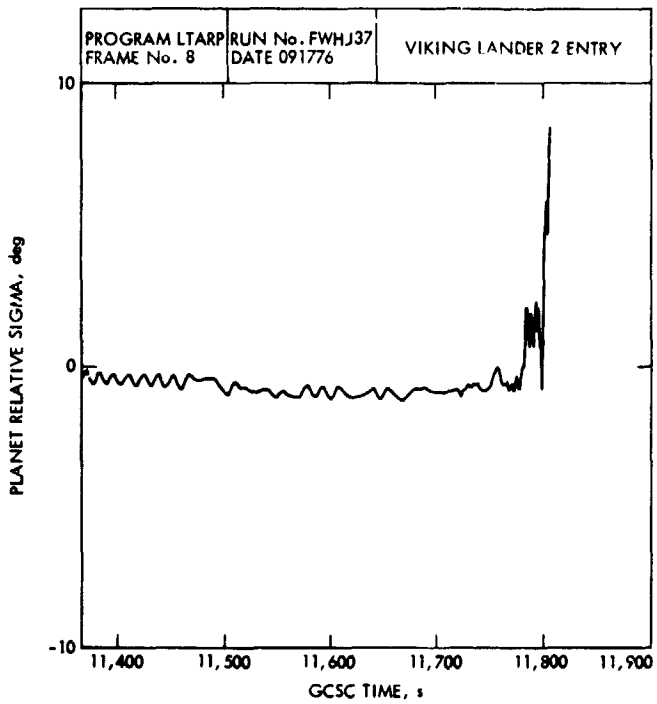


Fig. 59. VL-2 planet relative sigma vs time

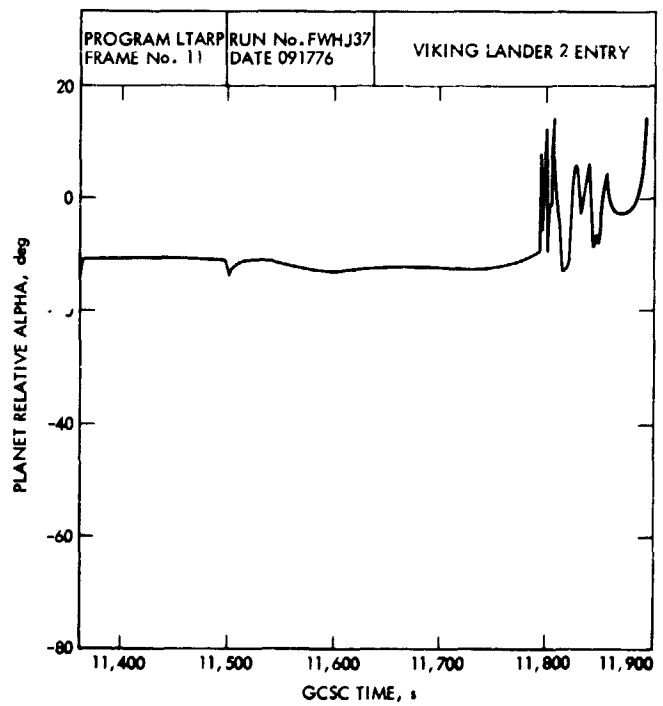


Fig. 61. VL-2 planet relative alpha vs time

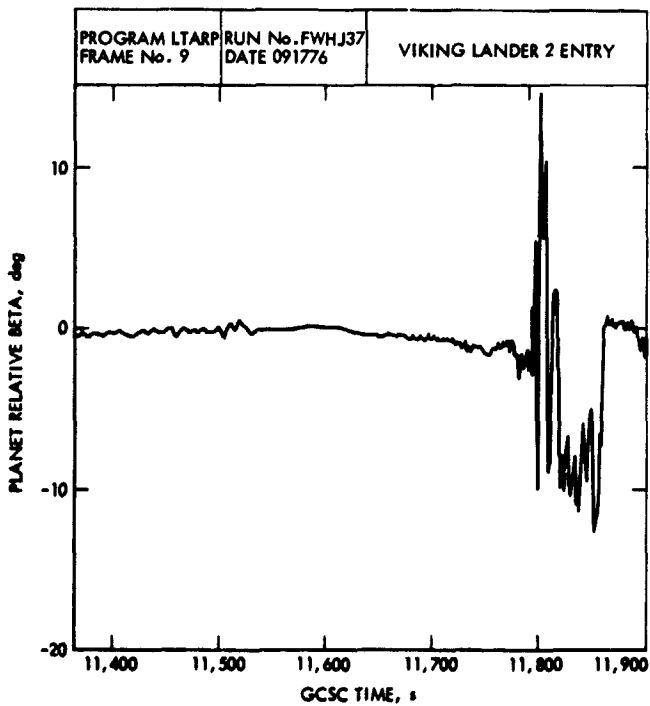


Fig. 60. VL-2 planet relative beta vs time

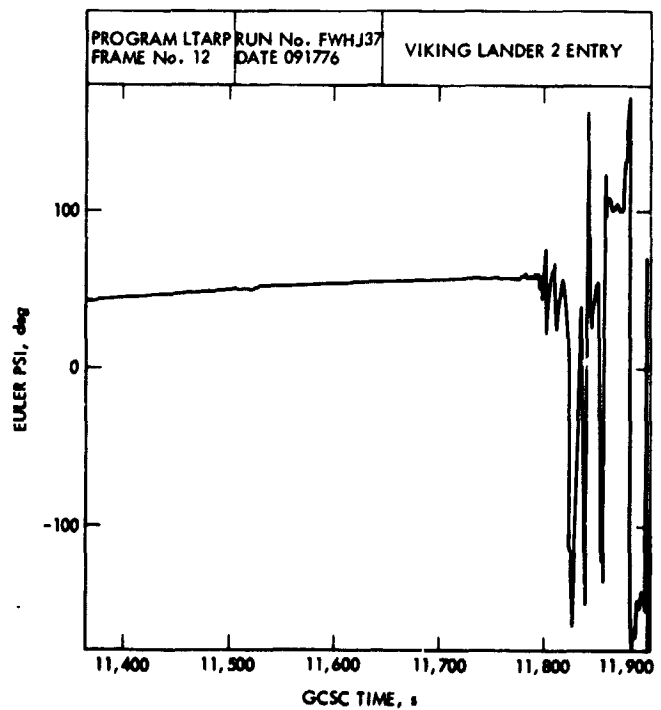


Fig. 62. VL-2 Euler PSI vs time

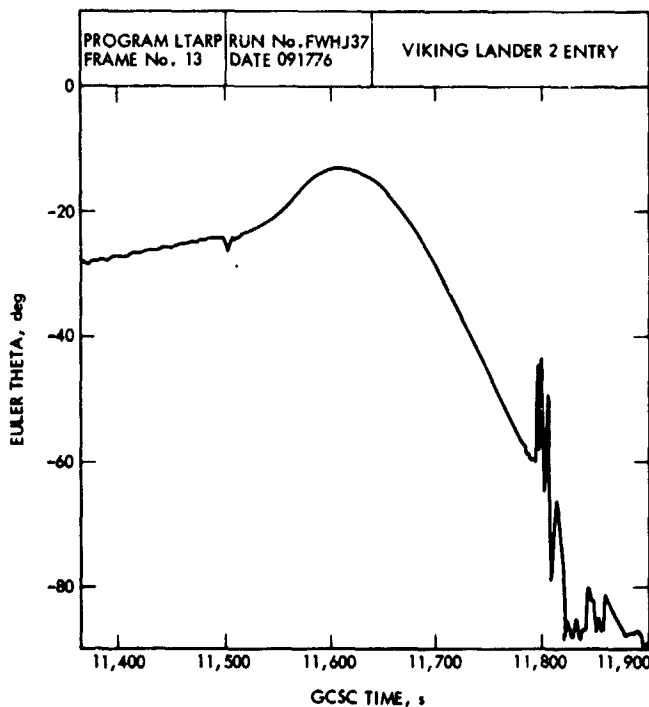


Fig. 63. VL-2 Euler theta vs time

excellent quality except for a short (i.e., approx 2 s) gap following parachute deployment for both VL-1 and VL-2.

That short gap, however, gave a great deal of trouble in both cases. It appeared in a region of great dynamic activity, and attempts to fill it by deducing a wave-form consistent with data on either side fell short of their mark. In effect, this resulted in a loss of attitude reference (several degrees) as LTARP reconstructed the trajectory through the gap such that excessively large TDLR residuals occurred when that measurement became available. Because the attitude errors were no longer consistent with the covariance matrix being propagated by LTARP, the Kalman filter responded to the TDLR residuals by making false corrections to velocity and to the position variables, which by that time were heavily correlated with velocity. Here another factor entered, in that the large TDLR residuals exceeded the linear range of the filter equations. Nevertheless, the filter was thus able to "explain" the initial large TDLR residuals and to keep the remaining ones to touchdown at near-respectable values. However, after processing the ODP position fix at touchdown, the smoothed (i.e., continuous) trajectory obtained by integrating the dynamic data back to time of entry was not of acceptable quality. Measurement residuals were not too bad back up to parachute deployment, but from there on back the RA residuals became progressively worse. To rephrase the above simply - with the

attitude error inherent in the gap-filled dynamic data, no continuous trajectory from entry to touchdown could be found which satisfactorily fit all the measurement data. While efforts were made to recover the lost dynamic data, a two-piece solution (with attitude discontinuities and small velocity discontinuities at the gap) was generated which fit the data quite well. Most of the atmosphere reconstruction was based on this two-piece trajectory. Finally, after playback of the entry data from the lander, the gap was filled with real data and a continuous dynamic file was generated by PREPR of a quality needed by LTARP for a good 1-piece trajectory reconstruction. This same story applied virtually without change to VL-2.

For both reconstructions the initial residuals for each type of measurement processed during the 1-piece filtering runs using the final versions of the dynamic data files are presented in Table 20. These were almost unbelievably small - especially those for VL-1. In particular, the VL-1 TDLR residuals imply that the relative velocity vector and vehicle attitude were known quite accurately before the TDLR went on, contrary to expectations based on premission studies. This attests to the accuracy of knowledge of the entry state, the low drift rate of

Table 20. Initial measurement residuals

Radar altimeter		
	VL-1	VL-2
GCSC time, s	11600.05	11446.45
Altitude (meas.), km	131.7	131.9
Residual, km	.28	.27
TDLR		
	VL-1	VL-2
GCSC time, s	11960.9	11812.8
Relative velocity magnitude, m/sec	71.2	63.6
Beam 1 residual, m/s	1.12	-5.27
Beam 2 residual, m/s	.123	-2.60
Beam 3 residual, m/s	1.18	.80
Beam 4 residual, m/s	1.54	-1.73
ODP touchdown position fix		
	VL-1	VL-2
Radius residual, km	.29	-3.29
Latitude residual, deg	.143	.062
Longitude residual, deg	-.0008	.147

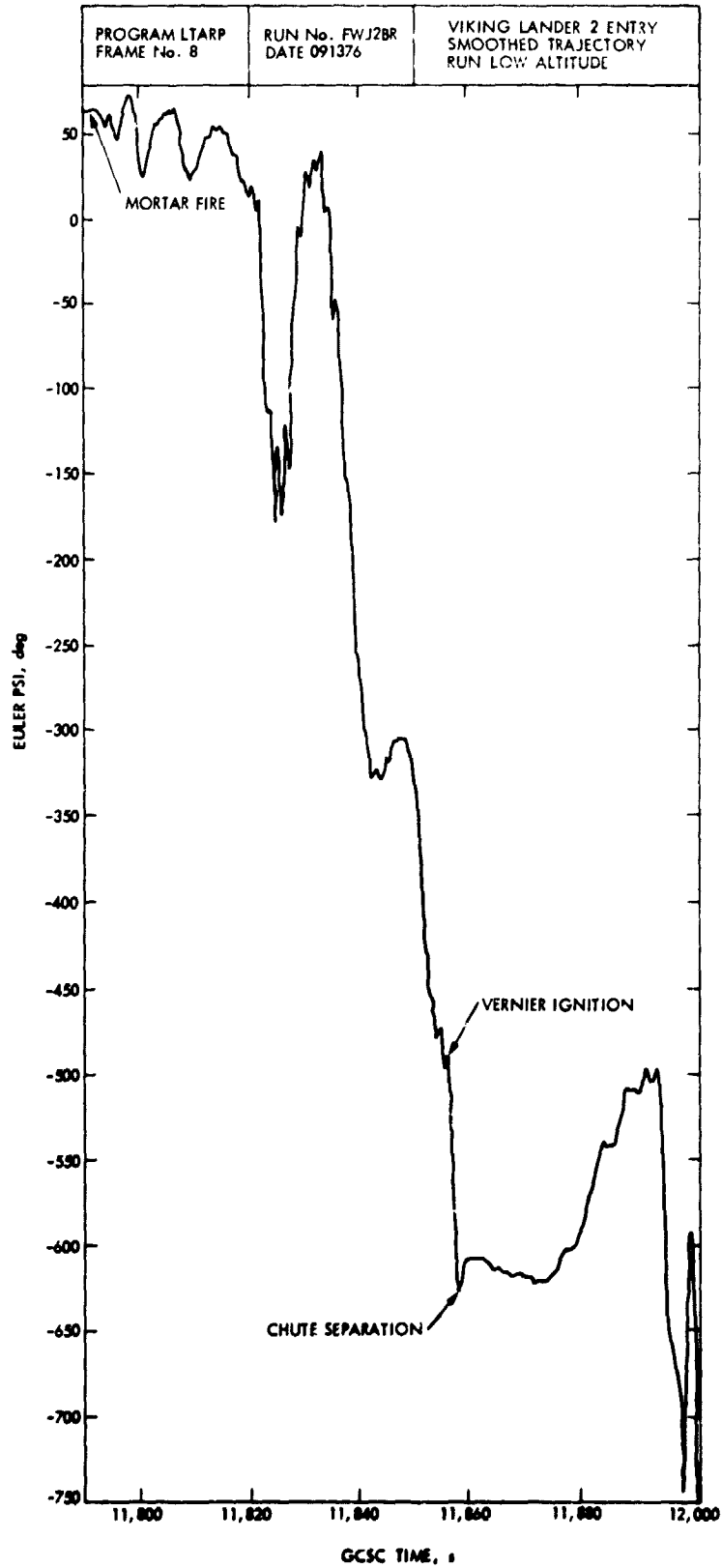


Fig. 64. VL-2 Euler PSI vs time (detail)

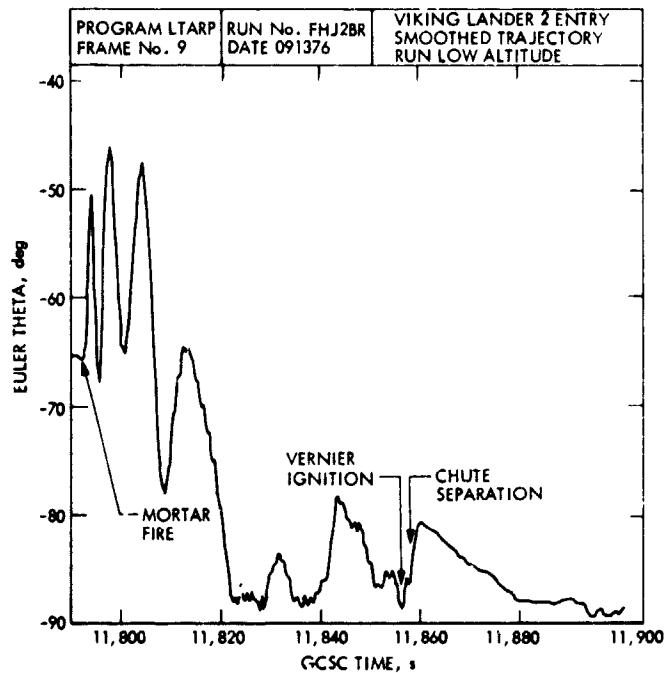


Fig. 65. VL-2 Euler theta vs time

the gyros during coast, the accuracy of the IRU and RA, and the high quality of the smoothed dynamic data processed. The landed position residuals were also quite small, corroborating the above. The radius residual of VL-2 indicated some inconsistency in the way the TDLR processing results in altitude changes through correlation with velocity which has built up in the covariance matrix. This effect, never observed in test activities with simulated data, was prominent in processing all the Viking dynamic data files (except the final one for VL-1), and is not yet understood. At any rate, its slight effect on position reconstruction accuracy was offset by the information in the ODP position fix.

The final continuous 1-piece reconstructed trajectories thus obtained for both VL-1 and VL-2 appear, on the basis of measurement residuals (see Table 21), to be highly accurate. In fact, they were much better than any obtained during development tests and flight team test and training activities using simulated telemetry data, and were excellent bases on which to reconstruct the atmosphere.

2. Solve-for parameters. Capability existed in LTARP to augment the state with solve-for parameters of significance, and most of the procedures were developed on this basis. Thanks to the precision of the IRU, RA, and TDLR, no significant effect on results could be noted by treating their scale factors, biases, etc., as solve-for or consider parameters.

Table 21. Measurement residuals, VL-1 and VL-2, smoothed trajectories

ODP touchdown position fix				
	VL-1	VL-2		
Radius, km	.05	-.18		
Latitude, deg	.057	.020		
Longitude, deg	.0041	.009		
TDLR residuals ^a				
GCSC time, s	Beam 1	Beam 2	Beam 3	Beam 4
VL-1				
11960.9	1.12	.41	.69	.82
11970.9	.15	-.11	-.18	.41
11980.9	.01	-.93	-.69	.18
11990.9	-.69	-.26	.19	-.42
12000.9	.07	.20	.06	-.09
12009.9	-.33	-.58	-.49	-.04
12019.1	-.25	-.27	-.46	-.29
12029.1	.38	.23	.66	.09
12039.1	.20	.26	.69	.22
12049.1	-.36	-.15	-.21	-.43
VL-2				
11812.8	.10	-.17	-.17	.24
11820.8	-.03	-.41	-.09	.05
11826.8	.01	-.36	1.05	.09
11830.8	-.24	-.54	-.45	-.05
11840.8	-.14	-.51	-.78	-.20
11850.8	-.35	-.77	-.11	.47
11860.8	-.58	-.85	-.76	-.22
11870.8	-.12	-.19	1.06	1.38
11880.8	-.15	-.47	.70	1.03
11884.8	-.16	-.35	.75	.91

^aFollowing is a tabulation of representative residuals in m/s obtained by sampling those printed out in the backward passes of the final filtering runs.

An exception, however, was terrain elevation from MSL. Because LTARP's equations of motion involved radial position from the center of the planet, which was observable to the RA only through an intermediate surface of uncertain location, inclusion of a bias to the nominal terrain height table as either a solve-for or consider parameter was necessary. The latter proved adequate in the Viking reconstruction due to the relative accuracy of the nominal terrain profiles deduced from the available contour maps. In spite of the above, however, accuracy figures in this report are derived from filtering runs in which the state was augmented with the most significant dynamic and measurement parameters as solve-fors. Estimates obtained were so near nominal that they will not be reported.

3. Local vs overall reconstruction accuracy The reconstruction philosophy underlying the results in this report is one of identifying a trajectory which best fits, in a minimum variance sense, a variety of measurement and other data taken at different times during entry. As a result, the local fit was not always as good in any given subregion as might be obtained by some less comprehensive method. Two examples of this are significant and will now be discussed.

a. Entry state. The estimated entry state was the final result of a deterministic run in negative time starting at touchdown and ending at entry. The nature of this trajectory was such that the entry state thus obtained was quite sensitive to small errors in the touchdown estimate, and in addition, primarily because of IRU uncertainties, the touchdown state uncertainty was amplified as the state was propagated back up to entry. It was thus often found that a better entry estimate (at least for selected variables) could be obtained by means of a restricted run that was terminated in the aeroshell phase after processing early RA data, with its final state being propagated back to entry. Though better in entry altitude and vertical velocity, such an entry state would, in general, be incapable of defining the other trajectory parameters to an accuracy suitable for the subsequent atmosphere reconstruction. The estimates presented in this report were obtained for both landers by backward integration of the touchdown state computed in a complete forward filtering run. The VL-1 and VL-2 entry states thus obtained are believed to be sufficiently accurate for all foreseen purposes because of the high quality of the dynamic data received from the landers.

b. Trajectory in vicinity of touchdown. As the reconstruction proceeded through the parachute and terminal descent phases, processing TDLR and RA data, the velocity and position (relative to touchdown position) were determined quite accurately. Throughout the long flight from entry, however, position and velocity became strongly correlated, such that the post-touchdown ODP position fix not only corrected radius, latitude, and longitude, but applied a correction to velocity as well. The velocity history, though improved on an overall basis over the entire trajectory, was thus degraded in the vicinity of touchdown. Although this may be by an insignificant amount for most purposes (e.g., only a fraction of a meter per second), it might be unacceptable, for example, for accurately inferring the terrain slope in the neighborhood of the landing site from RA measurements. Similarly, the terminal velocity and position histories may not be sufficiently accurate for deducing physical properties of the soil from landing impact velocities and the ground track leading to touchdown, or for assessing vehicle behavior during touchdown. For such uses a limited reconstruction fitting only selected data in the vicinity of touchdown would be preferable. Even for this, however, a

better tie point with the planet is needed, i.e., through availability of IRU data to the point where the vehicle is at rest.

4. Integration step size and PREPR smoother length. The PREPR smoothers selected were short (i.e., 7 point) during the first few seconds encompassing entry and the pitch maneuver following entry, long (i.e., 49 point) from there until just before mortar fire, and short (i.e., 7 point) the rest of the way down. These lengths were chosen to provide accurate tracking of the large amplitude changes during periods of great dynamic activity and to filter out the high-frequency, low-amplitude effects unwanted in a trajectory intended for atmosphere reconstruction. They also allowed use of a larger integration step size in LTARP down to the parachute phase. It should be pointed out, however, that the trajectory thus reconstructed is uniquely mated to the smoother-integration step size combination used. Although a different combination will, by means of an LTARP filtering run, result in an entry state and trajectory with apparently only insignificant differences, a deterministic run starting with an entry state unmatched to the smoother-integration step size combination being used may differ significantly (e.g., several hundred meters in altitude at touchdown).

For the Viking reconstruction the fundamental choice was smoother length. The integration step size schedule was then chosen so as to minimize computer run time without degrading accuracy of results. Step sizes thus varied from 0.1 to 0.5 s, depending on prevailing smoother length and nature of run.

D. Vehicle Subsystem Performance

1. Aerodynamics. Reconstructed dynamic pressure and Mach number time histories are presented in Figs. 66 to 69 for both landers. Figure 70 gives reconstructed trim angle of attack curves, together with design curves.

2. Aeroshell phase. The α_{trim} vs M curves for the two landers are qualitatively similar to each other, but differ distinctly in shape from the a priori curves of Ref. 2. Above Mach 3 the reconstructions were based on planet-relative rather than air-relative velocity, but are believed accurate, in that unreasonably large winds would be required to alter them significantly. At Mach 5, where flight path angle was approximately zero, for example, the results were virtually insensitive to horizontal wind. There, a vertical wind of about 18 m/s would be required to explain a 1-deg difference. Although such a vertical wind might not be totally unreasonable considering surface slopes, it was fairly well ruled out as a factor by the similarity of the VL-1 and VL-2 curves.

Below Mach 3, where winds were being estimated, the accuracy of the a priori curve became quite important. Here

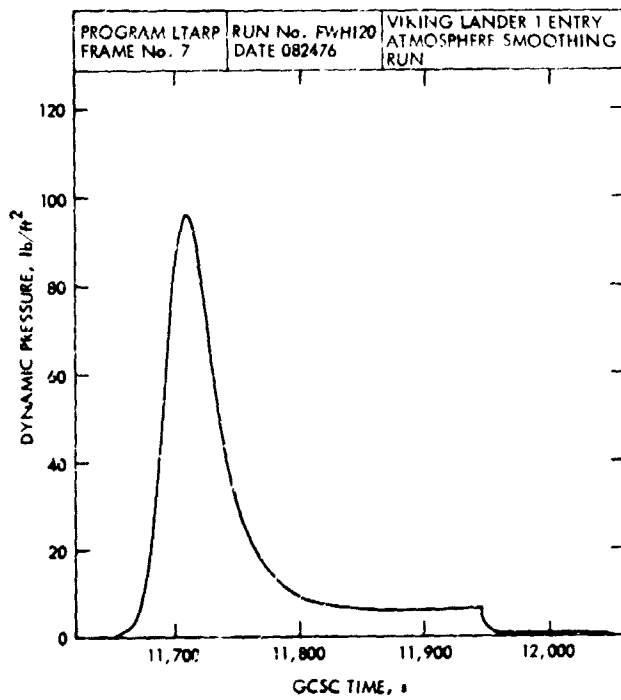


Fig. 66. VL-1 dynamic pressure vs time

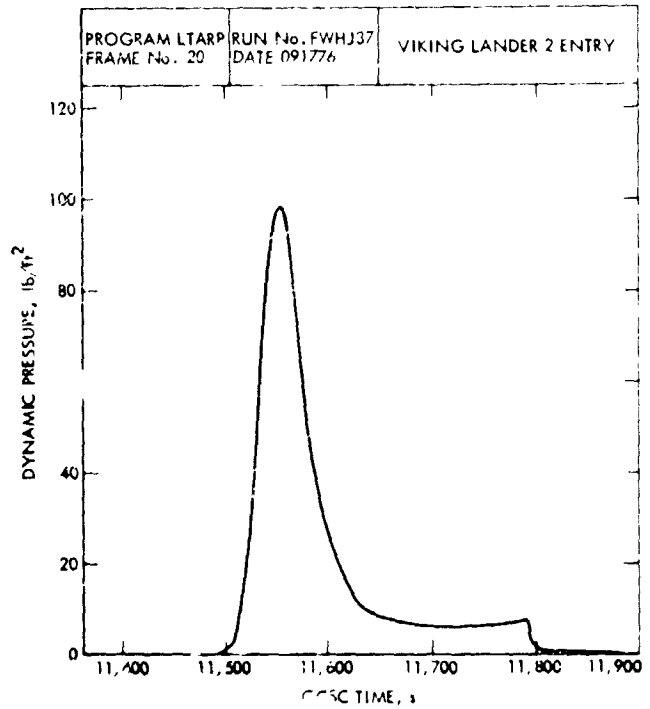


Fig. 68. VL-2 dynamic pressure vs time

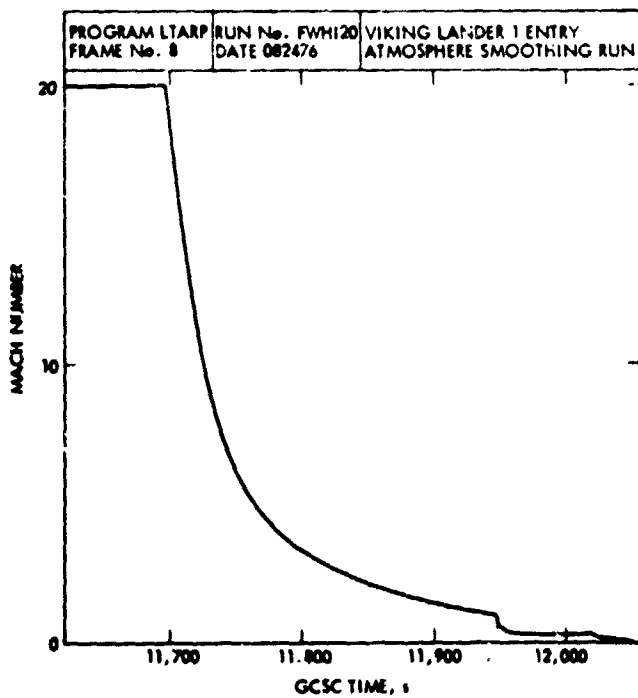


Fig. 67. VL-1 Mach No. vs time

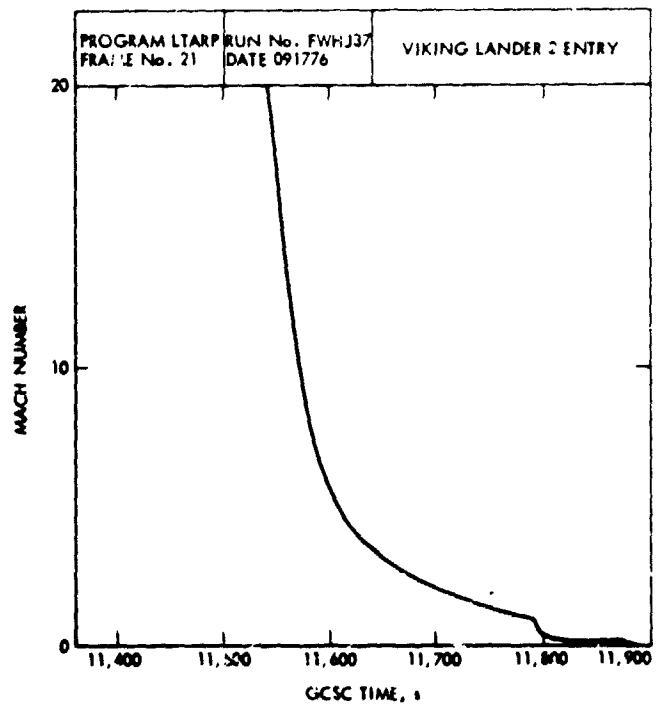


Fig. 69. VL-2 Mach No. vs time

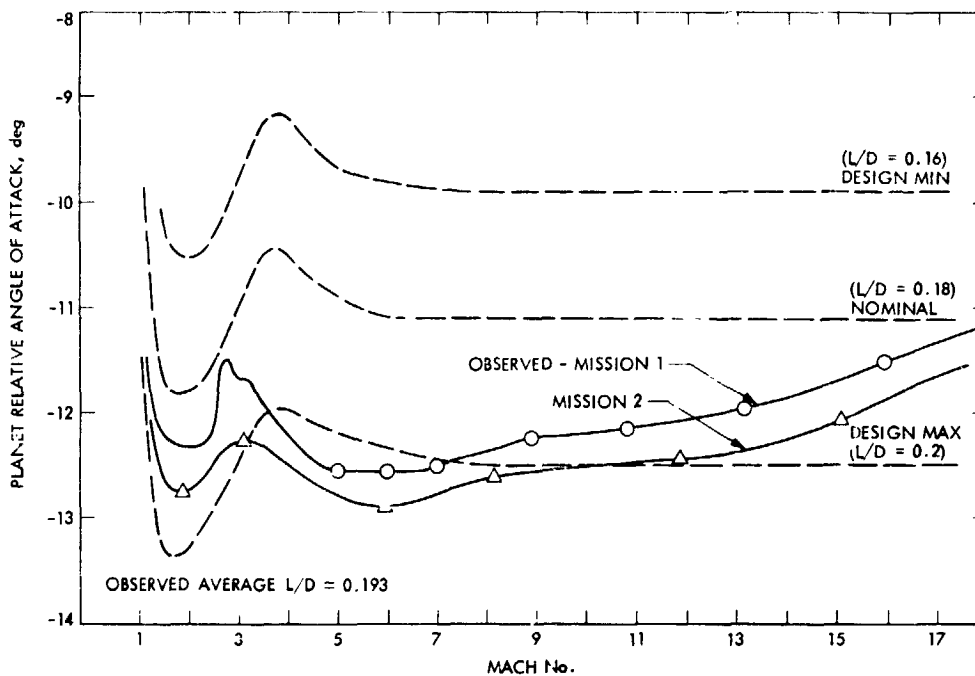


Fig. 70. Planet relative angle of attack vs Mach No.

LTARP tended to reconstruct a wind which, when combined with planet-relative velocity, resulted in a reconstructed α_{trim} curve qualitatively similar to the a priori nominal, though biased away from it.

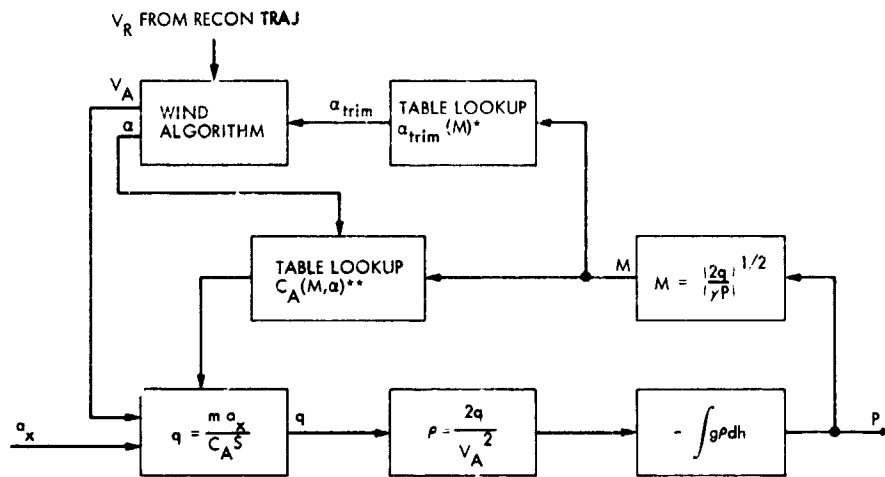
Characteristics of the atmospheric computation algorithm below Mach 3 deserve discussion. The feedback loops were rather involved, as can be seen from Fig. 71. Mach number was computed from dynamic pressure and then used in a table lookup of aero coefficients, which were subsequently used to compute dynamic pressure. Accuracy (and indeed stability) of the process in some Mach regions was of concern. The same holds to a lesser extent for angle-of-attack feedback effects. In particular, in the neighborhood of Mach 1.2, α_{trim} was highly sensitive to Mach number, which was reflected in the wind estimation uncertainties given in Fig. 72. Fortunately, this occurred at the end of the aeroshell phase, where the trajectory was bending over rapidly and the atmosphere reconstruction was becoming less sensitive to wind estimates.

At higher Mach numbers the accuracy of the LTARP atmospheric estimates was sensitive to real gas effects. The 5% 3 σ tolerance on axial force coefficient was assumed to adequately cover these, but recent analyses exploiting stagnation pressure measurement data indicated that that value was too low and that LTARP final dynamic pressure and density above Mach 3 might be on the order of 6% too high due to real gas effects not being modeled. LTARP, however, by processing end-of-

phase pressure and temperature measurements, estimated scale factor corrections to be applied uniformly over the entire Mach range to the nominal axial force coefficient table as follows:

C_A scale factor	
VL-1	1.012
VL-2	1.007

3. Parachute phase. The attitude reconstructions of Figs. 46, 47, 64, and 65 showed large-amplitude pitch and yaw oscillations following mortar fire, for both VL-1 and VL-2, with recognizable coning motion continuing thereafter. The density reconstruction for VL-2 was well-behaved, with a plausible (after smoothing out oscillations attributed to attitude excursions) density vs altitude plot over the entire parachute phase. Pressure and temperature measurement processing gave an estimated scale factor correction of 1.08 to be applied uniformly to the nominal drag coefficient over the entire parachute phase. Similar treatment of VL-1 data, however, seemed to indicate that for about 18 sec following deployment the parachute was not fully reefed, with the product $C_D S$ being about 15% less than nominal. At that point $C_D S$ jumped rather suddenly to about 7% greater than nominal. The interpretation here given was that the drag coefficient was 7% high over the entire phase, with the parachute being only about 80% reefed for 18 s following mortar fire. Other inter-



*IN PARACHUTE PHASE THIS BECOMES $\alpha_{trim}(M) \equiv 0$
 **IN PARACHUTE PHASE THIS TABLE IS $C_D(M)$

Fig. 71. Atmosphere estimation loops

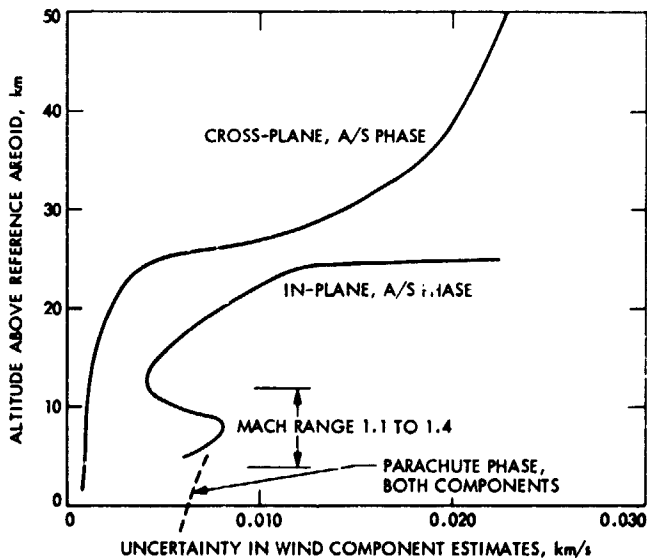


Fig. 72. VL-1 and VL-2 wind estimation uncertainties

pretations involving wind and attitude situations were perhaps equally plausible but did not lead to different atmosphere conclusions.

Ground track plots (Figs. 40 and 57) show the manner in which the motion of the landers was rapidly arrested after deployment, with motion relative to the planet defining the wind direction thereafter.

4. Terminal descent performance. Altitude-velocity plots (Figs. 41 and 58) indicate that the terminal descent phase was nominal for each lander, with the velocity contours being closely followed after intersection. Figures 40 and 57 show the ground tracks during terminal descent. VL-2 took a rather interesting turn just before touchdown, accompanied by an unscheduled change in velocity (possibly the result of the TDLR locking on a cloud of dust, as has been conjectured).

5. Inertial reference unit. Results of the trajectory reconstruction indicate that uncertainties associated with the IRU were well within tolerance and the least significant of all those affecting the process. Gyro accuracy is illustrated by attitudes at entry:

	Targeted	Actual	Δ
VL-1			
σ deg	0	.6	.6
β deg	0	.1	.1
α deg	-19.5	-18.8	.7
VL-2			
σ deg	0	-.3	-.3
β deg	0	-.1	-.1
α deg	-19.5	-19.3	.2

The a priori 1σ uncertainty for each of these was regarded as 1 deg, primarily allowing for gyro drift during coast.

Leg 1 azimuth at touchdown was another measure of gyro accuracy:

	LTARP	Gyrocompassing
VL-1 deg	321.6	321.6
VL-2 deg	210.1	209.2

Estimated corrections to the accelerometer scale factors were essentially zero.

6. Radar altimeter and TDLR. Estimated corrections to the RA and TDLR scale factors were essentially zero. RA bias was inseparable from the terrain height estimate.

VII. Environmental Estimates

A. Reconstructed Atmosphere/Winds

The atmosphere estimates based on VL-1 entry data are presented in Table 16 and Figs. 73 to 77; those on VL-2 data in Table 17 and Figs. 78 to 82. Uncertainties in these estimates are presented in Tables 18 and 19 and Fig. 83.

Wind estimates are presented in Figs. 84 and 85 for VL-1 and Figs. 86 and 87 for VL-2. Uncertainties in these estimates were presented in Fig. 72.

Reconstructed terrain profiles are presented in Figs. 88 and 89. The wind and atmosphere reconstructions are inseparable and will be discussed together. The figures and data presented are a composite of results obtained from runs made addressing individual phases, within an overall iterative procedure. The discussion follows in a like manner.

1. Upper aeroshell phase. For both VL-1 and VL-2 the accelerometer threshold for computation of density occurred at about 115 km altitude above the areoid. Above that altitude sensed axial acceleration was rather erratic, with attitude control disturbance predominating. Density at 115 km was found to be about $5.E-11$ g/cc and pressure on the order of $1.E-5$ mb. Because of the inaccuracy associated with picking a starting value for pressure, its estimate did not become reasonably accurate until the increase in pressure below 115 km had exceeded the starting value several fold. This was at an altitude of about 100 km. Temperature, being computed from pressure and density, thus had a threshold of about 100 km. VL-1 and VL-2 altitude and velocity time histories were quite similar during their respective aeroshell phases, with flight path angle staying near zero over a period of about 100 sec, during which velocity decreased from about 4 km/s to about 0.6 km/s. In this region it was not possible to obtain a good wind estimate (the uncertainty in the estimate would have greatly exceeded

the estimate), so planet-relative, rather than the unknown air-relative velocity was the basis for density computation. At small γ_R an unknown in-plane wind V_W will introduce a fractional error of $-2V_W/V_R$ in computed density, which becomes significant as velocity decreases. For Viking this occurred where altitude was changing only slowly, thus contributing to a physically implausible jog in each of the preliminary density-altitude plots. The upper aeroshell phase data of Figs. 73 to 82 reflect zero-wind assumption down to the point where wind becomes significant in the density calculation. Inherent are estimated scale factor corrections to the axial force coefficient made on the basis of pressure and temperature measurement processing during lower phases and post-touchdown.

2. Lower aeroshell phase. Wind estimation was begun for both landers at a point where γ_R had dropped below about -6 deg ($M \sim 3$, altitude ~ 24 km). This process in LTARP involved comparing a priori trim α and β with planet-relative values emanating from the trajectory reconstruction process. The difference was attributed primarily to a combination of horizontal wind and error in the a priori trim characteristics, with estimates of each being made in accordance with their uncertainties. The resulting wind estimates are presented in Figs. 84 to 87. These were manually extended above the altitude threshold defined by $\gamma = -6$ deg in such a manner as to include cross-plane estimates not subject to γ limitation and in-plane estimates which improve the density plots in the vicinity of the jogs described in the previous paragraph. The VL-1 wind profile above 25 km also includes results of a study made to force consistency between reconstructed wind, trajectory, and event times. Uncertainties in the wind estimates presented vs altitude in Fig. 72 reflect 1σ uncertainties of 0.4 and 0.3 deg in knowledge of α_{trim} and β_{trim} , respectively, including both aerodynamic and CG offset uncertainties.

Note that the wind uncertainties were of the same order of magnitude as the estimates themselves, especially in the case of VL-2, for which the winds appear to have been small enough during the aeroshell phase to be ignored in the atmosphere computations.

Atmosphere estimates of Figs. 73 to 82 were obtained for the lower aeroshell phase by means of LTARP runs in which the wind profiles of Figs. 84 to 87 were approximated by tabular input. Final results incorporated the axial force coefficient scale factor estimates based on pressure and temperature measurements processed below the aeroshell phase.

3. Parachute phase. Atmosphere reconstruction in the parachute phase was complicated by the large-amplitude attitude excursions that followed parachute deployment. These are presented in terms of the Euler angles $\bar{\psi}$ and $\bar{\theta}$ (yaw and pitch)

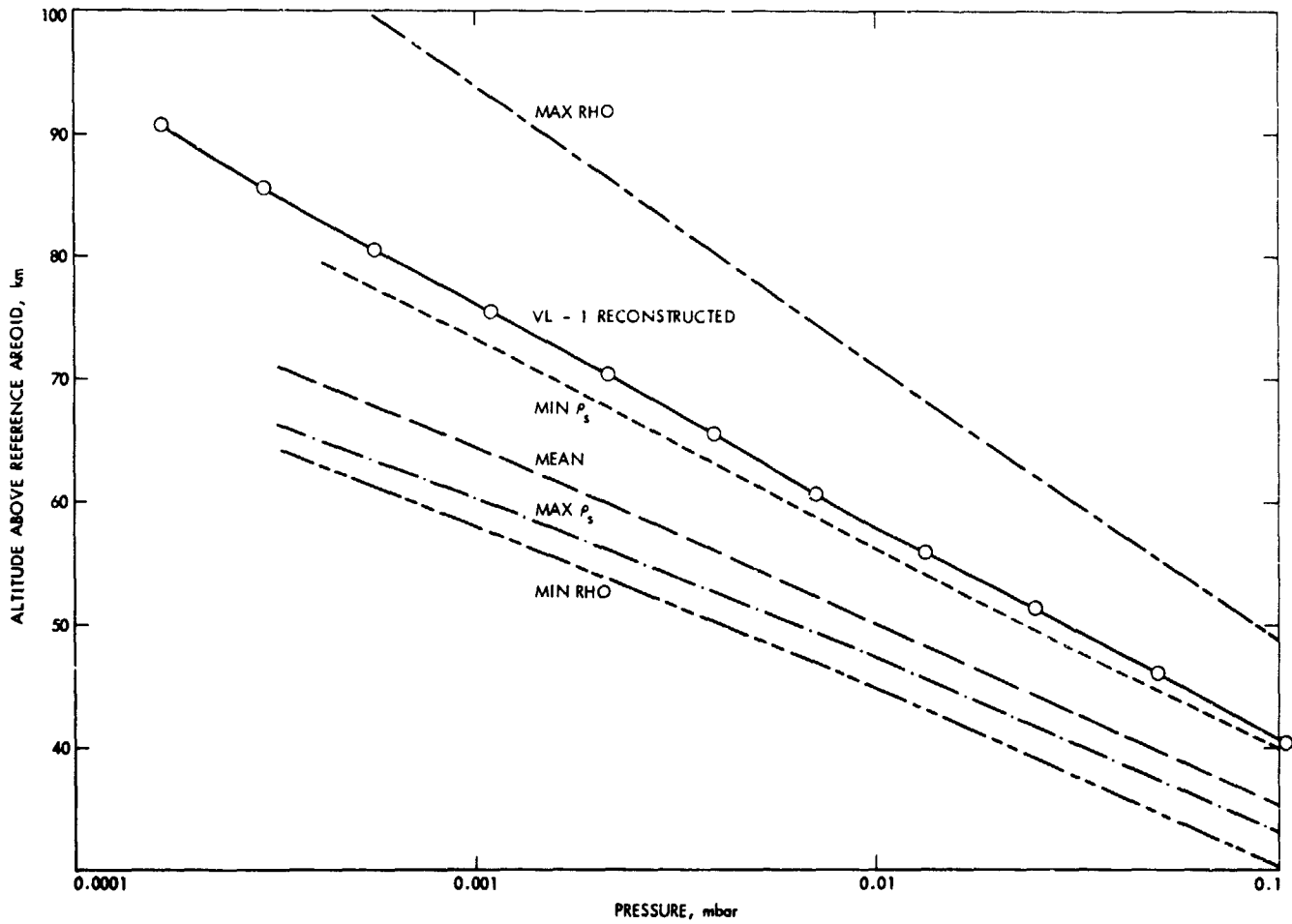


Fig. 73. VL-1 ambient pressure (< .1 mb) vs altitude

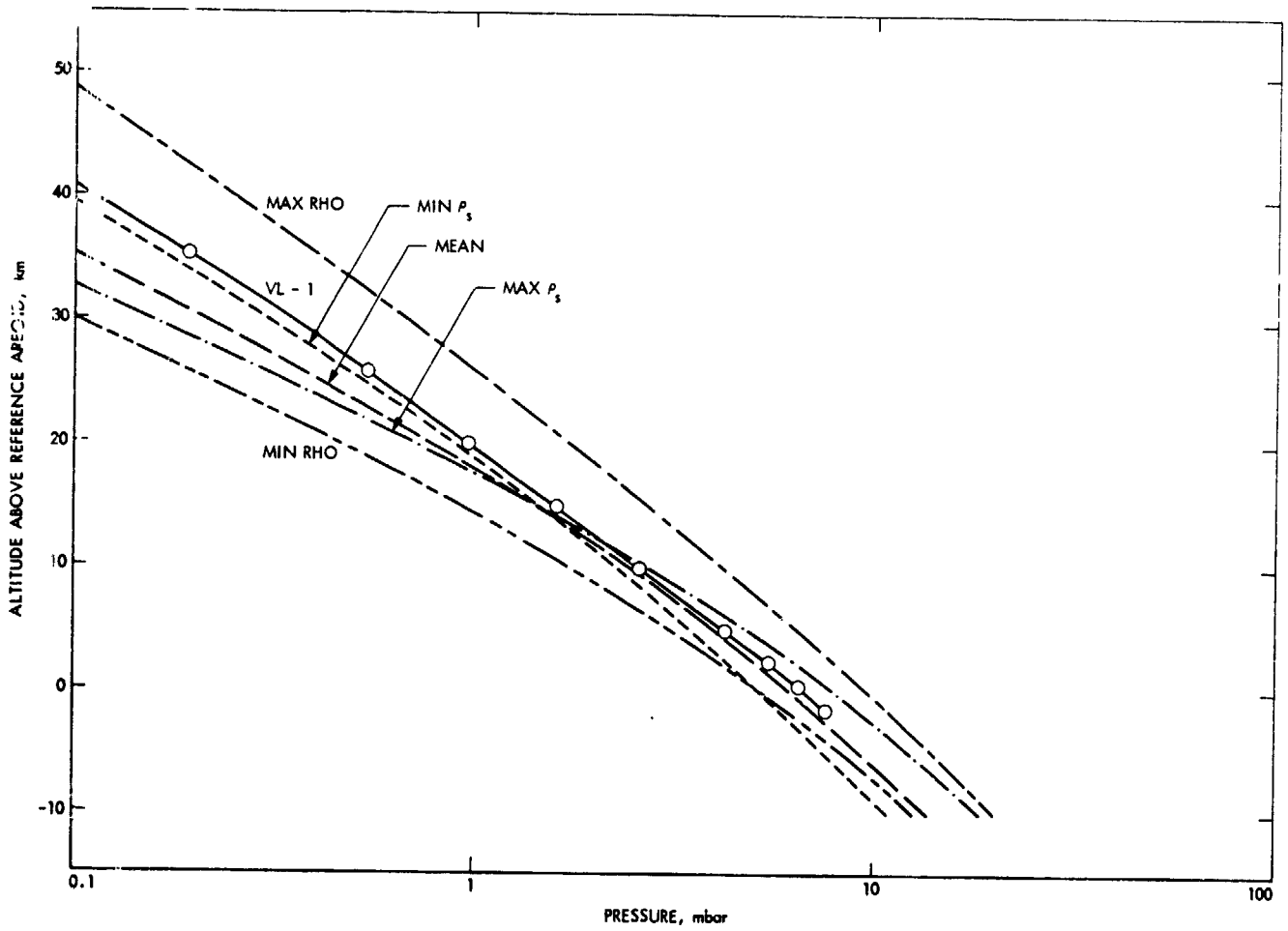


Fig. 74. VL-1 ambient pressure (> .1 mb) vs altitude

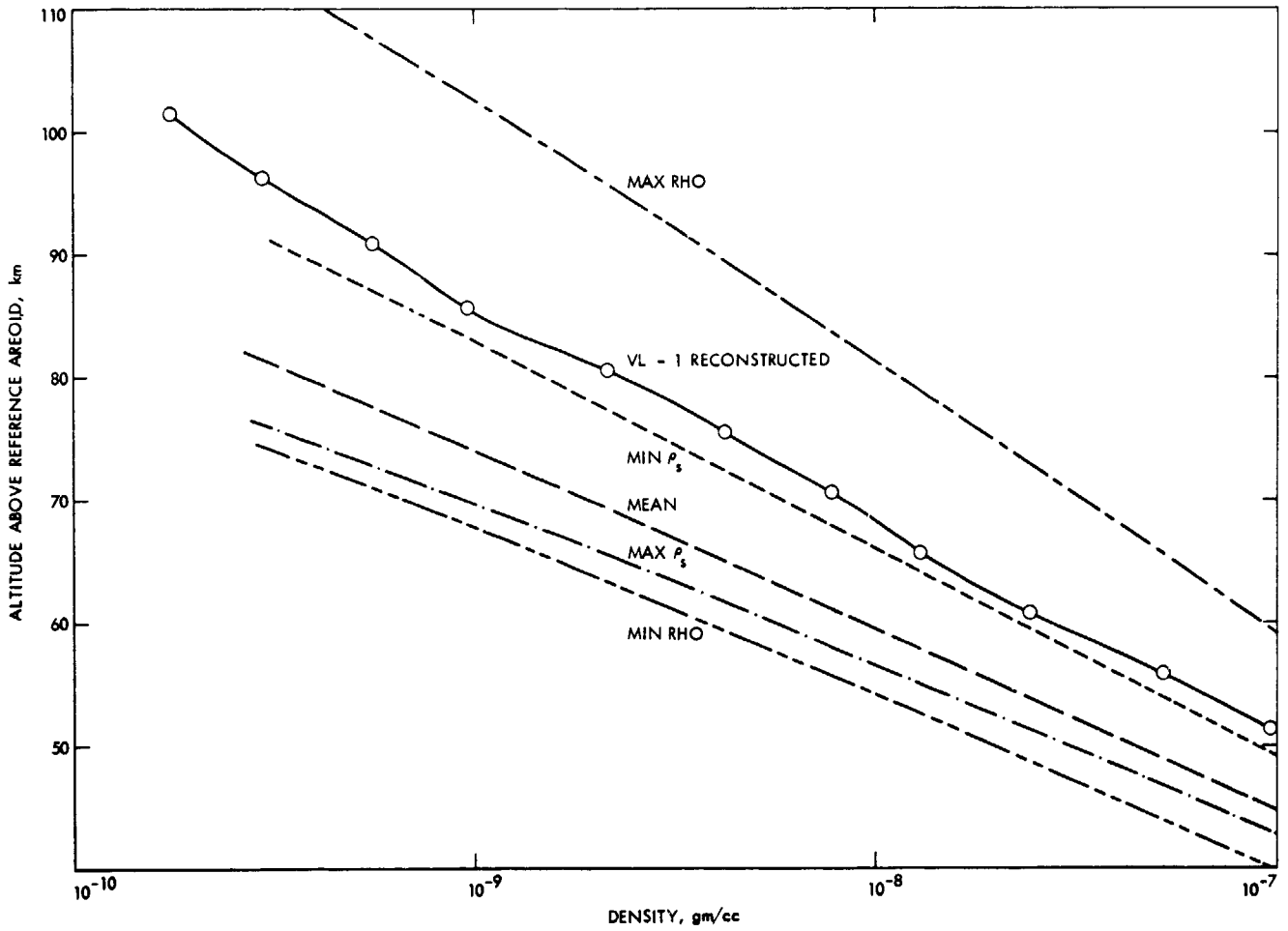


Fig. 75. VL-1 density ($<10^{-7}$ gm/cc) vs altitude

ORIGINAL PAGE IS
OF POOR QUALITY

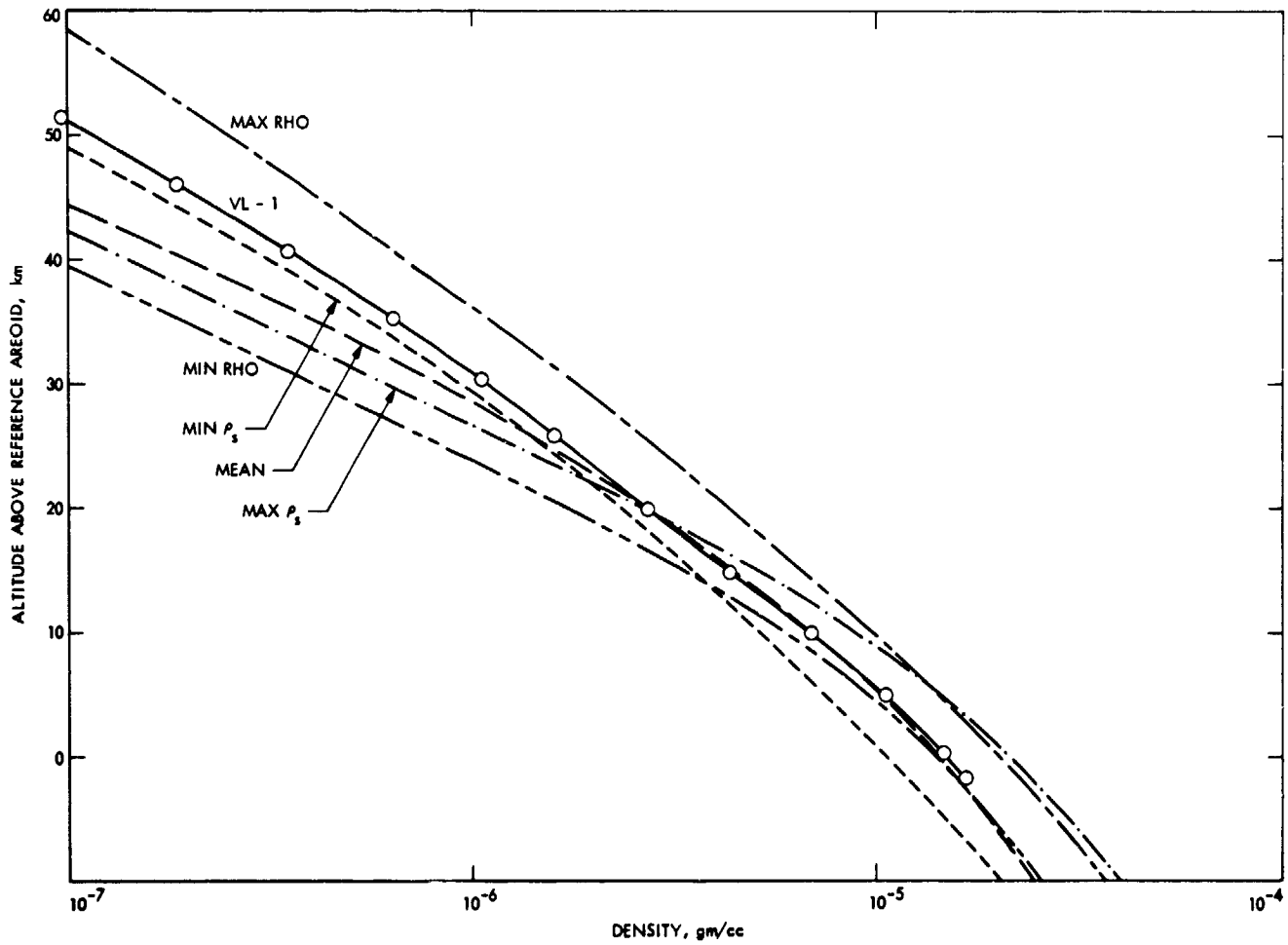


Fig. 76. VL-1 density ($>10^{-7}$ gm/cc) vs altitude

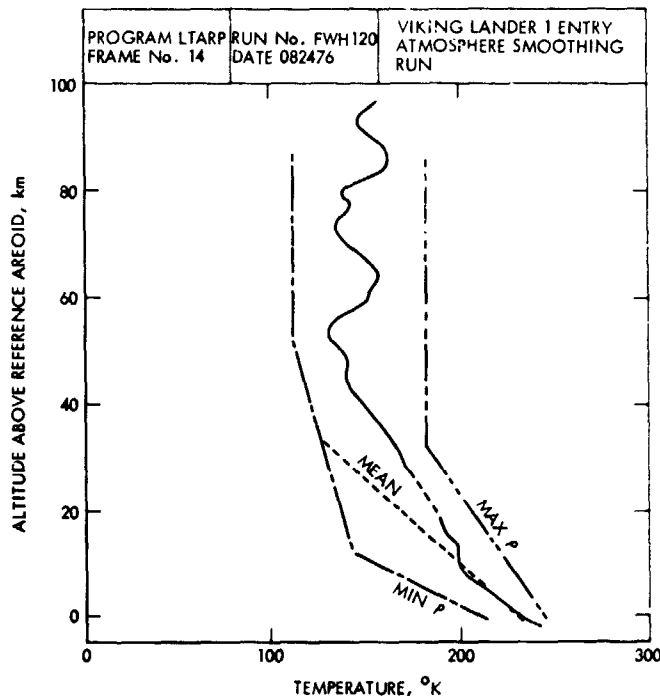


Fig. 77. VL-1 altitude above reference areoid vs temperature

in Figs. 46, 47, 64 and 65. The wind estimation algorithm for the parachute phase assumed that, on the average, the direction defined by these angles lay on a 6 deg cone about the air-relative velocity vector. A horizontal wind was then defined by the difference between planet-relative and air-relative velocity vectors. Inherent in this approach was an error during most of the parachute phase (after the initial rapid decrease in relative velocity to around 60 m/s) of about 6 m/s in the horizontal wind estimate. This was the main contributor to the wind uncertainties reported for the parachute phase in Fig. 72. Again, especially for VL-2, the uncertainties in the estimates were of the same order of magnitude as the estimates themselves.

The wind profiles of Figs. 84 to 87 reflect rather drastic manual smoothing of the original estimates to remove questionable large oscillations following parachute deployment. Parachute phase atmosphere runs were then made, with these profiles being approximated by tabular input. Final results incorporated parachute drag coefficient scale factor estimates based on pressure and temperature measurements processed during the parachute phase and post-touchdown.

4. Terminal descent phase. Atmospheric variables were computed by LTARP during terminal descent by propagating the final values of the parachute phase to touchdown assuming hydrostatic equilibrium and a constant temperature lapse rate deduced from lower parachute phase and post-touchdown

temperature measurements. Because of the erratic nature of the density estimate during the parachute phase, the actual times of start of the terminal descent phase were not used. Rather, carefully selected points were chosen for both VL-1 and VL-2 several seconds back into the parachute phase, where computed density had a mean value between peaks of oscillation.

5. Pressure and temperature measurement processing. The reconstructed aeroshell and parachute phase atmospheres for both VL-1 and VL-2 were "adjusted" as a final step by processing selected measurements:

- (1) Stagnation pressure: just before mortar fire.
- (2) Pressure and temperature: just before vernier ignition.
- (3) Pressure and temperature: post-touchdown.

This yielded estimates of overall scale factor corrections to be applied to the aeroshell phase axial force coefficient table and to the parachute phase drag coefficient table which, in combination with the wind table based on a priori trim characteristics, resulted in an atmosphere that fit the measurement data at the ends of the aeroshell, parachute, and terminal descent phases. It should be noted that this procedure artificially explains, by means of fixed scale factor corrections of the aerodynamic coefficients, differences due to the combined effects of:

- (1) Errors in the reconstructed wind.
- (2) Neglect of real gas effects in generation of the aerodynamic coefficient tables.
- (3) Use of free-stream Mach number, rather than that behind the shock wave, in table lookup.

B. Terrain Profiles

The terrain profiles of Figures 88 and 89 were obtained by means of LTARP runs which compared altitude estimates of the VL-1 and VL-2 reconstructed trajectories with corresponding radar altimeter measurements. Nominal scale factors were used for the latter. Also shown on the figures are the profiles deduced from Mars topographical maps and table-input to the program as nominal.

The 1σ uncertainty associated with the VL-1 terrain height estimates varies from about 0.2 km at touchdown to 0.9 km at entry. For the VL-2 estimates corresponding uncertainties are 0.5 and 1 km.

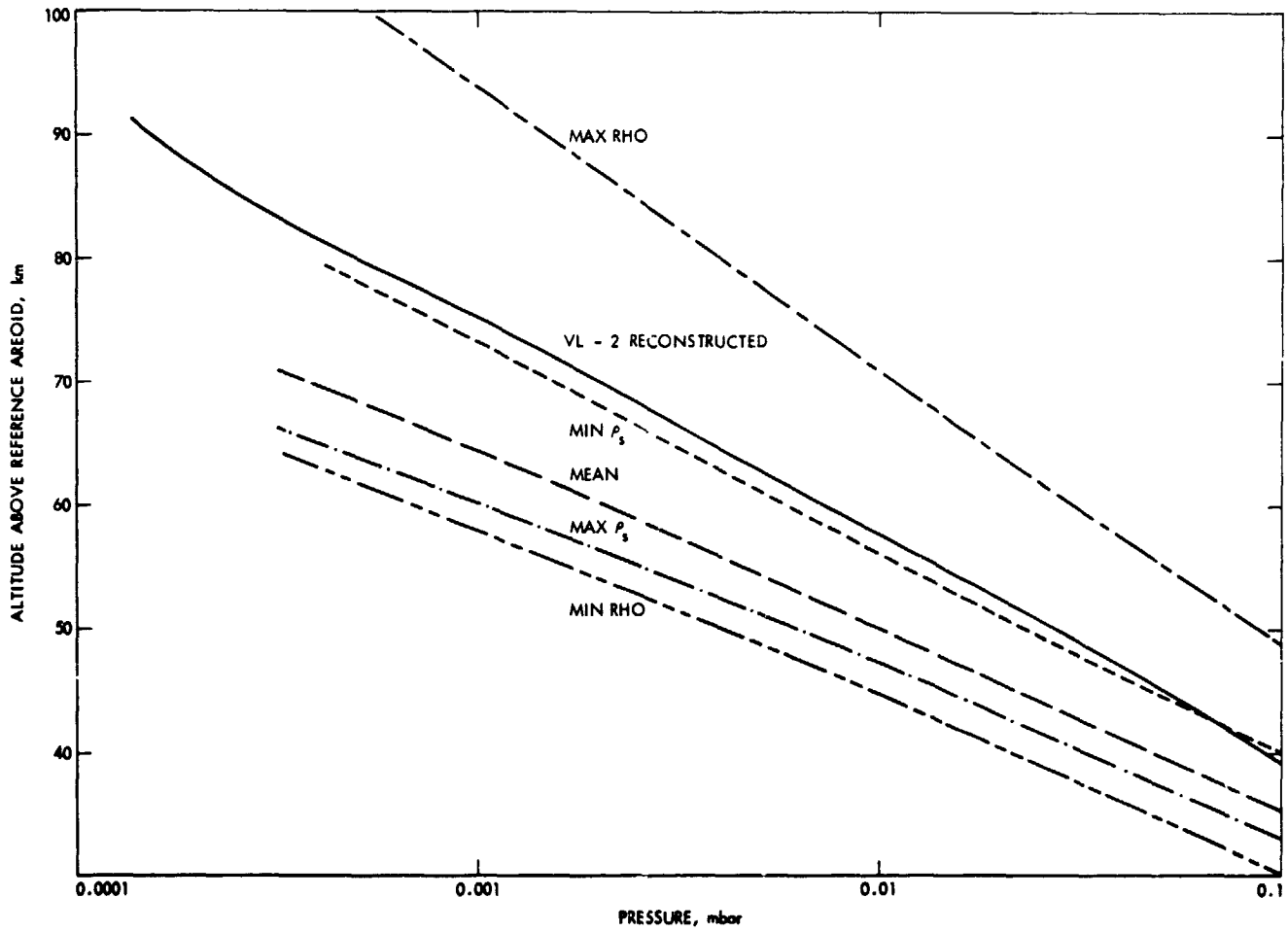


Fig. 78. VL-2 ambient pressure (< .1 mb) vs altitude

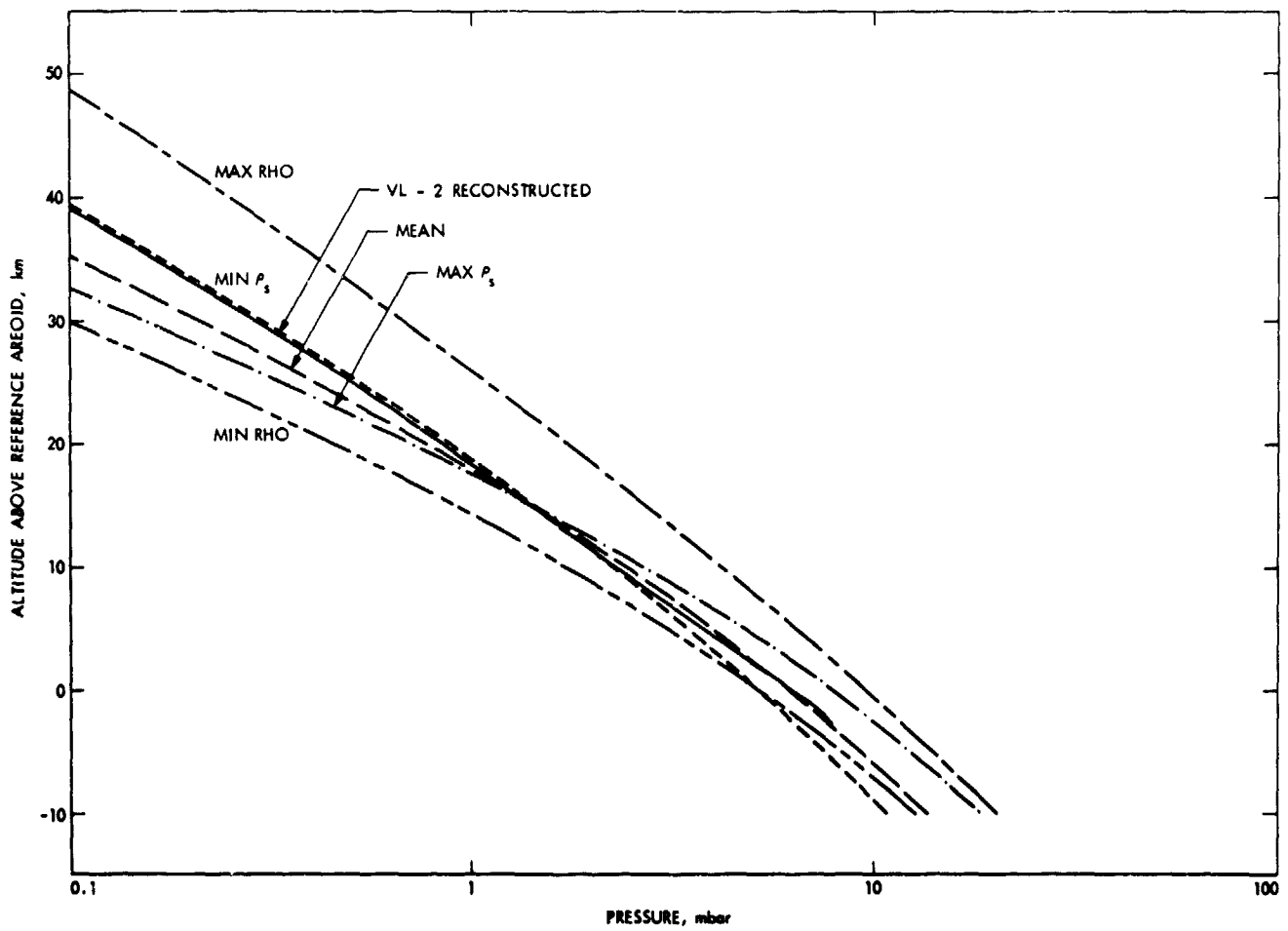


Fig. 79. VL-2 ambient pressure ($> .1$ mb) vs altitude

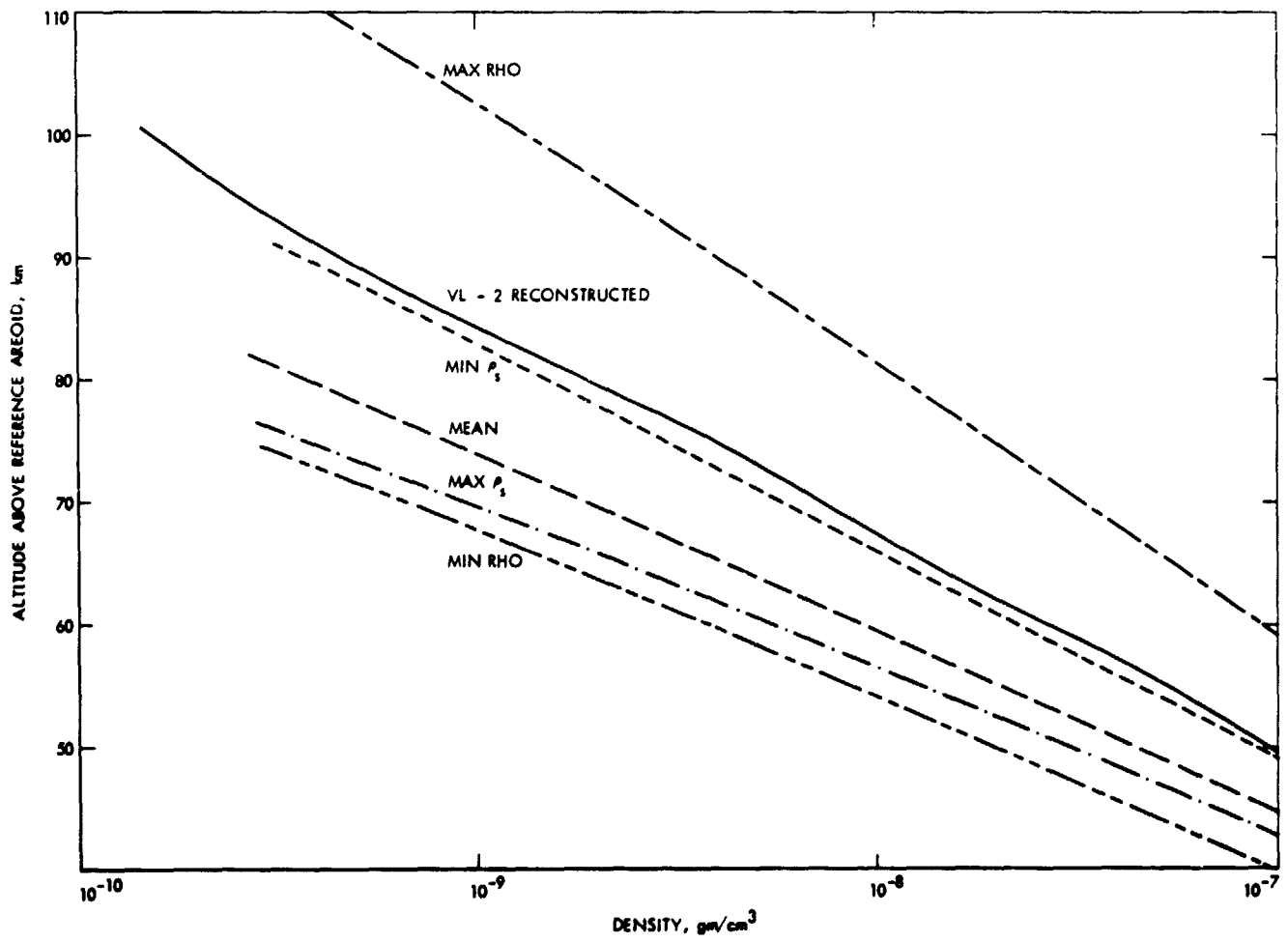


Fig. 80. VL-2 density ($< 10^{-7}$ gm/cc) vs altitude

ORIGINAL PAGE IS
OF POOR QUALITY

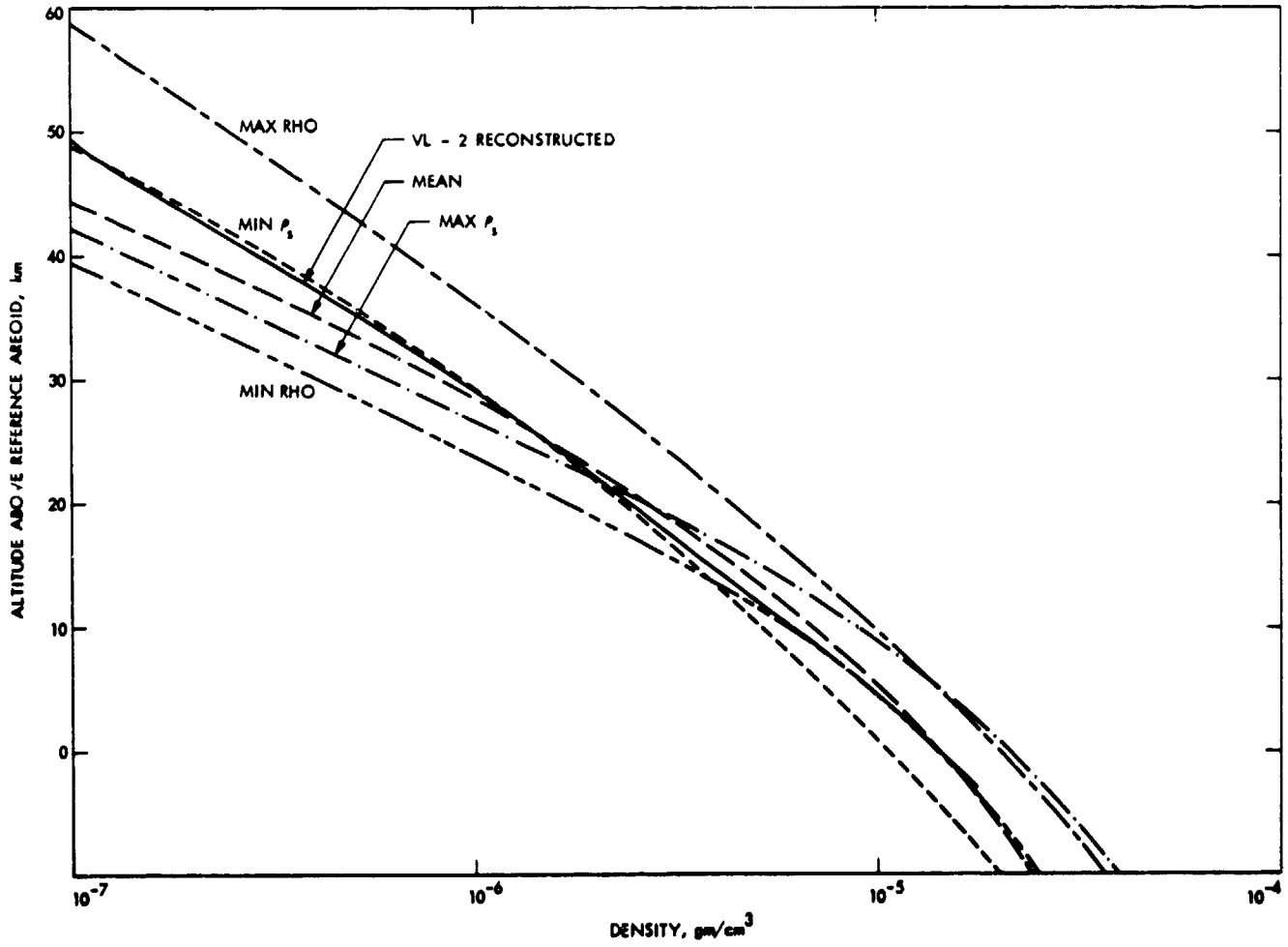


Fig. 81. VL-2 density (> 10⁻⁷ gm/cc) vs altitude

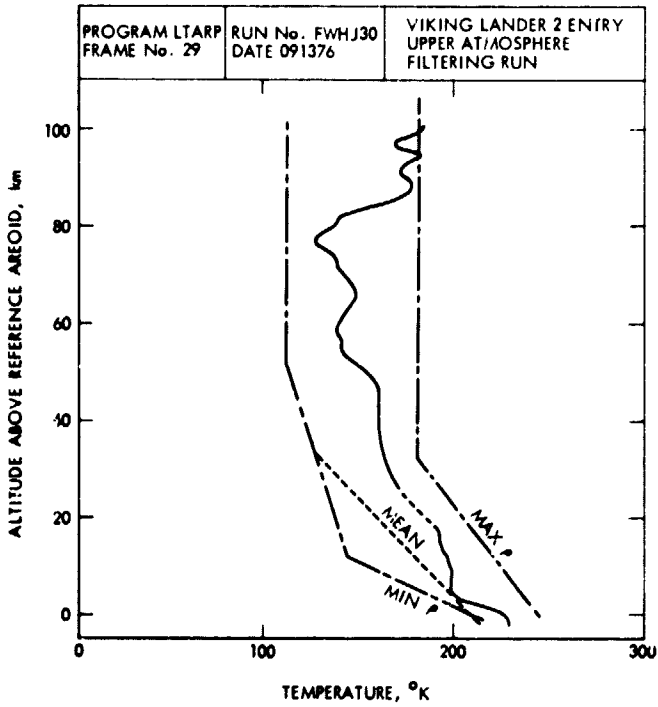


Fig. 82. VL-2 altitude above reference areoid vs temperature

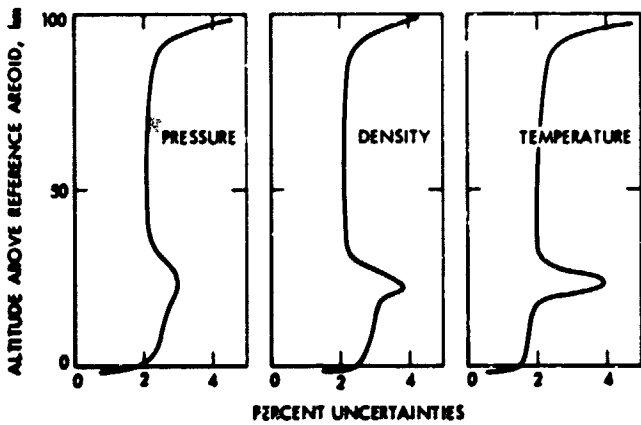


Fig. 83. Atmosphere estimation uncertainties (1σ)

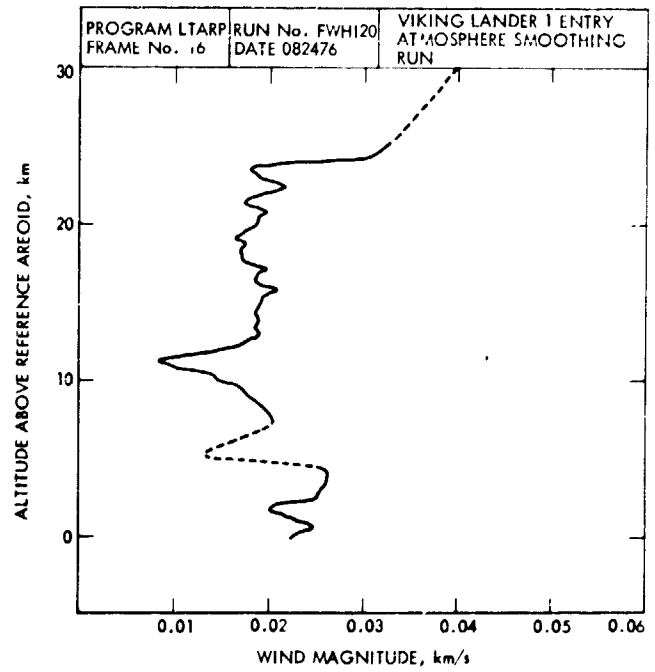


Fig. 84. VL-1 altitude above reference areoid vs wind magnitude

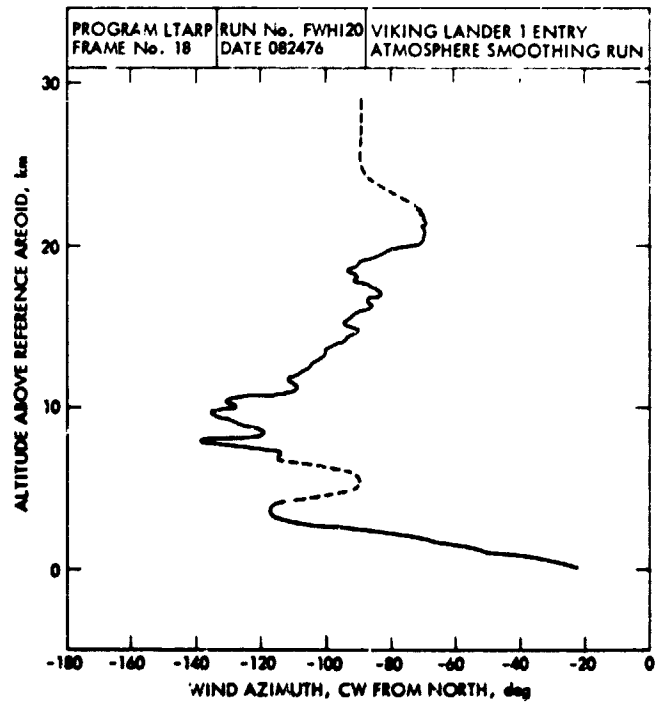


Fig. 85. VL-1 altitude above reference areoid vs wind azimuth

ORIGINAL PAGE IS
OF POOR QUALITY

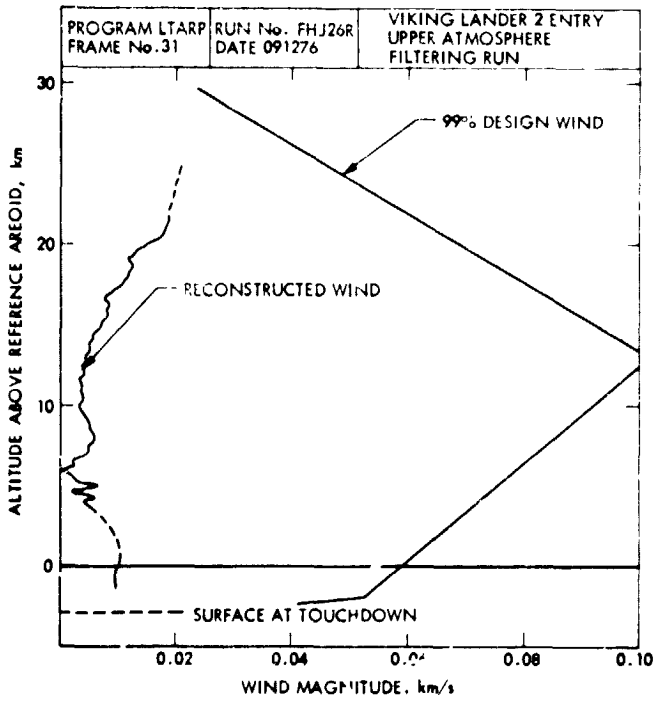


Fig. 86. VL-2 altitude above reference surface vs wind magnitude

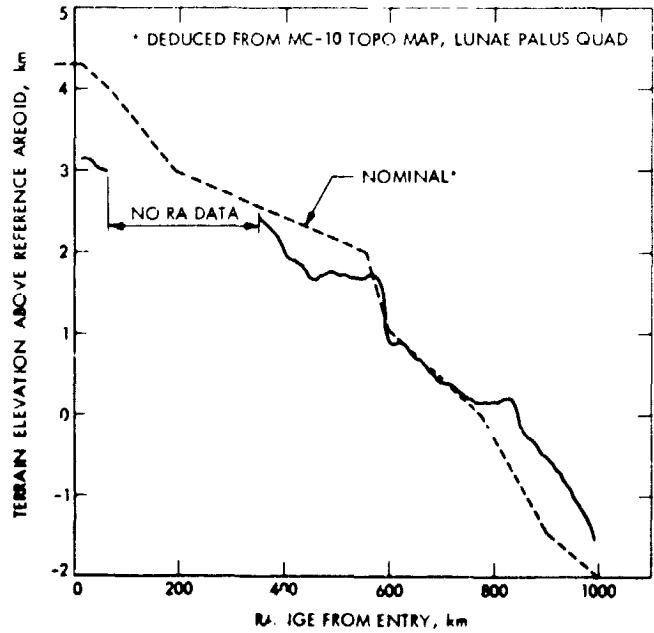


Fig. 88. VL-1 terrain height profile

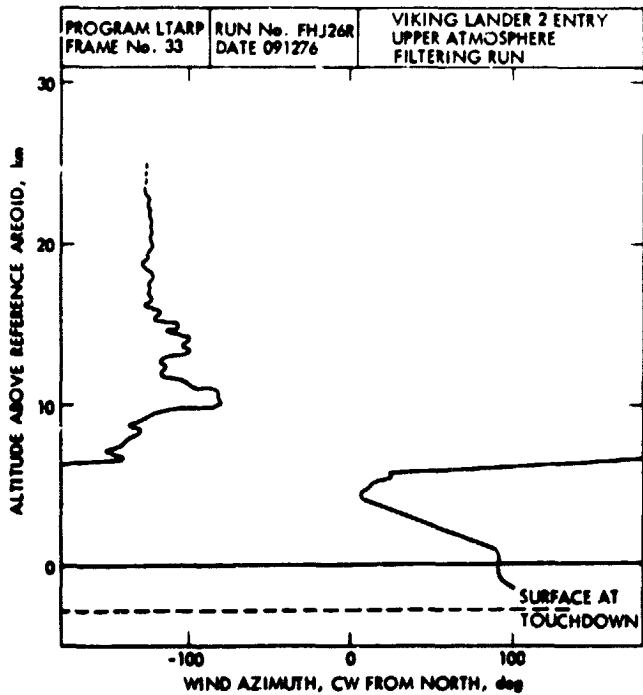


Fig. 87. VL-2 altitude above reference surface vs wind azimuth

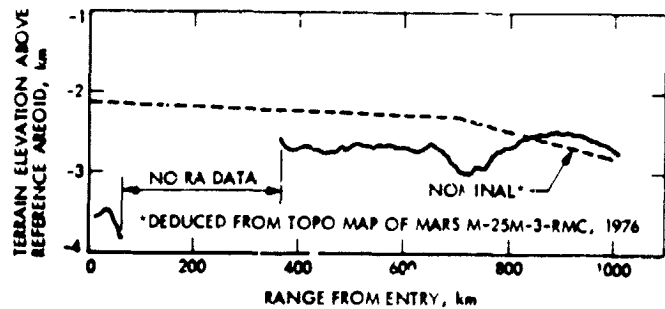


Fig. 89. VL-2 terrain height profile

VIII. Postland Relay Link

The discussion of the VL/VO postland relay links will be divided into two parts. The first part discusses the procedures and requirements which were used in flight operations for the various relay link phases. Also discussed in this section is the process of defining the relay transmission start times in the Initial Computer Load (ICL). The second part treats the actual relay link performance history from Sol 1 to the end of the primary mission for both landers.

A. Procedures, Requirements, and ICL Definition

To protect against failure to achieve a command link with the VL after touchdown, it was necessary that a preprogrammed mission be defined (and loaded into the VL GCSC prior to separation) to enable the landed VL to function and collect science data until a link could be established. The set of commands corresponding to this preprogrammed mission constituted the ICL. A subset of the ICL was the set of preprogrammed VL relay link transmission start times. The procedures and requirements relating to the preprogrammed transmission start times were fundamentally different from those employed during the postland primary mission. Preprogrammed mission relay link planning acknowledged increased uncertainty in predicting relay link performance and timing because of a lack of knowledge of VL landed position and attitude and of communications subsystem performance. Earlier Monte Carlo studies showed that 17.1-min link durations at bit error rates less than or equal to 3×10^{-3} could be achieved with 99% probability during this mission phase for VL-1; 17.2-minute durations at bit error rates less than or equal to 5×10^{-4} for VL-2. These durations reflected dispersions in VL landed position and attitude, VO orbit uncertainties, and communications systems performance at the QSS of adverse tolerances. Lower bit error rates were predicted for VL-2 links because of the more favorable relay geometry between VL-2 and VO-2.

Mission Planning responded to this situation by recording only 17.1 minutes of playback (two tape recorder tracks) and by transmitting this data in the "loop mode" such that the 17.1 minutes of data would be transmitted twice to account for start time uncertainties. This ensured that no data would be lost in the event that the relay performance window shifted as a result of the actual landed position and attitude. In defining the relay transmission start times in the ICL, the LFPAT positioned the middle of the playback data structure (end of first loop, beginning of second loop) defined by Mission Planning at the middle of the predicted QSS adverse link. This midpoint was based on bit error rates of 3×10^{-3} and 5×10^{-4} for VL-1 and VL-2, respectively. The final start times corresponding to this positioning of the recorded data were uplinked at SEP-39 hours.

Figure 90 shows the final VL-1 ICL update in relation to the original onboard ICL (which assumed a landing at the A1 site on July 4) and the July 10 baseline ICL (which assumed a landing at the A1WNW site on July 20). The total sequence of events stored onboard the VL was structured so that the relay playback sequence could be shifted by up to ± 40 minutes in Lander Local Time without introducing conflicts with other scheduled events. A station-keeping trim (SKT-2) was assumed in the design of the final ICL update to avoid violating this ± 40 -minute constraint. Since a communication link with VL-1 was established, the ICL beyond Sol 12 was not executed. However, as is described in the *Maneuver Analysis* Chapter, SKT-2 was redesigned to accomplish another purpose.

Figure 91 shows the final VL-2 ICL update in relation to the original onboard ICL (which assumed a landing at the original B1 site on September 4) and a preliminary ICL for the final site.

After touchdown the actual VL landed attitude and latitude were extracted from the GCSC octal memory readout. In addition, estimates of the VL latitude, longitude, and radius were obtained from the SATOD team after a few days of VL tracking. All this information, along with actual observed relay link performance, was used to reduce the uncertainty in predicting relay link performance on future Sols. Because of the long lead time (approximately 20 days) in the Long Range Planning cycle, where the relay link playback durations were set, the reduced uncertainty in relay geometry and performance was not fully utilized in the onboard VL data acquisition and playback sequences until Sol 19 for VL-1 and Sol 18 for VL-2.

B. Actual VL Relay Link Performance History

1. **VL-1/VO-1 relay links.** All VL-1 relay links were with VO-1. The VL-1 relay links were complicated by VL-1 power mode anomalies. Originally designed to transmit at 30 watts during relay links, VL-1 inexplicably transmitted in the 1-watt mode on Sols 2 and 3. This precipitated a redesign of SKT-2 on Sol 12 to provide favorable geometry in case the 1-watt-mode anomaly recurred. However, this anomaly did not reappear after Sol 3. Transmissions continued in the 30-watt mode for Sols 4 through 39. The power mode was intentionally reduced to 10 watts for the final links on Sols 40 through 43 because of observed VL transmitter power degradation on earlier links.

Relay link start times after Sol 11 utilized the CBE of actual VL-1 landed attitude and position. The landed position (LAT, LONG) was tabulated earlier in Table 9. The following

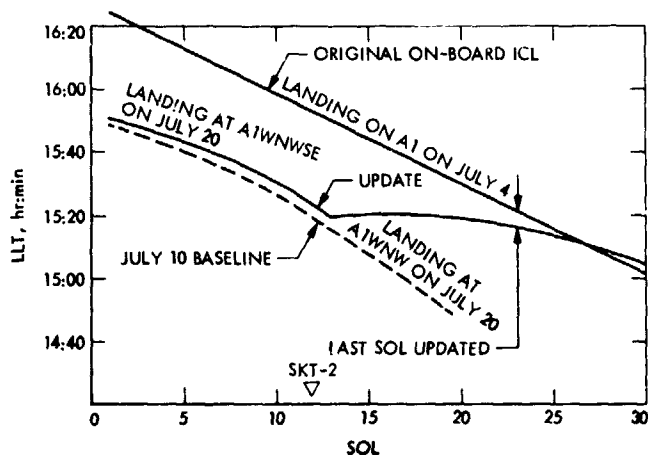


Fig. 90. VL-1 transmission start times

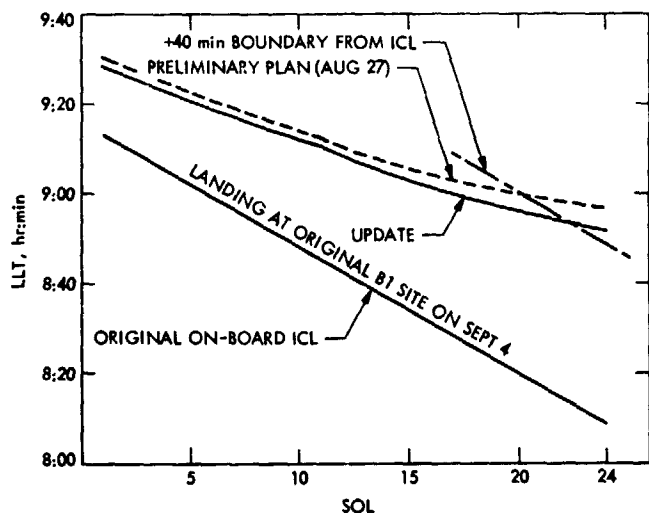


Fig. 91. VL-2 transmission start times

reconstructed VL-1 landed orientation was obtained from the postland memory readout: a landing slope magnitude of 2.99 deg, a landing site downslope azimuth of 285.18 deg, and a leg 1 azimuth of 321.91 deg. For all VL-1/VO-1 links, VO-1 was locked on Canopus.

The observed VL-1/VO-1 relay link performance was generally close to the predicted nominal performance. Figure 92 shows a typical preprogrammed VL-1/VO-1 (Sol 9) relay link. The received signal power (dBm) is plotted as a function of Earth received time (ERT). Also shown on the plot are the threshold power levels for bit error rates of 2×10^{-2} and 5×10^{-4} . These are the bit error levels crucial to real-time imaging (RTI) and recorded data playback (P/B), respectively. At the bottom of the plot is shown the actual link utilization,

i.e., the relative positioning of RTI and, in this case, four tracks of P/B in the loop mode.

Examples of typical relay link performance during other phases of the VL-1 landed mission are shown in subsequent figures. Figure 93 shows an example of the anomalous 1-watt-mode transmissions that occurred on Sols 2 and 3 of the preprogrammed mission. An example of the standard 30-watt relay link performance during the primary mission phase is shown in Figure 94. Finally, an example of the 10-W relay link performance during the final 4 Sols of the primary mission is shown in Figure 95.

Typical look vector traces through the VL-1 and VO-1 antenna patterns can be seen in Figs. 96 and 97, respectively. In these antenna pattern traces, rise and set refer to the predicted start and stop of the 2×10^{-2} BER links.

2. VL-2/VO-2 relay links. The initial relay links with VL-2 were, of course, with VO-2. These links were maintained through Sol 26, at which time the VO-2 orbit plane change maneuver was performed. Relay link start times after Sol 11 utilized the CBE of actual VL-2 landed attitude and position. The landed position (LAT, LONG) was tabulated earlier in Table 9. The reconstructed VL-2 landed orientation was obtained from the postland GCSC memory readout: a landing slope magnitude of 8.2 deg, a landing site down slope azimuth of 277.7 deg, and a leg 1 azimuth of 209.1 deg. Unlike certain VL-1 relay links, VL-2 always transmitted in the 30-W power mode. For VL-2/VO-2 links, VO-2 was locked on Vega.

The observed VL-2/VO-2 relay link performance was very close to the predicted nominal performance. Figure 98 shows a typical VL-2/VO-2 (Sol 5) relay link. As can be seen in Fig. 99, VO-2 passes directly overhead so that the VL-2/VO-2 look vector traced through a good region of the VL-2 antenna pattern. In this figure are shown the look vector traces for Sols 1 and 26 to show how the antenna trace drifted from the first to the last VL-2/VO-2 link. The prelanding predict of the Sol 1 trace was about midway between the actual Sol 1 and Sol 26 traces. Figure 100 shows the corresponding look vector traces through the VO-2 antenna pattern. In these antenna pattern traces, rise and set refer to the predicted start and stop of the 2×10^{-2} BER links.

Figure 101 presents a plot of a typical VL-2/VO-2 relay link following the completion of the preprogrammed mission. At the bottom of the plot is shown how the link was utilized during this phase of the mission, i.e., three tracks of recorded data transmitted in the standard mode (not the loop mode). Note that additional RTI was scheduled at the tail end of the link in order to take into account the unexpected beneficial

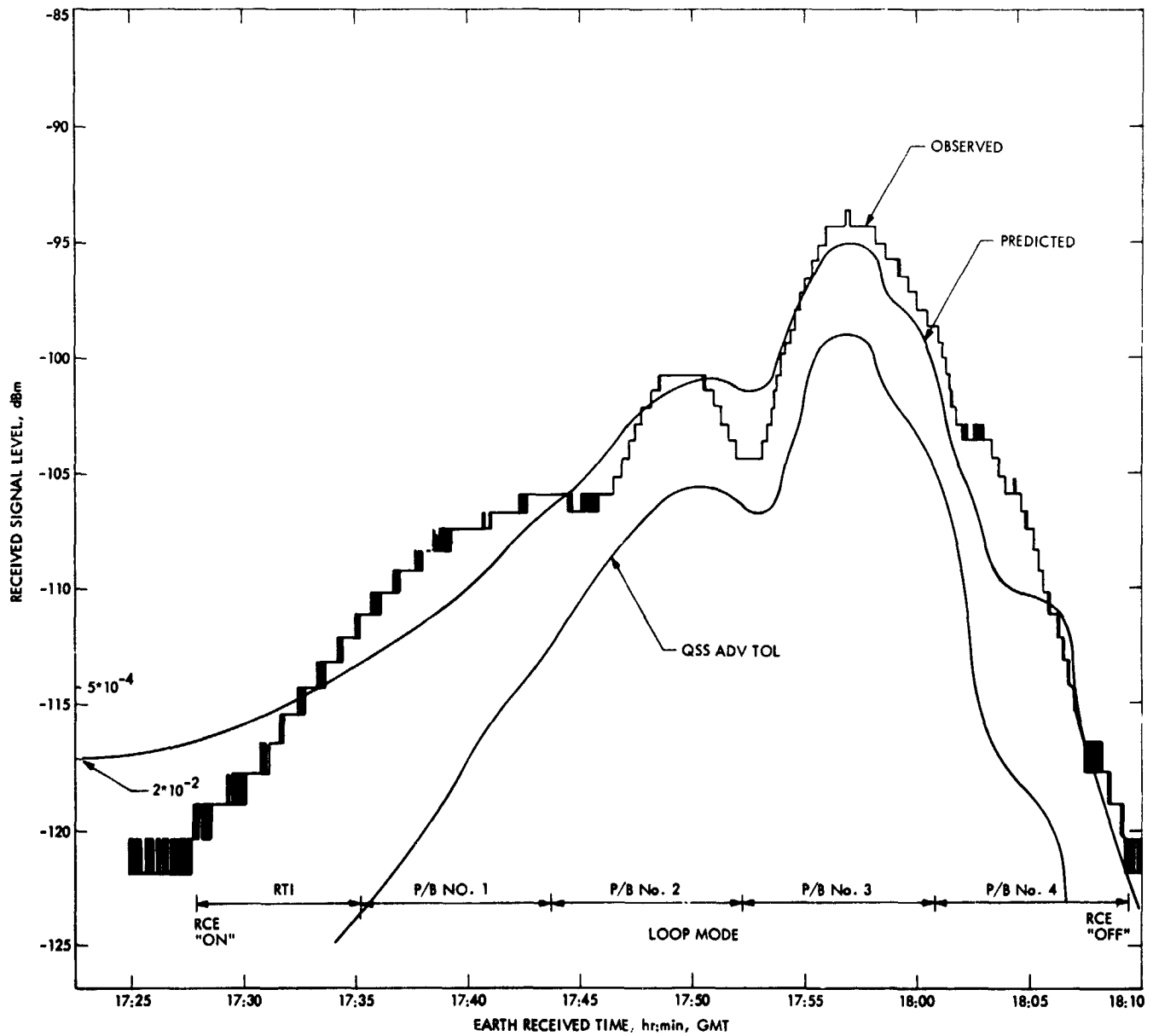


Fig. 92. VL-1/VO-1 relay link performance (Sol 9/ICL)

ORIGINAL PAGE IS
OF POOR QUALITY

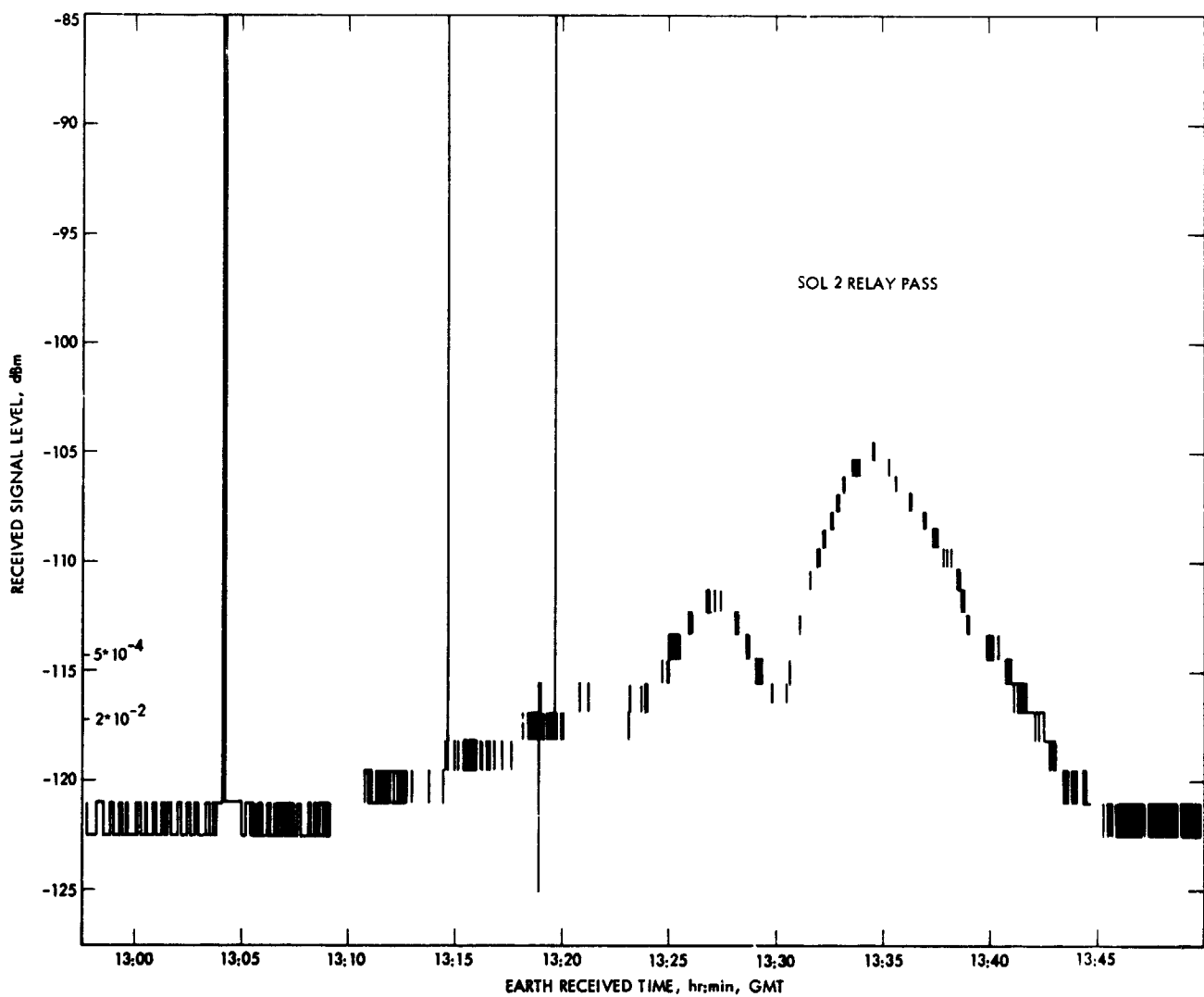


Fig. 93. VL-1/VO-1 1-W mode relay link performance (Sol 2)

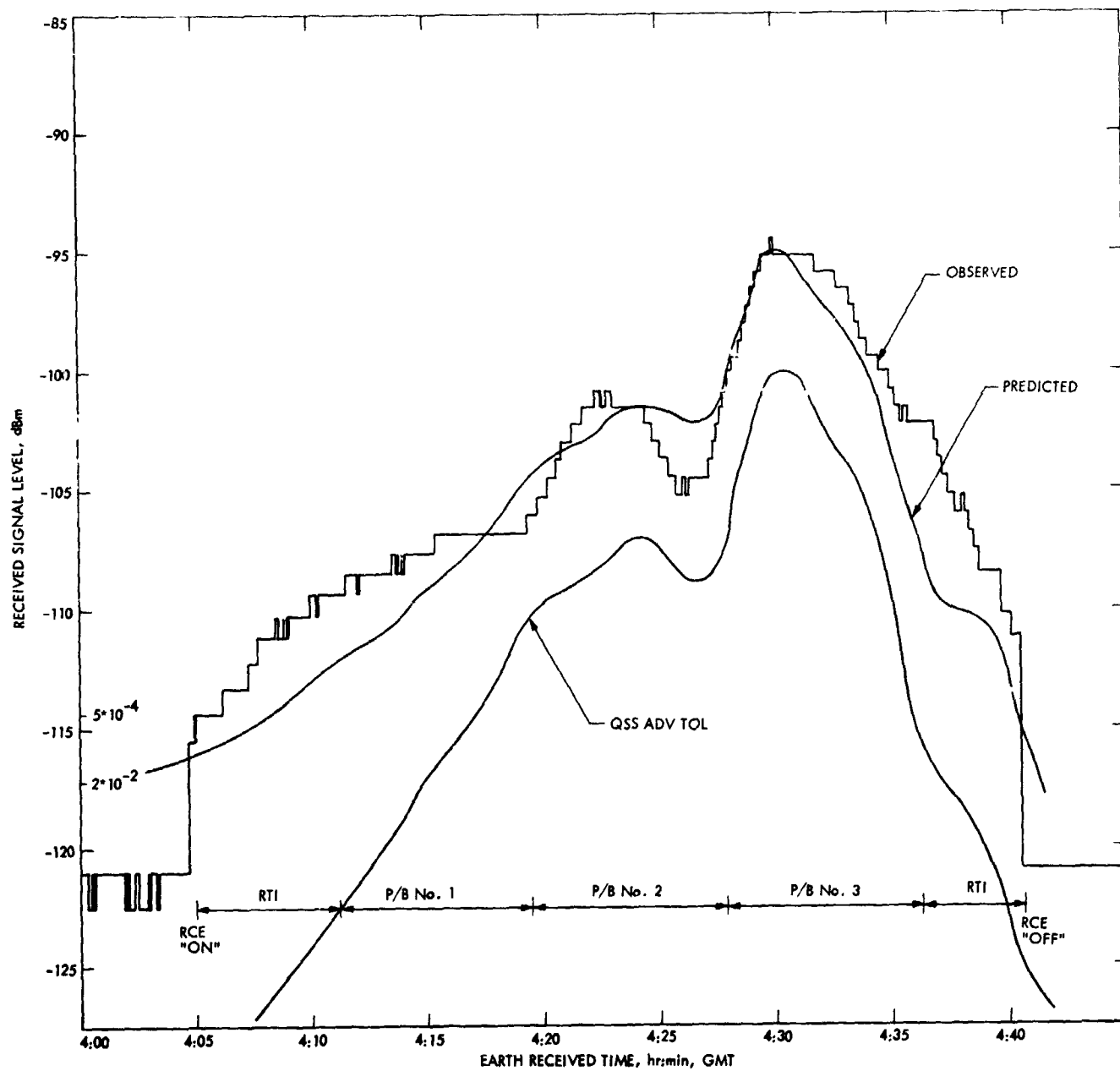


Fig. 94. VL-1/VO-1 relay link performance (Sol 28)

ORIGINAL PAGE IS
OF POOR QUALITY

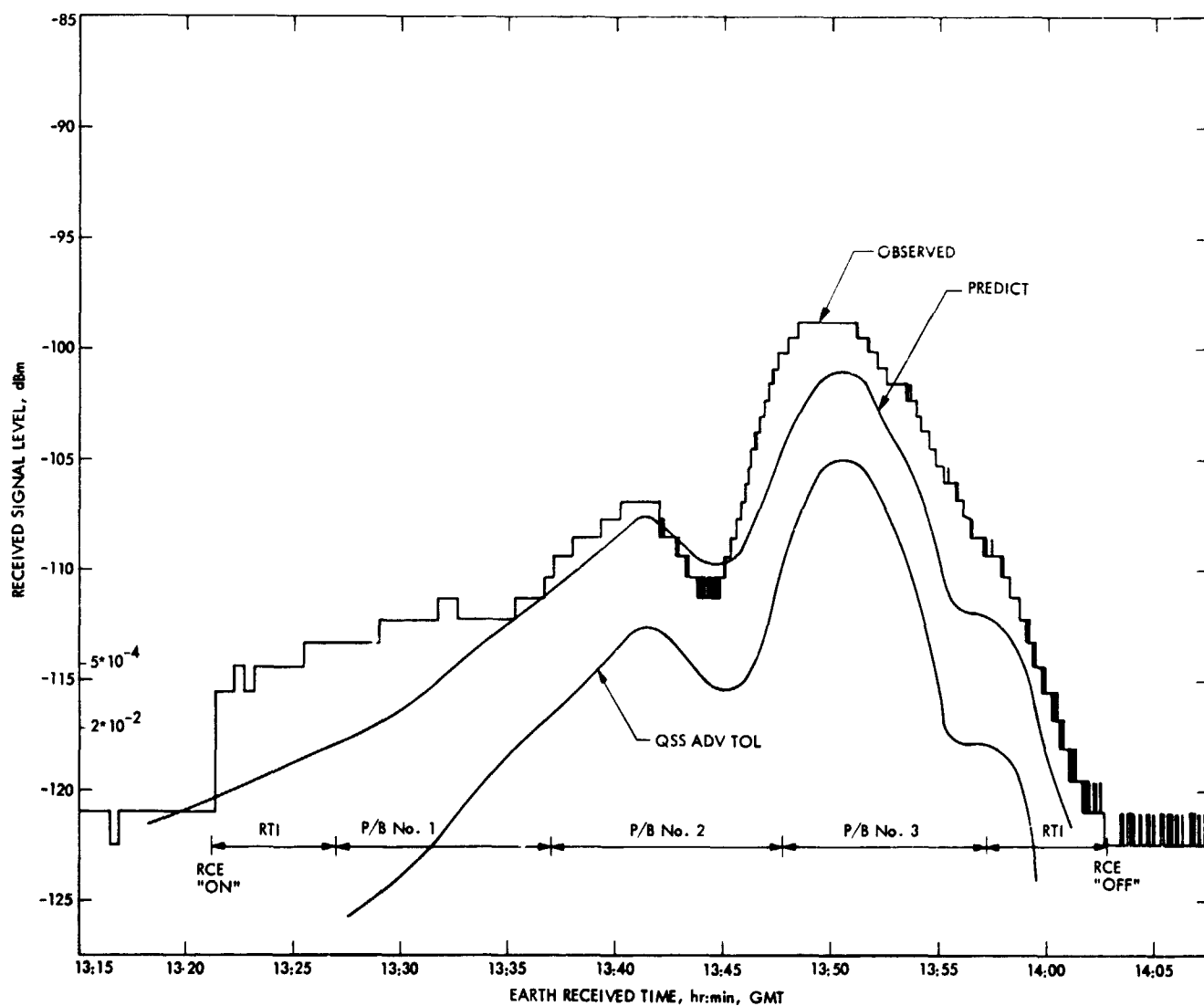


Fig. 95. VL-1/VO-1 10-W relay link performance (Sol 42)

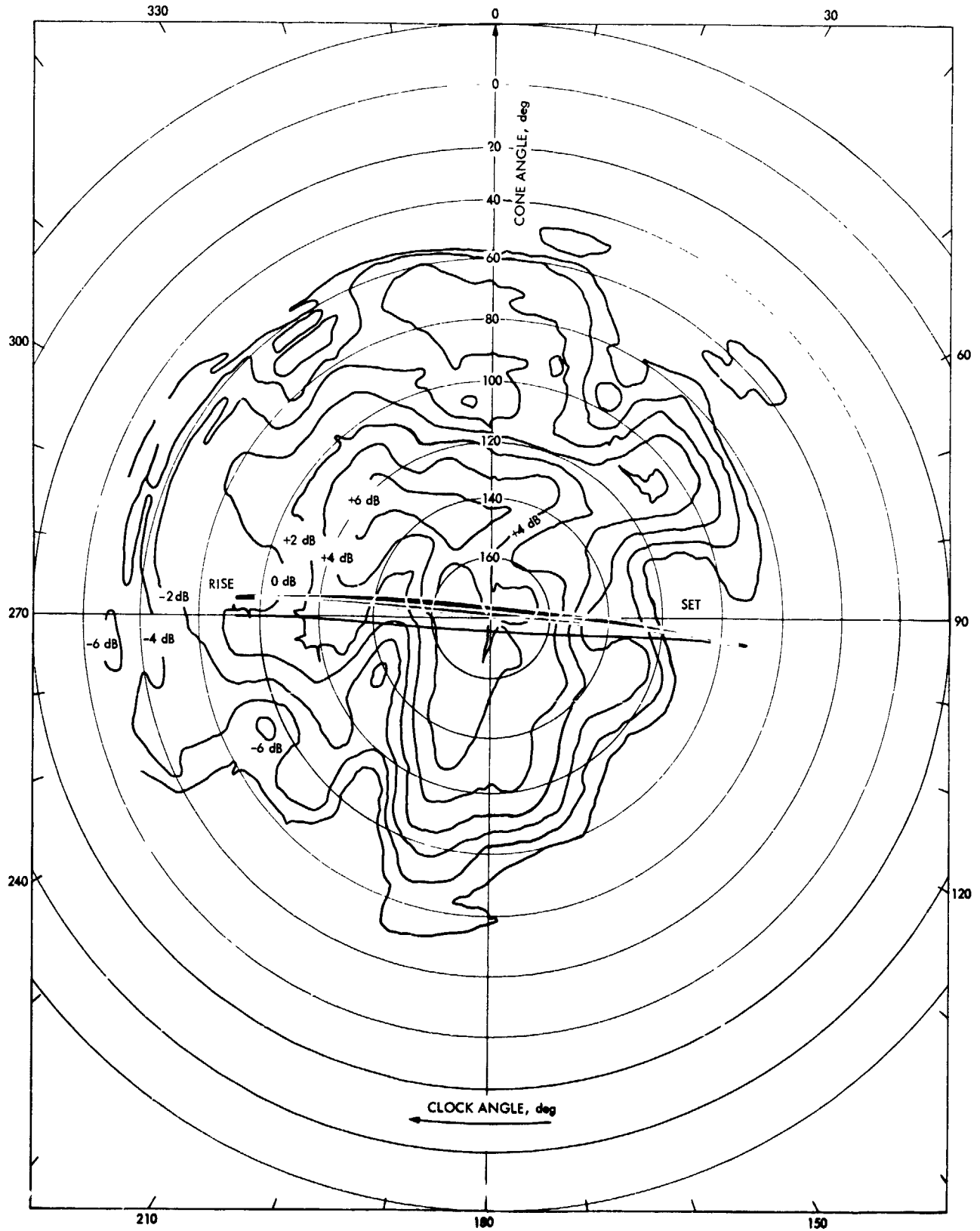


Fig. 96. VL-1 antenna pattern traces

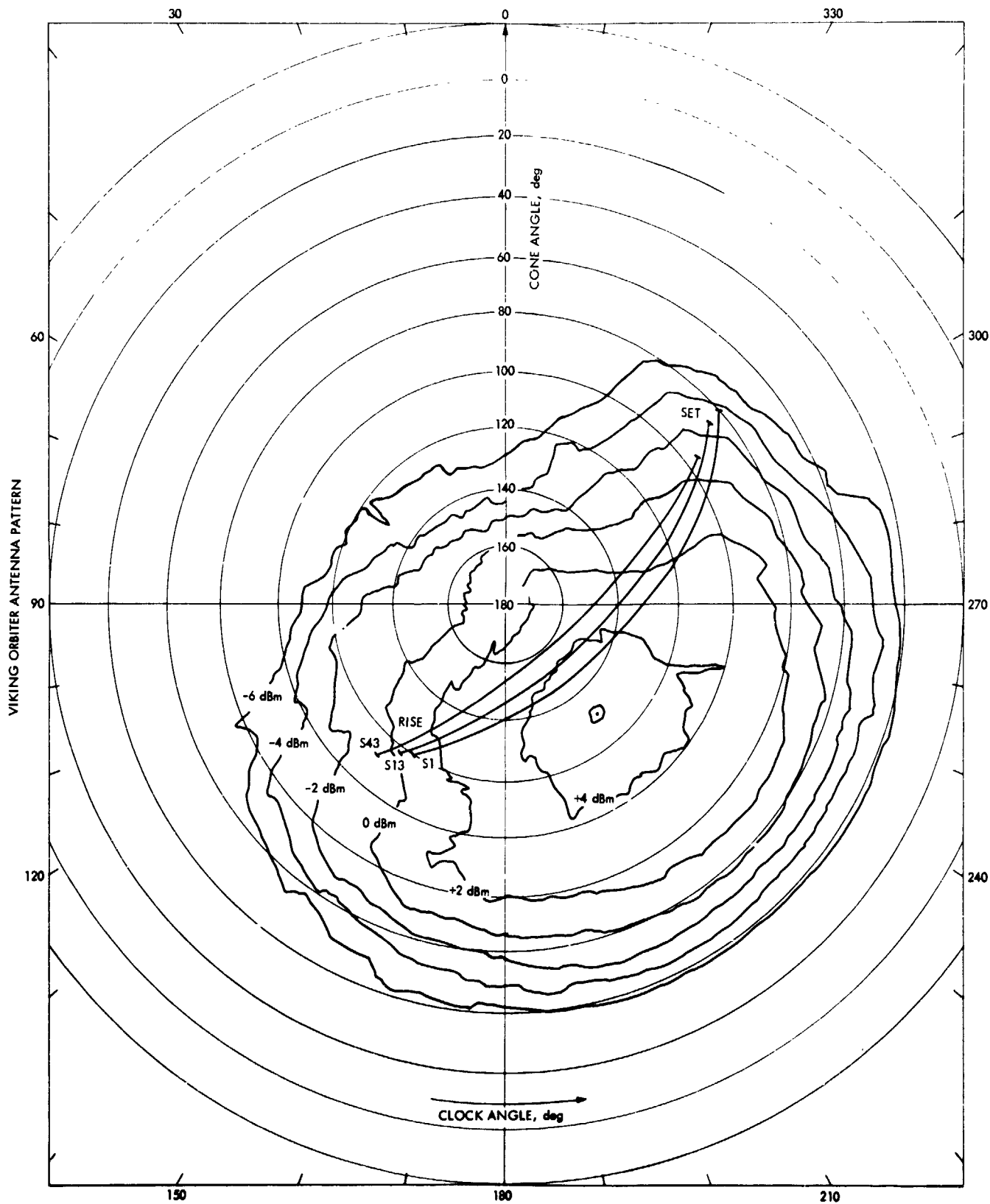


Fig. 97. VO-1 antenna pattern traces

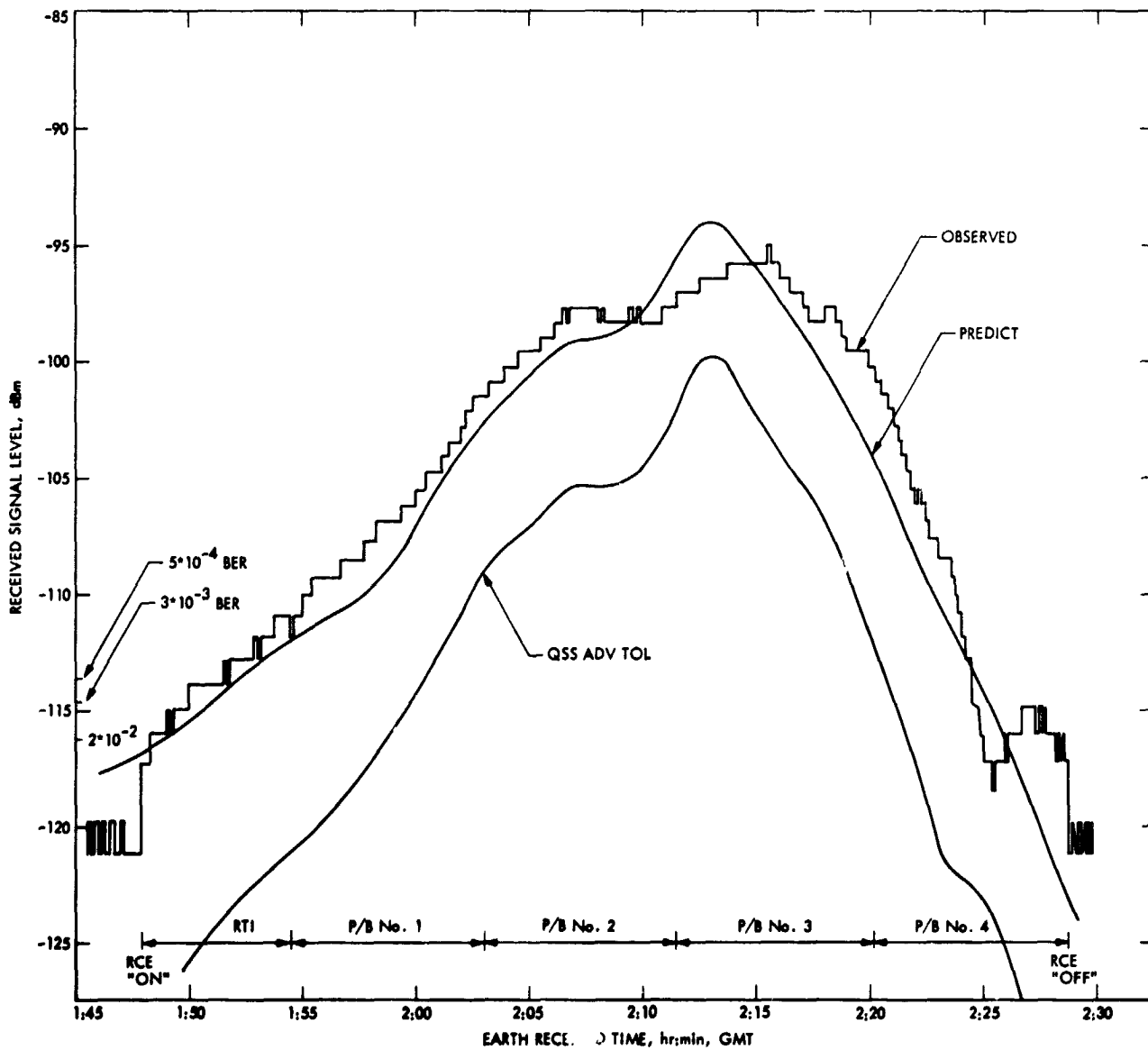


Fig. 98. VL-2/VO-2 relay link performance (Sol 5/ICL)

ORIGINAL PAGE IS
OF POOR QUALITY

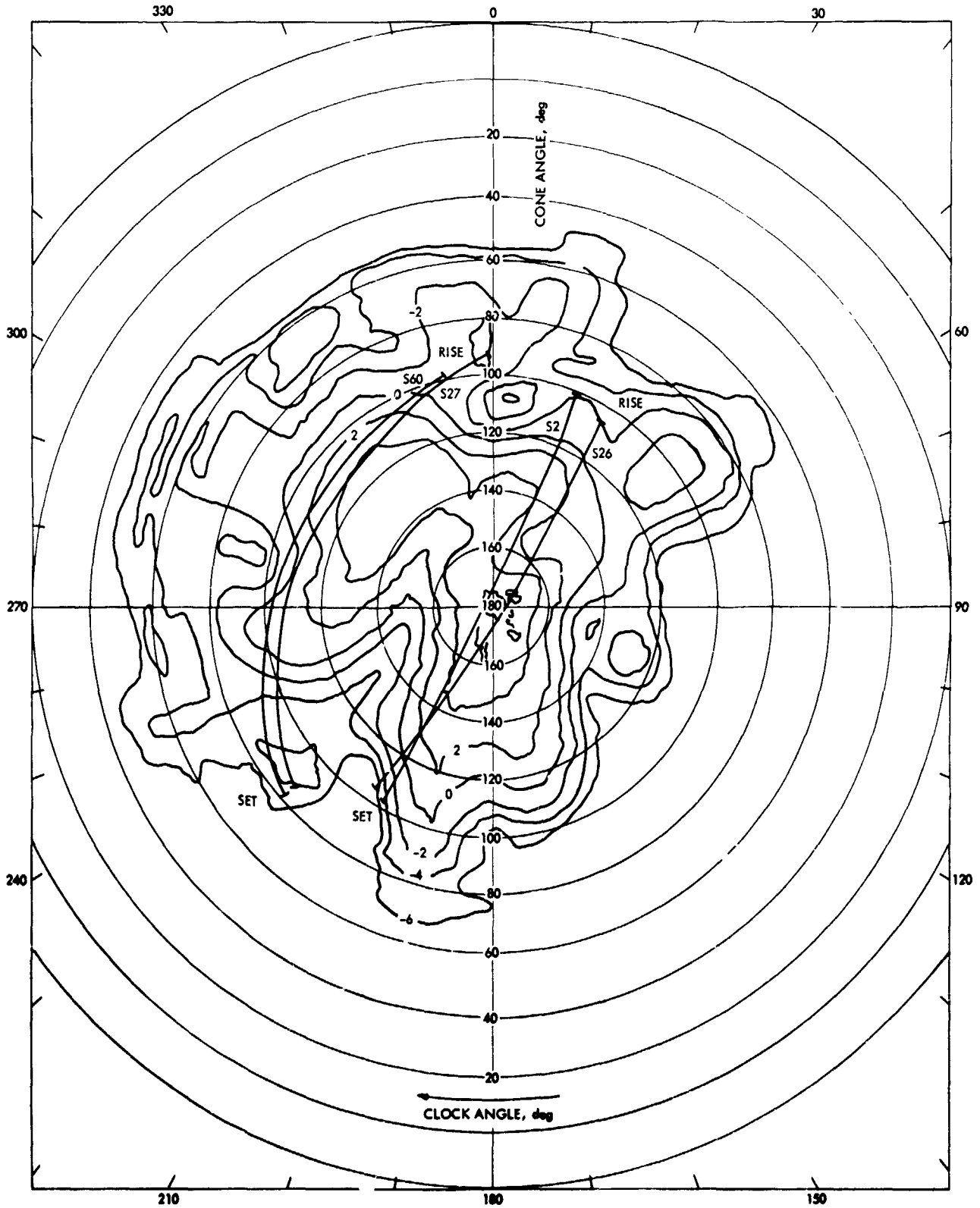


Fig. 99. VL-2 antenna pattern traces for VO-2 and VO-1 relay links

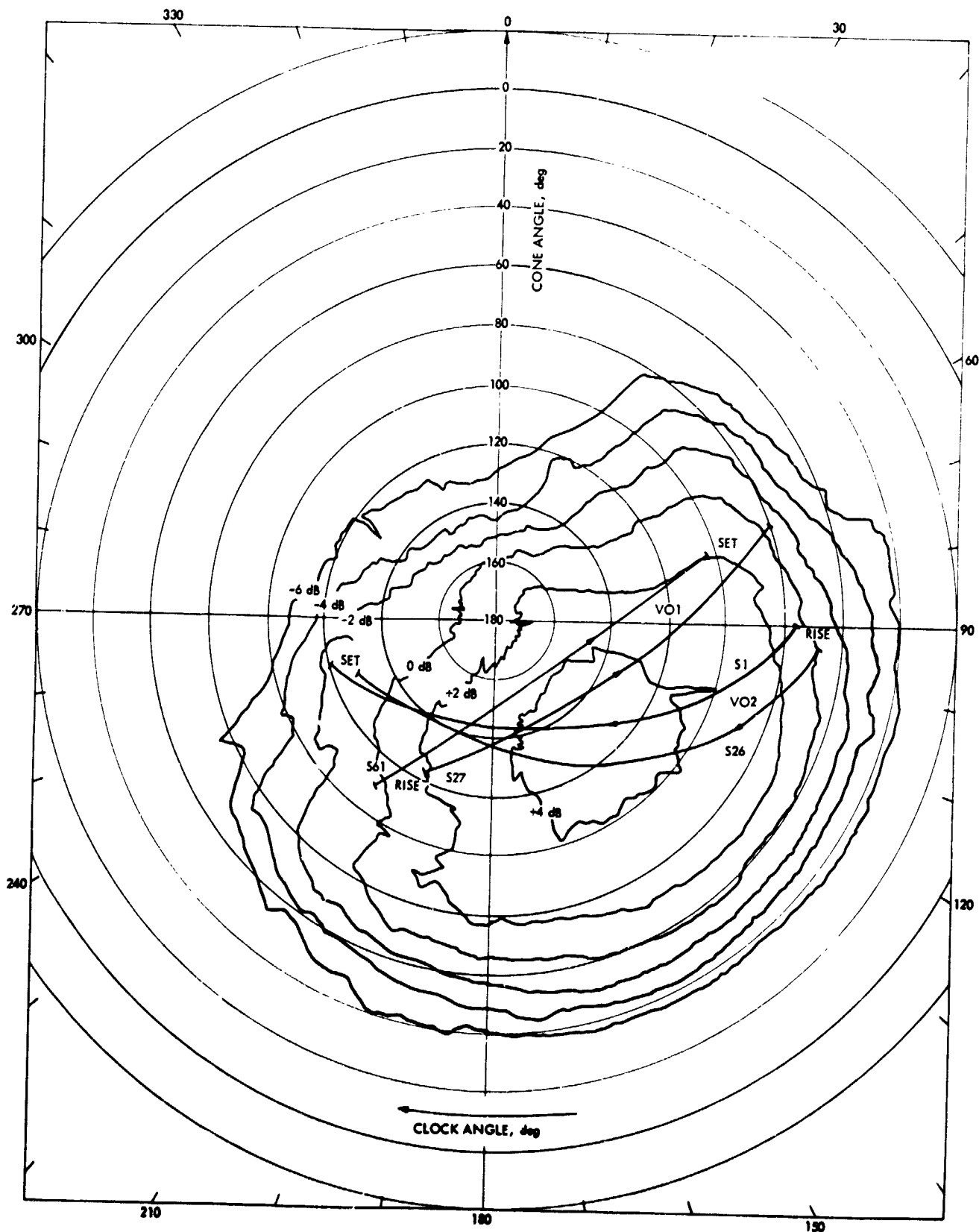


Fig. 100. VO antenna pattern traces for VL-2/VO-2 and VL-2/VO-1 relay links

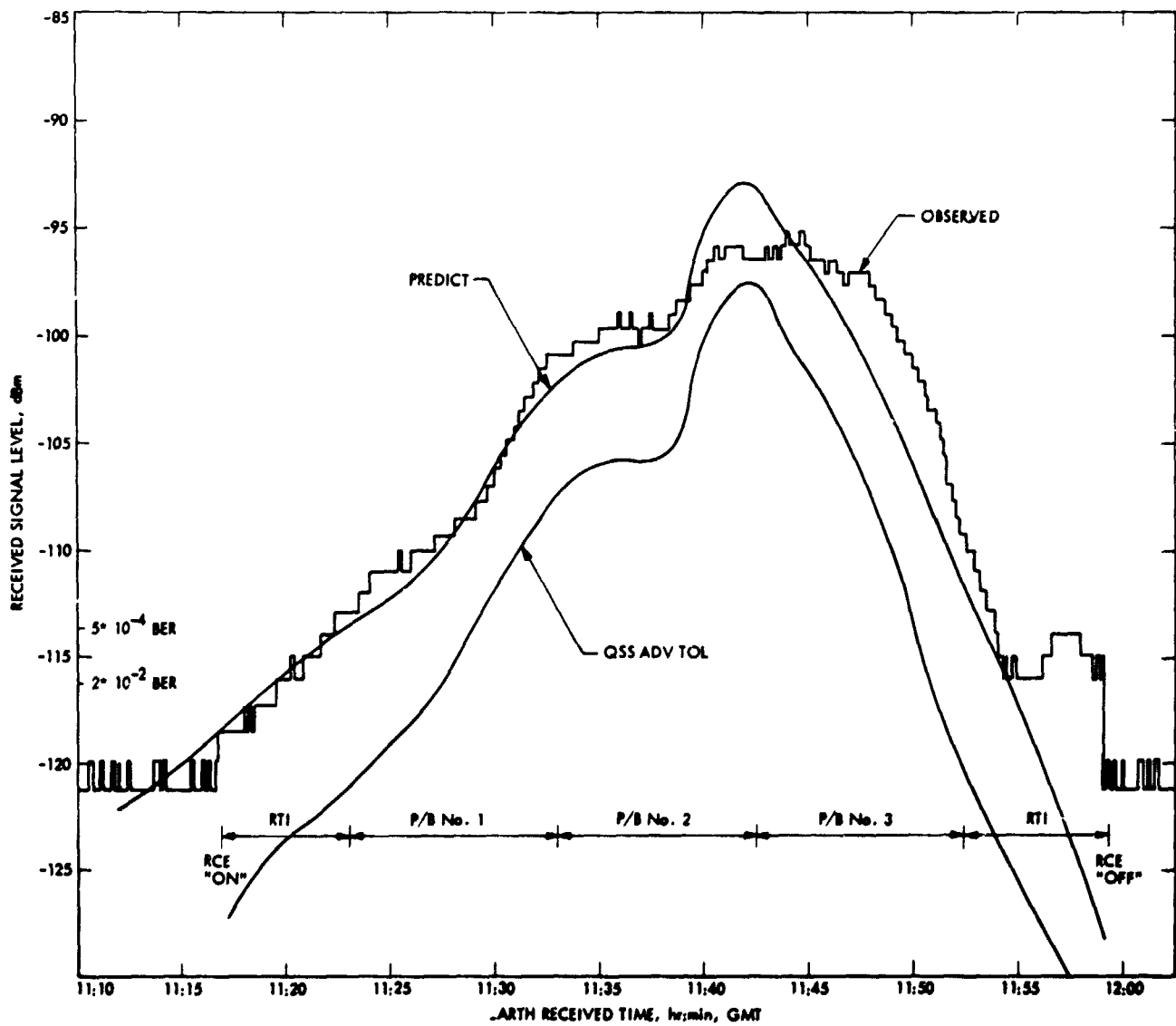


Fig. 101. VL-2/VO-2 relay link performance (Sol 20)

multipath effect on link performance at the tail end of the link.

3. VL-2/VO-1 relay links. On VL-2 Sol 20 VO-1 performed a maneuver to resynch it over VL-2. Test links between VL-2 and VO-1 were conducted on Sols 21, 23, and 25 to verify that VL-2/VO-1 links were acceptable before terminating VL-2/VO-2 links. The test links were acceptable, although they did show significant multipath effects. From Sol 27 to Sol 61 (end of primary mission) all VL-2 relay links

were handled by VO-1. All these links were characterized by low elevation angles of VO-1 with respect to VL-2, which is in direct contrast to the overhead links with VO-2 (Fig. 99). The traces through the VO-1 antenna pattern are shown in Fig. 100. The observed and predicted received signal power for a typical VL-2/VO-1 relay link (Sol 45) is shown in Fig. 102. Unlike VL-2/VO-2 relay link utilization, for VL-2/VO-1 the data playback was shifted earlier in time to take advantage of the beneficial multipath effect at link rise. For all VL-2/VO-1 links, VO-1 was locked on Canopus.

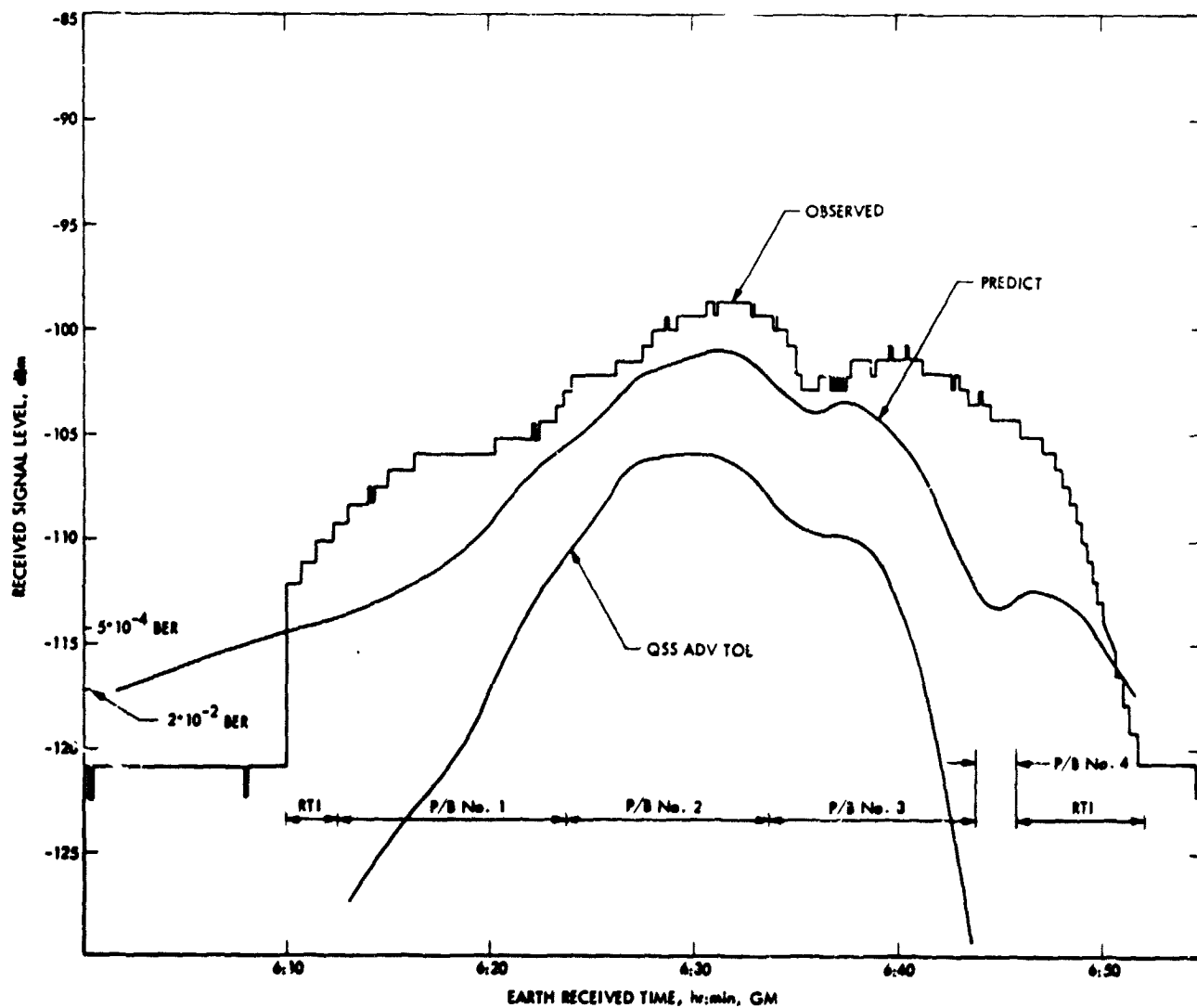


Fig. 102. VL-2/VO-1 relay link performance (Sol 45)

References

1. Viking 1975 Navigation Plan, 612-32, Jet Propulsion Laboratory, Pasadena, Calif., May 1975 (an internal document).
2. Viking '75 Project Aerodynamics Data Book, TR-3709014, prepared for JPL under Contract NAS1-900 by Martin Marietta Corp., Dec. 1974 (an internal document).
3. Hopper, F., "Trajectory Atmosphere and Wind Reconstruction from Viking Measurements," AAS Paper No. 75-068, July 28, 1975.